European Commission

9th International Conference on the Chemistry and Physics of the Actinide Elements

21-26 July 2013, Karlsruhe, Germany
Abstract Booklet

Editor: Roberto Caciuffo

2013

EUR 26163 EN

Joint Research Centre

As the Commission's in-house science service, the Joint Research Centre's mission is to provide EU policies with independent, evidence-based scientific and technical support throughout the whole policy cycle. Working in close cooperation with policy Directorates-General, the JRC addresses key societal challenges while stimulating innovation through developing new methods, tools and standards, and sharing its know-how with the Member States, the scientific community and international partners.

The mission of ITU is to provide the scientific foundation for the protection of the European citizen against risks associated with the handling and storage of highly radioactive material. JRC-ITU's prime objectives are to serve as a reference centre for the fundamental properties of nuclear materials, to contribute towards effective safety and safeguards systems for the nuclear fuel cycle, to enhance nuclear security and to study technological and medical applications of radionuclides.

European Commission
Joint Research Centre
Institute for Transuranium Elements

Contact information
European Commission – Joint Research Centre (JRC) – Institute for Transuranium Elements (ITU) – Unit Actinide Research
D-76125 Karlsruhe, P. O. Box 2340, Germany
E-mail: jrc-itu-info@ec.europa.eu
Tel.: (+49-7247)951-382
Fax: (+49-7247)951-590

http://itu.jrc.ec.europa.eu/
http://www.jrc.ec.europa.eu/

EUR 26163 EN
ISBN 978-92-79-33192-3 (online)
Catalogue Number LC-NA-26163-EN-N
JRC84465
doi:10.2789/16401

Publications Office of the European Union, Luxembourg

This publication was compiled and edited by Roberto Caciuffo.

9th International Conference on the Chemistry and Physics of the Actinide Elements

ACTINIDES 2013

21 – 26 July 2013
Karlsruhe, Germany

P R O G R A M

International Scientific Advisory Committee

Manuel Leite de ALMEIDA	ITN, Portugal
Polly L. ARNOLD	University of Edinburgh, UK
Roberto CACIUFFO	EC-JRC-ITU, Germany
Melissa A. DENECKE	KIT, INE, Germany
Yoshinori HAGA	JAEA, Japan
Richard G. HAIRE	Oak Ridge Nat. Lab., USA
Itzhak HALEVY	NRCN, Israel
Ladislav HAVELA	Charles University, Czech Republic
Stepan N. KALMYKOV	Lomonosov University, Russia
Jens V. KRATZ	University of Mainz, Germany
Francis R. LIVENS	University of Manchester, UK
Klaus LÜTZENKIRCHEN	EC-JRC-ITU, Germany
Marinella MAZZANTI	CEA, France (ISAC Chair)
Karsten MEYER	University of Erlangen, Germany
Kazuo MINATO	JAEA, Japan
Heino NITSCHE	UC Berkeley/LBNL, USA
Yoshichika ONUKI	Osaka University, Japan
Peter OPPENEER	Uppsala University, Sweden
John SARRAO	LANL, USA
David K. SHUH	LBNL, USA
Baldev RAJ	IGCAR, India
James TOBIN	LLNL, USA
Vinh Hung TRAN	Polish Academy of Sciences, Poland
Dominique WARIN	CEA, France
Jong-Il YUN	KAIST, Korea
Yongjun ZHU	Tsinghua University, China

ACTINIDES 2013 is organized by European Commission, Joint Research Centre, Institute for Transuranium Elements (EC-JRC-ITU) and the Karlsruhe Institute of Technology, Institute for Nuclear Waste Disposal (KIT-INE), with Professors Roberto CACIUFFO, Thomas FANGHÄNEL and Horst GECKEIS acting as conference chairs.

Local Organizing Committee

Roberto CACIUFFO	EC-JRC-ITU
Kathy DARDENNE	KIT-INE
Melissa A. DENECKE	KIT-INE
Rachel ELOIRDI	EC-JRC-ITU
Alfred JIMENEZ-SEGARRA	EC-JRC-ITU
Petra J. PANAK	KIT-INE
Bernd SCHIMMELPFENNIG	KIT-INE
Thorsten STUMPF	KIT-INE
Gabriele TAMBORINI	EC-JRC-ITU
Krisztina VARGA	EC-JRC-ITU
Franck WASTIN	EC-JRC-ITU

e-mail: JRC-ACTINIDES2013@ec.europa.eu
website: http://actinides13.ine.kit.edu/

Time	Sun, 21 July	Monday, 22 July		Tuesday, 23 July		Wednesday, 24 July		Thursday, 25 July		Friday, 26 July		Time
08:30-08:40	Congress Center Karlsruhe, Stadthalle	Hans Thoma Saal **Opening**		Hans Thoma Saal		Hans Thoma Saal		Hans Thoma Saal		Hans Thoma Saal		
08:40-09:25		Physics **Gabriel Kotliar**		Environmental Science **Katherine Morris**		Application Technologies **Moris S. Eisen**		Materials Science **Takanari Ogata**		Materials Science **Rudy Konings**		08:40-09:25
		Thoma Saal	Hebel Saal	Thoma Saal	Hebel Saal	Thoma Saal	Hebel Saal	Thoma Saal	Hebel Saal	Thoma Saal	Hebel Saal	
09:30-10:00		Physics **Paolo Santini**	Env.Sci. **Maria Marques F.**	Env.Sci. **David Shuh**	Chemistry **Den Auwer**	Appl.Tech. **Klaus Mayer**	Chemistry **Valérie Vallet**	Mat.Sci. **Thomas Gouder**	Chemistry **Peter Burns**	Physics **Tonya Vitova**	Appl.Tech. **MasahideTakano**	09:30-10:00
10:00-10:30		Physics **Johann Bouchet**	Env.Sci. **Dirk Bosbach**	Env.Sci. **Moritz Schmidt**	Chemistry **C. Walther**	Appl.Tech. **Itzhak Halevy**	Chemistry **V. Domanov**	Mat.Sci. **Euo Chang Jung**	Chemistry **V. Brendler**	Physics **James Tobin**	Appl.Tech. **K. Ananthasivan**	10:00-10:30
10:30-11:00		**Coffee break**		**Coffe break**		**Coffee break**		**Coffee break**		**Coffee break**		10:30-11:00
11:00-11:20		Physics **Tanmoy Das**	Chemistry **Andrew Gaunt**	Env.Sci. **Karin Popa**	Chemistry **Ondrej Benes**	Mat.Sci. **T. Matsumoto**	Chemistry **M. Schädel**	Mat.Sci. **Michael Ling**	Chemistry **Clément Falaise**	Physics **Anna L. Smith**	Appl.Tech. **Ksenia Lipkina**	11:00-11:20
11:20-11:40		Physics **Alexander Shick**	Chemistry **Tsuyoshi Yaita**	Env.Sci. **Nina Huittinen**	Chemistry **E. V. Alekseev**	Mat.Sci. **Sven C. Vogel**	Chemistry **Tetsuya K. Sato**	Mat.Sci. **Fanny Lalire**	Chemistry **Andy Kerridge**	Physics **Silvie Maskova**	Appl.Tech. **Peter Kunz**	11:20-11:40
11:40-12:00		Physics **Peter Oppeneer**	Chemistry **Yasuhisa Ikeda**	Env.Sci. **Katharina Müller**	Chemistry **Chao Xu**	Mat.Sci. **Patrick Allen**	Chemistry **Lozano Rodriguez**	Mat.Sci. **Sue Ennaceur**	Chemistry **Elena Lapshina**	Physics **Wenhua Luo**	Appl.Tech. **Nobuaki Sato**	11:40-12:00
										Thoma Saal		
12:00-12:20		Physics **Andrei Rogalev**	Chemistry **Lucile Chatelain**	Env.Sci. **Robert Baker**	Chemistry **David Rodrigues**	Mat.Sci. **William Weber**	Chemistry **M. W. Löble**	Mat.Sci. **Laura Martel**	Chemistry **Mark Sarsfield**	Presenting Actinides 2017		12:00-12:20
12:20-12:40		Physics **J-C Griveau**	Chemistry **Claude Berthon**	Env.Sci. **Annie Kersting**	Chemistry **T. Murakami**	Mat.Sci. **Nick Brincat**	Chemistry **Nicole Bauer**	Mat.Sci. **Gan Li**	Chemistry **Cécile Marie**	Closing Session 1: D.L. Clark		12:20-12:40
12:40-13:00		Poster Session 1 (Appl. Tech., Materials Sci., Physics) & working lunch		Env.Sci. **F. Quinto**	Chemistry **Kwang-W. Kim**	Poster Session 2 (Chemistry, Environmental Sci.) & working lunch		Mat.Sci. **W. Siekhaus**	Chemistry **Tae-Hong Park**	Closing Session 2: G.H. Lander		12:40-13:00
13:00-14:25				**Lunch break**				**Lunch break**				13:00-14:25
		Thoma Saal		Thoma Saal		Thoma Saal	Hebel Saal	Thoma Saal				
14:30-14:50		Chemistry **Jeffrey Long**		Physics **Eric Bauer**		Physics **A. P. Gonçalves**	Chemistry **G. P. Soldani**	Chemistry **Marcus Altmaier**				14:30-14:50
14:50-15:15						Physics **Greg Stewart**	Chemistry **A. Osipenko**					14:50-15:15
		Thoma Saal	Hebel Saal	Thoma Saal	Hebel Saal	Thoma Saal	Hebel Saal	Thoma Saal	Hebel Saal		Legend	
15:20-15:50		Mat.Sci. **Ian Farnan**	Chemistry **Polly Arnold**	Physics **G. Zwicknagl**	Mat.Sci. **Greg Lumpkin**	Physics **Hiroshi Yasuoka**	Appl.Tech. **Joseph Somers**	Mat.Sci. **A. Froideval-Z.**	Env.Sci. **Gareth Law**		Plenary talk	15:20-15:50
15:50-16:20		Mat.Sci. **Corwin Booth**	Chemistry **P. Diaconescu**	Physics **D. Kaczorowski**	Mat.Sci. **Louise Natrajan**	Physics **Yoshinori Haga**	Appl.Tech. **Kastriot Spahiu**	Mat.Sci. **C. Bessada**	Env.Sci. **T. Ohnuki**		Invited talk	15:50-16:20
16:20-16:40		Mat.Sci. **Damien Prieur**	Chemistry **Ch. Apostolidis**	Physics **Ladislav Havela**	Mat.Sci. **Tarik Saleh**			Mat.Sci. **Alexey Karavaev**	Env.Sci. **T. Kazakovskaya**		Contributed talk	16:20-16:40
16:40-17:10		**Coffee break**		**Coffee break**				**Coffee break**				16:40-17:10
17:10-17:40	17:30-19:30	Physics **Rebecca Flint**	Chemistry **Daniel Meyer**	Env.Sci. **T. Shinonaga**	Mat.Sci. **Michel Freyss**	**17:30 Transfer to Ettlingen, Tram stop "Konzerthaus"** 50th ITU Anniversary: *"Marie Curie and her time"* by Hélène Langevin-Joliot. Opera Recital by Norma Raccichini & Pietro Salvaggio		Physics **Jan Rusz**	Appl.Tech. **Andreas Geist**				17:10-17:40
17:40-18:10	Registration and Welcome Drink	Physics **Dai Aoki**	Chemistry **Karsten Meyer**	Env.Sci **A. C. Scheinost**	Mat.Sci. **Matthias Krack**			Physics **Nicola Magnani**	Appl.Tech. **C. Kratochwil**			17:40-18:10
18:10-18:30		Physics **A Schneidewind**	Chemistry **Stephen Liddle**	Env.Sci. **Heino Nitsche**	Mat.Sci. **François Bottin**			**18:20 Group Picture** **18:30 Transfer to Kühler Krug Tram stop "Konzerthaus"** Poster Award Ceremony Conference Banquet BBQ				18:10-18:30
18:30-18:50		Physics **A. V. Kolomiets**	Chemistry **Andreas Wilden**	Env.Sci. **Donald Reed**	Mat.Sci. **Gaël Ménard**							18:30-18:50
18:50-19:10			Chemistry **M. Mazzanti**									18:50-19:10

Registration & Welcome

Sunday, 21 July 2013/17:30-19:30 **Congress Center Karlsruhe**

Your badge serves as public transportation pass. Take care of your badge.

Registration

Monday, 22 July starting at 07:30 **Congress Center Karlsruhe**

Opening

Monday/08:30-08:40 **Thoma Saal** **Chair: Roberto Caciuffo**

Welcome: T. Fanghänel & H. Geckeis

Plenary session: Physics

Monday/08:40-09:25 **Thoma Saal** **Chair: Roberto Caciuffo**

08:40-09:25
Plenary talk

Signature of strong correlations in actinides and their compounds: a Dynamical Mean Field Theory perspective
Gabriel Kotliar
Center for Materials Theory, Department of Physics and Astronomy, Rutgers University, Piscatway, NJ 08854, USA

Parallel session: Physics

Monday/09:30-10:30 **Thoma Saal** **Chair: Roberto Caciuffo**

09:30-10:00
Invited talk

Elementary excitations in Uranium Dioxide: Unravelling the tangle
Paolo Santini[1], Stefano Carretta[1], Giuseppe Amoretti[1], Roberto Caciuffo[2], Nicola Magnani[6], Arno Hiess[5], Louis-Pierre Regnault[4], Gerry Lander[3]
[1]Dipartimento di Fisica e Scienze della Terra, Università di Parma, Parma, Italy, [2]European Commission, JRC, Institute for Transuranium Elements, Karlsruhe, Germany, [3]Institut Max von Laue-Paul Langevin, Grenoble, France, [4]SPSMS-CEA/UJF, Grenoble, France, [5]European Spallation Source, Lund, Sweden, [6]KIT, Institute of Nanotechnology, Karlsruhe, Germany

10:00-10:30
Invited talk

Vibrational properties of the light actinides
Johann Bouchet
CEA, Bruyeres-le-Chatel, France

Parallel session: Environmental Science

Monday/09:30-10:30 **Hebel Saal** **Chair: Katherine Morris**

09:30-10:00
Invited talk

The fate of trivalent actinides in clay based radioactive waste repositories
Maria do Sameiro Marques Fernandes, Rainer Dähn, Michael H. Bradbury, Bart Baeyens
Paul Scherrer Institut, Villigen PSI, Switzerland

10:00-10:30
Invited talk

Solid-solution-aqueous solution (SSAS) equilibria: experimental challenges and recent advances
Dirk Bosbach
Forschungszentrum Jülich, Jülich, Germany

Coffee Break

Monday/10:30-11:00

Parallel session: Physics

Monday/11:00-12.40 **Thoma Saal** **Chair: Ladislav Havela**

11:00-11:20 Emergent Fermi liquid physics in actinides within an intermediate coupling model

Tanmoy Das
Los Alamos National Laboratory, Los Alamos, NM, USA

11:20-11:40 Unified character of correlation effects in unconventional Pu-based superconductors and δ-Pu

Alexander Shick[1], Jindrich Kolorenc[1], Jan Rusz[2,1], Peter Oppeneer[2], Alexander Lichtenstein[3], Mikhail Katsnelson[4], Roberto Caciuffo[5]
[1]Institute of Physics, ASCR, Prague, Czech Republic, [2]Uppsala University, Uppsala, Sweden, [3]University of Hamburg, Hamburg, Germany, [4]Radboud University Nijmegen, Nijmegen, The Netherlands, [5]European Commission, Joint Research Centre, Institute for Transuranium Elements, Karlsruhe, Germany

11:40-12:00 Photoemission imaging of 3-dimensional Fermi surface pairing at the hidden order phase transition in URu_2Si_2

Peter M. Oppeneer[1], Jian-Qiao Meng[2], John A. Mydosh[3], Peter S. Riseborough[4], Krzysztof Gofryk[2], John J. Joyce[2], Eric D. Bauer[2], Yinwan Li[5], Tomasz Durakiewicz[2]
[1]Uppsala University, Uppsala, Sweden, [2]Los Alamos National Laboratory, Los Alamos, NM, USA, [3]Leiden University, Leiden, The Netherlands, [4]Temple University, Philadelphia, PA, USA, [5]Wolfram Research Inc., Champaign, IL, USA

12:00-12:20 Detection of a finite 5*f* orbital magnetic moment in Curium metal using XMCD.

Fabrice Wilhelm[1], Rachel Eloirdi[2], Ross Springell[3], Eric Colineau[2], Jean-Christpohe Griveau[2], Roberto Caciuffo[2], Andrei Rogalev[1], Gerard H. Lander[2]
[1]European Synchrotron Radiation Facility, Grenoble, France, [2]European Commission, Joint Research Centre, Institute for Transuranium Elements, Karlsruhe, Germany, [3]Royal Commission for the Exhibition of 1851 Research Fellow, Interface Analysis Centre, University of Bristol, Bristol, UK

12:20-12:40 Unconventional Superconductivity in Transuranium compounds : 10 years of research at ITU

Jean-Christophe Griveau[1], Krzysztof Gofryk[2], Eric Colineau[1], Eric D. Bauer[2], Paul Tobash[2], Rachel Eloirdi[1], Tomasz Klimczuk[3], Jean Rebizant[1], Richard G. Haire[4], Roberto Caciuffo[0]
[1]Institute of Transuranium, Karlsruhe, Germany, [2]Los Alamos National Laboratory, Los Alamos, USA, [3]Faculty of Applied Physics and Mathematics, Gdańsk, Poland, [4]Oak Ridge National Laboratory, Oak Ridge, USA

Parallel session: Chemistry

Monday/11:00-12:40 **Hebel Saal** **Chair: Karsten Meyer**

11:00-11:20 Molecular Transuranic Discovery Science

Andrew Gaunt[1], Sean Reilly[1], Matthew Jones[1], Brian Scott[1], Robert Paine[2], Nikolas Kaltsoyannis[3]
[1]Los Alamos National Laboratory, Los Alamos, NM 87545, USA, [2]University of New Mexico, Albuquerque, NM 87131, USA, [3]University College London, London, WC1H 0AJ, UK

11:20-11:40 Complex Formation Dynamics of Actinide and Lanthanide with Poly-dentate Ligands by Time Resolved XAFS.

Tsuyoshi Yaita, Daiju Matsumura, Toru Kobayashi, Shinichi Suzuki, Hideaki Shiwaku
QuBS, JAEA, Hyogo, Japan

11:40-12:00 Structural Studies on Uranyl Species in Acetonitrile and 1-Ethyl-3-methylimidazolium Nitrate ([EMI][NO_3]) Dissolved [EMI][$UO_2(NO_3)_4$] - Evidence for the Formation of $[UO_2(NO_3)_4]^{2-}$ -
Kotoe Sasaki[1], Tomoya Suzuki[2], Tsuyoshi Arai[1], Koichiro Takao[2], Shinichi Suzuki[3], Tsuyoshi Yaita[3], Yasuhisa Ikeda[2]
[1]Shibaura Institute of Technology, Toyosu, Koto-ku, Tokyo, Japan, [2]Tokyo Institute of Technology, Ookayama, Meguro-ku, Tokyo, Japan, [3]Japan Atomic Energy Agency, Ibaraki, Japan

12:00-12:20 Cation-Cation Complexes of pentavalent uranyl: towards polymetallic assemblies with unusual magnetic properties
Lucile Chatelain[1], Victor Mougel[1], Jacques Pécaut[1], Roberto Caciuffo[2], Eric Colineau[2], Jean-Christophe Griveau[2], Marinella Mazzanti[1]
[1]CEA Grenoble, Grenoble, France, [2]European Commission, Joint Research Centre, Institute for Transuranium Elements, Karlsruhe, Germany

12:20-12:40 Actinide paramagnetism and NMR
Claude Berthon[1], Thomas F. Wall[2], Steve Jan[1], Matthieu Autillo[1], Kenneth L. Nash[2], Claire Le Naour[3], Laetitia Guerin[1], Philippe Moisy[1]
[1]CEA, Bagnols/Ceze, France, [2]Whashington State University, Pullman, USA, [3]Paris XI University, Orsay, France

Poster session — Application Technologies, Materials Science, Physics

Place your poster on the board indicated with your poster number.
Posters are on display for 2 days (Monday-Tuesday)
Please remove your poster by 19:00, Tuesday, 23 July at the latest.

Monday/12:40-14.25 Congress Center Karlsruhe

Corner 1, Poster number 01-29

PS1-01 12:40-14:25 Mat.Sci. Influence of fluoride and oxide ions on the electrochemical behaviour of uranium in LiCl-KCl eutectic melt
Sergey Kuznetsov[1], Marcelle Gaune-Escard[2]
[1]Institute of Chemistry, Kola Science Centre RAS, Apatity, Russia, [2]Ecole Polytechnique U.M.R.-C.N.R.S. 6595, Marseille, France

PS1-02 12:40-14:25 Mat.Sci. Unalloyed uranium deformation curves under static and dynamic loading
Victor Pushkov, Margarita Andreeva, Alex Yurlov, Alex Kalmanov, Igor Shiberin
Russian Federal Nuclear Center – VNIIEF, Sarov, Russia

PS1-03 12:40-14:25 Mat.Sci. The high temperature heat capacity of thorium-plutonium mixed oxides
Octavian S. Valu[1,2], Ondrej Benes[1], Rudy J.M. Konings[1,2], Joseph Somers[1]
[1]European Commission, Joint Research Centre, Institute for Transuranium Elements, Karlsruhe, Germany, [2]Delft University of Technology, Faculty of Applied Sciences, Delft, The Netherlands

PS1-04 12:40-14:25 Mat.Sci. Numerical Investigation of Interfacial Flow in a Molten Immiscible LiCl-KCl/Cd System
Kwangrag Kim, Jun-Bo Shim, Seungwoo Paek, In-Tae Kim
Korea Atomic Energy Research Institute, Daejeon, Republic of Korea

PS1-05 12:40-14:25 Mat.Sci. Single and mixed f-elements sintered oxide pellets synthesis with tailored microstructures.
Elodie Remy[1], Sébastien Picart[1], Thibaud Delahaye[1], Isabelle Bisel[1], Olivier Dugne[1], Nicolas Clavier[2], Adila Azzou[3], Philippe Blanchart[4], André Ayral[5]
[1]CEA Marcoule, Bagnols sur Cèze/Gard, France, [2]ICSM UMR 5257 CEA-CNRS-UM2-ENSCM, Bagnols sur Cèze/Gard, France, [3]CRISMAT ENSICAEN, Caen/Calvados, France, [4]GEMH ENSCI, Limoges/Haute Vienne, France, [5]IEM UM2, Montpellier/Hérault, France

PS1-06 12:40-14:25 Mat.Sci. MD simulation of the effect of self-irradiation upon static strength characteristics of materials
Vladimir Dremov, Gennady Ionov, Alexey Karavaev, Philipp Sapozhnikov
Russian Federal Nuclear Center - Institute of Technical Physics, Snezhinsk, Chelyabinsk region, Russia

PS1-07
12:40-14:25
Mat.Sci.

Influence of adding niobium to uranium on the initial kinetics of hydriding
Ruiwen Li, Xiaolin Wang
China Academy of Engineering Physics, Mianyang,Sichuan, China

PS1-08
12:40-14:25
Mat.Sci.

Microstructure-related hydride nucleation sites on aged U-0.79 wt.% Ti alloy
Peng Shi, Xiaolin Wang, Fangfang Li, Ruiwen Li
China Academy of Engineering physics, Mianyang, Sichuan, China

PS1-09
12:40-14:25
Mat.Sci.

Microstructure and corrosion resistance of Cr/CrN multilayer film prepared by magnetron sputtering on depleted uranium
Shengfa Zhu[1], Yanping Wu[1], Tianwei Liu[2], Kai Tang[1], Qiang Wei[1]
[1]China Academy of Engineering and Physics, Mianyang, China, [2]Science and Technology on Surface Physics and Chemistry Laboratory, Mianyang, China

PS1-10
12:40-14:25
Mat.Sci.

Phase transformations in PuGa 1 at.% alloy: Elucidation of mechanisms of reversion process following martensitic transformation by coupling in situ experiments and CALPHAD-based calculations
Fanny Lalire, Brice Ravat, Aurélien Perron, Benoit Oudot, François Delaunay
CEA, Is sur Tille, France

PS1-11
12:40-14:25
Mat.Sci.

Corrosion of austenitic steels and their components in uranium-containing chloride melts
Alexandr Abramov, Ilya Polovov, Dmitriy Maltsev, Vladimir Volkovich, Oleg Rebrin
Ural Federal University, Ekaterinburg, Russia

PS1-12
12:40-14:25
Mat.Sci.

Interaction of prospective metallic construction materials with uranium-containing chloride melts
Robert Kamalov, Alexandr Bazhenov, Alexandr Abramov, Ilya Polovov, Dmitriy Maltsev, Vladimir Volkovich, Oleg Rebrin
Ural Federal University, Ekaterinburg, Russia

PS1-13
12:40-14:25
Mat.Sci.

Recent advances in the study of $U_{1-x}Am_xO_{2\pm\delta}$: solid solution synthesis, densification and structural properties
Florent Lebreton[1,4], Denis Horlait[1], Philippe M. Martin[2], Renaud C. Belin[3], Thibaud Delahaye[1], Philippe Blanchart[4]
[1]CEA, DEN, DTEC/SDTC/LEMA, Bagnols-sur-Cèze, France, [2]CEA, DEN, DEC/SESC/LLCC, Saint-Paul-lez-Durance, France, [3]CEA, DEN, DEC/SPUA/LMPC, Saint-Paul-lez-Durance, France, [4]GEMH/ENSCI, Limoges, France

PS1-14
12:40-14:25
Mat.Sci.

XRD monitoring of α self-irradiation effects in U1-xAmxO2±δ mixed-oxides
Denis Horlait[1], Florent Lebreton[1], Thibaud Delahaye[1], Roussel Pascal[2]
[1]CEA, Bagnols-sur-cèze, France, [2]Unité de Catalyse et de Chimie du Solide, Villeneuve d'Ascq, France

PS1-15
12:40-14:25
Mat.Sci.

Actinide oxalate compounds: structure directing role of the monovalent cations
Ana Gil-Martin[1], Bénédicte Arab-Chapelet[1], Murielle Rivenet[2], Philippe Martin[3], Andreas Scheinost[4], Isabelle Bisel[1], Stéphane Grandjean[5], Francis Abraham[2]
[1]Laboratoire de Conversion des Actinides et Radiolyse, CEA Marcoule DEN/DRCP/SERA, Bagnols sur Cèze, France, [2]UCCS, Equipe Chimie du Solide et Matériaux Nucléaires, Villeneuve d'Ascq, France, [3]Laboratoire des lois de comportement des Combustibles, DEN/DEC/SESC, Saint Paul lez Durance, France, [4]The Rossendorf Beamline at ESRF, Grenoble, France, [5]CEA Marcoule DEN/DRCP/DIR, Bagnols sur Cèze, France

PS1-16
12:40-14:25
Mat.Sci.

Submicron and nanostructured uranium carbides prepared by electrospinning
Margarida S. Henriques[1], Adelaide Cruz[1], Joaquim Marcalo[1], Martina Kratochvílová[2], Ladislav Havela[2], Thierry Stora[3], Antonio P. Goncalves[1]
[1]IST/ITN, Technical University of Lisbon, CFMC-UL, 2686-953-Sacavém, Portugal, [2]Dept. Condensed Matter Physics, Faculty of Mathematics and Physics, Charles University, 121 16 Prague, Czech Republic, [3]CERN - European Organization for Nuclear Research, CH-1211 Genève 23, Switzerland

PS1-17
12:40-14:25
Physics

Studies on the $UFeC_2$ uranium carbide
Margarida S. Henriques[1], Yuriy Verbovitskiy[1], Ladislav Havela[2], Antonio P. Goncalves[1]
[1]IST/ITN, Technical University of Lisbon, CFMC-UL, 2686-953-Sacavém, Portugal, [2]Dept. Condensed Matter Physics, Faculty of Mathematics and Physics, Charles University, 121 16 Prague, Czech Republic

PS1-18
12:40-14:25
Mat.Sci.

Persistence of the γ-phase in uranium-molybdenum alloy thin films
Anna Maria Adamska, T B Scott, R Springell
Interface Analysis Centre, University of Bristol, Bristol, UK

PS1-19
12:40-14:25
Mat.Sci.

Structure stability of the cubic γ-phase uranium molybdenum alloys.
Ilya Tkach[1], Nhu-Tarnawska Hoa Kim-Ngan[2], Silvie Mašková[1], Ladislav Havela[1], Alexander Warren[3], Camilla Stitt[3], Tomhas Scott[3]
[1]Charles University, Prague, Czech Republic, [2]Pedagogical University, Krakow, Poland, [3]University of Bristol, Bristol, UK

PS1-20
12:40-14:25
Mat.Sci.

German Joint Research Project on "Conditioning of long-lived Radionuclides in Ceramic Waste Forms" - An Introduction
Stefan Neumeier, Giuseppe Modolo, Dirk Bosbach
Forschungszentrum Jülich GmbH, Institute of Energy and Climate Research - IEK-6: Nuclear Waste Management, Jülich, Germany

PS1-21
12:40-14:25
Mat.Sci.

Non-destructive studies of fuel rodlets by neutron resonance absorption radiographyand thermal neutron radiography
Anton S. Tremsin[1], Sven C. Vogel[2], Michal Mocko[2], Mark A. M. Bourke[2], Vincent Yuan[2], Ron Nelson[2], Donald W. Brown[2], Bruce Feller[3]
[1]University of California at Berkeley, Berkeley, CA, USA, [2]Los Alamos National Laboratory, Los Alamos, NM, USA, [3]NOVA Scientific, Inc., Sturbridge, MA, USA

PS1-22
12:40-14:25
Mat.Sci.

Phase transformation inhibition in Pu-1.9 at.% Ga
Jason Jeffries, J. Bradley, Mark Wall
Lawrence Livermore National Laboratory, Livermore, CA, USA

PS1-23
12:40-14:25
Mat.Sci.

X-ray diffraction study of the eutectoid decomposition of γ-U(Mo) powder produced by magnesiothermic reduction.
Guillaume Champion[1,2], Mathieu Pasturel[1], Xavière Iltis[2], Olivier Tougait[1]
[1]ICSR/CSM, UMR 6226, CNRS-Université de Rennes1, Rennes, France, [2]CEA, DEN, DEC, Saint Paul Lez Durance, France

PS1-24
12:40-14:25
Mat.Sci.

Densification of uranium carbide pellets: Preliminary result of spark plasma sintering and comparison with conventional sintering techniques
Olivier Tougait[1], Matthieu Peniel[1], Mathieu Pasturel[1], Odile Merdrignac-Conanec[1], Christophe Lau[2], Sandrine Tusseau-Nenez[2]
[1]ICSR/CSM, UMR 6226, CNRS-Université de Rennes1, Rennes, France, [2]IPN-O, Pôle ALTO, Orsay, France

PS1-25
12:40-14:25
Mat.Sci.

Selective Actinide Separation Process by Amide Based New Ligands.
Shinichi Suzuki, Tohru Kobayashi, Tsuyoshi Yaita, Hideaki Shiwaku
Japan Atomic Energy Agency, Tokai, Ibaraki, Japan

PS1-26
12:40-14:25
Mat.Sci.

High-temperature experimental study on the U-Mo-C system
Matthieu Peniel, Mathieu Pasturel, Olivier Tougait
Insitut des Sciences Chimiques de Rennes, Rennes, France

PS1-27
12:40-14:25
Mat.Sci.

Pyrochlore - a promising host phase for actinide immobilisation
Sarah Finkeldei[1], Kiel Holliday[2,4], Eva de Visser-Týnová[3], Felix Brandt[1], Stefan Neumeier[1], Giuseppe Modolo[1], Thorsten Stumpf[4], Dirk Bosbach[1]
[1]Forschungszentrum Jülich GmbH, Institut für Energie- und Klimaforschung - IEK-6, Jülich, Germany, [2]Lawrence Livermore National Laboratory, Livermore, USA, [3]NRG, Petten, The Netherlands, [4]KIT, Institut für Nukleare Entsorgung, Karlsruhe, Germany

PS1-28
12:40-14:25
Mat.Sci.

Thermal conductivities of $(U_{1-y}, Pu_y)O_{2.00}$ (y = 0.00 - 0.46)
Kyoichi Morimoto[1], Masahiro Ogasawara[2]
[1]Japan Atomic Energy Agency, Naka-gun, Ibaraki, Japan, [2]Inspection development company, Naka-gun, Ibaraki, Japan

PS1-29
12:40-14:25
Mat.Sci.

Electronic Structure of Actinide Surface Reactions and Complexes
Krishnan Balasubramanian, Patrick Allen, William McLean II
Lawrence Livermore National Lab, Physical & Life Sciences Directorate,, Livermore CA 94551, USA

Corner 2, Poster number 30-60

PS1-30
12:40-14:25
Physics

Ab initio prediction and experimental verification of materials surface stability
Pablo Maldonado[1], José R. A. Godinho[2], Lena Z. Evins[3], Peter M. Oppeneer[1]
[1]Department of Physics and Astronomy, Uppsala University, Uppsala, Sweden, [2]Department of Geological Sciences, Stockholm University, Stockholm, Sweden, [3]Swedish Nuclear Fuel and Waste Management Co., Stockholm, Sweden

PS1-31
12:40-14:25
Physics

Physical properties of UBeGe and ThBeGe intermetallic compounds
Roman Gumeniuk, Andreas Leithe-Jasper, Walter Schnelle, Michael Nicklas, Ulrich Burkhardt, Horst Borrmann, Yuri Grin
MPI CPfS, Dresden, Germany

PS1-32
12:40-14:25
Physics

On the possibility of predicting the dynamic properties of light actinides
Elena Kosheleva, Alexander Uchaev, Valery Punin, Nadezda Selchenkova
Russian Federal Nuclear Center- VNIIEF, Sarov, Russia

PS1-33
12:40-14:25
Physics

Physical nature of Light Actinides Longevity in the Dynamic Failure Phenomenon
Nadezda Selchenkova, Alexander Uchaev, Valery Punin, Elena Kosheleva
Russian Federal Nuclear Center – VNIIEF, Sarov, Russia

PS1-34
12:40-14:25
Physics

Magnetization of U_2Fe_3Ge and $U_3Fe_4Ge_4$ under external pressure
Alexander Andreev[1], Zdenek Arnold[1], Denis Gorbunov[1,2], Margarida Henriques[3], Ladislav Havela[2], Antonio Gonçalves[3]
[1]Institute of Physics ASCR, Prague, Czech Republic, [2]Dept. Condensed Matter Physics, Charles University, Prague, Czech Republic, [3]Instituto Superior Técnico, Sacavém, Portugal

PS1-35
12:40-14:25
Physics

Electronic structure and Fermi surface of paramagnetic and antiferromagnetic UPt_2S_2
Saad Elgazar[1], Jan Rusz[2], Peter Oppeneer[2], John Mydosh[3]
[1]Dept. of Physics, Johannesburg, South Africa, [2]DMT, Uppsala, Sweden, [3]Dept. of Physics, Leiden, Norway

PS1-36
12:40-14:25
Physics

First-principles calculation of intrinsic and defective properties of UO_2 and ThO_2
Han Han, Cheng Cheng, Ping Huai
Shanghai Institute of Applied Physics, Chinese Academy of Sciences, Shanghai, China

PS1-37
12:40-14:25
Physics

Simulations of incipient damage and nanovoids in plutonium during alpha-decay
Boris Nadykto, Sergey Sokolov, Alexander Panov, Alexey Samodolov
Russian Federal Nuclear Center - VNIIEF, Sarov, Russia

PS1-38
12:40-14:25
Physics

Thermal and elastic properties of actinides on the example of americium and curium: a self-consistent thermodynamic approach
Anton Filanovich, Alexander Povzner, Varvara Oskina
Ural Federal University, Ekaterinburg, Russia

PS1-39
12:40-14:25
Physics

Microscopic theory of the insulating electronic ground states of actinides dioxides AnO_2 (with An = U, Np, Pu, Am and Cm)
Michi-To Suzuki[1,2], Nicola Magnani[3], Peter M. Oppeneer[1]
[1]Japan Atomic Energy Agency, Chiba, Japan, [2]Uppsala University, Uppsala, Sweden, [3]Lawrence Berkeley National Laboratory, Berkeley, CA, USA

PS1-40
12:40-14:25
Physics

^{119}Sn Mössbauer spectroscopy of 3d-, 4f- and U-intermetallic compounds
Vasily Krylov
Skobeltsyn Institute of Nuclear Physics, Moscow State University, Moscow, Russia

PS1-41
12:40-14:25
Physics

The screening effect of magnetic exchange interactionin the U- and Gd-based intermetallic compounds
Vasily Krylov[1], Vladimir Sechovský[2], Alexander Andreev[3]
[1]Skobeltsyn Institute of Nuclear Physics, Moscow State University, Moscow, Russia, [2]DSMP, Faculty of Mathematics and Physics, Charles University in Prague, Prague, Czech Republic, [3]Institute of Physics ASCR,, Prague, Czech Republic

PS1-42
12:40-14:25
Physics

The role of transition metals (TM) on the symmetry of Al-TM-Ac alloys (Ac= actinides and lanthanides)
Avraham I Bram[1,2], Arie Venkert[3], Louisa Meshi[1,2]
[1]Department of Materials Engineering, Ben-Gurion University of the Negev, Beer-Sheva, Israel, [2]Ilse Katz institute for nanotechnology, Ben Gurion University of the Negev, Beer-Sheva, Israel, [3]Nuclear Research Center-Negev, Beer-Sheva, Israel

PS1-43
12:40-14:25
Physics

On relationship between thermodynamic and dynamic properties of light actinides
Alexander Uchaev, Nadezda Selchenkova, Elena Kosheleva, Valery Punin
Russian Federal Nuclear Center – VNIIEF, Sarov, Russia

PS1-44
12:40-14:25
Physics

Structural, Electronic and Magnetic Properties of $NpNi_5$
Amir Hen[1,2], Eric Colineau[1], Rachel Eloirdi[1], Jean - Christophe Griveau[1], Itzhak Halevy[3,4], Itzhak Orion[2], Roberto Caciuffo[1]
[1]Institute for Transuranium Elements, Postfach 2340, D-76125 Karlsruhe, Germany, [2]Ben Gurion University, IL84105 Beer-Sheva, Israel, [3]Nuclear Research Center Negev, P.O. Box 9001, IL84190 Beer-Sheva, Israel, [4]California Institute of Technology, W. M. Keck Laboratory 138-78, Pasadena, California 91125, USA

PS1-45
12:40-14:25
Physics

Proposal for thermo-mechanical properties correlations of MOX bearing minor actinides fuels
Sara Perez-Martin, Michael Schikorr
Karlsruhe Institute of Technology, Karlsruhe, Germany

PS1-46
12:40-14:25
Physics

Structure and magnetism in $U_2Ni_{21}B_6$, $(U,Nb)_2Ni_{21}B_6$ and $(U,Nb)_3Ni_{20}B_6$
Alessia Provino[1,2], Amitava Bhattacharya[3], Sudesh K. Dhar[3], Cristina Bernini[2], Marcella Pani[1,2], Flavio Gatti[4], Pietro Manfrinetti[1,2]
[1]Department of Chemistry, University of Genova, Genova, Italy, [2]CNR-SPIN, Genova, Italy, [3]Condensed Matter Physics & Material Science, Tata Institute of Fundamental Research, Mumbai, India, [4]Department of Physics and INFN, University of Genova, Genova, Italy

PS1-47
12:40-14:25
Physics

Vibrational Properties of Uranium Hydride and Uranium Deuteride
Alice I. Smith, Luke L. Daemen, Joe R. Wermer, Jeffery Aguiar, Bogdan Mihaila, Roland K. Schulze
Los Alamos National Laboratory, Los Alamos, NM, USA

PS1-48
12:40-14:25
Physics

X-ray photoelectron spectroscopy of 7-at.% gallium δ-stabilized plutonium
Thomas Venhaus
Los Alamos National Laboratory, Los Alamos, NM, USA

PS1-49
12:40-14:25
Physics

Neutron Capture Cross Section on ^{236}U performed at the n_TOF facility at CERN
Mark James Vermeulen[1], Massimo Barbagallo[2], Carlos Guerrero[3], David Jenkins[1]
[1]University of York, York, UK, [2]Istituto Nazionale Fisica Nucleare, Bari, Italy, [3]European Organisation for Nuclear Research (CERN), Geneva, Switzerland

PS1-50
12:40-14:25
Physics

Production of Super Heavy Plutonium Isotopes for Basic Research
Stanislav Vesnovskii[2], Lev Kazakov[1], Alexey Kupriyanov[1], Evgeny Romanov[1], Valery Tarasov[1]
[1]JSC "State Scientific Centre - Research Institute of Atomic Reactors, Dimitrovgrad, Russia, [2]RFNC–VNIIEF, Sarov, Russia

PS1-51
12:40-14:25
Appl. Tech

New Concept of Designing Composite Fuel for Fast Reactors with Closing Fuel Cycle
Alexey Savchenko, Alexander Vatulin, Gennady Kulakov, Ksenia Lipkina, Vladimir Sorokin, Sergey Ershov, Sergey Maranchak, Zoya Petrova
A.A. Bochvar Institute (VNIINM), Moscow, Russia

PS1-52
12:40-14:25
Appl. Tech

Thermodynamic Aspects of Interphase Interaction in Heterogeneous Alloys and Its Influence on Alloys Properties
Alexey Savchenko, Andrey Laushkin, Yury Konovalov
A.A. Bochvar Institute (VNIINM), Moscow, Russia

PS1-53
12:40-14:25
Appl. Tech

Solubility of uranium and lanthanum in Ga-In eutectic based alloys at 25-800 °C
Vladimir Volkovich[1], Andrey Schetinskii[1], Dmitry Maltsev[1], Alexander Dedyukhin[1], Leonid Yamshchikov[1], Stanislav Melchakov[1], Viktor Ivanov[1], Alexander Osipenko[2], Sergey Raspopin[1], Mikhail Kormilitsyn[2]
[1]Ural Federal University, Ekaterinburg, Russia, [2]JSC "SSC Research Institute of Atomic Reactors", Dimitrovgrad, Russia

PS1-54
12:40-14:25
Appl. Tech

Post-Irradiation Examinations on PHENIX axially heterogeneous pins relevant to ASTRID fuel design: ZEBRE and PAVIX irradiations
Béatrice Rabu, Michel Pelletier, Christophe Valot, Isabelle Munoz, Mayeul Phelip
French Atomic Energy Commission (CEA), Saint Paul lez Durance, France

PS1-55
12:40-14:25
Appl. Tech

Oxidation of Uranium-Plutonium Mixed Nitrides
Andrei Shadrin, Alexey Glushenkov, Konstantin Dvoeglazov, Mikhail Skupov
Bochvar Institute (VNIINM), Moscow, Russia

PS1-56
12:40-14:25
Appl. Tech

In-situ measurement of a dissolved alpha emitter by electro-precipitation
Alexander Diener, Christoph Wilhelm, Ursula Hoeppener-Kramar
Karlsruhe Institute of Technology, Karlsruhe, Germany

PS1-57
12:40-14:25
Appl. Tech

Investigation of diformylhydrazine interaction with Pu in technological media of extraction SNF reprocessing
Vladimir Volk, Ekaterina Pavlyukevich, Konstantin Dvoyeglazov, Lubov Podrezova, Sergey Veselov
JSC SSC VNIINM, Moscow, Russia

PS1-58
12:40-14:25
Appl. Tech

Separation of uranium and lanthanides in "molten salt - liquid metal" system
Leonid Yamshchikov[1], Vladimir Volkovich[1], Andrey Schetinskii[1], Dmitry Maltsev[1], Alexander Dedyukhin[1], Viktor Ivanov[1], Stanislav Melchakov[1], Sergey Raspopin[1], Alexander Osipenko[2], Mikhail Kormilitsyn[2]
[1]Ural Federal University, Ekaterinburg, Russia, [2]JSC "SSC Research Institute of Atomic Reactors", Dimitrovgrad, Russia

PS1-59
12:40-14:25
Appl. Techn.

Ultra-Trace Determination of Pu and Np Isotopes by Resonance Ionization Mass Spectrometry
Michael Franzmann[1], Amin Hakimi[1], Gerd Passler[1], Sebastian Raeder[2], Tobias Reich[3], Pascal Schönberg[3], Nils Stöbener[3], Norbert Trautmann[3], Klaus Wendt[1]
[1]Institut für Physik, Johannes Gutenberg-Universität, Mainz, Germany, [2]TRIUMPF, ISAC RIB Division, Vancouver, Canada, [3]Institut für Kernchemie, Johannes Gutenberg-Universität, Mainz, Germany

PS1-60
12:40-14:25
Appl. Tech

μ-focus capabilities at the INE-Beamline for actinide science at ANKA
Kathy Dardenne[1], Jörg Rothe[1], Teresa Fernandes[2,3], Dieter Schild[1], Eva Soballa[1], Volker Metz[1], Christiane Bube[1], Bernhard Kienzler[1], Melissa Denecke[1], Horst Geckeis[1]
[1]KIT-INE, Karlsruhe, Germany, [2]Amphos 21, Barcelona, Spain, [3]ICTA, UAB, Bellaterra, Spain

Plenary session: Chemistry

Monday/14:30-15:15 Thoma Saal Chair: Melissa Denecke

14:30-15-15
Plenary talk

f-Element Single-Molecule Magnets
Katie Meihaus[1], Shuao Wang[1,2], Jeffrey Rinehart[1], Selvan Demir[1], Michael Nippe[1,2], Joseph Zadrozny[1], David Shuh[2], Jeffrey Long[1,2]
[1]University of California, Berkeley, Berkeley, CA, USA, [2]Lawrence Berkeley National Laboratory, Berkeley, CA, USA

Parallel session: Materials Science

Monday/15:20-16:40 Thoma Saal Chair: Joseph Somers

15:20-15:50
Invited talk

High-resolution Nuclear Magnetic Resonance Investigation into Chemical Shifts in UO_2 and ThO_2 and Ordering in Uranium-Thorium Oxide Solid Solutions.
Ian Farnan[1], Joseph Somers[2], Olivier Pauvert[2], Serge Fourcadot[2], Laura Martell[2], Kevin Boland[3], David Clark[3]
[1]University of Cambridge, Cambridge, UK, [2]European Commission, JRC, ITU, Karlsruhe, Germany, [3]Los Alamos National Laboratory, Los ALamos, NM, USA

15:50-16:20
Invited talk

Multiconfigurational Nature of 5f Orbitals in Uranium and Plutonium and Their Intermetallic Compounds
Corwin Booth
Lawrence Berkeley National Laboratory, Berkeley, CA, USA

16:20-16:40 Charge distribution and local structure of $M_{0.80}Am_{0.20}O_{2\pm x}$ (M: Th, U and Pu)
Damien Prieur[1], Ursula Carvajal-Nunez[1], Marika Vespa[1], Tonya Vitova[2], Joseph Somers[1]
[1]European Commission, Joint Research Centre, Institute for Transuranium Elements, Karlruhe, Germany, [2]Institut für Nukleare Entsorgung (INE), Karlsruhe, Germany

Parallel session: Chemistry

Monday/15.20-16:40 **Hebel Saal** **Chair: Melissa Denecke**

15:20-15:50 Invited talk Uranyl oxo group functionalisation, reduction, and migration reactions
Polly Arnold[1], Jason Love[1], Guy Jones[1], Anne-Frederique Pecharman[1], Emmalina Hollis[1], Roberto Caciuffo[2], Nicola Magnani[2], Laurent Maron[3], Ludovic Castro[3], Georg Schreckenbach[4], Samuel Odoh[4]
[1]EaStCHEM School of Chemistry, University of Edinburgh, Edinburgh, UK, [2]ITU, EC Joint Research Centre, Karlsruhe, Germany, [3]LPCNO, UPS, UNSA, University of Toulouse,, Toulouse, France, [4]Department of Chemistry, University of Manitoba, Winnipeg, Canada

15:50-16:20 Invited talk Unique advantages of organometallic supporting ligands for uranium complexes
Paula Diaconescu
University of California, Los Angeles, Los Angeles, CA, USA

16:20-16:40 $AnCp_4$: a grandfather of the organometallic chemistry of the actinides with young and attractive children
Christos Apostolidis, Jean Rebizant, Olaf Walter, Alfred Morgenstern
European Commission, Joint Research Centre, Institute for Transuranium Elements, Karlsruhe, Germany

Coffee Break

Monday/16:40-17:10

Parallel session: Physics

Monday/17:10-18:50 **Thoma Saal** **Chair: Eric D. Bauer**

17:10-17:40 Invited talk Spins, electrons and broken symmetries: realizations of two channel Kondo physics
Rebecca Flint
Massachusetts Institute of Technology, Cambridge, MA, USA

17:40-18:10 Invited talk Field reentrant superconductivity and Fermi surface instabilities in uranium ferromagnets
Dai Aoki[1,2]
[1]CEA-Grenoble, Grenoble, France, [2]IMR, Tohoku University, Oarai, Japan

18:10-18:30 Possible Pseudogap Phase in the Cubic Superconductor UBe13
Astrid Schneidewind[1], Arno Hiess[2,3], Oliver Stockert[4], Philipp Geselbracht[5], Paul Steffens[3], Zachary Fisk[6]
[1]JCNS, Forschungzentrum Jülich at Maier-Leibnitz-Zentrum, Garching, Germany, [2]European Spallation Source ESS AB, Lund, Sweden, [3]Institut Laue – Langevin, Grenoble, France, [4]MPI-CPfS, Dresden, Germany, [5]TU München, Maier-Leibnitz-Zentrum, Garching, Germany, [6]University of California, Irvine, USA

18:30-18:50 The increase of the Curie temperature of UGa_2 at high pressure
Alexandre V. Kolomiets[1,2], J. Prchal[2], J.-C. Griveau[3], L. Havela[2], A.V. Andreev[4]
[1]Department of Physics, Lviv Polytechnic National University, 12 Bandera Str., Lviv, Ukraine, [2]Department of Condensed Matter Physics, Charles University, Ke Karlovu 5, 121 16 Prague, Czech Republic, [3]European Commission, Joint Research Centre, Institute for Transuranium Elements, Postfach 2340, Karlsruhe, Germany, [4]Institute of Physics, ASCR, Na Slovance 2, 182 21 Prague, Czech Republic

Parallel session: Chemistry

Monday/17:10-19:10 **Hebel Saal** **Chair: Petra Panak**

17:10-17:40
Invited talk

Relation between the structure and the microstructure of a solid silicon hybrid based material and the plutonium and americium extraction behaviour from high level waste.
Daniel Meyer[1], Joel Moreau[2], Michel Wong Chi Man[3], Olivier Conocar[1], Stéphane Bourg[1]
[1]CEA, Marcoule, France, [2]ENSCM, Montpellier, France, [3]CNRS, Montpellier, France

17:40-18:10
Invited talk

Small Molecule Activation at Reactive Complexes of Uranium
Karsten Meyer
Friedrich-Alexander-University Erlangen-Nuremberg, Erlangen, Germany

18:10-18:30

Recent Advances in Terminal Uranium Nitride Triple Bond Chemistry
David King[1], Floriana Tuna[2], Eric McInnes[2], Jonathan McMaster[1], William Lewis[1], Alexander Blake[1], Stephen Liddle[1]
[1]University of Nottingham, Nottingham, UK, [2]University of Manchester, Manchester, UK

18:30-18:50

Development and laboratory-scale innovative-SANEX process demonstration for minor actinide partitioning using annular centrifugal contactors
Andreas Wilden[1], Giuseppe Modolo[1], Peter Kaufholz[1], Andreas Geist[2], Daniel Magnusson[2], Michal Sypula[1], Dirk Bosbach[1]
[1]Forschungszentrum Jülich GmbH, Jülich, Germany, [2]Karlsruhe Institute of Technology, Karlsruhe, Germany

18:50-19:10

Uranium chemistry: from nuclear to single molecule magnets and small molecule activation.
Marinella Mazzanti, Victor Mougel, Clement Camp, Lucile Chatelain, Jacques Pécaut
CEA, Grenoble, France

Plenary session: Environmental Science

Tuesday/08:40-09:25 **Thoma Saal** **Chair: Heino Nitsche**

08:40-09:25
Plenary talk

Radionuclide Biogeochemistry in the Nuclear Environmental Sciences.
Katherine Morris[1], Nicholas Bryan[1], Victoria Coker[1], Melissa Denecke[2], Gareth Law[1], Francis Livens[1], Jonathan Lloyd[1], Richard Pattrick[1], Sam Shaw[1], Pieter Bots[1], Diana Brookshaw[1], Timothy Marshall[1], Clare Thorpe[1], Adam Williamson[1]
[1]The University of Manchester, Manchester, M13 9PL, UK, [2]Karlsruhe Institute of Technology, Institut für Nukleare Entsorgung, Postfach 3640, 76021 Karlsruhe, Germany

Parallel session: Environmental Science

Tuesday/09:30-10:30 **Thoma Saal** **Chair: Heino Nitsche**

09:30-10:00
Invited talk

Actinide Environmental Science Utilizing Soft X-ray Synchrotron Radiation
David Shuh[1], Tolek Tyliszczak[1], Stefan Minasian[1,2], Stosh Kozimor[2], Tsuyoshi Yaita[3], Shinichi Suzuki[3]
[1]Lawrence Berkeley National Laboratory, Berkeley, CA 94720, USA, [2]Los Alamos National Laboratory, Los Alamos, NM 87545, USA, [3]Japan Atomic Energy Agency, SPRing-8, Hyogo, 67-5148, Japan

10:00-10:30
Invited talk

Plutonium reactivity at the mineral/water interface
Moritz Schmidt[1], Karah Knope[2], Sang Soo Lee[2], Francesco Bellucci[2], Richard Wilson[2], Joanne Stubbs[3], Peter Eng[3], Paul Fenter[2], L. Soderholm[2]
[1]Karlsruhe Institute of Technology, Institute for Nuclear Waste Disposal, Karlsruhe, Germany, [2]Argonne National Laboratory, Chemical Sciences and Engineering, Argonne, IL, USA, [3]University of Chicago, Consortium for Advanced Radiation Sources, Chicago, IL, USA

Parallel session: Chemistry

Tuesday/09:30-10:30 Hebel Saal Chair: Thorsten Stumpf

09:30-10:00
Invited talk

The role of phosphorous biochemistry in actinide human contamination
Claude Berthon[1], Marie Christine Charbonnel[1], Gaëlle Creff[3], Fabien Fontaine Vive[3], Domnique Guillaumont[1], Aurélie Jeanson[2], Sarah Mostapha[1], Lei Qi[1], Jérôme Roques[2], Samir Safi[2], Pier Lorenzo Solari[4], Claude Vidaud[1], Eric Simoni[2], Christophe Den Auwer[1]
[1]CEA Marcoule, Bagnols sur Cèze, France, [2]IPN Université Paris XI, Orsay, France, [3]ICN Université Nice Sophia Antipolis, Nice, France, [4]MARS Synchrotron Soleil, Saint Aubin, France

10:00-10:30
Invited talk

Radioecological Studies in Germany
Clemens Walther, Abdelouahed Daraoui, Beate Riebe, Stefan Bister
Leibniz University Hanover, Hannover, Germany

Coffee Break

Tuesday/10:30-11:00

Parallel session: Environmental Science

Tuesday/11:00-13:00 Thoma Saal Chair: Heino Nitsche

11:00-11:20

Sorption of uranium on lead hydrohyapatite
Karin Popa
'Alexandru Ioan Cuza' University, Iasi, Romania

11:20-11:40

A TRLFS study on the sorption of Cm(III) on natural kaolinite - The role of mineral dissolution in alkaline kaolinite suspensions
Nina Huittinen[1], Thomas Rabung[2], Andreas Schnurr[2], Martti Hakanen[1], Jukka Lehto[1], Horst Geckeis[2]
[1]Laboratory of Radiochemistry, Department of Chemistry, University of Helsinki, Helsinki, Finland, [2]Institute for Nuclear Waste Disposal, Karlsruhe Institute of Technology, Karlsruhe, Germany

11:40-12:00

Identification of Np(V) sorption complexes at the hematite-water interface studied by in-situ ATR FT-IR spectroscopy
Katharina Müller, Annett Gröschel
Helmholtz-Zentrum Dresden-Rossendorf e.V., Institute of Resource Ecology, Dresden, Germany

12:00-12:20

Characterisation of uranium minerals relevent to long term storage of spent nuclear fuel
Robert Baker[1], Aurora Walshe[1], Tonya Vitova[2]
[1]Trinity College, Dublin, Dublin, Ireland, [2]Karlsruhe Institute of Technology, Karlsruhe, Germany

12:20-12:40

Determining the Biogeochemical Mechanisms that Control Plutonium Transport
Annie Kersting[1], Mavrik Zavarin[1], Brian Powell[2], Pihong Zhao[1], James Begg[1], Zurong Dai[1], Ben Jacobsen[1], Mark Boggs[1]
[1]Lawrence Livermore National Laboratory, Livermore, CA, USA, [2]Clemson University, Clemson, SC, USA

12:40-13:00

Investigating the migration of trace levels of fallout plutonium and uranium in an ombrotrophic peat bog profile
Francesca Quinto[1], Erich Hrnecek[1], Michael Krachler[1], William Shotyk[2], Peter Steier[3], Stephan R. Winkler[3]
[1]European Commission Joint Research Centre, Institute for Transuranium Elements, P.O. Box 2340, 76125 Karlsruhe, Germany, [2]Department of Renewable Resources, University of Alberta, 839 General Services Building, Edmonton, AB, Canada T6G 2H1, Canada, [3]VERA Laboratory, Faculty of Physics, University of Vienna, Währinger Straße 17, A-1090 Vienna, Austria

Parallel session: Chemistry

Tuesday/11:00-13:00 Hebel Saal Chair: Marcus Altmaier

11:00-11:20 Thermodynamic investigation of the Th-U-Pu-O system
Ondrej Benes, Dario Manara, Octavian Valu, Robert Böhler, Rudy Konings
JRC-ITU, Karlsruhe, Germany

11:20-11:40 Influence of extreme conditions on the formation and structures of uranyl borates.
Evgeny V. Alekseev[1,2], Shijun Wu[3,4], Shuao Wang[5,6], Matthew Polinski[7], Wulf Depmeier[4], Thomas E. Albrecht-Schmitt[8]
[1]Institute of Energy and Climate Research (IEK-6), Forschungszentrum Jülich GmbH, Jülich, Germany, [2]Institut für Kristallographie, RWTH Aachen University, Aachen, Germany, [3]Guangzhou Institute of Geochemistry, Chinese Academy of Sciences, Guangzhou, China, [4]Institute of Geosciences, Kiel University, Germany, [5]Actinide Chemistry Group, Chemical Sciences Division, Lawrence Berkeley National Laboratory, Berkeley, California, USA, [6]Department of Chemistry, University of California, Berkeley, Berkeley, California, USA, [7]Department of Civil Engineering and Geological Sciences and Department of Chemistry and Biochemistry University of Notre Dame, Notre Dame, Indiana, USA, [8]Department of Chemistry and Biochemistry, Florida State University, Tallahassee, Florida, USA

11:40-12:00 Thermodynamic Study on the Complexation of Nd(III) and Cm(III) with Cyanex 301 in Ethanol
Chao Xu[1,2], Guoxin Tian[2], Linfeng Rao[2]
[1]Institute of Nuclear and New Energy Technology, Tsinghua University, Beijing, China, [2]Chemical Sciences Division, Lawrence Berkeley National Laboratory, Berkeley, CA, USA

12:00-12:20 Electrochemical behavior and speciation of thorium with fluorides in molten salt at high temperature
David Rodrigues, Sébastien Jaskierowicz, Sylvie Delpech
CNRS-IPNO, Orsay, France

12:20-12:40 Electrorefining of irradiated metallic fuel with limited Zr dissolution
Tsuyoshi Murakami[1], Tetsuya Kato[1], Tadafumi Koyama[1], Alcide Rodrigues[2], Michel Ougier[2], Jean-Paul Glatz[2]
[1]Central Research Institute of Electric Power Industry, Tokyo, Japan, [2]Institute of Transuranium Elements, Karlsruhe, Germany

12:40-13:00 Evaluation of stability of uranyl peroxide compounds in solution
Kwang-Wook Kim, Keun-Young Lee, Eil-Hee Lee, Dong-Yong Chung, Euo-Chang Jung, Jei-Kwon Moon
Korea Atomic Energy Research Institute, Daejeon, Republic of Korea

Lunch Break

Tuesday/13:00-14:30

Plenary session: Physics

Tuesday/14:30-15:15 Thoma Saal Chair: Peter Oppeneer

14:30-15-15 Plenary talk Recent Developments in $PuMGa_5$ and $PuMIn_5$ (M=Co, Rh) Heavy Fermion Superconductors
Eric Bauer
Los Alamos National Lab, Los Alamos, NM, USA

Parallel session: Physics

Tuesday/15:20-16:40 Thoma Saal Chair: Peter Oppeneer

15:20-15:50 Invited talk
5f electron correlations and core level photoelectron spectra of actinide compounds
Gertrud Zwicknagl
TU Braunschweig, Braunschweig, Germany

15:50-16:20 Invited talk
Diverse nature of 5*f* electrons in cage-compounds UT_2Zn_{20} and UT_2Al_{20}
Przemyslaw Swatek, Dariusz Kaczorowski
Institute of Low Temperature and Structure Research, Polish Academy of Sciences, Wroclaw, Poland

16:20-16:40
Amorphous 5*f* ferromagnet with high T_C: UH_3Mo_x
Ladislav Havela[1], Ilya Tkach[1], Zdenek Matej[1], Silvie Mašková[1], N.-T.H. Kim-Ngan[2], Alexander V. Andreev[3]
[1]Faculty of Mathematics and Physics, Charles University, Prague, Czech Republic, [2]Institute of Physics, Pedagogical University, Krakow, Poland, [3]Institute of Physics, Academy of Sciences, Prague, Czech Republic

Parallel session: Materials Science

Tuesday/15:20-16:40 Hebel Saal Chair: Takanari Ogata

15:20-15:50 Invited talk
Experimental and atomistic modelling studies of nuclear fuel cycle materials
Greg Lumpkin[1], Rob Aughterson[1], Dan Gregg[1], Eugenia Kuo[1], Simon Middleburgh[1], Meng Qin[1], Massey de los Reyes[1], Gordon Thorogood[1], Yingjie Zhang[1], Zhaoming Zhang[1], Marc Robinson[2], Nigel Marks[2]
[1]ANSTO, Sydney, NSW, Australia, [2]Curtin University of Technology, Perth, WA, Australia

15:50-16:20 Invited talk
Keeping Actinide Reactivity Under Surveillance Using Optical Fingerprinting
Louise Natrajan[1], Sean Woodall[1], Adam Swinburne[1], Simon Randall[1], Kurt Smith[1], Katherine Morris[1], Nicholas Bryan[1], Andrew Kerridge[2], Robert Baker[3], Emtithal Hashem[3]
[1]The University of Manchester, Manchester, UK, [2]University College London, London, UK, [3]Trinity College Dublin, Dublin, Ireland

16:20-16:40
Elastic Properties of Alpha Plutonium Measured Via Resonant Ultrasound Spectroscopy
Tarik Saleh, Adam Farrow, Franz Freibert
Los Alamos National Laboratory, Los Alamos, NM, USA

Coffee Break

Tuesday/16:40-17:10

Parallel session: Environmental Science

Tuesday/17:10-18:50 Thoma Saal Chair: Annie Kersting

17:10-17:40 Invited talk
Isotopic Composition of Uranium and Activity Concentration of $^{134, 137}Cs$ in Aerosol Samples Collected at 120 km from Fukushima before and after the Reactor Accidents
Taeko Shinonaga[1], Peter Steier[2], Markus Lagos[3], Takehisa Ohkura[4]
[1]Helmholtz Zentrum München, German Research Center for Environmental Health, Institute of Radiation Protection, Munich, Germany, [2]VERA Laboratory, Fakulität für Physik, Isotopenforschung, Universität Wien, Vienna, Austria, [3]Karlsruher Institut für Technologie (KIT), Institut für Nukleare Entsorgung, Karlsruhe, Germany, [4]Department of Radiation Protection, Nuclear Science Research Institute, Tokai Research and Development Center, Japan Atomic Energy Agency, Ibaraki, Japan

17:40-18:10
Invited talk

Interaction of plutonium with magnetite under anoxic conditions: Reduction, surface complexation, and structural incorporation
Andreas C. Scheinost[1], Regina Kirsch[1], Thomas Dumas[1], David Fellhauer[2], Xavier Gaona[3], Marcus Altmaier[3]
[1]HZDR Inst. for Resource Ecology, Dresden, Germany, [2]JRC Inst. for Transuranium Elements, Karlsruhe, Germany, [3]KIT Institut für Nukleare Entsorgung, Karlsruhe, Germany

18:10-18:30

Actinide Interactions with Ordered Mesoporous Carbon Materials
Heino Nitsche[1,2], Tashi Parsons-Moss[1,2], Harun Tüysüz[3], Jinxiu Wang[4], Deborah Wang[1,2], Stephen Jones[1,2], Daniel Olive[1], Erin Gantz[1,2], Dongyuan Zhao[4]
[1]University of California, Berkeley, Department of Chemistry, Berkeley, CA, USA, [2]Lawrence Berkeley National Laboratory, Nuclear Science Division, Berkeley, CA, USA, [3]Max-Planck-Institut für Kohlenforschung, Mülheim an der Ruhr, Germany, [4]Laboratory of Advanced Materials, Shanghai Key Laboratory of Molecular Catalysis and Innovative Materials, Department of Chemistry, Shanghai, China

18:30-18:50

Actinide Colloids in High Ionic-Strength Media
Donald Reed, Marian Borkowski, Michael Richmann, Jean-François Lucchini, Danielle Cleveland
Los Alamos National Lab, Carlsbad, NM, USA

Parallel session: Materials Science

Tuesday/17:10-18:50 Hebel Saal Chair: Takanari Ogata

17:10-17:40
Invited talk

First-principles modeling of nuclear fuels: strong 5f electron correlations and dispersive bonds
Emerson Vathonne[1], Michel Freyss[1], Marjorie Bertolus[1], Bernard Amadon[2]
[1]CEA, DEN, DEC, Centre de Cadarache, Saint-Paul-Lez-Durance, France, [2]CEA, DAM, DIF, DPTA, Arpajon, France

17:40-18:10
Invited talk

On the peculiarities of the DFT+U approach in the simulation of uranium dioxide
Matthias Krack
Paul Scherrer Institute, CH-5232 Villigen PSI, Switzerland

18:10-18:30

Thermodynamic stability of UO_2 surface by means of DFT+*U* calculations: interplay between polarity and overstoichiometry
François Bottin[1], Gérald Jomard[2], Grégory Geneste[1]
[1]CEA, DAM, DIF, Arpajon, France, [2]CEA, DEN, DEC, Saint-Paul-lez-Durance, France

18:30-18:50

Dissolution of innovative irradiated fuels: the case of HELIOS and CONFIRM
Gaël Ménard, Eva de Visser-Týnová
NRG, Petten, The Netherlands

Plenary session: Application Technologies

Wednesday/08:40-09:25 Thoma Saal Chair: Itzhak Halevy

08:40-09:25
Plenary talk

Actinides in Catalysis
Moris S. Eisen
Technion - Israel Institute of Technology, Haifa, Israel

Parallel session: Application Technologies

Wednesday/09:30-10:30 Thoma Saal Chair: Itzhak Halevy

09:30-10:00
Invited talk

Actinides in Scrap, Dirt and Deposits - A Challenge for Investigative Radiochemists
Klaus Mayer, Maria Wallenius, Magnus Hedberg, Zsolt Varga
European Commission JRC-ITU, Karlsruhe, Germany

10:00-10:30
Invited talk

New aspects in nuclear forensics. Aerial Radiation Monitoring before and after radiological event
Itzhak Halevy
NRCN, Beer-Sheva, Israel

Parallel session: Chemistry

Wednesday/09:30-10:30 Hebel Saal Chair: Marinella Mazzanti

09:30-10:00
Invited talk

How to build accurate macroscopic models of actinide ions in aqueous solvents?
Valérie Vallet[1], Florent Réal[1], Michael Trumm[2], Bernd Schimmelpfennig[2], Michel Masella[3]
[1]Université Lille 1 (Sciences et Technologies), PhLAM Institute, CNRS UMR 8523, Villeneuve d'Ascq, France, [2]Institut für Nukleare Entsorgung (INE), Karlsruher Institut für Technologie (KIT), Karlsruhe, Germany, [3]CEA Saclay, Laboratoire de Chimie du Vivant, Institut de biologie et de technologies de Saclay, CEA Saclay, Gif sur Yvette, France

10:00-10:30
Invited talk

Formation of New Exotic Curium Oxides CmO3 and CmO4 in the Gas Phase
Vladimir Domanov
JINR, Dubna, Moscow reg., Russia

Coffee Break

Wednesday/10:30-11:00

Parallel session: Materials Science

Wednesday/11:00-12:40 Thoma Saal Chair: Michel Freyss

11:00-11:20

Thermal conductivity measurement of $(Pu_{1-x},Am_x)O_2$ (x=0.03, 0.07)
Taku Matsumoto[1], Tatsumi Arima[1], Yaohiro Inagaki[1], Kazuya Idemitsu[1], Masato Kato[2], Kyoichi Morimoto[2], Masahiro Ogasawara[3]
[1]Kyushu university, Fukuoka, Japan, [2]Japan Atomic Energy Agency, Ibaraki, Japan, [3]Inspection development company, Ibaraki, Japan

11:20-11:40

Chemical Segregation of U-10wt.% Mo Fuel Foils During Simulated Bonding Cycles
Sven C. Vogel[1], Donald W. Brown[1], Maria Okuniewski[2]
[1]Los Alamos National Laboratory, Los Alamos, NM, USA, [2]Idaho National Laboratory, Idaho Falls, ID, USA

11:40-12:00

Insight Into The Mechanism Of Plutonium Hydride Formation
Patrick Allen, Long Dinh, William McLean, Scott McCall, Cheng Saw, John Haschke
Lawrence Livermore National Laboratory, Livermore, California, USA

12:00-12:20 *Ab initio* study of defect production and migration in thoria
William Weber[1,2], Haiyan Xiao[1], Bin Liu[2], Yanwen Zhang[2,1]
[1]University of Tennessee, Knoxville, TN, USA, [2]Oak Ridge National Laboratory, Oak Ridge, TN, USA

12:20-12:40 DFT Investigation of Uranium Oxides and Defect Structures
Nick Brincat[1], Steve Parker[1], Geoff Allen[2], Mark Storr[3]
[1]University of Bath, Bath, UK, [2]Interface Analysis Centre, University of Bristol, Bristol, UK, [3]AWE, Aldermaston, UK

Parallel session: Chemistry

Wednesday/11:00-12:40 Hebel Saal Chair: Marinella Mazzanti

11:00-11:20 The Redox Potential of Mendelevium (Md) Determined Atom-at-a-Time with a Flow Electrolytic Column
Matthias Schädel[1,2], Atsushi Toyoshima[1], Zijie Li[1], Masato Asai[1], Nozomi Sato[1], Takahiro Kikuchi[1], Yusuke Kaneya[1], Yoshihiro Kitatsuji[1], Kazuaki Tsukada[1], Yuichiro Nagame[1], Kazuhiro Ooe[1,3], Yoshitaka Kasamatsu[3], Yuka Kogoma[3], Atsushi Shinohara[3], Hiromitsu Haba[4], Julia Even[5]
[1]Japan Atomic Energy Agency (JAEA), Tokai, Japan, [2]GSI Helmholtzzentrum für Schwerionenforschung GmbH, Darmstadt, Germany, [3]Osaka University, Osaka, Japan, [4]RIKEN, Wako, Japan, [5]Mainz University, Mainz, Germany

11:20-11:40 The first successful ionization of Lr (Z=103) by a surface ionization technique
Tetsuya K. Sato[1], Masato Asai[1], Nozomi Sato[1], Kazuaki Tsukada[1], Atsushi Toyoshima[1], Sunao Miyashita[1], Kazuhiro Ooe[5], Matthias Schaedel[1], Yusuke Kaneya[2,1], Yuichiro Nagame[1], Akihiko Osa[1],
Shin-ichi Ichikawa[3], Thierry Stora[6], Jens Volker Kratz[4]
[1]Japan Atomic Energy Agency, Tokai, Japan, [2]Ibaraki University, Mito, Japan, [3]RIKEN, Wako, Japan, [4]Maintz University, Maintz, Germany, [5]Niigata University, Niigata, Japan, [6]CERN, Geneva, Switzerland

11:40-12:00 EXAFS Study of *f*-Elements Thiocianate Complexation
Marisol Janeth Lozano Rodriguez[1], Christophe Den Auwer[2], José Mustre de León[3]
[1]HELMHOLTZ Zentrum Dresden Rossendorf (HZDR), Institute of Resource Ecology, Dresden, Germany, [2]Université de Nice Sophia Antipolis, Institute de Chimie de Nice, Nice, France, [3]CINVESTAV, Mérida, Department of Physics, Mérida Yucatan, Mexico

12:00-12:20 Probing and Quantifying Orbital Mixing in f-Element Molecular Bonding
Matthias W. Loeble[1], Jason M. Keith[1], Paul H. Tobash[1], Brian L. Scott[1], Angela C. Olson[1], Stefan G. Minasian[1,2], Scott R. Daly[3], Kevin S. Boland[1], Eve Bauer[1], Kathy Dardenne[4], Joerg Rothe[4], Tonya Vitova[4], Tsu-Chien Weng[5], Dimosthenis Sokaras[5], Franz J. Freibert[1], Richard L. Martin[1], Enrique R. Batista[1], David L. Clark[1], Stosh A. Kozimor[1]
[1]Los Alamos National Laboratory, Los Alamos, New Mexico, USA, [2]Lawrence Berkeley National Laboratory, Berkeley, California, USA, [3]The George Washington University, Washington DC, USA, [4]Karlsruhe Institute of Technology (KIT), Karlsruhe, Baden-Wuerttemberg, Germany, [5]Stanford Synchrotron Radiation Lightsource (SSRL), Menlo Park, California, USA

12:20-12:40 Interaction of human serum transferrin with Cm(III) using Time-Resolved Laser Fluorescence Spectroscopy
Nicole Bauer[1,2], Petra Panak[2,1]
[1]Institute for Nuclear Waste Disposal (INE), Karlruhe Institute of Technology (KIT), Karlsruhe, Germany, [2]University of Heidelberg, Department of Physical Chemistry, Heidelberg, Germany

Poster session Chemistry, Environmental Science

Place your poster on the board indicated with your poster number.
Posters are on display for 2 days (Wednesday-Thursday)
Please remove your poster by 19:00, Thursday, 25 July at the latest

Wednesday/12:40-14:25 **Congress Center Karlsruhe**

Corner 1, Poster number 01-38

PS2-01 12:40-14:25 Chemistry
Study on the extracted complexes of purified Cyanex301 with Cm(III) and Ln(III) with spectrophotometry, fluorometry, and EXAFS
Guoxin Tian[1], Xihong He[1,2], Chao Xu[1,2], Linfeng Rao[1]
[1]Lawrence Berkeley National Laboratory, Berkeley, California, USA, [2]Tsinghua University, Beijing, China

PS2-02 12:40-14:25 Chemistry
Heavy metal extraction using advanced PUREX style partitioning systems
Kate Tucker[1], Robin Taylor[2], Clint Sharrad[1], Tamara Griffiths[1], Sarah Heath[1], Peter Kaden[3]
[1]The University of Manchester, Manchester, UK, [2]National Nuclear Lab, Cumbria, UK, [3]Karlsruhe Institute of Technology, Karlsruhe, Germany

PS2-03 12:40-14:25 Chemistry
Mechanism of $UO_2(NO_3)_2 \times 6H_2O$ Decomposition under Microwave Irradiation
Sergey Kulyukhin
Frumkin' Institute of Physical Chemistry and Electrochemistry, Russian Academy of Science, Moscow, Russia

PS2-04 12:40-14:25 Chemistry
Plutonium and uranium concentration from sea water
Sergey Kulyukhin[1], Irina Veleshko[2], Aleksander Veleshko[3]
[1]Frumkin' Institute of Physical Chemistry and Electrochemistry, Russian Academy of Science, Moscow, Russia, [2]Russian National Scientific Center "Kurchatov' Institute", Moscow, Russia, [3]Russian National Scientific Center "Kurchatov' Institute", Moscow, Russia

PS2-05 12:40-14:25 Chemistry
Interaction of UO_2^{2+} Aqueous Solutions with Sorbents Based on Modified Silica Gel Containing Cu, Ni, and Zn
Sergey Kulyukhin[1], Margarita Gorbacheva[2]
[1]Frumkin' Institute of Physical Chemistry and Electrochemistry, Russian Academy of Science, Moscow, Russia, [2]Frumkin' Institute of Physical Chemistry and Electrochemistry, Russian Academy of Science, Moscow, Russia

PS2-06 12:40-14:25 Chemistry
Discussion about the Universal Curves of Limiting Conductance of Electrolytes 1:3Study of Limiting Conductance of LaCl3, La(NO3)3 and TbCl3 in water-THF mixture (25% w)
Rafik Besbes[1], Abderabba Manef[2], Habib Latrous[3]
[1]Higher Institute of Education and Training – ISEFC 43, rue de la Liberté 2019 Tunisia, Le Bardo, Tunisia, [2]IPEST, route Sidi Bou Said,B.P:51 2075, La Marsa, Tunisia, [3]Faculté des Sciences de Tunis, 2092, El-Manar, Tunisia

PS2-07 12:40-14:25 Chemistry
Actinide colloids and nanoparticles: relevance to legacy waste, clean-up and geological disposal
Jennifer Rochford, Sarah Heath
University of Manchester, Manchester, UK

PS2-08 12:40-14:25 Chemistry
Arene-Actinide interactions in the Flexible Macrocyclic Ligand Environment of *trans*-Calix[2]benzene[2]pyrrolide
Joy Farnaby[1], Rebecca White[1], Michael Gardiner[2], Jason Love[1], Polly Arnold[1]
[1]University of Edinburgh, Edinburgh, UK, [2]University of Tasmania, Hobart, Australia

PS2-09 12:40-14:25 Chemistry
Optimization Criterions for H_2O-$UO_2(NO_3)_2$-TBP System.
Alexander Ochkin, Dmitriy Gladilov, Sergey Nekhaevskiy
D. Mendeleev University of Chemical Technology of Russia, Moscow, Russia

PS2-10 12:40-14:25 Chemistry
Dodecane effect on nitric acid extraction with TBP.
Alexander Ochkin, Dmitriy Gladilov, Sergey Nekhaevskiy
D. Mendeleev University of Chemical Technology of Russia, Moscow, Russia

PS2-11
12:40-14:25
Chemistry

Optical spectroscopy study into the bio-reduction of the uranyl(VI) ion and the uranyl(V) and uranium(IV) species generated.
Debbie Jones, Sean Woodall, Louise Natrajan, Adam Swinburne
University of Manchester, Manchester, UK

PS2-12
12:40-14:25
Chemistry

Luminescent properties of uranium complexes
Michael Andrews, Louise Natrajan, Adam Swinburne, Sean Woodall, Simon Randall
The University of Manchester, Manchester, UK

PS2-13
12:40-14:25
Chemistry

Vibrational spectroscopic study of some rare-earth metals trifluoromethylsulfonates enneahydrates and of corresponding salts of uranium(III) and curium(III)
Mikhail Skripkin[1], Patric Lindqvist-Reis[2], Christos Apostolidis[3], Reinhardt Klenze[2], János Mink[4]
[1]Saint-Petersburg State University, Saint-Petersburg, Russia, [2]Institut für Nukleare Entsorgung. Karlsruhe Institute of Technology, Karlsruhe, Germany, [3]Institute for Transuranium Elements, European Commission, Joint Research Centre, Karlsruhe, Germany, [4]Institute of Molecular Pharmacology, Research Centre of Natural Sciences, Hungarian Academy of Sciences, Budapest, Hungary

PS2-14
12:40-14:25
Chemistry

Self-assemblage of stable uranyl nano-clusters in the alkaline peroxide systems
Yingjie Zhang[1], Mohan Bhadbhade[2], Jason Price[3], Jiabin Gao[2], Inna Karatchevtseva[1], Gregory Lumpkin[1]
[1]Australian Nuclear Science & Technology Organisation, Sydney, Australia, [2]University of New South Wales, Sydney, Australia, [3]Australian Synchrotron, Melbourne, Australia

PS2-15
12:40-14:25
Chemistry

Structural studies of actinide complexes with picolinamide
Yingjie Zhang[1], Mohan Bhadbhade[2], Jiabin Gao[2], Inna Karatchevtseva[1], Gregory Lumpkin[1]
[1]Australian Nuclear Science & Technology Organisation, Sydney, Australia, [2]University of New South Wales, Sydney, Australia

PS2-16
12:40-14:25
Chemistry

Electrochemical and thermodynamic properties of uranium in low melting LiCl-KCl-CsCl eutectic
Dmitry Maltsev, Vladimir Volkovich, Evgeny Vladykin, Boris Vasin
Ural Federal University, Ekaterinburg, Russia

PS2-17
12:40-14:25
Chemistry

Synthesis and characterization of new heterometallic uranyl-based carboxylates
Christophe Volkringer, Ionut Mihalcea, Clement Falaise, Natacha Henry, Thierry Loiseau
University of Lille, Lille, France

PS2-18
12:40-14:25
Chemistry

TRLFS Study on the Complexation of Cm(III) and Eu(III) with methy-substituted Diglycolamides
Björn Beele[1,2], Andreas Wilden[3], Andrej Skerencak-Frech[2], Steve Lange[3], Fabian Sandowski[3], Giuseppe Modolo[3], Petra Panak[1,2], Mudassir Iqbal[4], Willem Verboom[4], Andreas Geist[2]
[1]Ruprecht-Karls-Universität Heidelberg, Physikalisch-Chemisches Institut, Heidelberg, Germany, [2]Karlsruher Institut für Technologie (KIT), Institut für Nukleare Entsorgung, Karlsruhe, Germany, [3]Forschungszentrum Jülich GmbH (FZJ), Institut für Energie- und Klimaforschung, Jülich, Germany, [4]University of Twente, Laboratory of Molecular Nanofabrication, Enschede, The Netherlands

PS2-19
12:40-14:25
Chemistry

Influence of the solvent on the complexation of Cm(III) with nPr-BTP studied by time-resolved laser fluorescence spectroscopy
Antje Bremer[1,2], Andreas Geist[1], Petra J. Panak[1,2]
[1]Karlsruhe Institute of Technology (KIT - Institute for Nuclear Waste Disposal (INE), Eggenstein-Leopoldshafen, Germany, [2]University of Heidelberg - Institute for Physical Chemistry, Heidelberg, Germany

PS2-20
12:40-14:25
Chemistry

Trivalent Lanthanide/Actinide Separation Using Aqueous-Modified TALSPEAK Chemistry
Travis Grimes, Leigh Martin
Aqueous Separations and Radiochemistry Department, Idaho National Laboratory, Idaho Falls, ID, USA

PS2-21
12:40-14:25
Chemistry

Solid Phase Extraction Materials for Separations of Actinides and Fission Products
Jennifer Shusterman, Eva Uribe, Tashi Parsons-Moss, Anthony Bruchet, Erin Gantz, Heino Nitsche
University of California, Berkeley, Berkeley, CA, USA

PS2-22
12:40-14:25
Chemistry

Effect of Hydrogen bonds on melting points and packing coefficients of uranyl nitrate complexes with cyclic urea derivatives

Tomoya Suzuki[1], Takeshi Kawasaki[1], Koichiro Takao[1], Masayuki Harada[1], Masanobu Nogami[2], Yasuhisa Ikeda[1]
[1]Tokyo Institute of Technology, Tokyo, Japan, [2]Kinki University, Osaka, Japan

PS2-23
12:40-14:25
Chemistry

Difference in the kinetics of Am(III) and Eu(III) extraction using TODGA in Ionic Liquid Medium

Maria Boltoeva, Ali Quadi, Sylvia Georg, Isabelle Billard
Université de Strasbourg, IPHC, Strasbourg, France

PS2-24
12:40-14:25
Chemistry

TALISMAN - Transnational Access to Large Infrastructures for a Safe Management of Actinides

Marcus Altmaier[1], S. Bourg[2], N. Bryan[3], P. Collings[4], N. Dacheux[5], B. Duplantier[6], Ch. Ekberg[7], D. Grolimund[8], L. Natrajan[3], Ch. Poinssot[2], Ph. Raison[9], T Schäfer[1], A.C. Scheinost[10], B. Schimmelpfennig[1]
[1]Karlsruhe Institute of Technology, Institute for Nuclear Waste Disposal, Karlsruhe, Germany, [2]Commissariat à l'Energie Atomique, Marcoule, France, [3]Centre for Radiochemistry Research, University of Manchester, Manchester, UK, [4]National Nuclear Laboratory, Sellafield, UK, [5]Centre National de la Recherche Scientifique, Paris, France, [6]LaGrange sarl (LGI Consulting), Paris, France, [7]Chalmers University of Technology, Gothenburg, Sweden, [8]Paul Scherrer Institut, Villigen, Switzerland, [9]Institute for Transuranium Elements, European Commission, Karlsruhe, Germany, [10]Helmholtz-Zentrum Dresden-Rossendorf, Dresden-Rossendorf, Germany

PS2-25
12:40-14:25
Chemistry

Curium-technetium complex oxide

Elena Pichuzhkina, Sergey Tomilin
JSC SSC "Research Institute of Atomic Reactors", Dimitrovgrad, Russia

PS2-26
12:40-14:25
Chemistry

UV-vis and fluorescence spectroscopic methods to evaluate the solution thermodynamic properties of hydroxypyridinonate actinide and lanthanide complexes

Manuel Sturzbecher-Hoehne, Gauthier Deblonde, Rebecca Abergel
Lawrence Berkeley National Laboratory, Berkeley, CA, USA

PS2-27
12:40-14:25
Chemistry

Receptor recognition of transferrin bound to f-block metals: a segregation step in cellular acquisition of actinides

Manuel Sturzbecher-Hoehne[1], Gauthier Deblonde[1], Christophe Goujon[1], Anne Mason[2], Rebecca Abergel[1]
[1]Lawrence Berkeley National Laboratory, Berkeley, CA, USA, [2]University of Vermont, Burlington, VT, USA

PS2-28
12:40-14:25
Chemistry

Actinide mixed oxide microspheres synthesis using Weak Acid Resin process: unconventional precursors for Minor Actinide Bearing Blanket fabrication

Sebastien Picart [1], Elodie Remy[1], Thibaud Delahaye[1], Isabelle Bisel[1], Olivier Dugne[1], Nicolas Clavier[2], Philippe Blanchart[3], André Ayral[4]
[1]CEA, Bagnols-sur-Cèze, France, [2]ICSM, Bagnols-sur-Cèze, France, [3]ENSCI, Limoges, France, [4]IEM, Montpellier, France

PS2-29
12:40-14:25
Chemistry

Thermodynamic evaluation of Np redox processes in dilute aqueous solutions at pH 4 - 10 under reducing conditions

David Fellhauer[1,3], Marcus Altmaier[1], Volker Neck[1], Xavier Gaona[1], Thierry Wiss[2], Markus Lagos[1], Jörg Runke[1,3], Thomas Fanghänel[2,3]
[1]Karlsruhe Institute of Technology, Institute for Nuclear Waste Disposal, Karlsruhe, Germany, [2]European Commission, JRC, Institute for Transuranium Elements, Karlsruhe, Germany, [3]Heidelberg University, Institute of Physical Chemistry, Heidelberg, Germany

PS2-30
12:40-14:25
Chemistry

Electronic Structure of Plutonium Dioxide

Yu. A. Teterin[1], K.I. Maslakov[1], M.V. Ryzhkov[2], A.Yu. Teterin[1], K.E. Ivanov[1], Vladimir G. Petrov[3], D.A. Enina[3], S.N. Kalmykov[3]
[1]NRC Kurchatov Institute, Moscow, Russia, [2]Institute of Solid State Chemistry UD RAS, Ekaterinburg, Russia, [3]Lomonosov Moscow State University, Moscow, Russia

PS2-31
12:40-14:25
Chemistry

Chemical Bond Nature in Neptunium Dioxide

Yu.A. Teterin[1], K.I. Maslakov[1], M.V. Ryzhkov[2], A.Yu. Teterin[1], K.E. Ivanov[1], Vladimir G. Petrov[3], D.A. Enina[3], S.N. Kalmykov[3]
[1]NRC Kurchatov Institute, Moscow, Russia, [2]Institute of Solid State Chemistry UD RAS, Ekaterinburg, Russia, [3]Lomonosov Moscow State University, Moscow, Russia

PS2-32 12:40-14:25 Chemistry
Synthesis and Characterization of U-doped Zircon and Baddeleyite
Vladimir G. Petrov, I.E. Vlasova, E.B. Furkina, M.V. Yevsunina, S.N. Kalmykov
Lomonosov Moscow State University, Moscow, Russia

PS2-33 12:40-14:25 Chemistry
Structure and spectroscopic evidence of hexavalent neptunyl and plutonyl mono- and dinitrate complexes in aqueous nitric acid
Patric Lindqvist-Reis[1], Christos Apostolidis[2], Olaf Walter[2], Remi Marsac[1], Nidhu Lal Banik[1], Mikhail Yu. Skripkin[3], Jörg Rothe[1], Alfred Morgenstern[2], Rachel Eloirdi[2]
[1]Institut für Nukleare Entsorgung. Karlsruhe Institute of Technology, Karlsruhe, Germany, [2]Institute for Transuranium Elements, European Commission, Joint Research Centre, Karlsruhe, Germany, [3]Department of Chemistry, St. Petersburg State University, St. Petersburg, Russia

PS2-34 12:40-14:25 Chemistry
Raman Spectroscopic Study on Uranyl and Neptunyl Complexes in Concentrated Chloride Solutions
Toshiyuki Fujii[1], Akihiro Uehara[1], Yoshihiro Kitatsuji[2], Hajiumu Yamana[1]
[1]Research Reactor Institute, Kyoto University, Osaka, Japan, [2]Nuclear Science and Engineering Directorate, Japan Atomic Energy Agency, Ibaraki, Japan

PS2-35 12:40-14:25 Chemistry
Development of a simplified soft-donor technique for trivalent actinide-lanthanide separations.
Madeleine Langford Paden[1], Louise Natrajan[1], Clint Sharrad[1], Leigh Martin[2], Sarah Hendley[1]
[1]The University of Manchester, Manchester, UK, [2]Idaho National Laboratory, Idaho, USA

PS2-36 12:40-14:25 Chemistry
Understanding molecular speciation of actinides in the PUREX process
Tamara Griffiths[1], Kate Tucker[1], Clint Sharrad[1], Francis Livens[1], Leigh Martin[2], Peter Kaden[3]
[1]University of Manchester, Manchester, UK, [2]Idaho National Laboratory, Idaho, USA, [3]Karlsruher Institut für Technologie, Institut für Nukleare Entsorgung, Eggenstein-Leopoldshafen, Germany

PS2-37 12:40-14:25 Chemistry
In-situ XAFS analysis of electrochemical reduction of uranium(VI) in highly concentrated LiCl
Akihiro Uehara[1], Toshiyuki Fujii[1], Hajimu Yamana[1], Yoshihiro Okamoto[2]
[1]Research Reactor Institute, Kyoto University, Osaka, Japan, [2]Nuclear Science and Engineering Directorate, Japan Atomic Energy Agency, Ibaraki, Japan

PS2-38 12:40-14:25 Chemistry
Selective recovery of actinides from An-Zr-fuel by electrorefining in molten LiCl-KCl
Roland Meier[1,2], Pavel Souček[1], Rikard Malmbeck[1], Claux Bennoit[1], Jean-Paul Glatz[1], Thomas Fanghaenel[1,2]
[1]European Commission, JRC Institute for Transuranium Elements, Karlsruhe, Germany, [2]Heidelberg University, Institute of Physical Chemistry, Heidelberg, Germany

Corner 2, Poster number 39-76

PS2-39 12:40-14:25 Chemistry
Actinide extraction and complexation properties of oxygen-nitrogen hetero donor ligand PTA
Tohru Kobayashi, Shinichi Suzuki, Hideaki Shiwaku, Tsuyoshi Yaita
Japan Atomic Energy Agency, 1-1-1 Koto, Sayo-cho, Sayo-gun, Hyogo, Japan

PS2-40 12:40-14:25 Chemistry
Formation of actinide(IV) carboxylate complexes in aqueous solution - the unexpected predominance of hexanuclear species
Christoph Hennig[1,5], Koichiro Takao[2], Shinobu Takao[3], Stephan Weiss[1], Werner Kraus[4], Franziska Emmerling[4], Andreas C. Scheinost[1,5]
[1]Helmholtz-Zentrum Dresden-Rossendorf, Institute of Resource Ecology, Dresden, Germany, [2]Department of Materials and Life Science, Seikei University, Tokyo, Japan, [3]Department of Engineering Science, University of Electro-Communications, Tokyo, Japan, [4]BAM Federal Institute for Materials Research and Testing, Berlin, Germany, [5]The Rossendorf Beamline at ESRF, Grenoble, France

PS2-41 12:40-14:25 Chemistry
XAFS and solubility investigations of penta- and hexavalent actinides in dilute to concentrated salt brines
Jörg Rothe[1], Kathy Dardenne[1], David Fellhauer[1,2], Xavier Gaona Martinez[1], Marcus Altmaier[1], Thomas Fanghänel[2]
[1]Karlsruhe Institute of Technology, Institute for Nuclear Waste Disposal (INE), Karlsruhe, Germany, [2]JRC Institute for Transuranium Elements (ITU), Karlsruhe, Germany

PS2-42
12:40-14:25
Chemistry

Preparation, phase composition, microstructure and electrochemical properties of UPd_3 and URu_3 in the solutions of nitric acid

Semen Zavarzin[1], Alexandre Maslennikov[2], Alexandre Osipenko[2], Alexandre Maershin[2], Irina Vlasova[3], Andrei Shiryaev[1]
[1]A.N. Frumkin Institute of Physical Chemistry and Electrochemistry of Russian Academy of Sciences, Moscow, Russia, [2]Open joint stock company State Scientific Research Institute of Atomic Reactors, Dimitrovgrad, Russia, [3]M.V. Lomonosov Mowcow State University, Chemistry Dept., Moscow, Russia

PS2-43
12:40-14:25
Chemistry

Redox Mechanism of Nd(III) Ions in High Temperature LiCl-KCl Eutectic Observed by UV-Vis Absorption Spectroscopy in Combination of Electrolysis

Seung Park, Jong-Il Yun
KAIST, Daejeon, Republic of Korea

PS2-44
12:40-14:25
Chemistry

Investigation of Plutonium Trifluoride Solubility in Molten Fluorides

Alexander Maershin, Alexander Osipenko, Andrey Lizin
Research Institute of Atomic Reactors, Dimitrovgrad-10, Russia

PS2-45
12:40-14:25
Chemistry

Investigation in field of partitioning of minor actinides and rare elements in chloride melt

Alexander Maershin, Alexander Osipenko, Mikhail Kormilitsyn
Research Institute of Atomic Reactors, Dimitrovgrad-10, Russia

PS2-46
12:40-14:25
Chemistry

Coordination Chemistry of Actinides with Hydroxamic Siderochelates

Alejandra Sornosa Ten, Pawel Jewula, Lé Vi Nguyen, Mélanie Bourdillon, Stéphane Brandès, Christine Stern, Jean-Claude Chambron, Michel Meyer
Institut de Chimie Moléculaire de l'Université de Bourgogne (ICMUB, DIJON, France

PS2-47
12:40-14:25
Chemistry

Preparation, stabilization, spectroscopic, computational studies of tetravalent protactinium in aqueous solution

Nidhu Banik[1], Christian Marquardt[1], Marcus Altmaier[1], Clemens Walter[1], Jörg Rothe[1], Bernd Schimmelpfennig[1], Florent Réal[2], Valérie Vallet[2]
[1]Karlsruhe Institute of Technology (KIT), Institute for Nuclear Waste Disposal (INE), Karlsruhe, Germany, [2]University Lille1, CNRS, PhLAM Institute, Villeneuve d'Ascq, France

PS2-48
12:40-14:25
Chemistry

The Thermodynamics of Extraction of Lanthanides and Actinides by Solvating and Ion-Exchanging Ligands: A Comparative Study

Leigh Martin, Peter Zalupski, Travis Grimes
Idaho National Laboratory, Idaho Falls, Idaho, USA

PS2-49
12:40-14:25
Chemistry

Radiolysis of adsorbed water on actinides oxides surface: investigations on the surface state evolution by hydration

Jérémy Gaillard[1], Laurent Venault[1], Philippe Moisy[1], Jackie Vermeulen[1], Rachel Calvet[2], Nicolas Clavier[3]
[1]CEA Marcoule/DRCP, Bagnols sur Cèze, France, [2]b Université de Toulouse, Mines Albi, CNRS, Centre RAPSODEE, Albi, France, [3]ICSM-UMR5257, Bagnols sur Cèze, France

PS2-50
12:40-14:25
Chemistry

Effect of trivalent dopant, Gd^{3+}, on the reaction of $U_{1-y}Gd_yO_2$ and Cs_2O

Jong-Goo Kim, Eun-Sil Jang, Yang-Soon Park, Yeong-Keong Ha, Kyuseok Song
Korea Atomic Energy Research Institute, Daejeon, Republic of Korea

PS2-51
12:40-14:25
Chemistry

Apparent Solubility of Thorium in the Presence of Humic Substances

Takayuki SASAKI, Yuka MATSUURA, Taishi KOBAYASHI, Ikuji TAKAGI, Hirotake MORIYAMA
Kyoto University, Kyoto, Japan

PS2-52
12:40-14:25
Chemistry

Temperature Effect on the Solubility and Solid Phase Stability of Thorium Hydroxide

Taishi Kobayashi, Takayuki Sasaki, Ikuji Takagi, Hirotake Moriyama
Kyoto University, Kyoto, Japan

PS2-53
12:40-14:25
Chemistry

EXAFS investigation of substituent effect of the hybrid type PDA complexes for actinides and lanthanides separation.

Hideaki Shiwaku, Toru Kobayashi, Yoshihiro Okamoto, Shin-ichi Suzuki, Tsuyoshi Yaita
Japan Atomic Energy Agency, Sayo, Hyogo, Japan

PS2-54
12:40-14:25
Chemistry

Mathematical model for crystallization purification of uranyl nitrate hexahydrate in continuous crystallization column

Vladimir Kascheev, Olga Shmidt, Pavel Poluektov, Svetlana Tretyakova
Bochvar Institute (VNIINM), Moscow, Russia

PS2-55
12:40-14:25
Chemistry

Sulfurization behaviour of uranium and zirconium oxides with CS_2
Yuhei Fukuda, Akira Kirishima, Nobuaki Sato
Institute of Multidisciplinary Research for Advanced Materials, Tohoku University, Sendai, Japan

PS2-56
12:40-14:25
Chemistry

Nuclear Fallout Debris Formation and Fractionation in Aerodynamic Particles
Kiel Holliday[1], Mischa Monroe[2], Richard Gostic[1], John McClory[2], Ian Hutcheon[1]
[1]Lawrence Livermore National Lab, Livermore, CA, USA, [2]Air Force Institute of Technology, Dayton, OH, USA

PS2-57
12:40-14:25
Chemistry

Complexation of actinides by the 1,4,7,10-tetraazacyclododecane-1,4,7,10-tetraacetic acid (DOTA)
Matthieu Audras, Laurence Berthon, Claude Berthon, Nicole Zorz, Dominique Guillaumont, Thomas Dumas, Philippe Moisy
CEA Marcoule, Bagnols-sur-Cèze, France

PS2-58
12:40-14:25
Chemistry

Evidence for covalence in a *N*-donor complex of Americium(III)
Peter Kaden[1], Christian Adam[1,2], Björn B. Beele[1,2], Udo Müllich[1], Sascha Trumm[1], Andreas Geist[1], Petra J. Panak[1,2], Melissa A. Denecke[1]
[1]Karlsruhe Institute of Technology (KIT), Institute for Nuclear Waste Disposal (INE), Karlsruhe, Germany, [2]University of Heidelberg, Department of Physical Chemistry, Heidelberg, Germany

PS2-59
12:40-14:25
Chemistry

Towards stability rules of extractants involve in minor actinides partitioning processes: Study of TODGA degraded samples under different experimental conditions.
Hitos Galán[1], Ana Nuñéz[1], Amparo G. Espartero[1], Aritz Durana[2], Javier de Mendoza[2], Joaquín Cobos[1]
[1]Centro de Investigaciones Energéticas, Medioambientales y Tecnológicas (CIEMAT), Madrid, Spain, [2]Institute of Chemical Research of Catalonia (ICIQ), Tarragona, Spain

PS2-60
12:40-14:25
Chemistry

Structural and Spectroscopic studies of Mononuclear Uranyl(VI) Complex Containing O,O,N,N-tetradentate ligand
Mohammad Azam, Saud Al-Resayes
King Saud University, Riyadh, Saudi Arabia

PS2-61
12:40-14:25
Chemistry

Temperature and Ionic Strength Effects on Neptunium Speciation in Simplified Brine Systems
Donald Reed, Marian Borkowski, Michael Richmann,
Jean-François Lucchini
Los Alamos National Lab, Carlsbad, NM, USA

PS2-62
12:40-14:25
Chemistry

Scanning phase diagrams to discover new phases with original properties: Examples from U-T Ge (T = Fe, Co, Ru) ternary systems.
Olivier Tougait[1], Mathieu Pasturel[1], David Berthebaud[1,4], Arnaud Soude[1], Thierry Roisnel[1], Margarida Henriques[2], Antonio Goncalves[2], Adam Pikul[3], Dariusz Kaczorowski[3]
[1]ICSR/CSM, UMR 6226, CNRS-Université de Rennes1, Rennes, France, [2]IST/ITN, Universidade Técnica de Lisboa, Sacavém, Portugal, [3]INTiBS PAN, Wroclaw, Poland, [4]CRISMAT, UMR CNRS 6508, Caen, France

PS2-63
12:40-14:25
Chemistry

Some progress made in f-element chalcogenide chemistry
Jean-Marie Babo, Peter C. Burns
University of Notre Dame, Notre Dame, IN, USA

PS2-64
12:40-14:25
Envir. Sci

The Hydrothermal Behavior of Depleted Uranium Oxides
Tatiana Kazakovskaya[1], Elena Zakharova[2], Vyacheslav Shapovalov[1]
[1]Russian Federal Nuclear center –All-Russia Scientific Institute of Experimental Physics, Sarov, Russia, [2]Institute of Physical and Electro- Chemistry, Russian Academy of Sciences, Moscow, Russia

PS2-65
12:40-14:25
Envir.Sci.

New Ionic Liquid compounds for liquid/liquid extraction of actinides and other metallic ions
Dariia Ternova[1,2], Isabelle Billard[1], Valérie Mazan[1], Ali Ouadi[1], Stanislav Miroshnychenko[2], Vitaly Kalchenko[2]
[1]CNRS and Université de Strasbourg, Strasbourg, France, [2]Institute of organic chemistry, NAS of Ukraine, Kiev, Ukraine

PS2-66
12:40-14:25
Envir.Sci.

Chemiluminescence specroscopy of actinides and lanthanides in solutions
Igor Izosimov[1], Nikolai Firsin[2], Nikolai Gorshkov[2], Vladimir Mikhalev[2], Sergei Nekhoroshkov[2]
[1]Joint Institute for Nuclear Research, Dubna, Moscow region, Russia, [2]Khlopin Radium Institute, St. Petersburg, Russia

PS2-67
12:40-14:25
Envir.Sci.

The fate of uranium and technetium during magnetite crystallisation at hyperalkaline pH

Timothy Marshall[1], Katherine Morris[1], Gareth Law[2], Frederick Mosselmans[3], Samuel Shaw[1]
[1]Research Centre for Radwaste and Decommissioning and Williamson Research Centre, School of Earth, Atmospheric and Environmental Sciences, The University of Manchester, Manchester, UK, [2]Centre for Radiochemistry Research and Research Centre for Radwaste and Decommissioning, School of Chemistry, The University of Manchester, Manchester, UK, [3]Diamond Light Source Ltd., Diamond House, Harwell Science and Innovation Campus, Didcot, Oxfordshire, UK

PS2-68
12:40-14:25
Envir.Sci.

Purification and separation of U, Pu and Am isotopes in environmental samples by extraction chromatography for alpha-spectrometry analyses

Silvia Stoica, Cristian Dulama, Alexandru Toma, Cristina Ciocirlan, Relu Dobrin
Institute for Nuclear Research, Pitesti, Romania

PS2-69
12:40-14:25
Envir.Sci.

Biogeochemistry of uranium in the southern Baltic ecosystem

Alicja Borylo, Bogdan Skwarzec, Grzegorz Olszewski
University of Gdańsk, Pomorskie, Poland

PS2-70
12:40-14:25
Envir.

The radiochemical contamination (^{234}U and ^{238}U) of zone around phosphogypsum waste heap in Wiślinka (northern Poland)

Grzegorz Olszewski, Alicja Borylo, Bogdan Skwarzec
University of Gdańsk, Pomorskie, Poland

PS2-71
12:40-14:25
Envir.Sci.

^{241}Pu in the southern Baltic Sea

Dagmara Struminska-Parulska, Grzegorz Olszewski, Bogdan Skwarzec
University of Gdańsk, Pomorskie, Poland

PS2-72
12:40-14:25
Envir.Sci.

Study of the behaviors and the transfers of $^{238,239+240}$Pu and ^{241}Am in different natural compartments (soil, water, sediment)

Amélie Leclercq[1], Violaine Philippini[1], Christophe Den Auwer[1], Hervé Michel[1], Tiina-Leena Lavonen[1,2], Pier Lorenzo Solari[3], Samir Safi[4], Vittorio Barci[1], Geneviève Barci-Funel[1]
[1]Université de Nice-Sophia Antipolis, Institut de Chimie de Nice, UMR CNRS 7272, PCRE, Nice, Alpes Maritimes, France, [2]Laboratory of Radiochemistry, Falculty of Science, University of Helsinki, Helsinki, Finland, [3]Synchrotron SOLEIL, MARS beam line, Gif sur Yvette, France, [4]Université Paris Sud, Institut de Physique Nucléaire d'Orsay, Orsay, France

PS2-73
12:40-14:25
Envir.Sci.

Sorption Characteristics of the Rocks Confining a Radioactive Waste Repository

Yulia Konevnik
IPHE RAS, Moscow, Russia

PS2-74
12:40-14:25
Envir.Sci.

Romanian perspective on iron nano-particles utilization as remediators for radioactive polluted environment

Ioana-Carmen Popescu[1], Eugenia Panturu[1], Antoneta-Constantina Olteanu-Filcenco[1], Thomas Bleigh Scott[2], Richard Andrew Crane[2]
[1]R&D National Institute for Metals and Radioactive Resources, Bucharest, Romania, [2]Interface Analysis Centre, University of Bristol, Bristol, UK

PS2-75
12:40-14:25
Envir.Sci.

New insights into uranyl interaction with proteins at physiological pH

Quentin Raffy, Isabelle Billard, Catherine Galindo, Mireille Del Nero,
Rémi Barillon
Université de Strasbourg, IPHC, CNRS, UMR7178, 67037 Strasbourg, France

PS2-76
12:40-14:25
Envir.Sci.

Uranium(VI) sorption on aluminium(hydr)oxides - inferring a functional relationship between sorption complex structures and physicochemical parameters by application of artificial neural networks

André Rossberg[1,2], Andreas C. Scheinost[1,2]
[1]Helmholtz-Zentrum Dresden-Rossendorf e.V. (HZDR), Dresden, Germany, [2]The Rossendorf Beamline at ESRF (ROBL)), Grenoble, France

Parallel session: Physics

Wednesday/14:30-15:15 Thoma Saal Chair: Paolo Santini

14:30-14:50 The UCoGe ferromagnetic superconductor: results from HRTEM studies
Antonio P. Goncalves[1], Margarida S. Henriques[1], Elsa B. Lopes[1], Laura C.J. Pereira[1], Arne Janssen[2], Thierry Wiss[2], Silva Maskova[3], Jan Prokleska[3], Ladislav Havela[3]
[1]IST/ITN, Technical University of Lisbon, CFMC-UL, 2686-953-Sacavém, Portugal, [2]European Commission, Joint Research Centre, Institute for Transuranium Elements, D-76125 Karlsruhe, Germany, [3]Dept. Condensed Matter Physics, Faculty of Mathematics and Physics, Charles University, 121 16 Prague, Czech Republic

14:50-15:10 New Uranium Heavy Fermion Antiferromagnet, γ>400 mJ/UmolK^2
Greg Stewart, Jungsoo Kim
Physics University of Florida, Gainesville, Florida, USA

Parallel session: Chemistry

Wednesday/14:30-15:15 Hebel Saal Chair: Tsuyoshi Yaita

14:30-14:50 Thermal stability of ammonium actinide(IV) nitrate
Guillaume Peter Soldani[1,2], Eléonore Welcomme[1], Catherine Renard[2], Stéphane Grandjean[1], Francis Abraham[2]
[1]CEA Marcoule, Bagnols sur Cèze, France, [2]UCCS, Université Lille Nord de France, Villeneuve d'Ascq, France

14:50-15:10 Promising alloy for separation actinides from lanthanides in molten salt - liquid metal system
Alexander Osipenko[1], Valeri Smolenski[2], Alena Novoselova[2], Alexander Maershin[1], Mikhail Kormilitsyn[1]
[1]Reasearch Institute of Atomic Reactors, Dimitrovgrad, Russia, [2]Institute of High-Temperature Electrochemistry, Ekaterinburg, Russia

Parallel session: Physics

Wednesday/15:20-16:20 Thoma Saal Chair: Paolo Santini

15:20-15:50 Invited talk Observation of ^{239}Pu NMR in PuO_{2-x} – Facts and Perspective –
Hiroshi Yasuoka, Geogios Koutroulakis, Scott Richmond, Kirk Veirs, Eric Bauer, Joe Thompson, Jarvinen Gordon, David Clark
Los Alamos National Laboratory, Los Alamos, NM, USA

15:50-16:20 Invited talk High quality single crystal growth and electronic state investigation of actinide intermetallic compounds
Yoshinori Haga
Japan Atomic Energy Agency, Tokai, Ibaraki, Japan

Parallel session: Application Technologies

Wednesday/15:20-16:20 Hebel Saal Chair: Klaus Mayer

15:20-15:50 Invited talk Synthesis and characterisation of minor actinide fuels and compounds
Joseph Somers
JRC-ITU, Karlsruhe, Germany

15:50-16:20 Invited talk Recent developments on the evaluation of spent fuel as a waste form.
Kastriot Spahiu[1,2]
[1]SKB, Stockholm, Sweden, [2]Chalmers University of Technology, Göteborg, Sweden

17:30 Transfer by tram to Ettlingen Stadthalle. (Friedrichstraße 14, 76275 Ettlingen)

Special tram **"Sonderfahrt" Departure at 17:30** from tram stop "Konzerthaus", (tram stationed on the middle-rails).

Arrival to Tram stop S1/S11 S-Bahn S1 / S-Bahn S11 "Ettlingen Stadt".

If you miss the direct tram, take tram S-Bahn S1 / S-Bahn S11 from "Kongresszentrum" Direction: Ettlingen, Ittersbach, Bad Herrenalb. Get off at "Ettlingen Stadt".

Reception, snack buffet at Ettlingen Stadthalle (Friedrichstraße 14, 76275 Ettlingen)
Wednesday/17.45-18:15 Refer to ANNEX 2

Hélène Langevin-Joliot: *"Marie Curie and her time"*
Wednesday/18:15-19:15 Ettlingen Stadthalle **Chair: Gerard H. Lander**

Norma Raccichini's Aria recital, accompanied by Pietro Salvaggio
Wednesday/19:30-20:30 Ettlingen Stadthalle

Plenary session: Materials Science

Thursday/08:40-09:25 Thoma Saal Chair: Ian Farnan

08:40-09:25
Plenary talk

Development Issues of Metal Fuels for Fast Reactors
Takanari Ogata
Central Research Institute of Electric Power Industry, Komae, Tokyo, Japan

Parallel session: Materials Science

Thursday/09:30-10:30 Thoma Saal Chair: Ian Farnan

09:30-10:00
Invited talk

Surface Science Study of Spent Fuel Corrosion Processes using Thin Films Model Systems
Thomas Gouder
EC-JRC-ITU, Karlsruhe, Germany

10:00-10:30
Invited talk

Spectroscopic characteristics of U(VI)-lanthanide(III) complexes adsorbed onto a silica surface and U(VI)-carbonate complexes in aqueous solutions
Euo Chang Jung, Kyoung Kyun Park, Hee-Jung Im, Wansik Cha, Hye-Ryun Cho, Kwang-Wook Kim
Korea Atomic Energy Research Institute, Daejeon, Republic of Korea

Parallel session: Chemistry

Thursday/09:30-10:30 Hebel Saal Chair: Polly Arnold

09:30-10:00
Invited talk

Recent progress in the synthesis, properties, and applications of uranyl peroxide nanoscale cage clusters
Peter Burns
University of Notre Dame, Notre Dame, IN, USA

10:00-10:30
Invited talk

Uranium sorption onto single mineral phases - approaching consistency and robustness
Vinzenz Brendler
Helmholtz-Zentrum Dresden-Rossendorf, Dresden, Germany

Coffee Break

Thursday/10:30-11:00

Parallel session: Materials Science

Thursday/11:00-13:00 Thoma Saal Chair: Corwin Booth

11:00-11:20

Solid state phase transformation study on Pu-Ga alloys containing 0.18 to 0.63 wt.% Ga
Michael Ling, Nigel Park
AWE, Reading, UK

11:20-11:40

Kinetic study of delta to alpha' isothermal martensitic transformation in PuGa 1at%
Fanny Lalire[1], Brice Ravat[1], Aurélien Perron[1], Benoit Oudot[1], Elisabeth Aeby-Gautier[2], François Delaunay[1]
[1]CEA, Is sur Tille, France, [2]École des Mines, Nancy, France

11:40-12:00

The effects of thermal conditioning and recovery processes on the δ →γ phase transformation mechanisms in plutonium.
Sue Ennaceur
AWE, Reading, UK

12:00-12:20 The unique solid-state NMR facility at JRC-ITU for the study of highly radioactive compounds
Laura Martel[1], Jean-Christophe Griveau[1], Chris Selfslag[1], Jacobus Boshoven[1], Olivier Pauvert[1], Ian Farnan[2], Joseph Somers[1]
[1]JRC-ITU, Karlsruhe, Germany, [2]University of Cambridge, Cambridge, UK

12:20-12:40 Raman spectroscopic characteristics of stoichiometric and non-stoichiometric uranium oxides
Gan Li, Wenhua Luo, Junbo Lv
China Academy of Engineering Physics, Mianyang, China

12:40-13:00 SIMS analysis of hydrogen and carbon co-precipitation in uranium and SEM/FIB analysis of its effect on surface reactions.
Patrick Allen, Ian Hutcheon, Jenny Matzel, Wigbert Siekhaus, Nick Teslich, Peter Weber
Lawrence Livermore National Laboratory, Livermore, CA, USA

Parallel session: Chemistry

Thursday/11:00-13:00 Hebel Saal Chair: Polly Arnold

11:00-11:20 Molecular and 3D hybrid architectures with tetravalent uranium
Clément Falaise, Christophe Volkringer, Natacha Henry, Thierry Loiseau
University of Lille, Lille, France

11:20-11:40 Oxidation state and aromaticity in f-element metallocenes $M(C_8H_8)_2$
Cina Foroutan-Nejad[2], Andy Kerridge[1]
[1]University College London, London, UK, [2]Masaryk University, Brno, Czech Republic

11:40-12:00 Separation of ^{225}Ac from radionuclides generated by proton irradiation of natural thorium using extraction chromatography
Elena Lapshina[1], Stanislav Ermolaev[1], Boris Zhuikov[1], Stepan Kalmykov[2], Ramiz Aliev[2], Valentina Ostapenko[2], Alexander Vasiliev[2]
[1]Institute for Nuclear Research of Russian Academy of Sciences, Moscow, Russia, [2]Lomonosov Moscow State University, Moscow, Russia

12:00-12:20 Americium and Plutonium Purification by Extraction (the AMPPEX process)
Mark Sarsfield[1], Keith Stephenson[2], Katie Bell[1], Jamie Brown[1], Michael Carrott[1], Colin Gregson[1], Christopher Maher[1], Chris Mason[1], Robin Taylor[1]
[1]National Nuclear Laboratory, Sellafield, Cumbria, UK, [2]European Space Agency, Noordwijk, The Netherlands

12.20-12:40 Separation of Americium alone from a Concentrated Raffinate by Liquid-Liquid Extraction
Cécile Marie, Marie-Thérèse Duchesne, Vincent Pacary, Vincent Vanel, Marc Montuir, Manuel Miguirditchian
CEA (DRCP/SMCS/LEPS), Bagnols-sur-Cèze, France

12:40-13:00 Spectroscopic study of redox behaviour of neptunium ions in molten LiCl-KCl eutectic
Tae-Hong Park, Dae-Hyeon Kim, Sang-Eun Bae, Jong-Yun Kim, Young-Hwan Cho, Jei-Won Yeon, Kyuseok Song
Korea Atomic Eenergy Research Institute, Daejeon, Republic of Korea

Lunch Break

Thursday/13:00-14:25

Plenary session: Chemistry

Thursday/14:40-15:15 Thoma Saal Chair: David K. Shuh

14:30-15-15 Plenary talk Recent Advances in Aqueous Neptunium Chemistry and Thermodynamics
Marcus Altmaier
Karlsruhe Institute of Technology, Institute of Nuclear Waste Disposal, Karlsruhe, Germany

Parallel session: Materials Science

Thursday/15:20-16:40 Thoma Saal Chair: Thomas Gouder

15:20-15:50
Invited talk

Uranyl speciation at the water/mineral interface: XPS, TRLFS and XAFS studies
Annick Froideval Zumbiehl[1], Mireille Del Nero[2], Rémi Barillon[2], Clotilde Gaillard[3], Klaus Lützenkirchen[4], Jean Hommet[5], Jean-Louis Hazemann[6]
[1]Paul Scherrer Institute, Nuclear Energy and Safety Research Department, Villigen, Switzerland, [2]Institut Pluridisciplinaire Hubert Curien, , Département de Recherches Subatomiques, Strasbourg, France, [3]University of Lyon, Institut de Physique Nucléaire de Lyon, Villeurbanne, France, [4]European Commission Joint Research Centre, Institute for Transuranium Elements, Karlsruhe, Germany, [5]Centre National de la Recherche Scientifique, Laboratoire de Physique Corpusculaire, Caen, France, [6]Institut Néel, Grenoble, France

15:50-16:20
Invited talk

Dynamics and speciation in molten actinide fluorides
Catherine Bessada[1], Louis Maksoud[1], Vincent Sarou-Kanian[1], Haruaki Matsuura[2], Anne Laure Rollet[3], Christian Simon[3], Mathieu Salanne[3], Mathieu Gibilaro[4], Laurent Massot[4], Pierre Chamelot[4]
[1]CEMHTI CNRS, Orleans, France, [2]Tokyo Institute of Technology, Tokio, Japan, [3]PECSA CNRS UPMC, Paris, France, [4]LGC, Toulouse, France

16:20-16:40

Relative thermodynamic stability of radiation defect clusters and He bubbles in δ-Pu-Ga alloys and their interaction with preexisting extended defects
Alexey Karavaev, Vladimir Dremov, Gennady Ionov
Russian Federal Nuclear Center - Institute of Technical Physics, Snezhinsk, Chelyabinsk Region, Russia

Parallel session: Environmental Science

Thursday/15.20-16:40 Hebel Saal Chair: David K. Shuh

15:20-15:50
Invited talk

Neptunium Biogeochemistry in Systems Representative of the Nuclear Legacy
Gareth Law[1], Clare Thorpe[1], Pieter Bots[1], Sam Shaw[1], Jon Lloyd[1], Francis Livens[1], Melissa Denecke[2], Jorg Rothe[2], Kathy Dardenne[2], Diana Brookshaw[1], Katherine Morris[0]
[1]The University of Manchester, Manchester, UK, [2]KIT-INE, Karlsruhe, Germany

15:50-16:20
Invited talk

Effect of organic acids on the adsorption and reduction of uranium(VI) by microorganisms
Toshihiko Ohnuki[1], Yoshinori Suzuki[2]
[1]Japan Atomic Energy Agency, Tokai, Ibaraki, Japan, [2]Tokyo University of Technology, Hachioji, Tokyo, Japan

16:20-16:40

^{237}Np Sorption by UO_2 Under Repository Conditions
Tatiana Kazakovskaya[1], Elena Zakharova[2]
[1]Russian Federal Nuclear Center - VNIIEF, Sarov, Russia, [2]Institute of Physical Chemistry and Electrochemistry RAS, Moscow, Russia

Coffee Break

Thursday/16:40-17:10

Parallel session: Physics

Thursday/17:10-18:10 Thoma Saal Chair: Dai Aoki

17:10-17:40 Invited talk
Magnetic circular dichroism with x-rays and electrons
Jan Rusz
Department of Physics and Astronomy, Uppsala University, Uppsala, Sweden

17:40-18:10 Invited talk
Fundamental magnetic interaction in actinide-based nanomagnets
Nicola Magnani
Institute of Nanotechnology, Karlsruhe Institute of Technology (INT-KIT), Karlsruhe, Germany

Parallel session: Application technologies

Thursday/17:10-18:10 Hebel Saal Chair: Daniel Meyer

17:10-17:40 Invited talk
An(III)/Ln(III) separation: N-donors do the job - but how?
Andreas Geist
Karlsruher Institut für Technologie (KIT), Karlsruhe, Germany

17:40-18:10 Invited talk
Current Status and Future Application of Actinide based Radiopharmaceuticals in Nuclear Medicine
Clemens Kratochwil[1], Frank Bruchertseifer[2], Frederik Giesel[1], Alfred Morgenstern[2]
[1]UniversityHospital Heidelberg, Department of Nuclear Medicine, Heidelberg, Germany, [2]EC-JRC, Institute for Transuranium Elements, Karlsruhe, Germany

18:20 Group Photo, Entrance stairs of Karlsruhe Congress Center

18:30 Transfer by tram to Kühler Krug. (Wilhelm-Baur-Straße 3, 76135 Karlsruhe) Ref. ANNEX 3

Special tram **"Sonderfahrt" Departure at 18:30** from **tram stop "Konzerthaus"** (tram stationed on the middle rails). Tram arrival to tram stop "Kühler Krug"

Banquet Kühler Krug, Barbecue (BBQ)

Thursday/18.45-22.00
40€, non-alcoholic beverages included until 22:00.
After 22:00 beverages at your own expenses.

Poster Prize Award

Thursday/19:00-19:15

Individual return from Banquet using KVV public transportation. Public transportation pass is printed on the back-side of your badge. Tram line network map: ref. ANNEX 1.

Kühler Krug on city map: ANNEX 3.

Plenary session: Materials Science

Friday/08:40-09:25 Thoma Saal Chair: Tatiana Kazakovskaya

08:40-09:25
Plenary talk

The high temperature behaviour of actinide fuels
Rudy Konings
EC,JRC-ITU, Karlsruhe, Germany

Parallel session: Physics

Friday/09:30-10:30 Thoma Saal Chair: Gertrud Zwicknagl

09:30-10:00
Invited talk

Structural investigations of actinides with advanced X-ray spectroscopy techniques
Tonya Vitova
Karlsruhe Institute of Technology, Karlsruhe, Germany

10:00-10:30
Invited talk

Soft X-ray Spectroscopy of the Actinides
James G. Tobin
Lawrence Livermore Natl Lab, Livermore, CA, USA

Parallel session: Application technologies

Friday/09:30-10:30 Hebel Saal Chair: Tatiana Kazakovskaya

09:30-10:00
Invited talk

Recent advances in material properties and behavior of transuranium compounds for application to nuclear fuel cycle
Masahide Takano, Tsuyoshi Nishi, Hirokazu Hayashi, Kunihisa Nakajima, Haruyoshi Otobe
Japan Atomic Energy Agency, Tokai, Ibaraki, Japan

10:00-10:30
Invited talk

Techniques for measuring the temperature of phase transitions involving liquids in actinide bearing systems.
Ananthasivan Krisnamurthy, Balakrishnan Subramanian, Nagarajan Krisnamurthy, Vasudeva Rao
Indira Gandhi Centre For Atomic Research, Kalpkkam, Tamilnadu, India

Coffee Break

Friday/10:30-11:00

Parallel session: Physics

Friday/11:00-12:00 Thoma Saal Chair: Gertrud Zwicknagl

11:00-11:20

Study of the phase equilibria in the Na-U-O, Na-Pu-O and Na-Np-O systems, and application to the safety of Sodium cooled Fast Reactors
Anna Louise Smith[1,2], Philippe Raison[1], Emmanuelle Suard[4], Laura Martel[1], Joseph Somers[1], Jean-Yves Colle[1], Ondrej Benes[1], Christos Apostolidis[1], Gilles Wallez[5], Ian Farnan[3], Anthony Cheetham[2], Rudy Konings[1]
[1]Institute for Transuranium Elements, Karlsruhe, Germany, [2]Department of Materials Science and Metallurgy, University of Cambridge, Cambridge, UK, [3]Department of Earth Sciences, University of Cambridge, Cambridge, UK, [4]Institut Laue Langevin, Grenoble, France, [5]Laboratoire de Chimie de la matière condensée, UPMC, Chimie ParisTech, Paris, France

11:20-11:40

Impact of hydrogen absorption on onset of magnetism in $U_2(Ni_{1-x}Fe_x)_2Sn$
Silvie Maskova[1], Ladislav Havela[1], Aleksandre Kolomiets[1,2], Khrystyna Miliyanchuk[3], Alexander V. Andreev[4], Heinz Nakotte[5], Joe Peterson[5]
[1]Department of Condensed Matter Physics, Charles University, Prague, Czech Republic, [2]Department of Physics, Lviv Polytechnic National University, Lviv, Ukraine, [3]Faculty of Chemistry, Ivan Franko National University, Lviv, Ukraine, [4]Institute of Physics, ASCR, Prague, Czech Republic, [5]Department of Physics, New Mexico State University, Las Cruces, USA

11:40-12:00

Density Functional Study of CO Adsorption on Pu (100) Surface
Wenhua Luo, Daqiao Meng, Gan Li, Huchi Chen
China Academy of Engineering Physics, Mianyang,Sichuan, China

Parallel session: Application Technologies

Friday/11:00-12:00 Hebel Saal Chair: Tatiana Kazakovskaya

11:00-11:20 Inert Matrix Fuel with Isolated Arrangement of PuO_2 or MA to Achieve Ultra-High Burn-up
Ksenia Lipkina, Alexey Savchenko, Alexander Vatulin, Gennady Kulakov, Sergey Ershov
A.A. Bochvar Institute (VNIINM), Moscow, Russia

11:20-11:40 Development and characterization of composite uranium carbide targets at TRIUMF
Peter Kunz[1], Nicole Erdmann[2], Pierre Bircault[1], Marik Dombsky[1], Vicky Hanemaayer[1], Klaus Lützenkirchen[2], John Wong[1]
[1]TRIUMF, 4004 Wesbrook Mall, Vancouver, B.C V6T 2A3, Canada, [2]JRC - Institute for Transuranium Elements, P.O. Box 2340, D-76125 Karlsruhe, Germany

11:40-12:00 Phase relations of uranium and zirconium oxides at high temperatures for fuel debris treatment
Nobuaki Sato[1], Yuhei Fukuda[1], Akira Kirishima[1], Takayuki Sasaki[2]
[1]Institute Multidisciplinary Research for Advanced Materials, Tohoku University, Sendai, Japan, [2]Department of Nuclear Engineering, Kyoto University, Kyoto, Japan

Presenting Actinides 2017

Friday/12:00-12:20 Thoma Saal

Closing session: D. L. Clark

Friday/12:20-12:40 Thoma Saal

Closing session: G. H. Lander

Friday/12:40-13:00 Thoma Saal

Presenting Author Index

Presenting Author Index

Presenting Author Index

Programme number index

1-20 Single and mixed f-elements sintered oxide pellets synthesis with tailored microstructures.
Elodie Remy, Sébastien Picart, Thibaud Delahaye, Isabelle Bisel, Olivier Dugne, Nicolas Clavier, Adila Azzou, Philippe Blanchart, André Ayral*

1-21 MD simulation of the effect of self-irradiation upon static strength characteristics of materials
Vladimir Dremov, Gennady Ionov, Alexey Karavaev, Philipp Sapozhnikov*

1-22 Influence of adding niobium to uranium on the initial kinetics of hydriding
Ruiwen Li, Xiaolin Wang*

1-23 Microstructure-related hydride nucleation sites on aged U-0.79 wt.% Ti alloy
Shi Peng, Wang Xiaolin, Li Fangfang, Li Ruiwen*

1-25 Phase transformations in PuGa 1 at.% alloy: Elucidation of mechanisms of reversion process following martensitic transformation by coupling in situ experiments and CALPHAD-based calculations
Fanny Lalire, Brice Ravat, Aurélien Perron, Benoit Oudot, Francois Delaunay*

1-26 Corrosion of austenitic steels and their components in uranium-containing chloride melts
Alexandr Abramov, Ilya Polovov, Dmitriy Maltsev, Vladimir Volkovich, Oleg Rebrin*

1-27 Interaction of prospective metallic construction materials with uranium-containing chloride melts
Robert Kamalov, Alexandr Bazhenov, Alexandr Abramov, Ilya Polovov, Dmitriy Maltsev, Vladimir Volkovich, Oleg Rebrin*

1-28 Recent advances in the study of $U_{1-x}Am_xO_{2\pm\delta}$: solid solution synthesis, densification and structural properties
Florent Lebreton, Denis Horlait, Philippe M. Martin, Renaud C. Belin, Thibaud Delahaye, Philippe Blanchart*

1-29 Thermal conductivities of $(U_{1-y}, Pu_y)O_{2.00}$ (y = 0.00 - 0.46)
Kyoichi Morimoto, Masahiro Ogasawara*

1-30 Actinide oxalate compounds: structure directing role of the monovalent cations
Ana Gil-Martin, Bénédicte Arab-Chapelet, Murielle Rivenet, Philippe Martin, Andreas Scheinost, Isabelle Bisel, Stéphane Grandjean, Francis Abraham*

1-31 Submicron and nanostructured uranium carbides prepared by electrospinning
*Margarida S. Henriques, Adelaide Cruz, Joaquim Marcalo, Martina Kratochvílová, Ladislav Havela, Thierry Stora, Antonio P. Goncalves**

1-32 Numerical Investigation of Interfacial Flow in a Molten Immiscible LiCl-KCl/Cd System
Kwangrag Kim, Jun-Bo Shim, Seungwoo Paek, In-Tae Kim*

1-33 Persistence of the γ-phase in uranium-molybdenum alloy thin films
A M Adamska, T B Scott, R Springell*

1-34 Structure stability of the cubic γ-phase uranium molybdenum alloys.
Ilya Tkach, Nhu-Tarnawska Hoa Kim-Ngan, Silvie Mašková, Ladislav Havela, Alexander Warren, Camilla Stitt, Tomhas Scott*

1-35 German Joint Research Project on "Conditioning of long-lived Radionuclides in Ceramic Waste Forms" - An Introduction
Stefan Neumeier, Giuseppe Modolo, Dirk Bosbach*

1-36 Non-destructive studies of fuel rodlets by neutron resonance absorption radiographyand thermal neutron radiography
Anton S. Tremsin, Sven C. Vogel, Michal Mocko, Mark A. M. Bourke, Vincent Yuan, Ron Nelson, Donald W. Brown, Bruce Feller*

1-37 Phase transformation inhibition in Pu-1.9 at.% Ga
Jason Jeffries, J. Bradley, Mark Wall*

1-38 X-ray diffraction study of the eutectoid decomposition of γ-U(Mo) powder produced by magnesiothermic reduction.
*Guillaume Champion, Mathieu Pasturel, Xavière Iltis, Olivier Tougait**

1-39 Selective Actinide Separation Process by Amide Based New Ligands.
Shinichi Suzuki, Tohru Kobayashi, Tsuyoshi Yaita, Hideaki Shiwaku*

1-40 Densification of uranium carbide pellets: Preliminary result of spark plasma sintering and comparison with conventional sintering techniques
Olivier Tougait, Matthieu Peniel, Mathieu Pasturel, Odile Merdrignac-Conanec, Christophe Lau, Sandrine Tusseau-Nenez*

1-41 High-temperature experimental study on the U-Mo-C system
Matthieu Peniel, Mathieu Pasturel, Olivier Tougait*

1-42 Pyrochlore - a promising host phase for actinide immobilisation
Sarah Finkeldei, Kiel Holliday, Eva de Visser-Týnová, Felix Brandt, Stefan Neumeier, Giuseppe Modolo, Thorsten Stumpf, Dirk Bosbach*

1-43 XRD monitoring of α self-irradiation effects in U1-xAmxO2±δ mixed-oxides
Denis Horlait, Florent Lebreton, Thibaud Delahaye, Roussel Pascal*

1-44 Electronic Structure of Actinide Surface Reactions and Complexes
Krishnan Balasubramanian, Patrick Allen, William McLean II*

1-45 On relationship between thermodynamic and dynamic properties of light actinides
Alexander Uchaev, Nadezda Selchenkova, Elena Kosheleva, Valery Punin*

1-46 Physical properties of UBeGe and ThBeGe intermetallic compounds
Roman Gumeniuk, Andreas Leithe-Jasper, Walter Schnelle, Michael Nicklas, Ulrich Burkhardt, Horst Borrmann, Yuri Grin*

1-47 On the possibility of predicting the dynamic properties of light actinides
Elena Kosheleva, Alexander Uchaev, Valery Punin, Nadezda Selchenkova*

1-48 Physical nature of Light Actinides Longevity in the Dynamic Failure Phenomenon
Nadezda Selchenkova, Alexander Uchaev, Valery Punin, Elena Kosheleva*

1-49 Magnetization of U_2Fe_3Ge and $U_3Fe_4Ge_4$ under external pressure
Alexander Andreev, Zdenek Arnold, Denis Gorbunov, Margarida Henriques, Ladislav Havela, Antonio Gonçalves*

1-50 Electronic structure and Fermi surface of paramagnetic and antiferromagnetic $UPt2S_2$
Saad Elgazar, Jan Rusz, Peter Oppeneer, John Mydosh*

1-51 First-principles calculation of intrinsic and defective properties of UO_2 and ThO_2
Han Han, Cheng Cheng, Ping Huai*

1-52 Simulations of incipient damage and nanovoids in plutonium during alpha-decay
Boris Nadykto, Sergey Sokolov, Alexander Panov, Alexey Samodolov*

1-53 Thermal and elastic properties of actinides on the example of americium and curium: a self-consistent thermodynamic approach
Anton Filanovich, Alexander Povzner, Varvara Oskina*

1-54 Microscopic theory of the insulating electronic ground states of actinides dioxides AnO_2 (with An = U, Np, Pu, Am and Cm)
Michi-To Suzuki, Nicola Magnani, Peter M. Oppeneer*

1-55 ^{119}Sn Mössbauer spectroscopy of 3d-, 4f- and U-intermetallic compounds
*Vasily Krylov**

1-56 The role of transition metals (TM) on the symmetry of Al-TM-Ac alloys (Ac= actinides and lanthanides)
Avraham I Bram, Arie Venkert, Louisa Meshi*

1-57 Screening effect of magnetic exchange interaction in U- and Gd-based intermetallic compounds
Vasily Krylov, Vladimir Sechovský, Alexander Andreev*

1-58 Studies on the $UFeC_2$ uranium carbide
*Margarida S. Henriques, Yuriy Verbovitskiy, Ladislav Havela, Antonio P. Goncalves**

1-59 Ultra-Trace determination of Pu and Np isotopes by resonance ionization mass spectrometry
Michael Franzmann, Amin Hakimi, Gerd Passler, Sebastian Raeder, Tobias Reich, Pascal Schönberg, Nils Stöbener, Norbert Trautmann, Klaus Wendt*

1-60 Proposal for thermo-mechanical properties correlations of MOX bearing minor actinides fuels
Sara Perez-Martin, Michael Schikorr*

1-61 Structure and magnetism in U2Ni21B6, (U,Nb)2Ni21B6 and (U,Nb)3Ni20B6
Alessia Provino, Amitava Bhattacharya, Sudesh K. Dhar, Cristina Bernini, Marcella Pani, Flavio Gatti, Pietro Manfrinetti*

1-62 Vibrational Properties of Uranium Hydride and Uranium Deuteride
Alice I. Smith, Luke L. Daemen, Joe R. Wermer, Jeffery Aguiar, Bogdan Mihaila, Roland K. Schulze*

1-63 X-ray photoelectron spectroscopy of 7-at.% gallium δ-stabilized plutonium
*Thomas Venhaus**

1-64 Neutron Capture Cross Section on 236U performed at the n_TOF facility at CERN
Mark James Vermeulen, Massimo Barbagallo, Carlos Guerrero, David Jenkins*

1-65 Production of Super Heavy Plutonium Isotopes for Basic Research
Stanislav Vesnovskii, Lev Kazakov, Alexey Kupriyanov, Evgeny Romanov, Valery Tarasov*

1-66 New Concept of Designing Composite Fuel for Fast Reactors with Closing Fuel Cycle
Alexey Savchenko, Alexander Vatulin, Gennady Kulakov, Ksenia Lipkina, Vladimir Sorokin, Sergey Ershov, Sergey Maranchak, Zoya Petrova*

1-67 Separation of uranium and lanthanides in "molten salt - liquid metal" system
Leonid Yamshchikov, Vladimir Volkovich, Andrey Schetinskii, Dmitry Maltsev, Alexander Dedyukhin, Viktor Ivanov, Stanislav Melchakov, Sergey Raspopin, Alexander Osipenko, Mikhail Kormilitsyn*

1-68 Solubility of uranium and lanthanum in Ga-In eutectic based alloys at 25-800 °C
Vladimir Volkovich, Andrey Schetinskii, Dmitry Maltsev, Alexander Dedyukhin, Leonid Yamshchikov, Stanislav Melchakov, Viktor Ivanov, Alexander Osipenko, Sergey Raspopin, Mikhail Kormilitsyn*

1-69 Post-Irradiation Examinations on PHENIX axially heterogeneous pins relevant to ASTRID fuel design: ZEBRE and PAVIX irradiations
Béatrice Rabu, Michel Pelletier, Christophe Valot, Isabelle Munoz, Mayeul Phelip*

1-70 Oxidation of Uranium-Plutonium Mixed Nitrides
Andrei Shadrin, Alexey Glushenkov, Konstantin Dvoeglazov, Mikhail Skupov*

1-71 In-situ measurement of a dissolved alpha emitter by electro-precipitation
Alexander Diener, Christoph Wilhelm, Ursula Hoeppener-Kramar*

1-72 Investigation of diformylhydrazine interaction with Pu in technological media of extraction SNF reprocessing
Volk Vladimir, Pavlyukevich Ekaterina, Dvoyeglazov Konstantin, Podrezova Lubov, Veselov Sergey*

1-73 Thermodynamic Aspects of Interphase Interaction in Heterogeneous Alloys and Its Influence on Alloys Properties
Alexey Savchenko, Andrey Laushkin, Yury Konovalov*

1-74 Structural, Electronic and Magnetic Properties of $NpNi_5$
Amir Hen, Eric Colineau, Rachel Eloirdi, Jean - Christophe Griveau, Itzhak Halevy, Itzhak Orion, Roberto Caciuffo*

1-75 μ-focus capabilities at the INE-Beamline for actinide science at ANKA
Kathy Dardenne, Jörg Rothe, Teresa Fernandes, Dieter Schild, Eva Soballa, Volker Metz, Christiane Bube, Bernhard Kienzler, Melissa Denecke, Horst Geckeis*

1-76 f-Element Single-Molecule Magnets
*Katie Meihaus, Shuao Wang, Jeffrey Rinehart, Selvan Demir, Michael Nippe, Joseph Zadrozny, David Shuh, Jeffrey Long**

1-77 High-resolution Nuclear Magnetic Resonance Investigation into Chemical Shifts in UO_2 and ThO_2 and Ordering in Uranium-Thorium Oxide Solid Solutions.
Ian Farnan, Joseph Somers, Olivier Pauvert, Serge Fourcadot, Laura Martell, Kevin Boland, David Clark*

1-78 Multiconfigurational Nature of 5f Orbitals in Uranium and Plutonium and Their Intermetallic Compounds
*Corwin Booth**

1-79 Charge distribution and local structure of $M_{0.80}Am_{0.20}O_{2+x}$ (M: Th, U and Pu)
Damien Prieur, Ursula Carvajal-Nunez, Marika Vespa, Tonya Vitova, Joseph Somers*

1-80 Uranyl oxo group functionalisation, reduction, and migration reactions
Polly Arnold, Jason Love, Guy Jones, Anne-Frederique Pecharman, Emmalina Hollis, Roberto Caciuffo, Nicola Magnani, Laurent Maron, Ludovic Castro, Georg Schreckenbach, Samuel Odoh*

1-81 Unique advantages of organometallic supporting ligands for uranium complexes
*Paula Diaconescu**

1-82 $AnCp_4$: a grandfather of the organometallic chemistry of the actinides with young and attractive children
Christos Apostolidis, Jean Rebizant, Olaf Walter, Alfred Morgenstern*

3-02 Actinides in Scrap, Dirt and Deposits - A Challenge for Investigative Radiochemists
Klaus Mayer, Maria Wallenius, Magnus Hedberg, Zsolt Varga*

3-03 New aspects in nuclear forensics. Aerial Radiation Monitoring before and after radiological event
*Itzhak Halevy**

3-04 How to build accurate macroscopic models of actinide ions in aqueous solvents?
Valérie Vallet, Florent Réal, Michael Trumm, Bernd Schimmelpfennig, Michel Masella*

3-05 Formation of New Exotic Curium Oxides CmO_3 and CmO_4 in the Gas Phase
*Vladimir Domanov**

3-06 Thermal conductivity measurement of $(Pu_{1-x}Am_x)O_2$ (x=0.03, 0.07)
Taku Matsumoto, Tatsumi Arima, Yaohiro Inagaki, Kazuya Idemitsu, Masato Kato, Kyoichi Morimoto, Masahiro Ogasawara*

3-07 Chemical Segregation of U-10wt.% Mo Fuel Foils During Simulated Bonding Cycles
Sven C. Vogel, Donald W. Brown, Maria Okuniewski*

3-08 Insight Into The Mechanism Of Plutonium Hydride Formation
Patrick Allen, Long Dinh, William McLean, Scott McCall, Cheng Saw, John Haschke*

3-09 *Ab initio* study of defect production and migration in thoria
William Weber, Haiyan Xiao, Bin Liu, Yanwen Zhang*

3-10 DFT Investigation of Uranium Oxides and Defect Structures
Nick Brincat, Steve Parker, Geoff Allen, Mark Storr*

3-11 The Redox Potential of Mendelevium (Md) Determined Atom-at-a-Time with a Flow Electrolytic Column
Matthias Schädel, Atsushi Toyoshima, Zijie Li, Masato Asai, Nozomi Sato, Takahiro Kikuchi, Yusuke Kaneya, Yoshihiro Kitatsuji, Kazuaki Tsukada, Yuichiro Nagame, Kazuhiro Ooe, Yoshitaka Kasamatsu, Yuka Kogoma, Atsushi Shinohara, Hiromitsu Haba, Julia Even*

3-12 The first successful ionization of Lr (Z=103) by a surface ionization technique
Tetsuya K. Sato, Masato Asai, Nozomi Sato, Kazuaki Tsukada, Atsushi Toyoshima, Sunao Miyashita, Kazuhiro Ooe, Matthias Schaedel, Yusuke Kaneya, Yuichiro Nagame, Akihiko Osa, Shin-ichi Ichikawa, Thierry Stora, Jens Volker Kratz*

3-13 EXAFS Study of f-Elements Thiocianate Complexation
Marisol Janeth Lozano Rodriguez, Christophe Den Auwer, José Mustre de León*

3-14 Probing and Quantifying Orbital Mixing in f-Element Molecular Bonding
Matthias W. Loeble, Jason M. Keith, Paul H. Tobash, Brian L. Scott, Angela C. Olson, Stefan G. Minasian, Scott R. Daly, Kevin S. Boland, Eve Bauer, Kathy Dardenne, Joerg Rothe, Tonya Vitova, Tsu-Chien Weng, Dimosthenis Sokaras, Franz J. Freibert, Richard L. Martin, Enrique R. Batista, David L. Clark, Stosh A. Kozimor*

3-15 Interaction of human serum transferrin with Cm(III) using Time-Resolved Laser Fluorescence Spectroscopy
Nicole Bauer, Petra Panak*

3-16 Study on the extracted complexes of purified Cyanex301 with Cm(III) and Ln(III) with spectrophotometry, fluorometry, and EXAFS
Guoxin Tian, Xihong He, Chao Xu, Linfeng Rao*

3-17 The Hydrothermal Behavior of Depleted Uranium Oxides
Tatiana Kazakovskaya, Elena Zakharova, Vyacheslav Shapovalov*

3-18 Mechanism of $UO_2(NO_3)_2 \times 6H_2O$ Decomposition under Microwave Irradiation
*Sergey Kulyukhin**

3-19 Plutonium and uranium concentration from sea water
Sergey Kulyukhin, Irina Veleshko, Aleksander Veleshko*

3-20 Interaction of UO_2^{2+} Aqueous Solutions with Sorbents Based on Modified Silica Gel Containing Cu, Ni, and Zn
Sergey Kulyukhin, Margarita Gorbacheva*

3-21 Discussion about the Universal Curves of Limiting Conductance of Electrolytes 1:3Study of Limiting Conductance of LaCl3, La(NO3)3 and TbCl3 in water-THF mixture (25% w)
Rafik Besbes, Abderabba Manef, Habib Latrous*

3-22 Actinide colloids and nanoparticles: relevance to legacy waste, clean-up and geological disposal
Jennifer Rochford, Sarah Heath*

3-23 Arene-Actinide interactions in the Flexible Macrocyclic Ligand Environment of *trans*-Calix[2]benzene[2]pyrrolide
Joy Farnaby, Rebecca White, Michael Gardiner, Jason Love, Polly Arnold*

3-24 Optimization Criterions for H_2O-$UO_2(NO_3)_2$-TBP System.
Alexander Ochkin, Dmitriy Gladilov, Sergey Nekhaevskiy*

3-25 Dodecane effect on nitric acid extraction with TBP.
Alexander Ochkin, Dmitriy Gladilov, Sergey Nekhaevskiy*

3-26 Optical spectroscopy study into the bio-reduction of the uranyl(VI) ion and the uranyl(V) and uranium(IV) species generated.
Debbie Jones, Sean Woodall, Louise Natrajan, Adam Swinburne*

3-27 Luminescent properties of uranium complexes
Michael Andrews, Louise Natrajan, Adam Swinburne, Sean Woodall, Simon Randall*

3-28 Vibrational spectroscopic study of some rare-earth metals trifluoromethylsulfonates enneahydrates and of corresponding salts of uranium(III) and curium(III)
Mikhail Skripkin, Patric Lindqvist-Reis, Christos Apostolidis, Reinhardt Klenze, Janos Mink*

3-29 Self-assemblage of stable uranyl nano-clusters in the alkaline peroxide systems
Yingjie Zhang, Mohan Bhadbhade, Jason Price, Jiabin Gao, Inna Karatchevtseva, Gregory Lumpkin*

3-30 Structural studies of actinide complexes with picolinamide
Yingjie Zhang, Mohan Bhadbhade, Jiabin Gao, Inna Karatchevtseva, Gregory Lumpkin*

3-31 Electrochemical and thermodynamic properties of uranium in low melting LiCl-KCl-CsCl eutectic
Dmitry Maltsev, Vladimir Volkovich, Evgeny Vladykin, Boris Vasin*

3-32 Synthesis and characterization of new heterometallic uranyl-based carboxylates
Christophe Volkringer, Ionut Mihalcea, Clement Falaise, Natacha Henry, Thierry Loiseau*

3-33 TRLFS Study on the Complexation of Cm(III) and Eu(III) with methy-substituted Diglycolamides
Björn Beele, Andreas Wilden, Andrej Skerencak-Frech, Steve Lange, Fabian Sandowski, Giuseppe Modolo, Petra Panak, Mudassir Iqbal, Willem Verboom, Andreas Geist*

3-34 Influence of the solvent on the complexation of Cm(III) with nPr-BTP studied by time-resolved laser fluorescence spectroscopy
Antje Bremer, Andreas Geist, Petra J. Panak*

3-35 Trivalent Lanthanide/Actinide Separation Using Aqueous-Modified TALSPEAK Chemistry
Travis Grimes, Leigh Martin*

3-36 Solid Phase Extraction Materials for Separations of Actinides and Fission Products
Jennifer Shusterman, Eva Uribe, Tashi Parsons-Moss, Anthony Bruchet, Erin Gantz, Heino Nitsche*

3-37 Effect of Hydrogen bonds on melting points and packing coefficients of uranyl nitrate complexes with cyclic urea derivatives
Tomoya Suzuki, Takeshi Kawasaki, Koichiro Takao, Masayuki Harada, Masanobu Nogami, Yasuhisa Ikeda*

3-38 Difference in the kinetics of Am(III) and Eu(III) extraction using TODGA in Ionic Liquid Medium
Maria Boltoeva, Ali Quadi, Sylvia Georg, Isabelle Billard*

3-39 TALISMAN - Transnational Access to Large Infrastructures for a Safe Management of Actinides
M. Altmaier, S. Bourg, N. Bryan, P. Collings, N. Dacheux, B. Duplantier, Ch. Ekberg, D. Grolimund, L. Natrajan, Ch. Poinssot, Ph. Raison, T Schäfer, A.C. Scheinost, B. Schimmelpfennig*

3-40 Curium-technetium complex oxide
Elena Pichuzhkina, Sergey Tomilin*

3-41 UV-vis and fluorescence spectroscopic methods to evaluate the solution thermodynamic properties of hydroxypyridinonate actinide and lanthanide complexes
Manuel Sturzbecher-Hoehne, Gauthier Deblonde, Rebecca Abergel*

3-42 Receptor recognition of transferrin bound to f-block metals: a segregation step in cellular acquisition of actinides
Manuel Sturzbecher-Hoehne, Gauthier Deblonde, Christophe Goujon, Anne Mason, Rebecca Abergel*

3-43 Actinide mixed oxide microspheres synthesis using Weak Acid Resin process: unconventional precursors for Minor Actinide Bearing Blanket fabrication
Picart Sebastien, Remy Elodie, Delahaye Thibaud, Bisel Isabelle, Dugne Olivier, Clavier Nicolas, Blanchart Philippe, Ayral André*

3-44 Thermodynamic evaluation of Np redox processes in dilute aqueous solutions at pH 4 - 10 under reducing conditions
David Fellhauer, Marcus Altmaier, Volker Neck, Xavier Gaona, Thierry Wiss, Markus Lagos, Jörg Runke, Thomas Fanghänel*

3-45 Electronic Structure of Plutonium Dioxide
Yu.A. Teterin, K.I. Maslakov, M.V. Ryzhkov, A.Yu. Teterin, K.E. Ivanov, V.G. Petrov, D.A. Enina, S.N. Kalmykov*

3-46 Chemical Bond Nature in Neptunium Dioxide
Yu.A. Teterin, K.I. Maslakov, M.V. Ryzhkov, A.Yu. Teterin, K.E. Ivanov, V.G. Petrov, D.A. Enina, S.N. Kalmykov*

3-48 Structure and spectroscopic evidence of hexavalent neptunyl and plutonyl mono- and dinitrate complexes in aqueous nitric acid
Patric Lindqvist-Reis, Christos Apostolidis, Olaf Walter, Remi Marsac, Nidhu Lal Banik, Mikhail Yu. Skripkin, Jörg Rothe, Alfred Morgenstern, Rachel Eloirdi*

3-49 Raman Spectroscopic Study on Uranyl and Neptunyl Complexes in Concentrated Chloride Solutions
Toshiyuki Fujii, Akihiro Uehara, Yoshihiro Kitatsuji, Hajiumu Yamana*

3-50 Development of a simplified soft-donor technique for trivalent actinide-lanthanide separations.
Madeleine Langford Paden, Louise Natrajan, Clint Sharrad, Leigh Martin, Sarah Hendley*

3-51 Understanding molecular speciation of actinides in the PUREX process
Tamara Griffiths, Kate Tucker, Clint Sharrad, Francis Livens, Leigh Martin, Peter Kaden*

3-52 In-situ XAFS analysis of electrochemical reduction of uranium(VI) in highly concentrated LiCl
Akihiro Uehara, Toshiyuki Fujii, Hajimu Yamana, Yoshihiro Okamoto*

3-53 Selective recovery of actinides from An-Zr-fuel by electrorefining in molten LiCl-KCl
Roland Meier, Pavel Souček, Rikard Malmbeck, Claux Bennoit, Glatz Jean-Paul, Fanghaenel Thomas*

3-54 Actinide extraction and complexation properties of oxygen-nitrogen hetero donor ligand PTA
Tohru Kobayashi, Shinichi Suzuki, Hideaki Shiwaku, Tsuyoshi Yaita*

3-55 Formation of actinide(IV) carboxylate complexes in aqueous solution - the unexpected predominance of hexanuclear species
Christoph Hennig, Koichiro Takao, Shinobu Takao, Stephan Weiss, Werner Kraus, Franziska Emmerling, Andreas C. Scheinost*

3-56 XAFS and solubility investigations of penta- and hexavalent actinides in dilute to concentrated salt brines
Jörg Rothe, Kathy Dardenne, David Fellhauer, Xavier Gaona Martinez, Marcus Altmaier, Thomas Fanghänel*

3-57 Preparation, phase composition, microstructure and electrochemical properties of UPd_3 and URu_3 in the solutions of nitric acid
Semen Zavarzin, Alexandre Maslennikov, Alexandre Osipenko, Alexandre Maershin, Irina Vlasova, Andrei Shiryaev*

3-58 Redox Mechanism of Nd(III) Ions in High Temperature LiCl-KCl Eutectic Observed by UV-Vis Absorption Spectroscopy in Combination of Electrolysis
Seung Park, Jong-Il Yun*

3-59 Investigation of Plutonium Trifluoride Solubility in Molten Fluorides
Alexander Maershin, Alexander Osipenko, Andrey Lizin*

3-60 Coordination Chemistry of Actinides with Hydroxamic Siderochelates
Alejandra Sornosa Ten, Pawel Jewula, Lé Vi Nguyen, Mélanie Bourdillon, Stéphane Brandès, Christine Stern, Jean-Claude Chambron, Michel Meyer*

3-61 Investigation in field of partitioning of minor actinides and rare elements in chloride melt
Alexander Maershin, Alexander Osipenko, Mikhail Kormilitsyn*

3-62 Preparation, stabilization, spectroscopic, computational studies of tetravalent protactinium in aqueous solution
*Nidhu Banik, Christian Marquardt, Marcus Altmaier, Clemens Walter, Jörg Rothe, Bernd Schimmelpfennig, Florent Réal, Valérie Vallet**

3-63 The Thermodynamics of Extraction of Lanthanides and Actinides by Solvating and Ion-Exchanging Ligands: A Comparative Study
Leigh Martin, Peter Zalupski, Travis Grimes*

3-64 Radiolysis of adsorbed water on actinides oxides surface: investigations on the surface state evolution by hydration
Jérémy Gaillard, Laurent Venault, Philippe Moisy, Jackie Vermeulen, Rachel Calvet, Nicolas Clavier*

3-65 Effect of trivalent dopant, Gd^{3+}, on the reaction of $U_{1-y}Gd_yO_2$ and Cs_2O
Kim Jong-Goo, Jang Eun-Sil, Park Yang-Soon, Ha Yeong-Keong, Song Kyuseok*

3-66 Apparent Solubility of Thorium in the Presence of Humic Substances
Takayuki Sasaki, Yuka Matsuura, Taishi Kobayashi, Ikuji Takagi, Hirotake Moriyama*

3-67 Temperature Effect on the Solubility and Solid Phase Stability of Thorium Hydroxide
Taishi Kobayashi, Takayuki Sasaki, Ikuji Takagi, Hirotake Moriyama*

3-68 EXAFS investigation of substituent effect of the hybrid type PDA complexes for actinides and lanthanides separation.
Hideaki Shiwaku, Toru Kobayashi, Yoshihiro Okamoto, Shin-ichi Suzuki, Tsuyoshi Yaita*

3-69 Mathematical model for crystallization purification of uranyl nitrate hexahydrate in continuous crystallization column
Vladimir Kascheev, Olga Shmidt, Pavel Poluektov, Svetlana Tretyakova*

3-70 Sulfurization behaviour of uranium and zirconium oxides with CS_2
Yuhei Fukuda, Akira Kirishima, Nobuaki Sato*

3-71 Nuclear Fallout Debris Formation and Fractionation in Aerodynamic Particles
Kiel Holliday, Mischa Monroe, Richard Gostic, John McClory, Ian Hutcheon*

3-72 Complexation of actinides by the 1,4,7,10-tetraazacyclododecane-1,4,7,10-tetraacetic acid (DOTA)
Matthieu Audras, Laurence Berthon, Claude Berthon, Nicole Zorz, Dominique Guillaumont, Thomas Dumas, Philippe Moisy*

3-73 Evidence for covalence in a *N*-donor complex of Americium(III)
Peter Kaden, Christian Adam, Björn B. Beele, Udo Müllich, Sascha Trumm, Andreas Geist, Petra J. Panak, Melissa A. Denecke*

3-74 Towards stability rules of extractants involve in minor actinides partitioning processes: Study of TODGA degraded samples under different experimental conditions.
Hitos Galán, Ana Nuñéz, Amparo G. Espartero, Aritz Durana, Javier de Mendoza, Joaquín Cobos*

3-75 Synthesis and Characterization of U-doped Zircon and Baddeleyite
V.G. Petrov, I.E. Vlasova, E.B. Furkina, M.V. Yevsunina, S.N. Kalmykov*

3-76 Temperature and Ionic Strength Effects on Neptunium Speciation in Simplified Brine Systems
Donald Reed, Marian Borkowski, Michael Richmann, Jean-Francois Lucchini*

3-77 Scanning phase diagrams to discover new phases with original properties: Examples from U-T-Ge (T = Fe, Co, Ru) ternary systems.
Olivier Tougait, Mathieu Pasturel, David Berthebaud, Arnaud Soude, Thierry Roisnel, Margarida Henriques, Antonio Goncalves, Adam Pikul, Dariusz Kaczorowski*

3-78 Some progress made in f-element chalcogenide chemistry
Jean-Marie Babo, Peter C. Burns*

3-79 Heavy metal extraction using advanced PUREX style partitioning systems
Kate Tucker, Robin Taylor, Clint Sharrad, Tamara Griffiths, Sarah Heath, Peter Kaden*

3-80 Structural and Spectroscopic studies of Mononuclear Uranyl(VI) Complex Containing O,O,N,N-tetradentate ligand
Mohammad Azam, Saud Al-Resayes*

3-81 Chemiluminescence specroscopy of actinides and lanthanides in solutions
Igor Izosimov, Nikolai Firsin, Nikolai Gorshkov, Vladimir Mikhalev, Sergei Nekhoroshkov*

3-82 The fate of uranium and technetium during magnetite crystallisation at hyperalkaline pH
Timothy Marshall, Katherine Morris, Gareth Law, Frederick Mosselmans, Samuel Shaw*

4-05 Uranium sorption onto single mineral phases - approaching consistency and robustness
*Vinzenz Brendler**

4-06 Solid state phase transformation study on Pu-Ga alloys containing 0.18 to 0.63 wt.% Ga
Michael Ling, Nigel Park*

4-07 Kinetic study of delta to alpha' isothermal martensitic transformation in PuGa 1at%
Fanny Lalire, Brice Ravat, Aurélien Perron, Benoit Oudot, Elisabeth Aeby-Gautier, Francois Delaunay*

4-08 The effects of thermal conditioning and recovery processes on the δ →γ phase transformation mechanisms in plutonium.
*Sue Ennaceur**

4-09 The unique solid-state NMR facility at JRC-ITU for the study of highly radioactive compounds
Laura Martel, Jean-Christophe Griveau, Chris Selfslag, Jacobus Boshoven, Olivier Pauvert, Ian Farnan, Joseph Somers*

4-10 Raman spectroscopic characteristics of stoichiometric and non-stoichiometric uranium oxides
Gan Li, Wenhua Luo, Junbo Lv*

4-11 SIMS analysis of hydrogen and carbon co-precipitation in uranium and SEM/FIB analysis of its effect on surface reactions.
Patrick Allen, Ian Hutcheon, Jenny Matzel, Wigbert Siekhaus, Nick Teslich, Peter Weber*

4-12 Molecular and 3D hybrid architectures with tetravalent uranium
Clément Falaise, Christophe Volkringer, Natacha Henry, Thierry Loiseau*

4-13 Oxidation state and aromaticity in f-element metallocenes $M(C_8H_8)_2$
*Cina Foroutan-Nejad, Andy Kerridge**

4-14 Separation of ^{225}Ac from radionuclides generated by proton irradiation of natural thorium using extraction chromatography
Elena Lapshina, Stanislav Ermolaev, Boris Zhuikov, Stepan Kalmykov, Ramiz Aliev, Valentina Ostapenko, Alexander Vasiliev*

4-15 Americium and Plutonium Purification by Extraction (the AMPPEX process)
Mark Sarsfield, Keith Stephenson, Katie Bell, Jamie Brown, Michael Carrott, Colin Gregson, Christopher Maher, Chris Mason, Robin Taylor*

4-16 Separation of Americium alone from a Concentrated Raffinate by Liquid-Liquid Extraction
Cécile Marie, Marie-Thérèse Duchesne, Vincent Pacary, Vincent Vanel, Marc Montuir, Manuel Miguirditchian*

4-17 Spectroscopic study of redox behaviour of neptunium ions in molten LiCl-KCl eutectic
Tae-Hong Park, Dae-Hyeon Kim, Sang-Eun Bae, Jong-Yun Kim, Young-Hwan Cho, Jei-Won Yeon, Kyuseok Song*

4-18 Recent Advances in Aqueous Neptunium Chemistry and Thermodynamics
*Marcus Altmaier**

4-19 Uranyl speciation at the water/mineral interface: XPS, TRLFS and XAFS studies
Annick Froideval Zumbiehl, Mireille Del Nero, Rémi Barillon, Clotilde Gaillard, Klaus Lützenkirchen, Jean Hommet, Jean-Louis Hazemann*

4-20 Dynamics and speciation in molten actinide fluorides
Catherine Bessada, Louis Maksoud, Vincent Sarou-Kanian, Haruaki Matsuura, Anne Laure Rollet, Christian Simon, Mathieu Salanne, Mathieu Gibilaro, Laurent Massot, Pierre Chamelot*

4-21 Relative thermodynamic stability of radiation defect clusters and He bubbles in δ-Pu-Ga alloys and their interaction with preexisting extended defects
Alexey Karavaev, Vladimir Dremov, Gennady Ionov*

4-22 Neptunium Biogeochemistry in Systems Representative of the Nuclear Legacy
Gareth Law, Clare Thorpe, Pieter Bots, Sam Shaw, Jon Lloyd, Francis Livens, Melissa Denecke, Jorg Rothe, Kathy Dardenne, Diana Brookshaw, Katherine Morris*

4-23 Effect of organic acids on the adsorption and reduction of uranium(VI) by microorganisms
Toshihiko Ohnuki, Yoshinori Suzuki*

4-24 ^{237}Np Sorption by UO_2 Under Repository Conditions
Tatiana Kazakovskaya, Elena Zakharova*

Presenter firstname	Presenter lastname	Type	Session	Categories	Title
Alexandr	Abramov	Poster	Mo-PS1	Materials science	Corrosion of austenitic steels and their components in uranium-containing chloride melts
A M	Adamska	Poster	Mo-PS1	Materials science	Persistence of the γ-phase in uranium-molybdenum alloy thin films
Evgeny V.	Alekseev	Oral	Tu-O2B	Chemistry	Influence of extreme conditions on the formation and structures of uranyl borates.
Patrick	Allen	Oral	We-O2A	Materials science	Insight Into The Mechanism Of Plutonium Hydride Formation
Marcus	Altmaier	Invited	Th-PL2	Chemistry	Recent Advances in Aqueous Neptunium Chemistry and Thermodynamics
M.	Altmaier	Poster	We-PS2	Chemistry	TALISMAN - Transnational Access to Large Infrastructures for a Safe Management of Actinides
Alexander	Andreev	Poster	Mo-PS1	Physics	Magnetization of U2Fe3Ge and U3Fe4Ge4 under external pressure
Michael	Andrews	Poster	We-PS2	Chemistry	Luminescent properties of uranium complexes
Dai	Aoki	Invited	Mo-O4A	Physics	Field reentrant superconductivity and Fermi surface instabilities in uranium ferromagnets
Christos	Apostolidis	Poster	We-PS2	Chemistry	AnCp₄: a grandfather of the organometallic chemistry of the actinides with young and attractive children
Polly	Arnold	Invited	Mo-O3B	Chemistry	Uranyl oxo group functionalisation, reduction, and migration reactions
Matthieu	Audras	Poster	We-PS2	Chemistry	Complexation of actinides by the 1,4,7,10-tetraazacyclododecane-1,4,7,10-tetraacetic acid (DOTA)
Mohammad	Azam	Poster	We-PS2	Chemistry	Structural and Spectroscopic studies of Mononuclear Uranyl(VI) Complex Containing O,O,N,N-tetradentate ligand
Jean-Marie	Babo	Poster	We-PS2	Chemistry	Some progress made in f-element chalcogenide chemistry
Robert	Baker	Oral	Tu-O2A	Environmental science	Characterisation of uranium minerals relevent to long term storage of spent nuclear fuel
Krishnan	Balasubramanian	Poster	Mo-PS1	Materials science	Electronic Structure of Actinide Surface Reactions and Complexes
Nicole	Bauer	Oral	We-O2B	Chemistry	Interaction of human serum transferrin with Cm(III) using Time-Resolved Laser Fluorescence Spectroscopy
Eric	Bauer	Invited	Tu-PL2	Physics	Recent Developments in PuMGa5 and PuMIn5 (M=Co, Rh) Heavy Fermion Superconductors
Björn	Beele	Poster	We-PS2	Chemistry	TRLFS Study on the Complexation of Cm(III) and Eu(III) with methy-substituted Diglycolamides
Ondrej	Benes	Oral	Tu-O2B	Chemistry	Thermodynamic investigation of the Th-U-Pu-O system
Claude	Berthon	Oral	Mo-O2B	Chemistry	Actinide paramagnetism and NMR
Rafik	BESBES	Poster	We-PS2	Chemistry	Discussion about the Universal Curves of Limiting Conductance of Electrolytes 1:3Study of Limiting Conductance of LaCl3, La(NO3)3 and TbCl3 in water-THF mixture (25% w)
Catherine	Bessada	Invited	Th-O3A	Materials science	Dynamics and speciation in molten actinide fluorides
Maria	Boltoeva	Poster	We-PS2	Chemistry	Difference in the kinetics of Am(III) and Eu(III) extraction using TODGA in Ionic Liquid Medium
Corwin	Booth	Invited	Mo-O3A	Materials science	Multiconfigurational Nature of 5f Orbitals in Uranium and Plutonium and Their Intermetallic Compounds
Dirk	Bosbach	Invited	Mo-O1B	Application technologies	Solid-solution-aqueous solution (SSAS) equilibria: experimental challenges and recent advances

François	Bottin	Oral	Tu-O4B	Materials science	Thermodynamic stability of UO₂ surface by means of DFT+U calculations: interplay between polarity and overstoichiometry
Johann	Bouchet	Invited	Mo-O1A	Physics	Vibrational properties of the light actinides
Avraham I	Bram	Poster	Mo-PS1	Physics	The role of transition metals (TM) on the symmetry of Al-TM-Ac alloys (Ac= actinides and lanthanides)
Antje	Bremer	Poster	We-PS2	Chemistry	Influence of the solvent on the complexation of Cm(III) with nPr-BTP studied by time-resolved laser fluorescence spectroscopy
Vinzenz	Brendler	Invited	Th-O1B	Chemistry	Uranium sorption onto single mineral phases - approaching consistency and robustness
Nick	Brincat	Oral	We-O2A	Materials science	DFT Investigation of Uranium Oxides and Defect Structures
Peter	Burns	Invited	Th-O1B	Chemistry	Recent progress in the synthesis, properties, and applications of uranyl peroxide nanoscale cage clusters
Lucile	Chatelain	Oral	Mo-O2B	Chemistry	Cation-Cation Complexes of pentavalent uranyl: towards polymetallic assemblies with unusual magnetic properties
Kathy	Dardenne	Poster	Mo-PS1	Application technologies	µ-focus capabilities at the INE-Beamline for actinide science at ANKA
Tanmoy	Das	Oral	Mo-O2A	Physics	Emergent Fermi liquid physics in actinides within an intermediate coupling model
Christophe	Den Auwer	Invited	Tu-O1B	Chemistry	The role of phosphorous biochemistry in actinide human contamination
Paula	Diaconescu	Invited	Mo-O3B	Chemistry	Unique advantages of organometallic supporting ligands for uranium complexes
Alexander	Diener	Poster	Mo-PS1	Application technologies	In-situ measurement of a dissolved alpha emitter by electro-precipitation
Vladimir	Domanov	Invited	We-O1B	Chemistry	Formation of New Exotic Curium Oxides CmO3 and CmO4 in the Gas Phase
Vladimir	Dremov	Poster	Mo-PS1	Materials science	MD simulation of the effect of self-irradiation upon static strength characteristics of materials
Moris S.	Eisen	Invited	We-PL1	Application technologies	Actinides in Catalysis
Pavlyukevich	Ekaterina	Poster	Mo-PS1	Application technologies	Investigation of diformylhydrazine interaction with Pu in technological media of extraction SNF reprocessing
Saad	Elgazar	Poster	Mo-PS1	Physics	Electronic structure and Fermi surface of paramagnetic and antiferromagnetic UPt2S₂
Sue	Ennaceur	Oral	Th-O2A	Materials science	The effects of thermal conditioning and recovery processes on the δ →γ phase transformation mechanisms in plutonium.
Clément	Falaise	Oral	Th-O2B	Chemistry	Molecular and 3D hybrid architectures with tetravalent uranium
Joy	Farnaby	Poster	We-PS2	Chemistry	Arene-Actinide interactions in the Flexible Macrocyclic Ligand Environment of trans-Calix[2]benzene[2]pyrrolide
Ian	Farnan	Invited	Mo-O3A	Materials science	High-resolution Nuclear Magnetic Resonance Investigation into Chemical Shifts in UO₂ and ThO₂ and Ordering in Uranium-Thorium Oxide Solid Solutions.

David	Fellhauer	Poster	We-PS2	Chemistry	Thermodynamic evaluation of Np redox processes in dilute aqueous solutions at pH 4 - 10 under reducing conditions
Anton	Filanovich	Poster	Mo-PS1	Physics	Thermal and elastic properties of actinides on the example of americium and curium: a self-consistent thermodynamic approach
Sarah	Finkeldei	Poster	Mo-PS1	Materials science	Pyrochlore - a promising host phase for actinide immobilisation
Rebecca	Flint	Invited	Mo-04A	Physics	Spins, electrons and broken symmetries: realizations of two channel Kondo physics
Michael	Franzmann	Poster	Mo-PS1	Application technologies	Ultra-Trace Determination of Pu and Np Isotopes by Resonance Ionization Mass Spectrometry
Michel	Freyss	Invited	Tu-04B	Materials science	First-principles modeling of nuclear fuels: strong 5f electron correlations and dispersive bonds
Annick	Froideval Zumbiehl	Invited	Th-03A	Materials science	Uranyl speciation at the water/mineral interface: XPS, TRLFS and XAFS studies
Toshiyuki	Fujii	Poster	We-PS2	Chemistry	Raman Spectroscopic Study on Uranyl and Neptunyl Complexes in Concentrated Chloride Solutions
Yuhei	Fukuda	Poster	We-PS2	Chemistry	Sulfurization behaviour of uranium and zirconium oxides with CS₂
Rupesh	Gaikwad	Poster	We-PS2	Chemistry	Synthesis of a phosphorus Schiff base and its application in Thorium (IV) coordination
Jérémy	Gaillard	Poster	We-PS2	Chemistry	Radiolysis of adsorbed water on actinides oxides surface: investigations on the surface state evolution by hydration
Hitos	Galán	Poster	We-PS2	Chemistry	Towards stability rules of extractants involve in minor actinides partitioning processes: Study of TODGA degraded samples under different experimental conditions.
Andrew	Gaunt	Oral	Mo-02B	Chemistry	Molecular Transuranic Discovery Science
Andreas	Geist	Invited	Th-04B	Application technologies	An(III)/Ln(III) separation: N-donors do the job - but how?
Ana	Gil-Martin	Poster	Mo-PS1	Materials science	Actinide oxalate compounds: structure directing role of the monovalent cations
Thomas	Gouder	Invited	Th-01A	Materials science	Surface Science Study of Spent Fuel Corrosion Processes using Thin Films Model Systems
Tamara	Griffiths	Poster	We-PS2	Chemistry	Understanding molecular speciation of actinides in the PUREX process
Travis	Grimes	Poster	We-PS2	Chemistry	Trivalent Lanthanide/Actinide Separation Using Aqueous-Modified TALSPEAK Chemistry
Jean-Christophe	Griveau	Oral	Mo-02A	Physics	Unconventional Superconductivity in Transuranium compounds : 10 years of research at ITU
Roman	Gumeniuk	Poster	Mo-PS1	Physics	Physical properties of UBeGe and ThBeGe intermetallic compounds
Yoshinori	Haga	Invited	We-04A	Physics	High quality single crystal growth and electronic state investigation of actinide intermetallic compounds
Itzhak	Halevy	Invited	We-01A	Application technologies	New aspects in nuclear forensics. Aerial Radiation Monitoring before and after radiological event
Han	Han	Poster	Mo-PS1	Physics	First-principles calculation of intrinsic and defective properties of UO₂and ThO₂

Ladislav	Havela	Oral	Tu-O3A	Physics	Amorphous 5f ferromagnet with high TC: UH3Mox
Amir	Hen	Poster	Mo-PS1	Physics	Structural, Electronic and Magnetic Properties of NpNi₅
Christoph	Hennig	Poster	We-PS2	Chemistry	Formation of actinide(IV) carboxylate complexes in aqueous solution - the unexpected predominance of hexanuclear species
Kiel	Holliday	Poster	We-PS2	Chemistry	Nuclear Fallout Debris Formation and Fractionation in Aerodynamic Particles
Nina	Huittinen	Oral	Tu-O2A	Environmental science	A TRLFS study on the sorption of Cm(III) on natural kaolinite - The role of mineral dissolution in alkaline kaolinite suspensions
Yasuhisa	Ikeda	Oral	Mo-O2B	Chemistry	Structural Studies on Uranyl Species in Acetoritrile and 1-Ethyl-3-methylimidazolium Nitrare ([EMI][NO3]) Dissolved [EMI][UO2(NO3)4] - Evidence for the Formation of [UO2(NO3)4]2-
Igor	Izosimov	Poster	We-PS2	Environmental science	Chemiluminescence specroscopy of actinides and lanthanides in solutions
Jason	Jeffries	Poster	Mo-PS1	Materials science	Phase transformation inhibition in Pu-1.9 at.% Ga
Debbie	Jones	Poster	We-PS2	Chemistry	Optical spectroscopy study into the bio-reduction of the uranyl(VI) ion and the uranyl(V) and uranium(IV) species generated.
Kim	Jong-Goo	Poster	We-PS2	Chemistry	Effect of trivalent dopant, Gd3+, on the reaction of U1-yGdyO2 and Cs2O
Euo Chang	Jung	Invited	Th-O1A	Materials science	Spectroscopic characteristics of U(VI)-lanthanide(III) complexes adsorbed onto a silica surface and U(VI)-carbonate complexes in aqueous solutions
Dariusz	Kaczorowski	Invited	Tu-O3A	Physics	Diverse nature of 5f electrons in cage-compounds UT2Zn20 and UT2Al20
Peter	Kaden	Poster	We-PS2	Chemistry	Evidence for covalence in a N-donor complex of Americium(III)
Robert	Kamalov	Poster	Mo-PS1	Materials science	Interaction of prospective metallic construction materials with uranium-containing chloride melts
Alexey	Karavaev	Oral	Th-O3A	Materials science	Relative thermodynamic stability of radiation defect clusters and He bubbles in δ-Pu-Ga alloys and their interaction with preexisting extended defects
Tatiana	Kazakovskaya	Poster	We-PS2	Environmental science	The Hydrothermal Behavior of Depleted Uranium Oxides
Tatiana	Kazakovskaya	Oral	Th-O3B	Environmental science	²³⁷Np Sorption by UO₂ Under Repository Conditions
Andy	Kerridge	Oral	Th-O2B	Chemistry	Oxidation state and aromaticity in f-element metallocenes M(C₈H₈)₂
Annie	Kersting	Oral	Tu-O2A	Environmental science	Determining the Biogeochemical Mechanisms that Control Plutonium Transport
Kwang-Wook	Kim	Oral	Tu-O2B	Chemistry	Evaluation of stability of uranyl peroxide compounds in solution
Kwangrag	Kim	Poster	Mo-PS1	Materials science	Numerical Investigation of Interfacial Flow in a Molten Immiscible LiCl-KCl/Cd System
Tohru	Kobayashi	Poster	We-PS2	Chemistry	Actinide extraction and complexation properties of oxygen-nitrogen hetero donor ligand PTA

Taishi	Kobayashi	Poster	We-PS2	Chemistry	Temperature Effect on the Solubility and Solid Phase Stability of Thorium Hydroxide
A.V.	Kolomiets	Oral	Mo-O4A	Physics	The increase of the Curie temperature of UGa₂ at high pressure
Yulia	Konevnik	Poster	We-PS2	Environmental science	Sorption Characteristics of the Rocks Confining a Radioactive Waste Repository
Rudy	Konings	Invited	Fr-PL1	Materials science	The high temperature behaviour of actinide fuels
Elena	Kosheleva	Poster	Mo-PS1	Physics	On the possibility of predicting the dynamic properties of light actinides
Gabriel	Kotliar	Invited	Mo-PL1	Physics	Signature of strong correlations in actinides and their compounds: a Dynamical Mean Field Theory perspective
Matthias	Krack	Invited	Tu-O4B	Materials science	On the peculiarities of the DFT+U approach in the simulation of uranium dioxide
Clemens	Kratochwil	Invited	Th-O4B	Application technologies	Current Status and Future Application of Actinide based Radiopharmaceuticals in Nuclear Medicine
Ananthasivan	Krisnamurthy	Invited	Fr-O1B	Application technologies	Techniques for measuring the temperature of phase transitions involving liquids in actinide bearing systems.
Vasily	Krylov	Poster	Mo-PS1	Physics	¹¹⁹Sn Mössbauer spectroscopy of 3d-, 4f- and U-intermetallic compounds
Vasily	Krylov	Poster	Mo-PS1	Physics	The screening effect of magnetic exchange interactionin the U- and Gd-based intermetallic compounds
Sergey	Kulyukhin	Poster	We-PS2	Chemistry	Mechanism of UO2(NO3)2×6H2O Decomposition under Microwave Irradiation
Sergey	Kulyukhin	Poster	We-PS2	Chemistry	Plutonium and uranium concentration from sea water
Sergey	Kulyukhin	Poster	We-PS2	Chemistry	Interaction of UO22+ Aqueous Solutions with Sorbents Based on Modified Silica Gel Containing Cu, Ni, and Zn
Peter	Kunz	Oral	Fr-O2B	Application technologies	Development and characterization of composite uranium carbide targets at TRIUMF
Sergey	Kuznetsov	Poster	Mo-PS1	Materials science	Influence of fluoride and oxide ions on the electrochemical behaviour of uranium in LiCl-KCl eutectic melt
Fanny	Lalire	Poster	Mo-PS1	Materials science	Phase transformations in PuGa 1 at.% alloy: Elucidation of mechanisms of reversion process following martensitic transformation by coupling in situ experiments and CALPHAD-based calculations
Fanny	Lalire	Oral	Th-O2A	Materials science	Kinetic study of delta to alpha' isothermal martensitic transformation in PuGa 1at%
Madeleine	Langford Paden	Poster	We-PS2	Chemistry	Development of a simplified soft-donor technique for trivalent actinide-lanthanide separations.
Elena	Lapshina	Oral	Th-O2B	Chemistry	Separation of ²²⁵Ac from radionuclides generated by proton irradiation of natural thorium using extraction chromatography
Gareth	Law	Invited	Th-O3B	Environmental science	Neptunium Biogeochemistry in Systems Representative of the Nuclear Legacy
Florent	Lebreton	Poster	Mo-PS1	Materials science	Recent advances in the study of U_{1-x}Am_xO_{2±δ}: solid solution synthesis, densification and structural properties
Florent	Lebreton	Poster	Mo-PS1	Materials science	XRD monitoring of α self-irradiation effects in U1-xAmxO2±δ mixed-oxides

Amélie	LECLERCQ	Poster	We-PS2	Environmental science	Study of the behaviors and the transfers of ^{238,239+240}Pu and ²⁴¹Am in different natural compartments (soil, water, sediment)
Ruiwen	Li	Poster	Mo-PS1	Materials science	Influence of adding niobium to uranium on the initial kinetics of hydriding
Gan	Li	Oral	Th-02A	Materials science	Raman spectroscopic characteristics of stoichiometric and non-stoichiometric uranium oxides
Stephen	Liddle	Oral	Mo-04B	Chemistry	Recent Advances in Terminal Uranium Nitride Triple Bond Chemistry
Patric	Lindqvist-Reis	Poster	We-PS2	Chemistry	Structure and spectroscopic evidence of hexavalent neptunyl and plutonyl mono- and dinitrate complexes in aqueous nitric acid
Michael	Ling	Oral	Th-02A	Materials science	Solid state phase transformation study on Pu-Ga alloys containing 0.18 to 0.63 wt.% Ga
Ksenia	Lipkina	Oral	Fr-02B	Application technologies	Inert Matrix Fuel with Isolated Arrangement of PuO₂ or MA to Achieve Ultra-High Burn-up
Matthias W.	Loeble	Oral	We-02B	Chemistry	Probing and Quantifying Orbital Mixing in f-Element Molecular Bonding
Jeffrey	Long	Invited	Mo-PL2	Chemistry	f-Element Single-Molecule Magnets
Marisol Janeth	Lozano Rodriguez	Oral	We-02B	Chemistry	EXAFS Study of f-Elements Thiocianate Complexation
Greg	Lumpkin	Invited	Tu-03B	Materials science	Experimental and atomistic modelling studies of nuclear fuel cycle materials
Wenhua	Luo	Oral	Fr-02A	Physics	Density Functional Study of CO Adsorption on Pu (100) Surface
Alexander	Maershin	Poster	We-PS2	Chemistry	Investigation of Plutonium Trifluoride Solubility in Molten Fluorides
Alexander	Maershin	Poster	We-PS2	Chemistry	Investigation in field of partitioning of minor actinides and rare elements in chloride melt
Nicola	Magnani	Invited	Th-04A	Physics	Fundamental magnetic interaction in actinide-based nanomagnets
Pablo	Maldonado	Poster	Mo-PS1	Physics	Ab initio prediction and experimental verification of materials surface stability
Dmitry	Maltsev	Poster	We-PS2	Chemistry	Electrochemical and thermodynamic properties of uranium in low melting LiCl-KCl-CsCl eutectic
Cécile	Marie	Oral	Th-02B	Chemistry	Separation of Americium alone from a Concentrated Raffinate by Liquid-Liquid Extraction
Maria do Sameiro	Marques Fernandes	Invited	Mo-01B	Chemistry	The fate of trivalent actinides in clay based radioactive waste repositories
Timothy	Marshall	Poster	We-PS2	Environmental science	The fate of uranium and technetium during magnetite crystallisation at hyperalkaline pH
Laura	Martel	Oral	Th-02A	Materials science	The unique solid-state NMR facility at JRC-ITU for the study of highly radioactive compounds
Leigh	Martin	Poster	We-PS2	Chemistry	The Thermodynamics of Extraction of Lanthanides and Actinides by Solvating and Ion-Exchanging Ligands: A Comparative Study
Silvie	Maskova	Oral	Fr-02A	Physics	Impact of hydrogen absorption on onset of magnetism in U₂(Ni_{1-x}Fe_x)₂Sn

Alexandre	Maslennikov	Poster	We-PS2	Application technologies	Preparation, phase composition, microstructure and electrochemical properties of UPd₃ and URu₃ in the solutions of nitric acid
Taku	Matsumoto	Oral	We-02A	Materials science	Thermal conductivity measurement of (Pu_{1-x},Am_x)O₂ (x=0.03, 0.07)
Klaus	Mayer	Invited	We-01A	Application technologies	Actinides in Scrap, Dirt and Deposits - A Challenge for Investigative Radiochemists
Marinella	Mazzanti	Oral	Mo-03B	Chemistry	Uranium chemistry: from nuclear to single molecule magnets and small molecule activation.
Roland	Meier	Group	We-PS2	Chemistry	Selective recovery of actinides from An-Zr-fuel by electrorefining in molten LiCl-KCl
Gaël	Ménard	Oral	Tu-04B	Materials science	Dissolution of innovative irradiated fuels: the case of HELIOS and CONFIRM
Karsten	Meyer	Invited	Mo-04B	Chemistry	Small Molecule Activation at Reactive Complexes of Uranium
Daniel	Meyer	Invited	Mo-04B	Chemistry	Relation between the structure and the microstructure of a solid silicon hybrid based material and the plutonium and americium extraction behaviour from high level waste.
Kyoichi	Morimoto	Poster	Mo-PS1	Materials science	Thermal conductivities of (U_{1-y}, Pu_y)O_{2.00}(y = 0.00 - 0.46)
Katherine	Morris	Invited	Tu-PL1	Environmental science	Radionuclide Biogeochemistry in the Nuclear Environmental Sciences.
Katharina	Müller	Oral	Tu-02A	Environmental science	Identification of Np(V) sorption complexes at the hematite-water interface studied by in-situ ATR FT-IR spectroscopy
Tsuyoshi	Murakami	Oral	Tu-02B	Chemistry	Electrorefining of irradiated metallic fuel with limited Zr dissolution
Boris	Nadykto	Poster	Mo-PS1	Physics	Simulations of incipient damage and nanovoids in plutonium during alpha-decay
Louise	Natrajan	Invited	Tu-03B	Materials science	Keeping Actinide Reactivity Under Surveillance Using Optical Fingerprinting
Stefan	Neumeier	Poster	Mo-PS1	Materials science	German Joint Research Project on "Conditioning of long-lived Radionuclides in Ceramic Waste Forms" - An Introduction
Heino	Nitsche	Oral	Tu-04A	Environmental science	Actinide Interactions with Ordered Mesoporous Carbon Materials
Alexander	Ochkin	Poster	We-PS2	Chemistry	Optimization Criterions for H₂O-UO₂(NO₃)₂-TBP System.
Alexander	Ochkin	Poster	We-PS2	Chemistry	Dodecane effect on nitric acid extraction with TBP.
Takanari	Ogata	Invited	Th-PL1	Materials science	Development Issues of Metal Fuels for Fast Reactors
Toshihiko	Ohnuki	Invited	Th-03B	Environmental science	Effect of organic acids on the adsorption and reduction of uranium(VI) by microorganisms
Grzegorz	Olszewski	Poster	We-PS2	Environmental science	Biogeochemistry of uranium in the southern Baltic ecosystem
Grzegorz	Olszewski	Poster	We-PS2	Environmental science	The radiochemical contamination (²³⁴U and ²³⁸U) of zone around phosphogypsum waste heap in Wiślinka (northern Poland)
Grzegorz	Olszewski	Poster	We-PS2	Environmental science	²⁴¹Pu in the southern Baltic Sea

Peter M.	Oppeneer	Oral	Mo-O2A	Physics	Photoemission imaging of 3-dimensional Fermi surface pairing at the hidden order phase transition in URu₂Si₂
Alexander	Osipenko	Poster	Mo-PS1	Application technologies	Separation of uranium and lanthanides in "molten salt - liquid metal" system
Alexander	Osipenko	Oral	We-O3B	Chemistry	Promising alloy for separation actinides from lanthanides in molten salt - liquid metal system
Antonio	P. Goncalves	Oral	We-O3A	Physics	The UCoGe ferromagnetic superconductor: results from HRTEM studies
Antonio	P. Goncalves	Poster	Mo-PS1	Materials science	Submicron and nanostructured uranium carbides prepared by electrospinning
Antonio	P. Goncalves	Poster	Mo-PS1	Physics	Studies on the UFeC₂ uranium carbide
Tae-Hong	Park	Oral	Th-O2B	Chemistry	Spectroscopic study of redox behaviour of neptunium ions in molten LiCl-KCl eutectic
Seung	Park	Poster	We-PS2	Chemistry	Redox Mechanism of Nd(III) Ions in High Temperature LiCl-KCl Eutectic Observed by UV-Vis Absorption Spectroscopy in Combination of Electrolysis
Shi	Peng	Poster	Mo-PS1	Materials science	Microstructure-related hydride nucleation sites on aged U-0.79 wt.% Ti alloy
Matthieu	Peniel	Poster	Mo-PS1	Materials science	High-temperature experimental study on the U-Mo-C system
Sara	Perez-Martin	Poster	Mo-PS1	Physics	Proposal for thermo-mechanical properties correlations of MOX bearing minor actinides fuels
Guillaume	Peter Soldani	Oral	We-O3B	Chemistry	Thermal stability of ammonium actinide(IV) nitrate
V.G.	Petrov	Poster	We-PS2	Chemistry	Electronic Structure of Plutonium Dioxide
V.G.	Petrov	Poster	We-PS2	Chemistry	Chemical Bond Nature in Neptunium Dioxide
V.G.	Petrov	Poster	We-PS2	Chemistry	Synthesis and Characterization of U-doped Zircon and Baddeleyite
Elena	Pichuzhkina	Poster	We-PS2	Chemistry	Curium-technetium complex oxide
Karin	Popa	Oral	Tu-O2A	Environmental science	Sorption of uranium on lead hydrohyapatite
Ioana-Carmen	Popescu	Poster	We-PS2	Environmental science	Romanian perspective on iron nano-particles utilization as remediators for radioactive polluted environment
Damien	Prieur	Oral	Mo-O3A	Materials science	Charge distribution and local structure of M_{0.80}Am_{0.20}O_{2±x} (M: Th, U and Pu)
Alessia	Provino	Poster	Mo-PS1	Physics	Structure and magnetism in U2Ni21B6, (U,Nb)2Ni21B6 and (U,Nb)3Ni20B6
Victor	Pushkov	Poster	Mo-PS1	Materials science	Unalloyed uranium deformation curves under static and dynamic loading
Francesca	Quinto	Oral	Tu-O2A	Environmental science	Investigating the migration of trace levels of fallout plutonium and uranium in an ombrotrophic peat bog profile
Béatrice	Rabu	Poster	Mo-PS1	Application technologies	Post-Irradiation Examinations on PHENIX axially heterogeneous pins relevant to ASTRID fuel design: ZEBRE and PAVIX irradiations
Quentin	Raffy	Poster	We-PS2	Environmental science	New insights into uranyl interaction with proteins at physiological pH
Donald	Reed	Poster	We-PS2	Chemistry	Temperature and Ionic Strength Effects on Neptunium Speciation in Simplified Brine Systems

Donald	Reed	Oral	Tu-O4A	Environmental science	Actinide Colloids in High Ionic-Strength Media
Elodie	Remy	Poster	Mo-PS1	Materials science	Single and mixed f-elements sintered oxide pellets synthesis with tailored microstructures.
Jennifer	Rochford	Poster	We-PS2	Chemistry	Actinide colloids and nanoparticles: relevance to legacy waste, clean-up and geological disposal
David	Rodrigues	Oral	Tu-O2B	Chemistry	Electrochemical behavior and speciation of thorium with fluorides in molten salt at high temperature
Andrei	Rogalev	Oral	Mo-O2A	Physics	Detection of a finite 5f orbital magnetic moment in Curium metal using XMCD.
André	Rossberg	Poster	We-PS2	Environmental science	Uranium(VI) sorption on aluminium(hydr)oxides - inferring a functional relationship between sorption complex structures and physicochemical parameters by application of artificial neural networks
Jörg	Rothe	Poster	We-PS2	Chemistry	XAFS and solubility investigations of penta- and hexavalent actinides in dilute to concentrated salt brines
Jan	Rusz	Invited	Th-O4A	Physics	Magnetic circular dichroism with x-rays and electrons
Tarik	Saleh	Oral	Tu-O3B	Materials science	Elastic Properties of Alpha Plutonium Measured Via Resonant Ultrasound Spectroscopy
Paolo	Santini	Invited	Mo-O1A	Physics	Elementary excitations in Uranium Dioxide: Unravelling the tangle
Mark	Sarsfield	Oral	Th-O2B	Chemistry	Americium and Plutonium Purification by Extraction (the AMPPEX process)
Takayuki	SASAKI	Poster	We-PS2	Chemistry	Apparent Solubility of Thorium in the Presence of Humic Substances
Tetsuya K.	Sato	Oral	We-O2B	Chemistry	The first successful ionization of Lr (Z=103) by a surface ionization technique
Nobuaki	Sato	Oral	Fr-O2B	Application technologies	Phase relations of uranium and zirconium oxides at high temperatures for fuel debris treatment
Alexey	Savchenko	Poster	Mo-PS1	Application technologies	New Concept of Designing Composite Fuel for Fast Reactors with Closing Fuel Cycle
Alexey	Savchenko	Poster	Mo-PS1	Application technologies	Thermodynamic Aspects of Interphase Interaction in Heterogeneous Alloys and Its Influence on Alloys Properties
Matthias	Schädel	Oral	We-O2B	Chemistry	The Redox Potential of Mendelevium (Md) Determined Atom-at-a-Time with a Flow Electrolytic Column
Andreas C.	Scheinost	Invited	Tu-O4A	Environmental science	Interaction of plutonium with magnetite under anoxic conditions: Reduction, surface complexation, and structural incorporation
Moritz	Schmidt	Invited	Tu-O1A	Environmental science	Plutonium reactivity at the mineral/water interface
Astrid	Schneidewind	Oral	Mo-O4A	Physics	Possible Pseudogap Phase in the Cubic Superconductor UBe13
Picart	Sebastien	Poster	We-PS2	Chemistry	Actinide mixed oxide microspheres synthesis using Weak Acid Resin process: unconventional precursors for Minor Actinide Bearing Blanket fabrication
Nadezda	Selchenkova	Poster	Mo-PS1	Physics	Physical nature of Light Actinides Longevity in the Dynamic Failure Phenomenon
Andrei	Shadrin	Poster	Mo-PS1	Application technologies	Oxidation of Uranium-Plutonium Mixed Nitrides

Alexander	Shick	Oral	Mo-O2A	Physics	Unified character of correlation effects in unconventional Pu-based superconductors and δ-Pu
Taeko	Shinonaga	Invited	Tu-O4A	Environmental science	Isotopic Composition of Uranium and Activity Concentration of ^{134, 137}Cs in Aerosol Samples Collected at 120 km from Fukushima before and after the Reactor Accidents
Hideaki	Shiwaku	Poster	We-PS2	Chemistry	EXAFS investigation of substituent effect of the hybrid type PDA complexes for actinides and lanthanides separation.
Olga	Shmidt	Poster	We-PS2	Chemistry	Mathematical model for crystallization purification of uranyl nitrate hexahydrate in continuous crystallization column
David	Shuh	Invited	Tu-O1A	Environmental science	Actinide Environmental Science Utilizing Soft X-ray Synchrotron Radiation
Jennifer	Shusterman	Poster	We-PS2	Chemistry	Solid Phase Extraction Materials for Separations of Actinides and Fission Products
Wigbert	Siekhaus	Oral	Th-O2A	Materials science	SIMS analysis of hydrogen and carbon co-precipitation in uranium and SEM/FIB analysis of its effect on surface reactions.
Mikhail	Skripkin	Poster	We-PS2	Chemistry	Vibrational spectroscopic study of some rare-earth metals trifluoromethylsulfonates enneahydrates and of corresponding salts of uranium(III) and curium(III)
Anna Louise	Smith	Oral	Fr-O2A	Physics	Study of the phase equilibria in the Na-U-O, Na-Pu-O and Na-Np-O systems, and application to the safety of Sodium cooled Fast Reactors
Alice I.	Smith	Poster	Mo-PS1	Physics	Vibrational Properties of Uranium Hydride and Uranium Deuteride
Joseph	Somers	Invited	We-O4B	Application technologies	Synthesis and characterisation of minor actinide fuels and compounds
Alejandra	Sornosa Ten	Poster	We-PS2	Chemistry	Coordination Chemistry of Actinides with Hydroxamic Siderochelates
Kastriot	Spahiu	Invited	We-O4B	Application technologies	Recent developments on the evaluation of spent fuel as a waste form.
Greg	Stewart	Oral	We-O3A	Physics	New Uranium Heavy Fermion Antiferromagnet, γ>400 mJ/UmolK²
Silvia	Stoica	Poster	We-PS2	Environmental science	Purification and separation of U, Pu and Am isotopes in environmental samples by extraction chromatography for alpha-spectrometry analyses
Manuel	Sturzbecher-Hoehne	Poster	We-PS2	Chemistry	UV-vis and fluorescence spectroscopic methods to evaluate the solution thermodynamic properties of hydroxypyridinonate actinide and lanthanide complexes
Manuel	Sturzbecher-Hoehne	Poster	We-PS2	Chemistry	Receptor recognition of transferrin bound to f-block metals: a segregation step in cellular acquisition of actinides
Michi-To	Suzuki	Poster	Mo-PS1	Physics	Microscopic theory of the insulating electronic ground states of actinides dioxides AnO₂ (with An = U, Np, Pu, Am and Cm)
Tomoya	Suzuki	Poster	We-PS2	Chemistry	Effect of Hydrogen bonds on melting points and packing coefficients of uranyl nitrate complexes with cyclic urea derivatives
Shinichi	Suzuki	Poster	Mo-PS1	Materials science	Selective Actinide Separation Process by Amide Based New Ligands.
Masahide	Takano	Invited	Fr-O1B	Materials science	Recent advances in material properties and behavior of transuranium compounds for application to nuclear fuel cycle
Dariia	Ternova	Poster	We-PS2	Chemistry	New Ionic Liquid compounds for liquid/liquid extraction of actinides and other metallic ions

Guoxin	Tian	Poster	We-PS2	Chemistry	Study on the extracted complexes of purified Cyanex301 with Cm(III) and Ln(III) with spectrophotometry, fluorometry, and EXAFS
Ilya	Tkach	Poster	Mo-PS1	Materials science	Structure stability of the cubic γ-phase uranium molybdenum alloys.
J. G.	Tobin	Invited	Fr-O1A	Physics	Soft X-ray Spectroscopy of the Actinides
Olivier	Tougait	Poster	Mo-PS1	Materials science	X-ray diffraction study of the eutectoid decomposition of γ-U(Mo) powder produced by magnesiothermic reduction.
Olivier	Tougait	Poster	Mo-PS1	Materials science	Densification of uranium carbide pellets: Preliminary result of spark plasma sintering and comparison with conventional sintering techniques
Olivier	Tougait	Poster	We-PS2	Chemistry	Scanning phase diagrams to discover new phases with original properties: Examples from U-T-Ge (T = Fe, Co, Ru) ternary systems.
Kate	Tucker	Poster	We-PS2	Chemistry	Heavy metal extraction using advanced PUREX style partitioning systems
Alexander	Uchaev	Poster	Mo-PS1	Physics	On relationship between thermodynamic and dynamic properties of light actinides
Akihiro	Uehara	Poster	We-PS2	Chemistry	In-situ XAFS analysis of electrochemical reduction of uranium(VI) in highly concentrated LiCl
Valérie	Vallet	Invited	We-O1B	Chemistry	How to build accurate macroscopic models of actinide ions in aqueous solvents?
Valérie	Vallet	Poster	We-PS2	Chemistry	Preparation, stabilization, spectroscopic, computational studies of tetravalent protactinium in aqueous solution
Octavian S.	Valu	Poster	Mo-PS1	Materials science	The high temperature heat capacity of thorium-plutonium mixed oxides
Thomas	Venhaus	Poster	Mo-PS1	Physics	X-ray photoelectron spectroscopy of 7-at.% gallium δ-stabilized plutonium
Mark James	Vermeulen	Poster	Mo-PS1	Physics	Neutron Capture Cross Section on 236U performed at the n_TOF facility at CERN
Stanislav	Vesnovskii	Poster	Mo-PS1	Physics	Production of Super Heavy Plutonium Isotopes for Basic Research
Tonya	Vitova	Invited	Fr-O1A	Physics	Structural investigations of actinides with advanced X-ray spectroscopy techniques
Sven C.	Vogel	Oral	We-O2A	Materials science	Chemical Segregation of U-10wt.% Mo Fuel Foils During Simulated Bonding Cycles
Sven C.	Vogel	Poster	Mo-PS1	Materials science	Non-destructive studies of fuel rodlets by neutron resonance absorption radiographyand thermal neutron radiography
Vladimir	Volkovich	Poster	Mo-PS1	Application technologies	Solubility of uranium and lanthanum in Ga-In eutectic based alloys at 25-800 ^oC
Christophe	Volkringer	Poster	We-PS2	Chemistry	Synthesis and characterization of new heterometallic uranyl-based carboxylates
Clemens	Walther	Invited	Tu-O1B	Environmental science	Radioecological Studies in Germany
William	Weber	Oral	We-O2A	Materials science	Ab initio study of defect production and migration in thoria
Andreas	Wilden	Oral	Mo-O4B	Chemistry	Development and laboratory-scale innovative-SANEX process demonstration for minor actinide partitioning using annular centrifugal contactors
Chao	Xu	Oral	Tu-O2B	Chemistry	Thermodynamic Study on the Complexation of Nd(III) and Cm(III) with Cyanex 301 in Ethanol
Tsuyoshi	Yaita	Oral	Mo-O2B	Chemistry	Complex Formation Dynamics of Actinide and Lanthanide with Poly-dentate Ligands by Time Resolved XAFS.

Hiroshi	Yasuoka	Invited	We-O4A	Physics	Observation of 239Pu NMR in PuO2-x – Facts and Perspective
Yingjie	Zhang	Poster	We-PS2	Chemistry	Self-assemblage of stable uranyl nano-clusters in the alkaline peroxide systems
Yingjie	Zhang	Poster	We-PS2	Chemistry	Structural studies of actinide complexes with picolinamide
shengfa	Zhu	Poster	Mo-PS1	Materials science	Microstructure and corrosion resistance of Cr/CrN multilayer film prepared by magnetron sputtering on depleted uranium
Gertrud	Zwicknagl	Invited	Tu-O3A	Physics	5f electron correlations and core level photoelectron spectra of actinide compounds

General information

➢**ACTINIDES 2013** is dedicated to discussion and information exchange for current research in physics and chemistry of the actinide and the transactinide elements. The conference will consist of presentations of new scientific results in plenary lectures, invited and contributed talks and presentations in poster formats. ACTINIDES 2013 also offers an excellent opportunity to establish or renew contacts with colleagues.

Session Topics

- Materials science
- Chemistry
- Physics
- Environmental science
- Application technologies

Contact

Prof. Roberto G. M. CACIUFFO
European Commission
Joint Research Centre
Institute for Transuranium Elements
JRC-ACTINIDES2013@ec.europa.eu

Plenary Speakers

Marcus ALTMAIER (KIT, Germany)
Chemistry

Eric D. BAUER (LANL, USA)
Physics

Moris S. EISEN (Technion, Israel)
Application Technologies

Rudy KONINGS (EC-JRC-ITU, Germany)
Materials Science

Gabriel KOTLIAR (Rutgers University, USA)
Physics

Jeffrey R. LONG (UC Berkeley, USA)
Chemistry

Katherine MORRIS (Uni Manchester, UK)
Environmental Science

Takanari OGATA (CRIEPI, Japan)
Materials Science

European Commission

Karlsruher Institut für Technologie

9th International Conference on the Chemistry and Physics of the Actinide Elements

ACTINIDES 2013

21 - 26 July 2013
Karlsruhe, Germany

ACTINIDES 2013
KARLSRUHE

Conference Schedule

Registration: March 20 - June 11, 2013
Late registration: after June 11, 2013
Abstract submission:
March 15-April 15 2013
Abstract acceptance notice: May 20, 2013
Conference registration: July 21, 2013
Conference: July 21-26, 2013
Conference banquet: July 25, 2013
Conference closes: noon, July 26, 2013

Organizers

➢**ACTINIDES 2013** is organized by European Commission, Joint Research Centre, Institute for Transuranium Elements (EC-JRC-ITU) and the Karlsruhe Institute of Technology, Institute for Nuclear Waste Disposal (KIT-INE), with Professors Roberto CACIUFFO, Thomas FANGHÄNEL and Horst GECKEIS acting as conference chairs.

Local Organizing Committee
Roberto CACIUFFO (EC-JRC-ITU)
Kathy DARDENNE (KIT-INE)
Melissa A. DENECKE (KIT-INE)
Rachel ELOIRDI (EC-JRC-ITU)
Alfred JIMENEZ-SEGARRA (EC-JRC-ITU)
Petra J. PANAK (KIT-INE)
Bernd SCHIMMELPFENNIG (KIT-INE)
Thorsten STUMPF (KIT-INE)
Gabriele TAMBORINI (EC-JRC-ITU)
Krisztina VARGA (EC-JRC-ITU)
Franck WASTIN (EC-JRC-ITU)

Venue

➢**ACTINIDES 2013** will be held at the Congress Centre in Karlsruhe, Germany, in the "Hebel" and "Thoma" conference rooms. Karlsruhe is situated in the sunny southern German section of the Rhine river and lies approximately between Strasbourg, France and Heidelberg, Germany. Karlsruhe can be easily reached via train or car from Frankfurt am Main, Strasbourg, or Stuttgart international airports.

Information links

➢**ACTINIDES 2013** conference website
http://actinides13.ine.kit.edu/

➢How to get there
Direction to Congress Center:
http://www.messe-karlsruhe.de/
click on English, then "Arrival"

➢**Accommodation**
www.messe-karlsruhe.de/messe_karlsruhe/anreise/hotels.php Click "Hotelbuchung"
for the event ACTINIDES 2013. Special rate if booking min. 4 weeks in advance.

➢ Info on **financial support**:
click Registration/Bursaries
http://actinides13.ine.kit.edu/72.php

International Scientific Advisory Committee

Manuel Leite de ALMEIDA (ITN, Portugal)
Polly L. ARNOLD (University of Edinburgh, UK)
Roberto CACIUFFO (EC-JRC-ITU, Germany)
Melissa A. DENECKE (KIT, INE, Germany)
Yoshinori HAGA (JAEA, Japan)
Richard G. HAIRE (Oak Ridge Nat. Lab., USA)
Itzhak HALEVY (NRCN, Israel)
Ladislav HAVELA (Charles University, Czech Republic)
Stepan N. KALMYKOV (Lomonosov University, Russia)
Jens V. KRATZ (University of Mainz, Germany)
Francis R. LIVENS (University of Manchester, UK)
Klaus LÜTZENKIRCHEN (EC-JRC-ITU, Germany)
Marinella MAZZANTI (CEA, France) (**ISAC Chair**)
Karsten MEYER (University of Erlangen, Germany)
Kazuo MINATO (JAEA, Japan)
Heino NITSCHE (UC Berkeley/LBNL, USA)
Yoshichika ONUKI (Osaka University, Japan)
Peter OPPENEER (Uppsala University, Sweden)
John SARRAO (LANL, USA)
David K. SHUH (LBNL, USA)
Baldev RAJ (IGCAR, India)
James TOBIN (LLNL, USA)
Vinh Hung TRAN (Polish Academy of Sciences, Poland)
Dominique WARIN (CEA, France)
Jong-Il YUN (KAIST, Korea)
Yongjun ZHU (Tsinghua University, China)

ANNEX

Abstracts sorted according to topics:

AT Application Technologies

CH Chemistry

ES Environmental Science

MS Materials Science

PH Physics

APPLICATION TECHNOLOGIES

PLENARY & INVITED

3-01

Actinides in Catalysis

Moris S. Eisen

Technion - Israel Institute of Technology, Haifa, Israel

Neutral and cationic organoactinide complexes have been extensively studied in the last decade as catalysts for several organic transformations. Polymerization of alkenes, oligomerization, intermolecular hydroamination, and hydrosilylation of terminal alkynes, comprise some of these processes (Equation 1).[1] In all these processes the rate determining step follows a four centered transition state.

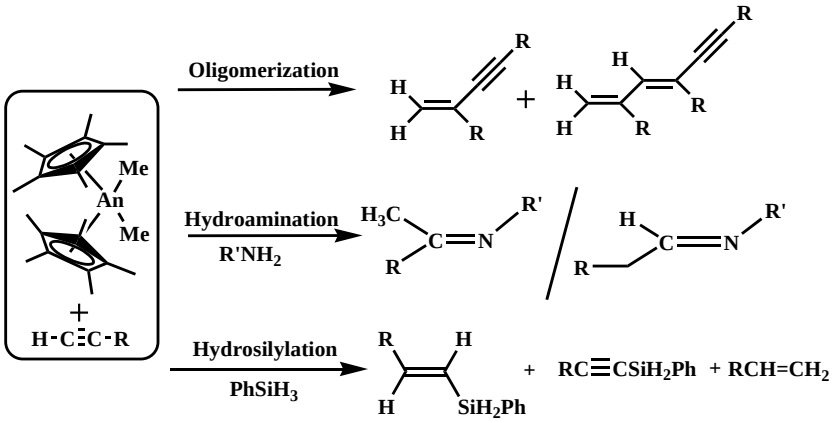

(1)

In the above mentioned processes mixtures of compounds are always obtained. Hence a conceptual question that will be addressed regards the possibility to tailor the same reactions in such a way that only in each one only one product is either chemo- and/or region-selectively obtained

As a continuation of our journey through catalysis we will ask the following question: Is possible to have a three centered transition state? For example the 1,1-insertion of isonitriles into terminal alkynes (Equation 2).[2]

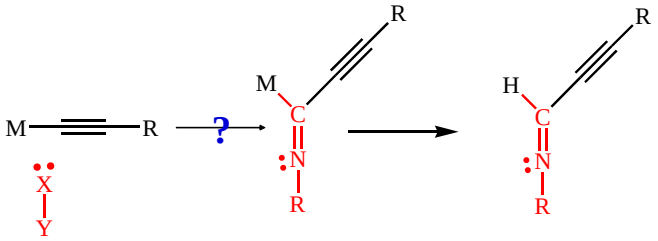

(2)

Remarkably, due to the high oxophilicity of the actinide complexes (Equation 3), all the substrates containing oxygen atoms have been excluded because of the expected low activity of the complexes due to the predictable oxygen-actinide interaction. Lin et al. have demonstrated this guideline in actinide chemistry, based on the extremely low activity of actinide complexes containing alkoxy ligands in the catalytic hydrogenation of olefins (Equation 4).[3]

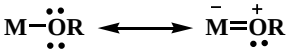

(3)

$$Cp^*_2ThMe_2 \xrightarrow{H_2\ 30^oC} [Cp^*_2ThH_2]_2 \qquad K = 3.6 \times 10^{-2}\ M^{-1}\ sec^{-1}$$

$$Cp^*_2ThMe(OR) \xrightarrow{H_2\ 100^oC} Cp^*_2ThH(OR) \qquad K = 5 \times 10^{-5}\ M^{-1}\ sec^{-1} \qquad (4)$$

In our attempts to discover new catalytic reactions for actinide-based complexes, we will show how is possible to perform the polymerization of cyclic monoesters (Equation 5).[4] This discovery opened the second conceptual question about the activity of actinide-alkoxo complexes.

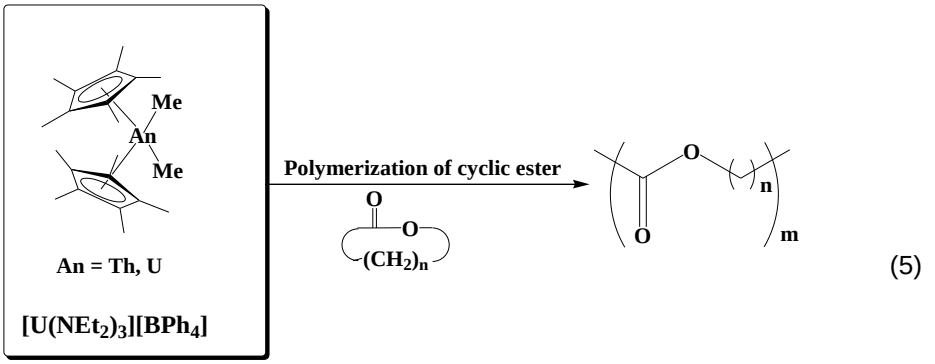

(5)

To expand the scope of the actinides in catalysis, we will show that actinides are extremely active catalysts in the dimerization of aldehydes to give the corresponding esters (Equation 6). The scope of the reaction will be presented with various organoactinide complexes in addition to kinetic and thermodynamic studies.[5]

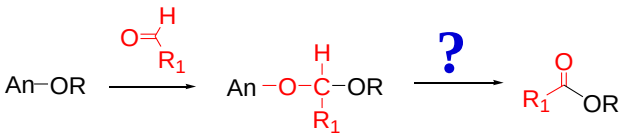

(6)

An = Th, U

Based on the observed reactivity by oxygen containing actinides, it was important to study the effect of coordinative unsaturation versus oxophilicity in actinide reactivity. To propose an answer for such difficult question, we will present the synthesis of oxo-bridged actinide complexes and their reactivity with alkynes and silanes. In addition we will introduce the concept of COPY and PASTE with actinides (Scheme 1).

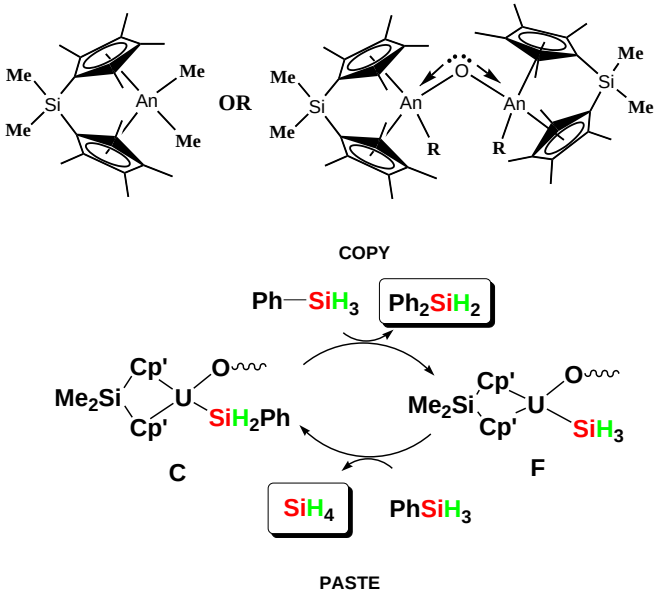

Scheme 1. Copy and paste catalytic pathways for a SiH_3 moiety promoted by actinides. The reaction is a remarkable example of a Ph-Si bond activation.

Interestingly, in all these catalytic processes, the most widely used organoactinide complexes contain the cyclopentadienyl $(C_5R_5)^-$ ancillary ligand. A new challenge will be the synthesis of organoactinide complexes containing for example a heteroatom ligands, which are by far less developed, but nonetheless reaching a high level of sophistication. Among these ligands, the amidinates, $[RC(NR')(NR'')]^-$ are very attractive due to their straightforward synthesis from simple starting materials, and the facile modification of both their steric bulk and electronic properties through the choice of proper backbone substituents. We will present the efficacy of amidinate actinide complexes in the precise formation of cyclic oligomers of e-caprolactone.[6] In addition we will show the unexpected results in the polymerization of ethylene catalyzed by these amidinate complexes when activated either poorly using a large excess of MAO (MAO = methylalumoxane) alone, improved by a mixture of trityl tetrakispentafluorophenylborate (TTPB) and a small amount of methylalumoxane (MAO), and amazingly providing the greatest activity, using only triisobutyl aluminum (TIBA). We will present a combination of ESR, C_{60} radical trapping, and MALDI-TOF studies describing the formation of the single-site active species.[7]

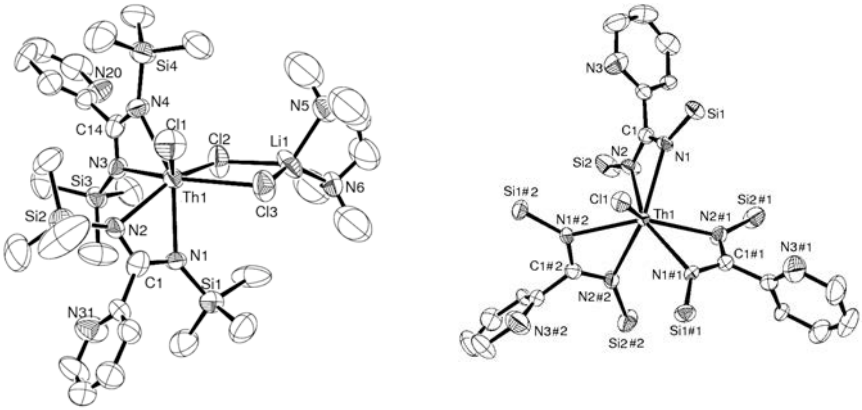

References

1. Andrea, T.; Eisen M. S. *Chem. Soc. Rev.* **2008**, *37,* 550.

2. Barnea, E.; Andrea, T.; Berthet, J.-C.; Ephritikhine, M.; Eisen, M. S. *Organometallics* **2008**, *27*, 3103.

3. Lin, Z.; Marks T. J. *J. Am. Chem. Soc.* **1987**, *109*, 7979.

4. Barnea E.; Moradov D.; Berthet, J.C.; Ephritikhine, M.; Eisen, M.S. *Organometallics* **2006**, *25*, 320.

5. Sharma, M.; Andrea, T.; Brookes, N. J.; Yates, B. F.; Eisen, M. S. *J. Am. Chem. Soc.*, **2011**, *133*, 1341.

6. Rabinovich, E.; Aharonovich, S.; Botoshansky, M.; Eisen, M. S. *Dalton Trans.* **2010,** *39*, 6667.

7. Domeshek, E.; Batrice, R. J.; Aharonovich, S.; Tumanskii, B.; Botoshansky, M.; Eisen, M. S. *Dalton Trans*. **2013**, in press.

3-02

Actinides in Scrap, Dirt and Deposits - A Challenge for Investigative Radiochemists

Klaus Mayer, Maria Wallenius, Magnus Hedberg, Zsolt Varga

European Commission JRC-ITU, Karlsruhe, Germany

The actinide elements are composed of radioactive isotopes. Their safe handling requires appropriate facilities. Some of these isotopes are fissile and, in consequence, measures for preventing their misuse have been implemented. A sophisticated system of physical protection and nuclear material safeguards was established in order to prevent theft or diversion of these actinide elements. In spite of all these measures, seizures of illicit uranium (and in very few cases also plutonium) have been reported. More recently, we have observed a number of incidents where scrap metal was found to be contaminated with uranium. Obviously, the question on the origin of the uranium arises, and nuclear forensic techniques are applied to provide hints on the place where the regulatory control of the material was lost.

Depending on the chemical form of the seized material, different radioanalytical techniques can be applied in order to measure characteristics parameters of the material. Chemical impurities in uranium ore concentrate, in particular the pattern of the rare earth elements, consist an important set of parameters pointing at the geological origin of the material. Enriched uranium associated with scrap metal was typically found to be rather inhomogeneous. By applying micro-analytical techniques we could reveal nature of the material and the isotopic composition of the individual uranium constituents.

The interpretation of the results and the attribution of the seized material to a potential origin required a comparative evaluation with literature data. The paper will describe the methodology and refer to real incidents for illustrating the application of investigative radioanalytical techniques to actinides in scrap, dirt and deposits.

3-03

New aspects in nuclear forensics Aerial Radiation Monitoring before and after radiological event

Itzhak Halevy

NRCN, Beer-Sheva, Israel

Radiological event can cause a large contamination area. Collection a good sample for forensic analysis or controlling the event could be very challenging in case of rough scenes. Aerial Radiation Monitoring (ARM) after radiological events is common and could be part of the solution for fast and all terrain monitoring. ARM before an event is done to measure the background at the scene, but no one knows where the scene will be: can we measure all the possible scenes?

Examples for radiation monitoring survey of small and large areas with different methods are given in figure 1.

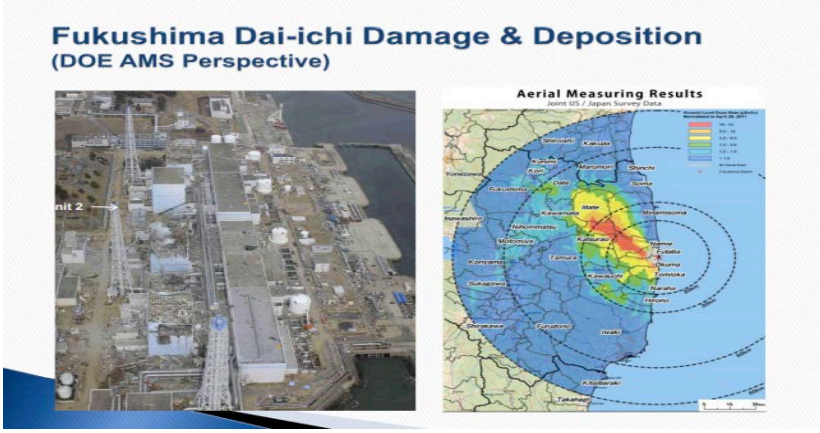

Fig 1: Left: Aerial Radiation Monitoring Survey of s Washington DC for background measurements. Right: Aerial Radiation Monitoring Survey Fukushima Dai-ichi after the event.

Are backgrounds similar in different regions? Looking at a wide Radiation Monitoring Survey, as shown in figure 2, indicates the wide variety of backgrounds as a function of intensity, energy and location. The source of radiation is a combination of natural sources in the ground and of nuclear activity.

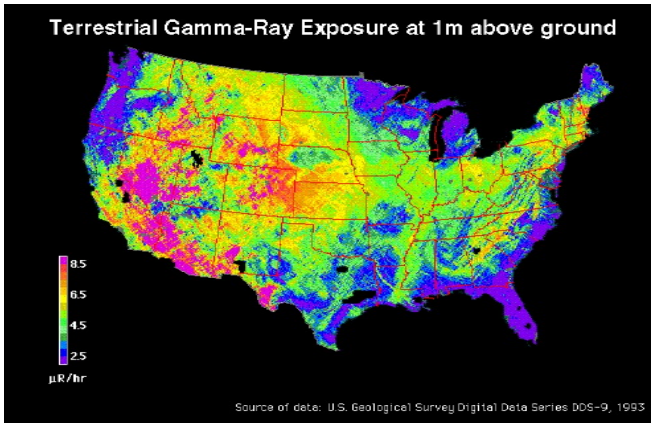

Fig 2: Terrestrial Gamma-Ray Exposure at 1m above ground in the USA.

Knowing that background differs a lot as function of location, force us to know the radiation background at the scene. We can say that there is contamination only by comparing the radiation measurements to the background at the same scene. More examples for pre-event Radiation Monitoring Survey are the surveys in populated areas and transportation lines.

Fig 3: Left: Survey 0f the Maracanazinho arena seats using a line of RIDs. Right: *The monitoring system near Vienna consisting of six chained portals.*

The mission of Aerial Radiation Monitoring after radiological event is to give the first overview on the radioactive scene and guide the first responders for detailed monitoring. There are three main concepts for Aerial Radiation Monitoring which are using different Air vehicle, namely, a plane or a chopper, unmanned plane or Mikro-Kopter. Those systems differ significantly in size, abilities and availability.

Concepts and monitoring results of "AIR RAM 2000" (chopper), "Caspar" (unmanned plane) and Mikro-Kopter will be compered. The ARM systems have the abilities to give a radiation map of the scene in terms of radiation exposure and spectrum analysis that indicates the radioactive isotopes involved.

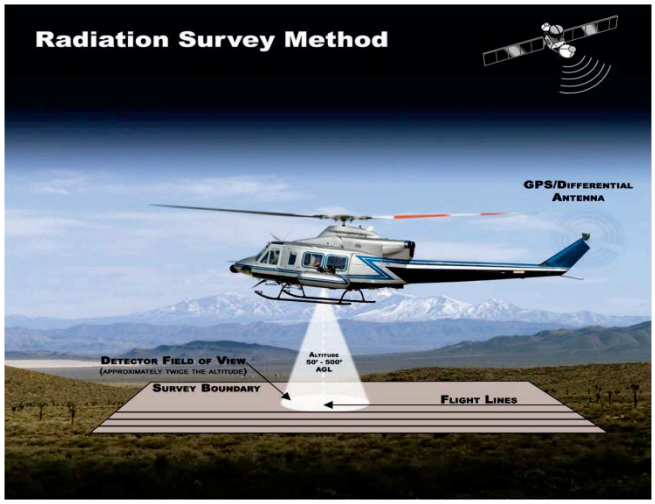

Fig 4: The method of Aerial Radiation Monitoring Survey before or after radiological event.

All the Aerial Radiation Monitoring systems have a telemetric system and the results are transmitted to a ground station in real-time. Special abilities of the Mikro-Kopter for Aerial Radiation Monitoring are dominant in indoor and outdoor scenes.

The "AIR RAM 2000" (chopper), "Caspar" (unmanned plane) and Mikro-Kopter are given as Aerial Radiation Monitoring examples in the figures. Measurements compered to models and simulations indicate the need for Aerial Radiation Monitoring systems. An Aerial Radiation Monitoring Survey of two hidden sources, 5Ci and 0.5Ci of ^{192}Ir is given in figure 6. Simulation of Aerial Radiation Monitoring Survey developed as shown if figure 7.

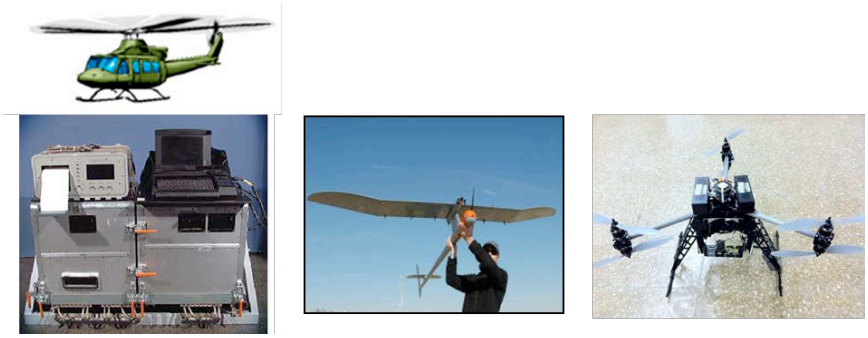

Fig 5: three different methods of Aerial Radiation Monitoring Survey before or after radiological event.

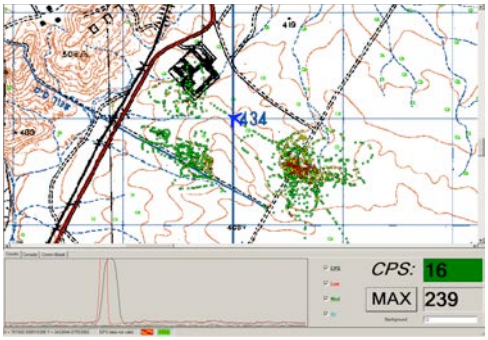

Fig 6: Aerial Radiation Monitoring Survey of two hidden sources, 5Ci and 0.5Ci of ^{192}Ir

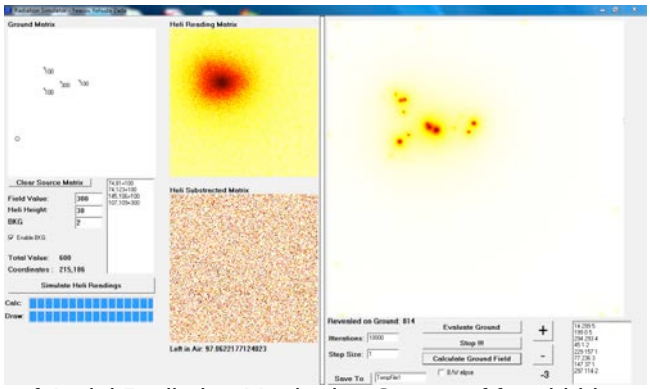

Fig 7: Simulation of Aerial Radiation Monitoring Survey of four hidden sources.

References

[1] "Illicit Nuclear Trafficking: Collective Experience and the way forward" Proceedings of an international conference, Edinburgh, 19-22 Nov 2007, IAEC

[2] Rashelle D. Mahan, "Radiological Survey of Downtown Washington DC for the 2009 Presidential Inauguration", NNSA DOE/NV/25946--684 March 2009

[3] I. Halevy, New aspects in nuclear forensics, Aerial radiological event monitoring.

JDA 42 16-21 April, Bristol, UK. (2012) School Lec.

3-99

Synthesis and characterisation of minor actinide fuels and compounds

Joseph Somers

JRC-ITU, Karlsruhe, Germany

Nuclear fuels operate under extreme conditions, due to the high power density of the reactor core. They have to withstand damage due to neutrons and large thermal gradients. They must show an adequate pellet cladding mechanical interaction (PCMI) and benign pellet cladding chemical interaction (PCCI). The chemical form of the fuel has largely concentrated on oxides, especially in Europe. Nitrides and carbides possess much higher melting points than metal fuel, and also have higher thermal conductivity than the oxides (see Table 1), which when coupled to their high metal content provide strong reasons to advocate their deployment in fast reactors. The minimisation of nuclear fuel cycle waste became an important research area in the last 20 years, whereby the long-lived radioisotopes (mostly the minor actinides (MA) neptunium, americium and curium) should be partitioned (P) from the nuclear waste for recycling and transmutation (T) in fast reactors.

Table 1. Representative physical properties of (U,20%Pu) oxide, carbide and nitride fuels

Fuel Type	**$(U,Pu)O_2$**	**(U,Pu)C**	**(U,Pu)N**
Melting point (^{0}C)	2750	2480	2650
Boiling point (^{0}C)	3150	4280	n/a
Theoretical density, ($g \cdot cm^{-3}$)	11.06	13.6	14.3
Heavy metal density, ($g \cdot cm^{-3}$)	9.7	12.9	13.5
Thermal conductivity, ($W \cdot m^{-1}K^{-1}$ at 1000°C)	3.0	20.5	20.0
Linear coefficient of thermal expansion ($x10^{-6}$)	10.7	14.7	12.5

MOX Fuels

The main synthesis routes for MOX fuels are based on powder metallurgy. Stored UO_2 and PuO_2 powders are mixed in the appropriate proportions. Without milling, the final product invariably exhibits two ceramic phases (CERCER) consisting of islands of PuO_2 distributed in a UO_2 matrix. Ball milling the precursor powders can result in a nearly perfect distribution of the Pu in the mixed oxide product.

Nitride and Carbide fuels

The synthesis of nitride and carbide fuels requires glove boxes operating in highly pure atmospheres. The carbothermal reduction route remains the synthesis route of choice. The problems of pyrophoricity can be addressed by synthesising the precursor UO_2-PuO_2-Carbon mixture in the form of large (> 50 µm) particles. This has been achieved in a sol gel step using external or internal gelation. Such methods have the advantage that the actinide precursor oxide for the carbothermal reduction is already in the form of a solid solution – $(U,Pu)O_2$. Spark Plasma Sintering (SPS) is an emerging technique for laboratory production of high quality, high density pellets.

Minor Actinide bearing fuels

Minor actinide bearing fuels can be synthesised by classical powder metallurgical routes. There are safety issues related with powder handling, especially on large scales. Liquid conversion routes for minor actinides have been developed at CEA and JRC-ITU laboratories.

The former concentrate on the preparation of the precursor powder using an oxalate precipitation. Excellent results have been obtained. Sol gel routes overcome the issue of dust. The JRC-ITU uses sol gel methods to prepare well defined particles with diameters in excess of 50 µm. Their porosity permits infiltration of an Am nitrate solution into the beads. Due to the resounding sintering nature of the sol gel material and the very small particle size of the AmO_2, high quality solid solutions are obtained. There have been very few attempts to produce minor actinide bearing nitride or carbide fuels. The volatility of Am is particularly problematic. First attempts at JRC-ITU have now been completed for their vapour pressure determination.

3-991

Recent developments on the evaluation of spent fuel as a waste form.

Kastriot Spahiu[1,2]

[1]SKB, Stockholm, Sweden, [2]Chalmers University of Technology, Göteborg, Sweden

The dissolution rate of spent nuclear fuel depends on intrinsic factors such as fuel structure and burn-up, as well as environmental factors, including groundwater composition where dissolved hydrogen originating from anoxic iron corrosion is a major component.

The burn-up of future spent fuel is expected to increase. Fuel burnup leads to complex and significant changes in the composition and properties of the fuel. The transformed microstructure, which is referred to as the high burnup structure (HBS) or rim structure in the outer region of the fuel, consists of small grains of submicron size and a high concentration of pores of typical diameter 1 to 2 μm. One of the primary driving forces behind the HBS formation is the significantly higher burnup experienced by the pellet periphery. This increased burnup is a result of neutron capture in ^{238}U that leads to a significant gradient in the radial distribution of Pu near the surface. The build-up of Pu results in corresponding gradients in fission rates and the concentrations of fission products and higher actinides. The increased actinide content in spent fuel at higher burn-ups leads to a higher α-dose rate. The same holds for beta and gamma dose rates, due to the increased amount of fission products at the rim zone. Usually when discussing high burn-up fuel dissolution, the effect of the increased radiation field with burn-up, as well as of the influence of the smaller grain size and increased porosity at the rim are mentioned as factors which contribute to increased dissolution rates. A third factor, which is the increase of fission product and actinide doping in high burn-up fuel, has been discussed extensively in connection with increased resistance to air oxidation of the fuel, but only recently in connection with fuel dissolution.

In an experimental series at Studsvik (further on referred to as *series 11*) performed using fuel material from a segment of a BWR stringer rod with burn-up varying between 21 and 49 MWd/kg U along the fuel column, the cumulative fractional release increased slightly, almost linearly, with burnup up to values of 40-45 MWd/kg U, but afterwards seemed to decrease slightly. In order to test if this decrease was really related to the burn-up, a series of tests with fuels of burnup 58-75 MWd/kg U was carried out under similar leaching conditions, i.e. dilute air saturated solutions containing carbonate (10 mM NaCl, 2 mM $NaHCO_3$).

The cumulative fractional releases of several radionuclides during 182 days contact time are shown in Fig.1 for the four high burnup fuel segments, together with data from series 11 with lower burn-up fuels, as function of the fuel burn-up. With the exception of segregated radionuclides, as e.g. Cs which forms part of IRF and has higher releases for HBU fuels, for most of matrix bound radionuclides the releases seem to be lower at higher burn-up. The concentrations of e.g. uranium, the major component of the matrix, are quite similar for the four high burn-up samples and about an order of magnitude lower than in the case of lower burn-up fuels (series 11).

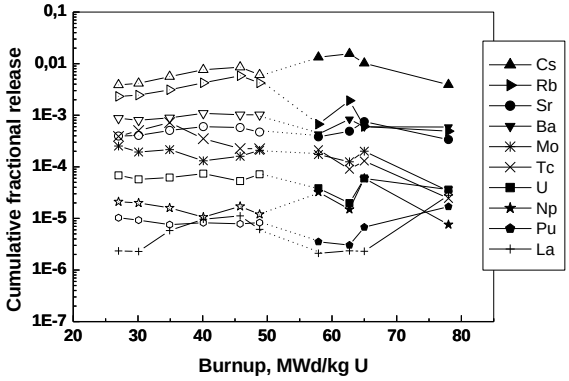

Fig. 1. Cumulative release fractions for a cumulative contact time of 182 days, compared to a selection of corresponding data from series 11 (open symbols).

Another indicator is the ratio $^{236}U/^{235}U$, which increases in fuel as the irradiation proceeds, because ^{236}U content increases at the expense of ^{235}U, which decreases due to both fission and neutron capture. This ratio varies radially in the pellet, with a marked increase at the rim and could serve as indicator of the corrosion site. The data show that in all cases the ratio $^{236}U/^{235}U$ in the leachate is always lower than the inventory value for the first contact periods and increases in the later samplings approaching the inventory value. This indicates that the central part of the pellet, where the ratio is lower, is corroded faster. Similar results, i.e. no marked influence of increased burn-up in fuel dissolution rates, have been observed also in all other fuel dissolution tests reported in the literature with fuels of variable burn-up or when comparing the leaching of the central part with the outer part for a fuel pellet.

A better insight in these results is obtained by considering data on the oxidative dissolution of other UO_2 based materials, which containing various amounts of non-uranium atoms. Thus the dissolution rates natural uraninites, containing various amounts of Th or lanthanide ions, decrease by orders of magnitude with the increase of the dopant concentration. The same holds for oxidative dissolution rates of Gd-doped UO_2(s), which decrease with the increase of the Gd-content. Especially low are the dissolution rates of SIMFUEL, and they decrease for specimens simulating higher burn-up.

All available experimental results show that the presence of fission products like lanthanides and other dopants in the UO_2 matrix has an inhibiting effect on UO_2 dissolution. The increase of non uranium cation concentration at high burn-up seems to counteract effectively the influence of higher surface area and higher dose rates.

Another development during the last decade has been the testing of spent fuel under conditions which mimic better the anoxic conditions expected in most repository concepts. The anoxic corrosion of massive iron containers considered in most deep disposal concepts produces large amounts of dissolved hydrogen in the groundwater. In several experimental studies during this period, a large impact of dissolved hydrogen on the dissolution of the LWR or MOX fuel and UO_2(s) doped with ^{233}U or ^{238}Pu has been observed.

This impact is much larger than the simple influence of molecular hydrogen in the homogeneous radiolysis of water, based in its reaction with the very oxidizing OH-radical to give water and atomic hydrogen. Most of the data indicate for a strong influence of the actinide oxide surfaces on the activation of hydrogen in the presence of radiation. In fact alpha radiation is an intrinsic property of the actinide oxides, which sometimes is neglected while discussing e.g. their interaction with small amounts of water.

In most spent fuel experiments carried out under hydrogen, a decrease in concentration of all redox sensitive nuclides originating from a pre-oxidized layer is observed (Fig.2). Other typical features observed during the leaching of spent fuel under hydrogen are the complete absence of radiolytic oxygen or hydrogen peroxide in the test solutions, a decrease of the concentrations of all redox-sensitive radionuclides with time until reaching levels which correspond to the solubility of their tetravalent oxides and practically constant concentrations of non-redox sensitive nuclides (as e.g. Cs).

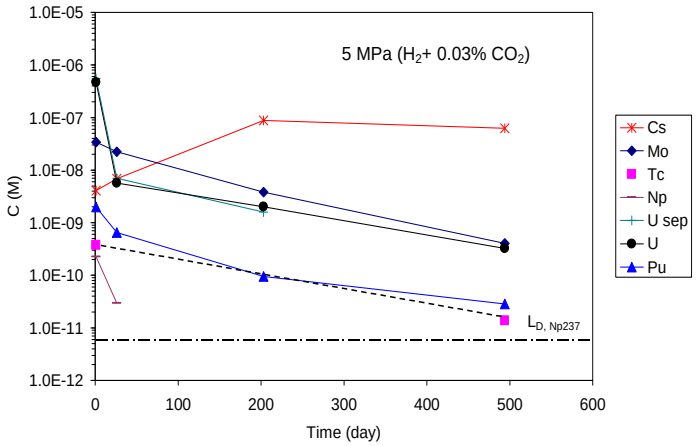

Fig.2. Evolution of concentrations of fission products and actinides during the leaching of MOX fuel (48 MWd/kg HM) with time.

Investigations with fuel fragments of different size, various temperatures and hydrogen pressures show that the reduction rate of pre-oxidized uranium depend strongly on the fuel surface area and temperature, but not very much on the surplus of hydrogen(Fig.3).

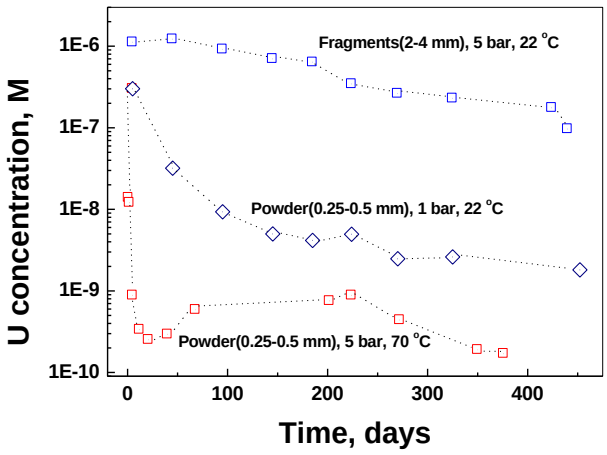

Fig.3. Evolution of pre-oxidized uranium concentrations with time during fuel leaching tests carried out with various fuel grain sizes, T and H_2 concentrations.

In spite of the experimental evidence that the pre-oxidized uranium or other redox sensitive nuclides probably precipitate on the surface of the fuel itself, a direct confirmation by surface investigation methods is difficult, given their low concentrations and their abundance in the fuel. Lately results with Cr(VI) oxyanions, employed as redox sensitive markers, have made possible to show that Cr(VI) precipitates as Cr(III) oxide on the catalyst that activates hydrogen, i.e. spent fuel surface (Fig.4).

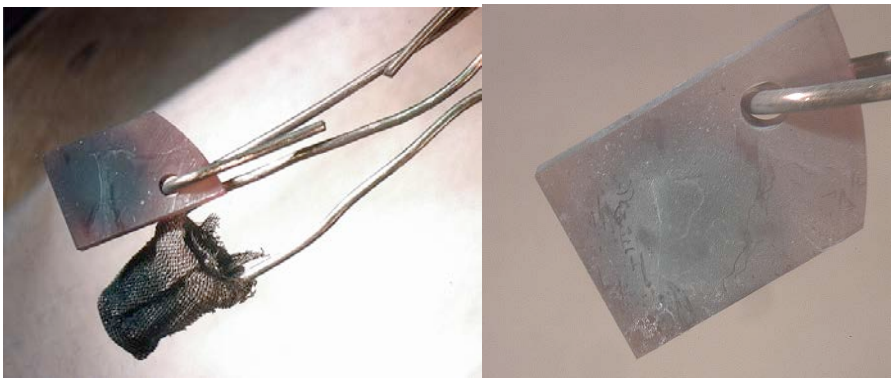

Fig.4. View of the dark green precipitate on the gold basket and on the SEM sample. The contours of the fuel fragment cast in epoxy are visible on the right.

In all repository concepts, it is expected that the container will avoid the contact of spent fuel with water for at least a thousand years, i.e. fuel will contact water when beta and gamma radiations have decayed to negligible levels and only alpha radiation can drive the oxidative dissolution of spent fuel. To mimic such “old” spent fuel, UO_2 containing different fractions of short-lived α-emitters, the so-called α-doped UO_2, is used. By varying the content of the α-emitter, the level of activity of spent fuel after different storage times can be simulated and

used to study the effects of radiolysis on the corrosion behavior of aged spent fuel exposed to groundwater in a geologic repository. Even in this case, a large effect of the presence of relatively small amounts of dissolved hydrogen is observed.

During the leaching of alpha doped pellets under argon in carbonate containing solutions other interesting observations was made. The releases of oxidized uranium were proportional with the doping level for relatively high doping levels, but when the doping levels were low (1% ^{233}U, mimicking 10^5 y old fuel), practically no effect of alpha radiolysis on the uranium releases could be detected. This is in line with observations made on natural analogue studies as in Cigar Lake (Canada), where less than 1% of the produced radiolytic oxidants is found in the form of sulfate. No other oxidized species were found and even sulfate can have other origins than oxidation of sulfide by radiolytic oxidants.

In conclusion, both in the case of spent fuel and alpha doped UO_2 there is a large amount of experimental evidence for the existence of surface mediated processes causing the reaction of hydrogen with radiolytic oxidants and oxidized forms of radionuclides. The detailed mechanism of this hydrogen activation on radioactive UO_2 surfaces is still unknown. Both theoretical and experimental efforts are necessary to increase our understanding of these processes in order to make reliable predictions over the long time scales relevant for spent fuel disposal.

4-27

An(III)/Ln(III) separation: *N*-donors do the job — but how?

Andreas Geist

Karlsruher Institut für Technologie (KIT), Karlsruhe, Germany

For three decades lipophilic *N*-donor extracting agents have been used to separate trivalent actinides from the chemically similar lanthanide ions[1,2,3] in the context of advanced nuclear fuel cycles. 15 years ago, bis-triazinyl-pyridines (BTP) were shown to achieve this separation under conditions relevant to the reprocessing of nuclear fuels, i.e. from nitric acid solutions.[4] BTP were later followed by the bis-triazinyl-bipyridines (BTBP).[5,6] More recently, water soluble BT(B)P were used as complexing agents selective for actinides.[7,8] These could be useful for simplified process schemes.[9]

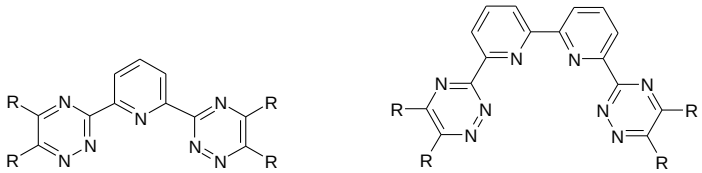

BTP (left) and BTBP (right).

Despite BT(B)P's advantageous properties, current work in international projcets is directed towards finding ligands with even better properties. This requires a deep understanding of how such ligands work on the molecular level. This question has been addressed in several studies, the outcome of which has recently been summarised.[10] The following conclusions are drawn: Only *N*-donor ligands forming strong complexes with actinides(III) show adequate performance in highly acidic solutions. Furthermore, high selectivity over lanthanides(III) seems to correlate with the ligands' ability of forming complexes with exclusive coordination via *N* atoms.

However, several important questions remain unanswered: Why are BT(B)P the only compounds able to extract actinide nitrates from nitric acid with high selectivity, while most other compounds require a more lipohilic anion to form extractable complexes? Is selectivity an intrinsic property of the ligand, or is it induced by its ability of forming complexes with pure *N*-donor coordination? Can we find even better ligands? Or are BT(B)P the holy grail of An(III)/Ln(III) separation?

This presentation discusses the development of *N*-donor ligands and their properties as selective extracting or complexing agents for actinides(III). Furthermore, it gives an overview of the more fundamental studies performed with BT(B)P (but also with some less efficient *N*-donor ligands). We show on the one hand how these studies have forwarded our understanding of *N*-donor-actinide interactions and on the other hand point out some of the open questions to be addressed in the future.

References

[1] C. Musikas et al., ACS symposium series 117, Washington DC, USA, 1980, 131.

[2] C. Musikas, P. Vitorge and D. Pattee, in *Proc. Internat. Solvent Extr. Conf. (ISEC 1983)*, Denver, Colorado, USA, 26/8–2/9/1983, 1983, pp. 6–8.

[3] C. Ekberg et al., *Radiochim. Acta*, 2008, **96**, 225.

[4] Z. Kolarik, U. Müllich and F. Gassner, *Solvent Extr. Ion Exch.*, 1999, **17**, 1155.

[5] M. G. B. Drew et al., *Inorg. Chem. Commun.*, 2005, **8**, 239.

[6] A. Geist et al., *Solvent Extr. Ion Exch.*, 2006, **24**, 463–.

[7] A. Geist et al., *Solvent Extr. Ion Exch.*, 2012, **30**, 433–.

[8] C. M. Ruff et al., *Dalton Trans.*, 2012, **41**, 14594.

[9] G. Modolo et al., *Radiochim. Acta*, 2012, **100**, 715.

[10] P. J. Panak and A. Geist, *Chem. Rev.*, 2013, **113**, 1199.

4-28

Current Status and Future Application of Actinide based Radiopharmaceuticals in Nuclear Medicine

Clemens Kratochwil[1], Frank Bruchertseifer[2], Frederik Giesel[1], Alfred Morgenstern[2]

[1]UniversityHospital Heidelberg, Department of Nuclear Medicine, Heidelberg, Germany, [2]EC-JRC, Institute for Transuranium Elements, Karlsruhe, Germany

First observations with relevant statistical power on human beings exposed to alpha radiation are available from the nuclear explosions in Hiroshima and Nagasaki. Despite the fact, that the subjects in the Japanese Hiroshima trial were exposed to a mixture of percutaneous (X-ray, gamma-ray) and the incorporation of both beta particle (e.g. Cs-137, I-131) and a variety of alpha particle emitters some important conclusions can be drawn: There was an absolute latency to develop radiation induced cancer of approximately five years and the max. incidence of leukemia and solid tumors were reach >10 and > 20 years later, respectively.

A more selective exposure to alpha radiation and more reliable dosimetry data are available from the historic usage of Thorium-232 as a contrast media in the early phase of roentgen angiography. Between 1929 and 1950 about 2-10 million patients worldwide were exposed before the radioactivity of the drug was realised. Thorium-232 accumulates in the reticular phagocyte system (liver, spleen, lymph node, bone marrow) with a biological half-life of approximately 22 years. In post mortem ex-vivo counting of single subjects cumulative doses of 300 Sv to the liver, 2420 Sv to the spleen and 80 Sv to the bone (marrow) were found (Kathren RL 1992, McInroy JF 1992). Thorotrast was found to be strong carcinogenic. In n=2326 Thorotrast patients 279 cases of liver cancer (1.7 expected in the normal population) and 57 cases of lymphoma, myeloma and leukemia (10.5 expected) were observed (van Kaick 2004). However, a long incubation time of >25 years to develop secondary cancers were reported and the latency period was independent form the amount of administered Thorium-232 (Fig.-1).

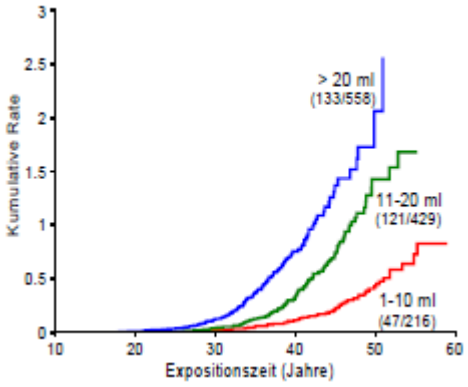

Figure-1: Incidence of secondary cancers after exposure to different doses of Thorotrast (Thorium-232). A dose independent latency time of >25 years was observed (van Kaick, 2004).

In Germany, the alpha emitter Radium-224 was use under different brand names (Peeosthor, Thorium-X, SpondylAT) as a reserve analgetics for patients with Bechterew's disease until 2006. 1006 patients treated 1948-1975 have been evaluated with a follow-up time of 30 years (Wick RR, 2008). Due to an increased risk for leukemia (19 cases vs 6.8 expected) it was finally considered obsolete for therapy of a benign disease with normal life-expectancy.

However, in cancer patients with poor prognoses the long-term effects of radioactive exposure might be less relevant and tumor targeted drugs tagged with an alpha emitting radionuclide were considered a promising option in cancer treatment. In contrast to the radioiodine treatment with the beta emitter I-131, which is established in clinical routine for decades, the limited availability, unfavourable half-life or incomplete understood chemistry of

the suitable nuclides prohibit the translation of targeted alpha therapy (TAT) into the clinical routine.

Recently Radium-223 (Alpharadin), which is an inherent bone seeker, demonstrated to prolong the overall survival of patients with bone metastases of prostate cancer in a prospectively, randomized, double-blind, placebo-controlled trial (Nilsson 2012). However, divalent Ra-223 cannot be easily linked to tumor targeting molecules.

In the recent years DOTA- or CHX-DTPA chelated antibodies, peptides or small molecules were evaluated in clinical pilot studies with different kind of cancer (Fig.-2). Most of them were based on the Actinides Bi-213 or Ac-225.

Leukemia	^{213}Bi-HuM195mAb	n=49	Jurcic et al, Blood 2002 Rosenblat et al, CCR 2010
	^{225}Ac-HuM195mAb	n=14	Jurcic et al, 7th TAT-Symp. 2011
Lymphoma	^{213}Bi-Rituximab	n=12	Schmidt et al, 4th TAT-Symp. 2004
Melanoma	^{213}Bi-9.2.27mAb	n=55	Allen et al, Cancer Biol Ther., 2005 Allen et al, Immunotherapy, 2011
Gliom	^{213}Bi-Substance P	n=13	Kneifel et al, CCR 2006 Cordier et al, EJNMMI 2010
	^{211}At-81C6mAb	n=18	Zalutsky et al, JNM 2008
Ovarian cancer	^{211}At-MX35 F(ab')2	n=9	Andersson et al, JNM 2009
NET	^{213}Bi-DOTATOC ^{225}Ac-DOTATOC	n=24 n=17	Kratochwil et al, 7th TAT-Symp. 2011

Figure-2: Summery of the clinical experience with TAT in cancer patients.

Most of the “carrier-molecules” have previously been evaluated when tagged with an beta emitter. The authors reported a favourable therapeutic range of the alpha emitter tagged compounds with low acute toxicity and promising efficacy.

In this talk we give an overview about the convincing results of the clinical studies available today (Fig.-2). In more detail we present our actual results of patients treated with Bi-213 or Ac-225 tagged DOTATOC - a peptide targeting the somatostatin receptors overexpressed on neuroendocrine tumors (NET); An investigation conducted as a collaboration of the University Hospital Heidelberg and the EC-JRC, ITU, Karlsruhe.

Due to the high toxicity even of single alpha particles, a highly tumor specific tracer, knowledge of the nuclide’s decay scheme and supportive medication (e.g. suitable chelators to enhance the biological clearance of daughter nuclides) are mandatory. A couple of such promising tracers are currently under development (e.g. small molecules targeting the prostate-specific-membrane-antigen (PSMA) overexpressed on prostate cancer). On the other hand, due to new accelerator driven production techniques the unlimited supply of alpha emitting actinides such as Bi-213 or Ac-225 will be feasible in near future. Therefore TAT is an emerging factor in the future of therapeutic nuclear medicine.

5-04

Recent advances in material properties and behavior of transuranium compounds for application to nuclear fuel cycle

Masahide Takano, Tsuyoshi Nishi, Hirokazu Hayashi, Kunihisa Nakajima, Haruyoshi Otobe

Japan Atomic Energy Agency, Tokai, Ibaraki, Japan

In the high-level radioactive wastes generated from reprocessing of spent nuclear fuels, so-called minor actinides (MA: Np, Am, Cm) are included. Because of their high radioactive toxicity, long life and decay heat, burning or transmutation of MA into short-lived nuclides is a realistic option for future nuclear fuel cycles. Although a variety of fuel or target concepts for MA transmutation are considered, the addition of MA, especially Am and Cm, into fuels gives impacts on material properties and behavior extensively, regardless of the chemical form of fuel. We have been studying on synthesis, thermophysical and thermochemical properties, and behavior of transuranium (TRU) compounds concerning MA transmutation and reprocessing of the fuels. In this paper, recent advances in these fields on TRU nitrides, chlorides, alloys and oxides are introduced.

1. Solid solubility and thermal properties of nitrides

TRU nitrides are considered as the fuel materials for MA transmutation, especially for accelerator driven system (ADS). In this case Pu and MA nitrides are diluted with inert matrix such as ZrN, in the form of (Zr,Pu,MA)N single-phase solid solution. Although PuN-ZrN system shows complete solid solubility, the solid solubility of AmN into ZrN is limited. By the systematic experiments on solid solution formation between ZrN and lanthanide/TRU nitrides, the solid solubility into ZrN has been determined as a function of relative lattice parameter difference (RLPD) [1]. RLPD (%) is defined as $100\cdot(a_{MN} - a_{ZrN})/a_{ZrN}$, where a_{MN} and a_{ZrN} are lattice parameters of solute nitrides (lanthanide or TRU) and solvent ZrN, respectively. When the solute is nitride solid solution like (Pu,MA)N, the corresponding a_{MN} value can be computed from the lattice parameters of components by Vegard's law. The solubility data obtained by powder metallurgy of the nitride mixtures are plotted against RLPD value in Fig. 1. The upper limit of RLPD value for complete solid solubility is then evaluated to be 8.6–8.9 % at heat treatment temperatures of 1773–1973 K. From these results, the composition limits in (Zr,Np,Pu,Am,Cm)N for single-phase solid solution formation can be predicted for various cases, although the actual solubility near the composition limit should be further confirmed experimentally.

Thermal properties of TRU nitrides and their solid solutions with ZrN have been also studied to establish the material database for fuel design works. Lattice thermal expansion is determined by the high temperature X-ray diffraction technique. In addition to NpN, PuN and AmN [2], the measurement on CmN has been successfully accomplished [3]. From the temperature dependence of lattice parameter, the averaged thermal expansion coefficient of CmN from 293 to 1273 K is determined to be 9.8×10^{-6} K^{-1}. This value lies between the higher expansive nitrides (PuN and AmN, $11.1–11.2\times10^{-6}$ K^{-1}) and the lower expansive nitrides (UN and NpN, $8.8–8.9\times10^{-6}$ K^{-1}). The averaged thermal expansion coefficients for TRU nitride solid solutions and even for those containing ZrN can be approximated by the linear mixture rule using the values for each component nitride [4].

Thermal conductivity of the sintered nitride specimens is determined from thermal diffusivity measured by laser flash method and specific heat measured by a drop calorimeter. Thermal conductivity of solid solutions between TRU nitrides and ZrN [5], as shown in Fig.2, is remarkably lower than the values expected from hypothetical linear dependence on ZrN fraction. A possible explanation for the obtained dependence on ZrN fraction is the big gap in atomic weight between Zr (91.22) and TRU elements (around 240), which may result in remarkable phonon scattering. The composition dependence of electrical conductivity should be also investigated for better understanding, since the electronic contribution predominates over the total thermal conductivity in these nitrides.

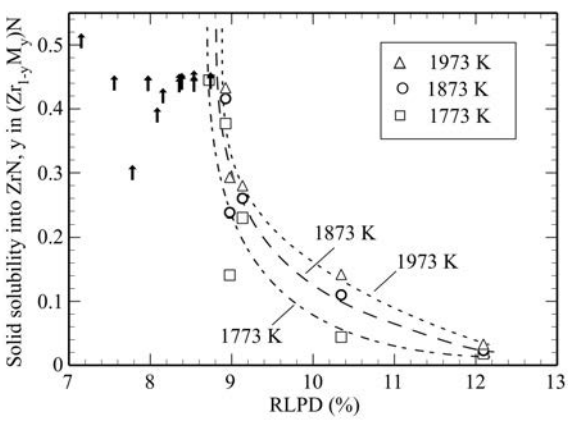

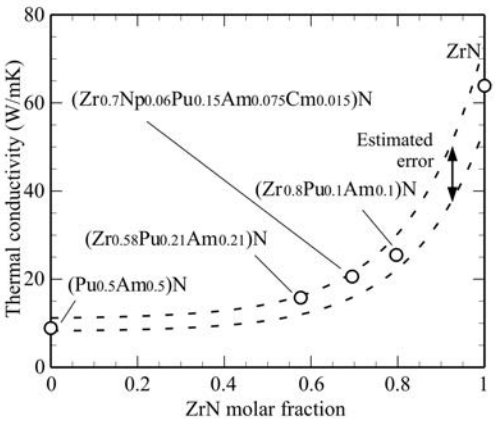

Fig.1 (left) Solid solubility of lanthanide and TRU nitrides into ZrN as a function of relative lattice parameter difference, examined by powder metallurgy of nitride mixture. Upward arrow symbol represents the solubility is higher than the indicated value.

Fig. 2 (right) Thermal conductivity of sintered (Zr,TRU)N solid solution specimens at 873 K as a function of ZrN molar fraction, normalized to theoretical density.

2. Synthesis and thermochemical data of chlorides

For the pyrochemical reprocessing of spent nitride fuel, we have been performing the electrochemical experiments using TRU chlorides in molten-salt bath. For the synthesis of TRU trichlorides, a new method based on solid-state reaction between TRU nitrides (MN) and $CdCl_2$ has been established. The unnecessity of any hazardous or corrosive gasses like Cl_2 or CCl_4 is the advantage of this method, especially in a hot cell facility for handling TRU. This reaction is expressed by,

$$MN + 3/2CdCl_2 = MCl_3 + 3/2Cd + 1/2N_2. \qquad (1)$$

The by-product Cd and remnant $CdCl_2$ in the product are distilled off under dynamic vacuum at temperatures up to 748 K. Up to now the powders of pure $NpCl_3$ [6], $AmCl_3$ [7] and $CmCl_3$ [8] have been successfully synthesized from the respective nitrides in 10 mg to several hundred mg scale. The trichloride samples are encapsulated into gold crucibles and subjected to differential thermal analysis (DTA) measurements. From the DTA curves the melting points of $NpCl_3$ and $CmCl_3$ are determined to be 1070±3 K and 970±3 K, respectively.

3. Vaporization of Am in alloy fuel

The high heavy-metal density of alloy fuel allows potentially better transmutation performance of MA than oxide fuels. However, there are some problems such as vaporization loss of Am and its miscibility during fuel fabrication process. At the fabrication temperatures up to 1720 K, Am has nearly three orders of magnitude higher vapor pressure than Pu. The addition of Am and lanthanides to ternary U-Pu-Zr alloy causes phase segregation into U-rich, Zr-rich and Am-Ce-Nd rich phases. Only Pu exhibits limited mutual solubility among these phases. Knowledge of vapor pressure and chemical activities of Am for the Am-containing phase is indispensible to perform quantitative analysis of vaporization loss and miscibility. Here the vaporization of a Pu–6.6Am alloy specimen was studied by Knudsen-effusion mass spectrometry technique. As a result, only atomic Am vapor species was detected and the equilibrium vapor pressure is expressed as the following equation in the temperature range of 1100–1380 K,

$$\log p_{Am}\,(Pa) = 9.061\pm0.087 - (12150\pm110)/T. \qquad (2)$$

The Am content in the alloy specimen was estimated to decrease from 6.6 to 6.4 % during the measurement. At 1500 K, the Am activity in the alloy was evaluated to be 0.096±0.062 using the Am vapor pressure computed from the thermodynamic data of liquid and gaseous Am [9]. Further, the partial heat of solution of Am was found to be positive because the heat of evaporation of Am over the alloy, 227.0±4.2 kJ/mol at 1500 K, which was computed from Eq. (2) and both the specific heats of liquid and gaseous Am, was clearly lower than that of pure Am [9]. The Am activity in this alloy is therefore suggested to be deviate positively from the Raoult's law.

4. Oxygen potentials vs. O/M of oxides

For oxide nuclear fuels, the oxygen defect in fluorite-type structured $MO_{2\pm x}$ is one of the important factors that characterize the material properties and behavior at high temperatures. Addition of transplutonium elements, namely Am and Cm, into the oxide fuels tends to lower the O/M to hypostoichiometry, because the tri-valent ions of Am and Cm are rather stable at high temperatures. We have studied the relation between oxygen potentials and oxygen-defect concentration x of fluorite-type or C-type MO_{2-x} such as AmO_{2-x} [10], $(Np,Am)O_{2-x}$ [11], $(Pu,Am)O_{2-x}$ [12] and $(Pu,Cm)O_{2-x}$ [13] by the electrochemical method using a zirconia solid electrolyte.

Another factor that may influence on the O/M is the solid fission products soluble into fuel matrix, like Zr or lanthanides. Recently, we have investigated the relation between oxygen potentials and oxygen-defect concentration y of pyrochlore-type $Am_2Zr_2O_{7+y}$ (O/M = (7+y)/4) [14], in comparison with the fluorite-type oxides. The oxygen potentials at 1333 K smoothly increased from -516.5 to 0 kJ/mol with increasing O/M from 1.75 to 1.89. They are higher than the oxygen potentials of either fluorite-type AmO_{2-x} and $Np_{0.5}Am_{0.5}O_{2-x}$ at the corresponding O/M for 1333 K. Such difference in the oxygen potentials is considered due to the difference in oxygen-defect structure between pyrochlore-type and fluorite-type oxides.

5. Material behaviour caused by self-irradiation damage

An inevitable phenomenon in MA-bearing fuels regardless of the chemical form is the self-irradiation damage by short-lived alpha-emitters represented by ^{238}Pu, ^{241}Am, ^{242}Cm and ^{244}Cm. The lattice expansion due to generation of Frenkel defect is well known. However, very few experimental data on the dimensional change of ceramic fuel pellets due to the self-irradiation damage are available so far. We have observed the lattice and bulk expansion of a sintered $(Pu_{0.95}Cm_{0.05})O_2$ specimen simultaneously as a function of storage time at room temperature [15]. In Fig. 3, the expansion data are plotted against fractional disintegration, lt (product of the effective decay constant and the storage time). It is found that the sintered pellet exhibits the expansion similar to its lattice, and that the expansion of both lattice and bulk saturates to a similar value (~0.3 %) at λt of $3–4x10^{-4}$, where the Frenkel defect concentration reaches equilibrium.

After a long period of storage, thermal recovery of the lattice and bulk expansion was also examined comparatively by isothermal annealing. The results are shown in Fig. 4 as a function of annealing temperature. By annealing up to 1429 K, the lattice parameter was recovered to the undamaged value, while the pellet expanded during annealing at 1433 K. From the SEM image on the fracture surface of the pellet after annealing, the traces of gas bubbles are found along grain boundaries. The dissolved He atoms migrated to the grain boundaries and formed gas bubbles during annealing, which resulted in the He gas swelling of the pellet.

Another influence of self-irradiation damage in fuel materials is a lowering of thermal conductivity, because the accumulated Frenkel defects cause phonon scattering. We have measured the thermal conductivity of sintered $(Pu_{0.91}Cm_{0.09})O_{1.99}$ [16] and $(Np_{0.20}Pu_{0.50}Am_{0.25}Cm_{0.05})O_{1.98}$ [17] specimens at 473–573 K as a function of storage time at room temperature. The thermal conductivity ratio of damaged specimen (K) to undamaged specimen (K_o) at 573 K is shown in Fig. 6 as a function of lt. The K/K_o ratio decreases with increasing defect concentration and saturates to 50–60 % of the undamaged value, corresponding to the saturation of lattice expansion. A possible reason of the difference in

saturated K/K_o values is the difference in O/M, since the lower O/M means the higher oxygen vacancy (defect) concentration at the initial undamaged state. The thermal diffusivity was measured again immediately after annealing at 1423 K, and recovery to the undamaged value was confirmed.

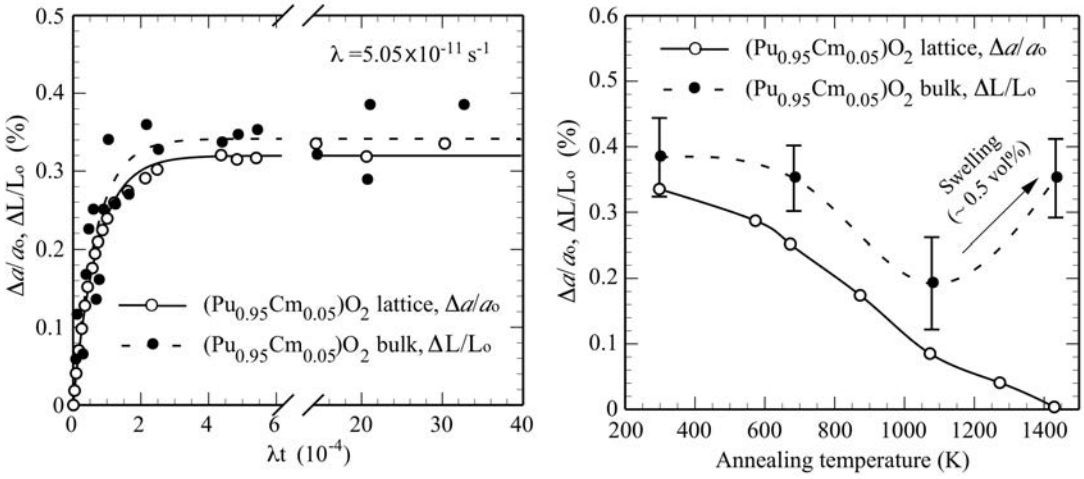

Fig. 3 (left) Comparison of linear expansion for lattice and bulk dimension of sintered $(Pu_{0.95}Cm_{0.05})O_2$ specimen as a function of fractional disintegration (λt).

Fig. 4 (right) Comparison of thermal recovery for the lattice and bulk dimension as a function of annealing temperature. The bulk finally swelled due to He bubble formation.

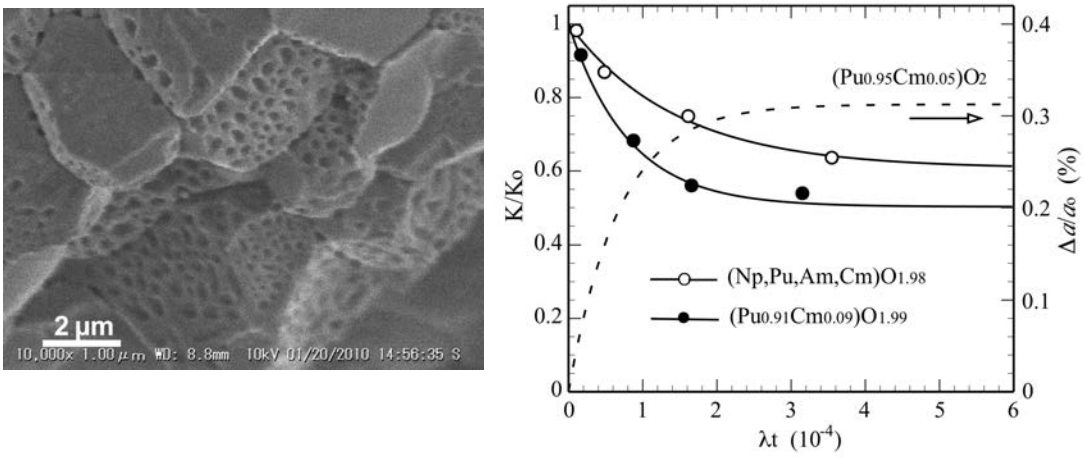

Fig. 5 (left) SEM image of fracture surface of the $(Pu_{0.95}Cm_{0.05})O_2$ pellet annealed at 1433 K. Traces of He bubbles are distributed along grain boundaries.

Fig. 6 (right) Thermal conductivity of damaged TRU dioxide specimens relative to undamaged value (K/K_o), in comparison with lattice expansion as a function of fractional disintegration (lt). Np/Pu/Am/Cm = 20/50/25/5 at%.

References

[1] M. Takano, Experimental evaluation of solid solubility of lanthanide and transuranium nitrides into ZrN matrix, to be published in J. Nucl. Mater.

[2] M. Takano, M. Akabori et al., J. Nucl. Mater. 376 (2008) 114-118.

[3] M. Takano, Lattice thermal expansion of CmN, to be published in J. Nucl. Mater.

[4] M. Takano, M. Akabori et al., J. Nucl. Mater. 389 (2009) 89-92.

[5] T. Nishi, M. Takano et al., J. Nucl. Sci. Technol. 48 (2011) 359-365.

[6] H. Hayashi, M. Takano et al., Syntheses of neptunium trichloride and measurements of its melting temperature, to be published in J. Nucl. Mater.

[7] H. Hayashi, M. Takano et al., J. All. Comp. 456 (2008) 243-246.

[8] H. Hayashi, M. Takano et al., Synthesis and thermal analyses of curium trichloride, to be published in J. Radioanal. Nucl. Chem.

[9] E.H.P. Cordfunke, R.J.M. Konings ed., Thermodynamic Data for Reactor Materials and Fission Products, North-Holland, Amsterdam, 1990.

[10] H. Otobe, M. Akabori et al., J. Am. Ceram. Soc. 91 (2008) 1981-1985.

[11] H. Otobe, M. Akabori et al., J. Am. Ceram. Soc. 92 (2009) 174-178.

[12] H. Otobe, M. Akabori et al., J. Nucl. Mater. 389 (2009) 68-71.

[13] H. Otobe, M. Akabori et al., IOP Conf. Ser.: Mater. Sci. Eng. 9 (2010) 012015.

[14] H. Otobe, M. Takano et al., J. Am. Ceram. Soc. 94 (2011) 3596-3599.

[15] M. Takano, M. Akabori et al., J. Nucl. Mater. 414 (2011) 174-178.

[16] T. Nishi, M. Takano et al., J. Nucl. Mater. 433 (2013) 531-533.

[17] T. Nishi, M. Takano et al., Thermal conductivity of $(Np_{0.20}Pu_{0.50}Am_{0.25}Cm_{0.05})O_{2-x}$ solid solutions, to be published in J. Nucl. Mater.

5-05

Techniques for measuring the temperature of transitions involving liquids in actinide bearing systems

Ananthasivan Krisnamurthy, Balakrishnan Subramanian, Nagarajan Krisnamurthy, Vasudeva Rao

Indira Gandhi Centre For Atomic Research, Kalpkkam, Tamilnadu, India

Information on the phase diagrams of actinide bearing systems are useful in the design and performance assessment of conventional as well as advanced fission reactor fuels. Melting temperature and thermal conductivity are the two most important thermophysical properties of the fuel materials that govern the fuel performance. Since most of these fuels are multiphasic the lowest temperature at which liquid appears first when the fuel is heated, is considered in place of melting temperature. It could be the solidus temperature or the temperature pertaining to a phase equilibria in which liquid is formed. A reasonably accurate knowledge of this temperature is necessary for the following reason. The most important parameter in the thermal design of the core of a nuclear reactor is the distribution of temperature in the core. Factors such as the specific power, power density and heat flux, all related to a given fuel lattice or cell dimensions, are to be so chosen that together with the heat removal system they would not result in temperatures that exceed fuel element material limitations leading to its failure [1]. Hence the melting temperature (solidus temperature) of the fuel often serves as a reference limit for the designer.

The melting point of both irradiated and fresh UO_2 and $UPuO_2$ have been experimentally determined many times in the past three decades [2-5]. The melting point of $(PuAm)O_{2-x}$ dispersed in MgO has been experimentally determined by using an innovative laser based technique [6]. Matzke [7] has given a detailed account of the investigations on the binary and multicomponent phase equilibria in systems of relevance to nuclear fuels. The solidus and liquidus temperatures pertaining to the system U_2C_3-Pu_2C_3 reported by various authors were collated by Matzke [7]. Earlier Dalton [8] had reported various isothermal sections and isopleths in the system U-Pu-C. Recently, a laser based technique has been used to determine the melting point of uranium carbides [9]. The systems U-C, Pu-C and U-Pu-C are of relevance to the mixed carbide fuel used in the Indian Fast Breeder Test Reactor (FBTR). The carbide fuel employed in FBTR could have different phase composition and the impurities such as oxygen and nitrogen present in the fuel can influence its melting point. In order to predict the melting point of the fuel, the multicomponent phase diagram U-Pu-C-O-N has to be established. This is a tedious exercise and involves experimental investigation on a large number of alloys. Hence, experimental investigations on fewer alloys supported by computation is often resorted to. Experiments on the fuel specimen itself would provide valuable information. Sengutpa et al. [10] measured the peritectic melting temperature of the U-Pu mixed carbide -containing both MC and M_2C_3 ($M = U_{1-x}Pu_x$) with a relative Pu content of 0.7 in the metal fraction (Mark I mixed carbide fuel used in FBTR) with an uncertainty of 25 K, while the. solidus temperature of the Mark II fuel with a relative Pu content of 0.55 was estimated from dilatometric measurements by Sengupta et al. [11]. The solidus temperatures have not been determined so far by using direct measurements. In view of the above, a new experimental facility was established at our laboratory in order to measure the phase transition temperatures involving liquids in actinide bearing systems.

Since the mixed carbide fuel is both radioactive and pyrophoric all the experiments involving the fuel material have to be carried out in custom-made inert atmosphere glove boxes. A variety of experimental techniques are available for the determination of phase diagrams [12]. These methods could be broadly classified as the methods based on i) the heat of phase transformation ii) microstructural characterization iii) measurement of chemical potential, iv) X-ray diffraction, v) phase segregation and vi) change in a physical property like emissivity, resistivity or volume with temperature. In order to establish a phase diagram often a combination of two or more of these techniques is required. Many of the commercially available equipments are not suitable for the present application. Thus in order carry out measurements on mixed carbide fuel an experimental facility capable of heating the sample under vacuum to temperatures above 1873 K was established [13]. The spot technique is one of the few methods that are particularly useful for the determination of the transitions involving actinide bearing liquids at high temperatures. The spot method originally devised by Ackermann and Raugh [14] makes use of the mirror effect of the molten phase of the sample

[15]. In this method a small amount of the sample, (usually less than a gram) of known composition is placed in an inert cup. This cup is centred inside a Knudsen cell and heated under high vacuum. The orifice of the Knudsen cell is viewed through a pyrometer. As long as the sample remains solid, the Knudsen orifice approximates a black body and appears as a uniformly lit bright disc and the temperature measured under such conditions would correspond to its brightness temperature. However, at the solidus temperature when a liquid phase begins to appear, a thin film of the liquid is formed on the surface of the sample. Now that a reflecting mirror surface is present, the orifice of the Knudsen cell exhibits a dual behaviour [16]. It is an incandescent object with respect to the pyrometer as the latter receives maximum radiation from it. However, for the liquid mirror it is a perfect black object since the surface receives radiation from all directions within the effusion cell except from the orifice. Hence the reflected image of the orifice appears as a black spot when observed through a pyrometer. The temperature, at which this dark spot is sighted first, corresponds to the solidus temperature of the alloy under investigation. On further heating several dark spots appear. Garg et al. [17] refer to this as a broken mirror image. When the melting is complete all the dark spots coalesce suddenly into a single large spot. This corresponds to the liquidus temperature. In order to observe the spot-effect it is necessary to use a non-contact mode of heating, viz., electron bombardment or radiofrequency (RF) induction.

Garg et al. [17] showed that the melting points of various metals viz. zirconium, hafnium, thorium and uranium taken in suitable cups could be determined within an accuracy of 5 K. Solidus and liquidus boundaries in several binaries have been determined by using this technique. Small sample size, in-situ alloying and suitability for remote measurements at high temperature make this technique suitable for exploring many refractory metal systems. Recently, in our laboratory we developed a modified apparatus which unlike the experimental systems used in earlier studies, was capable of providing an image with a higher magnification. Thus phase boundaries involving a liquid in the systems U-Sn [13], Ru-Sn [18], Cu-Ni [19] U-Zr [20] could be established. Recently the peritectic melting temperature of the Mark I U-Pu mixed carbide FBTR fuel was measured by using this technique.

One of the limitations of the conventional spot technique is its non-applicability at temperatures below incandescence. The spot effect could be observed at temperatures far below incandescence by illuminating the internals of the K-cell [21]. A new procedure called the “external illumination” was developed based on some observations made during the conventional spot-experiments, in our laboratory (Fig 1). In order to validate the measurement accuracy of the latter in situ differential thermal analysis was performed during the spot experiments. This experimental technique termed as the illuminated spot-DTA technique is suitable for glove box application and is useful for the determination of melting transitions of actinide alloys [22]. These two new techniques namely the illuminated-spot technique and the spot-DTA technique devised in our laboratory are very useful and complimentary to DTA measurements, especially in establishing steep liquidus boundaries.

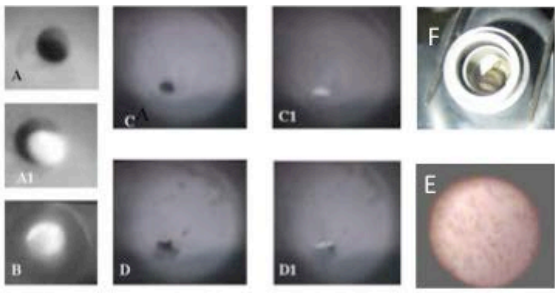

Figure 1 Photographs obtained during spot experiments and the illuminated-spot experiments Cu melting A) conventional spot A1) Illuminated spot B) Hg- Illuminated spot at room temperature; Cu- Ni [80 wt% Cu] C) solidus D) above solidus C1) & D1) illuminated spots pertaining to C and D; E. Peritectic transition Mark I mixed carbide fuel *2161 ± 3 K* F. Mark I mixed carbide fuel after melting

References

1 Ioan Ursu, Physics and Technology of Nuclear Materials, Pergamon Press, New York, 1985, p. 278.

2 H. Hausner J. of Nucl. Mater.15 (3)(1965) 179-183.

3 J.Lambert Bates J. of Nucl. Mater.36 (2)(1970) 234-236.

4 Junji Komatsu, Toshimichi Tachibana, Kenji Konashi J. of Nucl. Mater.154 (1)(1988) 179-183.

5 F. De Bruycker, Boboridis, R.J.M. Konings, M. Rini, R. Eloirdi, C. Guéneau, N. Dupin, D. Manara, J. of Nucl. Mater.419 (1-3)(2011) 186-193.

6 Shuhei Miwa, Isamu Sato, Kosuke Tanaka, Takashi Hirosawa, Masahiko Osaka J. of Nucl. Mater.400 (1)(2010) 32 - 36.

7 Hj. Matzke, Science of Advanced LMFBR Fuels, Elsevier Science Publishers B.V., Amsterdam, 1986.

8 J.T. Dalton in: Carbides in Nuclear Energy, L.E. Russell, B.T. Bradbury, J.D.L. Harrison, H.J. Hedger and P.G. Mardon, editors, Mcmillan & Co. Ltd., London, 1964, p. 77.

9 C.A. Utton, F. De Bruycker, K. Boboridis, R. Jardin, H. Noel, C. Guéneau, D. Manara J. of Nucl. Mater.385 (2)(2009) 443-448.

10 Sengupta et al. in Fast Reactor Fuel Cycle Symposium Ed. C.K. Mathews, 10-12, Feb 1986, Kalpakkam, India.

11 Sengupta et al. J. Nucl. Mater. 2009 (385) 161-164.

12 R.A. Buckley, in: Techniques of Metals Research, R.A. Rapp, editor, Interscience, New York, Vol. IV, part I, p. 425.

13 K.Ananthasivan Ph.D. thesis, University of Madras, 2002.

14 R.J. Ackermann and E.G. Rauh, J. Phys. Chem. 73 (1969) 769.

15 M.S. Chandrasekharaiah, J.L. Margrave and D. Das, in: J.F. Schooley, editor, Temperature – Its Measurement and Control in Science and Industry, Vol. 6, Part 1, American Institute of Physics, New York, 1992, p. 373.

16 S.P. Garg Ph.D. thesis, Bombay University, Bombay, India (1980).

17 S.P. Garg, Y.J. Bhatt and R. Venakatasubramani, Mater. Sci. Forum, Vol. 3, Trans Tech Publications Ltd., Switzerland, 1985, p. 419.

18 K. Ananthasian, I.Kaliappan, P.R. Vasudeva Rao, C.Sudha and A.L.E Terrance, J. Nucl. Mater. 305 (2002) 97.

19 K. Ananthasivan, S. Balakrishnan, I. Kaliappan, N. Pankajavalli, S. Anthonysamy and P.R. Vasudeva Rao, J. Alloys and Compds. (in press) 2007.

20 S. Balakrishnan, K. Ananthasivan, S. Anthonysamy, V. Ganesan, P.R. Vasudeva Rao and K. C. Hari Kumar" Solidus and liquidus measurements in the U-Zr binary system" presented at the Calphad XL meeting held at Rio de genero, Brazil May 2011.

21 A. Awasti, Y.J. Bhatt and S.P. Garg, Mater. Sci. Technol. 7 (1996) 753.

22 K. Ananthasivan, I. Kaliappan and P. R. Vasudeva Rao, J. Alloys and Compounds 2003.

ORAL

5-09

Inert matrix fuel with isolated arrangement of PuO_2 or MA to achieve ultra-high burn-up

Ksenia Lipkina, Alexey Savchenko, Alexander Vatulin, Gennady Kulakov, Sergey Ershov

A.A. Bochvar Institute (VNIINM), Moscow, Russia

Inert Matrix Fuel (IMF) is advanced nuclear fuel form that can potentially provide higher burn-up than current fuel form, making it a promising alterative for future - generation nuclear power reactors. It is considered as one of the variants for the incineration of excess Pu and MA in fast or thermal reactors.

Application of IMF in Fast and Thermal Reactors

Previously on the first place was incineration weapons grade Pu then reactor grade and then MA. Currently the situation has changed. Fast reactors (FR) are coming and need fissile Pu, especially weapons. Increasing of burn- up in thermal reactors and using MOX result in poor Pu composition in spent fuel as well as increasing of stock - piles of MA needs incineration in FR (Fig. 1).

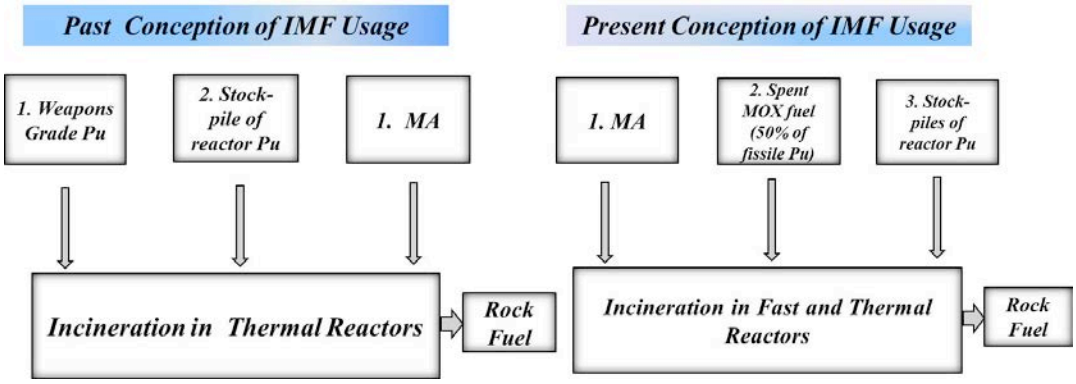

Fig. 1. IMF Usage Concepts.

The purpose of investigations is to propose the concept of IMF achieving high burn-ups that can be produced by simple technology and comply with requirement for “Rock-fuel”.

This can be achieved by replacing ceramics inert matrix of pelletized design on dispersion-type fuel element. A direct metallurgical bond between the fuel and cladding provides high thermal conductivity while serving to protect against fuel-cladding interactions. Dispersion – type metallic IMF is an ideal separable system, allowing each component to be studied separately (i.e., actinide fuel, inert metallic matrix and cladding.

One of the versions of dispersion type IMF that now is under development at A.A Bochvar Institute is a fuel element having a heat conducting metal matrix and an isolated arrangement of PuO_2 in a fuel minielement. The fuel minielement is a thin-walled stainless steel tube 1.8-2.4 mm in the diameter. It is filled with PuO_2 powder or granules (60-70 % vol.), sealed and placed within a fuel element. The volume fraction of PuO_2 in a fuel element might be varied from 5 to 25 %, *which is enough for the fast reactor fuel element.* Aside from PuO_2, also oxides of other actinides might be loaded into a fuel minielement. Actinide oxides can be produced by pyrochemical method as well as $(Er,Y,Pu,Zr)O_{2-x}$ microspheres, prepared by internal gelation process (such as at ITU and PSI) can be also implemented.

The fuel minielements (from 1 to 6) are inserted into fuel cladding followed by filling with matrix granules, and liquid-solid sintering (capillary impregnation method). After fuel element fabrication the melting temperature of the Zr matrix alloys increases up to 1100^0C. (Fig.2)

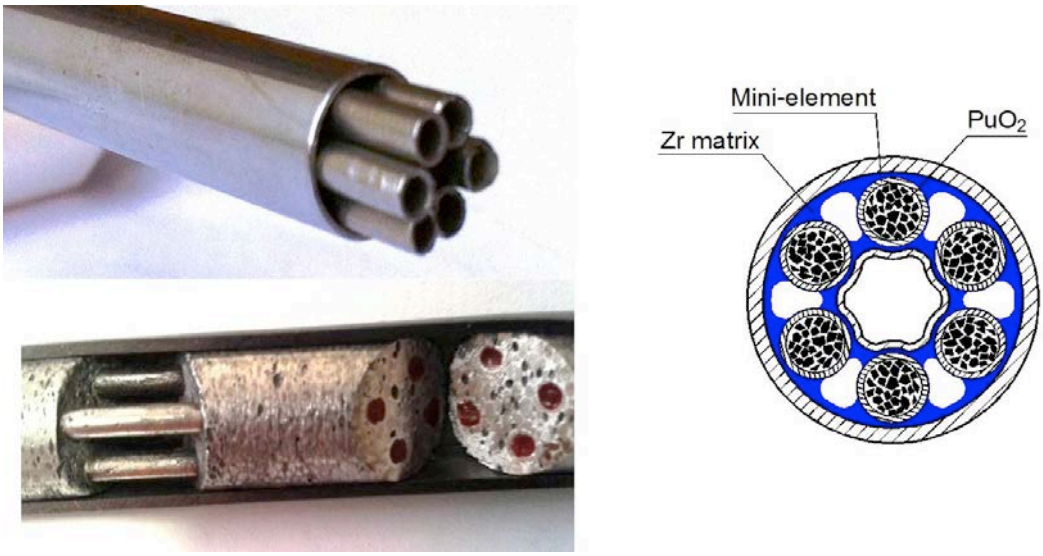

Fig. 2. IMF with separate arrangement of fuel.

Advantages of the proposed IMF design:

-Minimum dust-forming operations with Pu;

-three protection barriers against corrosion (Rock Fuel);

-Accommodation of swelling;

-Cold fuel.

Proposed IMF design simplifies nuclear fuel cycle: Pu of poor quality with MA from spent PWR fuel, particularly spent MOX fuel, after pyrochemical reprocessing can be used as a fissile material. Then it would be delivered to fast or thermal reactors with the achievement of very high burn-up, followed by direct geological disposal as a ROCK fuel. The other option – to use fertile Pu+MA from FR after mechanical separation in case of application composite U-PuO_2 fuel in FRs (Fig.3).

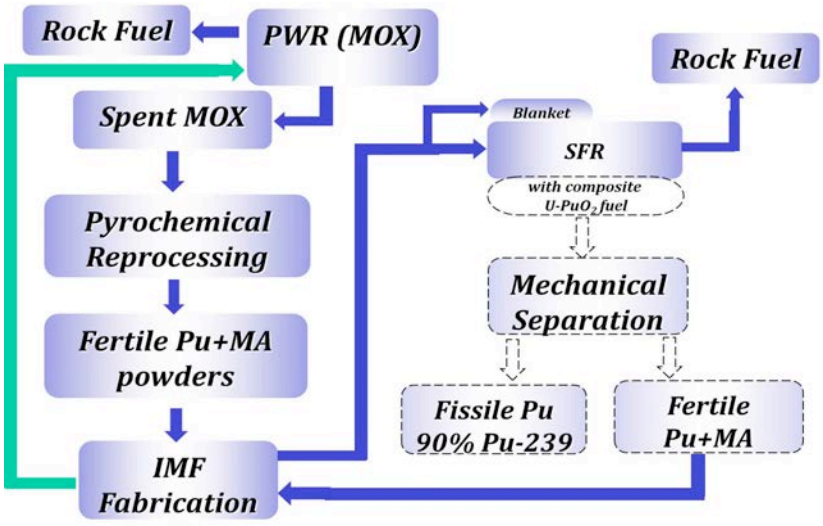

Fig. 3. Peculiarities of involving novel IMF design into nuclear fuel cycle.

5-10

Development and characterization of composite uranium carbide targets at TRIUMF

Peter Kunz[1], Nicole Erdmann[2], Pierre Bircault[1], Marik Dombsky[1], Vicky Hanemaayer[1], Klaus Lützenkirchen[2], John Wong[1]

[1]TRIUMF, 4004 Wesbrook Mall, Vancouver, B.C V6T 2A3, Canada, [2]JRC - Institute for Transuranium Elements, P.O. Box 2340, D-76125 Karlsruhe, Germany

The isotope separator and acceleration facility ISAC at TRIUMF is using thick targets for the production of radioactive ion beams (RIB) via spallation, fragmentation and fission reactions by irradiation with a 500 MeV proton beam at currents of up to 100 µA. Typical ISAC production targets are composed of a stack of thin foils of various refractory materials. The lamellar structure allows for the effective release of short-lived radioactive nuclei via diffusion from the target material matrix and effusion to the ion source while at the same time providing sufficient thermal conductivity to dissipate excess heat from the high power driver beam [1,2].

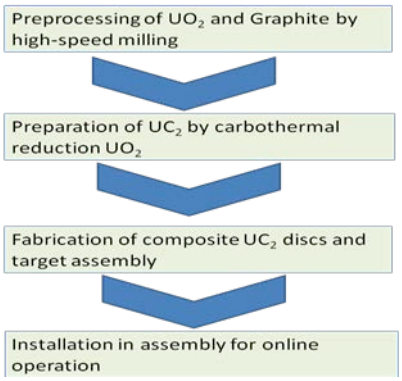

Figure 1: Production steps for the assembly of a uranium carbide target.

Among the suitable choices for target materials are refractory carbides with sufficiently high melting points and vapour pressures, not exceeding 10^{-6} mbar at temperatures of up to 2300 ºC. ISAC carbide targets are typically made of up to 400 D-shaped composite ceramic discs, consisting of a carbide layer coated onto a thin exfoliated graphite sheet. While not adding significantly to the total target reaction cross section, the graphite backing foil is crucial for the dissipation of thermal energy [3]. For the production of radioactive isotopes of heavy elements such as Ac, Ra, Fr, At and Rn as well as very neutron-rich isotopes a fabrication method for composite uranium carbide targets has been developed (Fig. 1). In a multi-step process, UC_2 has to be prepared with sufficient purity, the right grain size and carbon content by carbothermal reduction of UO_2 in a high temperature vacuum furnace. The second step consists of manufacturing the composite target discs. A slurry is produced by mixing organic solvents, binders, UC_2 and additional graphite powder. The average particle size is reduced to <10 µm by high-speed grinding in a planetary ball mill. The slurry is then slip-cast on an exfoiliated graphite sheet. After drying, composite target discs with a thickness of ~50 mg/cm^2 are cut out, loaded into a target container and finally conditioned at temperatures of up to 2000 ºC.

For the characterization of the composite UC_2/C target discs a variety of diagnostic methods were employed. Scanning electron microscopy (SEM) was used to analyse the particle structure. The molecular composition was investigated by x-ray diffraction (XRD) and contaminants were detected using x-ray fluorescence (XRF). The thickness of target discs was determined by L-edge densitometry (LED). This method was originally developed as transportable equipment for the analysis of liquid samples, e.g. uranium product samples (pellets and powders) after their dissolution. It is typically used in uranium fuel fabrication plants in support of international nuclear safeguard authorities (IAEA, EURATOM) during physical inventory verification (PIV) campaigns [4]. In collaboration between TRIUMF and JRC-ITU the setup was modified to perform spatially-resolved thickness measurements of UC_2/C target disks. Within the surface area of one target disc, fluctuations of up to 40% were detected (Fig. 2). This can be attributed to the fact that, so far, the slip-casting procedure has to be performed manually inside an inert gas glove box, the relatively quick evaporation of the organic solvent and the associated loss of viscosity [5].

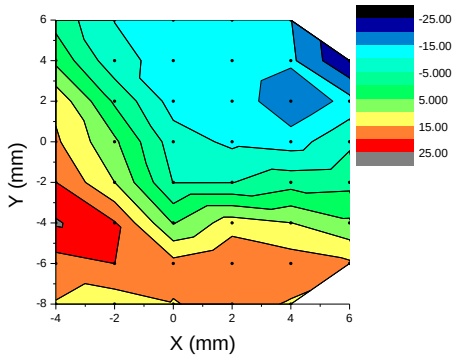

Figure 2: LED scan of a UC_2 target disc. The contour plots show the deviation from the median target disc

The TRIUMF operating license for actinide targets allows currently a maximum proton beam current of 10 µA on target. In online tests of composite UC_2/C targets a variety of RIB yields have been measured. Heavy elements like Ac, Ra, Fr and At as well as neutron-rich isotopes of Rb, Sr, and K could be detected by α-,β- and γ-spectroscopy. Short release times in the range of a few milliseconds were confirmed with the detection of short-lived isotopes like ^{214}Fr and ^{35}Mg.

References

[1] M. Dombsky, P. Bricault, V. Hanemaayer. Increasing beam currents at the TRIUMF-ISAC Facility; techniques and experiences. *Nuclear Physics A*, 746 (2004), 32c-39c.

[2] M. Dombsky, P. Bricault. High intensity targets for ISOL, historical and practical perspectives. *Nuclear Instruments and Methods in Physics Research B*, 266 (2008), 4240–4246.

[3] V. Hanemaayer, P. Bricault, M. Dombsky. Composite ceramic targets for high power proton irradiation. *Nuclear Instruments and Methods in Physics Research B*, 266 (2008), 4334–4337.

[4] N. Erdmann, P. Amador, P. Arboré, H. Eberle, K. Lützenkirchen, H. Ottmar, H. Schorlé, P. van Belle, F. Lipcsei, P. Schwalbach, R. Gunnink. COMPUCEA: a High-Performance Analysis Procedure for Timely On-site Uranium Accountancy Verification in LEU Fuel Fabrication Plants. *ESARDA BULLETIN*, 43 (2009), 30-39.

[5] Peter Kunz, Pierre Bricault, Marik Dombsky, Nicole Erdmann, Vicky Hanemaayer, John Wong, Klaus Lützenkirchen. *Composite uranium carbide targets at TRIUMF: development and characterization with SEM, XRD, XRF and L-edge densitometry*. 2013. submitted to Journal of Nuclear Materials.

5-11

Phase Relations of Uranium and Zirconium Oxides at High Temperatures for Fuel Debris Treatment

Nobuaki Sato[1], Yuhei Fukuda[1], Akira Kirishima[1], Takayuki Sasaki[2]

[1]Institute Multidisciplinary Research for Advanced Materials, Tohoku University, Sendai, Japan, [2]Department of Nuclear Engineering, Kyoto University, Kyoto, Japan

In March, 2011, reactors at Fukushima Daiichi NPP were severely damaged by the tsunami attack resulting in the formation of fuel debris. To study the fuel debris treatment at Fukushima Daiichi NPP, information on the phase relations of main constituents in the reactor, i.e., oxides and metals of uranium and zirconium is needed. In the case of TMI NPP accident, the alloy phase containing uranium and zirconium appeared in the fuel debris as well as mixed oxide phase. Though several phase diagrams were reported in 1950's and 1960's, they were not consistent. On the other hand, the fuel debris seemed to be exposed to the oxidative condition compared with the TMI case. In this paper, phase relations of uranium and zirconium oxides were analyzed by powder XRD method at high temperatures. After the heat treatment of the mixture of UO_2 and ZrO_2 in vacuum, the UO_2 solid solution phase such as $Zr_yU_{1-y}O_{2+x}$ seemed to be formed as well as the small amount of the monoclinic ZrO_2 phase at temperatures lower than 1273 K. However, phases with higher oxidation state such as, U_3O_7 and U_3O_8 seemed to appear in the temperature range from 1073 K to 1473 K with significant amount of the ZrO_2 phase. Over this temperature, a new phase similar to the UO_2 phase seemed to be formed showing the decomposition of U_3O_8 phase at high temperature. Also, the tetragonal ZrO_2 was also observed in the same sample since phase transition from monoclinic to tetragonal occurred at high temperature. When the mixture of zirconium to uranium oxides was treated by mechanochemical method under reducing condition, the X-ray pattern of the products showed that they were the same fluorite structure and the lattice parameter of this phase was linearly decreased with increasing zirconium ratio. This suggests that the UO_2 and ZrO_2 form the solid solution from low Zr/U ratio to high one. These results were also discussed with the phase diagram.

POSTERS

1-66

New Concept of Designing Composite Fuel for Fast Reactors with Closing Fuel Cycle

Alexey Savchenko, Alexander Vatulin, Gennady Kulakov, Ksenia Lipkina, Vladimir Sorokin, Sergey Ershov, Sergey Maranchak, Zoya Petrova

A.A. Bochvar Institute (VNIINM), Moscow, Russia

A possibility is considered for use in fast reactors in place of the base container type ceramic fuel: MOX, (U,Pu)N, or metallic U-Pu-Zr fuel, the dispersion type fuel elements (composite of metallic high uranium content fuel, U-Mo or U-Zr with PuO_2 powder distributed in Zr alloy matrix). Composite fuel combines the favorable features of metallic and ceramic fuels and improves characteristics of materials. In composite fuel metal fuel and PuO_2 powder have separate arrangement, hence includes both active core and inner blanket. Therefore we can manage to reach practically the same heavy atoms density under the cladding as for nitride and metallic type's fuel (fig. 1).

Density of heavy atoms (U+Pu) g/cm³		MOX $(U, Pu)O_2$	Nitride (U, Pu)N	Metallic Fuel U-19Pu-10Zr	Composite Fuel $U\text{-}PuO_2$
Under the cladding		8,3-8,5	10,5	10.5-11.0	10.5-11.5
Thermal conductivity of fuel W/m K		2-4	16-25	20-30	20-25
Conversion ratio	SFR	0,8-1,2	1,5		1,7
	FR-BREST	0,8-0,9	1,1		1,2

Fig 1. Design of container type fuels (ceramic and U-19Pu-10Zr metal fuel) and novel composite $U\text{-}PuO_2$ dispersion fuel for fast reactors

In the suggested design metal fuel of U-Zr, U-Zr-Nb, U-Mo or novel U-Mo-C alloys in the form of granules forms a porous frame, bonded by a zirconium matrix alloy; the pores of the frame contain PuO_2 powder manufactured by pyrochemical or other methods. The fuel meat metallurgically bonded to a cladding promotes the high thermal conductivity to such composite $U\text{-}PuO_2$ fuel, while the Zr-base matrix alloy improves the compatibility between fuel components.

This approach can be also implemented with the use of Th granules instead of dump uranium. It should be mentioned that when fabricating the fuel element Zr matrix alloy automatically coats inner surface of the cladding, hence, protects it against interaction with fuel. Composite fuel has the following advantages: higher thermal conductivity, higher uranium content, hence, high conversion ratio as compared to MOX fuel and lower damage of fuel by fission products and, hence, lower swelling as well as low interaction with cladding as compared to metallic U-Pu-Zr fuel. Fabrication technology is more simple and environmentally clean.

Mechanism of composite fuel operation: It should be noticed that composite fuel includes both active core with PuO_2 powder and inner blanket with U blank fuel simultaneously, since U and Pu have initially separate arrangement. Moreover, in U alloy granules Pu generates much higher due to more intensive neutrons flow. First PuO_2 powder burns up inside METMET fuel frame while Pu generates in the METMET fuel that first serves as a breeding

blanket and only then begins to burn up. Therefore plutonium dioxide powder will basically accumulate non-fissionable isotopes while the METMET fuel fissionable ones. We can receive practically weapons grade Pu in U alloy granules with atomic burn-up of 2-3%, and 8-10% of generated Pu. But in PuO_2 powder we can receive the burn-up of 33% with poor isotopic Pu composition and high quantities of MA as well as 80% of fission fragments. Then, without chemical reprocessing, using only mechanical separation methods we can separate high quality product from poor one. For MA incineration a novel IMF design with isolated arrangement of MA is suggested that complies fully the requirements for “Rock Fuel” and shall extend the burn-up.

***Peculiarities of fuel cycle closing with composite fuel**:* First, by mechanical separation, spent fuel is separated on high quality (U granules) and poor quality (PuO_2 powder). High quality fuel (fissile Pu isotopes) can be used again after pyrochemical reprocessing in fast reactors or, without reprocessing coarse granules can be used in fuel fabrication Plant for producing fuel elements for thermal reactors using capillary impregnation technology. Fuel of the low quality (PuO_2 powder) of poor Pu isotopic composition including fission fragments and MA can be used for IMF fabrication followed by incineration in thermal or fast reactors with direct geological disposal as (Rock fuel). Thus, the proposed fuel cycle looks more effective from the point of minimizing r/a waste and reused of generated Pu (fig.2).

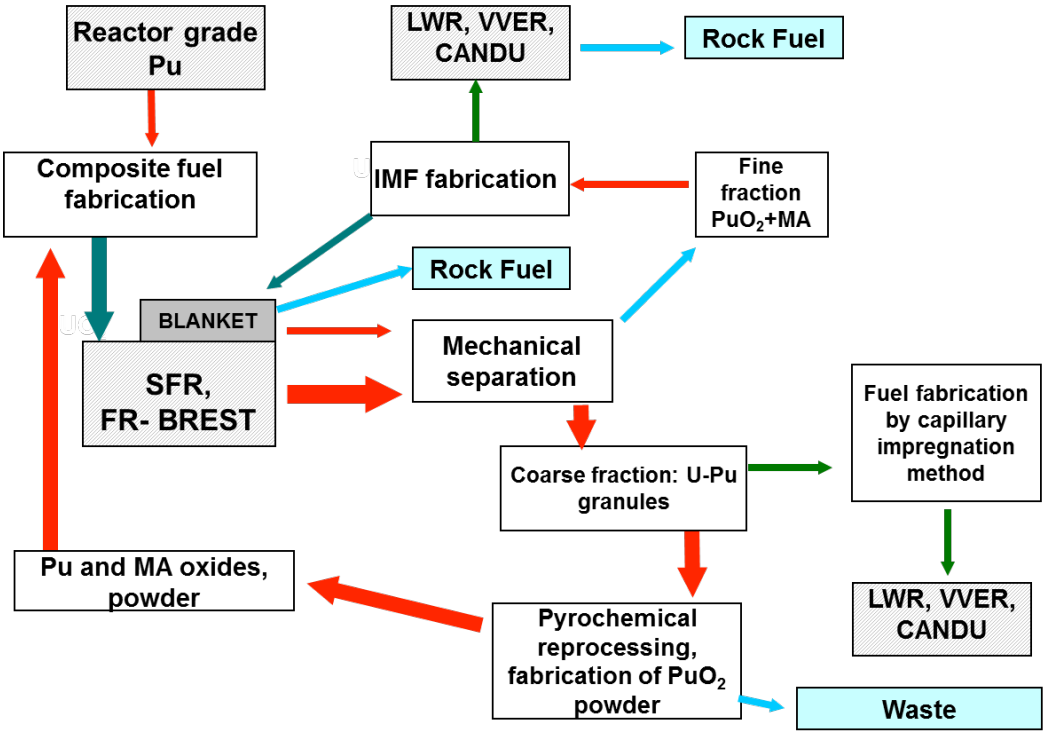

Fig. 2. SFR fuel cycle with composite fuel

1-67

Separation of uranium and lanthanides in "molten salt – liquid metal" system

Leonid Yamshchikov[1], Vladimir Volkovich[1], Andrey Schetinskii[1], Dmitry Maltsev[1], Alexander Dedyukhin[1], Viktor Ivanov[1], Stanislav Melchakov[1], Sergey Raspopin[1], Alexander Osipenko[2], Mikhail Kormilitsyn[2]

[1]Ural Federal University, Ekaterinburg, Russia, [2]JSC "SSC Research Institute of Atomic Reactors", Dimitrovgrad, Russia

High and constantly increasing amounts of spent fuel and radioactive wastes as well as not effective use of natural uranium constitute the major problems of nuclear power production based on U-235 fission. Realization of a more efficient closed fuel cycle is possible, for instance, with fast neutron reactors, including reactors with fused salt active zone. Such molten salt represents suitable electrolyte for reprocessing spent fuel employing electrochemical methods. The present work is aimed at studying processes of separating uranium from lanthanides as well as developing methods for separating minor actinides employing alkali chloride melts and Ga-In eutectic alloys.

Separation coefficient (Θ) of two elements (Me_1 and Me_2) in molten salt on a liquid alloy was determined from the formal standard potentials of these elements (E^*) and their activity coefficients (γ) in the liquid metal alloy:

$$\ln \Theta = \frac{nF}{RT}(E_2^* - E_1^*) + \ln \frac{\gamma_1}{\gamma_2}$$

Formal standard potentials of uranium and lanthanides have been studied in sufficient detail and can be found in the literature. Activity coefficients of uranium and lanthanides in Ga-In eutectic based alloys were calculated from the following equation

$$\lg\gamma_R = \lg a_R - \lg X_R,$$

where R = U, La, Nd, Pr, a is activity and X solubility of a given element in the metallic alloy. Activity of uranium and lanthanides in the Ga-In based alloys was determined employing the direct and most precise technique of electromotive force measurements.

Solubility of uranium and lanthanides in the Ga-In eutectic was determined between 298 and 1073 K using four independent methods (precipitation, filtration, centrifuging and electromotive force measurements). Separation coefficients of uranium and three studied lanthanides at 723 K are presented in the Table.

Table – Uranium and lanthanides formal standard potentials (in 3LiCl-2KCl based melts), activity coefficients of the super cooled metals in Ga-In eutectic based alloys and separation coefficients of U/Ln couples in "3LiCl-2KCl – Ga-In" system

R	$-E^*_R$, V	$-\lg\gamma_R$	lgΘ	Θ
La	3.116	13.37	4.11	$1.3\cdot10^4$
Pr	3.098	11.75	5.34	$2.2\cdot10^5$
Nd	3.070	12.70	3.81	$6.4\cdot10^4$
U	2.504	4.66	-	-

1-73

Thermodynamic Aspects of Interphase Interaction in Heterogeneous Alloys and Its Influence on Alloys Properties

Alexey Savchenko, Andrey Laushkin, Yury Konovalov

A.A. Bochvar Institute (VNIINM), Moscow, Russia

Properties of heterogeneous alloys are governed by both level of interatomic interaction and phase compositions of alloys, specifically, structure, morphology, size and distribution of phases as well as interphase interaction. The latter is particularly urgent for systems with developed interphase surfaces of nanostructure type, composite materials as well as for processes in which interphase boundaries play a decisive part, i.e., during corrosion, interaction between materials, that takes place during irradiation and often accompanies by structure changes and alloying by fission products. It is particularly actual for actinides systems when alloying of Pu^{241} with Am^{241} up to 21 at. % by natural decay did not result in delta phase stabilization. In this and many other cases the alloying does not influence on the thermodynamic state of an alloy and the energy state of electron shells of atoms.

In traditional thermodynamics interaction between phases has never been taken into account before, since heterogeneous alloy was considered to be a mechanical blend of phases while alloys are an unified thermodynamic system having a sophisticated physical-chemical phase interactions which is not available in the mechanical blend.

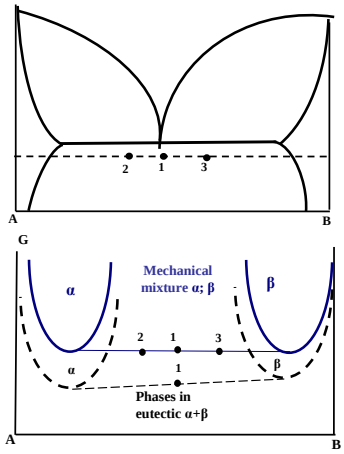

Fig 1. Description of equilibrium in eutectic: traditional - (solid blue line - reduced average value) - using free energies of isolated phases in an alloy – phase equilibrium does not depend on composition; Proposed in accordance with classical thermodynamics - (black dotted line) - using free energies of phases contacting each other in an alloy - phase equilibrium depends on composition

We treated heterogeneous alloy as a single thermodynamic system, for its description use is made of free energy values of not isolated phases as it is done presently, but free energies of the same phases contacting one another. Then, the free energy value of alloy and phases will be smaller than of isolated phases, while the energy state of alloy will be lower which distinguishes an alloy from the mechanical blend (fig. 1).

It follows from the fact that heat capacities of phases change (initial separate phases have lower value).

The reduce in Gibb's free energy associated with changes in average heat capacities of phases, influences many properties of alloys, particularly, actinides alloys. While forming alloy we observe changes in free energy, entropy, heat capacity and hence – in character and energy of atomic oscillations. Therefore it affects: temperature and enthalpy of melting, heat capacity, coefficient of thermal expansion, strength and high temperature strength as well as diffusion processes, which in turn influences on compatibility, corrosion, material performance, etc..

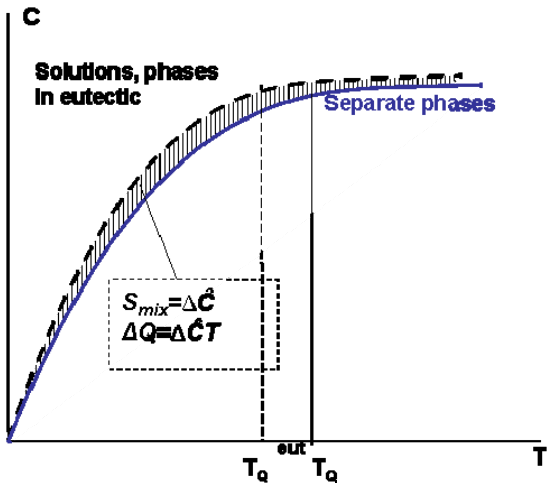

Fig. 2. Changes in specific heat (heat capacity) during mixing processes. Dotted line – eutectic, solid line – initial separate phases (reduced average value)

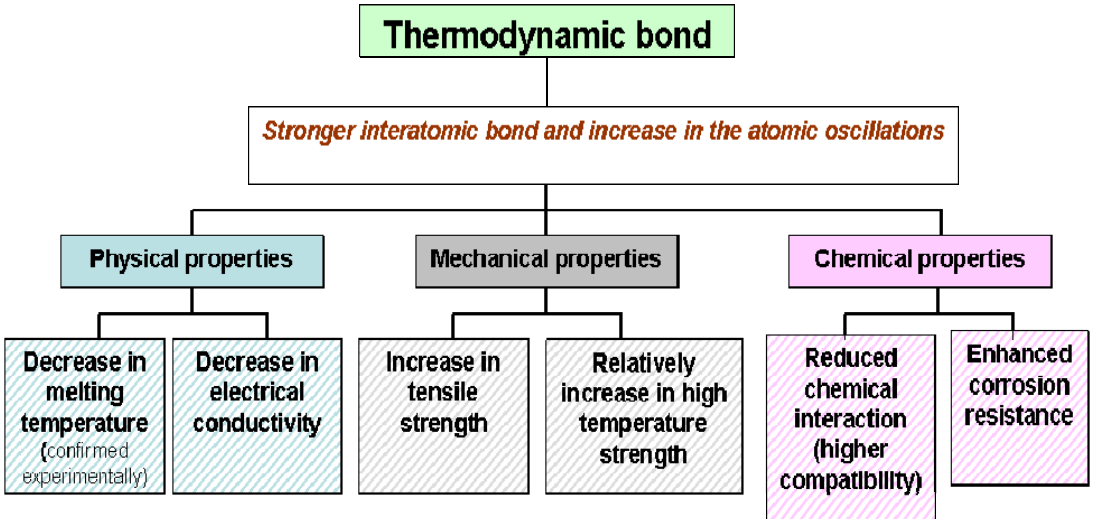

Fig. 3. Schematic presentation of Influence of interphase thermodynamic bond on properties of alloys

1-68

Solubility of uranium and lanthanum in Ga-In eutectic based alloys at 25-800 °C

Vladimir Volkovich[1], Andrey Schetinskii[1], Dmitry Maltsev[1], Alexander Dedyukhin[1], Leonid Yamshchikov[1], Stanislav Melchakov[1], Viktor Ivanov[1], Alexander Osipenko[2], Sergey Raspopin[1], Mikhail Kormilitsyn[2]

[1]Ural Federal University, Ekaterinburg, Russia, [2]JSC "SSC Research Institute of Atomic Reactors", Dimitrovgrad, Russia

Current technology (PUREX process) employed for reprocessing spent nuclear fuels (SNF) has a number of limitations due to radiation instability of organic reagents used and presence of neutron moderators. This process cannot therefore be used for work with highly concentrated in fissile materials systems of for treating high burn-up fuels after short cooling times. Molten salts and metals exhibit high thermal and radiation stability and can be employed as working media for pyrochemical reprocessing of spent nuclear fuels and practical realization of a short closed nuclear fuel cycle. Having the salt and the metal in liquid state, particularly at relatively low temperatures, simplifies phase separation in radiochemical technology. Understanding processes occurring in molten salts and liquid metals as well as behavior of uranium and SNF components is important for designing a feasible process. Low-melting metals can be effectively employed for separating SNF components in a "liquid metal – molten salt" system. Metal alloys of eutectic composition can be used for further reduction of the operation temperature. The information about the behavior and properties of SNF components in three-component liquid metal alloys is scares.

The present study was aimed at determining solubility of uranium (fissile material) and lanthanum (an example of a rare earth fission product) in one of the lowest melting point alloys – Ga-In eutectic (21.8 wt. % In, m.p. 16 °C). The measurements were performed in a wide temperature range from the room temperature (25 °C) to 800 °C. Several independent techniques were employed for the solubility determination including electromotive force (EMF) measurements method, supersaturated alloy filtration, precipitation and centrifuging. X-ray analysis of the solid precipitates formed in the supersaturated alloys showed that in uranium containing alloys the solid phase consisted of UGa_3 intermetallic compound, and in lanthanum containing alloys $LaGa_6$ or $LaGa_2$ is formed depending on temperature.

In the EMF method the solubility of studied metals was determined between 300 and 800 °C from the difference between experimentally measured uranium or lanthanum activity and activity coefficients values. Low melting ternary LiCl-KCl-CsCl eutectic containing uranium or lanthanum chlorides acted as the electrolyte in the electrochemical measurements. Direct physical methods (precipitation, filtration and centrifuging) were used between 25 and 420 °C. In case of lanthanum centrifuging was ineffective due to closeness of densities of solid lanthanum intermetallic compounds and Ga-In eutectic alloy.

Experimental data on uranium and lanthanum solubility are presented in Fig. 1. Upon lowering temperature from 800 °C to room temperature, uranium solubility decreases from *ca*. $3.1 \cdot 10^{-3}$ to $7.9 \cdot 10^{-7}$ mole fraction and lanthanum solubility changes from *ca*. 0.12 to $4.0 \cdot 10^{-7}$ mole fraction.

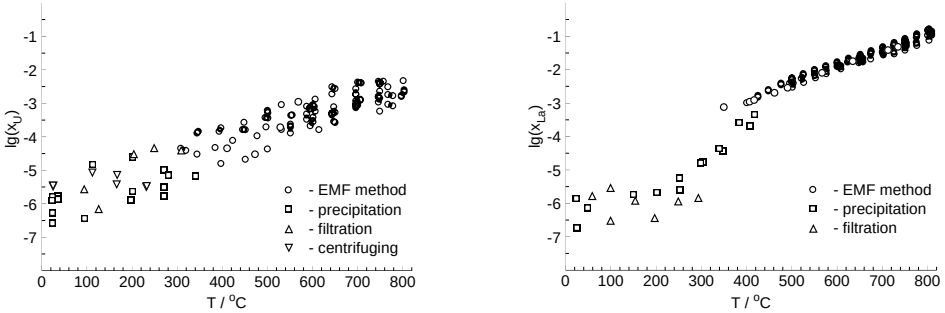

Figure 1. Solubility (in mole fraction) of uranium (left) and lanthanum (right) in Ga-In eutectic based alloys measured by various techniques (shown for each set of data).

1-69

Post-Irradiation Examinations on PHENIX axially heterogeneous pins relevant to ASTRID fuel design: ZEBRE and PAVIX irradiations

Béatrice Rabu, Michel Pelletier, Christophe Valot, Isabelle Munoz, Mayeul Phelip

French Atomic Energy Commission (CEA), Saint Paul lez Durance, France

Descriptors: Axially Heterogeneous Concept, ASTRID, Post-Irradiation Examinations, sodium fast reactors, PHENIX, internal corrosion, cladding material, ZEBRE, PAVIX

In the frame of **ASTRID reactor** development, an **Axially Heterogeneous Concept** (sequence of fertile and fissile fuel) is foreseen on the basis of the encouraging performance of ZEBRE experiment in PHENIX. This type of innovative fuel is potentially able to reach a higher mean burn-up than homogeneous pins because of both reduced maximum deformation and limited internal corrosion.

A large **Post-Irradiation Examinations program** (PIE) has been carried out on fuel pins (austenitic Ti stabilized steel cladding) from the 3 **ZEBRE sub-assemblies**. More than 250 pins have been examined non destructively and 13 pins subjected to detailed destructive examination. Main PIE results will be exposed.

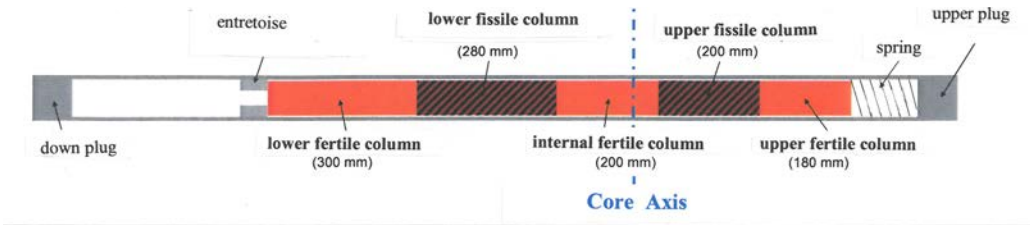

Figure 1: ZEBRE pin geometry

With regard to internal cladding corrosion, metallographic examinations are coherent with Eddy Current signals: in comparison with homogeneous pins in quite similar conditions, the mean corrosion is about 3 times lower in the heterogeneous pins (60 µm instead of 150 -200 µm). No evidence of clad corrosion or cracking damage was seen near the fissile-fertile interfaces. The behaviour of the $(UPu)O_2$ mixed oxide is consistent with the irradiation parameters. The behaviour of the internal (UO_2) fertile layer is promising without enhanced swelling. Electron Probe Microanalysis indicates that limited Pu diffusion occurred (< 200 µm) from the lower and upper fissile zones to the medium fertile zone; some Cs moving towards fertile columns (tens of mm) without reaction with UO_2. The absence of fissile-fertile interface reaction observed could be attributed to the presence of the upper fertile column avoiding concentration of corrosive fission products at the top of the fissile column.

Excellent behaviour of heterogeneous ZEBRE fuel has been observed up to a burn-up of 13.3 at% (ZEBRE 4), especially with respect to internal corrosion.

To enrich the state of the art of axially heterogeneous fuel pin concept, a Post-Irradiation Examinations (PIE) program on the **PAVIX experiment** dealing both with non-destructive and destructive exams is planned to be performed. Better behaviour of cladding material (15-15 Ti - AIM1) at the fuel fissile-fertile interface is expected.

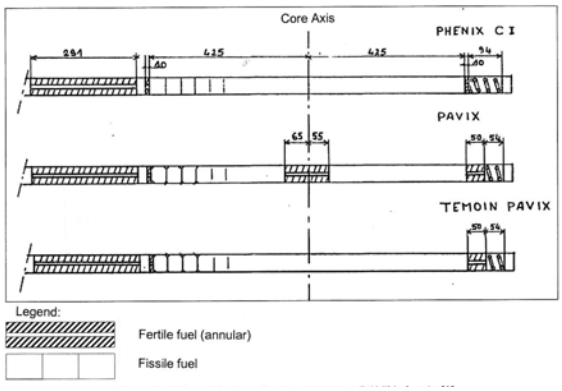

Figure 2 : PAVIX and Témoin PAVIX pin geometry compared to PHENIX Standard pin

Destructive exams	**Properties expected**
Pin puncturing and gas analysis	- % release of Fission Products, composition of the gas - internal pressure in the pin
Thermal gas retention	Total gas in the fuel pellets at various levels
Metallography -Maximum Flux Plan +axial metallography (fissile /fertile interface) Complementary exams if internal corrosion	Fuel thermics through following indicators: - state of fracturation - grain size and shape - porosity and gas bubbles distribution - gap evolution, formation of JOG ? - fuel restructuration ? - general state of the fuel (low power in PAVIX) for comparison with ZEBRE experiment - extension of the corroded zone
Secondary Electron Microscopy (SEM)+Possibly Focus Ion Beam	*performed on polished samples* In depth analyses
Electron Probe MicroAnalysis (EPMA)	Radial analysis of pellet constituants: - actinide redistribution - radial distribution of gas and volatile species - local BU by Nd measurement - X-ray species cartography (U, Pu, Mo, Ru, Pd, Te, Zr, Nd, Cs, O) - metallic precipitates analysis
SIMS	- radial isotopic analysis - analysis complementary to EPMA - in depth fission gas analysis
XRD	- on the cladding if corrosion: - JOG cristalline structure - Internal corrosion study - on thin slices (< 500 µm): - crystalline structure evolution vs. fuel restructuration

Table 1: Main destructive exams planned on PAVIX pins

The **Post-Irradiation Examinations program on PAVIX experiment** will be detailed :

- Non destructive exams will be performed on PAVIX pins both at CEI PHENIX in Marcoule (Irradiated Elements Cell) and at LECA/STAR facility in Cadarache: visual inspection, metrology, axial gamma spectrometry (fission products and activation products axial distribution, interpellet), Eddy currents (defaults localisation in the cladding), neutronography and possibly X-ray radiography (better precision expected).

- Destructive exams will be performed in a second step in LECA/STAR. The different examinations and expected properties figure in the following table:

The PIE program described above on PAVIX irradiation is planned to be performed at the end of 2014 at CEI Phenix in Marcoule and from 2015 at LECA-STAR facility in Cadarache center. Results will enlarge knowledge on axially heterogeneous concept for ASTRID.

Oxidation of Uranium-Plutonium Mixed Nitrides

Andrei Shadrin, Alexey Glushenkov, Konstantin Dvoeglazov, Mikhail Skupov

Bochvar Institute (VNIINM), Moscow, Russia

Most of experts suppose the future development of nuclear energy will be associated with the fast neutron reactors (FR) and use of dense fuels (i.e. mixed nitrides, uranium and plutonium carbides, metallic fuels). The program “New Generation Technologies for Nuclear Energetics” performing in Russian Federation is to provide development of BREST-OD-300 reactor with mixed U-Pu nitride fuel (MNUPF) by 2020 year. The FR implementation is closely interconnected with nuclear fuel cycle closure (CNFC). So the questions concerning spent nuclear fuel (SNF) reprocessing, especially SNF reprocessing safety, gain significance. Mixed nitride fuel application needs solution for several specific problems due to ability of uranium and plutonium nitrides to be oxidized with air oxygen at high temperatures.

This paper describes results of investigation of U and Pu nitrides oxidation at temperatures from 25 to 300°C in atmosphere of nitrogen containing oxygen and water with concentrations from 10 ppm to 3 vol.%. The samples of mixed nitrides of U and Pu and model nuclear fuel were used in experiments.

Scheme of experimental installation is shown on Figure 1. According to the results obtained intensive oxidation of UN (powder – 250 µm) takes place at temperature higher than 260 ^{o}C.

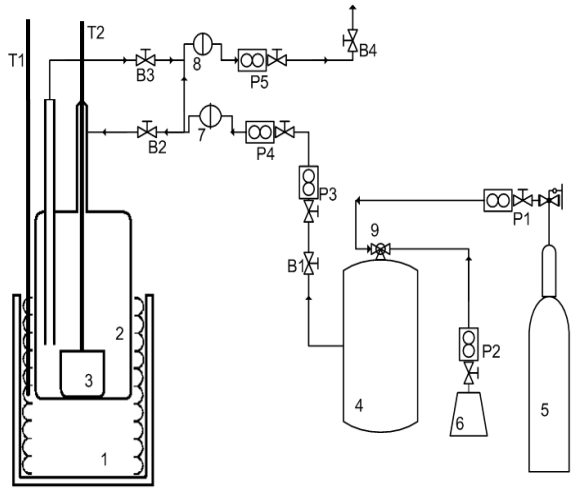

1 – electric heater; 2 – quartz glass reactor; 3 – crucible; 4 – receiver; 5 – nitrogen cylinder; 6 – compressor; 7 –inlet oxygen concentration sensor; 8 –outlet oxygen concentration sensor; 9 – mixer; T1, T2 – thermocouples

Figure 1 – Experimental installation for U(Pu)N powder oxidation investigation

Oxidation of mixed U(Pu)N powder (<25 µm and 800-1000 µm) was performed in Ar containing 2% O_2 at temperatures from 25 to 450 ^{o}C. The results (Figure 2 and Table 2) showed no intensive oxidation under these conditions. The similar results were obtained for model spent nuclear fuel containing U, Pu, Zr and Mo (Figure 3).

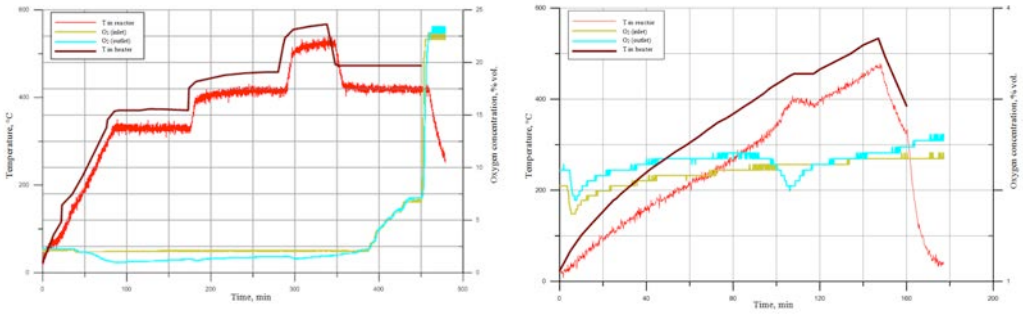

Figure 2 – Temperature in the crucible (T2 thermocouple) and oxygen concentrations during (UPu)N heating in 2% vol. oxygen containing media flow (particle size -25 μm (left), 800-1000 μm (right).

Table 1. Mixed nitride powders behavior in oxygen containing gaseous media at high temperature

Particles sizes, μm	Oxygen concentration, % vol.	Oxidation lowest temperature, °C	Temperature increase, °C	Process duration, min
<25	2	200	–	320
800-1000	2	300	50	20
	air		210	<20

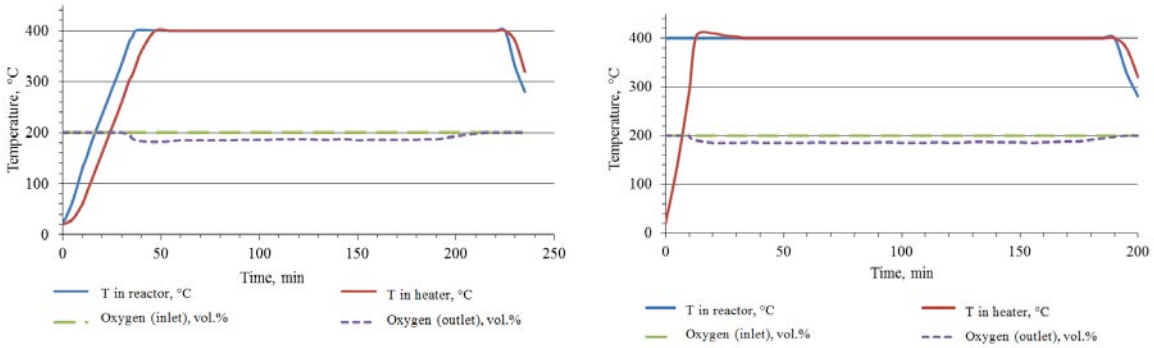

Figure 3 - Temperature in the crucible (T2 thermocouple) and oxygen concentrations during (UPu)N heating (gradual (left) and rapid (right) in 2% vol. oxygen containing media flow

The experiments carried out show nitride oxidation processes take place at temperature of 260°C and higher even in presence of trace amounts of oxygen and water. Although for the particle size over 100 μm exothermal effect of the reaction is relatively small even in presence of 3 vol. % of oxygen. Experiments with MNF showed no oxidation of mixed U and Pu nitrides below 260°C. The results obtained will be used in works on MNUP SNF reprocessing safety validation

1-72

Abstract for report: 'Investigation of diformylhydrazine interaction with Pu in technological media of extraction SNF reprocessing'

Volk Vladimir, Pavlyukevich Ekaterina, Dvoyeglazov Konstantin, Podrezova Lubov, Veselov Sergey

JSC SSC VNIINM, Moscow, Russia

At the stage of uranium and plutonium separation in hydrometallurgical spent nuclear fuel reprocessing hydrazine-stabilized U(IV) is usually used as a reducing agent. It leads to generation of products, which cause difficulties for following liquid nuclear waste reprocessing.

I|n order to find alternative reducing agent for Pu reextraction kinetis of Pu(IV) reduction by diformylhydrazine (DFH) in uranyl nitrate and pertechnetat-ion containing nitric acid solutions has been studied by means of spectrophotometric technique.

Investigation of U(VI) influence on the reaction rate was carried out under following conditions: initial concentration of U(VI) from 10 to 50 g/l, temperature 30°C, [DFH] = 0.1 mol/l, $[HNO_3]$ = 1 mol/l, [Pu] = $5 \cdot 10^{-3}$ mol/l.

DFH addition to the solution causes rapid decrease of Pu^{4+} ions concentration. Kinetic curves can be characterized by second-order equation with respect to Pu concentration. Reaction rate constant, order of reaction in respect to U were evaluated, reaction energy of activation was estimated.

As the extracts contain technetium besides U and Pu, seeveral experiments for investigation of Tc influence on Pu reduction were carried out under following conditions: $[HNO_3]$ = 1 mol/l, [Tc] from 0.1 to 0.5 mmol/l, temperature 30°C. Results obtained in these experiments showed that reduction rate was significantly higher in presence of Tc and kinetic curve character indicated autocatalytic nature of reaction investigated.

1-75

µ-focus capabilities at the INE-Beamline for actinide science at ANKA

Kathy Dardenne[1], Jörg Rothe[1], Teresa Fernandes[2,3], Dieter Schild[1], Eva Soballa[1], Volker Metz[1], Christiane Bube[1], Bernhard Kienzler[1], Melissa Denecke[1], Horst Geckeis[1]

[1]KIT-INE, Karlsruhe, Germany, [2]Amphos 21, Barcelona, Spain, [3]ICTA, UAB, Bellaterra, Spain

The INE-Beamline at ANKA [1] is dedicated to actinide research with emphasis on X-ray spectroscopic techniques. It has been constructed and is operated by the Institute for Nuclear Waste Disposal (INE) at KIT north campus. The necessary infrastructure and safety equipment is available at the INE-Beamline for basic and applied research on radioactive materials. Investigations on non-fissile radioisotopes up to 10^6 times the limit of exemption and fissile radioisotopes (Pu-239, U-235) up to 200mg, contained within two layers of protection, are possible. The available energy range at the INE-Beamline covers the K-edges from P (2.1 keV) to Pd (25 keV), including the L-edges of lanthanide elements and the lighter actinide elements (up to the Cf L_3-edge).

The synchrotron-based activities at the INE-Beamline are embedded in INE's in-house research, thereby allowing a combination of analytical and instrumental methods, notably laser techniques and microscopic methods. Its location on the same KIT-CN site as INE's controlled area labs offers a constellation unique in Europe for the spectroscopic and microscopic characterization of actinide samples. This symbiosis between beamline and labs has numerous advantages, including profiting from the existing infrastructure, safety equipment and expertise gathered over decades.

R&D at INE is largely aimed at long-term safety assessment of proposed deep geological repositories for high-level, heat-producing nuclear waste (HAW) disposal. To ensure sound safety assessment, a molecular understanding of processes determinant in the fate of radionuclides, notably the actinides (An), and their thermodynamic quantification is essential. Of central importance in such investigations is the determination of An speciation, or their molecular, chemical and physical form. An speciation determines transport properties (mobilization / immobilization), reactivity, bio-availability and, hence, their potential human and environmental risk. X-ray spectroscopic methods have proved to be valuable tools for An speciation research, providing information on the coordination and redox chemistry of An cations, e.g., sorbed onto surfaces or at mineral - water interfaces, occluded or included into the structure of precipitates, colloids, and secondary phases or into glass and spent fuel and their corrosion products. The flexibility of the INE-Beamline design enables various sample environments and detection systems required for answering many specific scientific questions. Besides well-established bulk techniques like XAFS spectroscopy, more advanced methods like (confocal) XAFS/XRF detection with a µ-focused beam or a combination of µ-XAFS and µ-XRD have been implemented. Additional instrumentation for high-energy resolution X-ray emission (HRXES) spectroscopy is actually under commissioning [2].

Since 2009 considerable efforts have been undertaken at the INE-Beamline to implement spatial resolution in the µm regime for the investigation of radioactive samples with heterogeneous elemental or phase distributions. In this context, µ-XAFS (µ-XANES/µ-EXAFS), µ-XRF and µ-XRD have been combined, e.g., to characterize U-rich regions in thin section samples of corroded cement matrices retrieved from the Asse II salt mine in Northern Germany after long-term exposure to salt (NaCl, $MgCl_2$) brines [3] or U contaminated sludge samples obtained from a decantation pond of a uranium treatment facility. Generally, in these samples regions of interest are pre-selected from SEM backscattering images, showing high contrast for U-rich aggregates (hot spots) embedded in the sample matrix. A polycapillary optic mounted on a hexapod positioning unit is used to focus monochromatic radiation to a beam spot-size of 25-30 µm for µ-XRF and µ-XAFS measurements. Samples are mounted on a three-axis positioning stage with the sample surface at a 45° angle to the incident beam for 2D scanning. The third axis defines the focal distance. A silicon drift detector is used for collecting X-ray fluorescence radiation. By mounting an identical polycapillary lens in front of the detector (confocal detection geometry, Fig. 1 - left), element characteristic fluorescence radiation excited below the sample surface can be detected in order to reconstruct 3D elemental distribution maps (Fig. 1 - right).

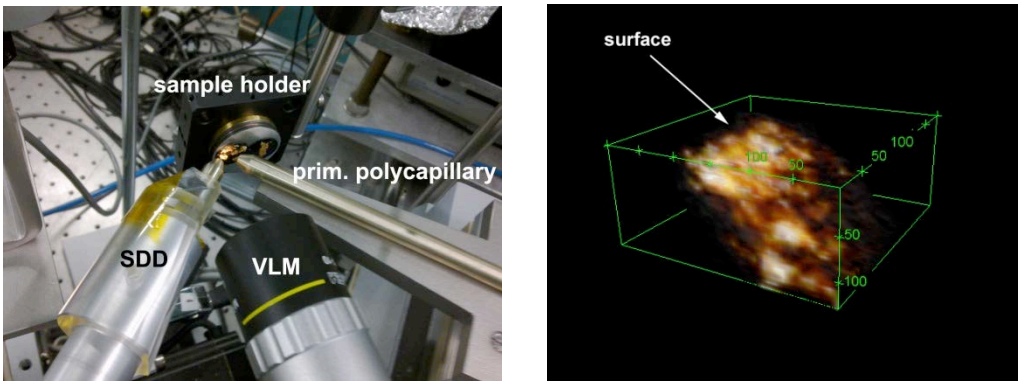

Fig. 1. *left: polycapillary setup for μ-XAFS/XRF measurements at the INE-Beamline – the silicon drift detector (SDD) is depicted with a secondary capillary mounted for confocal measurements (VLM: visible light microscope); right: 3D U distribution in contaminated sludge sample (scales in μm).*

Uranium hot spots identified in element distribution maps reconstructed from scanning μ-XRF data can be selected for μ-XAFS and μ-XRD analysis. Diffraction patterns are collected in Laue transmission mode on erasable X-ray sensitive films, mounted perpendicular to the beam, downstream from the sample. In this case, a single bounce capillary is used to deliver a low divergent ~35 μm focused beam. The setup for confocal μ-XAFS and μ-XRF measurements based on polycapillary half-lenses was completed by integrating a new x/y/z-stage, which allows precise positioning of the silicon drift fluorescence detector (SDD) relative to the primary focus. All components (primary capillary hexapod positioning system, sample stage, detector stage, and visible light microscope) were integrated and tested in the confocal geometry (Fig. 1 left). The first 3D reconstitution of the uranium distribution in a uranium rich sediment based on confocal measurement at different depth is shown in Fig. 1 right. The microfocus setup is available for general user operation since October 2010 and the confocal since April.

The INE-Beamline is a pooled facility of the EU FP-7 project TALISMAN [4], follow-up of the ACTINET-I3 initiative. The INE-Beamline is accessible for the general actinide and radiochemistry community through the ANKA proposal system [5].

Selected examples – with an emphasis on the μ-focus capabilities at the beamline - of on-going research projects will be presented. The available techniques will be extended to include high-resolution x-ray emission spectroscopy at the CAT-ACT beamline (projected starting date January 2015)

References

[1] J. Rothe et al., Rev. Sci. Instrum. 83, 043105 (2012)

[2] ANKA Annual Report 2010/2011, KIT (2012)

[3] B. Kienzler et al., Radiochim. Acta 98, 675 (2010)

[4] http://www.actinet-i3.eu

[5] http://www.anka.kit.edu/61.php

1-59

Ultra-Trace Determination of Pu and Np Isotopes by Resonance Ionization Mass Spectrometry

Michael Franzmann[1], Amin Hakimi[1], Gerd Passler[1], Sebastian Raeder[2], Tobias Reich[3], Pascal Schönberg[3], Nils Stöbener[3], Norbert Trautmann[3], Klaus Wendt[1]

[1]Institut für Physik, Johannes Gutenberg-Universität, Mainz, Germany, [2]TRIUMPF, ISAC RIB Division, Vancouver, Canada, [3]Institut für Kernchemie, Johannes Gutenberg-Universität, Mainz, Germany

The sensitive and element-specific determination of long-lived isotopes of plutonium and the minor actinides neptunium to curium, which dominate the radiotoxicity of spent nuclear fuel after thousand years, has always been a challenge. For α-emitters with long half-lives, like ^{239,240,242}Pu, ^{237}Np, ^{243}Am, and ^{248}Cm, the radiometric determination is limited by their low specific activity or hampered by interferences from the decay of neighboring isotopes. The approach of counting the atoms in a sample by using mass spectrometric (MS) techniques is often favorable compared to the analysis of the nuclear decay. Nevertheless, conventional mass spectrometer ion sources, as used in stable isotope inorganic MS, usually operate in a non-selective mode and known elemental isotope patterns serve for clear and sensitive element identification. This approach fails in the analysis of nuclear materials and corresponding contaminations as isotopic compositions exhibit strong variations. Detection limits for Pu and Np are predetermined by isobaric interferences, caused by species of the highly abundant element uranium, e.g. $^{238}U^{1}H$ in the case of ^{239}Pu. Due to its exceptional elemental selectivity, incorporated in the ionization process, resonance ionization mass spectrometry (RIMS) is one of the promising techniques for the sensitive and specific analysis of low-level contents in samples.

The laser resonance ionization process uses step-wise multi-photon excitation of the sample atoms along a chain of characteristic optical resonance lines of the specific element. As an example an excitation scheme for plutonium is given in Fig. 1. Due to the high cross sections for optical excitation processes and the availability of powerful and reliable laser sources, high ionization efficiencies in the % region as well as almost complete isobaric and high isotopic selectivity can be achieved. The latter is somewhat constrained, as thermal atomization of the sample is a prerequisite for RIMS, which leads to some unavoidable contributions of surface ionization or electron emission. Different approaches of RIMS have been worked out to optimize either the aspect of elemental selectivity or the overall efficiency:

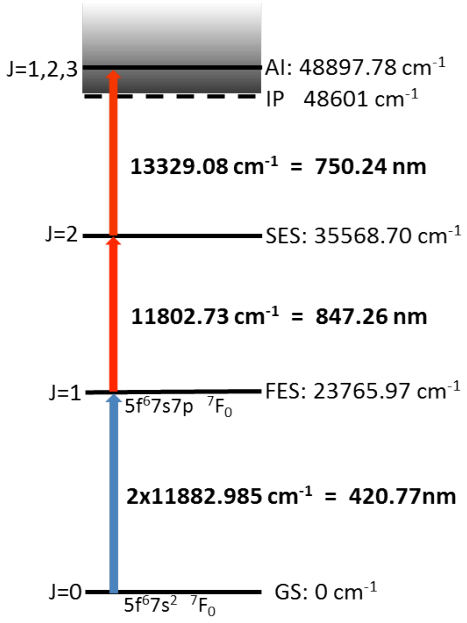

Fig 1: Scheme for three-step excitation and ionization of ^{242}Pu

(1) Filament-TOF-RIMS:
Highest selectivity is achieved by introducing the sample on a filament and performing laser resonance ionization directly within the acceleration field of a time-of-flight MS. Surfaced ionized species are completely suppressed by two consecutive electrode apertures installed between the filament and the ionization region. Even though complete atomization of the actinide of interest is supported by elaborate filament preparation, the efficiency is limited by the low spatial and temporal overlap of the atomic vapor and the laser pulses. Routine operation of this technique is reported with an overall efficiency of $3\cdot10^{-5}$ for Pu and ~10^{-6} for Np, which gives very low LODs of 10^6 atoms for Pu and 10^7 atoms for Np due to an almost vanishing background [1].

(2) In-Source-RIMS:
Based on the ongoing development of laser ion sources at on-line radioisotope production facilities [2], in-source laser resonance excitation has been investigated for the analysis of actinides. The atomization in a graphite furnace, rather similar as in AAS techniques, is combined with resonance ionization at a compact quadrupole mass filter and subsequent quantitative ion counting. The sample is wrapped in a small piece of titanium foil, which acts as reducing agent, and is introduced into the furnace. Direct irradiation of the laser beams into the hot graphite cavity serves for highest ionization efficiency, as an atom inside the cavity typically experiences up to 40 laser pulses of the high-power, high repetition rate laser system. On the other hand, some interfering surface ions are generated in the graphite furnace, which cannot be suppressed. Hence, the gain in efficiency of up to a factor of 100 is accompanied by a trade-off in selectivity. A full characterization of this technique is under way. So far an overall efficiency of ~10^{-3} with an LOD of 10^5 atoms for Pu isotopes has been reported [3], while an efficiency value of $3 \cdot 10^{-3}$ for Np has been determined [4]. In a recent study the LOD of $1 \cdot 10^5$ atoms of Pu could be confirmed, while for Np a LOD value of $2 \cdot 10^5$ atoms could be extracted from a slightly enhanced overall efficiency of $7 \cdot 10^{-3}$.

For analytic applications of RIMS on Pu, the suppression of interfering contaminations from ^{238}U and its hydrides $^{238}U^1H$ and $^{238}U^1H_2$ is of major concern. As has been verified initially for the highly efficient but less selective In-Source-RIMS approach, atomization and spurious ionization of the elemental fraction of ^{238}U exceed the contributions of the uranium hydrides by more than three orders of magnitude. Correspondingly, the elemental selectivity of In-Source RIMS has been studied by investigating the isotope ratio of $^{242}Pu/^{238}Pu$ of $8.83 \cdot 10^{-3}$ in the reference material IRMM043. Samples of $2.9 \cdot 10^8$ atoms of ^{238}Pu and $3.3 \cdot 10^{10}$ atoms of ^{242}Pu each were analyzed as function of an artificially introduced surplus of uranium of $^{238}U/^{238}Pu = 10^2$ to 10^6. Lasers were adjusted on the plutonium ionization scheme as given in Fig. 1 and operated with powers well above optical saturation levels, which ensured that all Pu isotopes are equally ionized. Independent of the uranium surplus on mass 238 of up to 6 orders of magnitude, the ratio of the two Pu isotopes was perfectly reproduced within the experimental precision of typically 10% for furnace temperatures below the melting temperature of the reducing agent titanium of 1670 °C.

A number of experiments are in preparation for further extending the application of RIMS in the field of highly sensitive ultra-trace determination of plutonium and minor actinides. Presently, suitable excitation schemes for RIMS on the minor actinides Am and Cm are being developed. The next steps concern analyses of the Pu content in environmental samples involving both experimental set-ups for intercomparison.

References

[1] N. Trautmann, K. Wendt, Radiochim. Acta 100, 675-685 (2012)

[2] N. Lecesne, Rev. Sci Instrum. 83, 02A916 (2012)

[3] S. Raederet al., Anal. Bio. Chem. 404, 2163-2172 (2012)

[4] S. Raeder, et al., Spectrochim. Acta B 66, 242-247 (2011)

1-71

In-situ measurement of a dissolved alpha emitter by electro-precipitation

Alexander Diener, Christoph Wilhelm, Ursula Hoeppener-Kramar

Karlsruhe Institute of Technology, Karlsruhe, Germany

The vulnerability of drinking water distribution systems to contaminations, which would have major public health, economic, and psychosocial consequences, is one of the main issues of concern to governmental agencies and water supply authorities. A horrific radioactive contamination could arise by nuclear accidents or by terrorist's attack with alpha emitters (e.g. Po-210, U-235, Np-237, Pu-239, Am-241) brought into reservoirs, groundwater cares or water treatment plants. Commonly, there is no continuous observation of the drinking water regarding ionizing radiation. The lack of available online measurement systems with reasonable detection limits is one important reason. For that reason, the task of our joint research project is the development of an in situ measurement system which bases upon electro-precipitation of the dissolved alphas on artificial surfaces.

Therefore, we wanted to figure out which elements in drinking water disturb our activity measurements of alpha emitters in solution. It consists of the sensor (diamond doped Si-waver), $NaNO_3$ or $NaSO_4$ as electrolytes and Am-241 as radioactive tracer. Published median or maximum concentrations for European drinking water were the basis for the synthesis of typical or highly concentrated drinking water for main (HCO_3, Ca, SO_4, Cl, Na, K, Mg, NO_3) and minor elements (Sr, F, Ba, PO_4, Zn, B, Br, Cu, I, Fe, Li, Al).

The electro-deposition itself is reversible. In the average, 99% of the precipitated Am-241 becomes dissolved if the sensor is used as cathode. A comparison between the efficiency in the yield of the electrolytes reveals that $NaNO_3$ is much more effective (~25% yield) than $NaSO_4$ (~7% yield). Figure 1 shows three different runs for each electrolyte, demonstrating the residual activity in the solution after the experiment, the activity of precipitated Am-241 and finally the yield. Regarding the potential disturbance of the activity measurements due to dissolved main and minor elemental components, the results (Figure 2) show that the chemical yield is highest, if there is only the radioactive tracer next to the electrolyte present in solution. The median concentrations of the main and minor elements disturb only slightly. Only at high concentrations especially of Ca, Mg, F, Ba, PO_4, the yield decrease significantly, with a loss of up to 50%. To sum up, the investigation of alphas in solution with a reasonable yield is working well except for rare, extraordinarily high inorganic concentrations.

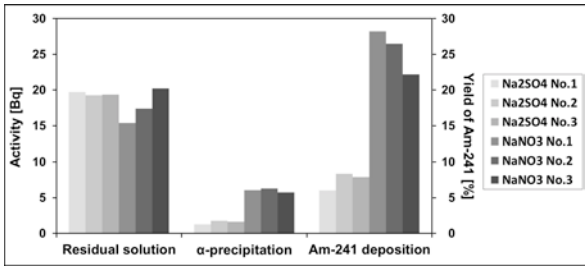

Figure 1

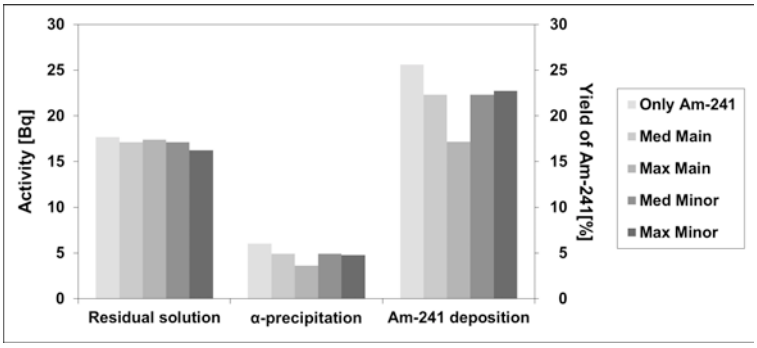

Figure 2

CHEMISTRY

PLENARY & INVITED

1-76

f-Element Single-Molecule Magnets

Katie Meihaus[1], Shuao Wang[1,2], Jeffrey Rinehart[1], Selvan Demir[1], Michael Nippe[1,2], Joseph Zadrozny[1], David Shuh[2], Jeffrey Long[1,2]

[1]University of California, Berkeley, Berkeley, CA, USA, [2]Lawrence Berkeley National Laboratory, Berkeley, CA, USA

Scientists have long employed lanthanide elements in the design of materials with extraordinary magnetic properties, including the strongest magnets known, $SmCo_5$ and $Nd_2Fe_{14}B$. The properties of these materials are largely a product of fine-tuning the interaction between the lanthanide ion and the crystal lattice. Recently, synthetic chemists have begun to utilize f-elements—both lanthanides and actinides—for the construction of single-molecule magnets, resulting in a rapid expansion of the field. The desirable magnetic characteristics of the f-elements are contingent upon the interaction between the single-ion electron density and the crystal field environment in which it is placed.[1] Taking advantage of this interaction, new approaches for synthesizing single-molecules magnets based upon lanthanide and actinide ions will be presented. Focus will be on recent work involving: (i) the synthesis and characterization of radical-bridged dilanthanide complexes exhibiting strong magnetic exchange and record high blocking temperatures,[2] (ii) the observation of ferromagnetic exchange coupling between uranium(IV) and transition metal ions in chloride-bridged complexes,[3] (iii) the observation of slow magnetic relaxation in mononuclear uranium(III) complexes,[4] and (iv) the synthesis and characterization of related new transuranium complexes.

References

[1] Rinehart, J. D.; Long, J. R. *Chem. Sci.* **2011**, *2*, 2078.

[2] (a) Rinehart, J. D.; Fang, M.; Evans, W.; Long, J. R. *Nat. Chem.* **2011**, *3*, 538. (b) Rinehart, J. D.; Fang, M.; Evans, W.; Long, J. R. *J. Am. Chem. Soc.* **2011**, *133*, 14236. (c) Demir, S.; Zadrozny, J. M.; Nippe, M.; Long, J. R. *J. Am. Chem. Soc.* **2012**, *134*, 18546.

[3] (a) Kozimor, S. A.; Bartlett, B. M.; Rinehart, J. D.; Long, J. R. *J. Am. Chem. Soc.* **2007**, *129*, 10672. (b) Rinehart, J. D.; Bartlett, B. M.; Kozimor, S. A.; Long, J. R. *Inorg. Chim. Acta* **2008**, *361*, 3534. (c) Rinehart, J. D.; Harris, T. D.; Kozimor, S. A.; Bartlett, B. M.; Long, J. R. *Inorg. Chem.* **2009**, *48*, 3382.

[4] (a) Rinehart, J. D.; Long, J. R. *J. Am. Chem. Soc.* **2009**, *131*, 12558. (b) Rinehart, J. D.; Meihaus, K. R.; Long, J. R. *J. Am. Chem. Soc.* **2010**, *132*, 7572. (c) Meihaus, K. R.; Rinehart, J. D.; Long, J. R. *Inorg. Chem.* **2011**, *50*, 8484. (d) Rinehart, J. D.; Long, J. R. *Dalton Trans.* **2012**, *41*, 13572.

4-18

Recent Advances in Aqueous Neptunium Chemistry and Thermodynamics

Marcus Altmaier

Karlsruhe Institute of Technology, Institute of Nuclear Waste Disposal, Karlsruhe, Germany

Actinides have a unique electronic configuration and specific chemical properties and the aquatic chemistry of actinides therefore emerges as a very multifold, lively and scientifically challenging field of inorganic chemistry [1]. The chemistry of long-lived actinides has been investigated by the international scientific community over the last decades from many different perspectives. Owing to the exceptionally high importance in many nuclear waste disposal scenarios, the detailed study of aqueous actinide chemistry is an especially important focus of research activities. The disposal of long-lived nuclear waste in deep underground repositories is the safest option to separate highly hazardous radionuclides from the environment over geological timescales. On an international level, three different host rock formations (crystalline, clay, rock salt) are currently considered. For all present disposal options, a detailed understanding of fundamental (geo)chemical processes is required in order to critically assess the long-term safety. As it is important to predict the geochemistry of the respective aqueous systems potentially generated, the behavior of the highly radioactive and radiotoxic actinide elements under these conditions likewise must be understood in detail. This defines the need to investigate fundamental aspects of aqueous actinide chemistry and the need to supply reliable thermodynamic data for the accurate and quantitative modeling of actinide chemistry.

Focusing on aqueous actinide chemistry it is a mandatory task to investigate and quantify the main factors controlling solution chemistry, i.e. characterize solubility limiting solid phases, aqueous actinide complexation reactions, redox phenomena and ion-interaction processes. Each individual aspect requires dedicated research efforts in order to guarantee reliable process understanding and enable a consistent assessment and prediction of actinide (geo)chemistry. Regarding experimental studies, the technical progress in modern analytics achieved over the last decade and input from quantum chemical theory have resulted in a significantly improved understanding of actinide chemistry. Especially advanced spectroscopic tools for investigating speciation at the molecular level have been a driving force for progress in aquatic actinide chemistry. Based upon improved chemical and structural information, a more detailed picture of radionuclide speciation becomes available, thus generating scientific input for improved chemical models and improved thermodynamic data.

In view of the high relevance in the context of nuclear waste disposal and considerable complexity of actinide chemistry it is essential to continuously reduce experimental and systematic uncertainties, fill relevant gaps in thermodynamic databases and improve knowledge and available data for more complex (geo)chemical systems, e.g. high ionic strength systems, kinetically controlled processes, actinide-organics complexation reactions or actinide chemistry at elevated temperatures.

This presentation focuses on aqueous neptunium chemistry as an especially interesting case of actinide science and good example of the overall experimental and conceptual approach employed in investigation actinide solubility. Examples are mainly taken from recent studies performed at the Institute for Nuclear Waste Disposal at KIT. Based upon several studies on neptunium redox transformation processes designed to substantiate main Np redox stability fields, separate series of solubility experiments were performed for each of the oxidation states Np(IV), Np(V) and Np(VI) in dilute to concentrated carbonate free NaCl and $CaCl_2$ solutions. Investigations with other actinides, i.e. Th(IV), Pu(IV) and Pu(VI), are discussed in order to support the interpretation of the Np studies. In addition to the comprehensive solubility data, several spectroscopic tools were used to derive detailed pictures of the solid and aqueous Np speciation. Studies in $CaCl_2$ media evidence the formation of hitherto unknown ternary Ca-An-OH complexes and solid Ca-neptunate phases. Solubility studies in NaCl solution revisit the aqueous Np(V)-NaCl system and indicate the presence of solubility limiting Na-neptunate phases at alkaline pH conditions. Extending the work to more oxidising conditions, the solubility and speciation of Np(VI) in alkaline NaCl systems has been investigated in close analogy to the respective U(VI) system.

All studies discussed in this presentation aim to derive comprehensive quantitative models of the investigated systems over the entire relevant pH range from dilute solutions to highly concentrated brine systems. The fundamental site-independent thermodynamic data obtained in the studies include consistent sets of the relevant solubility products, complex formation constants and ion-interaction parameters derived within both the SIT and Pitzer approaches.

References

[1] Altmaier, M., Gaona, X., Fanghänel, Th., *Recent Advances in Aqueous Actinide Chemistry and Thermodynamics*, Chem. Rev. (2013), 113, 901-943.

Uranyl oxo group functionalisation, reduction, and migration reactions

Polly Arnold[1], Jason Love[1], Guy Jones[1], Anne-Frederique Pecharman[1], Emmalina Hollis[1], Roberto Caciuffo[2], Nicola Magnani[2], Laurent Maron[3], Ludovic Castro[3], Georg Schreckenbach[4], Samuel Odoh[4]

[1]EaStCHEM School of Chemistry, University of Edinburgh, Edinburgh, UK, [2]ITU, EC Joint Research Centre, Karlsruhe, Germany, [3]LPCNO, UPS, UNSA, University of Toulouse,, Toulouse, France, [4]Department of Chemistry, University of Manitoba, Winnipeg, Canada

The strong, linear and covalent U=O bonds in the uranyl dication render the oxo groups particularly inert and poorly Lewis basic, which explains the dominance of this ion in the laboratory and its persistence as an environmental contaminant. The oxo groups can be rendered more basic, and thus more susceptible to interactions with other metal ions, by one electron reduction to the f^1 U^V uranyl ion, $[UO_2]^+$. The more radioactive, neighbouring neptunyl and plutonyl ions, with f^1 and f^2 electron configurations, exhibit oxo-group chemistry and cluster formations that hamper nuclear waste separations, and could be better modelled by the U^V uranyl ion. Furthermore, the U(V) uranyl ion is implicated in environmental uranium immobilisation processes through a disproportionation to U^{VI} uranyl and insoluble U^{IV} oxides. It is precisely this redox-instability that has made the $[UO_2]^+$ ion such a difficult ion to study.

We use macrocyclic ligands to block equatorial uranyl ligand chemistries and guide the coordination of other metal cations to one or both uranyl oxo groups, activating the ion towards oxo functionalisation, C-H bond activation, and single electron transfer chemistry.

A range of kinetically inert, isolable U(V) uranyl complexes can be isolated, including dimeric f^1 f^1 U_2O_4 ions in which the uranyl character is (reversibly) lost, and oxo group migration has occurred.

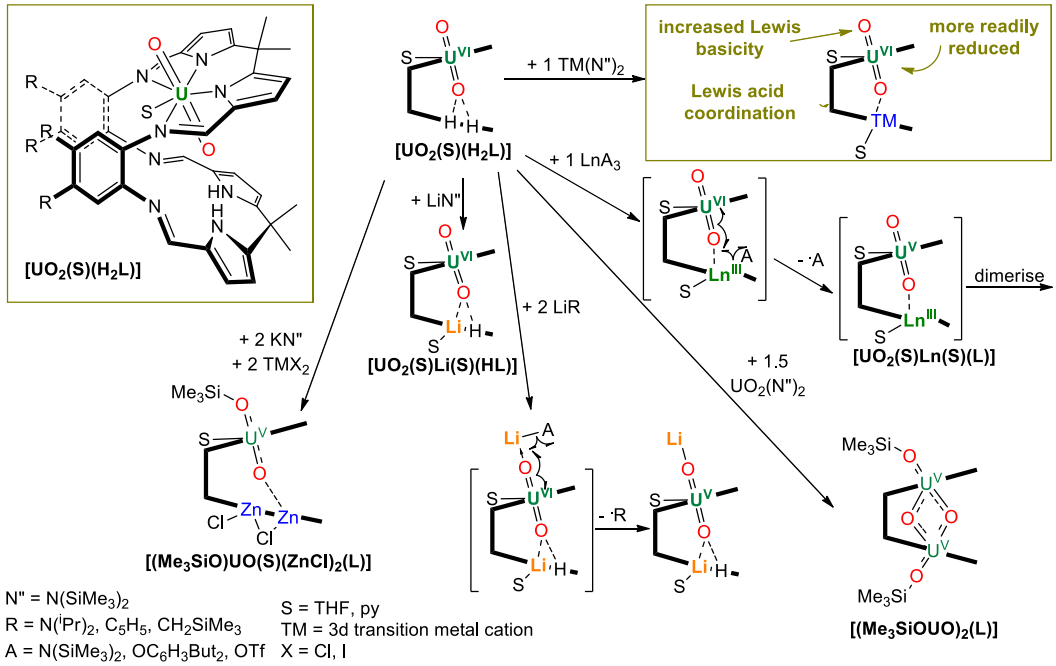

1-81

Unique advantages of organometallic supporting ligands for uranium complexes

Paula Diaconescu

University of California, Los Angeles, Los Angeles, CA, USA

Ancillary ligand design in organometallic chemistry is drawing increasingly on inducing ligand participation in reactions of the metal. Chelating ferrocene diamides possess unique electronic characteristics that make them especially versatile in supporting a wide range of reactivity behaviors for the resulting metal complexes. When combined to the unique properties of uranium, new avenues can be opened. Oxidation of uranium(IV) bis(1,1'-diamidoferrocene) complexes gives products that are best described as mixed valence bisferrocenes, in which uranium mediates the electronic communication. The characterization of these complexes and comparisons with non-actinide analogues will be presented.

1-87

Relation between the structure and the microstructure of a solid silicon hybrid based material and the plutonium and americium extraction behaviour from high level waste.

Daniel Meyer[1], Joel Moreau[2], Michel Wong Chi Man[3], Olivier Conocar[1], Stephane Bourg[1]

[1]CEA, Marcoule, France, [2]ENSCM, Montpellier, France, [3]CNRS, Montpellier, France

In this study we have developed the synthesis and the characterisation of silicon based hybrid material obtained by molecular and supramolecular engineering. These materials have been synthesised in order to extract and separate plutonium and americium from high level radioactive wastes.

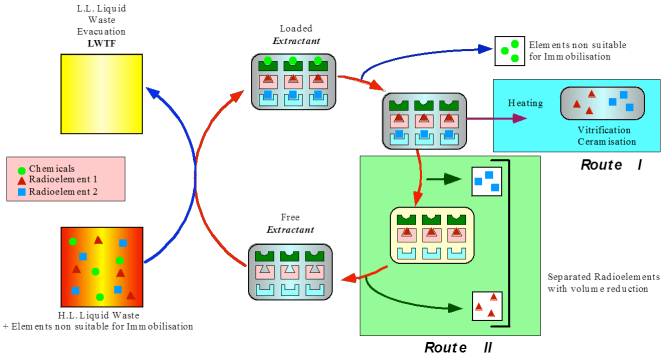

The materials were synthesized by hydrolysis and condensation of silicon alcoxides. The co-condensation of tetra-alcoxides and functionalised tri-alcoxides allow the implanting of an organic extractant in a silica material.

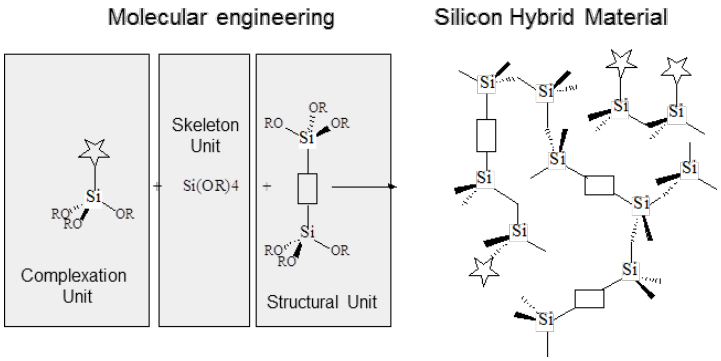

The impacts of some aspects of the material on the extraction properties of plutonium and americium have been extensively studied. In this frame, different organic parts were evaluated (amine, ether, pyridine, diamide…).

Several materials showing different ratios between the organic extractant and the silicon skeleton and different microstructures (specific surface, porosity…) were synthesised and studied in order to get some informations about the relation between the structure of the materials and the interactions with several actinides.

Also, different imprinting techniques were used to get some “labelled” materials and the impact on some extraction properties was determined. First, molecular imprinting was applied using lanthanides complexes and the Am/lanthanide separation was studies by comparison with a reference non imprinted material. Second, a supramolecular imprinting by surfactant was used in order to get mesoporous material. Finally, imprinting using a surfactant molecule and a lanthanide complex was used to obtain a double “labelled” material.

The main results shows that these materials are good candidate for a high level americium and plutonium decontamination, showing good performance and good loading properties, without any optimisation. The original strategy to use this silicon based materials was developed in order to recover the actinides for reuse, but they are also compatible with a final disposal in a silica glass matrix.

1-88

Small Molecule Activation at Reactive Complexes of Uranium

Karsten Meyer

Friedrich-Alexander-University Erlangen-Nuremberg, Erlangen, Bavaria, Germany

We recently reported the formation of a bridging carbonate complex *via* reductive cleavage of CO_2, yielding a μ-oxo bridged complex, followed by the insertion of another molecule CO_2. In a similar strategy, we were able to isolate and characterize several mixed carbonate complexes U–CO_2E–U, U–CS_2E–U, and even U–OC(S)Se–U by reacting bridged chalcogenide complexes U–E–U (E = S, Se) with CO_2, CS_2, and COS. These chalcogenido mixed-carbonate complexes represent the first of their kind.

Activation of elemental chalcogenides has been investigated for transition metals but is mostly unexplored for the actinide elements. The bonding between actinide ions and hard ligands, containing nitrogen or oxygen, is predominantly ionic, whereas bonding interactions with softer, heavier chalcogenide ligands could help to understand M–L covalency in actinide complexes.

Bridged chalcogenide complexes U–E–U (E = S, Se) also show remarkable reactivity towards an excess amount of the corresponding elemental chalcogen; thus, forming dinuclear uranium complexes bridged by highly unusual μ-E_m^{n-} ligand fragments (with m = 2, 4 and n = 2 for Se; m = 2 and n = 1 for S). Some of these compounds engage in chalcogen atom transfer chemistry.

2-04

The role of phosphorous biochemistry in actinide human contamination

Claude Berthon[1], Marie Christine Charbonnel[1], Gaëlle Creff[3], Fabien Fontaine Vive[3], Dominique Guillaumont[1], Aurélie Jeanson[2], Sarah Mostapha[1], Lei Qi[1], Jérôme Roques[2], Samir Safi[2], Pier Lorenzo Solari[4], Claude Vidaud[1], Eric Simoni[2], Christophe Den Auwer[1]

[1]CEA Marcoule, Bagnols sur Cèze, France, [2]IPN Université Paris XI, Orsay, France, [3]ICN Université Nice Sophia Antipolis, Nice, France, [4]MARS Synchrotron Soleil, Saint Aubin, France

Introduction

In case of accidental exposure to radioelements, internal actinide toxicity is related to both emitted radiation and to the in-vivo circulation scheme [1]. Blocking the biological pathways of the actinides in the human (or more generally mammalian) systems and/or increasing their elimination rate would considerably decrease the toxicity of these elements. While actual decorporating agents like DTPA (diethylenetriaminepentaacetic acid) are effective for plutonium(IV), clinical studies showed that extended treatment may cause liver failure [2]. Overall the need for a better understanding of the actinide pathways in biological systems is of fundamental importance with regards to the assessment of nuclear risk. The use of bio-mimicking molecules or molecular building blocks (like simple aminoacids with important chelating groups, small peptides etc) is one of the methods to better understand these chemical pathways that drive actinide incorporation into cells and organs. Our present strategy has focused on the cation coordination itself in a so-called bioactinidic approach corresponding to actinide chelation by important biological actors or building blocks of biological molecules that may be considered as simplified mimicking actors. Note that actinide chemistry is complicated by complex RedOx behavior and large ionic size radius that induces significant changes in ligand conformation with respect to the essential biological cations such as iron. These complications are why a fundamental and simplified approach to the question of actinide transfer in biological systems is essential.

The phosphate chemical function is ubiquitous in biological systems. The phosphorylations of proteins are transient phenomena which play a key role in the signalization cascades, and actinide bound to the phosphorylated groups might disturb some biochemical pathways. While it is involved in phosphorylated proteins it is also one of the major functions of the nucleotides. For instance photo oxidation and consequent cleavage of oligodeoxynucleotides by the uranyl ion is greatly enhanced in the presence of a terminal 5'-or 3'-phosphate group. It has been suggested that the uranyl ion forms a coordination complex with terminal phosphates and that photocleaveage is taking place proximal to the phosphate to which the uranyl is bound [3]. Uranium (VI) can also cause the inhibition of some cellular metabolisms by replacing Mg(II) in the active ATP-Mg(II)-hexokinase (ATP = adenosine triphosphate) where the glucose can't be phosphorylated. This observation served as the basis for the first studies of the interaction of uranium(VI) with adenine nucleotides.

Evidently phosphorylated amino acid building blocks as well as phosphorylated proteins may be considered as possible targets for actinide complexation in the various compartments of the biological machinery. This was evidenced in our previous studies aiming at identifying proteins able to bind uranyl starting from cell extracts [4]. The proteins known to have phosphorylated groups were largely represented (69%) among a population of proteins isolated by affinity chromatography on immobilized uranyl. This is statistically higher than in the global proteome (about 30%). Furthermore, half of these identified proteins were potentially poly-phosphorylated. While inorganic actinide phosphates have been thoroughly studied in the framework of underground storage very little is known about the structural molecular chemistry of actinides with phosphorylated biological molecules [5]. One of the rare studies describes the interaction of uranyl with phosphoserine and phosphothreonine building blocks by fluorescence spectroscopy (TRLFS) but no structural data have been reported [6] With nucleotide derivatives, the complex formation of U(VI) with AMP (adenosine monophosphate) has been studied in the alkaline pH range 8.5-12, by Szabo et al. [7]. This study showed that only two complexes were formed with all ligands in this pH range. Although, the coordination of the 5'-phosphate group and the 2'-and 3'-hydroxyl groups of the ribose to the U(VI) is similar to that suggested earlier by Feldman, the number and the structures of the formed complexes are different [8]. With transuranium elements, very

recently, a first crystallographic structure of a Pu-nucleotide complex has been published in the literature with the deoxycytidinemonophosphate-Pu(IV) complex [9].

We have undertaken a systematic structural analysis of complexes involving actinides and surrogates with phosphorylated biochemical species, as of essential chemical fragments, peptides and proteins. This includes simple building blocks like phosphoserine (p-Ser), important biochemical units like nucleotides (AMP, ATP), biomimetic simplified peptides of phosphorylated proteins (Osteopontin, OPN).

This presentation will browse some examples of actinide coordination with phosphorylated amino acids, peptides and proteins since a thorough investigation of the complex topology is necessary to better assess the incorporation mechanisms. Three cations have been targeted : thorium(IV) as a representative of actinide(IV), uranyl(VI) as the most ubiquitous example of actinyl oxocations and americium(III) as a representative of oxidation state +III. In addition, lutetium(III) will be also discussed as a chemical analogue of the middle actinides (Am, Cm, Cf). Some elements of the presentation are discussed here after.

Discussion

Two biological systems have been described : a phosphorylated, intrinsically disordered protein responsible for regulating bone growth, osteopontin; and nucleotides that occur as coenzymes intermediates and are also the building blocks for nucleic acids.

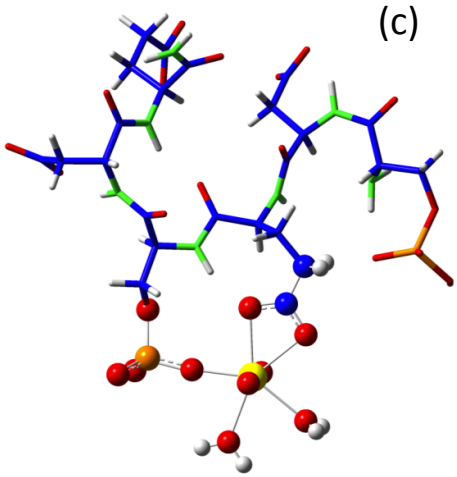

Figure 1 : Theoretical model calculated using DFT for a possible U(VI) interaction with the H8V peptide.

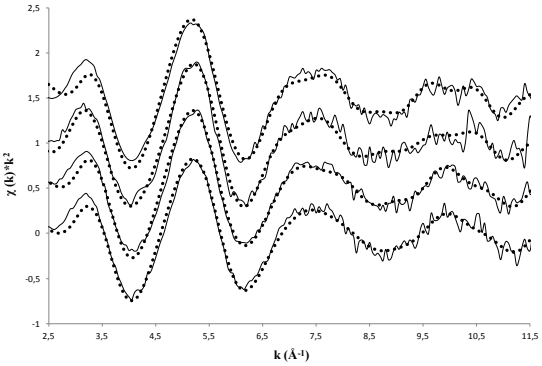

Figure 2 : k^2-weighted U-L_{III} edge EXAFS spectra of H8V - uranyl complex species under various pH conditions (1.5 - 5.5 from bottom to top) and OPN – uranyl at pH = 5.5 (top spectrum)

Osteopontin (OPN) is a secreted multifunctional protein also located in considerable concentrations in U(VI) target organs (kidney and bone matrix) [10]. The screening of several peptides present in the sequence of the protein for bone growth regulation led to the identification of a phosphorylated hexapeptide "pSDEpSDE" (codename H8V used further in the text), as the most potent calcium growth inhibitor and thus as one possible OPN active site [11]. We thus decided to investigate the structural and thermodynamic aspects of U(VI) coordination with the phosphorylated H8V peptide by combining thermodynamics, spectroscopic techniques and quantum chemical calculations. Lacking crystallographic data for the peptide and protein complex, the only indications about the coordination scheme come from knowledge of the peptide amino acidic sequence and preliminary IR data. Various

geometrical combinations have been tested *in silico* as shown in Figure 1. The k^2-weighted EXAFS spectra of the obtained at different pH are shown in Figure 2. The EXAFS data for the H8V complex at pH 1.5 and 3.5 consist of a similar interference pattern, indicating a similar type of coordination for both complexes. In contrast, at pH 5.5, the presence of different interferences patterns at k= 7.5 and 10.5 $Å^{-1}$ suggests a small modification of the uranium coordination sphere. Finally we have fitted the EXAFS spectrum of the OPN protein-U(VI) prepared under the same fairly acidic pH conditions (pH = 5.5). We observed equivalent values within the error range to those obtained with the peptide at pH 5.5. This strongly supports the starting assumption that the same coordinating environment exists in both cases. This result clearly shows that the description of the major interaction site for uranyl in OPN can be modeled using the H8V peptide [12].

It has been reported based on known metabolic pathways and the extent of the world's biomass, that **Adenosine** mono- (AMP) and triphosphate (ATP) are involved in more chemical reactions than any other compound on the Earth's surface, except water [13]. Despite the large range of the available experimental techniques, data concerning the metal binding and the stoichiometry of the lanthanide(III) complexes formed with various nucleotides are often controversial, and almost inexistent with actinide cations [7,9]. We compare here the coordination mode of Lu(III) and Am(III) for adenosine mono- and triphosphate (experiment in progress for americium).

In the case of the AMP-Lu complex elemental analysis indicates a 1:2 ratio between Lu and P, in agreement with crystallographic data of the lutetium ciliatine complex that exhibits 6 bridges of the phosphate groups per Lu cation [14]. IR spectroscopy, NMR and EXAFS have been used as complementary structural probes in combination with quantum chemical calculations in an analogous way as for the OPN system.

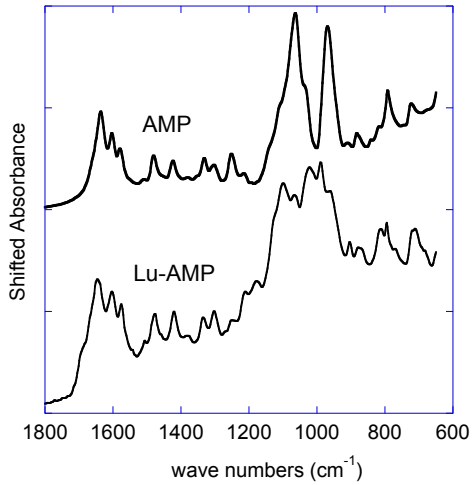

Figure 3 : FT-IR spectra of the Lu-AMP complex compared to the free AMP ligand.

In Figure 3, the IR spectra of the Lu-AMP system in comparisons with the free AMP ligand are presented. The phosphate vibrations of the free AMP ligand at 1063 cm^{-1} (anti symmetric (C-O), $v(PO_3^{2-})$) and 969 cm^{-1} (symmetric $v(PO_3^{2-})$) exhibit drastic changes upon complexation with Lu. Both of these stretching bands show a splitting in the complex spectrum indicating a direct coordination of Lu with phosphate.

Compared coordination of Lu and Am with AMP and ATP have been further assed using a combination of NMR and EXAFS data. Although work is still in progress for Am, the EXAFS data clearly show the participation of the phosphate group in order to form polymeric structures for Lu-AMP and monomeric 1:2 complexes for Lu-ATP.

Conclusion

The experimental/theoretical approach presented here proved to be extremely useful for studying exogenous metal interaction with such unstructured flexible target peptides or proteins. Indeed structural investigation of intrinsically unstructured proteins through amino acid sequence analysis, can lead to the identification of possible new metal interaction sites. Our work widens the classical study scope found in the literature, that mostly deals with known metalloprotein binding sites, thus ignoring all possible uncharacterized binding sequences

Combination of EXAFS data with computed cluster fragment, IR and other spectroscopic techniques brings information about the local atomic environment of the actinide cations plus the lutetium surrogate. Furthermore the experimental/theoretical approach allowed us to establish a basis for future computer simulations and topological characterization of biological molecules affected by actinide coordination. This will enable to develop coordination models for larger biomolecular entities like proteins that may be involved in actinide transport or storage. This is essential given the crucial role of this chemical function in the biological systems.

Acknowledgements

The authors wish to thank ARLA Food Group for providing OPN-enriched samples of cow's milk. The authors would like to thank B. Sitaud, S. Schultig and I. Llorens of the MARS beam line of synchrotron SOLEIL for beam line assistance. This work is supported by the ToxNuc3 CEA program within the SPECULOS project and CEA/DEN under the RBPCH Program of Basic Research in Chemistry

References

[1] P.W. Durbin, Actinides in animals and man, *the chemistry of actinide and transactinide elements* Vol. 5 pp 3339

[2] B.D. Breitenstein and H.E. Palmer, *Radiat. Prot. Dosim.*, **26** (1989) 317

[3] A.R. Hill Jr., L.E. Orgel, *Bioconjugate Chem.* **2** (1991) 431

[4] A. Dedieu, F. Bérenguer, C. Basset, O. Prat, E. Quéméneur, O. Pible, C. Vidaud, *Journal of Chromatography A*, **1216** (2009) 5365

[5] O. Terra, N. Dacheux, N. Clavier, R. Podor, F. Audubert, *J. Am. Cer. Soc.* **91** (2008) 3673.

[6] A. Gunther, G. Geipel, G. Bernhard, *Radiochim. Acta* **94** (2006) 845

[7] I. Szabo, I. Furo, Csoregh, *J. Am. Chem. Soc.* **127** (2005) 15236

[8] R.P. Agarwal, I. Feldman, *J. Am. Chem. Soc.* **90** (1968) 6635

[9] G. Andreev, N. Budantseva, M. Sokolova, I. Tananaev, B. Myasoedov, *Inorg.Chem.* **48** (2009) 2343.

[10] O. Prat, E. Ansoborlo, N. Sage, D. Cavadore, J. Lecoix, P. Kurttio, E. Quemeneur, *Environ. Int.* **37** (2011) 657

[11] L. D. Silverman, M. Saadia, J. S. Ishal, N. Tishbi, E. Leiderman, I. Kuyunov, B. Recca, C. Reitblat, R. Viswanathan, *Langmuir* **26** (2010) 9899

[12] S. Safi, G. Creff, A. Jeanson, L. Qi, C. Basset, J. Roques, P. Lorenzo Solari, E. Simoni, C. Vidaud, C. Den Auwer, *Chem. Eur. J.* accepted

[13] P. D. Boyer, *Biochemistry* **26** (1995), 8503

[14] T. Głowiak, E. Huskowska, J. Legendziewicz, Polyhedron **10** (1991) 175

2-05

Radioecological Studies in Germany

Clemens Walther, Abdelouahed Daraoui, Beate Riebe, Stefan Bister

Leibniz University Hanover, Hannover, Germany

The nuclear reprocessing plants Sellafield and La Hague release large amounts of the long lived fission product I-129 into the north sea. By resuspension and formation of aerosols, this radionuclide is transported inland and finds its way into air masses, soil and water reservoirs. While the radiological impact is still very low, the natural isotope ratio I-129/I-127 changed dramatically over the past decades from 10^{-12} to 10^{-7} in some places. We investigate pathways and speciation of iodine at several sampling locations in Germany. We find a pronounced gradient of I-129 intake from north to south and from west to east and in addition local effects that are correlated to weather conditions. Possible additional sources in Germany or close to the border are discussed. A second - radiologically relevant - large scale contamination of radionuclides is still present in the former uranium mining areas in Saxony. Though remediation strongly decreased the contamination of land and the Mulde river, the late effects of the mining activities are still evident. The concentrations and isotope ratio of uranium at different ecosystems are measured in soils, water and plants. Investigations of the propagation pathways up to the radiation exposure of men are performed with several analytical methods, in part on a microscopic level to the chemical speciation up to the action of microorganisms to achieve a comprehensive understanding of the underlying processes. The radiation exposure of the population is calculated on a conservative basis. Except for very small chidren a total effective dose of 1mSv/a is not exceeded.

3-04

How to build accurate macroscopic models of actinide ions in aqueous solvents?

Valérie Vallet[1], Florent Réal[1], Michael Trumm[2], Bernd Schimmelpfennig[2], Michel Masella[3]

[1]Université Lille 1 (Sciences et Technologies), PhLAM Institute, CNRS UMR 8523, Villeneuve d'Ascq, France, [2]Institut für Nukleare Entsorgung (INE), Karlsruher Institut für Technologie (KIT), Karlsruhe, Germany, [3]CEA Saclay, Laboratoire de Chimie du Vivant, Institut de biologie et de technologies de Saclay, CEA Saclay, Gif sur Yvette, France

Investigating at the molecular scale the fundamental processes affecting the chemistry and the thermodynamic of actinide ions in liquid phase is a major topic in the nuclear waste and disposal research fields. Despite the fact that most of the available experimental spectroscopic techniques (such as EXAFS, HEXS, NMR, or TRFLS) were used to investigate for instance lanthanides and actinide ions in solution, there are still many debates concerning their hydration properties, such as the structure of their first hydration shell, the residence time of first-shell water molecules and ion transport properties.

Thanks to the developments of both computer power and theoretical approaches, numerical experiment offers an alternative technique to determine new data and reduce the experimental uncertainties, providing that the accuracy and prediction capability of the models are assessed. Classical molecular dynamics (MD) based on parameterized force fields allow one to simulate large molecular systems on significantly long simulation times (usually, at the ns scale and above). Hence, they provide statistically relevant sampled sets of data, which may then be post-processed to estimate specific properties. However, the study of the ligand coordination dynamics around heavy ions requires the use of sophisticated force fields accounting for in particular polarization phenomena, as well as for the charge-transfer effects affecting ion/ligand interactions, which are shown to be significant in several heavy element systems. Our current efforts focus on the development of force-field models for radionuclides, with the intention of pushing as far as possible the accuracy of all competing interactions between the various elements present in solution, that is the metal, the ligands, the solvent, and the counter-ions.

This presentation will drive you through the complexity of the development of accurate force-field models, which are completely free from experimental input data. All the model parameters are adjusted from geometrical and energetic data corresponding to gas phase water clusters, metal-water, counter-ion water clusters, and computed from state-of-the-art *ab initio* calculations at the CCSD(T) or MP2 level. The force-field model can reproduce ab initio data within an accuracy of 1-2 kcal/mol.

To validate our model for the description of negatively charged hydrated counter-ions we have studied the properties of three counter-ions fluoride, chloride and bromide in aqueous solution. Even if we use no condensed phase data to assign its parameters, our model is able to reproduce all the experimental (EXAFS, HEXS) and theoretical (CPMD and QM/MM) data published to date concerning the anion solvation in liquid water at ambient conditions. Unlike all available models published so far, we show here our model to be particularly well suited to model anion-water systems in different physical conditions [1].

The interaction between a positively charged radionuclide and a ligand, being either water or another counter-ion is complex, as it includes beyond the well-known electrostatic interaction other effects of the many-body type, such as “covalency”. We are exploring several physical and mathematical models to account for these many-body effects. The sensitivity of the hydration properties to the choice of the model can then be explored in a systematic way by performing series of MD trajectories for a given system. This is possible with the use high-performance computing platforms from the French and Argonne National Laboratory Supercomputer centers.

Two actinide test cases, trivalent curium and tetravalent thorium, and a selection of trivalent lanthanide ions have been studied. For both ions, all many-body models lead to close results in terms of structure in solution: the coordination number is included within 8 and 9, and the mean ion/water oxygen distances are 2.45 and 2.49 Å respectively for Th(IV) and Cm(III).

While, transport properties are rather insensitive to the choice of the interaction model, solvent-exchange reaction rate may vary by a factor of two. We will present our preliminary results on Ln(III) hydration properties (See Figure) [2, 3].

To reduce the uncertainties on the solvent-exchange kinetics, improvements on the treatment of many-body effects are needed. In particular, on-going ab initio density analysis are helping us understanding how a positively charged radionuclides perturbs the water hydrogen bond network of the water molecules present in the first hydration shells, an effect that has so far been ignored in force-field models.

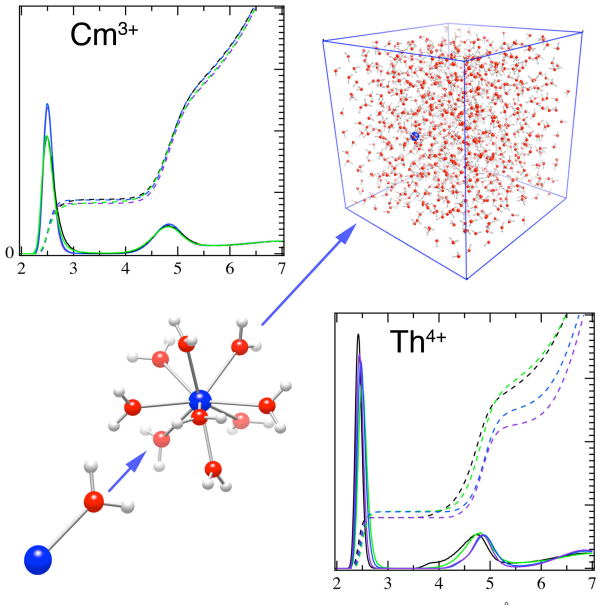

Our modelling results will finally be discussed in the light of new experimental data obtained from synchrotron experiments including high-energy x-ray scattering (HEXS) and x-ray absorption fine structure (XAFS), conducted at the APS synchrotron by the Heavy Element and Separation Chemistry group at Argonne National Laboratory.

[1] Trumm, M., Guerrero Martínez, Y. O., Réal, F., Masella, M., Vallet, V., Schimmelpfennig, B., J. Chem. Phys., **2012**, *136*, 044509.

[2] Réal, F., Trumm, M., Vallet, V., Schimmelpfennig, B., Masella, M., Flament, J.-P., J. Phys. Chem. B **2010,** *114*, 15913–15924

[3] Réal, F., Trumm, M., Vallet, V., Schimmelpfennig, B., Masella, M., Vallet, V., J. Comput. Chem. **34**, 707 (2013).

3-05

Vladimir Domanov

JINR, Dubna, Moscow reg., Russia

Chemical properties of microcomponents have some peculiarities which appear both in the liquid and the gas phase. The low probability of collisions between two microcomponents leads to the limitation of isotopic exchange, redox and self-redox reactions in solutions [1, 2]. While the reactions $2Pu(IV) + U(IV) \rightarrow 2Pu(III) + U(VI)$ and $2U(V) \rightarrow U(VI) + U(IV)$ are quite common in macrochemistry, so they do not occur at concentrations of actinides $<10^{-10}$ M.

Considerable differences in chemical behaviour between micro- and macroquantities of actinides in the gas phase are also found [3-7]. In the thermochromatographic (TC) studies of thermal oxidation at ~700ºC of U, Np, Pu and Am trace quantities in a stream of $He + O_2$ mixtures, their transfer from the starting zone of the quartz TC column to its thermal gradient section is observed. It is experimentally established that actinides form volatile compounds which are adsorbed at 500–400, 300–200 and 150–50ºC. It is shown that the first adsorption zone is due to the deposition of dioxides, the second zone is formed due to adsorption of trioxides and the last one arises from acid or hydroxide condensation. In the experiments with plutonium there is one more adsorption zone at a negative temperature around ~ –100ºC. The adsorption enthalpy $-\Delta H^0_a$ for di- and trioxides on quartz are 172 ± 6 (UO_2) and 126 ± 6 (UO_3); 167 ± 6 (NpO_2) and 124 ± 6 (NpO_3); 175 ± 7 (PuO_2) and 122 ± 7 (PuO_3); 180 ± 10 (AmO_2) and 144 ± 7 kJ mol^{-1}(AmO_3).

At the same time, annealing of macroquantities of U in the presence of O_2 leads to formation of non- volatile U_3O_8. The other studied actinides in ponderable quantities and in similar conditions form non- volatile dioxides.

It has long been agreed that the maximal valence state of curium is +4. Nevertheless, Peretrukhin et al [8] report on preparation of Cm(VI) in solution. Merini[9] and Fargeas [10] confirm this statement. They produced Cm(VI) in the gas phase in the form of volatile hexafluoride CmF_6.

In view of these facts and our data [3-7], it was assumed that volatile CmO_3 also could be existed and we undertook an attempt at its preparation.

EXPERIMENTS AIMED AT Cm(VI) PREPARATION

The experimental installation is shown in Fig. 1. The carrier gas was He, and reagent gas was O_2. The gases were fed from cylinders 1 and 3. Then they were fed to mixer 5, dried to remove water vapour in trap 6, and purified to remove possible aerosols on the surface of fibrous filter 7. Fine purification of the gas was achieved in the volume of cryogenic trap 8 filled with activated quartz sand and cooled to a temperature from -90 to -95ºC. The purified gas was fed to the inlet of a hollow quartz thermochromatographic (TC) column 9 (d_{int} = 3 mm). To prepare the initial radioactive sample (IRS), we used nitric acid solution of ^{244}Cm. The obtained sample contained 10^9 -10^{10} Cm atoms in a form of the hydride CmH_{2-3} that was adsorbed on the surface of purified quartz sand. The procedure of IRS preparation is described comprehensively in Ref.[7]. We placed the prepared IRS in the start zone of the TC column 11.At the outlet of the TC column, we arranged fibrous filter 15 and carbon filter 16. The flow rate of the gases was monitored with flow meters 2, 4, and 17.

The typical experimental conditions were as follows: the flow rate ($He + O_2$)20 cm^3 min^{-1},He : O_2 = 1 : 1, heating IRS to 720 − 730ºC, the temperature gradient å was –15 deg cm^{-1}, time of en experiment τ = 30 min. The temperature distribution along the column was maintained with the tubular furnace 12 and running water 14. After the experiment was terminated, the surfaces of the separated parts of the column (l = 3 cm) and start zone 11 were treated with 5 M HNO_3. From the radioactive solutions thus obtained, we prepared thin-layer α-ray sources which were subjected to measurements on α-ray spectrometer. The spectrometer contained a semiconductor surface-barrier Si(Au) detector and the required electronic units with data saving on a computer disc. The measurements results were presented in the form of thermochromatograms. As the temperature of the deposition of volatile species T_a we took the temperature corresponding to the maximum of the adsorption peak. The total α-activity of the thermal gradient section was taken equal to 100%. We also determined the chemical yield of Cm from the start zone *Y*. The α-activity of fibrous filter 15 was measured on a PSO2-2eM α-

ray counter equipped with a Na(I) detector and a photoelectron multiplier. The installation background was taken equal to the results of the measurements of the initial filter samples.

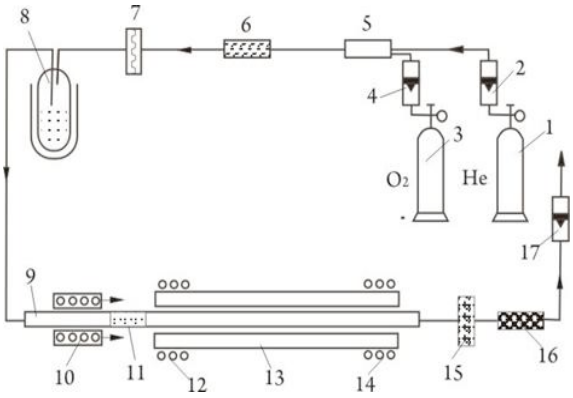

Fig. 1 Scheme of the installation for studying the volatility of ^{244}Cm oxidation products: (1) cylinder with compressed helium, (2, 4, 17) gas flow meters, (3) cylinder with compressed oxygen, (5) gas mixer, (6) trap with P_2O_5, (7, 15) fibrous filters, (8) cooled trap, (9) TC column, (10) tubular electric furnace, (11) start zone of TC column, (12) heating, (13) thermal gradient furnace, (14) cooling, and (16) carbon filter

The α-ray spectrometric measurements showed that the Cm oxidation products are two volatile compounds. The total chemical yield *Y* of both fractions was about 30%. The result is shown in Fig.2. It is seen that the first compound is deposited at 550 ± 25ºC, and the second, at 390 ± 25ºC. TC experiments with Am [7] presented in the upper part of Fig.2, showed that AmO_2 was deposited at 500 ± 25ºC, and AmO_3 at 330 ± 25ºC. The correlation we showed allowed us to suggest the chemical composition of the isolated compounds: the first adsorption peak belongs to CmO_2, and the second, to CmO_3.

We calculated the enthalpies of adsorption of the assumed CmO_2 and CmO_3 on the quartz surface. They appear to be equal to 185 ± 6 (CmO_2) and 157 ± 6 kJ mol^{-1} (CmO_3). As can be seen, the Am and Cm oxides are less volatile than the isostructural oxides of U, Np, and Pu.

This difference is in agreement with Haissinsky's concept [11] according to which the chemical (and physicochemical) properties gradually vary in the row U-Np-Pu-Am with a decrease in the actinide ionic radius along the actinide series. Thus, the suggested interpretation of the chemical composition of the Cm oxidation products does not contradict the known theoretical concepts.

The installation background did not exceed $(8\text{-}9)\times10^{-2}$ s^{-1}, whereas the α-activity of the spent fibrous filters 15 was $(1.5\text{-}2)\times10^{-1}$ s^{-1}. We failed firstly to account for this excess activity.

EXPERIMENTS AIMED AT Cm(VIII) PREPARATION

Considering the prospects for studying transplutonium elements, Spitsyn and Ionova suggested that new oxidation states should be primarily expected for Cm [12]. They noted that the stability of a given valence state depends on the number of electron localized on *f* orbitals. A trend was observed toward relative stabilization of valence forms with even number of electrons on *f* orbitals not involved in chemical bonding. They also assumed that Cm(VIII) should be more stable than Am(VIII) and could be comparable in stability with Pu(VIII).

Increased the α-activity of the fibrous filters 15 could be connected with the transfer of Cm in the form of volatile CmO_4 and so the prediction [12] is confirmed. An alternative interpretation of this effect was uncontrollable transfer of Cm by aerosol mechanism. The next experiments were performed to check these assumptions. They were done at the same installation shown in Fig. 1. Some changes were carried out: the zone 14 was cooled by liquid N_2; the value of å = –17 deg cm^{-1}; α-spectrometric filter was installed in the position 15 and the IRS contained ^{244}Cm(85%), ^{243}Cm(~15%), and concomitant ^{242}Cm. Final experiments were performed with $C(O_2)$ = 5 and 1%. After their completing, the cooled zone was not cut into fragments, and the deposited nuclides were washed out from the whole surface of the 6-cm column section that had been located in the temperature interval from –30 to –130ºC. We also subjected to chemical treatment the CmO_2 (550 - 450ºC) and CmO_3 (450 - 350ºC) deposition zones.

The thermochromatogram obtained with $C(O_2)$ = 50% is shown in Fig. 3(a) (solid line). The same figure shows by the dashed line the PuO_4 distribution [5]. As can be seen, both thermochromatograms partially overlap, and the centres of the two deposition zones are close and are located in the adjacent sections of the cut column. For the volatile species assumed CmO_4, *Y* was 17%.

Figure 3(b) shows the result of a repeated experiment performed under the same conditions. Here the adsorption zone of the volatile Cm species shifted towards more negative temperatures, with the maximum at –105 ± 25ºC and *Y* = 75%. For comparison, we show in Fig. 3b by the dashed line the PuO_4 distribution in Ref [6], p.16, Fig. 2a. As can be seen, in this case the centres of the deposition zones of the volatile Cm species and PuO_4 fully coincide. The adsorption peaks formed by the two compounds are similar in shape. They have also high contrast, with 80 to 95% of the α-activity concentrated in the maximum (3-cm section). The fact that the adsorption peaks of assumed CmO_4 in Figs. 3a and 3b do not coincide may be due to location of peaks near the point of cutting the TC column. At high concentration of the activity near the peak maximum, as, e.g., in Ref. [6] , p. 16, Fig. 2c, where about 75% of PuO_4 was concentrated in a 2-cm section, slight variation of the experimental conditions could lead to predominant deposition of the volatile species in one of the two adjacent sections of the column.

The adsorption temperature T_a of supposed CmO_4, estimated from the results of two experiments, was –80 ± 50ºC. This value is in good agreement with deposition temperatures of PuO_4: –105 ± 25 [5] and –97 ± 18ºC [6]. Closeness of T_a of PuO_4 and assumed CmO_4 counts in favour of the suggested chemical composition of the volatile Cm species. Week α-activity of fibrous filter 15, detected in the first part of this paper, also finds explanation. Apparently, Cm was transported beyond the column also in the form of CmO_4. This assumption is also supported by absence of extra α-activity of used α-spectrometric filters 15 in these two experiments.

The calculated value of $-\Delta H^0_a$ of CmO_4 on the quartz surface appeared to be equal to 47 ± 12 kJ mol^{-1}. This value is close to $-\Delta H^0_a$ of PuO_4 (41 ± 6 [5]), 43 ± 4 kJ mol^{-1} [6], OsO_4 (50 ± 5 [13]), 47 ± 8 kJ mol^{-1}[5,6] and RuO_4 (55 ± 4 kJ mol^{-1} [14]). Comparison of these data also supports our assumption that the species we detected is CmO_4.

To finally check this assumption, we performed similar experiments with decreased concentration of O_2 in He (5 and 1%). The data obtained are given in Fig. 4. The results of single experiments with Pu and Cm are shown by filled and hollow circles, respectively, and the averaged results of two experiments, encircled circles. As can be seen, both dependences $Y = f[C(O_2)]$ are fitted by parabolic curves. Their similarity indicates that the chemical behaviour of the two compounds is also similar. In the examined range of $C(O_2)$, the chemical yield of PuO_4 exceeded that of CmO_4, suggesting higher stability of PuO_4 in the gas phase.

Thus, PuO_4 and assumed CmO_4 are similar not only in thermochromatographic characteristics (T_a, shape of thermochromatograms), but also in physicochemical parameters (enthalpy of adsorption) and in chemical behaviour. This indicates that the two chemical species are similar in composition. Hence, the volatile Cm compound whose deposition from the gas phase was detected at negative temperature is in fact described by the formula CmO_4.

Apparently, the exotic species CmO_4, like PuO_4, can be obtained only in trace amounts. At its excess concentration in the gas phase , collisions of tetraoxide molecules with each other will lead to the reaction $CmO_4 + CmO_4 \rightarrow 2CmO_3 + O_2$, followed by self-reduction of the trioxide molecules, $CmO_3 + CmO_3 \rightarrow 2CmO_2 + O_2$, and formation of known curium dioxide.

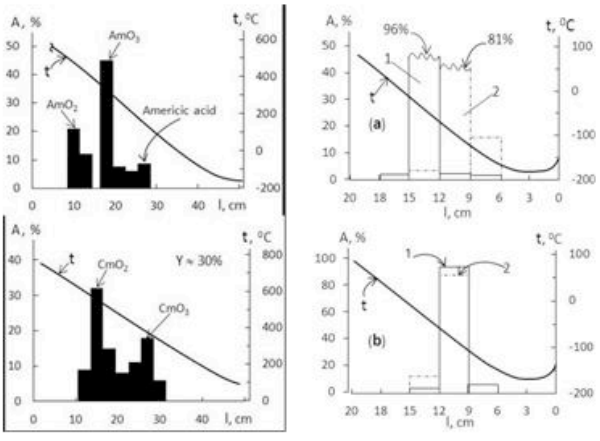

Fig. 2 Thermochromatograms of oxygen-containing compounds of Am and Cm

Fig. 3 Thermochromatograms of CmO_4 (1) and PuO_4 (2); (a) first and (b) second experiment

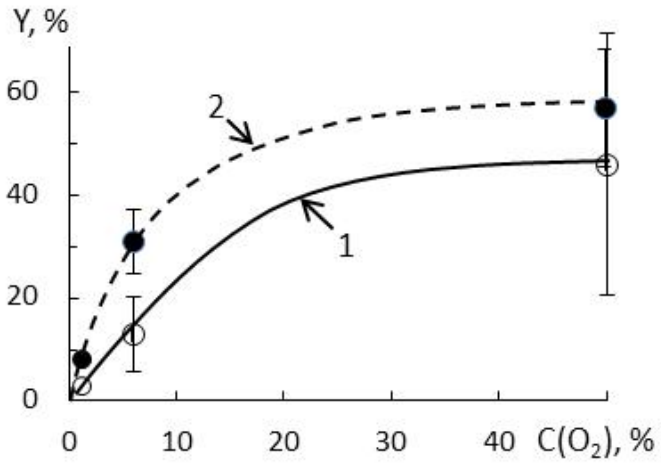

Fig. 4 Chemical yield of CmO_4 (1) and PuO_4 (2) as a function of $C(O_2)$

References

1. Guillaumont R et al. Radiochim. Acta, vol. 46,1989, p.169.

2. Guillaumont R. Radiochim. Acta, vol. 54, 1991, p.1.

3. Domanov V.P., Lobanov, Yu.A. JINR FLNR Scientific Reports, 1997-1998, E7- 2000-232, p. 169.

4. Domanov V.P. Radiokhimiya, 2009, vol. 51, no. 4, p.308 (in Russian).

5. Domanov V.P. et al. J. Nucl. Sci. Technol., 2002, Suppl. 3, p.579.

6. Domanov V.P.,Lobanov, Yu.A. Radiokhimiya, 2009, vol. 51, no.1, p.14 (in Russian).

7. Domanov V.P. Radiochemistry, 2010, vol. 52, no. 3, p. 230.

8. V.F. Peretruhin et al., Dokl. Akad.Nauk SSSR, vol. 242,1978, p.1359 (in Russian).

9. Merini J. et al. C.R. Acad., Paris, Ser.II, vol. 296, 1983, p.1773.

10. Fargeas R. et al. J. Less-Comm. Met., vol. 121, 1986, p 439.

11. Haissinsky M., Adloff J.-P.. Radiochemical Survey of the Elements, Elsevier Publish. Comp., Amsterdam/London/New York, (1965) pp.164,165.

12. Spitsyn V.I., Ionova G.V. Radiokhimiya, 1978, vol. 20, no.3, p.328 (in Russian).

13. Eichler B., Domanov V.P. J. Radioanal. Chem., vol. 28, 1975, p.143.

14. Duelman C.E. et al. PSI Annual Rep., 1998, p.4.

4-04

Recent progress in the synthesis, properties, and applications of uranyl peroxide nanoscale cage clusters

Peter Burns

University of Notre Dame, Notre Dame, IN, USA

One of the research themes of the Energy Frontier Research Center *Materials Science of Actinides* is development of the ability to control actinides at the nanometer scale. Most of our effort in this area has focused on development of a large family of uranium-based cage clusters that self-assemble in aqueous solution under ambient conditions.[1] We have reported more than 40 nanometer scale cage clusters built from uranyl ions that are bridged by bidentate peroxide groups. Most of these clusters contain additional bridges between uranyl ions, including hydroxyl, oxalate, pyrophosphate, and phosphite groups. A partially covalent interaction between the peroxide and uranyl ion favors a bent U-O_2-U interaction, which in turn fosters curvature and formation of the cage clusters.[2] Of the many possible cluster topologies, those with higher symmetry tend to be favored,[3] and counter ions are important in determining the cluster size.[2]

We have recently focused much of our attention to the behavior of uranyl peroxide cage clusters in aqueous solution under a variety of conditions. Monitoring mother solutions using electrospray ionization mass spectrometry (ESI-MS), dynamic light scattering (DLS) and small-angle X-ray scattering (SAXS) provides evidence that clusters assemble in solution. However, the formation process typically results in a range of cluster sizes in the same system. In order to obtain a mono-disperse solution, clusters may be crystallized, with the crystals subsequently harvested and re-dissolved in pure water.

Subsequent to dissolution of crystals containing a single uranyl peroxide cluster, ESI-MS, DLS and SAXS all provide evidence that a mono-disperse solution results, and that the clusters persist in solution for months. Detailed studies of U60 (containing 60 uranyl polyhedra) and U24Py12 (containing 24 uranyl polyhedra and 12 pyrophosphate groups) and their behavior in solution are currently underway. Zeta potential measurements indicate U60 resides in aqueous solution with an approximate charge of -18, indicating that about 42 cations (Li and K) are closely associated with the shell of uranyl polyhedra. We have identified locations for cations to bind to the clusters both inside the cage, and on the outer surface. In the case of U24Py12, the pyrophosphate groups provide sites that may be protonated and thus the clusters have a pH-dependent charge.

Upon dissolution of U60 in water, within the resolution of DLS and SAXS the clusters are present as isolated entities. Addition of alkali or alkaline earth cations to the solution triggers rapid aggregation of the clusters into much larger objects, which are designated as blackberries by analogy to the use of this title for aggregates of transition metal polyoxometalates (Fig. 1). Once they are formed, the blackberry size stabilizes after a few hours and they remain in solution without detectable changes for several months. On the basis of SAXS measurements and their corresponding pair distribution functions, it is likely that blackberry formation is fostered by the addition of inner sphere cations to the cluster, thereby lowering their charges and aiding aggregation. Although we have not yet been able to directly image the blackberries, the preponderance of evidence indicates they are likely approximately spherical and hollow.

Cluster U24Py12 in aqueous solution can be induced to aggregate into blackberry structures either by addition of an alkali or alkaline earth cation, or by reduction of the pH, both of which will lower the overall charge of the cluster.

We are interested in the behavior of nanoscale uranyl cage clusters in solution in part because of their potential role in a process to separate uranium from irradiated nuclear fuel in a more cost-effective and environmentally sustainable fashion than current methods involving solvent extraction. We are currently examining the dissolution of surrogate UO_2 fuel in an alkaline system containing peroxide. Under these conditions, the fuel dissolves as U(IV) is oxidized to U(VI), and cage clusters form. We are developing methods to separate these cage clusters from other constituents in solution using filtration in a stirred cell apparatus. Preliminary results indicate that this approach is highly effective at recovering the uranium

from solution, but also that some of the fission products are following the uranium in the process. This is most likely because the fission product cations are bound to the uranyl peroxide cage clusters. Ongoing work is focused on controlling the interaction of aqueous species with the cage clusters in order to achieve a superior separation.

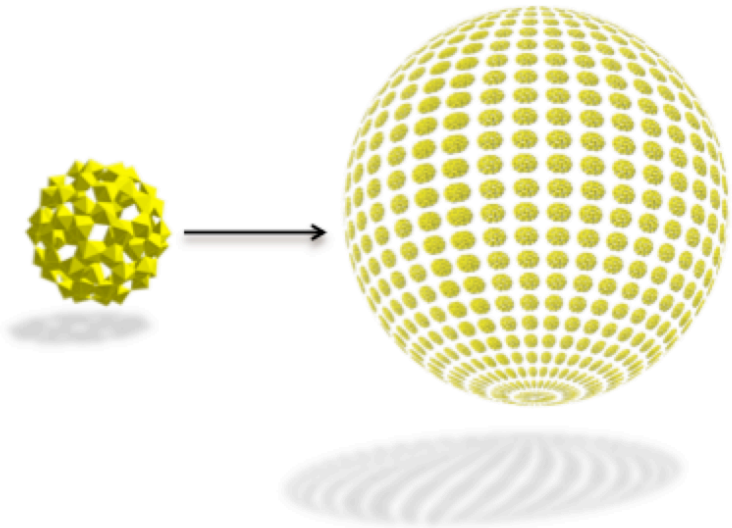

Figure 1. Aggregation of U60 (left) into a much larger blackberry (right). The shape of the blackberry may be spherical and it is likely hollow, as it does not continue to grow beyond several hours after formation.

References

(1) (a) Nyman, M.; Burns, P. C. *Chemical Society Reviews* **2012**, *41*, 7354(b) Qiu, J.; Burns, P. C. *Chemical Reviews* **2012**, *113*, 1097.

(2) Vlaisavljevich, B.; Gagliardi, L.; Burns, P. C. *Journal of the American Chemical Society* **2010**, *132*, 14503.

(3) Sigmon, G. E.; Unruh, D. K.; Ling, J.; Weaver, B.; Ward, M.; Pressprich, L.; Simonetti, A.; Burns, P. C. *Angewandte Chemie-International Edition* **2009**, *48*, 2737.

4-05

Uranium sorption onto single mineral phases – approaching consistency and robustness

Vinzenz Brendler

Helmholtz-Zentrum Dresden-Rossendorf, Dresden, Germany

One of the contaminants gaining special public attention is uranium. Though in almost all cases natural uranium (or depleted uranium) is of concern – and thus its chemotoxicity – radioactivity dominates most debates. But in any case the environmental fate of uranium and factors retarding or enhancing its transport are of high relevance. There are many studies addressing the sorption properties of uranium(VI) – and to a much lesser amount also of uranium(IV) – that produce a very patchy figure when it comes to a generalized view based on quasi-thermodynamic surface complexation models (SCM). This talk summarizes the current state-of-the-art with respect to and tries to homogenize the facts, also pointing out some steps to be done next.

An overview about SCM reactions and parameters published so far can be, e.g., obtained from the RES³T database (Brendler et al., 2003), see also http://www.hzdr.de/res3t. As of April 2013 it lists more than 600 data records for U(VI) – compared to only 11 for U(IV). The mineral coverage is very unbalanced (number of records in parentheses): Fe-(oxy)hydroxides (324), SiO_2 (88), 3-layer silicates (76), Zr-oxides (58), Al-(oxy)hydroxides (19), and kaolinite (15). A similar picture emerges when looking at the composition of background electrolytes and the experimental temperatures. The list of surface species proposed from the various authors is impressive (restricting ourselves to the ternary system U-OH-solid) with 9 different inner-sphere and 8 different outer-sphere surface species proposed.

a) inner-sphere complexes: »X-O-UO_2<1+>, (»X-O)$_2$-UO_2, (»X-O)$_2$-$UO_2(OH)_3$<3->, »X-O-$UO_2(OH)$, »X-O-$UO_2(OH)_2$<1->, »X-O-$UO_2(OH)_3$<2->, »X-O-$(UO_2)_3(OH)_5$, »X-O-$(UO_2)_3(OH)_7$<2->, and »X-O-$(UO_2)_2(OH)_2$<+>
b) outer sphere complexes: »X-OH-UO_2<2+>, »X-OH-$UO_2(OH)$<1+>, »X-OH-$UO_2(OH)_2$, »X-OH-$UO_2(OH)_4$<2->, »X-OH_2-$UO_2(OH)_2$<1+>, »X-OH_2-$UO_2(OH)_3$, »X-OH_2-$UO_2(OH)_4$<1->, and »X-$(OH)_2$-UO_2<2+>

Unfortunately, only a minority of them has any spectroscopic backup although several respective tools have been developed during the last two decades. Also quantum chemical modeling may provide valuable support when it comes to decide between several similar structures / stoichiometries. Recent prominent publications addressing Uranium(VI) sorption include works exploiting TRLFS (Baumann et al., 2005, Walter et al., 2005, Arnold et al., 2006, Chang et al., 2006, Vandenborre et al., 2007, Křepelová et al., 2007), GIXAFS: (Catalano et al., 2005, Den Auwer et al., 2003;), EXAFS (Walter et al., 2005, Froideval et al., 2006; Hattori et al., 2009, Gückel et al., 2013), vibrational spectroscopy (Lefevre et al., 2008, Veilly et al., 2008, Müller et al, 2012, Gückel et al., 2013), and DFT calculations (Veilly et al., 2008; Hattori et al., 2009).

The above list of postulated complexes contains several oligomeric uranyl surface species where the authors put a direct analogy between structures assumed for the aqueous speciation and the one on mineral surfaces. This at least for inner-sphere complexes is questionable as there are not enough coordination sites available to allow for additional bonds to the surface (or such bonds have to be extraordinarily long and thus weak). Other species structures only differ by one H_2O unit – which is both very difficult to prove and to distinguish from solvation shell water. Clearly, there is some room for reduction of complexity.

Applying the principle of parsimony and discussing the most recent papers seeking for spectroscopic evidence a reduced set of uranyl surface species is suggested. It then should be used to re-fit experimental raw data from as many independent investigations as being accessible. Such a multi-institutional task would also take profit from a formalized sorption raw data storage scheme, comprising uniform notation and data structures as well as user-friendly storage and access tools. The talk intends to initiate respective discussions by providing first proposals. Eventually such an approach may promote the transfer of surface complexation models, together with other thermodynamic models e.g. describing ion exchange and surface precipitation, into more general reactive transport codes used to predict contaminant transport in the environment.

References

[1] Arnold, A., S. Utsunomiya, G. Geipel, R.C. Ewing, N. Baumann and V. Brendler: “Adsorbed U(VI) surface species on Muscovite identified by Laser Fluorescence Spectroscopy and Transmission Electron Microscopy”. Environ. Sci. & Technol., 40(2006), 4646.

[2] Baumann, N., V. Brendler, T. Arnold, G. Geipel and G. Bernhard: "Uranyl sorption onto gibbsite studied by time-resolved laser-induced fluorescence spectroscopy (TRLFS)". J. Colloid Interface Sci. 290(2005), 318.

[3] Brendler, V.,A. Vahle, Th. Arnold, G. Bernhard and Th. Fanghänel: “RES³T-Rossendorf expert system for surface and sorption thermodynamics”. J. Contaminant Hydrology, 61(2003), 281.

[4] Catalano, J.G., Trainor, T.P., Eng, P.J., Waychunas, G.A., Brown, G.E.: “CTR diffraction and grazing-incidence EXAFS study of U(VI) adsorption onto α-Al_2O_3 and α-Fe_2O_3 ($11\bar{0}2$) surfaces”. Geochim. Cosmochim. Acta 69(2005), 3555.

[5] Chang, H.S., Korshin, G.V., Wang, Z.M., Zachara, J.M.: “Adsorption of uranyl on gibbsite: a time-resolved laser-induced fluorescence spectroscopy study”. Environ. Sci. & Technol. 40(2006), 1244.

[6] Den Auwer C., Drot R., Simoni E., Conradson S. D., Gailhanou M. and de Leon J. M.: “Grazing incidence XAFS spectroscopy of uranyl sorbed onto TiO_2 rutile surfaces”. New J. Chem. 27(2003), 648.

[7] Froideval, A., M. Del Nero, C. Gaillard, R. Barillon, I. Rossini, J.L. Hazemann: “Uranyl sorption species at low coverage on Al-hydroxide: TRLFS and XAFS studies”. Geochim. Cosmochim. Acta 70(2006), 5270.

[8] Gückel, K., Rossberg, A., Brendler, V. and Foerstendorf, H.: „Binary and ternary surface complexes of U(VI) on the gibbsite/water interface studied by vibrational and EXAFS spectroscopy“. Chemical Geology 326-327(2012), 27.

[9] Hattori, T., Saito T., Ishida K., Scheinost A. C., Tsuneda T., Nagasaki S., and Tanaka S.: “The structure of monomeric and dimeric uranyl adsorption complexes on gibbsite: a combined DFT and EXAFS study”. Geochim. Cosmochim. Acta 73(2009), 5975.

[10] Křepelová, A., V. Brendler, S. Sachs, N. Baumann and G. Bernhard: "U(VI)-Kaolinite surface complexation in absence and presence of humic acid studied by TRLFS". Environ. Sci. & Technol., 41(2007), 6142.

[11] Müller, K., Foerstendorf, H., Meusel, T., Brendler, V., Lefèvre, G., Comarmond, M.J. and Payne, T.E.: “Sorption of U(VI) on the TiO_2 – water interface: An in situ vibrational spectroscopic study”. Geochim. Cosmochim. Acta 76(2012), 191.

[12] Lefevre G., Kneppers J. and Fedoro□ M.: “Sorption of uranyl ions on titanium oxide studied by ATR-IR spectroscopy”. J. Colloid Interface Sci. 327(2008), 15.

[13] Vandenborre J., Drot R. and Simoni E.: “Interaction mechanisms between uranium(VI) and rutile titanium dioxide: from single crystal to powder”. Inorg. Chem. 46(2007), 1291.

[14] Veilly, E., Roques J., Jodin-Caumon M.C., Humbert B., Drot R., Simoni E.: “Uranyl interaction with the hydrated (001) basal face of gibbsite: a combined theoretical and spectroscopic study”. J. Chemical Physics 129(2008), 244704.

[15] Walter, M.; Arnold, T.; Geipel, G.; Scheinost, A.; Bernhard, G.: “An EXAFS and TRLFS investigation on uranium(VI) sorption to pristine and leached albite surfaces”. J. Colloid Interface Sci. 282(2005), 293.

ORAL

1-11

Molecular Transuranic Discovery Science

Andrew Gaunt[1], Sean Reilly[1], Matthew Jones[1], Brian Scott[1], Robert Paine[2], Nikolas Kaltsoyannis[3]

[1]Los Alamos National Laboratory, Los Alamos, NM 87545, USA, [2]University of New Mexico, Albuquerque, NM 87131, USA, [3]University College London, London, WC1H 0AJ, UK

Increasing our understanding of the reactivity, structural, and bonding properties of the early to middle actinide elements can support, at the molecular level, advances in applications such as novel separation schemes for advanced nuclear fuel cycles and waste disposition strategies. Despite the importance of the transuranic elements, their chemistry and detailed comprehension of electronic structure and bonding is relatively poorly developed. We are studying the f-element coordination chemistry of a range of hard and soft ligands that are related to extractant molecules. The research is conducted mainly in organic solvents and under one of two regimes: air/moisture-stable or air/moisture-sensitive. Chemistry open to the atmosphere tends to have more direct relevance to conditions encountered in the fuel cycle and typically encompasses hard donors that are likely to engage predominately in ionic bonding to both lanthanides and actinides. On the other hand, while chemistry performed under inert atmospheres may be less applied, a wide range of ligands and soft donors become accessible that can inform, in depth, upon fundamental electronic structure and the extent to which 5f metals can participate in covalent bonding contributions, a factor that is thought to be influential in trivalent actinide/lanthanide separations by S and N donor extractants.

One the prerequisites for successful synthetic coordination chemistry endeavours is an easily accessible array of starting materials to choose from that best facilitates the preparation of the target molecules. For plutonium, the choice of non-aqueous precursors is rather limited and is an area that we have attempted to expand recently. Specifically, tetrabutyl ammonium salts of Pu(IV) hexanitrate (Figure 1) and hexachloride have been synthesized. Both compounds are ideal starting materials for reactions in organic solvents since they are readily soluble, isolated in high yield, are accessed from readily available acidic stock solutions of Pu, and are well characterized by single crystal X-ray diffraction and optical spectroscopy (solution and solid-state).

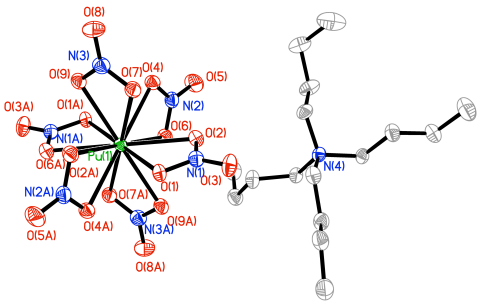

Figure 1. Solid-state molecular structure of a Pu(IV)-hexanitrate non-aqueous synthetic starting material, isolated as a tetrabutyl ammonium salt (only one of two cations is shown).

On the topic of hard O donors, the binding of Pu(IV) to a phosphine oxide decorated dibenzofuran platform was investigated by spectroscopic and structural analysis. Electronic absorption spectroscopy following Pu(IV) acid stock addition to organic solutions containing increasing equivalents of ligand indicates that a 1:1 complex is the limiting species. This suggestion is supported by the crystal structure of 1:1 neutral complex obtained from THF/methanol solution. The ligand is bidentate, bonding to the Pu(IV) center through both P=O groups, while the furan O atom is unable to coordinate (Figure 2). Future studies are being directed towards investigating S and Se donor analogs of the phosphine oxide ligand framework.

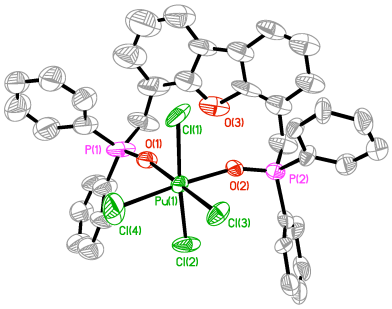

Figure 2. Solid-state structure of the 1:1 complex formed between Pu(IV) and the dibenzofuran ligand that has two diphenylphosphine oxide groups appended.

On the topic of soft donor chemistry, a diselenophosphinate ligand was chosen as a softer Se donor analog of known S donor extractants. This ligand was previously unstudied for any of the f-elements and is well suited for a systematic coordination chemistry investigation. The aim was to uncover bonding trends and differences both between 4f and 5f trivalent metals and across the 5f series in the tetravalent oxidation state. Series of 1:3 and 1:4 complexes with several trivalent lanthanides and Pu(III) have been prepared and analyzed by structural determination (Figure 3), spectroscopy, and DFT calculations. Results reveal that consistently shorter Pu-Se versus Ce-Se bond lengths are probably a reflection a modest increase in the metal-ligand orbital overlap in the actinide bonding relative to the lanthanide bonding. Conversely, the changes in U-Se versus Np-Se bond lengths in the An(IV) molecules appear to be consistent with the expected effect of the actinide contraction, namely an increase in the metal-ligand electrostatic interactions from left to right across the 5f series.

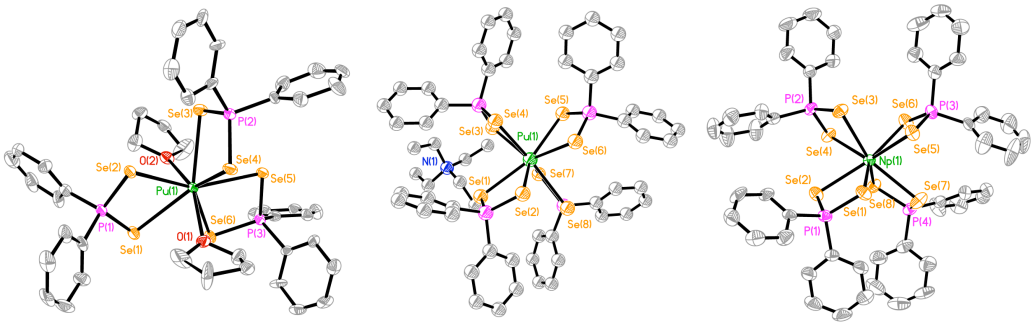

Figure 3. Solid-state structures of a Pu(III) 1:3 neutral complex (left), a Pu(III) 1:4 anionic complex (middle), and a Np(IV) 1:4 neutral complex (right), all with the diphenyldiselenophosphinate ligand.

1-12

Complex formation dynamics of actinide and lanthanide with poly-dentate ligands by time resolved XAFS.

Tsuyoshi Yaita, Daiju Matsumura, Toru Kobayashi, Shinichi Suzuki, Hideaki Shiwaku

QuBS, JAEA, Hyogo, Japan

Introduction. The chemical bond properties of *f*-elemets with neutral N-donor ligands provide key information for design of new ligand for separation of trivalent actinides from lanthanides. Hence, we have studied the electronic structures regarding N-donor complexes with actinides:Th, Pu, Cm and lanthanides by the SOR-based XAS/XES and DFT calculation methods. From these results, it has been clarified that actinides having 5*f*-electron significantly interacted with nitrogen through both ionic and covalent interactions. Interestingly, the 5f-orbital and the 6s- and 6p-orbitals might participate in covalent and ionic bonds, independently. It means that the ionic interaction mainly depends on the s- and p-orbitals charge density and however, the f-orbital, which participates in covalent bond, might not effectively contribute to increase in charge density of ion. If such the independency exists in complex formation of f-element, it would become to be an important factor for considering ion separation. On these backgrounds, in this study, we carried out chemical formation dynamics study using TR-DXAFS in order to elucidate U(IV), Eu(III)-N donor ligand in solution. The TR-DXAFS provides time dependent EXAFS parameters: chemical shift (E_0), bond distance(R), coordination number (N), Debye-Waller factor (σ^2) and so on, possibly giving us detailed information regarding chemical bond formation features about *f*-elements. Especially, we are interesting in time differences between structural formation (probably driven by ionic interaction) (N, R) and chemical shift (probably driven by covalent interaction) (E_0). The N-donor ligands used in this study were 1,10-phenanthroline (Phen) and phenanthroline amide (PTA).

Experimental. Metal (U(IV, VI) or Eu(III)) in methanol was prepared as initial solution, and then concentrated ligand (Phen or PTA) solution was added by titration with remote control system, after EXAFS measurement started. TR-DXAFS was performed at the BL14B1 of SPring-8. Resolution of DXAFS in this system was 0.1ms.

Results and Discussion. Figure 1 shows the time dependent radial structural functions (RSF) of EXAFS for Eu(III)-PTA-methanol system. The EXAFS RSF after 200s consists of two peaks: peak-1 around 2 Å and peak-2 at 2.7 Å, arising from O, N(C=O, Phen) and C around N donor atoms, respectively. At first, oxygen of carbonyl group coordinated immediately replacing with water oxygen and the peak-2 also appeared. After 5s, the peak-1 slightly broadened and the peak-2 slightly shifted for shorter distance, indicating that PTA coordination occurred by two steps coordination. Figure 2 shows the time resolved RSF of U(IV,VI)-PTA-methanol system. The EXAFS RSF after 2000s consists of three peaks: peak-1 around 1.5 Å, peak-2 at 2 Å, and peak-3 at 3.1 Å, arising from O (axial oxygen), O, N of PTA, and C of PTA around N donor atoms, respectively. This solution was mixture of uranium (IV, VI) solution; however, we confirmed the rapid coordination of PTA after mixing solution because the peak-3 around 3.1 Å appeared at Time=0s (just after mixing with ligand solution). After mixing solution, although PTA coordination was already completed, it was observed that a part of water oxygen had changed to uranyl oxygen during oxidation of uranium. In this presentation, we will also present that time resolved EXAFS fitting parameters for complex formation dynamics of U(IV or VI) and Eu(III)-Phen, PTA solution system.

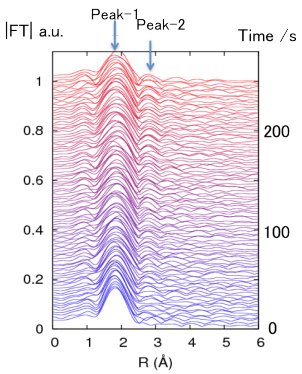

Fig. 1 TR-RSF of Eu(III)-PTA-methanol system

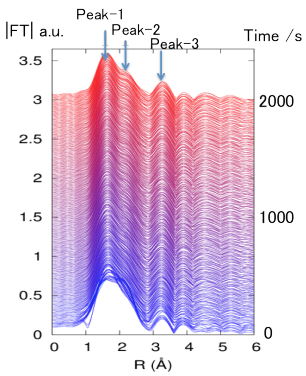

Fig. 2 TR-RSF of U(IV, VI)-PTA-methanol system

1-13

Structural Studies on Uranyl Species in Acetonitrile and 1-Ethyl-3-methylimidazolium Nitrate ([EMI][NO_3]) Dissolved $[EMI]_2[UO_2(NO_3)_4]$ – Evidence for the Formation of $[UO_2(NO_3)_4]^{2-}$ –

Kotoe Sasaki[1], Tomoya Suzuki[2], Tsuyoshi Arai[1], Koichiro Takao[2], Shinichi Suzuki[3], Tsuyoshi Yaita[3], Yasuhisa Ikeda[2]

[1]Shibaura Institute of Technology, Toyosu, Koto-ku, Tokyo, Japan, [2]Tokyo Institute of Technology, Ookayama, Meguro-ku, Tokyo, Japan, [3]Japan Atomic Energy Agency, Ibaraki, Japan

Uranyl trinitrato complex in non-aqueous solvents and in solid state has been known to exist as $[UO_2(NO_3)_3]^-$ with D_{3h} symmetry [1-3]. Uranyl nitrato complexes in ionic liquids (ILs) have also been examined using spectroscopic methods such as UV-visible, EXAFS, and so on [4-7]. Such studies have clarified that the uranyl nitrato complexes in ILs exist as $[UO_2(NO_3)_3]^-$ with D_{3h} symmetry. However, recently it was reported that $[DMI]_2[UO_2(NO_3)_4]$ (DMI =1,3-dimethylimidazolium) is obtained as a single crystal and that uranyl species exist as $[UO_2(NO_3)_4]^{2-}$ in [BMI][NO_3] (BMI = 1-butyl-3-methylimidazolium). In these complexes, the equatorial plane of uranyl moiety is coordinated by two bidentate and two unidentate nitrates [8, 9].

In the present study, to get more detail information on the structure of uranyl nitrato complexes, we have examined the structures of uranyl species in CH_3CN and [EMI][NO_3] dissolved $[EMI]_2[UO_2(NO_3)_4]$(EMI = 1-ethyl-3-methylimidazolium). The $[EMI]_2[UO_2(NO_3)_4]$ complex was synthesized by adding four equivalent of $AgNO_3$ to $[EMI]_2[UO_2Cl_4]$ in CH_3CN, followed by filtration for removing AgCl and evaporation of CH_3CN. Sample solutions were prepared by dissolving $[EMI]_2[UO_2(NO_3)_4]$ complex into CH_3CN or [EMI][NO_3]. The UV-visible absorption spectra of solutions were measured by Shimadzu UV-3150 spectrophotometer. EXAFS measurements were carried out using PF BL27B at High Energy Accelerator Organization.

UV-visible absorption spectrum of sample solution prepared by dissolving $[EMI]_2[UO_2(NO_3)_4]$ complex(0.024 M, M = mol dm^{-3}) into CH_3CN was measured and found to be consistent with that of the $[UO_2(NO_3)_3]^-$ species with D_{3h} symmetry. We also measured the absorption spectral changes with the addition of [EMI][NO_3] (0.074, 0.12, 0.52, 1.5 M) to the above CH_3CN solution dissolved $[EMI]_2[UO_2(NO_3)_4]$ (0.024 M). The results are shown in Figure 1.The absorbance in the range of 420 to 440 nm is found to increase with appearance of isosbestic points at 465 and 469 nm. This phenomenon is similar to that reported by Ryan [2], i.e., the absorption spectra of CH_3NO_2 solutions dissolved $(C_2H_5)_4UO_2(NO_3)_3$ and $(C_2H_5)_4NNO_3$ showed the isosbestic points at 465.5 and 470.0 nm. From these results, it is proposed that the following equilibrium reaction exists in the present system.

$$[UO_2(NO_3)_3]^- + NO_3^- = [UO_2(NO_3)_4]^{2-},$$

Based on the absorption spectral changes, the equilibrium constant (K) was evaluated as 3.85 M^{-1}, which is in agreement with the data reported by Ryan, 4.74 M^{-1} [2]. Furthermore, we measured UV-visible absorption and EXAFS spectra of [EMI][NO_3] solution dissolved $[EMI]_2[UO_2(NO_3)_4]$ at 50 ºC. The UV-visible absorption spectrum (Figure 1, neat) was found to be consistent with that of [EMI][NO_3] dissolved $UO_2(NO_3)_2{\cdot}6H_2O$. From the EXAFS data, it was supported that the uranyl species in [EMI][NO_3] are present as $[UO_2(NO_3)_4]^{2-}$ and its equatorial plane is coordinated by two bidentate and two unidentate nitrates.

From these results, it is proposed that in media containing a large excess of NO_3^- the $[UO_2(NO_3)_4]^{2-}$ species is formed.

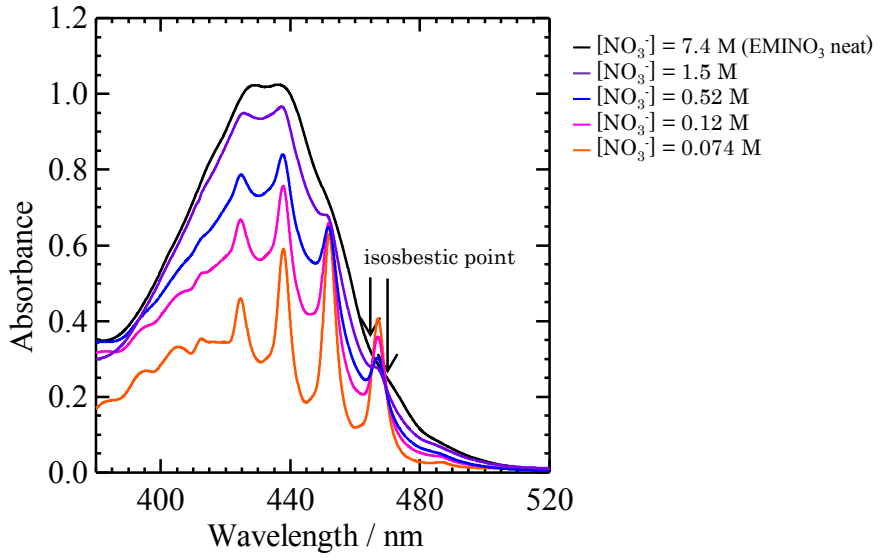

Figure 1. UV-visible absorption spectral changes with addition of [EMI][NO_3] to the solutions prepared by dissolving $[EMI]_2[UO_2(NO_3)_4]$(0.024 M) into CH_3CN, and UV-visible absorption spectrum of [EMI][NO_3] solution dissolved $[EMI]_2[UO_2(NO_3)_4]$(0.024 M). Temp. = 25 ºC.

References

1. L.K. Kaplan, R.A. Hildebrandt, and M. Ader, *J. Inorg. Nucl., Chem.*, **2**, 153 (1956).

2. J.L. Ryan, *J. Phys. Chem.*, **65**, 1099 (1961).

3. R.D. Denning, D.N.P. Foster, T.R. Snellgrove, and D.R. Woodwark, *Mol. Phys.*, **37**, 1089 (1979).

4. K. Servaes, C. Hennig, I. Billard, C. Gaillard, K. Binnemans, C.G-.Walrand, and R.V. Deun, *Eur. J. Inorg. Chem*., 5120 (2007).

5. P. Nockemann, K. Servaes, R.V. Deun, K.V. Hecje, L.V. Meervelt, K. Binnemans, and C.G-Walrand, *Inorg. Chem*., **46**, 11335 (2007).

6. D.L. Quach, C.M. Wai, and S.P. Pasilis, *Inorg. Chem*., **49**, 8568 (2010).

7. S. Georg, I. Billard, A. Ouadi, C. Gillard, L. Petitjean, M. Picquet, and V. Solo'ev, *J. Phys. Chem. B*, **114**, 4276 (2010).

8. A.E. Bradley, C. Hardacre, M. Nieiwenhuyzen, W.P. Pitner, D. Sanders, K.R. Seddon, and R.C. Thied, *Inorg. Chem*., **43**, 2503 (2004).

9. C. Gaillard, O. Klimchuk, A. Ouadi, I. Bikkard, and C. Hennig., *Dalton Trans.*, **41**, 5476 (2012).

1-14

Cation-Cation Complexes of pentavalent uranyl: towards polymetallic assemblies with unusual magnetic properties

Lucile Chatelain[1], Victor Mougel[1], Jacques Pécaut[1], Roberto Caciuffo[2], Eric Colineau[2], Jean-Christophe Griveau[2], Marinella Mazzanti[1]

[1]CEA Grenoble, Grenoble, France, [2]European Commission, Joint Research Centre, Institute for Transuranium Elements, Karlsruhe, Germany

The design of multinuclear molecular actinide complexes is of high current interest because of their efficiency to provide practical models of species involved in the uranium mobility in the environment and to investigate the magnetic interaction and the electronic structure of actinide materials. Accordingly we have become interested in studying the chemistry of pentavalent uranyl (UO_2^+) compounds. A key property of an uranyl(V) moiety is its ability to bind to another actinyl moiety through the axial oxygen (commonly known as cation-cation interaction, CCI).

The synthesis of stable pentavalent uranyl complexes presenting CCI's also provides a route to the self-assembly of multinuclear uranium complexes trough the mutual coordination of the UO_2^+ groups. We have thus recently shown that a suitable choice of ligand and conditions can lead to the isolation of multinuclear complexes of pentavalent uranyl with different nuclearities. Such assemblies show unambiguously an intermetallic communication between $5f^1$ complexes and these magnetic properties can be tuned by appropriate structural modifications. We have thus recently observed that these simple uranyl building units can be assembled with d block ions to form mixed 3d-5f complexes acting as single molecule magnets. The structure and magnetic properties of new polymetallic assemblies of uranyl(V) will be reported.

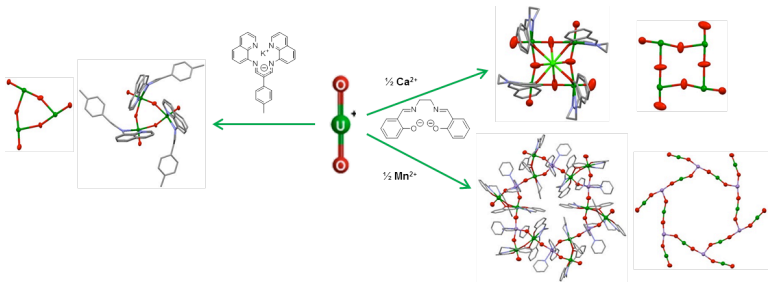

1-15

Actinide paramagnetism and NMR

Claude Berthon[1], Thomas F. Wall[2], Steve Jan[1], Matthieu Autillo[1], Kenneth L. Nash[2], Claire Le Naour[3], Laetitia Guerin[1], Philippe Moisy[1]

[1]CEA, Bagnols/Ceze, France, [2]Whashington State University, Pullman, USA, [3]Paris XI University, Orsay, France

Nuclear Magnetic Resonance spectroscopy offers considerable insights into fundamental characteristics of nuclei. It has been applied to the lanthanide series to probe hydration sphere size, ordering, resonance times or aggregation states for both non-complexed cations and bound cations[4,3]. The paramagnetism of trivalent lanthanide cations, arising from partially filled electron orbitals, has been exploited in NMR spectroscopy to observe nuclear relaxation processes and lanthanide induced shifts (LIS)[7,6]. All these investigations have led to a better understanding of lanthanide electron behavior, their magnetic properties as well as structural information of complex formed. Moreover influencing parameters on NMR spectra due to lanthanide paramagnetic behaviors have been tabulated[1,5,2]. Extension of these techniques to actinides would be of interest, particularly in nuclear fuel re-processing systems.

In spite of main advances many questions still remain unanswered on the actinide series, particularly on the behavior of the 5*f* unpaired electrons, their magnetic properties in solutions, the importance of spin-orbit coupling, the covalency within actinide-ligand bounds, etc.

A systematic determination of actinide paramagnetic behavior was then undertaken by NMR through two complementary approaches which are the paramagnetic induced chemical shifts d_{para} and the molar magnetic susceptibility c_M measurements.

$$\delta_{para} = \delta_{dia} + \delta_{con} + \delta_{dip}$$

$$\delta_{con} \propto \frac{A}{\hbar}(g_J - 1)\chi_M \qquad \delta_{dip} \propto (\chi_{//} - \chi_{\perp})\frac{3\cos^2\vartheta - 1}{r^3}$$

In the first approach, magnetic susceptibilities of the most stable ions in solution from uranium to californium, for various oxidation states (Th^{IV} - U^{IV} -U^{VI}, Np^{IV} -Np^{V} -Np^{VI}, Pu^{III} -Pu^{IV} -Pu^{VI}, Am^{III}, Cm^{III} et Cf^{III}), were measured by NMR in perchloric media thanks to the Evans' method. In these conditions, cations are all surrounded by a field ligand made of water molecules. An(IV) exhibit experimental values lower than theoretical values based on the free-ion's ground state determined by Hund's rule. Some actinide(III) also differ from their lanthanide counterparts but for some other reasons because experimental values are higher than expected for free ions. Magnetic susceptibilities of actinide ions exhibit a temperature dependence in good agreement with a Curie law around room temperature except for Am(III), Pu(IV) and $5f^0$ configurations.

In the second approach, chemical shifts of actinide(IV)-dipicolinate (DPC) paramagnetic complexes were studied and analysed in dimethylformamide. DPC ligands have been used successfully to characterize paramagnetic behaviour of lanthanide(III). Thanks to available X-Ray diffraction data of An(IV):DPC_3 which exhibit isostructural complexes, ^1H and ^{13}C paramagnetic chemical shifts were analysed comparatively to calculated geometric factors. Ethyl-DPC complexed to An(IV) were also studied in order to check dipolar effects by increasing nuclei remoteness with An(IV) paramagnetic center. This separation method of contact and dipolar contributions that has been proved efficient for lanthanide(III) fails in the case of actinide(IV) complexes. This method nevertheless highlights that contact interaction terms are greater than for lanthanide(III) and can be directly interpreted as a covalence proof of an(IV). A second separation method based on the temperature dependence of contact and dipolar interactions fails too but for other reasons which are related to An(IV) magnetic susceptibility properties.

Determination of An(IV) paramagnetic parameters which would be only characteristic of the cation and independent of the ligand, similarly to Ln(III) case, does not appear straightforward.

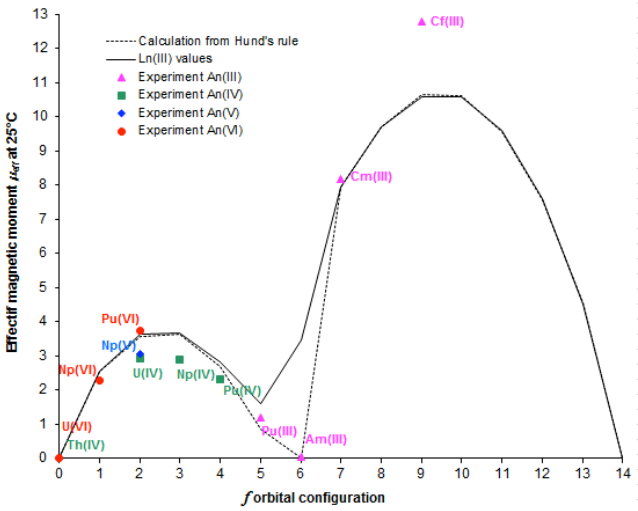

Experimental effective magnetic moments of actinide cations studied as a function of their electronic configuration at 25°C

References

[1] B. Bleaney. Nuclear magnetic resonance shifts in solution due to lanthanide ions. *J. Magn. Reson.*, 8:91–100, 1972.

[2] B. Bleaney, C. M. Donbson, B. A. Levine, R. B. Martin, R. J. P. Williams, and A. V.. Xavier. Origin of lanthanide nuclear magnetic resonance shifts and their uses. *J. Chem. Soc., Chem. Commun.*, pages 791–793, 1972.

[3] P. Caravan, Parisa Mehrkhodavandi, and Chris Orvig. Cationic Lanthanide Complexes of N,N'-Bis(2-pyridylmethyl)ethylenediamine-N,N'-diacetic Acid ($h_2$bped). *Inorg. Chem.*, 36(7):1316–1321, 1997.

[4] Jean F. Desreux. Nuclear magnetic relaxation studies on actinide ions and models of actinide complexes. In Rudi van Eldik and Ivano Bertini, editors, *Advances in Inorganic Chemistry*, volume 57, pages 381–403. Elsevier Science, New York, 2005.

[5] R. M. Golding and M. P. Halton. A theoretical study of the ^{14}n and ^{17}o nmr shifts in lanthanide complexes. *Aust. J. Chem.*, 25:2577–2581, 1972.

[6] F. Inagaki and T. Miyazawa. Nmr analyses of molecular conformations and conformational equilibria with the lanthanide probe method. *Prog. NMR spectrosc.*, 14:67–111, 1981.

[7] J. A. Peters, J. Huskens, and D. J. Raber. Lanthanide induced shifts and relaxation rate enhancements. *Prog. NMR spectrosc.*, 28:283–350, 1996.

1-82

Cp_4An: one grandfather in the organometallic chemistry of actinides with young and attractive grandchildren

Christos Apostolidis, Jean Rebizant, Olaf Walter, Alfred Morgenstern

European Commission, Joint Research Centre, Institute for Transuranium Elements, Karlsruhe, Germany

The organometallic complexes [Cp4An] (An: actinide) of the tetravalent actinides are among the first organometallic compounds of these elements which have been synthesised and described in the literature [1-4].

They can be prepared relatively easily by metathesis reaction in high yields. Kinetic shielding of the nuclei by the four organometallic Cp-ligands in a tetrahedral arrangement around the central metal contributes to their resulting good stability.

However, under careful control of the reaction conditions reaction with broensted acidic compounds might proceed to well defined organometallic products exhibiting interesting spectroscopic and magnetic properties.

A brief summary of the presented chemistry is given in the scheme, examples will be presented on Th, U, and Np, respectively. Pa will be subjected to later presentations.

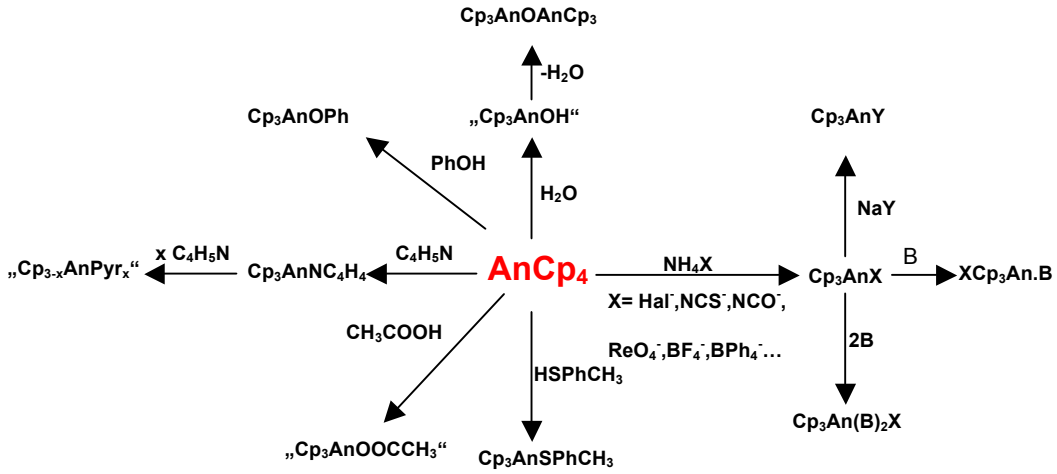

References

[1] E. O. Fischer, Z. Naturforsch., Teil B 1962, 17, 276

[2] E.O. Fischer, Z. Naturforsch., Teil B 1962,17, 275

[3] B. Kanellakopulos, Angew. Chem. Int. Ed. Engl. 1968, 7, 634

[4] B. Kanellakopulos, Angew. Chem. Int. Ed. Engl. 1969, 8, 202

1-89

Recent Advances in Terminal Uranium Nitride Triple Bond Chemistry

David King[1], Floriana Tuna[2], Eric McInnes[2], Jonathan McMaster[1], William Lewis[1], Alexander Blake[1], Stephen Liddle[1]

[1]University of Nottingham, Nottingham, UK, [2]University of Manchester, Manchester, UK

There is currently great interest in the nature and reactivity of molecular uranium-ligand multiple bonds.[1] This is because the nature and extent of 5f/6d orbital participation in uranium-ligand bonding is still a topic of debate and the unique orbital-hybridisation patterns available to uranium promises novel applications in atom-efficient catalysis and small molecule activation.[2]

Molecular uranium nitrides are of special interest because of their potential as precursors to uranium nitride materials via 'soft' routes, but more importantly because in contrast to commonly observed U=O, U=NR, and U=CR_2 linkages the U≡N triple bond was prominent for its paucity.[3] For example, the only examples of the U≡N triple bond were previously confined to matrix isolation experiments at ~5 K and attempts to prepare molecular species under ambient conditions in exploitable quantities resulted in compounds where the nitride bridges to 2-4 metal atoms or is trapped by a covalently bound borane group. The U≡N triple bond was proposed by calculations to be a transient species formed during photolysis of uranium(IV)-azides, but it could not be trapped and instead reacts with ancillary-ligand C-H bonds to give amide derivatives.

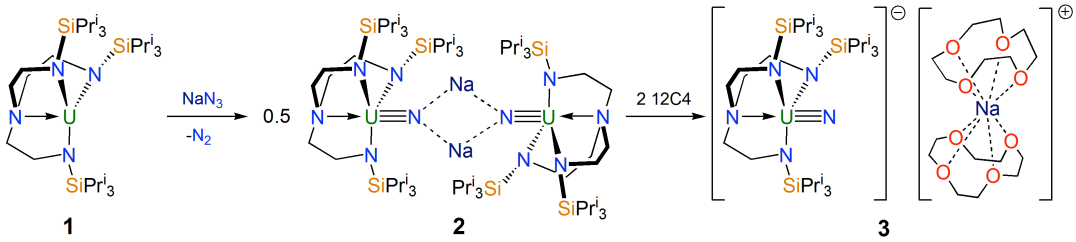

Recently, we reported that a sterically encumbered uranium(III)-triamidoamine complex [U($Tren^{TIPS}$)] [**1**, $Tren^{TIPS}$ = $N(CH_2CH_2SiPr^i_3)_3$] reacts with sodium azide to afford the bridging uranium(V)-nitride complex [{U($Tren^{TIPS}$)(μ-N)(μ-Na)}$_2$] (**2**). Abstraction and sequestration of the sodium ion by 12-crown-4 ether results in the separated ion pair complex [U($Tren^{TIPS}$)(N)][Na(12-crown-4)$_2$] (**3**) which contains the terminal U≡N triple bond linkage under ambient conditions and in multi-gram quantities.[4]

We will discuss this chemistry and the factors that contributed to the success of this relatively simple strategy and will detail more recent work in this area including the isolation and reactivity of the long-sought terminal uranium(VI)-nitride triple bond,[5] and if time permits the single molecule magnetism of a related uranium(V)-mono-oxo complex.[6]

References

1. T. W. Hayton, *Chem. Commun.*, **2013**, *49*, 2956.
2. A. R. Fox, S. C. Bart, K. Meyer, C. C. Cummins, *Nature*, **2008**, *455*, 341.
3. B. M. Gardner, S. T. Liddle, *Eur. J. Inorg. Chem.*, **2013**, Microreview in press.
4. D. M. King, F. Tuna, E. J. L. McInnes, J. McMaster, W. Lewis, A. J. Blake, S. T. Liddle, *Science*, **2012**, *337*, 717-720.
5. D. M. King, F. Tuna, E. J. L. McInnes, J. McMaster, W. Lewis, A. J. Blake, S. T. Liddle, *Nat. Chem.*, **2013**, in press.
6. D. M. King, F. Tuna, J. McMaster, W. Lewis, A. J. Blake, E. J. L. McInnes, S. T. Liddle, *Angew. Chem. Int. Ed.*, **2013**, in press.

1-90

Development and laboratory-scale innovative-SANEX process demonstration for minor actinide partitioning using anular centrifugal contactors

Andreas Wilden[1], Giuseppe Modolo[1], Peter Kaufholz[1], Andreas Geist[2], Daniel Magnusson[2], Michal Sypula[1], Dirk Bosbach[1]

[1]Forschungszentrum Jülich GmbH, Jülich, Germany, [2]Karlsruhe Institute of Technology, Karlsruhe, Germany

For the advanced minor actinide (MA) partitioning following the PUREX process, several multi-cycle processes have been developed. Recent research in Europe focused on the development of single-cycle processes, e.g. 1-cycle SANEX[1], EXAm[2]. Single cycle processes are advantageous, as they make the advanced MA partitioning more economical and easier.

In this paper the development and laboratory-scale demonstration of a so-called “innovative-SANEX” process is presented. In this strategy, the An(III) and Ln(III) are co-extracted from the PUREX raffinate, and the loaded solvent in subjected to several stripping steps. A solvent using the TODGA extractant with addition of 5 vol.-% 1-octanol showed very good extraction of Am(III) and Cm(III) together with the trivalent lanthanides (Ln(III)) from simulated PUREX raffinate solution without 3rd phase formation. The problem of co-extraction of Zr and Pd was overcome using CDTA as masking agent[3].

The An(III) are selectively stripped using either polyamino carboxylic acids (e.g. DTPA) or other selective complexing agents. A recent improvement of the selective stripping of An(III) was the use of the hydrophilic complexing agent SO_3-Ph-BTP[4]. This complexing agent for the first time enabled a selective An(III) stripping at nitric acid concentrations up to 0.5 mol/L.

A 32-stage process flow-sheet was designed using computer-code calculations[5] and tested in annular miniature centrifugal contactors in counter-current mode. For stripping of the Ln(III), a citric acid based solution was used.

The results of this test are presented and discussed.

References

[1] Wilden, A. et al. (2013): Solvent Extr. Ion Exch. Vol. 31 (5), accepted, DOI:10.1080/07366299.07362013.07775890

[2] Poinssot, C. et al. (2012): Proc. Chem. Vol. 7, 358-366.

[3] Sypula, M. et al. (2012): Solvent Extr. Ion Exch. Vol. 30 (7), 748-764.

[4] Geist, A. et al. (2012): Solvent Extr. Ion Exch. Vol. 30 (5), 433-444.

[5] Magnusson, D. et al. (2012): Proc. Chem. Vol. 7, 245-250.

1-91

Uranium Chemistry: from Nuclear to Single Molecule Magnets and Small Molecule Activation.

Marinella Mazzanti, Victor Mougel, Clement Camp, Lucile Chatelain, Jacques Pécaut

CEA, Grenoble, France

Uranium has very different magnetic properties and chemical reactivity from lanthanide and d-block metal ions because of its large size, the availability of 5f orbitals for bonding and the multiple oxidation states. Such reactivity plays a crucial role in many aspects of nuclear technology including nuclear fuel design, reprocessing and safe disposal and in determining the mobility of actinides in the environment. Moreover, uranium with its unconventional properties and reactivity is well poised for the development of efficient catalysts and functional materials such as molecular magnets (SMM) with improved properties. We have recently shown that multidentate Schiff bases can be used to stabilize uranium in the elusive pentavalent oxidation state. Recent reactivity studies of such uranium compounds shed light on the mechanism of disproportionation of pentavalent uranyl and afford polynuclear complexes with new topologies and interesting magnetic properties (Figure 1).

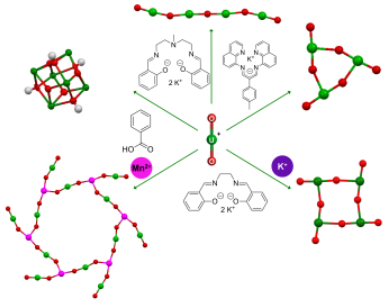

Figure 1. Polynuclear complexes from pentavalent uranyl.

In particular the observation of magnetic bistability with an open hysteresis loop and high relaxation barrier in a 5*f*-3*d* $U_{12}Mn_6$ wheel assembled trough cation-cation interaction, suggests that uranium might provide an avenue to magnetic storage devices. Uranium compounds are also very attractive because of their ability to promote the activation of small molecules (CO_2, azides, arenes, O_2) which is an important goal in contemporary catalysis. We have recently prepared the first dinuclear U(III) siloxide complex which acts as a two-electron reducing agent in the reaction with a variety of small molecules such as CS_2 and CO_2 and reduces toluene to afford a di-uranium inverted-sandwich (Figure 2). Such dinuclear arene-bridged complexes are attractive for understanding the involvement of f-orbitals in actinide bonding, for their potential magnetic properties and reactivity, but they remain rare. Usually, inverted-sandwich complexes are synthesized by reduction of halide metal complexes in the presence of an arene, rendering rather difficult the isolation of complexes in different states of charge. We have prepared three toluene-bridged diuranium inverted-sandwich complexes supported by siloxide ligands in different state of charge and studied their structure, bonding and magnetic behavior. Recent uranium redox chemistry carried out in our laboratory will be presented together with the structure and properties of new original polynuclear uranium compounds.

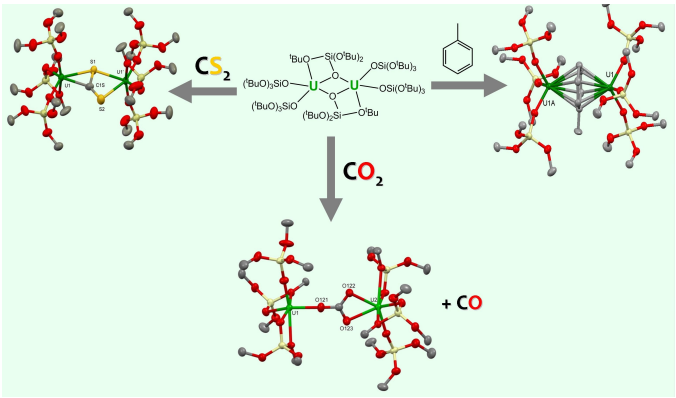

References

1. V. Mougel, J. Pecaut and M. Mazzanti, *Chem. Commun.*, 2012, **48**, 868-870.

2. L. Chatelain, V. Mougel, J. Pecaut and M. Mazzanti, *Chem. Sci.*, 2012, **3**, 1075-1079.

3. V. Mougel, L. Chatelain, J. Pecaut, R. Caciuffo, E. Colineau, J. C. Griveau and M. Mazzanti, *Nat. Chem.*, 2012, **4**, 1011-1017.

4. V. Mougel, C. Camp, J. Pecaut, C. Coperet, L. Maron, C. E. Kefalidis and M. Mazzanti, *Angew Chem. Int. Ed.*, 2012, **51**, 12280-12284.

2-12

Thermodynamic investigation of the Th-U-Pu-O system

Ondrej Benes, Dario Manara, Octavian Valu, Robert Böhler, Rudy Konings

JRC-ITU, Karlsruhe, Germany

Understanding of nuclear fuel behaviour under normal as well as under accidental conditions is one of the key points for the safety assessment of nuclear reactors. The commercial solid oxide fuel, which is based on either UO_2 or $(U_{1-x},Pu_x)O_2$ (MOX), is a rather complex system to study as the properties of such fuel are modified with composition change that takes place upon nuclear fission and are also highly depending on the actual O/M ratio, which is determined by the imposed local oxygen potential and temperature. Addition of Th, which is envisioned as fertile material in advanced nuclear reactor designs, increases the complexity of the fuel and therefore, in order to predict the thermochemical properties of a fuel, the solution is to develop a thermodynamic database that gives a systematic description of the whole Th-U-Pu-O system. With such database it is straightforward to identify the exact chemical form for any composition of interest with respect to external variables, such temperature, oxygen potential or pressure.

The thermodynamic assessment of the MOX fuel system has been described in previous studies [1-3] as part of the FUELBASE development and in this paper we present the extension of the U-Pu-O system by addition of the Th component. This includes the assessments of all Th-containing sub-binary systems, namely Th-U (Figure 1), Th-Pu (Figure 2) and Th-O, which are further used to assess the full Th-U-Pu-O system. For the optimization of the former two binary phase diagrams experimental data from the literature were used, whereas in case of the Th-O system, our own measurements of the melting temperatures using a laser method have been considered. These measurements revealed increased liquidus temperature of hypostochiometric ThO_{2-x} compared to the melting point of stochiometric ThO_2 and this observation has been well correlated with the optimized Th-O phase diagram. Furthermore, the data of the heat capacity of $(Th,U)O_2$ and $(Th,Pu)O_2$ mixed oxides plus vapour pressure data measured using a Knudsen effusion cell coupled with mass spectrometry obtained as part of this study as well were used to optimize the Gibbs energy data of ternary phases.

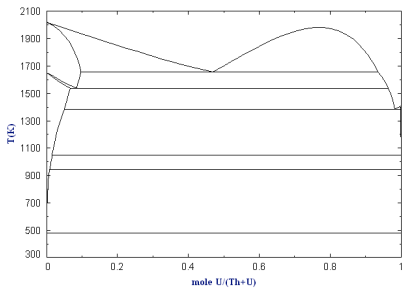

Fig.1: The optimized Th-U phase diagram

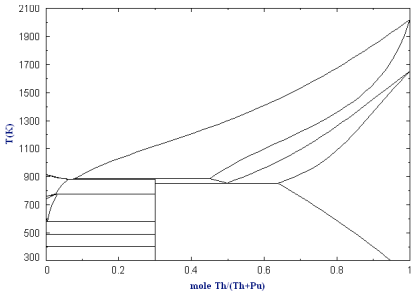

Fig.2: The optimized Th-Pu phase diagram

With the thus obtained database we will show how one can simulate the fuel behaviour under accidental conditions, i.e. at very high temperature at which the fuel matrix starts to vaporize, hence releasing the actinide containing species from the fuel element. Using the model it is possible to predict the exact composition of the vapour as well as that of the condensed matter at equilibrium for given temperature. It will be also shown how this vaporization behaviour is dependent on O/M ratio of the fuel. Comparisons will be made between the UO_2 fuel and fuel containing thorium and plutonium.

References

[1] C. Guéneau et al., *J. Nucl. Mater.* **304**, 161-175 (2002).

[2] C. Guéneau et al., *J. Nucl. Mater.* **378**, 257-272 (2008).

[3] M. Kurata, Calphad **23**, 305-337 (1999)

2-13

Influence of extreme conditions on the formation and structures of uranyl borates.

Evgeny V. Alekseev[1,2], Shijun Wu[3,4], Shuao Wang[5,6], Matthew Polinski[7], Wulf Depmeier[4], Thomas E. Albrecht-Schmitt[8]

[1]Institute of Energy and Climate Research (IEK-6), Forschungszentrum Jülich GmbH, Jülich, Germany, [2]Institut für Kristallographie, RWTH Aachen University, Aachen, Germany, [3]Guangzhou Institute of Geochemistry, Chinese Academy of Sciences, Guangzhou, China, [4]Institute of Geosciences, Kiel University, Germany, [5]Actinide Chemistry Group, Chemical Sciences Division, Lawrence Berkeley National Laboratory, Berkeley, California, USA, [6]Department of Chemistry, University of California, Berkeley, Berkeley, California, USA, [7]Department of Civil Engineering and Geological Sciences and Department of Chemistry and Biochemistry University of Notre Dame, Notre Dame, Indiana, USA, [8]Department of Chemistry and Biochemistry, Florida State University, Tallahassee, Florida, USA

Most of the nuclear borosilicate glasses contain some uranium and plutonium as well as minor transuranium elements such as neptunium and americium together with B_2O_3, Al_2O_3 and SiO_2. The chemistry of actinide silicates (especially uranium silicates) is well developed. Before our research, the chemistry of actinide borates was essentially uninvestigated. To understand the formation of actinide borates, as well the structures and properties, we have systematically studied the $A^I – An^{n+} – B_2O_3 – H_2O$ systems (where A^I – alkali elements and Ag, Tl; An^{n+} - actinide cations in different valence states).

Over the past three years, we developed the actinide borate chemistry by using boric acid as a reactive flux. The coordination sphere of An^{n+} coordination provided by oxo-borate polyhedra in the phases obtained from boric acid flux (normal conditions experiments) is quite similar. All phases (with only one exception, β-$UO_2B_2O_4$) possess six oxygen atoms donated by planar BO_3 triangles and/or BO_4 tetrahedra to an equatorial plane of the An^{n+} coordination environment. The An^{n+} cations are located in triangular holes of the polyborate 2D or 3D frameworks. This coordination remains in different actinide borates obtained from low/mild temperature conditions, even when different valences of the An atoms (from +3 to +6) is observed. It is noteworthy that in all these phases, the boron to actinides atomic ratios are greater than or equal to 1.

Next, we investigated structure-property relationships of actinide borates obtained from extreme conditions of both pressure and temperature (high-temperature/high-pressure, HT/HP). These phases demonstrate dramatic change in chemistry and structural properties. First of all, the chemical composition is different. We have synthesized several phases under extreme conditions and in all pure uranium borates the B/U ratio was smaller than 1. This observation shows a significant difference in thermodynamic stability of actinide borates with excess of the boron atoms at HT/HP conditions. The second point is the dramatic increase of the structural complexity of uranium borates from HT/HP reactions. The structure of the layers in HT/HP phases is totally different from the phases obtained under normal and mild conditions. U polyhedra are edge- or corner-sharing to form infinite 2D sheets. All boron oxo-polyhedra are BO_3 triangles and this is quite different from the phases obtained at normal conditions where BO_4 groups are the major content of the polyborate nets. The variation of UO_2^{2+} to BO_3 coordination is significant in HT/HP phases. For example, 10 different coordination schemes were observed in three HT/HP uranyl borates, viz. $K_{12}[(UO_2)_{19}(UO_4)(B_2O_5)_2(BO_3)_6(BO_2OH)O_{10}] \cdot nH_2O$, $K_4[(UO_2)_5(BO_3)_2O_4]\cdot H_2O$, and $K_{15}[(UO_2)_{18}(BO_3)_7O_{15}]$.

We then implemented the HT/HP methods for the preparation of mixed anion borates – aluminoborates and boronsilicates. It is necessary to mention that we were not able to get such phases from reactions at normal conditions. The borosilicates keep the pure HT/HP borate motifs with uranium polyhedra polymerization. In contrast, the uranium coordination in aluminoborate prepared at extreme conditions is practically identical to that we found in phases from normal conditions.

In conclusion, the structural and chemical complexity of uranyl borates obtained from HT/HP conditions is quite unusual for actinide borates from boric acid flux and for actinide oxo-salts chemistry in general.

2-14

Thermodynamic Study on the Complexation of Nd(III) and Cm(III) with Cyanex 301 in Ethanol

Chao Xu[1,2], Guoxin Tian[2], Linfeng Rao[2]

[1]*Institute of Nuclear and New Energy Technology, Tsinghua University, Beijing, China,* [2]*Chemical Sciences Division, Lawrence Berkeley National Laboratory, Berkeley, CA, USA*

Purified Cyanex 301, namely bis(2,4,4-trimethylpentyl)dithiophosphinic acid, has shown extremely high selectivity to An(III) over Ln(III) in solvent extraction.[1,2] Several experimental and theoretical studies have been performed to understand the driving force of this selectivity.[3-6] Thermodynamic study on the complexation of Ln(III) and An(III) with Cyanex 301 in homogeneous media would hopefully provide some additional knowledge and help to better understand the biphasic extraction behavior. In this work, complexation of Nd(III) and Cm(III) with purified Cyanex 301 (ammonium bis(2,4,4-trimethylpentyl)dithiophosphinate) has been investigated in ethanol with 1% v/v water. The species formed in the solution and their conditional stability constants were determined by spectrophotometric titration (Figure 1). For Nd(III), three successive complexes, NdL^{2+}, NdL_2^{+}, and NdL_3, where L^{-1} stands for the bis(2,4,4-trimethylpentyl)dithiophosphinate anion, formed in the solution. In contrast, four complexes, CmL^{2+}, CmL_2^{+}, CmL_3, and CmL_4^{-} were found to form successively during the titration. The formation of CmL_4^{-} was also confirmed by fluorescence lifetime measurements that suggested the presence of less than one water molecule remaining in the primary coordination sphere of Cm(III) with excess Cyanex 301 ligand (> 8 : 1 ligand to metal) in the solution. Meanwhile, the conditional stability constants for Cm(III)/Cyanex 301 complexes were found to be much higher than those of corresponding Nd(III) complexes. With the known stability constants, the enthalpies for the complexation of Nd(III) and Cm(III) with Cyanex 301 were measured by microcalorimetry, and the entropies were calculated thereby. Highly unfavourable enthalpies were found for both metals, which is mainly due to the energy required for the desolvation of both the cations (Nd and Cm) and the ligand. Interestingly, the enthalpy values were found to be similar for the complexes of Nd(III) and Cm(III). Therefore, the stronger complexation of Cm(III) with Cyanex 301 seems to result from more positive entropies of complexation.

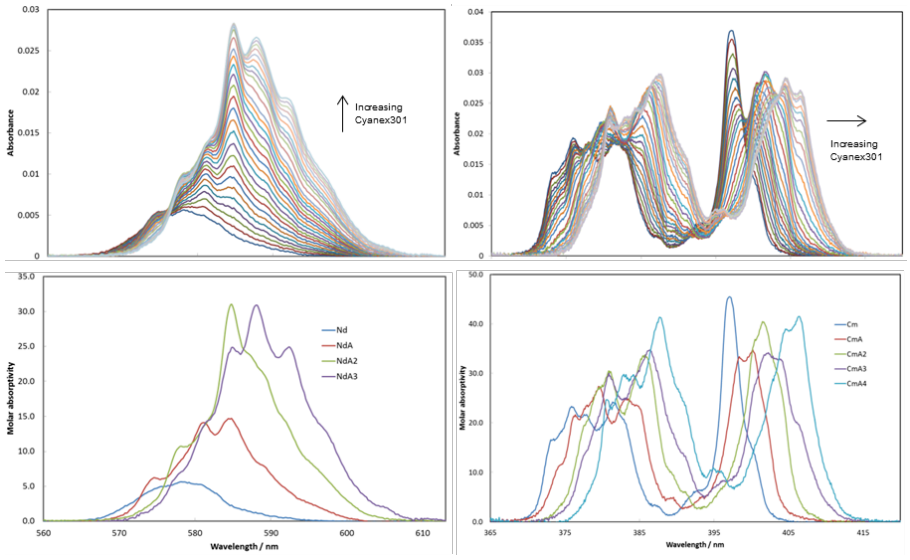

Figure 1. Spectrophotometric titrations of Nd(III) and Cm(III) with Cyanex 301 in ethanol (1% water). Up: absorption spectra normalized in terms of metal. Bottom: calculated molar absorptivity for different species.

References

[1] Chen, J.; Zhu, Y.; Jiao, R. *Sep. Sci. Technol.* **1996**, 31, 2723.

[2] Zhu, Y.; Chen, J.; Jiao, R. *Solvent Extr. Ion Exch.* **1996**, 14, 61

[3] Tian, G.; Zhu,Y.; Xu, J.; Hu, T.;Xie, Y. *J. Alloys Compd.* **2002**, 334, 86.

[4] Tian, G.; Zhu, Y.; Xu, J.; Zhang, P.; Hu, T.; Xie, Y.; Zhang, J. *Inorg. Chem.* **2003**, 42, 735.

[5] Jensen M.P.; Bond A.H. *J. Am. Chem. Soc.* **2002**, 124, 9870

[6] Cao X.; Heidelberg D.; Ciupka J.; Dolg M. *Inorg. Chem.* **2010**, 49, 10307

2-15

Electrochemical behavior and speciation of thorium with fluorides in molten salt at high temperature

David Rodrigues, Sébastien Jaskierowicz, Sylvie Delpech

CNRS-IPNO, Orsay, France

Thorium is currently studied as a fertile element in the nuclear fuel cycle for nuclear power plants of future generations. Under irradiation, thorium fuel produces ^{232}U which decreases to a very high radiotoxic element, ^{208}Tl. This type of fuel requires very special facilities and American researchers advocate the use of this fuel under liquid state, as a molten salt. The last concept of molten salt reactor, the MSFR (Molten Salt Fast Reactor) was developed by CNRS in France and the salt is constituted of $LiF\text{-}ThF_4\text{-}UF_4$ (77.5-19.5-3 mol%). The knowledge of the chemical and physical properties of this media is required to optimize the reactor operation and the reprocessing unit associated to this concept. In the frame of this work, we have studied the speciation of thorium with fluoride ions in a molten salt at high temperature.

This approach is based on the electrochemical study of ThF_4 in a chloride media (eutectic LiCl-KCl at 480°C) with fluoride ions. The complexa tion of Th(IV) with fluoride ions which increases the stability of Th(IV) is clearly observed on the cyclic voltammograms recorded. The analysis of potentiometric and voltammetric curves combined with an analytical and mathematical approach leads to the determination of complexation constants (β_i) [1] and to the calculation of the speciation diagram of Th(IV) with fluoride ions (figure 1).

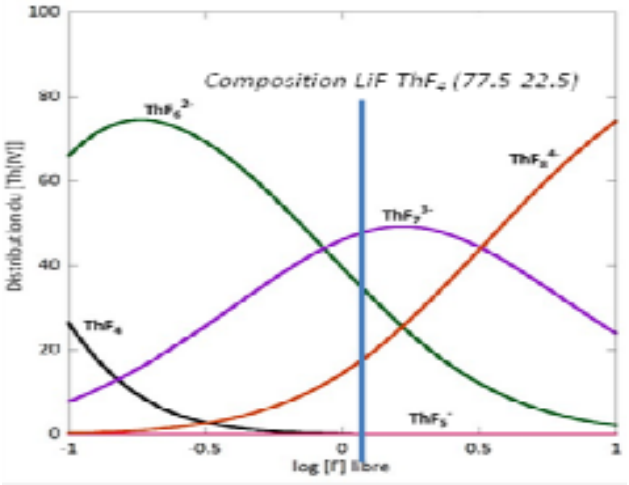

Fig.1: Speciation diagram of Th(IV) with fluoride ions in molten salt at high temperature

These results are in agreement with those obtained by NMR and EXAFS spectroscopy and reported by Pauvert and Bessada [2].

References

[1] F. Séon, These de l'UPMC, 1981

[2] O. Pauvert, Thèse de l'Université d'Orléans, 2009

2-16

Electrorefining of irradiated metallic fuel with limited Zr dissolution

Tsuyoshi Murakami[1], Tetsuya Kato[1], Tadafumi Koyama[1], Alcide Rodrigues[2], Michel Ougier[2], Jean-Paul Glatz[2]

[1]Central Research Institute of Electric Power Industry, Tokyo, Japan, [2]Institute of Transuranium Elements, Karlsruhe, Germany

Pyroprocessing is one of the key processes to provide a nuclear energy cycle which is regarded as a prospective energy source for the next generation [1]. The pyroprocessing technology is also applied in partitioning and transmutation scenarios and is considered to be one of the feasible options to stabilize damaged spent nuclear fuel debris. Electrorefining, which uses a molten salt as the electrolyte, is the main step for the spent metallic fuels pyroprocessing. Actinides, which anodically dissolve, are recovered on the cathode. Rare earth, alkaline and alkaline earth fission products dissolve from the anode and remain in the melt, while noble metal fission products remain in the anode. A part of Zr (one of main components of metallic fuel) dissolves from the anode, burdening the pyroprocessing; the dissolved Zr is deposited on the wall of electrorefiner and collected on the cathode as U-Zr alloy. A periodical operation to remove the deposited Zr on the wall is required. Due to the higher melting point of the U-Zr alloy than that of U metal, higher temperature is required to consolidate the deposits for a following cathode process. Therefore, it is obvious that the electrorefining should be operated minimizing the amount of dissolved Zr. In this study, three electrorefining runs (RUN-1, RUN-2 and RUN-3) using irradiated metallic fuels (U-19wt%Pu-10wt%Zr alloy irradiated at the PHENIX reactor in France, approximate maximum burn-up: 2.5 at%, diameter including the cladding: 6.55 mm, so-called METAPHIX-1 fuel [2], Fig. 1) were performed to demonstrate the limited Zr dissolution.

All experiments were carried out using a small scale electrorefiner installed in a shielded caisson at the Institute of Transuranium Elements. Both oxygen and water concentrations in the caisson were kept below 20 ppm. Eutectic LiCl-KCl, initially containing 1.26 mol% UCl_3 and 0.05 mol% $PuCl_3$, was melted at 773 K. METAPHIX-1 fuel segments were loaded in an anode basket (Table 1). A low carbon steel rod was used as the cathode and rotated at 50 rpm during the electrolysis. Although a conventional Ag/AgCl reference electrode is often used to investigate the electrochemical behavior of actinides in the LiCl-KCl melt, a previous study revealed that the life time of the Ag/AgCl reference electrode was significantly shorten in a high radiation environment [3]. Therefore, a W wire on which U metal was electrochemically deposited in the melt was used as a quasi-reference electrode. The potential of the quasi-reference electrode was calibrated against a Ag/AgCl reference electrode by immersing this reference electrode shortly in the melt.

Since Zr metal was found to dissolve in the melt at more positive potential than -1.0 V based on the polarization measurement of Zr metal, the anodic potential or applied current was controlled to limit the Zr dissolution as listed in Table 1. At the end of each run, a dendritic deposit was obtained on the solid cathode (Fig. 2) and the remnants in the anode basket (anode residues) were recovered (Fig. 3). SEM-EDX observations revealed that the anode residue was composed of three distinct concentric areas: porous Zr at the center and outer areas and aggregated Zr particles at the middle area. It was also observed that noble metals were retained in the structures of the anode residue. ICP-MS analysis confirmed that electrorefining of METAPHIX-1 fuel segments with a high dissolution ratio of actinides (U: 98.9 %, Pu: 99.8 %, Np: 99.0 %, Am: 98.9 %) was successfully demonstrated leaving most of Zr (remaining ratio: 82.5 %) and noble metals (remaining ratio: 80~90 %) in the anode residues. Likewise it was found that the actinides and rare earths dissolved in the melt with the progress of the electrolysis, while the dissolution of alkalis and alkaline earths occurred independently of the progress of the electrolysis.

References

[1] T. Koyama, T. Ogata, M. Myochin and Y. Arai, Proceedings of Global 2011, Makuhari, Japan, December 11-16, 2011, Paper No. 452983.

[2] H. Ohta, T. Ogata and T. Yokoo, Nucl. Technol., 165 (2009) 96.

[3] T. Kato et al., Proceedings of Global 2011, Makuhari, Japan, December 11-16, 2011, Paper No. 452983.

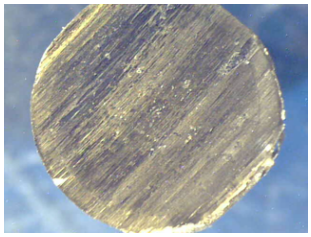

Fig. 1 Cross section of METAPHIX-1 fuel segment before electrorefining.

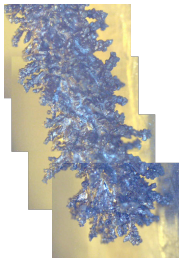

Fig. 2 U metal dendrite deposited on the solid cathode.

Fig 3 Cross section of METAPHIX-1 fuel segment after electrorefining. The surface was polished.

Table 1 Experimental condition of RUN-1, RUN-2 and RUN-3.

	METAPHIX-1 fuel segment		Electrolysis	Total passed charge (C)
	Length (mm)	Weight (g)		
RUN-1	5.60	2.11	Potentiostatic electrolysis at -1.0 V vs. Ag/AgCl	5262
	5.35	1.97		
	4.85	1.93		
RUN-2	5.45	2.03	Galvanostatic electrolysis (upper limit potential -1.0 V vs. Ag/AgCl)	4887
	5.47	2.04		
	5.80	2.03		
RUN-3	3.40	1.26	Potentiostatic electrolysis at -1.04 V vs. Ag/AgCl	3777
	8.80	3.17		

2-17

Evaluation of stability of uranyl peroxide compounds in solution

Kwang-Wook Kim, Keun-Young Lee, Eil-Hee Lee, Dong-Yong Chung, Euo-Chang Jung, Jei-Kwon Moon

Korea Atomic Energy Research Institute, Daejeon, Republic of Korea

A carbonate-based process, which is for recovery of uranium from dirty UO_2 fuel scraps generated during nuclear fuel fabrication, has been recently developed [1]. In the process, UO_2 is selectively dissolved to form uranyl peroxo carbonate complex ion, $UO_2(O_2)(CO_3)_2^{4-}$, with a high solubility in carbonate solutions that contain H_2O_2. On the other hand, the impurity solids-contaminating the uranium scraps such as Fe, Ni, Al materials, etc. are hardly dissolved, because of their very low solubilities in the carbonate solution at high pH. The uranium is recovered as a precipitate of uranyl peroxide,UO_4 with very low solubility by acidifying the uranyl peroxo-carbonato complex ion solution to pH 2 to 3, while partially-dissolved impurity metal ions remaining in the UO_4 supernatant at acidic condition.

H_2O_2 is known to be easily decomposed into water and oxygen in heated alkaline solutions. Accordingly, evaluation of the stability of uranyl peroxo compounds of $UO_2(O_2)(CO_3)_2^{4-}$ and UO_4 is very necessary to ensure the concentration does not change during prolonged storage in the carbonate-based process. When $UO_2(O_2)(CO_3)_2^{4-}$ and UO_4 lose their peroxide component, they change into stable species of $UO_2(CO_3)_3^{4-}$ and UO_2^{2+}, respectively. However, there have been very little studies on the stability of such uranyl peroxide materials to date. In this study, decomposition rate of the uranium peroxo-carbonato complex in carbonate solution and stability of UO_4 in several solutions were investigated at several temperatures using absorption and Raman spectroscopies.

Fig.1 shows the changes in peroxide concentrations with time in the solutions at 25, 40, 60, 80°C in a uranyl peroxo carbonate solution which was prepared by dissolving UO_2 powder (4.2×10^{-2} M) in 0.5 M Na_2CO_3 containing 1.0 M H_2O_2. The initial rapid decrease in O_2^{2-} concentration is attributed to the decomposition of excess H_2O_2 that remained in the solution after completely dissolving the UO_2, where all the uranium in the solution was confirmed to form the $UO_2(O_2)(CO_3)_2^{4-}$ ion. From that time on, the very slow change in O_2^{2-} concentration in the solution is ascribed to the decomposition of O_2^{2-} complex in the $UO_2(O_2)(CO_3)_2^{4-}$ change into $UO_2(CO_3)_3^{4-}$ by releasing O_2^{2-} into solution. Fig.2 shows the change in absorption spectrum of a diluted $UO_2(O_2)(CO_3)_2^{4-}$ solution of 2.8×10^{-4} M at 80°C with time. The initial solution showed a typical absorption spectrum of $UO_2(O_2)(CO_3)_2^{4-}$ with a peak near 341 nm and a shoulder near 410 nm. The absorption spectrum gradually disappeared with time. Instead, the trace of absorption peaks of $UO_2(CO_3)_3^{4-}$ complex appeared at 435, 448, and 462 nm. Too high extinction coefficient of $UO_2(O_2)(CO_3)_2^{4-}$ solution made the absorbance spectroscopy difficult in evaluation of the solution stability.

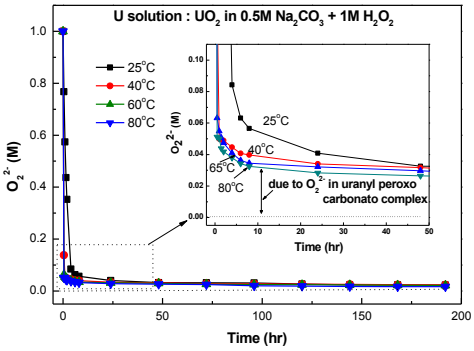

Fig.1 Change of O_2^{2-} concentration in $UO_2(O_2)(CO_3)_2^{4-}$ solutions at different temperatures.

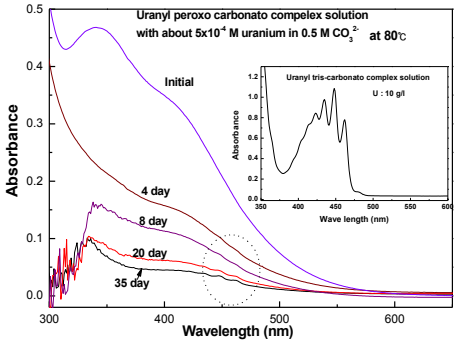

Fig.2 Change of absorbance of $UO_2(O_2)(CO_3)_2^{4-}$ solution 80°C with time.

Fig.3 shows the change of Raman spectra of $UO_2(O_2)(CO_3)_2^{4-}$ solution at 60°C with time. The relative ratio of the Raman band intensities of $UO_2(O_2)(CO_3)_2^{4-}$ at 769 cm^{-1} to $UO_2(CO_3)_3^{4-}$

at 811 cm^{-1} decreased with time. However, the intensities of the Raman bands at 848 cm^{-1} and 727 cm^{-1}, which are thought to be $UO_2(O_2)_2^{2-}$ and $UO_2(CO_3)_x(OH)_y^{2-2x-y}$, were not almost changed without a significant shift of Raman bands. These results indicate that only $UO_2(O_2)(CO_3)_2^{4-}$ continuously changes into $UO_2(CO_3)_3^{4-}$ because of the instability of O_2^{2-} in $UO_2(O_2)(CO_3)_2^{4-}$ in alkaline condition. When the initial concentration of $UO_2(O_2)(CO_3)_2^{4-}$ is known, the concentration of $UO_2(O_2)(CO_3)_2^{4-}$ in the mixture of $UO_2(O_2)(CO_3)_2^{4-}$ and $UO_2(CO_3)_3^{4-}$ can be evaluated by measuring the concentration of $UO_2(CO_3)_3^{4-}$ in the solution, because the calibration curve of $UO_2(CO_3)_3^{4-}$ solution by Raman spectroscopy can be stalely and correctly made, as shown in Fig.4. Table 1 shows the comparison between the concentrations of $UO_2(O_2)(CO_3)_2^{4-}$ measured by Raman and the concentrations of O_2^{2-} measured directly in the solution as time elapsing after the preparation of $UO_2(O_2)(CO_3)_2^{4-}$ solution. The concentrations agree relatively well, within a deviation of less than 5%, which confirms that the molar ratio of U and O_2^{2-} in the uranyl peroxo carbonato complex ion is 1:1. These results reveal that measurement of O_2^{2-} in the mixture solution of $UO_2(O_2)(CO_3)_2^{4-}$ and $UO_2(CO_3)_3^{4-}$ can represent the concentration of $UO_2(O_2)(CO_3)_2^{4-}$ in the solution.

Table 1 Change of measured concentrations of $UO_2(O_2)(CO_3)_2^{4-}$ by Raman and O_2^{2-}

day	by Raman spectroscopy (M)	by peroxide assay (M)	deviation (%)
4	$7.33x10^{-2}$	$7.61x10^{-2}$	3.9
16	$6.94x10^{-2}$	$7.27x10^{-2}$	4.7
240	$3.59x10^{-2}$	$3.77x10^{-2}$	4.8

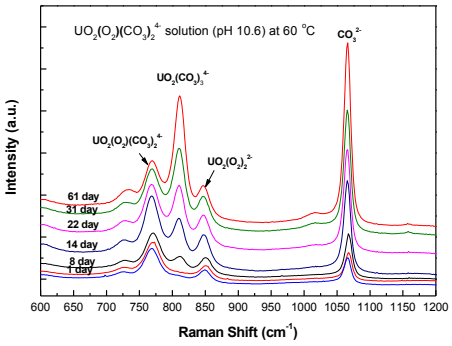

Fig.3 Change of O_2^{2-} concentration in $UO_2(O_2)(CO_3)_2^{4-}$ solutions at different temperatures.

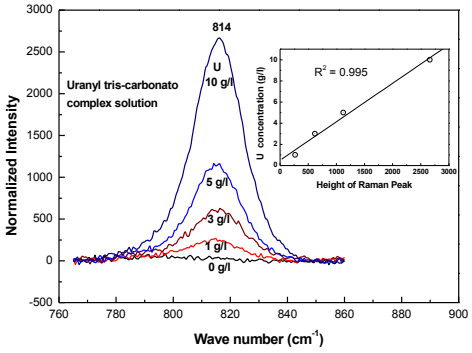

Fig.4 Raman spectrum of $UO_2(CO_3)_3^{4-}$ with different U concentrations.

Based on the above results, the decomposition rate of $UO_2(O_2)(CO_3)_2^{4-}$ into $UO_2(CO_3)_3^{4-}$ could be evaluated using data on the change of O_2^{2-}in the solution in Fig.1. The liner plot of ln k (rate constant) vs. 1/T could be obtained, as shown in Fig.5 with an assumption of the decomposition reaction with first order, and the decomposition rate was able to be expressed as shown in Eq.(1).

$$- r = -dC/dt = 78.5 \exp(- 8.59x10^2/T)\, C, \qquad (1)$$

where r, C, T. t are the decomposition rate (mole/s), concentration of $UO_2(O_2)(CO_3)_2^{4-}$ (mole/l), temperature (K), time (s) respectively.

Fig.6 shows the concentration change of UO_2^{2+} dissolved from UO_4 that was stored in several conditions. UO_4 was not significantly dissolved from all the samples at 25℃ in the conditions adjusted by pH and ionic strength. However, all the samples at higher temperatures in acidic conditions showed significant uranium dissolution with time.

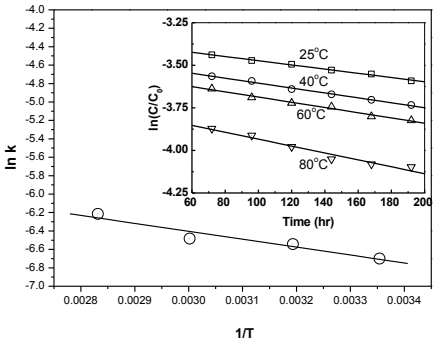

Fig.5 Dependence of the rate constant on temperature for the decomposition reaction

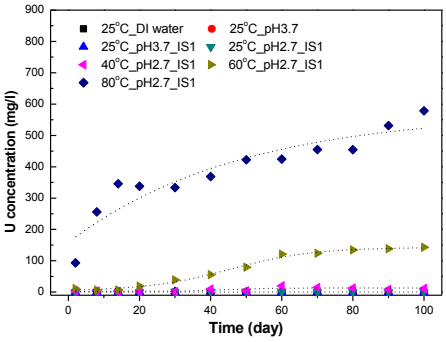

Fig.6 Changes of dissolved uranium concentrations from UO_4 in several conditions

References

[1] K.-W. Kim, et al, J. Nucl. Mat., **418**, 93 (2011)

3-11

The Redox Potential of Mendelevium (Md) Determined Atom-at-a-Time with a Flow Electrolytic Column

Matthias Schädel[1,2], Atsushi Toyoshima[1], Zijie Li[1], Masato Asai[1], Nozomi Sato[1], Takahiro Kikuchi[1], Yusuke Kaneya[1], Yoshihiro Kitatsuji[1], Kazuaki Tsukada[1], Yuichiro Nagame[1], Kazuhiro Ooe[1,3], Yoshitaka Kasamatsu[3], Yuka Kogoma[3], Atsushi Shinohara[3], Hiromitsu Haba[4], Julia Even[5]

[1]Japan Atomic Energy Agency (JAEA), Tokai, Japan, [2]GSI Helmholtzzentrum für Schwerionenforschung GmbH, Darmstadt, Germany, [3]Osaka University, Osaka, Japan, [4]RIKEN, Wako, Japan, [5]Mainz University, Mainz, Germany

It is fascinating and challenging to determine chemical properties of the heaviest elements to unravel the interplay between increasingly strong relativistic and shell effects at the far end of the Periodic Table [1]. For the actinides, theory shows that the relativistic expansion of the 5f orbital leads to the actinide contraction because the central nuclear charge becomes less shielded by the expanded 5f electrons. This leads to shrinkage of the outer valence orbitals [2]; i.e., the 5f orbital gets relativistically destabilized while the outer orbitals are stabilized. Beyond fermium, these energetic levels are not yet directly accessible in spectroscopic studies. However, radiochemical measurements of M^{3+} to M^{2+} redox potentials, which are related to the third ionization potential, can provide insights into the stability of valence electrons.

Beginning with element 101, mendelevium (Md), all these elements are only accessibly through heavy-ion reactions at accelerators. Therefore, only short-lived radioisotopes of these elements become available atom-at-a-time. This significantly constrains the use of chemical techniques and procedures. Hulet et al. [3] reduced Md^{3+} with reducing agents and determined properties for the reduced species typical for divalent actinide ions. They deduced the redox potential to be about -0.2 V vs. a normal hydrogen electrode (NHE). From similar experiments Maly and Cunningham [4] deduced a redox potential of about -0.1 V vs. a NHE. However, the limited exactness of measurements with reducing agents and other potential imperfections of these experiments called for a precise determination of the redox potential of the $Md^{3+} + e^- \rightleftarrows Md^{2+}$ couple.

Our present study of the Md redox potential exploits a novel electrochemical method of flow electrolytic column (FEC) chromatography developed for single ions [5]. Carbon fibres modified with Nafion perfluorinated cation-exchange resin simultaneously serve as working electrodes and as cation-exchanger. Earlier, this technique was successfully applied to the oxidation of No^{2+} to No^{3+} [6].

^{255}Md was produced at the JAEA tandem accelerator in reactions of ^{11}B with ^{248}Cm and was transported to the chemistry set-up by a He/KCl gas-jet. In a first step, Md was separated from KCl by column chromatography. Dried Md samples were dissolved in 0.1 M HCl and were fed onto the FEC modified by a Nafion perfluorinated ion-exchange resin. An appropriate pretreatment of solvents and the FEC ensured oxygen-free operation. Potentials between -0.3 and -0.9 V vs. a Ag/AgCl reference electrode (SSE) in 1.0 M LiCl were applied to the working electrode. The effluent (0.1 M HCl) passed through the column at a flow rate of 0.8 mL/min. The elution position of divalent Md ions was determined by collecting samples on Ta discs. Remaining trivalent products were stripped from the column with 3.0 M HCl and were also collected. All samples were evaporated to dryness. Alpha spectroscopic measurements started ~12 min after end of the last KCl collection and were performed for ~90 min. The counting efficiency and energy resolution was ~30% and ~60 keV (FWHM), respectively. After these measurements, the content of ^{250}Bk, present in these samples as a nuclear reaction by-product, was determined by γ-spectroscopy. Bk served as one of the reference elements for the behaviour or trivalent actinides. Prior to the Md experiments, the elution behaviour of trivalent lanthanides from the FEC has been determined as well as their separation from Sr^{2+} and (reduced) Eu^{2+} ions. Preparatory experiments showed that at an applied potential of -0.2 V Eu^{3+} is stripped with 3 M HCl together with trivalent lanthanides while at -1.0 V Eu^{2+} appeared quantitatively together with Sr^{2+} in the 0.1 M HCl. This shows that at this potential Eu^{3+} is completely reduced to Eu^{2+} and that it is clearly separated from trivalent ions.

In the Md experiment, reduction probabilities (%Red), defined by %Red = 100 × A_1 / (A_1 + A_2) where A_1 and A_2 are the amounts of Md and Eu observed in 0.1 M HCl and 3.0 M HCl fractions, respectively, were measured as a function of the applied potential. The reduction probability of Md sharply increases to about 100% when going from -0.3 V to -0.6 V while a similar behaviour for Eu is observed between -0.6 V to -0.9 V. From the 50% reduction probability values, redox potentials of the $Md^{2+} \rightleftarrows Md^{3+} + e^-$ and $Eu^{2+} \rightleftarrows Eu^{3+} + e^-$ couples are presently evaluated and will be discussed in our presentation. These results will be compared with the ones from previous experiments [3, 4] and with empirical and theoretical predictions.

References

1. Schädel, M. (Ed.) The Chemistry of Superheavy Elements, Kluwer Academic Publishers, Dordrecht (2003); Schädel, M. Angew. Chem. Int. Ed. **45**, 368 (2006); Türler, A. and Pershina, V. Chem. Rev. **113**, 1237 (2013).

2. Pyykkö, P. Chem. Rev. **88**, 563 (1988); Küchle, W., Dolg, M., Stoll, H. J. Phys. Chem. A **101**, 7128 (1997).

3. Hulet, E.K. et al. Science **158**, 486 (1967).

4. Maly, J., Cunningham, B. B. Inorg. Nucl, Chem. Lett. **3**, 445 (1967).

5. Toyoshima, A. et al. Radiochim. Acta **96**, 323 (2008).

6. Toyoshima, A. et al. J. Am. Chem. Soc. **131**, 9180 (2009).

3-12

The first successful ionization of Lr (Z=103) by a surface ionization technique

Tetsuya K. Sato[1], Masato Asai[1], Nozomi Sato[1], Kazuaki Tsukada[1], Atsushi Toyoshima[1], Sunao Miyashita[1], Kazuhiro Ooe[5], Matthias Schaedel[1], Yusuke Kaneya[2,1], Yuichiro Nagame[1], Akihiko Osa[1], Shin-ichi Ichikawa[3], Thierry Stora[6], Jens Volker Kratz[4]

[1]Japan Atomic Energy Agency, Tokai, Japan, [2]Ibaraki University, Mito, Japan, [3]RIKEN, Wako, Japan, [4]Maintz University, Maintz, Germany, [5]Niigata University, Niigata, Japan, [6]CERN, Geneva, Switzerland

The first ionization potential (IP) is a fundamental physical and chemical property of an element. It directly reflects the electronic configuration of the element. Relativistic effects which affect the electronic configuration of the element would be particularly noticeable for heavy elements. Information on the IP of the heaviest elements, therefore, can provide a better understanding of relativistic effects. The elements heavier than fermium (Fm, Z = 100) must be produced at accelerators using reactions of heavy ions with heavy target materials. Moreover, both half-lives and cross sections of the isotopes of the still heavier elements are rapidly decreasing. Thus, they are usually available in quantities of a few atoms only at a time. Consequently, beginning with about the end of the actinides, properties of the heaviest elements must be studied on an atom-at-a-time scale. The IP values of the heavier actinides with Z > 100, therefore, have not been measured using well-established methods like resonance ionization mass spectroscopy (RIMS) [1].

Lawrencium (Lr, Z = 103) is the heaviest actinide element. The electronic configuration in its ground-state is predicted to be [Rn]$5f^{14}7s^{2}7p_{1/2}$, which is different from that of the lanthanide homolog lutetium (Lu) [Xe]$4f^{14}6s^{2}5d$. The reason for this change in the ground-state configuration is that the 7p orbital of Lr is stabilized below the 6d orbital by strong relativistic effects [2]. The weakly-bound outermost electron results in a significantly lower IP of Lr as compared to those of neighbouring heavy actinides [3]. With an experimentally determined IP of Lr, we can contribute to a better understanding of shell effects and how relativistic effects play a role in the electronic structure of heavy atoms.

For this purpose, we have been developing a novel IP measurement method for the heavy actinide elements on an atom-at-a-time scale as an application of an ISOL (Isotope Separator On-Line) technique. We have developed a surface ionization type ion-source as part of the JAEA-ISOL setup [4], which is coupled to a gas-jet transport system with novel aerosol material, CdI_2 [5]. The surface ionization process in the ion-source depend on the temperature, and the work function of the surface of the ion-source, and on the IP of the atom of interest. Thus the ionization behaviour of the element would provide us information on its IP. As a first step to determine the IP of Lr, we ionized a short-lived Lr isotope by using the ion-source under several ionization conditions.

The isotope ^{256}Lr ($T_{1/2}$ = 27 s) was produced in the reaction of ^{249,250,251}Cf(^{11}B, xn)^{256}Lr [6]. A ^{249,250,251}Cf target (^{249}Cf : 63%, ^{250}Cf : 12%, and ^{251}Cf : 25%) with 185 ± 25 μg/cm^2 on a 1.85 mg/cm^2 thick Be backing foil was irradiated with a 67.9-MeV $^{11}B^{4+}$ beam from the JAEA tandem accelerator. The beam energy was calculated to be 63 MeV in the middle of the target. For comparison, the lutetium isotopes ^{168m}Lu and ^{168g}Lu, with half-lives of 6.7 min and 5.5 min, respectively, were synthesized in the ^{162}Dy(^{11}B, 5n) reaction. The reaction products recoiling from the targets were transported to the ion-source by the He/CdI_2 gas-jet transport system. The products were ionized in the ion-source at 2600 K, accelerated with 30-kV, and then mass-separated with a mass-separator being part of the ISOL. The amount of collected ions at the end of the ISOL after mass-separation was determined by α-particle or γ-ray measurements. To calculate ionization efficiencies, nuclear reaction products transported from a target recoil chamber were collected directly and measured in advance of the ionization experiments.

To compare the ionization efficiency on a surface material of the ion-source, a rhenium (Re) surface and a tantalum (Ta) surface were employed in this study. The temperature of the ion-source was measured with a radiation thermometer. The ionization efficiencies of Lr and Lu on the Re surface were 42^{+20}_{-19}% and 19.9 ± 7.0%, respectively. In the case of the Ta surface, the ionization efficiencies of Lr and Lu were 19^{+9}_{-8}% and 4.0 ± 1.4 %, respectively. In both ionization conditions, the ionization efficiency of Lr is larger than that of Lu. The results

indicate that the IP of Lr must be lower than that of Lu, 5.426 eV [7], which is consistent with the prediction by a theoretical calculation [3].

We will report on the first experimental determination of the IP of Lr based on these results.

References

1. Köhler, S. et al. Angew. Chem. Int. Ed. **35**, 2856 (1996).

2. Zou, Y. and Fischer, C. F. Phys. Rev. Lett. **88**, 183001 (2002).

3. Borschevsky, A. et al. Eur. Phys. J. D**45**, 115 (2007).

4. Ichikawa, S. et al. Nucl. Instr. and Meth. A **374**, 330 (1996).

5. Sato, T. K. et al. Rev. Sci. Instrum. **84**, 023304 (2013).

6. Sato, N. et al. JAEA Rev. **2010-056**, 52 (2010).

7. Handbook of Chemistry and Physics, 65th ed., edited by W. H. Beyer et al. (CRC, 1985).

3-13

EXAFS Study of *f*-Elements Thiocyanate Complexation

Marisol Janeth Lozano Rodriguez[1], Christophe Den Auwer[2], José Mustre de León[3]

[1]HELMHOLTZ Zentrum Dresden Rossendorf (HZDR), Institute of Resource Ecology, Dresden, Germany, [2]Université de Nice Sophia Antipolis, Institute de Chimie de Nice, Nice, France, [3]CINVESTAV, Mérida, Department of Physics, Mérida Yucatan, Mexico

The search for alternative ways of exploring and understanding the intra-molecular interactions in lanthanide and actinide molecules with adequate ligands has always been essential to progresses in the chemistry of the actinide elements. In the case of the light actinides, the 5*f* orbital are partially screened, thus allowing a greater radial expansion. As a result there is a versatility of oxidation states for the first half of the series. For heavy actinides the increase in nuclear charge causes an additional contraction of the 5*f* orbitals. This decreases the metal-ligand overlap, making the trivalent oxidation state the dominant one. This behaviour is similar to that of the lanthanides where the 4*f* orbitals are less screened by the external influence of the 5*s* and 5*p* electrons, where the trivalent state being the dominant oxidation state just like it is for the heavy actinides.

Comparative studies of chemical reactivity between heavy trivalent actinides (An) and lanthanides (Ln) have always been a challenging issue because of their analogous behaviour. In an effort to better understand the complexation of the lanthanides and actinides elements we have chosen the thiocyanate ligand $(NCS)^-$ to their study. Because this anion is highly versatile, monodentate or bidentate coordination is often found, where it has two possible reaction centers, one *via* nitrogen and other one *via* sulfur, depending on the response of the cation to the nucleophilic behavior of the ligand. For this study, lutetium, neodymium and thorium, have been selected as hard acids according Person's theory.

Crystal structures of $[n\text{-}(C_4H_9)_4N]_3[Lu(NCS)_4(NO_3)_2]$ **(1)**, $K_4[M(NCS)_4(H_2O)_4(NCS)_3(H_2O)_2$ where M= Nd^{3+} **(2)**, Lu^{3+} **(3)**, and $[n\text{-}(C_4H_9)_4N]_3[Th(NCS)_4(NO_3)_3]$ **(4)** were obtained. XRD data show that these hard acids cations are N-bonded thiocyanate complexes as expected. The structure of **1** includes two values for Lu-N bond distances at 2.332(2) Å and 2.313(2) Å which are slightly shorter than in $[Yb(NCS)_4(NO_3)_2]^{3-}$ structure at 2.342(10) Å and even shorter than in the analogous $[Nd(NCS)_4(NO_3)_2]^{3-}$ at 2.452(11) Å, both reported previously [3]. These results are consistent with the lanthanide contraction when crossing the series from Nd to Lu.

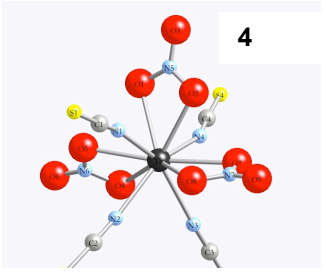

Fig. 1 Crystal structure of $[Th(NCS)_4(NO_3)_3]_{3-}$

Complexes **2** and **3** are isomorphous and each cation is coordinated to four thiocyanate ligands through Ln-N bond. The average Ln-N distance decreases in the order Nd to Lu, 2.477 Å and 2.331 Å respectively, according to the lanthanide contraction [1]. Finally the Th^{4+} compound **4** is bound to four N atoms of thiocyanate where the average Th-N bond is 2.481(10) Å (Fig. 1). The M-O bidentate nitrate distances are consistent with the values reported in the literature [2].

EXAFS spectroscopy was also carried out at the Lu L_{III}-edge (9244 eV) and Th L_{III}-edge (16300 eV) at the MARS beamline of SOLEIL and at Rossendorf Beamline (BM20) of ESRF, respectively. In order to validate the fitting method of such family compounds, the spectra of **1** and **4** were recorded. Distances around the absorbing atom were consistent with the XRD values (Table). EXAFS spectra of **1** and **4** are shown in Fig. 2 (top). Fourier transform of the EXAFS spectra show characteristic peaks related with the local structure around the metal, thiocyanate and nitrate ligands, mainly (bottom). Single scattering contributions of the first neighbors of N_{thio} and O_{nit} are convoluted in the first peak (A). Single and multiple scattering contributions from the carbon atoms of the thiocyanate (B), from the distal oxygen atoms of the nitrate (C) and from sulfur atoms of the thiocyanate (D) represented in the subsequent peaks have been taken account to fit the data. Applying the knowledge of similar behaviour of the lanthanide to heavy actinides, one americium compound has been synthesized following

the same procedure. EXAFS measurement of Am L_{III}-edge (18510 eV) was used to characterize the final red paste compound of Am. Results of the fit are shown in Table. Fig. 2 exhibits the EXAFS spectrum for Am **5**.

		XRD	EXAFS		
Complex		R(Å)	R(Å)	CN	σ^2(Å^2)
1	Lu-N_{thio}	2.322 (2)	2.32 (3)	4	0.0012 (4)
	Lu-O_{nit}	2.400 (2)	2.44 (3)	4	0.0030 (4)
	Lu---S	5.093 (5)	5.12	4	0.0085 (3)
S_0^2= 0.99, E_0=2.56 eV, R factor=2.3%					
4	Th-N_{thio}	2.481 (10)	2.50 (3)	4	0.0058 (3)
	Th-O_{nit}	2.57 (3)	2.61 (3)	6	0.0012 (3)
	Th---S	5.22	5.23	4	0.0094 (3)
S_0^2= 1.32, E_0=1.44 eV, R factor=6.8%					
5	Am- N_{thio}	-	2.49 (3)	2	0.0018 (3)
	Am-O_{nit}	-	2.61 (3)	8	0.0137 (3)
	Am---S	-	5.32	2	0.0072 (3)
S_0^2= 1.09, E_0=2.72 eV, R factor=3.1%					

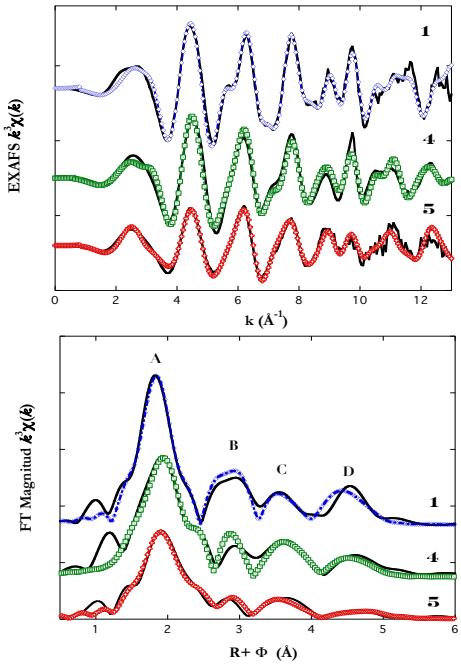

Fig. 2 Lu, Th and Am L_{III} edge EXAFS spectra and their Fourier Transform. Experimental data are displayed in line, fit are displayed in symbols.

Fourier transform of the EXAFS is also shown at the bottom of the Figure. In a first attempt, the coordination number was maintained fixed according to the structure of $[Nd(NCS)_2(NO_4)_4]^{3+}$ reported previously, where the mean Nd-N and Nd-O bond distances are 2.506(4) Å and 2.57(3) Å, respectively [3]. The Am-N_{thio} distance at 2.49 Å is in agreement with the value reported by Farmer and with the Nd-N_{thio} distance found in **2** in this work. However a decrease on the contribution of sulfur peak at ~5 Å was found, revealing a diminution of the thiocyanate coordination. This is in contrast with the nitrate contributions for which the peak ~3 Å is still present. These EXAFS results suggest that thiocyanate ligands are weaker coordinated than nitrate ligands to heavy actinides -as americium-.

References

[1] M. J. Lozano-Rodriguez et al., *New, J. Chem.*, 2011, **35**, 2755

[2] M. J. Lozano-Rodriguez et al., *Acta Cryst.* (2011) **E67**, m487

[3] J. M. Farmer et al., *J. Chem Crystallogr.*, 2000, **30**, 301

3-14

Probing and Quantifying Orbital Mixing in *f*-Element Molecular Bonding

Matthias W. Loeble[1], Jason M. Keith[1], Paul H. Tobash[1], Brian L. Scott[1], Angela C. Olson[1], Stefan G. Minasian[1,2], Scott R. Daly[3], Kevin S. Boland[1], Eve Bauer[1], Kathy Dardenne[4], Joerg Rothe[4], Tonya Vitova[4], Tsu-Chien Weng[5], Dimosthenis Sokaras[5], Franz J. Freibert[1], Richard L. Martin[1], Enrique R. Batista[1], David L. Clark[1], Stosh A. Kozimor[1]

[1]Los Alamos National Laboratory, Los Alamos, New Mexico, USA, [2]Lawrence Berkeley National Laboratory, Berkeley, California, USA, [3]The George Washington University, Washington DC, USA, [4]Karlsruhe Institute of Technology (KIT), Karlsruhe, Baden-Wuerttemberg, Germany, [5]Stanford Synchrotron Radiation Lightsource (SSRL), Menlo Park, California, USA

The covalent sharing of electrons between elements to form chemical bonds represents a fundamental concept in chemistry. Covalency is routinely used to explain reactivity and physical properties across the periodic table. For transition metals, the 3*d*- 4*d*, and 5*d*-orbitals extend well into the periphery of the atom and can interact with valence orbitals of the ligand to form covalent chemical bonds. The situation is more complicated for *f*-elements, and the extent to which these elements participate in covalent bonding remains uncertain.[1]

This is especially true for the 5*f*-elements, where decades of study using optical spectroscopy to probe valence 5*f*-orbitals have supported the viewpoint that 5*f*-orbitals are core-like, only weakly perturbed by ligand fields, and not generally involved in covalent bonding.

As we could show recently, octahedral binary chlorides MCl_6^{2-} (M = Ti, Zr, Hf, U) provide a highly symmetric platform for directly comparing the electronic structure and bonding of *d*-block transition metal elements to those of the actinides.[2] Based on the structural metrics, one might anticipate that bonding for these compounds is best be described as ionic with little variation in orbital mixing down the periodic table (Ti to Th) and across the actinide series (Th to Pu). However, Ligand K—edge absorption spectroscopy (XAS) on the chlorine K-edge in combination with time-dependent density functional theory (TDDFT) and hybrid ground state DFT calculations provided unambiguous evidence for M–Cl covalency with a clear trend toward increased orbital mixing from Ti, to Zr, to Hf and to U in the MCl_6^{2-} (M = Ti, Zr, Hf, U) compounds.

In this presentation, we will extend these efforts in Ligand Cl K-edge XAS to assess the roles of n*f vs.* (n+1)*d*-orbitals (n = 4, 5) in bonding and compare lanthanide with actinide MCl_6^{n-} compounds. We will show trends how orbital mixing changes within both periods (4*f*: M = Ce, Nd, Sm, Eu, Gd; 5*f*: M = Th, U, Pu) and between both groups of elements. Furthermore we will discuss the influence of the oxidation state of selected systems of lanthanide ($CeCl_6^{3-}$ vs $CeCl_6^{2-}$) and actinide hexachloro compounds (UCl_6^{3-}, UCl_6^{2-}, UCl_6^{1-}) on orbital mixing.

Next to our well established Cl K—edge methodology we will show first examples of our efforts to broaden our spectroscopical portfolio to the metal point of view via complementary spectroscopic techniques, namely high-energy resolution fluorescence detection XAS (HERFD-XAS) and X-ray emission spectroscopy (XES).

References

1. Neidig, M. L.; Clark, D. L.; Martin, R. L., Covalency in *f*-element complexes. *Coord. Chem. Rev.* **2013,** *257* (2), 394-406.

2. Minasian, S. G.; Keith, J. M.; Batista, E. R.; Boland, K. S.; Clark, D. L.; Conradson, S. D.; Kozimor, S. A.; Martin, R. L.; Schwarz, D. E.; Shuh, D. K.; Wagner, G. L.; Wilkerson, M. P.; Wolfsberg, L. E.; Yang, P., Determining Relative *f* and *d* Orbital Contributions to M–Cl Covalency in MCl_6^{2-} (M = Ti, Zr, Hf, U) and $UOCl_5^-$ Using Cl K-Edge X-ray Absorption Spectroscopy and Time-Dependent Density Functional Theory. *J. Am. Chem. Soc.* **2012,** *134* (12), 5586-5597.

LA-UR-13-22278

3-15

Interaction of human serum transferrin with Cm(III) using Time-Resolved Laser Fluorescence Spectroscopy (TRLFS)

Nicole Bauer[1,2], Petra Panak[2,1]

[1]Institute for Nuclear Waste Disposal (INE), Karlsruhe Institute of Technology (KIT), Karlsruhe, Germany, [2]University of Heidelberg, Department of Physical Chemistry, Heidelberg, Germany

If radionuclides are accidentally released to the environment especially actinides can cause a serious health risk upon incorporation. Since they have no essential function in the human body there is only deficient knowledge about the biochemistry of actinides in man. With regard to the development of potential decontamination therapies, a detailed understanding of the mechanisms of relevant biochemical reactions is necessary.[1] One potential reaction that incorporated actinides might undergo is the coordination to human serum transferrin, an iron carrier protein in the blood. It is folded into two lobes housing the metal binding sites for Fe(III) (fig. 1).[2] In regular blood serum, only 30 % of transferrin is saturated with iron, indicating a high capacity for the complexation of other metal ions, e.g. the actinides.

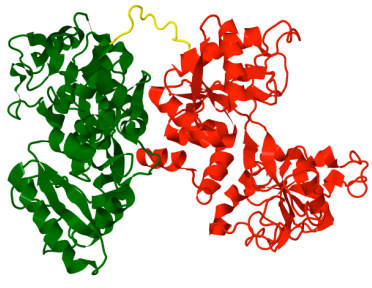

Fig. 1: 3D structure of human serum transferrin with N-lobe (green) and C-lobe (red). Each lobe houses one metal binding site.

Our previous results on Cm(III) transferrin complexation demonstrated that commercial human serum transferrin is contaminated with EDTA. After purification with size-exclusion chromatography and filtration the complexation of Cm(III) with transferrin was investigated in the pH range from 3.5 to 11.0 at room and physiological temperature using TRLFS. Two Cm(III) transferrin species were identified for the first time and characterized spectroscopically. In the pH range from 6.3 to 7.7 a Cm(III) sorption species is formed (fig. 2). The fluorescence lifetime of 130 µs correlates with partial coordination to transferrin.[3] [4] The complexation occurs presumably at the Fe(III) binding site although sorption at a nonspecific site cannot be excluded. Above pH 7.7 the fluorescence spectra are dominated by the emission band of an additional Cm(III) transferrin species at 619.9 nm (fig. 2). The extraordinary bathochromic shift of the emission band of 26.6 nm relative to the emission band of the Cm(III) aquo ion is very unusual for organic ligands and has so far only been reported for Cm(III) incorporated e.g. into calcite or Ca-montmorillonite.[5] [6] The peak position together with the fluorescence lifetime of 221 µs indicate incorporation of Cm(III) at the transferrin binding site resulting in a 4-fold coordination via amino acid groups (Asp-63, Tyr-95, Tyr-188 and His-249) of the protein and coordination of two water molecules and three additional ligands, e.g. synergistic anions (fig. 3).

Kinetic studies on the complexation of Cm(III) with transferrin were performed at different pH. As an important result no variation in the emission spectra with time is observed implying a fast complexation reaction.

The complexation of transferrin to Cm(III) shows a distinct temperature effect upon increasing the temperature from 23°C to physiological temperature. At 37.5°C the formation of both Cm(III) transferrin species increases and they are formed at pH values that are 0.5 units lower than the respective pH values at room temperature. Under physiological conditions (pH 7.4,

37.5°C, c(NaCl) = 150 mM) about 70 % of the incorporated Cm(III) transferrin species and 30 % of the sorbed Cm(III) transferrin species are formed. The presence of both species indicates that the Cm(III) transferrin system in the literature is more complicated as only the incorporated Cm(III) transferrin species might bind to the receptor followed by endocytosis. Furthermore, the complexation of Eu(III) with human serum transferrin was investigated at T < 20K using TRLFS. The results obtained at pH 7.4 show the formation of an Eu(III) transferrin species with a sevenfold coordination of Eu(III) via amino acid groups and synergistic anions. This species corresponds to the incorporated Cm(III) transferrin species. Further structural investigations were performed by EXAFS spectroscopy. They also confirm the formation of an Eu(III) transferrin complex at pH 7.2 and an Am(III) transferrin complex at pH 8.5. The results presented in this study focus on the speciation and structures of An(III) transferrin complexes. Together with in vivo studies they might contribute to a better understanding of relevant biochemical reactions of actinides upon incorporation and can be of major importance for the future development of potential decontamination therapies.

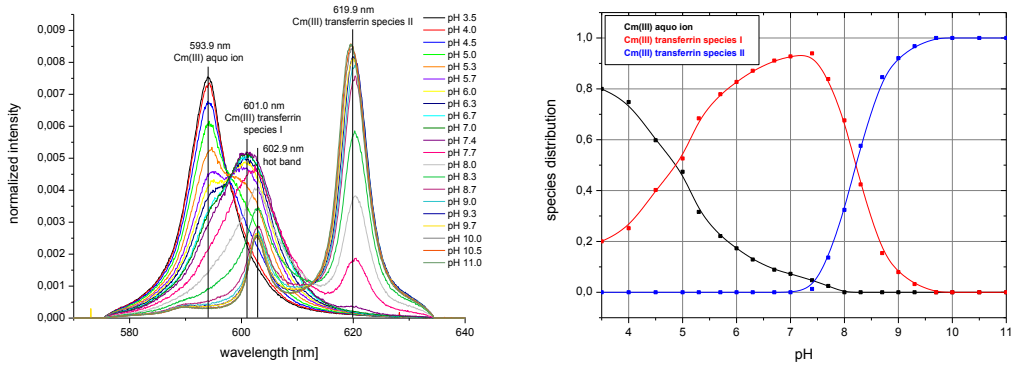

Fig. 2: Left: Normalized fluorescence emission spectra of the Cm(III) transferrin complexation in the pH range between 3.5 and 11.0 at room temperature. c(Cm) = $1 \cdot 10^{-7}$ M, c(Tf) = $5.1 \cdot 10^{-6}$ M; Right: Fractions of the three species Cm(III) aquo ion, Cm(III) transferrin species I and Cm(III) transferrin species II depending on the pH.

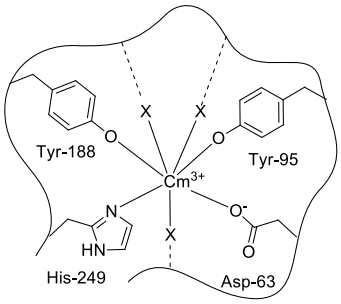

Fig. 3: Proposed structure of the Cm(III) transferrin species with Cm(III) incorporated at the binding site; X represents additional ligands such as carbonate, bicarbonate and/or hydroxide (the two coordinating water molecules are not shown).

References

[1] A. E. V. Gorden et al., *Chem. Rev.* **2003**, *103*, 4207-4282.

[2] H. Z. Sun, H. Y. Li, P. J. Sadler, *Chem. Rev.* **1999**, *99*, 2817-2842.

[3] T. Kimura, G. R. Choppin, *J. Alloys Compd.* **1994**, *213/214*, 313-317.

[4] T. Kimura, G. R. Choppin, Y. Kato, Z. Yoshida, *Radiochim. Acta* **1996**, *72*, 61-64.

[5] T. Stumpf, M. M. Fernandes, C. Walther, K. Dardenne, T. Fanghänel, *J. Colloid Interface Sci.* **2006**, *302*, 240-245.

[6] M. M. Fernandes, T. Stumpf, T. Rabung, D. Bosbach, T. Fanghänel, *Geochim. Cosmochim. Acta* **2008**, *72*, 464-474.

Thermal stability of ammonium actinide(IV) nitrate

Guillaume Peter Soldani[1,2], Eléonore Welcomme[1], Catherine Renard[2], Stéphane Grandjean[1], Francis Abraham[2]

[1]CEA Marcoule, Bagnols sur Cèze, France, [2]UCCS, Université Lille Nord de France, Villeneuve d'Ascq, France

In the nuclear fuel reprocessing cycle, nitric acid media are widely used. During concentration of laboratory nitric effluent containing actinide, formation of solid actinide compounds was observed. Tetravalent actinide elements are known to form hexanitrates in highly concentrated nitrate solution and XRD analysis allowed us to detect $(NH_4)_2An^{IV}(NO_3)_6$ in the solid residue. Structural information on ammonium actinide(IV) nitrates is available in the literature [1] but there is a lack of data concerning their relative thermal stability.

We synthesized the pure thorium, uranium and plutonium analog salts by slow evaporation of each corresponding actinide(IV) nitrate solution containing ammonium nitrate (with an antinitrous reagent for U(IV)). TGA/DSC analyses were performed for each compound. The decomposition starts around 210°C for the thorium based compound and leads directly to the formation of thorium dioxide at 350°C. The thermogravimetric analysis of the uranium salt indicates the formation of two intermediate phases between 170°C and 570°C (Figure 1), both identified bytemperature-dependent X-ray diffraction. From 170°C to 260°C, the initial $(NH_4)_2U^{IV}(NO_3)_6$ salt loses one NH_4NO_3 and the U(IV) is oxidised to U(VI). This uranyl ammonium nitrate intermediate is $NH_4UO_2(NO_3)_3$, whose structure has recently been solved by Belomestnykh *et al*. [2]. The uranium oxide produced by the decomposition of the U(VI) salt is amorphous UO_3, reduced at 570°C into U_3O_8 via an endothermic transformation.

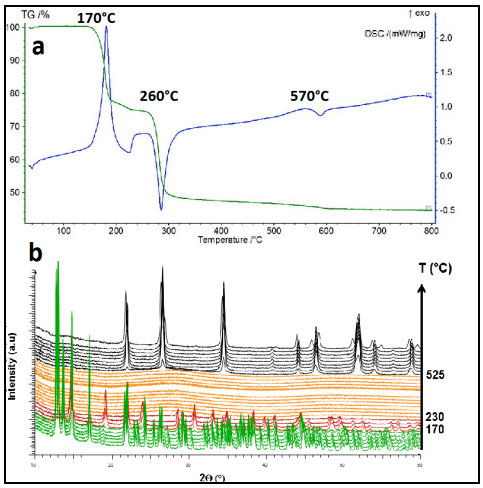

Figure 1: TGA/DSC (a) and temperature-dependent X-ray diffraction patterns (b) for $(NH_4)_2U(NO_3)_6$ in air atmosphere (heating rate: 10°C.min^{-1}).

The plutonium ammonium nitrate compound is more stable, the decomposition occurring between 195°C and 320°C. Thanks to thermogravimetric analysis in rate-controlled mass change mode (instead of constant heating rate) two intermediate phases were isolated and investigated by X-ray diffraction analysis. Thus, the gradual decomposition of $(NH_4)_2Pu^{IV}(NO_3)_6$ leads to a mixture of $(NH_4)_2Pu^{IV}(NO_3)_6$ and $NH_4PuO_2(NO_3)_3$ at 207°C. PuO_2 is formed from 270°C up to 320°C when all the $NH_4PuO_2(NO_3)_3$ is decomposed. The uranium and plutonium based compounds are stable until 170°C and 195°C and are thermally decomposed via an intermediate An(VI) phase while the thorium salt is directly decomposed to oxide at 210°C.

References

[1] M.R. Spirlet et al., *Acta Crystallogr. C* 48, 1161 (1992).
[2] V.I. Belomestnykh et al. , Russ. J. Inorg. Chem 56, 1894–1898 (2011)

3-96

Promising alloy for separation actinides from lanthanides in molten salt – liquid metal system

Alexander Osipenko[1], Valeri Smolenski[2], Alena Novoselova[2], Alexander Maershin[1], Mikhail Kormilitsyn[1]

[1]Reasearch Institute of Atomic Reactors, Dimitrovgrad, Russia, [2]Institute of High-Temperature Electrochemistry, Ekaterinburg, Russia

Actinides recycling by separation and transmutation are considered worldwide as one of the most promising strategies for more efficient use of the nuclear fuel as well as for nuclear waste minimization, thus contributing to make nuclear energy sustainable. With this purpose, two major fuel reprocessing technologies have been explored so far to separate the actinides from the fission products arising from nuclear energy production: hydrometallurgical and pyrometallurgical processes. The actinide – lanthanide separation efficiency can be estimated from the thermodynamic equilibrium constants and the activity coefficients which give the idea of the interactions between the elements and molten salts or liquid metals.

Selectivity of pyrochemical separation process taking place at the molten salt – liquid metal interface depends on the properties of both phases. Knowing thermodynamic properties of all spent nuclear fuel components in working media is essential for determining applicability of a particular system for practical application. There is no information on thermodynamic properties of neodymium in ternary metallic alloys containing low melting metals. In the present study the behaviour of neodymium was investigated in the alloys based on Ga-In eutectic. The activity coefficient of the neodymium in liquid gallium – indium alloy was determined in fused 3LiCl-2KCl eutectic by measuring the electromotive force of the galvanic or semi-galvanic cells:

Mo(s) (Nd) | molten salt, Nd(III) || molten salt | C(s), Cl_2(g) (1)

Nd (alloy) | molten salt, Nd(III) || molten salt | C(s), Cl_2(g) (2)

The formal standard potentials of $E^{*}_{Nd(III)/Nd(0)}$ and $E^{**}_{Nd(Ga-In)}$ vs. Cl-/Cl_2 reference electrode have been obtained from expressions (1) and (2), correspondingly, by using potentiometry at zero current method on potentiostat-galvanostat AUTOLAB PGSTAT 30 (Eco Chemie) The results of calculations are the following:

$$\log\gamma_{Nd(Ga-In)} = \frac{3F}{2.303RT}(E^{*}_{Nd(III)/Nd} - E^{**}_{Nd(III)/Nd(Ga-In)}) \quad (3)$$

$$\log\gamma_{\alpha-Nd(Ga-In)} = 4.59 - \frac{12960}{T} \pm 0.15 \quad (4)$$

Partial excess Gibbs energy of α-Nd in liquid Ga-In alloy was calculated according by equation (6) using expression (4):

$$\Delta G^{ex}_{\alpha-Nd(Ga-In)} = \Delta H^{ex}_{\alpha-Nd(Ga-In)} - T\Delta S^{ex}_{\alpha-Nd(Ga-In)} \quad (5)$$

$$\Delta G^{ex}_{\alpha-Nd(Ga-In)} = 2.303RT\log\gamma_{\alpha-Nd(Ga-In)} \quad (6)$$

$$\Delta G^{ex}_{\alpha-Nd(Ga-In)} = -247.66 + 87.73\cdot10^{-3}T \pm 3.60 \quad kJ/mol \quad (7)$$

The obtained data of the temperature dependences of the activity coefficient and partial excess Gibbs energy of neodymium in liquid gallium – indium eutectic alloy at the temperature investigation range 723-823 K show the perspective of used this system in future innovation method of recovery of nuclear waste.

4-12

Molecular and 3D hybrid architectures with tetravalent uranium

Clément Falaise, Christophe Volkringer, Natacha Henry, Thierry Loiseau

University of Lille, Lille, France

For the past decade, the number of synthesis reports dealing with metallic carboxylates has grown exponentially because of their implication in the construction of metal−organic frameworks (MOFs), exhibiting porosity and fascinating atomic architectures. Transition elements are the most used metals for the construction of such compounds, but actinide cations were also involved in the elaboration of a large variety of hybrid organic−inorganic assemblies. Since the use of the oxalate ligand in the industrial process for actinide extraction and separation, a significant effort has been focused on the reactivity of different organic polycarboxylate anions, mainly with uranyl cations, $[UO_2]^{2+}$, resulting in multidimensional (1D, 2D, and 3D) extended uranyl−organic frameworks (UOFs). Although tetravalent uranium carboxylates have been identified for more than 50 years, only a very few reports described the different varieties of its coordination complexes involved in low-dimensional networks.

This submission deals with the syntheses and the crystal structures of new architectures constructed from carboxylate ligands and U^{4+}. We will discuss about the crucial role of water and solvothermal conditions for the generation of new U^{4+}-based polynuclear species. Among the various solids isolated in our team, 3 systems highlight very well our approach.

- The association of benzoic acid and U^{4+} lead to the production of a large cluster containing 38 cations of uranium (U^{4+}), closely related to the $\{Pu_{38}\}$ entity.[1]
- Isoreticular 3D MOF-type architectures containing the uranium hexanuclear motif (U_6O_8) were synthesized with a series of rigid ditopic ligands (see figure).[2]
- The mixing of two organic ligands (formic acid and dicarboxylic ligands) or the use of tricarboxylic acid (trimesic acid) were favorable for the isolation U^{4+}-based bricks like hexamer, tetramer or trimer.[3]

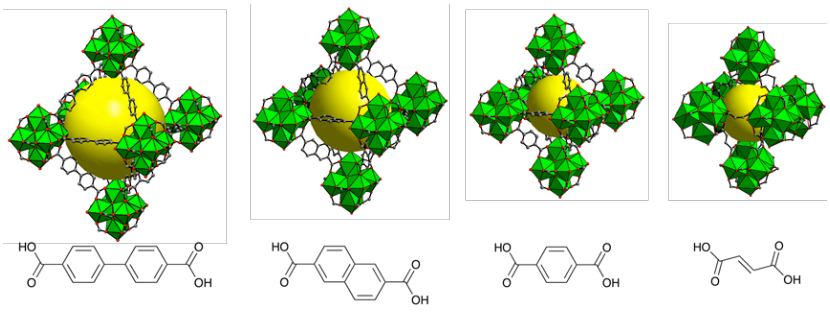

3D MOF-type architectures with tetravalent uranium hexanuclear motif

References:

1- C. Falaise, C. Volkringer, J-F. Vigier, A. Beaurain, P. Roussel, P. Rabu, T. Loiseau ; submitted

2- C. Falaise, C. Volkringer, J-F. Vigier, N. Henry, A. Beaurain, T. Loiseau ; *Chem. Eur. J.* **2013**, DOI : 10.1002/chem.201203914

3- C. Volkringer, I. Mihalcea, J-F. Vigier, A. Beaurain, M. Visseau, T. Loiseau ; *Inorg. Chem*. **2011**, 50, 11865

4-13

Oxidation state and aromaticity in f-element metallocenes $M(C_8H_8)_2$

Cina Foroutan-Nejad[2], Andy Kerridge[1]

[1]*University College London, London, UK,* [2]*Masaryk University, Brno, Czech Republic*

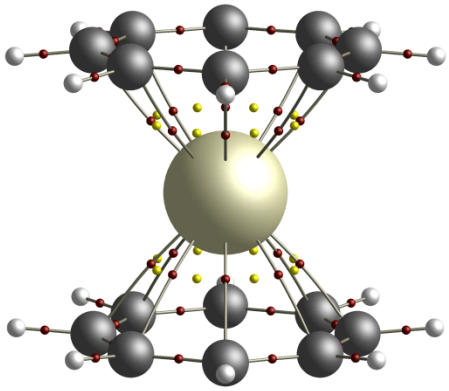

Figure 1: QTAIM- calculated molecular graph of cerocene

Whilst the thorocene molecule $ThCOT_2$ (COT = C_8H_8) is universally regarded as a Th(IV) compound, with two electrons donated to each COT ligand in order to achieve aromatic stability[1,2], the picture is less clear for its lanthanide analogue cerocene, $CeCOT_2$. Here, the close proximity of a highly oxidising Ce^{4+} ion to two highly reducing COT^{2-} ligands seems unlikely, although experimental evidence for such an assignment exists[3]. As an alternative, it has been suggested[4] that cerocene may be an example of a molecular Kondo system, and multiconfigurational self-consistent field (MCSCF) studies appear to support this view[1]. In these calculations, the electronic ground state of cerocene was found have an open-shell singlet leading configuration involving occupation of a single 4f orbital. Further evidence for a Ce(III) complex was provided by Ce L_{III}-edge XANES data[5], however a recent complete-active-space self-consistent-field (CASSCF) study[2] has suggested that such an assignment is a matter of interpretation; whilst the weight of the leading configuration was found to be highly sensitive to details of the calculation, it could nonetheless be concluded that there was significant accumulation of charge density on the Ce ion through occupation of strongly hybridised orbitals, leading to measures of the effective oxidation state to be lower than the formal +4 value. In this contribution, CASSCF studies of cerocene and thorocene are combined with topological analysis of the electron density employing the quantum theory of atoms in molecules (QTAIM) in order to consider the degree of electron delocalisation between the central ion and complexing ligands. Measures of COT ligand aromaticity are also considered in order to unambiguously characterise the electronic ground states of both complexes.

References

[1] M. Dolg, *et al.*, *J. Chem. Phys.* **94**:3011 (1991); M. Dolg, *et al.*, *Chem. Phys.* 1**95**:71 (1995)
[2] A. Kerridge, R. Coates and N. Kaltsoyannis, *J. Phys. Chem. A* **113**:2896 (2009)
[3] A. Streitwieser, *et al.*, *J. Am. Chem. Soc.* **107**:7786 (1985)
[4] C.-S. Neumann and P. Fulde, *Z. Phys. B-Cond. Matt.* **74**: 277 (1989)
[5] C. H. Booth, *et al.*, *Phys. Rev. Lett.* **95**:267202 (2005)

4-14

Separation of ^{225}Ac from radionuclides generated by proton irradiation of natural thorium using extraction chromatography

Elena Lapshina[1], Stanislav Ermolaev[1], Boris Zhuikov[1], Stepan Kalmykov[2], Ramiz Aliev[2], Valentina Ostapenko[2], Alexander Vasiliev[2]

[1]Institute for Nuclear Research of Russian Academy of Sciences, Moscow, Russia, [2]Lomonosov Moscow State University, Moscow, Russia

Alpha-emitters are promising for targeted radiotherapy of cancer due to high linear energy transfer (LET) of about 100 keV/μm and low range of alpha particles of about 50-100 μm in biological tissue. Application of alpha-emitters is determined by the requirements of half-life, medical applicability and production possibilities. ^{225}Ac is one of appropriate candidates and it may be used either directly or as a mother radionuclide in ^{213}Bi isotope generator.

Among the existing production approaches, irradiation of natural thorium with protons having energy 200-60 MeV is one of the most prospective. It can provide curie amounts of ^{225}Ac during a 10-day irradiation [1]. A number of fission and spallation radionuclide products are also generated in proton irradiation of thorium. The isolation of pure actinium fraction using extraction chromatography resins produced by Eichrom Company is studied in this work. The resins tested in the experiments are: TEVA (mixture of trioctyl and tridecyl methyl ammonium chloride as an extractant), DGA (N,N,N`,N`tetroctyldiglicolamide), LN (di(2-ethylhexyl)orthophosphoric acid) and TRU (octylphenyl-N,N-di-isobutyl carbomoylphosphine oxide).

Although the radionuclide composition of the irradiated target comprises several tens of various elements, the main difficulties were to separate Ac from Th and rare earth elements especially La and Ce. First, irradiated thorium was dissolved in 6 M HNO_3 solution in the presence of catalytic amount of hydrofluoric acid (0.003-0.004 M HF). Then most part of Th was extracted with commonly used extraction agents: tributyl phosphate, or di(2-ethylhexyl)orthophosphoric acid, or tri(n-octyl)phosphine oxide dissolved in toluene. The extraction was repeated with a fresh organic phase until the Th content in aqueous phase is diminished significantly lower than the sorption capacity of the investigated resins.

TEVA resin is proposed for sorption of **TE**tra**VA**lent actinides. The distribution coefficient (*k'*) for Th(IV) increases with HNO_3 concentration up to 400 in 6 M HNO_3. The value of Th sorption capacity is 70 mg/g (manufacturer's data), whereas the sorption of trivalent ions is negligible. So we use a column filled with TEVA resin after the liquid extraction to remove the traces of Th from the solution.

DGA and LN resins have been chosen for the next processing step because they have a steep dependence of *k'* for trivalent ions on HNO_3 concentration. *k'* (DGA) reaches maximum in 6-7 M HNO_3 solution and drops down to 1-2 in 10^{-2} M HNO_3 solution. *k'* (LN) demonstrates inverse acidity dependence [2,3]. We used these resins to adsorb actinium and lanthanides from HNO_3 solution of favorable acidity, while mono- and divalent ions (Cs^+, Ra^{2+}, Ba^{2+}, Sr^{2+}) as well as most of Ru, Zr, Nb, and others were washed out of the column. Then we changed HNO_3 concentration to strip off the purified actinium and lanthanides. TRU resin displays a moderate *k'* values ~10^2 for trivalent ions in the range of 1-5 M HNO_3 [3]. Optimization of acidity and column length allowed us to separate actinium from lanthanides. *Figure 1* illustrates the chromatographic behavior of Ac, La and Ce on TRU resin in 2 and 4 M HNO_3 solution.

Radionuclidic purity of the obtained ^{225}Ac fraction was better than 99.5%, and chemical yield was not less than 85%.

Acknowledgment. The authors would like to thank Dr. Steffen Happel and TrisKem International company for providing the samples of extraction chromatography resins.

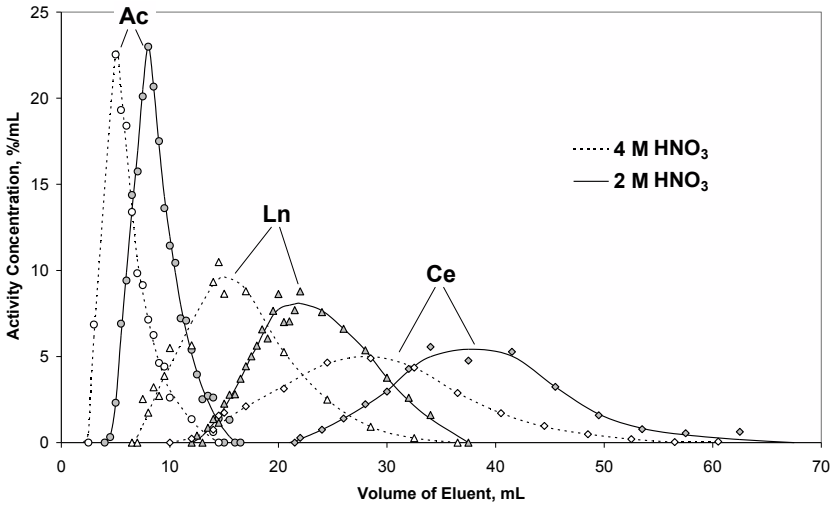

Figure 1. Separation of actinium, lanthanum and cerium on TRU resin column in 2 M HNO_3 and 4 M HNO_3 solutions.

References

1. S.V. Ermolaev, B.L. Zhuikov, V.M. Kokhanyuk, V.L. Matushko, S.N. Kalmykov, R.A. Aliev, I.G. Tananaev and B.F. Myasoedov. Production of actinium, thorium and radium isotopes from natural thorium irradiated with protons up to 141 MeV, Radiochim. Acta, 2012, V.100, P. 223-229.

2. D.R. McAlister., E.P. Horwitz, Solvent Extraction and Ion Exchange, 2007, V.25, P.757-769.

3. E.P. Horwitz, D.R. McAlister, A.H. Bond, R.E. Barrans, Solvent Extraction and Ion Exchange, 2005, V.23, P.319-344.

4-15

Americium and Plutonium Purification by Extraction (the AMPPEX process)

Mark Sarsfield[1], Keith Stephenson[2], Katie Bell[1], Jamie Brown[1], Michael Carrott[1], Colin Gregson[1], Christopher Maher[1], Chris Mason[1], Robin Taylor[1]

[1]National Nuclear Laboratory, Sellafield, Cumbria, UK, [2]European Space Agency, Noordwijk, The Netherlands

The UK has more than 100 t of plutonium dioxide (PuO_2) powder in storage from the reprocessing of spent nuclear fuel. Within this material there was initially 4-11% w/w of the isotope Pu-241 some of which has undergone beta decay resulting in > 2000 kg of Am-241. This isotopically pure material is a potential asset with the ability to provide small amounts of power for centuries and so it is not surprising that there is an increasing interest in utilising Am-241 as a heat source for use in Radioisotope Thermoelectric Generators (RTGs) and Radioisotope Heating Units (RHUs). These power systems may provide key enabling technology for space applications, particularly in Europe.

This paper provides an overview of a process for separating Am-241 from PuO_2 and gives details on the progress made so far in establishing proof of concept for a flowsheet that not only provides a sufficiently pure Am-241 product but also results in a PuO_2 product that meets storage requirements and is easier to handle when making into MOx fuel.

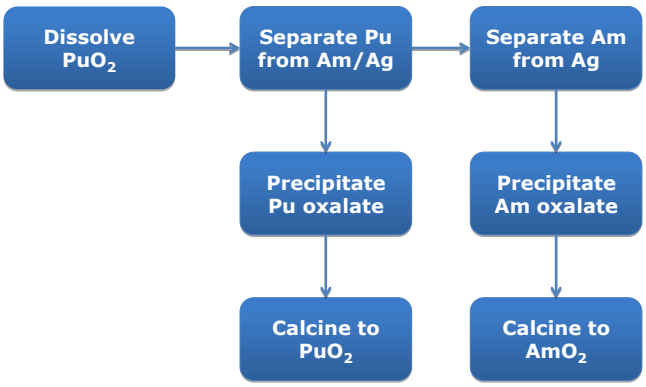

An overview of the AMPPEX process

4-16

Separation of Americium alone from a Concentrated Raffinate by Liquid-Liquid Extraction

Cécile Marie, Marie-Thérèse Duchesne, Vincent Pacary, Vincent Vanel, Marc Montuir, Manuel Miguirditchian

CEA (DRCP/SMCS/LEPS), Bagnols-sur-Cèze, France

Recycling americium (Am) alone from the spent fuel is an important option studied for the future nuclear cycle (Generation IV systems) since Am is one of the main contributor to the long-term radiotoxicity and heat power of ultimate waste. Since 2008, a liquid-liquid extraction process called EXAm has been developed by the CEA to allow the recovery of Am alone from a PUREX or COEX^{TM} raffinate (already cleared from U, Np and Pu). A mixture of DMDOHEMA (*N,N'*-dimethyl-*N,N'*-dioctyl-2-(2-(hexyloxy)ethyl)-malonamide) and HDEHP (di-2-ethylhexylphosphoric acid) in TPH is used as the solvent and the Am/Cm selectivity is improved using TEDGA (tetraethyldiglycolamide) as a selective complexing agent to maintain Cm and heavier lanthanides in the acidic aqueous phase (HNO_3 5M). Americium is then stripped selectively from light lanthanides at low acidity (pH 2-3) with a polyaminocarboxylic acid (DTPA). The feasibility of this Am separation was demonstrated during a hot test in ATALANTE facility in April 2010 on a genuine PUREX/Np raffinate.

In order to improve the compactness of the process and the future plant, the objective is now to adapt the EXAm process to a concentrated raffinate. The acquisition of data in batch experiments performed to sustain the development of the EXAm process will be reported. Solvent formulation, TEDGA and HNO_3 concentrations, pH buffer nature were optimized to manage high concentrations of americium and lanthanides in the loaded solvent and to avoid 3rd phase formation but still keeping a sufficient Am/Cm and Am/fission products separation.

4-17

Spectroscopic study of redox behaviour of neptunium ions in molten LiCl-KCl eutectic

Tae-Hong Park, Dae-Hyeon Kim, Sang-Eun Bae, Jong-Yun Kim, Young-Hwan Cho, Jei-Won Yeon, Kyuseok Song

Korea Atomic Eenergy Research Institute, Daejeon, Republic of Korea

The pyrochemical process based on electrochemical methods in molten salts has made progress as an alternative technology for the development of advanced spent nuclear fuel cycle. This dry reprocessing process separates uranium, plutonium, and minor actinides from fission products via electrochemical codeposition of mixed oxide, MOX, at the cathode. Therefore, the knowledge of the chemical behaviour of minor actinides as well as uranium in high temperature molten salts is of great important to understand and improve electrorefining and electrowinning processes. Neptunium, an anthropogenic transuranic element, may exist as minor actinides with plutonium, americium, and curium, and there is limited information on chemical behaviour of Np ions in eutectic melts. In the present study, we focus on the measurement of the UV-vis spectra of Np ions. The oxidation states of Np ions were controlled electrochemically and spectral modification with different oxidation states was monitored in the UV and visible regions.

All the experiments were carried out in the glove box, where O_2 and H_2O levels were maintained to be less than 1 ppm. A small piece of LiCl-KCl eutectic containing $NpCl_x$ (x = 3 and 4) prepared from ^{237}Np oxide salt was added to a quartz cell containing a molten LiCl-KCl eutectic salt at 460 °C. After all solid was melt, a set of three electrodes was carefully immersed into the melt to avoid blocking the light path of a spectro-electrochemical cell within a furnace. A glassy carbon rod was used as working electrode. Ag-AgCl (1 wt % AgCl in LiCl-KCl) and a silver wire were placed in a thin Pyrex tube, and used as reference and counter electrodes, respectively. The potential of 1.1 V vs Ag|AgCl was applied to the Np eutectic solution and Cl_2 gas was electrochemically evolved to convert any Np oxide compound to Np^{4+}. In addition, such environment reduced any Np^{3+} to Np^{4+}, resulting in a brown melt.

Figure 1 shows the electronic absorption spectra of Np ions in a LiCl-KCl melt at 460 °C obtained after performing chronoamperometry at 0.6 → 0.1 → 1.1 V vs Ag|AgCl for certain period. The initial two spectra after Cl_2 evolution and application of 0.6 V display nearly identical features and the oxidation state of all Np ions is 4+. Although several research groups reported the Np spectra in molten salts in the visible region (> 400 nm), which exhibit a few weak f-f transitions ($\varepsilon < 20\ M^{-1}cm^{-1}$), it should be noted that we clearly observed strong f-d transitions of Np^{4+} peaked at 252 nm as well as relatively much weaker f-f bands at 600-1000 nm. The determination of molar extinction coefficient is currently in progress.

Under reduction conditions (at 0.3 → 0.1 V vs Ag|AgCl), the spectral features of Np^{4+} significantly varied. The absorbance of Np^{4+} at 252 nm considerably decreased whereas a new band at 380 nm appeared. Because a cyclic voltammetric measurement displays the reduction of Np^{4+} to Np^{3+} at ~0.5 V vs Ag|AgCl, the new absorption peak at 380 nm is apparently attributed to Np^{3+}. In addition, the absorbance is comparable to that of the Np^{4+} f-d band and much higher than that of the f-f transitions at 600-1000 nm, indicating that the Np^{3+} absorption band peaked at 380 nm is also derived from inter-configurational transitions.

After little spectral changes were observed at the reduction potential of 0.1 V, indicating that most of Np species exited as Np^{3+}, we applied an oxidation potential of 0.6 V to the melt. As a result, the absorption band of Np^{3+} at 380 nm gradually disappeared whereas the absorption signal of Np^{4+} at 250 nm rapidly arose within 15 min. However, the spectral change became much slower with consumption of Np^{3+} and the shoulder at 380 nm still remained even after applying the potential for 65 min, suggesting that the oxidation was not complete. Then, chronoamperometry was carried out at 1.1 V vs Ag|AgCl, where Cl_2 gas evolves. The much higher oxidation potential with combination of Cl_2 evolution converted most of the Np species in the melt to Np^{4+}, displaying an intense absorption at 250 nm without the Np^{3+} spectral signal at 380 nm.

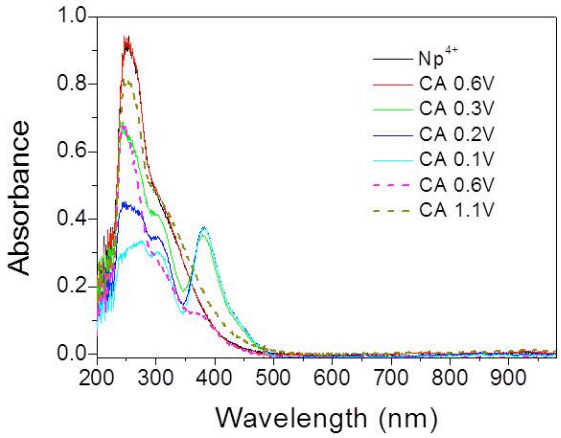

Figure 1. Electronic absorption spectra of Np ions obtained after chronoamperometry at different potentials for certain period.

In addition, the spectroscopic measurement can present information on chemical interactions between components in a molten salt system. We measured electronic absorption spectra of a mixture of Np and lanthanide ions, which likely coexist in the molten salt during the pryoprocess. To a LiCl-KCl solution containing Np^{4+} at 460 °C, added was the LiCl-KCl eutectic containing $CeCl_3$ (~10 wt %), which was prepared by dissolving $CeCl_3$ as purchased without further purification in LiCl-KCl. Figure 2 displays the spectra of Np^{4+} in red and the mixture in green. The addition of $CeCl_3$ gave rise to a new absorption peak at 380 nm as well as the band at 318 nm assigned to a Ce^{3+} f-d transition. Moreover, a slight decrease of the absorbance at 250 nm was observed. Such spectral variation in the UV region interestingly resembles that obtained during reduction of Np^{4+} to Np^{3+} in Figure 1, indicating that there presumably happened a reduction reaction of Np^{4+} after adding of a lanthanide compound, which are currently under our investigation.

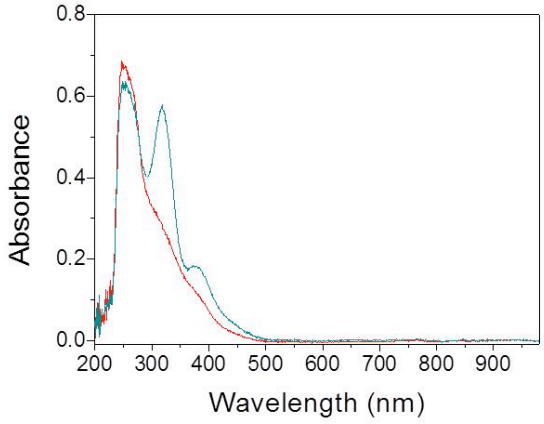

Figure 2. Electronic absorption spectra of Np^{4+} and the mixture after addition of $CeCl_3$ in a LiCl-KCl eutectic at 460 °C.

We measured the electronic absorption spectra of Np^{4+} and Np^{3+} in the LiCl-KCl eutectic melt at 460 °C, and in particular, we determined the energies of the f-d transitions of Np ions in the UV region via electrochemical reactions. We also observed changes in the spectrum of Np^{4+} with the addition of a $CeCl_3$ containing eutectic mixture and currently we focus on revealing the origins of such observation.

POSTERS

3-16

Study on the extracted complexes of purified Cyanex301 with An(III) and Ln(III) with spectrophotometry, fluorometry, and EXAFS

Guoxin Tian[1], Xihong He[1,2], Chao Xu[1,2], Linfeng Rao[1]

[1]Lawrence Berkeley National Laboratory, Berkeley, California, USA, [2]Tsinghua University, Beijing, China

The extracted complexes of purified Cyanex301 with Cm(III), Nd(III), Sm(III), and Tb(III) have been studied with spectrophotometric and fluorometric titrations, and EXAFS. We found that only one extracted complex species of Cm(III) is formed in the organic phase while two or three species of Ln(III) are identified in the organic phase using 0.1-0.5 M purified Cyanex301 in toluene as organic phase and 1.0 M $NaNO_3$ as aqueous phase. The absorption spectra, fluorescence spectra, and fluorescence lifetime measurement of the extracted complex species of Cm(III) suggest that the only one complex in the organic phase might be $HCmA_4$ (A stands for Cyanex301). For Ln(III), the extracted complexes may contain three or four Cyanex301 molecules and various water molecules.

3-18

Mechanism of $UO_2(NO_3)_2 \cdot 6H_2O$ Decomposition under Microwave Irradiation

Sergey Kulyukhin

Frumkin' Institute of Physical Chemistry and Electrochemistry, Russian Academy of Science, Moscow, Russia

The influence of microwave irradiation (MWI) on the decomposition of $UO_2(NO_3)_2 \cdot 6H_2O$ was studied. The $UO_2(NO_3)_2 \cdot 6H_2O$ decomposition products arising under MWI were investigated using thermogravimetric and X-ray phase studies, as well as IR spectroscopy and electron microscopy. The results of the physicochemical studies of the decomposition products were compared with the literature data for different uranium compounds, including $UO_2(NO_3)_2 \cdot 6H_2O$.

Physicochemical studies of the decomposition products, the measurements of $[UO_2^{2+}]$ and $[NO_3^-]$, and of the molar ratio between NO_3^- and UO_2^{2+} in different fractions of the decomposition product show that, in addition to gaseous products, the end decomposition products of 2-10 g of $UO_2(NO_3)_2 \cdot 6H_2O$ under MWI during 35 minutes (a maximum temperature of the process 170-320 ^oC is achieved in the first 2-5 minutes of the irradiation) are the uranyl hydroxinitrate $UO_2(OH)NO_3$ and the uranium trioxide UO_3, or their hydrates. The solubility of $UO_2(OH)NO_3$ in H_2O at 20^oC was measured. It was equal to $6.83 \cdot 10^{-2}$ mol/L. The obtained results are consistent with the $UO_2(NO_3)_2 \cdot 6H_2O$ decomposition under MWI which can be described by the following reactions: (1) $UO_2(NO_3)_2 \cdot 6H_2O \rightarrow UO_2(OH)NO_3 + 5H_2O + HNO_3$ and 2) $UO_2(OH)NO_3 \rightarrow UO_3 + HNO_3$.

The mechanism of the $UO_2(NO_3)_2 \cdot 6H_2O$ decomposition under MWI differs from its thermal decomposition mechanism during convection heating in that the major precursor for UO_3 as a $UO_2(NO_3)_2 \cdot 6H_2O$ decomposition product is only $UO_2(OH)NO_3$ or its hydrates. No formation of $UO_2(NO_3)_2$ or its hydrates is observed.

A study of the MWI effect on the decomposition of $UO_2(NO_3)_2 \cdot 6H_2O$ placed in a silica gel matrix showed that after MWI of the silica gel - $UO_2(NO_3)_2 \cdot 6H_2O$ system during 35 minutes, the water leaching of uranium from silica gel during 24 hours was not higher than 10-15% of the total uranium content in the silica gel matrix.

3-19

Plutonium and uranium concentration from sea water

Sergey Kulyukhin[1], Irina Veleshko[2], Aleksander Veleshko[3]

[1]Frumkin' Institute of Physical Chemistry and Electrochemistry, Russian Academy of Science, Moscow, Russia, [2]Russian National Scientific Center "Kurchatov' Institute", Moscow, Russia, [3]Russian National Scientific Center "Kurchatov' Institute", Moscow, Russia

During the development of the method of Pu and U concentration, a quantitative assessment of the physicochemical state of Pu and U in sea water was carried out.

At first, we measured the quantity of Pu occurring in solutions in ionic and colloid forms. The obtained data on the Pu distribution shows that about 38% of it is sorbed on suspended particles, and 20.9% is in the ionic form. The remaining Pu is either in the colloid state, or sorbed on other colloid particles to form pseudocolloids. Therefore, the flocculation precipitation of colloids and suspended particles on freshly precipitated chitosan could be an effective method to concentrate plutonium. The obtained results on the Pu and U coprecipitation on low-molecular chitosan (LMC) in salt solutions allowed us to consider the possibility of using LMC for Pu and U concentration in sea water. Using LMC already forming a bulk precipitate at pH 6 excluded the possibility of its simultaneous coprecipitation with Ca^{2+} and Mg^{2+} occurring in sea water in microquantities (0.39 and 1.23 g/L, respectively).

To develop the method, we studied the influence of the LMC content in the 0-1 g/L concentration range on the Pu and U coprecipitation degree in the Barents Sea water. The data on the kinetics of the Pu and U coprecipitation from the Barents Sea water show that the kinetic equilibrium on LMC was reached over 20-30 min for either element. Also it was found that coprecipitation degree for Pu was 92% at [LMC] = 0.2 g/L, and it slightly increased (up to 95%) in the 0.2-0.7 g/L concentration range. Increasing the chitosan concentration further on, had hardly any effect on the Pu coprecipitation efficiency. In contrast to Pu, the U coprecipitation degree increased monotonically over the entire LMC concentration range studied. Thus, the coprecipitation degree for U was 50% at [LMC] = 0.2 g/L, whereas at [LMC] = 1.0 g/L, it increased to 70%; i.e., virtually 1.5-fold. Therefore, the investigations were carried out at [LMC] = 0.2 g/L, at which the difference in coprecipitation degree for U and Pu was the highest. Based on the obtained results, we proposed a method of sea water analysis for Pu and U concentration.

Thus, the usage of chitosan for concentrating radionuclides during the ecological monitoring of natural waters showed wide prospects for its practical uses. One of the options could be the reprocessing of low-level salt waste.

The research was carried out using financial support by the Russian Fund for Fundamental Research (Grand N 11-03-00106).

3-20

Interaction of UO_2^{2+} Aqueous Solutions with Sorbents Based on Modified Silica Gel Containing Cu, Ni, and Zn

Sergey Kulyukhin[1], Margarita Gorbacheva[2]

[1]Frumkin' Institute of Physical Chemistry and Electrochemistry, Russian Academy of Science, Moscow, Russia, [2]Frumkin' Institute of Physical Chemistry and Electrochemistry, Russian Academy of Science, Moscow, Russia

Uranium radionuclides are one of the biologically hazardous nuclear fuel elements penetrating into the environment as a result of human activity in nuclear engineering. Uranium may be present in the environment in different oxidation states. However, the most widely spread is mobile form is UO_2^{2+}.

In addition, the presence of CO_3^{2-} ions in aqueous solutions leads to the formation of neutral and negative complexes with UO_2^{2+}, having high migration ability. To decrease the uranium migration, it has been proposed to carry out the reduction of UO_2^{2+} to U^{4+} with the help of materials containing Fe or Fe-Ni nanoparticles [1]. The UO_2^{2+} reduction results in the formation of UO_2. It was found that adding Ni to Fe leads not only to the stabilization of Fe nanoparticles, but also an increase in the UO_2^{2+}reduction degree.

The aim of this work was to study the interaction of UO_2^{2+} in aqueous solutions of varied compositions with modified sorbents based on large-pore silica gels containing Cu, Ni, and Zn.

A study of the interaction of aqueous solutions of UO_2^{2+} with the modified sorbents based on the large-pore silica gel (brand MSCG) containing Cu, Ni, and Zn was carried out. It was shown that the sorption of UO_2^{2+} occurred on all sorbents. The decontamination factors for 10^{-2} M aqueous solutions of UO_2^{2+} on pure MSCG, as well as on the sorbents containing Cu, Ni, and Zn are of the same order of magnitude and were not higher than 100. For $1.1 \cdot 10^{-1}$ M aqueous solutions of UO_2^{2+}, the decontamination factors on the pure MSCG and modified sorbents containing Cu, Ni, and Zn were also of the same order of magnitude, but their values were not higher than 10.

The interaction of the modified Ni-containing sorbent with the UO_2^{2+} solution yielded a dark-green residue of the composition $NiU(OH)_6 \cdot 4N_2H_5OH$; i.e., the reduction of UO_2^{2+} to U^{4+} took place.

References

1. Riba O., Scott Th.B., Allen G.C. // Abstracts. 11th Inter. Conf. on Chemistry and Migration Behaviour of Actinides and Fission Products in the Geosphere "Migration'07", 2007, Munich, Germany. P. 201.

3-21

Discussion about the Universal Curves of Limiting Conductance of 1:3 Electrolytes: A Study of the Limiting Conductance of $LaCl_3$, $La(NO_3)_3$ and $TbCl_3$ in H_2O-THF mixtures

Rafik Besbes[1], Abderabba Manef[2], Habib Latrous[3]

[1]Higher Institute of Education and Training – ISEFC 43, rue de la Liberté 2019 Tunisia, Le Bardo, Tunisia, [2]IPEST, route Sidi Bou Said,B.P:51 2075, La Marsa, Tunisia, [3]Faculté des Sciences de Tunis, 2092, El-Manar, Tunisia

The concept of universality of limiting conductance of electrolytes in mixed solvents assumes that the variation of the ionic mobility is essentially due to the variation of the medium viscosity and the dielectric constant (Bjerrum length L_B), without taking into account structural and dynamical changes in the solvation shells of the solvated ions [1-2]. The latter effect is particularly important for dissymmetric 1:3 electrolytes, which will be discussed in more detail in the present study.

In this work we measured the variation of conductance of solvated lanthanide chloride and nitrate salts ($LaCl_3$, $La(NO_3)_3$, and $TbCl_3$) in pure water and in mixed water-tetrahydrofuran (THF) solvents (25% *w*) at 298.15 K. Previous studies have shown that mixtures of water and the aprotic solvent THF have good solvating properties for trivalent lanthanides ions. Willey et al. and Drew et al. [3-4] determined the crystal and molecular structures of $LnCl_3(THF)_n$ (n = 2-4), $[PrCl(\mu\text{-}Cl)_2(THF)_2]_n$, $[Nd(\mu\text{-}Cl)_3(H_2O)(THF)]_n$ and $GdCl_3(THF)_4$ using single-crystal X-ray diffraction methods. The differences in the structures and compositions of these complexes reflect the decrease of the ionic radii across lanthanide series as a consequence of the lanthanide contraction. Moreover, since these compounds crystallized from solutions containing a small amount of water, most of them are anhydrous. In our study, we used the universal curves [1-2] for KCl to calculate $\lambda^{\circ}_{Cl^-}$, the limiting conductance of the chloride ion in water-THF mixture (25% w of THF) at infinite dilution. Thus, having deduced $\lambda^{\circ}(Cl^-)$ we then calculated the corresponding values for the lanthanum and terbium ions, $\lambda^{\circ}(La^{3+})$ and $\lambda^{\circ}(Tb^{3+})$. The apparent ionic volumes of the solvation shells of the lanthanum and terbium ions are calculated in the water-THF mixtures and compared to the volumes calculated in pure water. We observe slightly smaller solvation shell volumes for both lanthanum and terbium in the mixed solvent as compared to the volumes in pure water. Table 1 summarizes the calculated results for the limiting conductance in water and in water-THF mixtures, as well as the ionic radius of the different ion species under study.

Table 1: Calculated Limiting Conductance and Ionic Radii of Solvated K^+, Cl^-, NO_3^-, La^{3+}, and Tb^{3+} Ions in Water and in Water-THF Mixtures (25% w)

	K^+	Cl^-	NO_3^-	La^{3+}	Tb^{3+}
[a] limiting conductance in water	73.52	76.35	71.46	69.75[5]	63.66[6]
[a] limiting conductance in water-THF	36.91	41.33	42.92	40.23	41.23
[b] crystallographic ionic radius[7]	1.41	1.80	1.77	1.14	1.01
[b] ionic radius in water	4.43	4.36	4.48	4.528	4.72
[b] ionic radius in water-THF	4.40	4.33	4.45	4.40	4.614

[a] the unit of limiting conductance is S cm^2 mol^{-1}; [b] all ionic radii are in Å.

The ionic radius of $[Tb(THF)_3]^{3+}$ and $[La(THF)_2(H_2O)_3]^{3+}$ corresponds to the ionic radii in Table 1. If x_W is the mole fraction of the water in the bulk solution and x^L_W is the local molar fraction of water in the vicinity of the ion, the preferential solvation is expressed by δ_W with : $\delta_W = x^L_W - x_W$. The preferential solvation of hydrogen ions by water is positive in water-THF mixtures, meaning that water molecules show a greater tendency to be in the immediate vicinity of a given hydrogen ion than THF molecules, as studied in detail by Barrón et al. [8]. In our case, THF molecules show a greater tendency to be in the immediate vicinity of solvated La^{3+} and

Tb^{3+} ions than do water molecules. On the contrary, K^+, Cl^-, and NO_3^- are preferentially solvated by water and preserve their hydration shell structures the in water-THF mixtures (cf. Table 1).

In summary, comparison of the experimental limiting values of conductance for $LaCl_3$, $La(NO_3)_3$, and $TbCl_3$ in water and in water-THF mixtures with the universal curves of limiting conductance shows significant differences. In order to utilize the universality law of limiting conductance, it is important to take into account the change of affinity of ion solvation.

References

1. A. Apelblat, *Acta. Chim. Slov* (2009), **56**, 1-17.

2. A. Apelblat, *J. Solution. Chem* (2011), **40**, 1544-1562.

3. G. R. Willey, T. J. Woodman, M. G. B. Drew, *Polyhedron* (1997), **16**, 3385-3393.

4. P.D. Beer, M.G.B. Drew, M. Kan, P.B. Leeson, M.I. Ogden, G. Williams, *Inorg. Chem*. (1996), **35**, 2202.

5. J. M'Halla, F. David, *Bulletin de la Société Chimique de France*, (1984), **34**, 85-90.

6. F. H. Spedding, G. Atkinson "The Structure of Electrolytic Solutions", J. HAMER (Wiley, New York), 1959.

7. Y. Marcus, *Chem. Rev* (1988), **88**, 1475-1498.

8. D. Barrón, S. Butí, M. Ruizb, J. Barbosa, *Polyhedron* (1999), **18**, 3281-3288.

Acknowledgements: We thank Prof. B. Jamoussi and Dr. L. Zayeni for their encouragement and support of this work.

3-22

Actinide colloids and nanoparticles: relevance to legacy waste, clean-up and geological disposal

Jennifer Rochford, Sarah Heath

University of Manchester, Manchester, UK

The hydrolysis of actinides needs to be understood at a molecular level to ensure thorough decontamination of waste water streams in effluent treatment facilities and if final disposal is to take place. The hydrolysis of actinides can be more fully understood by attempting to control complexation and hydrolysis reactions by restricting the number of free binding sites that are available for hydrolysis. The speciation of early actinides with simple organic ligands, primarily those which can occur in storage ponds and effluent streams, have been studied in aqueous systems over a wide pH range. The effects of eight ligands (thme, TEA, bicine, Heidi, NTA, ADA, citric acid and 5Me-HXTA) on the speciation and hydrolysis of Th^{4+} and UO_2^{2+} have been studied using various methods including $^{1}H/^{13}C$ NMR spectroscopy, UV/Vis spectroscopy, potentiometry and elemental analysis. The results have been interpreted using speciation modelling (PHREEQC).

The alcohol functionalities show no binding between 2 < pH < 13. The pK_a of an alcohol group is typically around 14 and hydrolysis has been seen at pH 5 for both Th^{4+} and UO_2^{2+}; so occurs before deprotonation and binding can take place. Reflecting this, at the high pH found in storage ponds, alcohol groups will not alter the chemistry of the actinides. Ligands containing one carboxylic acid functional group have been observed to bind between 2 < pH < 5. Through the presence of broad signals in the NMR, it has been determined that the ligands are fluxional and that as pH increases, hydrolysis occurs with the precipitation of hydroxide species. As further carboxylate groups are incorporated in the ligand, they become multidentate, and as a consequence, they become less labile preventing hydrolysis until the solution is at a higher pH. In some instances (citric acid and NTA) the actinide species is soluble up to pH 12.

Ligands containing both carboxylic acid and amide groups have also been investigated. At pH < 7 both the amide and carboxylate groups bind to the actinide, stabilising the species with respect to hydrolysis. However, as pH is increased further, only the carboxylate groups bind to the metal allowing partial hydrolysis to occur on the free site and by pH 9 a precipitate forms.

The functionalities of organic ligands have been shown to have a profound effect on the hydrolysis and partial hydrolysis of the actinides. This work is crucial to the nuclear industry and its environment impact.

3-23

Arene-Actinide interactions in the Flexible Macrocyclic Ligand Environment of *trans*-Calix[2]benzene[2]pyrrolide

Joy Farnaby[1], Rebecca White[1], Michael Gardiner[2], Jason Love[1], Polly Arnold[1]

[1]*University of Edinburgh, Edinburgh, UK,* [2]*University of Tasmania, Hobart, Australia*

We have recently shown the spontaneous activation and C-H bond functionalisation of simple aromatic hydrocarbons such as benzene, using the strong δ-backbonding from low-oxidation state uranium centres.[1] The bonding of actinide centres to soft arenes is of importance to the fundamental understanding of actinide covalency,[2] which is of relevance to the separation of minor actinides from nuclear waste mixtures.[3] The dianionic macrocyclic *meso*-octamethyl-*trans*-calix[2]benzene[2]pyrrolide ligand (L) has been shown both to stabilize Sm(II) and adopt a variety of bonding modes in complexes of the lanthanides.[4] Here we show how the varied binding modes, and reaction chemistry of this conformationally-flexible ligand with uranium and thorium cations, offer an ideal chance to explore the subtleties and differences in actinide-arene bonding in a well-defined molecular environment and compare covalency in actinide ions.[5]

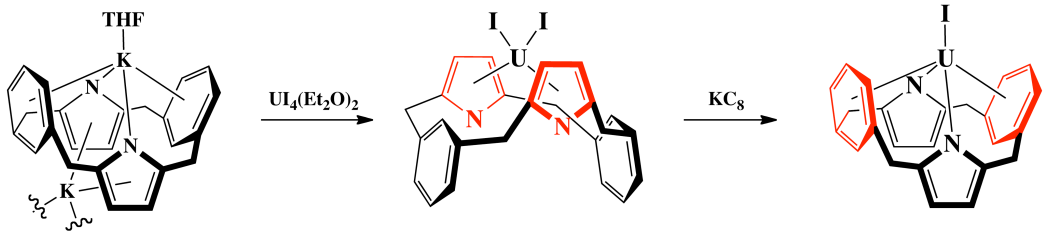

Figure 1: Synthetic route to UI_2L and UIL with η-pyrrolide and η-benzene binding highlighted in red and *meso*-methyl groups omitted for clarity.

The synthesis and characterization of UI_2L and $ThCl_2L$ are reported. The solid-state structures of both complexes show η^5-binding of the pyrrolide rings and no interaction with the benzene rings. Reduction of the thorium(IV) complex results in C-H activation and double metalation of the ligand; whereas reduction of UI_2L allows the isolation of the U(III) complex UIL. This has, in contrast to the U(IV) precursor, a η-benzene, κ^1-pyrrolide $\kappa^1{:}\eta^6{:}\kappa^1{:}\eta^6$ binding mode. Some studies on the magnetic and electronic structure, and the reaction chemistry of these complexes will be presented.

References

[1] P. L. Arnold, S. M. Mansell, L. Maron, D. McKay, *Nat. Chem.* **2012**, 4, 668.

[2] M. I. Neidig, D. L. Clark, R. L. Martin, *Coord. Chem. Rev.* **2013**, 257, 394.

[3] N. Kaltsoyannis, *Inorg. Chem.* **2013**, 52, 3407.

[4] A. S. P. Frey, M. G. Gardiner, A. J. Wilson, P. Jensen, P. Turner, *Angew. Chem. Int. Ed.* manuscript submitted.

[5] J. H. Farnaby, R. C. White, M. G. Gardiner, J. B. Love, P. L. Arnold, manuscript in submission.

3-24

Optimization Criterions for H_2O-$UO_2(NO_3)_2$-TBP System

Alexander Ochkin, Dmitriy Gladilov, Sergey Nekhaevskiy

D.Mendeleev University of ChemicalTechnology of Russia, Moscow, Russia

H_2O-HNO_3-$UO_2(NO_3)_2$-TBP-diluent system is the basic one for PUREX process. Usually this system is divided in some separate sub-systems. H_2O-$UO_2(NO_3)_2$-TBP system is being one of the most important sub-systems. Two variants of the description of this system were presented [1,2].

Experimental data were presented in [3] and included molar concentrations of uranyl nitrate c_U and water c_w in the organic phase, molal concentrations of uranyl nitrate m_U in the aqueous phase and densities d in the organic phase. Concentrations of TBP c_{tt} (total) and c_{tf} (free) were calculated from d.

Equilibrium concentrations were calculated using mole fractions x_i as it is presented in [2]. The aim of the calculation is a minimization of the sum of deviation of relative errors of calculated molar concentrations from experimental ones δ and the determination of extraction constant K_{ex} and the parameter b_1 of interaction of TBP and di-solvate.

Two problems arise due to experimental dispersions are not being homogeneous:

1. An equilibrium water concentration could not be properly determined when uranyl nitrate concentration is low. Therefore the experimental values of c_w in three points were two high and were changed to values from regression equation.

2. Errors of c_{tf} significantly increased when uranyl nitrate concentration reached high values.

In order to solve the first problem values of c_w from the regression equation have been used instead of experimental ones. It results in a decrease of δ_w. The second problem has been solved the inclusion of first experimental point in the special group in which a sum of δ_U and δ_{tf} is minimized. A sum of δ_U is minimized in the group of 27 points. The results are given in Table 1.

Table 1. Variants of optimization criterions.

	K_{ex}	b_1	δ_U %	δ_{tf} %	δ_w %
[1]	329	0.268	5.6	0.46 (δ_{tt})	7.2
[2]	311	0.341	6.1	10	7.4
17 points	304.5	0.288	7.5	2.1	-
27 points	303.9	0.283	6.1	18	3.1

It can be concluded that the value of K_{ex} is equal to 305±10 and the value of b_1 ~ 0.285±0.020.

References

[1] A.Ochkin et al. 19th International Solvent Extraction Conference. 3-7 October 2011 Santiago. Chile. 2011. Paper 131.

[2] A.Ochkin et al. *Procedea Chem.***7,** 315 (2012).

[3] W.Davis et al. Solvent Extraction Chemistry. Proceedings of the International Conference held at Gotheborg. Sweden. 27 August – 1 September 1966. North Holland Publishing Company. Amsterdam. 1967. p. 343-351.

3-25

Dodecane effect on nitric acid extraction with TBP

Alexander Ochkin, Dmitriy Gladilov, Sergey Nekhaevskiy

D.Mendeleev University of Chemical Technology of Russia, Moscow, Russia

H_2O-HNO_3-TBP-hydrocarbon solvent is one of the most important sub-systems of PUREX-process. The aim of this paper is to compare results of calculation of H_2O-HNO_3-TBP and H_2O-HNO_3-TBP-dodecane systems in order to estimate the effect of dodecane on the equilibrium. However in order to achieve this aim it is necessary to create a right way to determine a permissible interval of constants. The extraction of nitric acid with TBP can be calculated as

$$x_{ij} = K_{ij} \cdot a_a^{\ i} \cdot a_t^{\ j} / f_{ij} \quad (1)$$

Here a_a and a_t are activities of acid and TBP, f_{ij} is activity coefficient of solvate, K_{ij} is a constant of a formation of a solvate from i acid molecules and j TBP molecules, h_{ij} is a hydration ratio. Besides $K_{0.5}$ and $h_{0.5}$ are a constant and a hydration ratio of ion pair formation, b_2 is a solvent parameter and K and Δh are a constant and a hydration ratio of solvate formation through the reaction

$$H^+ + NO_3^- + (HNO_3)_n \cdot TBP \leftrightarrow (HNO_3)_{n+1} \cdot TBP \quad (2)$$

Table 1. Values of constant of solvate formation

	$K_{0.5}$	$h_{0.5}$	K_{11}	K_{12}	h_{12}	$K_{21} \cdot 10^4$	h_{21}	$K \cdot 10^4$	Δh
[1] 100% TBP	0.2956	3.5	0.2667	1.807	1.330	1.038	1.195	9.54	4.24
[2] TBP+n-$C_{12}H_{24}$	small	-	0.2692	1.764	1.246	0.304	0	-	-

Obviously the formation of mono-solvate, di-solvate and semi-solvate is sufficient to describe H_2O-HNO_3-TBP-dodecane system. However the values of constants are average ones obtained for 30%, 12% and 5 % TBP solutions and it is impossible now to determine a permissible interval of constants. The procedure of the calculation of the interval is given in Table 2.

Table 2. Calculation of interval of constants for 12% TBP

Other constants	b_2	h_{21}	δ_a %	δ_{tt} %	δ_{a+tt} %
K_{11} = 0.2692, K_{12} = 1.764, h_{12} = 1.246, $K_{21} \cdot 10^5$ = 3.543	0.606	-0,0225	3.51	2.67	3.12
	0.606	0	3.51	2.67	3.12
	0.606	1	3.45	3.21	3.33
	0.606	2	3.41	3.91	3.66
	0.606	3	3.38	4.43	3.94
the same	0.707	0	3.48	3.13	3.33

In Table 2 δ_a and δ_{tt} are the average relative deviations of calculated molar concentrations of acid and TBP from the experimental ones, $\delta_{a+tt} = [(\delta_a^2 + \delta_{tt}^2)/2]^{0.5}$. The alteration of h_{21} results in the alteration of values δ_a, δ_{tt} and δ_{att}. It is obvious that $h_{21} \geq 0$. Increasing of h_{21} from 0 to 3 results in the rise of δ_{a+tt} but the choice of a permissible interval of h_{21} depends on comparison of results found for systems with 30%, 12% and 5% TBP. It is necessary to compare results step by step.

[1] A.Ochkin et al. Russian Journal of Physical Chemistry, V. 83(10), pp. 1803 (2009).

[2] A.Ochkin et al. Russian Journal of Physical Chemistry, V. 84(9), pp. 1526 (2010).

3-26

Optical spectroscopy study into the bio-reduction of the uranyl(VI) ion and the uranyl(V) and uranium(IV) species generated.

Debbie Jones, Sean Woodall, Louise Natrajan, Adam Swinburne

University of Manchester, Manchester, UK

There is currently great concern regarding the release of radioactive materials into the environment from nuclear fission and related activities including future geological disposal scenarios. Uranium is common in most medium- and low-level radioactive wastes and is mostly found as the soluble uranyl(VI) ion (UO_2^{2+}), which is highly mobile and therefore poses a problem within the environment [1]. Studies into the bio-reduction of uranyl(VI) to the more insoluble and therefore environmentally manageable uranium(IV) ion have shown that the reduction may occur by a one electron process forming the unstable pentavalent uranyl ion (UO_2^{+}) as an intermediate [1]. The chemistry of uranyl(V) species and its role as an intermediate in the reduction of uranyl(VI) is important for the nuclear industry as it may be associated with potential uranium release during the storage of spent nuclear fuel [2].

We have attempted to understand the redox chemistry of this elusive uranyl(V) species and to develop an understanding of its electronic properties using optical spectroscopy by using a range of SiR_3 substituted 2,2'-bipyridine groups (where R= tert-butyldimethylsilyl, triisopropylsilyl, trimethylsilyl, tert-butyldiphenylsilyl). 2,2'-bipyridine ligands have previously been shown to be useful for optical studies of uranyl(VI) oligopyridyl complexes and were chosen for this reason [3]. We have also studied the redox reactions of uranyl(VI) in bacteria that contain one and two electron containing enzymes in order to follow the uranyl(VI)/(V)/uranium(IV) redox speciation in situ by optical techniques to further understand the bio-reduction of uranyl(VI).

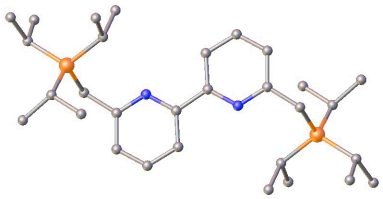

Figure 1: Crystal structure of 6,6'-bis-(triisopropylsilylmethyl)-2,2'-bipyridine4

References

[1] J.C Renshaw; L. Butchins; F.R Livens; I. May; J.M Charnock; J.R. Lloyd, Environ. Sci. Technol, 2005, 39, 5657-5660.

[2] Y. Suzuki; S. D. Kelly; K. M. Kemner; J. F. Banfield, Nature, 2002, 419, 134.

[3] G. Zucchi; O. Maury; P. Thuery; F. Gumy; J-C.G. Bunzli; M. Ephritikhine, Chem. Eur. J., 2009, 15, 9686-9696.

[4] D.Jones, M, Chem Report, University of Manchester, 2012.

3-27

Luminescent properties of uranium complexes

Michael Andrews, Louise Natrajan, Adam Swinburne, Sean Woodall, Simon Randall

The University of Manchester, Manchester, UK

The development of reprocessing strategies and long-term management programs for nuclear waste requires a detailed understanding of actinide behaviour in the environment. While the use of radiometric counting techniques is well developed as a means of following actinide migration, techniques based around the photophysical properties of uranium are relatively under-utilised. This is despite the potential for luminescence spectroscopy to provide valuable information regarding the oxidation state and speciation of uranium ions in solution. Here we present our efforts to study underexplored aspects of the green LMCT fluorescence of the $U(VI)O_2^{2+}$ species[1] as well as the first experimental studies of the f-f transitions of the U(IV) ion.[2] We also look at the little-known uranium(VI) terminal oxo complex $UOCl_5$ with the aim of furthering the knowledge of the non-trivial oxidation redox properties of uranium species in solution.

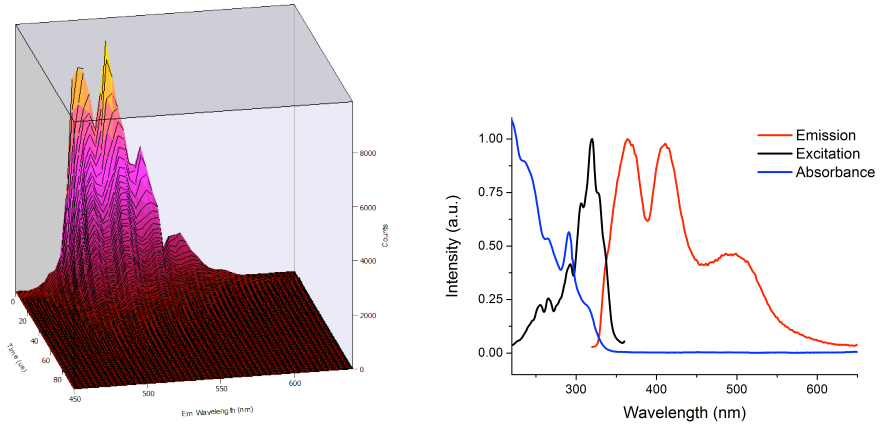

Time resolved luminescence of UO_2^{2+} (left) and spectra of U(IV) ion (right).

References

[1] M.P. Redmond, S.M. Cornet, S.D. Woodall, D. Whittaker, M. Helliwell, D. Collison, L.S. Natrajan, *Dalton Trans*., **2011**, *40*, 3914-3926.

[2] E. Hashem, A.N. Swinburne, C. Schulzke, R.C. Evans, J.A. Platts, A. Kerridge, L.S. Natrajan, R.J. Baker. *RSC Advances,* **2013**, *in press, DOI:* 10.1039/c3ra22712j.

3-28

Vibrational spectroscopic study of some rare-earth metals trifluoromethylsulfonates enneahydrates and of corresponding salts of uranium(III) and curium(III)

Mikhail Skripkin[1], Patric Lindqvist-Reis[2], Christos Apostolidis[3], Reinhardt Klenze[2], Janos Mink[4]

[1]Saint-Petersburg State University, Saint-Petersburg, Russia, [2]Institut für Nukleare Entsorgung, Karlsruhe Institute of Technology, Karlsruhe, Germany, [3]Institute for Transuranium Elements, European Commission, Joint Research Centre, Karlsruhe, Germany, [4]Institute of Molecular Pharmacology, Research Centre of Natural Sciences, Hungarian Academy of Sciences, Budapest, Hungary

Both lanthanides (Ln) and actinides (An) are f-block elements, corresponding to the filling of the 4f and 5f electron shells, respectively. Hence one would expect that their similar electronic structure result in similar coordination chemistry in aqueous systems; this is only partly true. While the later actinides (curium and beyond) form primarily trivalent cations and thus resemble the lanthanides in their coordination chemistry, the early actinides (up to americium) have several accessible oxidation states, all of which with their particular coordination chemistry.[1]

In order to study structural trends and bonding in lanthanide and actinide aqua complexes, it is important to compare complexes having very similar coordination structure. We chose the well-characterized isotypic series $[M(H_2O)_9](CF_3SO_3)_3$ (M = Ln, U-Cm, Cf) because of the recent established procedure for the preparation of the oxidation sensitive U and Np compounds.[2-3] In these structures the metal ions are surrounded by six equidistant water oxygen atoms at the vertices of a trigonal prism and three capping water oxygen atoms in the equatorial plane at somewhat longer distances. The MO_9 polyhedron (C_{3h} symmetry) is stabilized by hydrogen bonds to the triflate anions, which control the orientation of the coordinated waters (Figure 1). Because the hydrated complexes in this series mimic well the structure of the first hydration shell of nonahydrated Ln^{3+}/An^{3+} ions in aqueous solution,[4] we have carried out vibrational spectroscopic studies and normal coordinate analysis of $[M(H_2O)_9](CF_3SO_3)_3$ (M = Ln, U, Cm) to analyse the dependency of the M-O bond strength on the M^{3+} ionic radii. Of great importance was to ascertain whether the hydrated actinide ions follow the trend of the lanthanides. Infrared and Raman were used to study the vibrational spectra for M = Ln and U, while vibronic sideband spectroscopy (VSBS) was used for Cm. The advantage with the latter technique is that extremely small amounts of Cm^{3+} is needed in the doped $[M(H_2O)_9](CF_3SO_3)_3$ (M = La, Y) hosts to obtain low-temperature fluorescence emission spectra of high quality with detailed vibronic sideband structures, which consist almost exclusively of vibrational bands of $[Cm(H_2O)_9]^{3+}$.

Complete assignment of the vibrational bands of both $[M(H_2O)_9]^{3+}$ and $CF_3SO_3^-$ ions at room and low (77 and 20 K) temperatures was achieved. Site-symmetry effects, which result in splitting of the vibrational bands at low temperature, were clearly revealed and explained. Force field analysis of the vibrational spectra at generalized valence force field level was fulfilled and a full set of force constants in internal coordinates were obtained. The results clearly show that the metal-oxygen bonds in trivalent, isostructural lanthanide and actinide aqua complexes follow the same trend and is determined primarily by the metal-oxygen distance, which in turn is governed by the metal ionic radii.[3] This suggests that the metal-oxygen bonds are primarily electrostatic in nature. No evidence of bond covalence was revealed.

We gratefully acknowledge European Commission under the Euratom Research and Training Programme on Nuclear Energy for the financial support via ACTINET-13 programme (JPR 232631).

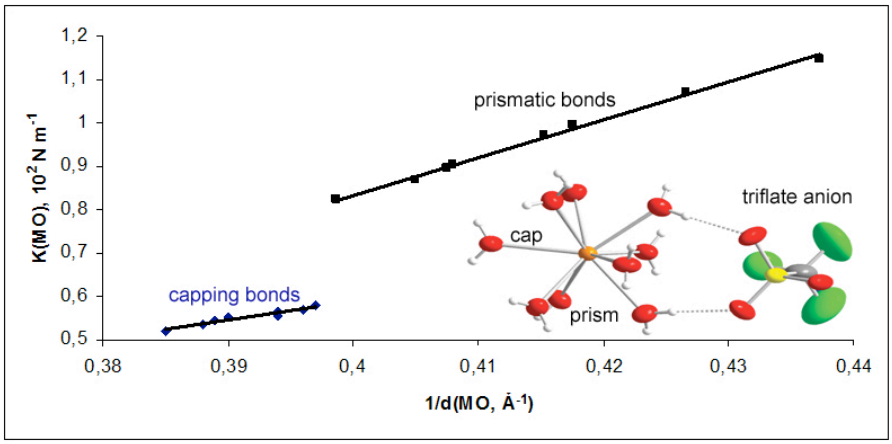

Figure 1. Correlation between M-O stretch force constants *K*(M-O) and reciprocals of the M-O bond distances *d*(M-O) for $[M(H_2O)_9](CF_3SO_3)_3$ (M = Ln, U, Cm). ■ – prismatic bonds, ♦ – capping bonds. Also depicted is a thermal ellipsoid plot (40 % probability) of the $[Cm(H_2O)_9]^{3+}$ cation hydrogen bonded to a $CF_3SO_3^-$ anion.

References

[1] Neidig, M.L.; Clark, D. L.; Martin, R. L., *Coord. Chem. Rev*. **2013**, *257*, 394.

[2] Lindqvist-Reis, P.; Apostolidis, C.; Rebizant, J.; Morgenstern, A.; Klenze, R.; Walter, O.; Fanghänel, T.; Haire, R. G. *Angew. Chem., Int. Ed.* **2007**, *46*, 919.

[3] Apostolidis, C.; Schimmelpfennig, B.; Magnani, N.; Lindqvist-Reis, P.; Walter, O.; Sykora,R.; Morgenstern, A.; Colineau, E.; Caciuffo, R.; Klenze, R.; Haire, R. G.; Rebizant, J.; Bruchertseifer, F.; Fanghänel, T. *Angew. Chem., Int. Ed.* **2010**, *49*, 6343.

[4] Persson, I.; D'Angelo, P.; De Panfilis, S.; Sandström, M.; Eriksson, L.; *Chem.-Eur. J.*, **2008**, *14*, 3056.

3-29

Self-assemblage of stable uranyl nano-clusters in the alkaline peroxide systems

Yingjie Zhang[1], Mohan Bhadbhade[2], Jason Price[3], Jiabin Gao[2], Inna Karatchevtseva[1], Gregory Lumpkin[1]

[1]Australian Nuclear Science & Technology Organisation, Sydney, Australia, [2]University of New South Wales, Sydney, Australia, [3]Australian Synchrotron, Melbourne, Australia

Actinide peroxide phases form in aqueous solutions throughout the nuclear fuel cycle and the nuclear medicine production processes such as uranium yellow cake production, nuclear wasteform and nuclear fuel in storage, as well as alkaline processing of LEU targets for ^{99}Mo production [1-3]. Thus the peroxide ligand must be considered in developing nuclear fuel reprocessing and separation of actinides, as well as models for actinide transport in the bio-geo-environment. Self-assemblage of nano-clusters of uranyl peroxide and/or hydroxide polymetalate anions in aqueous solutions has been reported [4] featuring edge-sharing $UO_2(O_2)_3$ polyhedra into spherical cages up to 60 uranium atoms. U24 and U28 are among the most stable uranium nano-spheres reported so far. In this work, we report two new U24 spherical clusters formed in the simulated processing conditions for the production of ^{99}Mo with pure Na^+ ions for charge balancing and templating. Two new U28 will also be reported with either Cs^+ or TeO_4^{2-} at the spherical centre. These spherical uranyl peroxide/hydroxide clusters are stable in aqueous solutions, proven by means of X-ray small angle scattering and particle size distribution studies, which provide direct evidence that their solution speciation is similar to their crystal structures in solid state.

References

[1] M. Nyman, M.A. Rodriguez and T.M. Alam, *Eur. J. Inorg. Chem*., 2011, 14 (2011) 2197-2205.

[2] B.A. Buchholz and G.F. Vandegrift, Processing of LEU targets for ^{99}Mo production, International Meeting on Reduced Enrichment for Research and Test Reactors, 18-21, Sept., 1994, Paris, France.

[3] A. Gil, D. Karhánek, P. Miró, M.R. Antonio, M. Nyman and C. Bo, *Eur. J. Inorg. Chem*., 18 (2012) 8340-8346.

[4] P.C. Burns, K.-A. Kubatko, G. Sigmon, B.J. Fryer, J.E. Gagnon, M.R. Antonio and L. Soderholm, *Angew. Chem. Int. Ed*., 44: 2039, 2005, doi: 10.1002/anie.200590044.

3-30

Structural studies of actinide complexes with picolinamide

Yingjie Zhang[1], Mohan Bhadbhade[2], Jiabin Gao[2], Inna Karatchevtseva[1], Gregory Lumpkin[1]

[1]Australian Nuclear Science & Technology Organisation, Sydney, Australia, [2]University of New South Wales, Sydney, Australia

The calixarene-based picolinamide ligands have been proposed and successfully tested for separation of actinide and rare earth elements [1]. However, the aqueous and solid state chemistries of actinides with simple picolinamide-based ligands are still poorly understood. There is an urgent need to study systematically the structural diversity for various actinide ions with such ligands. In this work, we report the first two crystal structures of uranyl(VI) and thorium(IV) complexes with picolinamide.

$(C_6H_6N_2O)_3(UO_2SO_4)_2$ (**1**) was crystallised in orthorhombic space group (*Cc*) with cell parameters of *a* 15.752(1), *b* 14.282(1), *c* 13.5345(8), β 116.583(4)^o, V 2722.94, Z=8 with final R-factor of 0.0502. The asymmetric unit contains two uranyl groups bridge-linked by two sulphate groups and an uncoordinated picolinamide. One uranyl group is quite normal with U-O bond length of 1.738 and 1.777 Å whilst the other uranyl group has relatively shorter U-O bonds (1.618 and 1.717 Å). A coordinated picolinamide (N, O) and three O from three sulphate groups occupy the equatorial plane forming pentagonal bipyramid uranium geometry. The sulphate group is tridentate (O, O', O'') to three uranium centres forming one dimensional ladder-type polymeric structure.

$[Th(C_6H_6N_2O)(H_2O)_3(SO_4)_2]\cdot H_2O$ (**2**) was crystallised in triclinic space group (*P*-1) with cell parameters of *a* 6.891(1), *b* 10.652(2), *c* 10.936(2), α 72.34(3), β 79.62(3), γ 77.92(3)^o, V 742.078, Z=2 with final R-factor of 0.0327. The Th atom is coordinated by a picolinamide (N,O), four sulphate O atoms and three coordinated water molecules forming an approximately capped square antiprismatic geometry for Th. One sulphate group is monodentate to a Th atom and the other sulphate group is tridentate (O, O', O'') to three Th atoms forming one dimensional polymeric chain structure.

References

[1] A. Casnati, N. Della Ca', M. Fontanella, F. Sansone, F. Ugozzoli, R. Ungaro, K. Liger and J.F. Dozol, *Eur. J. Org. Chem.*, 2005, 2338–2348.

3-31

Electrochemical and thermodynamic properties of uranium in low melting LiCl-KCl-CsCl eutectic.

Dmitry Maltsev, Vladimir Volkovich, Evgeny Vladykin, Boris Vasin

Ural Federal University, Ekaterinburg, Russia

One of the prospective scenarios of development of sustainable nuclear power is associated with short closed fuel cycle with at-station reprocessing of spent nuclear fuel (SNF). Reprocessing of SNF after short cooling time is possible only employing non-aqueous pyroelectrochemical methods that have a number of obvious advantages in comparison with the existing aqueous extraction processes. These advantages include significantly lower volumes of liquid radioactive wastes, high radiation stability of alkali chlorides used as working media, absence of neutron moderators. Pyrochemical methods, however, require high temperatures for keeping the melts in liquid state and conducting the process. Lowering working temperatures can be achieved by employing low-melting eutectic mixtures instead of individual alkali chlorides. Ternary lithium-potassium-cesium chloride eutectic has the lowest melting point (256 ^{o}C) of all known alkali chloride systems. Developing and optimization of pyroelectrochemical methods of SNF reprocessing requires reliable and comprehensive information concerning behaviour and properties of uranium and fission products in the chosen melt. The main objective of the present work was therefore studying the behaviour and determining main electrochemical and thermodynamic properties of uranium in LiCl-KCl-CsCl eutectic melt in a wide temperature range including:

- experimental determination of the formal standard electrode potential of U(III)/U(0) couple and the formal standard red-ox potential of U(IV)/U(III) couple;

- calculating major thermodynamic functions of U chlorides (Δ*G* of formation, mixing, *etc*.);

- determination of diffusion coefficients of uranium (III) and (IV) chloro-species in the melt.

Measurements were performed between 573-1073 K employing potentiometry, cyclic and square wave voltammetry. U concentration in the melt and the average oxidation state were determined by chemical analysis after each experiment. U formal standard electrode potentials in LiCl-KCl-CsCl eutectic melt were determined using electromotive force method. $E^*_{U(III)/U(0)}$ linearly increases with temperature and between 576-1067 K can be described by the following equation:

$$E^*_{U(III)/U(0)} = -2.901 + 6\cdot10^{-4} \cdot T\ (\pm\ 0.029)\ V$$

From the results of the electrochemical measurements Gibbs free energy change of the formation of uranium trichloride in LiCl-KCl-CsCl melt at 576-1067 K was calculated:

$$\Delta G^*_{UCl3} = -839.8 + 161.7\cdot10^{-3} \cdot T\ (\pm\ 2.6)\ (kJ/mol)$$

The results ($E^*_{U(III)/U(0)}$, ΔG^*_{UCl3}) obtained in the present work for LiCl-KCl-CsCl melt are in a good agreement with the literature data for the melts of other cationic compositions, Fig. 1.

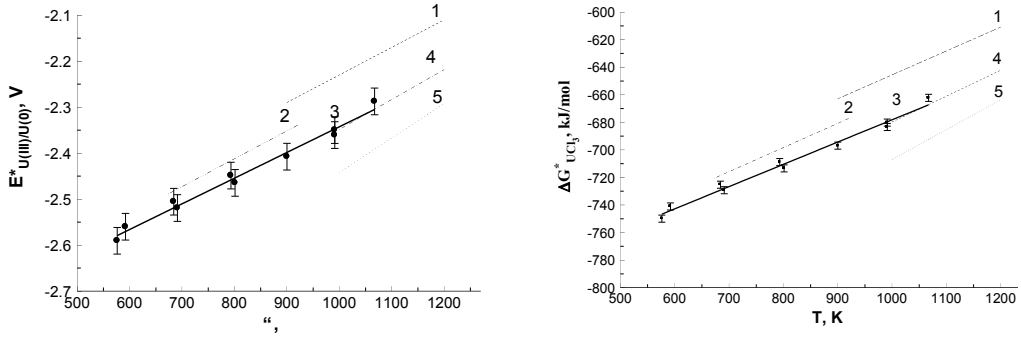

Fig. 1. Temperature dependence of $E^*_{U(III)/U(0)}$ (left) and $\Delta G^*_{U(III)/U(0)}$ (right) in alkali chloride melts: 1, LiCl; 2, LiCl-KCl; 3, LiCl-KCl-CsCl; 4, NaCl; 5, CsCl. 1, 2, 4, 5 – literature, 3 – present work. WE – W, RE – $2Cl^-/Cl_2$

Uranium (IV)/(III) electrochemical reduction was studied using cyclic and square wave voltammetry. Examples of the experimental results are shown in Figs 2-4. Analysis of the experimental data showed that U(IV) → U(III) reduction is a reversible one-electron diffusion controlled process.

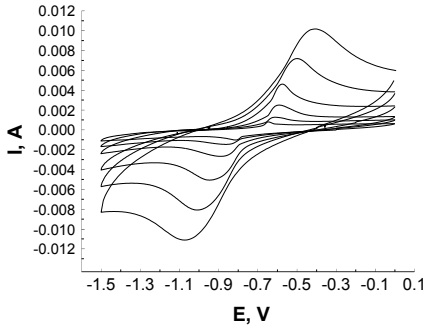

Fig. 2. Cyclic voltammograms measured in the region of U(IV)/U(III) reduction/oxidation in LiCl-KCl-CsCl melt at 573 K, 0.5 wt.% U. Scan rates: 10, 30, 60, 100, 500, 2000 mV/sec.

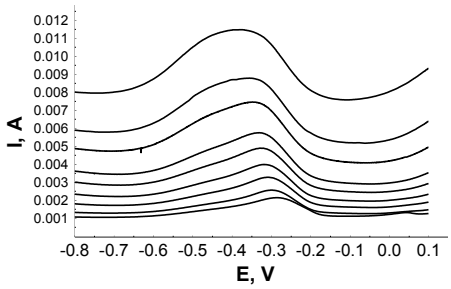

Fig. 3. Square wave voltammograms, measured at 773 K in uranium containing LiCl-KCl-CsCl melt. Frequency (bottom to top), Hz: 8, 12, 20, 30, 45, 60, 100, 140, 240. WE – W, RE – Ag/AgCl, 0.5 wt.% U.

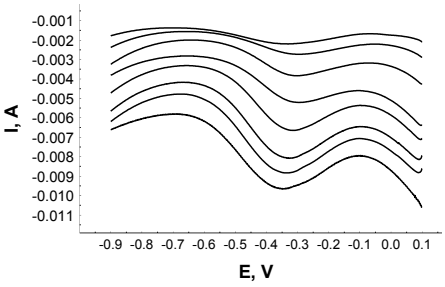

Fig. 4. Square wave voltammograms, measured at 773 K in uranium containing LiCl-KCl-CsCl melt. Frequency (top to bottom), Hz: 8, 12, 20, 30, 45, 60, 100, 140, 240. WE – W, RE – Ag/AgCl, 2.5 wt.% U.

Information concerning diffusion of ions of the same metal in different oxidation states is important for explaining the mechanism of diffusion of polyvalent metal ions in molten salt media. Therefore in the present work diffusion coefficients of uranium (III) and (IV) ions were determined between 573-1073 K employing cyclic voltammetry. The results obtained are presented in Figs. 5 and 6 in lg$D$ – 1/T coordinates. The experimental results are satisfactorily described by the following equations:

$\lg D_{U(III)} = -3781.14/T - 0.42\ (\pm 0.27)\ cm^2/s$

$\lg D_{U(IV)} = -3126.3/T - 1.43\ (\pm 0.16)\ cm^2/s$

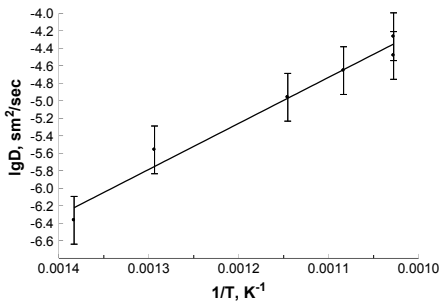

Fig. 5. U(III) chloro-species diffusion coefficients in LiCl-KCl-CsCl eutectic based melts.

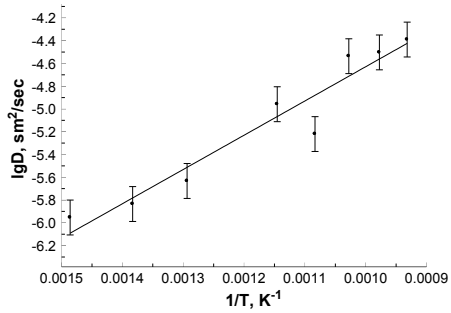

Fig. 6. U(IV) chloro-species diffusion coefficients in LiCl-KCl-CsCl eutectic based melts.

3-32

Synthesis and characterization of new heterometallic uranyl-based carboxylates

Christophe Volkringer, Ionut Mihalcea, Clement Falaise, Natacha Henry, Thierry Loiseau

University of Lille, Lille, France

The formation of coordination polymers involving actinide cations with O-donor organic ligands (i.e., multidentate carboxylates) has been extensively investigated in the past decades, especially with hexavalent uranium. A large number of hybrid organic−inorganic architectures have thus been reported with different dimensionalities, exhibiting various coordinations for uranyl cations together with diverse building units. For the organic part, the reactivity of aliphatic or aromatic polycarboxylate has been explored and successfully led to the so-called uranyl organic frameworks (UOFs). Surprisingly, the association of a hetero metal such as rare-earth elements or other transition elements was rarely reported in literature, instead of different field of applications. Indeed, the use of lanthanide elements may simulate the chemical reactivity of the radionuclides plutonium or other highly radioactive actinides. Furthermore, transitions metals are present in many natural minerals or as fission products, and need to be separate from valuable actinides.

Through this presentation, we are going to talk about syntheses and crystal structure of heterometallic carboxylates formed from uranyl and either lanthanides (Ce, Nd) or 3d transition metals (Cu, Zn).

In the case of mixed lanthanide-uranyl, we will discuss about a unique case of heterometallic cation-cation interaction with U^{VI}=O-Ln^{III} bonding[1] (Ln = Ce, Nd) (figure 1.a). The series of mixed U-Ln solids were also thermally decomposed in order to analyze the formation of mixed oxides, from the perspective of producing new types of nuclear fuels or extraction setups.[1, 2]

The synthesis of mixed solids containing copper[3] or zinc[4] leads to a series of heterometallic compounds with particular chemistry, and unexpected dehydration behavior for some of them (figure 1.b).

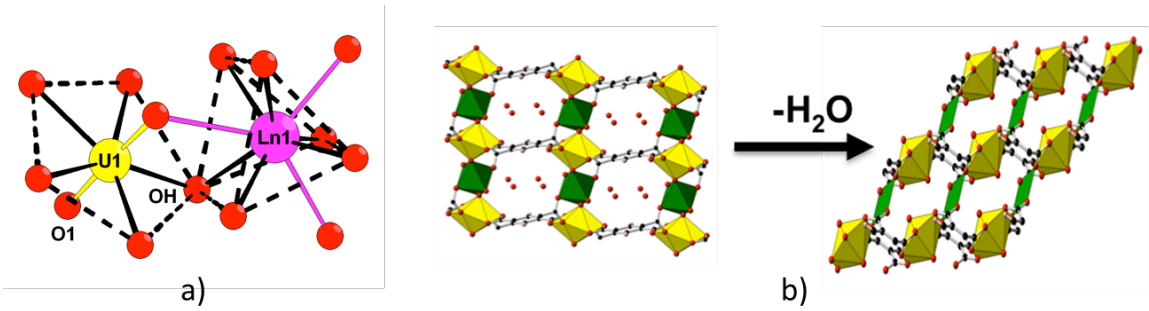

Figure 1: Illustration of heterometallic cation-cation interaction with U^{VI}=O-Ln^{III} (a) and topotactic transformation occurring in mixed U-Cu pyromellitate upon dehydration (b).

References:

1- C. Volkringer, N. Henry, S. Grandjean, T. Loiseau, *J. Am. Chem. Soc.* **2012**, 134, 1275
2- I. Mihalcea, C. Volkringer, N. Henry, T. Loiseau, *Inorg. Chem.* **2012**, 51, 9610
3- J. Olchowka, C. Falaise, C. Volkringer, N. Henry, T. Loiseau, *Chem. Eur. J.* **2013**, 19, 2012
4- J. Olchowka, C. Volkringer, N. Henry, T. Loiseau, *Eur. J. Inorg. Chem.* **2013**, DOI: 10.1002/ejic.201201349

3-33

TRLFS study on the complexation of Cm(III) and Eu(III) with methyl-substituted diglycolamides

Björn Beele[1,2], Andreas Wilden[3], Andrej Skerencak-Frech[2], Steve Lange[3], Fabian Sandowski[3], Giuseppe Modolo[3], Petra Panak[1,2], Mudassir Iqbal[4], Willem Verboom[4], Andreas Geist[2]

[1]Ruprecht-Karls-Universität Heidelberg, Physikalisch-Chemisches Institut, Heidelberg, Germany, [2]Karlsruher Institut für Technologie (KIT), Institut für Nukleare Entsorgung, Karlsruhe, Germany, [3]Forschungszentrum Jülich GmbH (FZJ), Institut für Energie- und Klimaforschung, Jülich, Germany, [4]University of Twente, Laboratory of Molecular Nanofabrication, Enschede, The Netherlands

Numerous processes based on oxygen and nitrogen-donor ligands have been developed in order to achieve separation of trivalent actinides, An(III) and trivalent lanthanides, Ln(III).[1] Hereby diglycolamide ligands like TODGA (*N*,*N*,*N*',*N*'-tetraoctyldiglycolamide) are widely-used as efficient O-donor ligands for the An(III) and Ln(III) co-separation by solvent extraction.[2,3]

The extraction behavior of An(III), Ln(III) and other fission products is significantly influenced by structural changes in the back-bone of the TODGA ligands.[4] In this work, the TODGA molecule was modified by adding one or two methyl groups to the carbon-atoms in α-position to the ether oxygen atom (Fig. 1).

In liquid-liquid extraction studies using TODGA **1** and the methyl-substituted derivatives Me-TODGA **2** and Me_2-TODGA **3** a distinct influence of the degree of substitution on the extraction performance is observed: Significantly lower distribution ratios for trivalent lanthanides and trivalent actinides are found using Me-TODGA or Me_2-TODGA in comparison to TODGA.

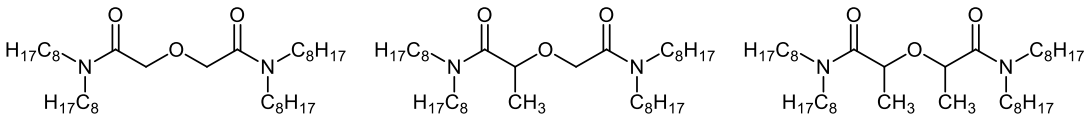

1 **TODGA** | **2** **Me-TODGA** | **3** **Me_2-TODGA**

Fig 1. Molecular structures of TODGA 1, Me-TODGA 2, and Me_2-TODGA 3.

In order to obtain information about the stoichiometry of the formed complexes and thermodynamic data of the complexation reactions the complexation of Cm(III) and Eu(III) with TODGA, Me-TODGA and Me_2-TODGA is studied.

Hereby Time-resolved laser fluorescence spectroscopy (TRLFS) as very versatile spectroscopic method for these metal ions is used.[3,5] As an example the Cm(III) emission bands upon increasing TODGA concentration are shown in Fig. 2. Three emission bands with emission maxima at 600.9 nm, 603.3 nm and 608.4 nm are found. These emission bands are assigned to solvated Cm(III), Cm-TODGA 1:1 and Cm-TODGA 1:3 complex species via slope analysis. According emission bands were obtained in TRLFS studies of the complexation of Cm(III) with Me-TODGA **2** and Me_2-TODGA, **3** respectively. The following conditional stability constants were determined: $\log \beta_3(Cm(TODGA)_3) = 14.92 \pm 0.30$, $\log \beta_3(Cm(Me\text{-}TODGA)_3) = 14.85 \pm 0.31$, $\log \beta_3(Cm(Me_2\text{-}TODGA)_3) = 12.72 \pm 0.25$.

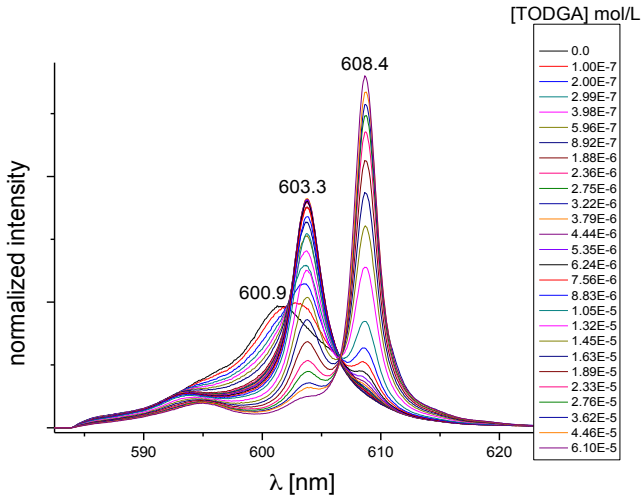

Fig. 2 Normalized fluorescence spectra of Cm(III) with increasing TODGA concentration in ethanol; $[Cm(III)]_{ini} = 1.0 \cdot 10^{-7}$ mol/L.

The complexation of Eu(III) with the diglycolamide ligands was studied by recording the $^5D_0 \rightarrow {}^7F_1$, $^5D_0 \rightarrow {}^7F_2$ und $^5D_0 \rightarrow {}^7F_4$ emission bands at different ligand concentrations. The following conditional stability constants were determined: log β_3(Eu(TODGA)$_3$) = 15.69 ± 0.22, log β_3(Eu(Me-TODGA)$_3$) = 15.45 ± 0.20, log β_3(Eu(Me$_2$-TODGA)$_3$) = 15.47 ± 0.24.

Furthermore, to verify that the 1:3 metal complex species formed in monophasic titration experiments are the same species which are formed by extraction into kerosene the organic phases of two-phase extraction experiments are characterized by TRLFS. The results show that the emission spectra of the Cm(III) complexes prepared by liquid-liquid extraction into a solvent consisting of TODGA, Me-TODGA or Me$_2$-TODGA, in kerosene were identical with the emission bands observed in the titration experiment in ethanol.

Our studies show that results obtained by TRLFS are in good agreement with results from liquid-liquid extraction. Calculated separation factors $SF_{Cm(III)/Eu(III)} = \beta_{3,Cm(III)} / \beta_{3,Eu(III)}$ are in excellent accordance with the experimental values obtained by extraction experiments.

References

[1] G. Modolo, A. Wilden, A. Geist, D. Magnusson, R. Malmbeck, *Radiochim. Acta* **2012**, *100* (8–9), 715–725.

[2] D. Magnusson, B. Christiansen, J.-P. Glatz, R. Malmbeck, G. Modolo, D. Serrano-Purroy, C. Sorel, Solvent Extr. Ion Exch. **2009**, *27* (1), 26-35.

[3] P. Panak, A. Geist, *Chem. Rev.* **2013***, 113*, 1199–1236.

[4] M. Iqbal, J. Huskens, W. Verboom, M. Sypula, G. Modolo, *Supramol. Chem.* **2010**, *22*, 827-837.

[5] N. M. Edelstein, R. Klenze, T. Fanghänel, S. Hubert, Coord. Chem. Rev. **2006**, *250*, 948.

3-34

Influence of the solvent on the complexation of Cm(III) with nPr-BTP studied by time-resolved laser fluorescence spectroscopy

Antje Bremer[1,2], Andreas Geist[1], Petra J. Panak[1,2]

[1]Karlsruhe Institute of Technology (KIT - Institute for Nuclear Waste Disposal (INE), Eggenstein-Leopoldshafen, Germany, [2]University of Heidelberg - Institute for Physical Chemistry, Heidelberg, Germany

An efficient separation of trivalent actinide and lanthanide ions by liquid-liquid extraction is an essential part of innovative nuclear fuel cycles which are under consideration in many countries.[1] This separation is a very challenging task due to the distinctive chemical similarity of An(III) and Ln(III) and a lot of effort has been put into the development of selective extractants. Alkylated 2,6-bis(1,2,4-triazin-3-yl)pyridines (BTPs) belong to the most promising extracting agents so far.[2] Although a multitude of BTP-like ligands has been synthesized, the molecular reason for the high selectivity of these soft N-donor ligands is not fully understood. To gain a better understanding, further investigations on the complexation of An(III) and Ln(III) with BTP-type ligands of particular interest.

Unfortunately, these investigations cannot be performed in the same solvent for the various ligands e.g. due to solubility problems or slow complexation kinetics. In previous studies numerous different conditions and solvents have been applied, most often using a mixture of alcohol (MeOH, EtOH or 2-PrOH) and water as solvent. A comparison of these studies has shown that the water content as well as the alkyl chain of the alcohol have a distinct impact on the stability constants of the formed complexes.[3] Therefore, a detailed knowledge on the influence of the solvent is indispensable for a reliable comparison between different ligands investigated in different solvents.

Time-Resolved Laser Fluorescence Spectroscopy (TRLFS) is a very sensitive spectroscopic method which makes it possible to follow the complex formation of fluorescing ions like Cm(III) in solution.[4] Spectroscopic parameters like position and shape of an emission band provide information on the number and the type of coordinating ligands. This method is a very powerful and established tool for investigations on the complexation behaviour of ligands.

In the present work, TRLFS is used for a detailed investigation on the influence of water content in the solvent mixture on the stability constants of the complexation of Cm(III) with nPr-BTP (2,6-bis(5,6-dipropyl-1,2,4-triazin-3-yl)pyridine).

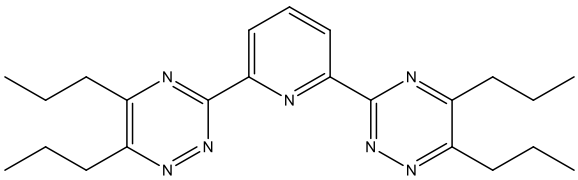

Figure 1: Molecular structure of nPr-BTP (2,6-bis(5,6-dipropyl-1,2,4-triazin-3-yl)pyridine.

The well-known nPr-BTP ligand is used as a test ligand with good solubility and complexation properties. The stability constant for the $[Cm(nPr\text{-}BTP)_3]^{3+}$ complex in MeOH:water 1:1 is log $b_3 = 14.4 \pm 0.1$[5]. In our studies, we performed several experiments with varying water content in the solvent mixture, with the lowest water ratio being 1.5 vol%. As an example, the fluorescence spectra of Cm(III) with increasing concentration of nPr-BTP measured in this solvent mixture are presented in Figure 2.

Our results prove a strong influence of the water content on the stability constant. We observed a significant increase of $\log\beta_3$ for the Cm(III)-nPr-BTP 1:3-complex of approximately 2 orders of magnitude with reducing the water content from 50 vol% to 1.5 vol%. These results are important for the evaluation and comparison of stability constants for various ligands determined under different conditions.

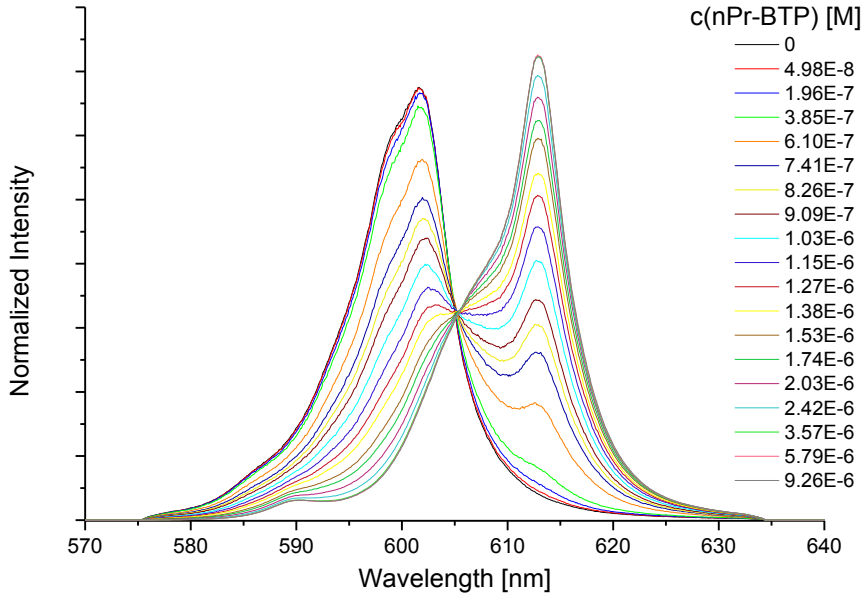

Figure 2: Normalized fluorescence spectra of Cm(III) with increasing concentration of nPr-BTP in methanol with 1.5 vol% water.

References

[1] a)Actinide and Fission Product Partitioning and Transmutation, Status and Assessment Report, OECD Nuclear Energy Agency, Paris, **1999**. b) M. Salvatores, G. Palmiotti, Prog. Part. Nucl. Phys. **2011**, *66*, 144-166.

[2] a) Z. Kolarik, U. Müllich, F. Gassner, *Solvent Extr. Ion Exch.* **1999**, *17*, 1155-1170. b) S. Trumm, A. Geist, P. J. Panak, Th. Fanghänel, *Solv. Extr. Ion Exch.* **2011**, *29*, 213-229.

[3] P. J. Panak, A. Geist, *Chem. Rev*. **2013**, *113*, 1199-1236.

[4] R. Klenze, J. I. Kim, H. Wimmer, *Radiochim. Acta* **1991**, *52/53*, 97-103.

[5] S. Trumm, P. J. Panak, A. Geist, T. Fanghänel, *Eur. J. Inorg. Chem.* **2010**, 3022-3028.

3-35

Trivalent Lanthanide/Actinide Separation Using Aqueous-Modified TALSPEAK Chemistry

Travis Grimes, Leigh Martin

Aqueous Separations and Radiochemistry Department, Idaho National Laboratory, Idaho Falls, ID, USA

A key step in the development of a sustainable closed nuclear fuel cycle is transmutation of the long-lived minor actinides Am^{3+} and Cm^{3+}. Efficient transmutation of these elements is only achievable once they are separated from the trivalent lanthanides since the lanthanides (in particular Nd^{3+}, Sm^{3+}, Eu^{3+}, Gd^{3+}) have large thermal neutron capture cross sections that act as neutron poisons and could compete with the minor actinides for neutrons. In the U.S., the TALSPEAK process has received the most attention for accomplishing the lanthanide/actinide group separation. This system uses a complex aqueous medium with a high concentration of lactic acid (HL) buffer, and diethylenetriamine-N,N,N',N",N"-pentaacetic acid (DTPA) as an aqueous "holdback" reagent for the actinides at pH 3-4. The aqueous phase is contacted with an immiscible organic phase containing the monoacidic dialkyl bis(2-ethylhexyl)phosphoric acid extractant (HDEHP). DTPA selectively coordinates the actinides holding them in the aqueous phase, and HDEHP extracts the trivalent lanthanides into the organic phase. Although TALSPEAK has been proven successful at pilot plant scale, recent fundamental studies have highlighted complex chemical interactions occurring in the aqueous and organic phases during the extraction process. Previous work has attempted to model the traditional TALSPEAK system has shown thermodynamic models do not accurately predict the observed extraction trends in the $p[H^+]$ range 2.5-4.8.

The purpose of this study is to explore the Ln^{3+}/An^{3+} group separation and potentially improve thermodynamic predictability of the TALPSEAK process. By substituting the lactic acid buffer, with a variety of amino acids (which buffer between pH 2.0-2.4), TALSPEAK can possibly be operated at conditions reduced by 1.0-1.6 pH units. We proposed that operating TALSPEAK in a lower pH range and substituting the aromatic 1,4-diisopropylbenzene (DIPB) organic diluent with n-dodecane (an aliphatic diluent) would create a more "ideal" solvent extraction system that can be modeled using thermodynamic data found in the literature. The amino acid buffers chosen for study are shown in Figure 1.

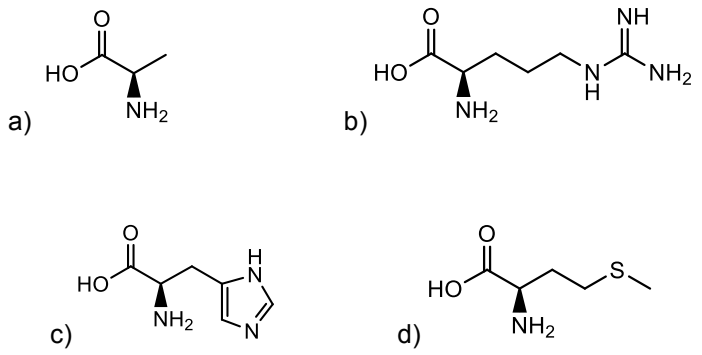

Figure 1. a) L-alanine, b) L-arginine, c) L-histidine, d) L-methionine

Initially, solvent extraction studies were conducted using three different concentrations of L-alanine buffer (0.5, 1.0, and 1.5 M) with varied aqueous phase acidities, pH 1, pH 2, and pH 3 to determine the effect of reducing buffer concentration and aqueous acidity. A representative sample of results from these studies is shown in Figure 2.

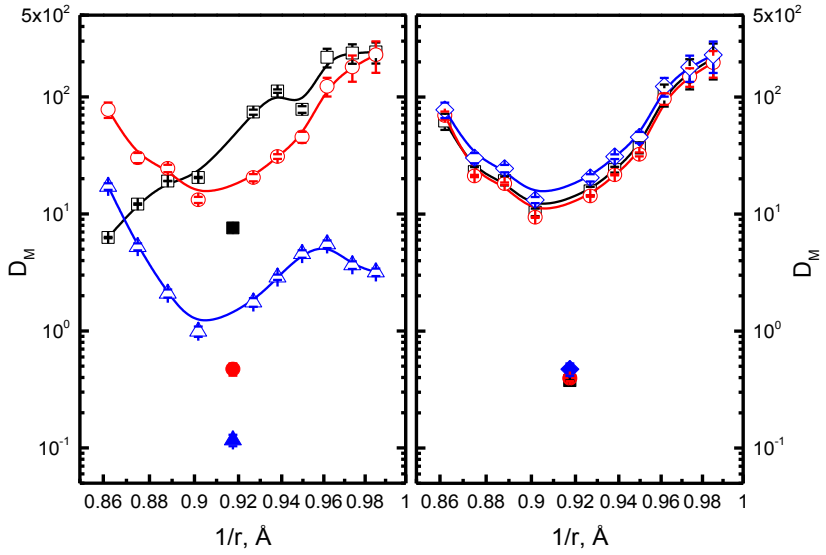

Figure 2. Left panel: Comparison of trivalent lanthanide/Am^{3+} extraction using L-alanine buffered TALSPEAK at pH 1(□,■), pH 2 (○,●), and pH 3 (△,▲). Organic phase: 0.2 M HDEHP in n-dodecane, aqueous phase: 0.5 M L-alanine, 0.050 M DTPA. **Right panel:** Demonstration of the successful separation of Ln^{3+} from Am^{3+} at varying concentrations of L-alanine, 1.5 M (□,■), 1.0 M (○,●), 0.5 M (◇,◆). Aqueous phase: 0.050 M DTPA, acidity adjusted to pH 2, organic phase: 0.2 M HDEHP in n-dodecane. Open symbols represent the lanthanide series (La^{3+}-Ho^{3+}, excluding Pm^{3+}), closed americium.

In this presentation, the effects of varying amino acid, buffer concentration and pH will be discussed in terms of separation performance. The modified TALSPEAK process will be shown to operate with a reduced buffer concentration and at lower pH. The results also demonstrate that the modified TALSPEAK process operates without any phase-transfer kinetics issues that are known to occur in traditional TALSPEAK. Successful modeling of the aqueous-modified TALSPEAK process (p[H^+] 1.6-3.1) using a simplified thermodynamic model will also be presented.

3-36

Solid Phase Extraction Materials for Separations of Actinides and Fission Products

Jennifer Shusterman, Eva Uribe, Tashi Parsons-Moss, Anthony Bruchet, Erin Gantz, Heino Nitsche

University of California, Berkeley, Berkeley, CA, USA

The ability to separate radionuclides quickly and with high separation factors and simple procedures, is necessary for a number of reasons, including purification of long-lived materials present in spent nuclear fuel (SNF) for storage and/or reuse. Spent nuclear fuel and legacy waste contain primarily uranium, but there are also significant contributions from plutonium, minor actinides, and both stable and radioactive fission products. Developing procedures to separate these components has long been a goal of the radiochemistry community due to the necessity for either long-term storage or reprocessing of the radioactive materials. Safe storage of this high level waste (HLW), both to prevent proliferation and introduction to the biosphere, requires that radionuclides are separated based on both chemical and radiolytic properties. The Plutonium URanium Extraction (PUREX) process is used to extract plutonium and uranium (Pu and U) from these wastes; however, the remaining actinide and fission product constituents are stored together. Developing a separation that can isolate the minor actinides, namely Np, Am, and Cm, from the fission products and then isolate each of the minor actinides from one another would allow for a smaller volume of long-lived radiotoxic waste.

Challenges in separation procedures for reprocessing legacy wastes and SNF are encountered mainly due to the large volumes that ultimately must be treated. Large volumes of highly radioactive materials tend to have elevated temperatures from decay energy, which can potentially destroy materials used for separations. Additionally these materials are usually in acidic, oxidizing solutions with high salt content, which creates a very corrosive environment. Radioactive decay can also degrade materials via radiolysis reactions. Thus, ideal materials used for separations must be resistant to high temperatures, corrosion, radiolysis, and hydrolysis.

The majority of separations methods in the literature and, in turn, implemented industrial processes in this field, use solvent extraction. Solvent extraction, while a well understood and successful technique for selective separations of elements, produces large amounts of waste and can be complicated by a number of factors. These complications include third-phase formation and extractant degradation due to time and radiation effects. Additionally, due to phase transfer kinetics, solvent extract processes are sometimes kinetically hindered. To minimize hazardous waste production and third-phase formation, and to potentially increase reaction kinetics, solid-liquid methods can be used.

In this work, we have focused on solids that either have ligands grafted or coated on them. The coated material was a commercial diglycolamide (DGA) based extraction chromatography resin that we tested with various trivalent lanthanides and actinides in highly acidic conditions. The results were not as expected, likely due to instability of the extraction chromatography resin. Because the material most likely degrades from the ligand falling off of the polymer bead support, we would like to improve stability by chemically bonding the ligands to the surface of the solid. We are particularly interested in mesoporous silica as a solid support. The benefits of mesoporous silica include high surface area, ordered structure, potential for incorporation of silica into a vitrified waste matrix, and chemical and thermal stability of the material. The high surface area will lend to increased ligand density compared to coated chromatography resins. The ligands of interest have links to current solvent extraction methodologies. By grafting a ligand with known liquid-liquid extraction behavior to mesoporous silica, we are comparing the behavior of functionalized materials and the free ligand.

In choosing ligands to graft to the silica surface, we are focusing on those pertinent to complexation and subsequent separation of the transuranic elements and lanthanide fissions products. Elements of particular concern are the minor actinides (Np, Am, Cm) as they contribute to the long term radioactivity in spent nuclear fuel after U and Pu have been removed. Separations of these elements from fission products are important to reduce the overall heat loading from the fission products. The focus of this work will be on grafting

ligands that have been shown to strongly complex Np, Am, or Cm in solvent extraction procedures to mesoporous silica. These separations will be tested in the presence of Pu to determine if they can be added to spent fuel treatment processes after only U has been extracted.

We tested an acetamide phosphonate ligand (Ac-Phos) grafted to SBA-15 type mesoporous silica (Figure 1), a system originally introduced by Fryxell (Fryxell et al., 2007). We performed batch contact experiments with Pu(IV), Pu(VI), Ce(III), and Eu(III). It was determined that there was very high sorption of Pu(VI), but that it was not easily stripped from the material, which makes it a poor separations material. Additionally, the Ac-Phos bound all species under all tested conditions, so it would not be a selective material. There were fast kinetics for this sorption, however, which supports the hypothesis that solid-liquid extractions may have faster kinetics than liquid-liquid extraction. Recently, a hydroxyquinoline based ligand has been tested (Figure 2) and compared to a pyridine based ligand (Figure 3), both functionalized to SBA-15 type mesoporous silica. The pyridine ligand contains a binding site with three nitrogens that, due to their soft-donor nature, were expected to bind actinides more strongly than lanthanides. The hydroxyquinoline based ligand contains a binding site with two nitrogens and one oxygen. The addition of oxygen, a hard donor, was expected to increase complexation with lanthanides because of their ionic character. Both materials showed little to no sorption of Eu(III), a model fission product, which led to studies to test the stability of these materials. It was determined that the functionalized material was breaking down at the imine linkage that attached the ligand to the silane anchor holding it to the surface. Based on this work, new functionalization methods will be used to graft future ligands to the mesoporous surface. Repetition of pyridine and hydroxyquinonline based materials will be done with the new grafting techniques.

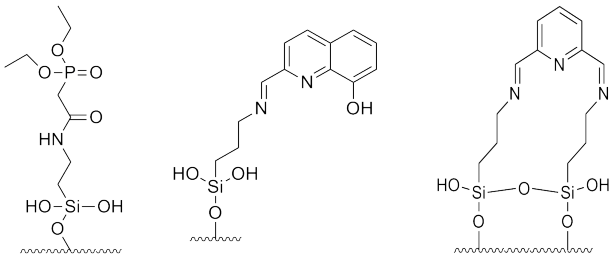

Figure 1 (left) Ac-Phos, Figure 2 (middle) Pyridine based ligand, Figure 3 (right) Hydroxyquinoline

Currently, we are developing a different morphology of SBA-15 material that has spherical particles and uniform particle size to allow for potential chromatographic separations. Additionally, we are testing new ligands that are aimed at complexing trivalent actinides and/or lanthanides. Our current studies will include detailed material characterization after silica synthesis, ligand grafting, contact with acidic solutions, and metal sorption. By including characterization at all steps of the process, we aim to determine the fundamental chemistry in these silica-supported metal-ligand complexes.

References

[1] Fryxell, G. E., Mattigod, S. V., Lin, Y., Wu, H., Fiskum, S., Parker, K., Zheng, F., et al. (2007). Design and synthesis of self-assembled monolayers on mesoporous supports (SAMMS): The importance of ligand posture in functional nanomaterials. *Journal of Materials Chemistry*, *17*(28), 2863. doi:10.1039/b702422c

3-37

Effect of hydrogen bonds on melting points and packing coefficients of uranyl nitrate complexes with cyclic urea derivatives

Tomoya Suzuki[1], Takeshi Kawasaki[1], Koichiro Takao[1], Masayuki Harada[1], Masanobu Nogami[2], Yasuhisa Ikeda[1]

[1]Tokyo Institute of Technology, Tokyo, Japan, [2]Kinki University, Osaka, Japan

In our previous study, we found out that *N*-alkylated 2-pyrrolidone derivatives selectively precipitate U(VI) from HNO_3 solution. On this basis, we have proposed an advanced reprocessing system for spent nuclear fuels of fast breeder reactors [1]. In this system, U and Pu are recovered through two precipitation processes after dissolution of the spent nuclear fuels in HNO_3 solution. We have proposed that solubility of the uranyl precipitates or precipitation ability to U(VI) and Pu(IV) are determined by hydrophobicity of precipitants and melting points (mps) of the precipitates [2]. Hydrophilic precipitants which can form U(VI) precipitates with high mps are expected to exhibit high selectivity to U(VI). The low hydrophobicity can be achieved by simply designing a precipitant structure, e.g., introduction of hydrophilic groups or shortening of alkyl groups. In contrast, requirements to form U(VI) precipitates with high mp are not clear. Lattice energy of crystal is known to be related closely to mp. Formation of intermolecular hydrogen bonds (HBs) is expected to raise the lattice energy and hence mp of U(VI) precipitates. Therefore, HB sites should be introduced in the precipitant structures. On these contexts, we have examined the crystal structures of U(VI) nitrates with cyclic urea derivatives (L) shown in Fig. 1. We prepared $UO_2(NO_3)_2(L)_2$ complexes and determined their molecular structures by X-ray crystallography. The aims of this study are to confirm if HBs are formed in these crystals as expected, and to clarify HB effect on mps of this kind of compounds.

Geometrical analyses were performed by PLATON using crystal structures of $UO_2(NO_3)_2(L)_2$ [3]. Melting points of ground U(VI) complexes were also measured under Ar atmosphere. Figure 2 shows two types of intermolecular HBs observed in $UO_2(NO_3)_2(\mathbf{0a})_2$. As seen from this figure, N1-H forms a bifurcated HB with oxygen of carbonyl group and nitrate of the neighboring molecule. In contrast, N2-H interacts with an axial oxygen atom of uranyl moiety in the neighbor. In the $UO_2(NO_3)_2(\mathbf{0b})_2$, similar interactions were also found to be formed. In **2a** or **2b**, there are no possibilities to form HBs through the >NH, whereas two C-H···O HBs were observed in $UO_2(NO_3)_2(\mathbf{2a})_2$ and $UO_2(NO_3)_2(\mathbf{2b})_2$. It has been reported that bond strength of C-H···O bonds are 25 - 50 % of O-H···N or N-H···O bonds. Vishweshwar et. al. assumed that three C-H···O HB are energetically equivalent to one O-H···N HB [4]. Therefore, we also regard three C-H···O HB as one N-H···O and calculated conversion number of N-H···O HBs as (conversion number of N-H···O HBs) = (number of N-H···O HBs) + 0.33 × (number of C-H···O HBs). The results are listed in Table 1 together with mp values and packing coefficients. From this table, it is recognized that mp of $UO_2(NO_3)_2(L)_2$ certainly depends on the conversion number of HBs. Furthermore, tendency of packing coefficients indicates that an increase in the conversion number of HBs results in the closer packing. From these results, it is suggested that formation of intermolecular HBs is an important factor for forming $UO_2(NO_3)_2(L)_2$ with high mp.

We are now investigating the crystal structures of $UO_2(NO_3)_2(1a)_2$ and $UO_2(NO_3)_2(1b)_2$, which are the intermediates of both cyclic urea series and expected to provide more detailed understanding on the relationship between HBs and mp.

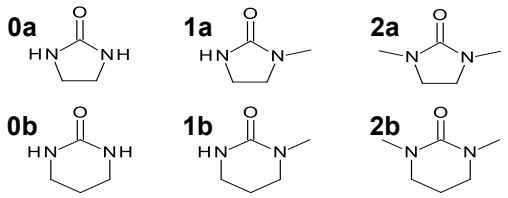

Figure 1. Structural formula of cyclic urea compounds, 2-imidazolidone (**0a**), 1-methyl-2-imidazolidone (**1a**), 1,3-dimethyl-2-imidazolidone (**2a**), tetrahydro-2-pyrimidinone (**0b**), 1-methyltetrahydro-2-pyrimidinone (**1b**), 1,3-dimethyl-3,4,5,6- tetrahydro-2-pyrimidinone (**2b**).

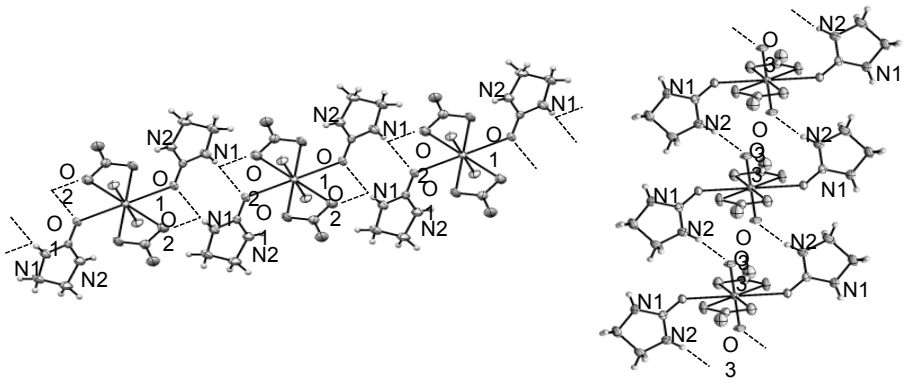

Figure 2. Formation of intermolecular hydrogen bonds in $UO_2(NO_3)_2$(**0a**)$_2$, bifurcated N1-H···O HBs (left), N2-H···O HB.

Table 1 Relationship between hydrogen bonds, melting points, and packing coefficients for each complex

	0a	0b	2a	2b
number of C-H···O HBs	0	0	2	2
number of N-H···O HBs	3	3	0	0
conversion number of N-H···O HBs	3	3	0.66	0.66
mp /ºC	280 (dec)	280 (dec)	211	211
packing coefficient	0.739	0.740	0.710	0.697

References

[1] T. R. Varga et. al., *Inorg. Chem. Commun*., **2000**, 3, 637-639.

[2] T. Suzuki et. al., *J. Nucl.Sci. Technol.,* **2012**, 49, 1010-1017.

[3] A.L. Spek, *Acta Crystallogr.*, **2009**, D65,148-155.

[4] P. Vishweshwar et. al., *Cryst. Growth Des.*, **2003**, 3, 783-790.

3-38

Difference in the kinetics of Am(III) and Eu(III) extraction using TODGA in Ionic Liquid Medium

Maria Boltoeva, Ali Quadi, Sylvia Georg, Isabelle Billard

Université de Strasbourg, IPHC, Strasbourg, France

Context: **Why ionic liquids for separation of lanthanides and actinides?**

Ionic Liquids (ILs) are intensively studied in liquid-liquid solvent extraction, particularly in extraction of metal ions,[1] due to their important advantages over conventional organic solvents as extracting phase. First, the unique physicochemical properties of ILs as low vapor pressure, non-flammability, good thermal, chemical and radiolytic stability, *etc.* would **reduce the potential hazards**.[2] Second, ILs offer the possibility to design a solvent for a specific application by the appropriate selection of the cation and anion and their combination, which justifies them being regarded as "**designer solvents**".[3] Third, the use of ILs as diluents to liquid-liquid extraction of metallic ions leads in many cases to remarkably **high extraction performance** in comparison with traditional molecular solvents.[1b]

One of the issues that is presently attracting attention is the possible application of ILs as extraction media to the reprocessing of spent nuclear fuel, especially to the separation of trivalent minor actinides (An) namely Am(III) and Cm(III) from the trivalent lanthanides (Ln) from aqueous acidic medium.[4] In fact, these *f*-block elements are difficult to be separated due to the similarity of their physical and chemical properties in aqueous systems. However, there is a small but significant difference between the affinity of An and Ln toward certain reagents, namely soft N- and O-donor ligands, which makes possible the An/Ln separation by solvent extraction.[5] It is shown that in ionic liquid medium, the chemical behavior of metal ions is dramatically different owing to a unique solvation environment of different nature (cationic and anionic). In this context, Stumpf *et al.* reported the different reaction kinetics for complexation of Eu(III), Cm(III) and Am(III) by N_3^- as a model system for organic N-based extractants.[6] Thus, the difference in the chemical reactivity of the *f*-elements toward extractant molecules could be exorbitant in ILs and may provide the opportunity for an highly efficient and highly selective An(III)/Ln(III) separation.

Objectives

In the present study we aim to investigate the extraction behavior of the trivalent *f*-elements, namely Eu(III) and Am(III), to evaluate the potential of ionic liquids as diluents for An(III)/Ln(III) separations. We employ 1-methyl-3-butyl-imidazolium *bis*(trifluoromethanesulphonyl)imide ($C_1C_4imTf_2N$) as the IL solvent and *N,N,N',N'*-tetra(*n*-octyl) diglycolamide (TODGA) as the extractant molecule. TODGA is a neutral tridentate ligand composed of C, H, O and N atoms ("green extractant"). TODGA is considered one of the promising extractants for the recovery of actinides and lanthanides the nuclear industry. [7] It is shown that by using TODGA in *n*-dodecane Eu(III) is preferentially extracted over Am(III). [8]

Recent Experimental Results:

Different kinetics

We report a noticeable difference between Eu(III) and Am(III) extraction behavior with TODGA in $C_1C_4imTf_2N$. The preliminary results show that the extraction of Eu(III) using 4 mM TODGA at 4 M HNO_3 is more efficient in comparison with Am(III) with a separation factor of Eu/Am~7. This separation factor is higher than values reported for TODGA in various molecular solvents [8] and it is comparable to the value found for the same extraction system but slightly different chemical conditions (3 M HNO_3 and 10 mM TODGA). [9]

Insights into the kinetic process

We studied in details the effect of various parameters such as nitric acid and TODGA concentrations on the Eu(III) extraction. The results reveal the kinetics of Eu transfer depends on the chemical conditions (Fig. 1). It is fast at low and very high acidity ([HNO_3]> 7 M), but slow at medium range of the acidity. These data corroborate a multiple mechanism takes place in the system (cationic and/or anionic exchange).

Modeling

We propose a phenomenological model to account for the kinetic results, for Am and Eu under all the chemical conditions of this work as:

$$M + \bar{L} \underset{k_2}{\overset{k_1}{\rightleftarrows}} \ddot{X} + p\bar{L} \overset{K_3}{\rightleftarrows} \bar{Y}$$

Where the first equilibrium is between the bulk aqueous phase and possibly the interface, with two kinetic constants, k_1 et k_2. The second equilibrium reaction, which is assumed to be a fast equilibrium of constant K_3, describes the transfer from the interface complex to the bulk of the IL possibly with an increase in the TODGA stoichiometry.

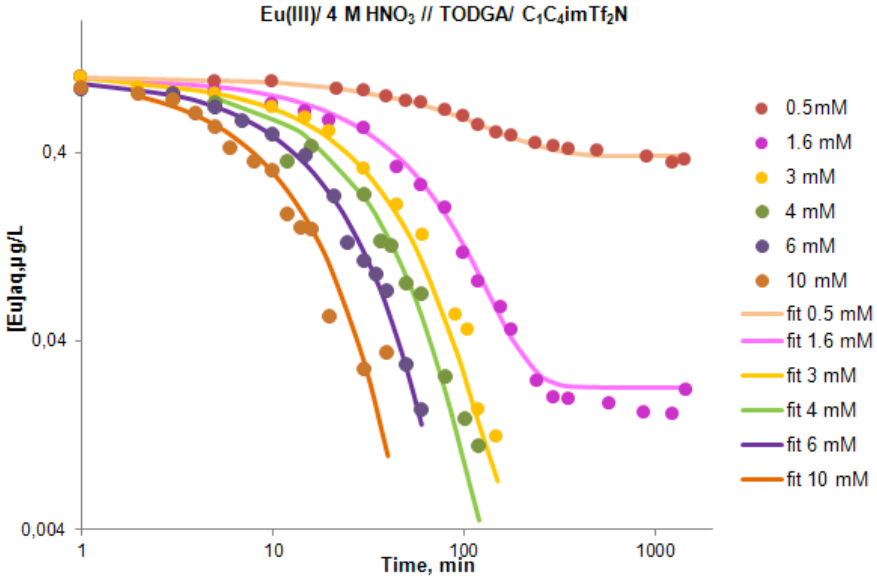

Fig. 1. Extraction of Eu as a function of mixing time for variable concentrations of TODGA.

The agreement between calculated and experimental $Eu(III)_{tot}$ values is very good (Fig. 1). The fitted value of TODGA stoichiometry in the extracted Eu species is close to three. Similarly, the Am data can be satisfactorily fitted on the basis of the model for Eu. Differences in the TODGA stoichiometry between Am and Eu and reaction rates will be discussed.

References

[1] a) A. Stojanovic and B. K. Keppler, *Sep. Sci. Technol.* **2011**, *47*, 189-203; b) I. Billard in *Ionic Liquids: New Hopes for Efficient Lanthanide/Actinide Extraction and Separation?*, *Vol. 43* (Ed. Bünzli&Pecharsky), **2012**, pp. 213-275; c) X. Sun, H. Luo and S. Dai, *Chem. Rev.* **2012**, *112*, 2100-2128.

[2] A.-V. Mudring and S. Tang, *Eur. J. Inorg. Chem.* **2010**, *2010*, 2569-2581.

[3] M. Freemantle, *Chem.Eng. News* **1998**, *76*, 32-37.

[4] a) A. Rout, S. Karmakar, K. A. Venkatesan, T. G. Srinivasan and P. R. Vasudeva Rao, *Sep.Pur. Technol.* **2011**, *81*, 109-115; b) M. E. Mincher, D. L. Quach, Y. J. Liao, B. J. Mincher and C. M. Wai, *Solv. Extr. Ion Exch.* **2012**, *30*, 735-747.

[5] M. J. Hudson, L. M. Harwood, D. M. Laventine and F. W. Lewis, *Inorg. Chem.* **2012**.

[6] S. Stumpf, I. Billard, C. Gaillard, P. J. Panak and K. Dardenne, *Inorg. Chem.* **2008**, *47*, 4618-4626.

[7] K. Shimojo, K. Kurahashi and H. Naganawa, *Dalton Trans.* **2008**, 5083-5088.

[8] Y. Sasaki et al., *Solv. Extr. and Ion Exch.* **2007**, *25*, 187-204.

[9] P. K. Mohapatra, P. Kandwal, M. Iqbal, J. Huskens, M. S. Murali and W. Verboom, *Dalton Trans.* **2013**, *42*, 4343-4347.

3-39

TALISMAN - Transnational Access to Large Infrastructures for a Safe Management of Actinides

M. Altmaier[1], S. Bourg[2], N. Bryan[3], P. Collings[4], N. Dacheux[5], B. Duplantier[6], Ch. Ekberg[7], D. Grolimund[8], L. Natrajan[3], Ch. Poinssot[2], Ph. Raison[9], T Schäfer[1], A.C. Scheinost[10], B. Schimmelpfennig[1]

[1]Karlsruhe Institute of Technology, Institute for Nuclear Waste Disposal, Karlsruhe, Germany, [2]Commissariat à l'Energie Atomique, Marcoule, France, [3]Centre for Radiochemistry Research, University of Manchester, Manchester, UK, [4]National Nuclear Laboratory, Sellafield, UK, [5]Centre National de la Recherche Scientifique, Paris, France, [6]LaGrange sarl (LGI Consulting), Paris, France, [7]Chalmers University of Technology, Gothenburg, Sweden, [8]Paul Scherrer Institut, Villigen, Switzerland, [9]Institute for Transuranium Elements, European Commission, Karlsruhe, Germany, [10]Helmholtz-Zentrum Dresden-Rossendorf, Dresden-Rossendorf, Germany

TALISMAN is a large international project funded within the European Commission FP7 EURATOM framework. The aim of TALISMAN is to offer transnational access to large infrastructures for a safe management of actinides. TALISMAN project is coordinated by CEA (contact: stephane.bourg@cea.fr).

Safety issues are of fundamental importance for the acceptance and sustainable application of nuclear energy as was strongly reinforced following the Fukushima accident. Actinides play a central role in the nuclear fuel cycle from mining, fuel fabrication, energy production, up to reprocessing, partitioning and transmutation treatment of used fuel, and finally the management and disposal of radioactive waste. Fundamental understanding of actinide properties and behaviour in fuel materials during the separation processes and in geological repositories is an imperative prerequisite to tackle all the related safety issues.

Unravelling the complexity of the actinide components of used nuclear fuel certainly represents one of the great challenges in nuclear science. To meet the needs of safe and sustainable management of nuclear energy, it is essential to maintain a high level of expertise in actinide sciences in Europe and to prepare the next generation of scientists and engineers who will contribute to developing safe actinide management strategies. Because actinides are radioactive elements, their study requires specific tools and facilities that are only available to a limited extent in Europe.

Only a few academic and research organisations have the capabilities and licenses to work on actinide elements. It is therefore strategic to coordinate the existing actinide infrastructures in Europe and to strengthen the community of European scientists working on actinides. Within TALISMAN we offer (for positively evaluated scientific research proposals submitted in reply to a specific TALISMAN call) access to the previous ACTINET Pooled Facilities (CEA Atalante and CEA DPC, France; ITU Laboratories & hot-cells, European Commission; KIT-INE laboratories and KIT-INE beamline, Germany; HZDR-IRE & ROBL, Germany; PSI microXAS Beamline, Switzerland) to which two new facilities have been added: NNL Central Lab in the UK and CHALMERS in Sweden.

TALISMAN leads and coordinates a network of actinide facilities across Europe, but also manages a network between facilities and users to increase the knowledge for a safer management of actinides. TALISMAN also enhances the efforts made to support education and training issues by continuing the former ACTINET Summer School series and travel grant attributions for attending international conferences.

The TALISMAN project website http://www.talisman-project.eu offers detailed information on all TALISMAN activities, including contact addresses, TALISMAN newsletters, announcements and description of open and forthcoming calls for transnational user access and indicates several other options to perform actinide research within the TALISMAN context.

Figure 1: The project website of TALISMAN is located at http://www.talisman-project.eu

3-40

Curium-technetium complex oxide

Elena Pichuzhkina, Sergey Tomilin

JSC SSC "Research Institute of Atomic Reactors", Dimitrovgrad, Russia

Over a number of years, RIAR has been synthesizing and studying transplutonics compounds, in particular, curium and americium compounds with other elements of the periodic system [1-3].

This paper presents the results of synthesis and study of an unknown tertiary oxide based on curium-244 and technetium generated when studying curium-244 and technetium alloying. The compound was generated by condensing metal curium vapor onto a metal technetium substrate. Mixed oxide Cm_6TcO_{12} with hexagonal lattice of Ho_6MoO_{12} type was identified by X-raying and characterized. Crystalline lattice parameters were identified as (*a* = 10,552(3) Å, *c* = 9,879(5) Å).

The crystalline lattice of this compound was found to be stable to the long-term internal self-irradiation of curium-244; the complete amorphisation was not observed even after 1000 days of exposure, though the diffraction picture intensity decreased significantly (fig.). During the time period of ~1000 days, phase Cm_6TcO_{12} accumulated about $2 \cdot 10^{20}$ α-dec/g; it remained crystalline and underwent some swelling, mainly at the beginning of self-irradiation. It is noted that curium remains insoluble in the hexagonal closed-packed technetium lattice.

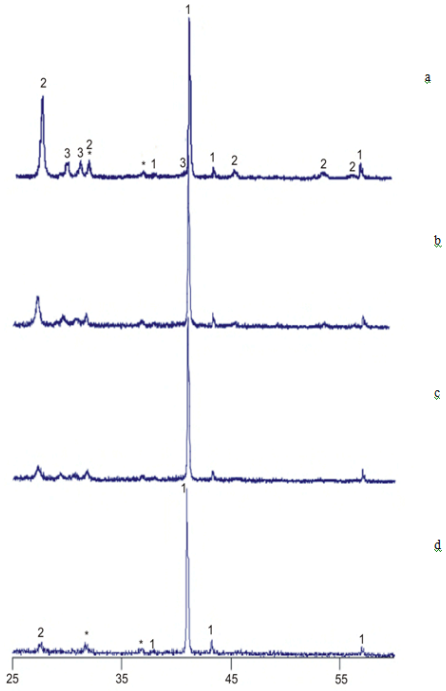

Figure 1. X-ray of sample of the Cm-Tc system: *a*– t = 0,2 days; b - t = 314 days; c - t = 597 days; d - t = 1006 days; 1 – Tc; 2 – Cm_6TcO_{12}; 3 – *B*-Cm_2O_3; * - teflon

References

[1] Radchenko V.M., Ryabinin M.A., Seleznev A.G. et al., Radiokhimiya, 2004, V. 46, edition 5, P. 385-388.
[2] Radchenko V.M., Seleznev A.G., Droznik R.R. et al., Radiokhimiya, 2004, V. 46, edition 1, P. 3-6.
[3] Radchenko V.M., Pichuzhkina E.M., Ryabinin M.A. et al., Radiokhimiya, 2006, V. 48, edition 4, P. 289-293.

3-41

UV-vis and fluorescence spectroscopic methods to evaluate the solution thermodynamic properties of hydroxypyridinonate actinide and lanthanide complexes

Manuel Sturzbecher-Hoehne, Gauthier Deblonde, Rebecca Abergel

Lawrence Berkeley National Laboratory, Berkeley, CA, USA

Introduction The only practical treatment after a large-scale internal contamination by radioactive materials such as actinides (An) and lanthanide (Ln) fission products would be the use of chelating agents. Currently, the only approved therapeutic agent to reduce internal actinide contamination is diethylenetriaminepentaacetic acid, generally referred to as DTPA (Fig 1A). Unfortunately, DTPA is not potent when administered orally, moderately effective for the removal of trivalent ions such as Am(III), less efficient for Pu(IV), and barely active for removing U(VI) and Np(V) from the body.[1,2]
On the other hand, one of the most promising candidates for new decorporation therapies, ideally of low toxicity, orally available and active for Ln(III), An(III) and An(IV) ions, is the linear octadentate 1-hydroxy-2-pyridinonate ligand 3,4,3-LI(1,2-HOPO) (Fig. 1B).[2] An other ligand under investigation is the tetradentate *N*-Me-3-hydroxy-2-pyridinonate ligand 5-LIO(Me-3,2-HOPO)(Fig. 1C). To complement on going *in vivo* decorporation studies, the *in vitro* coordination properties of these two compounds with An and Ln ions have been investigated. UV-vis and fluorescence titrations, in manual, automated and competition batch modes, were used as tools to determine coordination chemistry and thermodynamic properties.

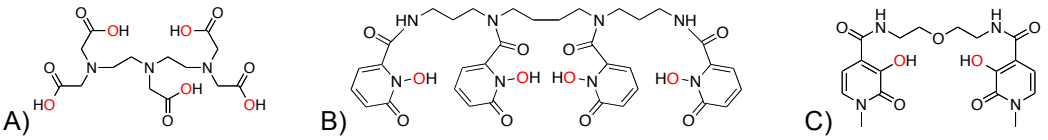

Figure 1. Decorporation agents A) DTPA, B) 3,4,3-LI(1,2-HOPO), and C) 5-LIO(Me-3,2-HOPO).

Results and Discussion The lanthanide complex stabilities increase over the series from La(III) towards Lu(III) and all formed complexes have higher stabilities than DTPA (Fig. 2, left).[3–5] 3,4,3-LI(1,2-HOPO) acts as antenna that sensitizes the emission of Eu(III), which was used as a spectroscopic tool in competition batch titrations to evaluate the thermo-dynamic stabilities of the remaining Ln(III) complexes. In contrast, direct UV-vis titrations were performed for the complexation of 5-LIO(Me-3,2-HOPO) with the Ln(III) series.
The special case of Ce in the Ln series allowed the determination of complex stabilities for the tetravalent Ce(IV) and Th(IV) ions, using the ligand-to-metal charge transfer band of [Ce(IV)3,4,3-LI(1,2-HOPO)] (Fig. 2 right). The [Th(IV)3,4,3-LI(1,2-HOPO)] complex (log β_{110} 40.1) is 10^{13} times more stable than the Th(IV) complex of the currently used decorporation agent DTPA.
Similar trends of stabilities were observed for U(VI) complexes: 3,4,3-LI(1,2-HOPO) and 5-LIO(Me-3,2-HOPO) form 10^9 and 10^6 times more stable complexes than DTPA.[6]
For Cm(III), both ligands are capable to function as antennae and sensitize its emission in high yields (Fig. 3). This effect allowed the direct investigation of the complex thermodynamic stabilities through an automated titration setup, by reducing the activity/concentration of metal used by a factor of 50. The determined stabilities (pM) are 22.7 and 20.0 for 3,4,3-LI(1,2-HOPO) and 5-LIO(Me-3,2-HOPO), respectively, both relatively similar to DTPA (21.1).[7]

Conclusion The solution thermodynamic stabilities of Ln(III), Ce(IV), U (VI), Th(IV) and Cm(III) complexes of the decorporation agents 3,4,3-LI(1,2-HOPO) and 5-LIO(Me-3,2-HOPO) were evaluated. The stability constants determined in this research evidence the remarkable high affinities of multidentate hydroxypyridinonate ligands for these metal ions and corroborate the observations made in *in vivo* studies.[2] Because of the extremely high stabilities of the higher valence metals, a direct determination of the thermodynamic properties is impossible. Hence, the methods implemented to probe the solution thermodynamics of [Ce(IV)(3,4,3-LI(1,2-HOPO))] and [Th(IV)(3,4,3-LI(1,2-HOPO))] will be applied to characterize the corresponding U(IV), Np(IV) and Pu(IV) complexes.

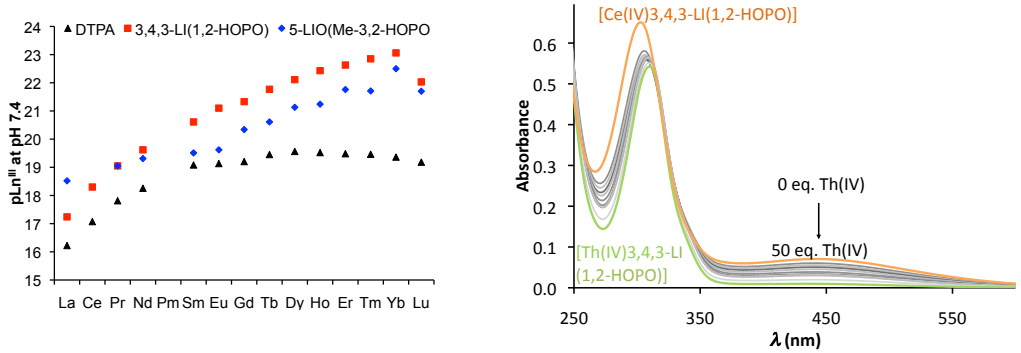

Figure 2 left. pM values of all three complexes for the lanthanide series. The stabilities increase for the ligands with decreasing radii of the lanthanides. Triangle = DTPA; Square = 3,4,3-LI(1,2-HOPO); Diamond = 5-LIO(Me-3,2-HOPO). Both experimental ligands have higher stabilities than DTPA. **Right.** Metal competition batch titration of [Ce(IV)(3,4,3-LI(1,2-HOPO))] with Th(IV). [Ce(IV)] = [3,4,3(LI-1,2-HOPO)] = 30 μM, [Th(IV)]:[Ce(IV)] = 0 to 50, [H_2SO_4] = 0.05 M, pH 1.0, I = 0.15 (Na_2SO_4), T = 20°C. Major changes were observed between 350 and 550 nm for the disappearance of the charge transfer band of Ce(IV).

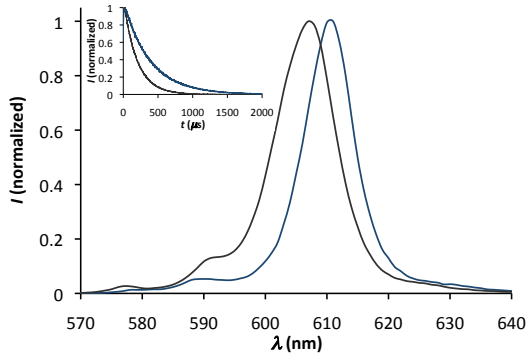

Figure 3. Fluorescence spectra of 1.27 μM [Cm(III)(3,4,3-LI(1,2-HOPO)]$^-$ (blue) and 1.53 μM [Cm(III)((5-LIO(Me-3,2-HOPO$_2$)]$^-$ (black) upon excitation at 320 nm and 345 nm, respectively (in 0.1 M HEPES at pH 7.4). **Inlet.** Luminescence decay of both ligands at the maximum emission.

Acknowledgement We thank Prof. Kenneth N. Raymond, Dr. David K. Shuh, Dr. Norman M. Edelstein, and Dr. Guoxin Tian for helpful discussions, and Tiffany Pham for assistance with the cyclic voltammetry experimental setup. This research was supported by the National Institutes of Health (National Institute of Allergy and Infectious Diseases, RAI087604Z) through the U.S. Department of Energy under Contract No. DE-AC02-05CH11231.

References

1. P. W. Durbin, *Health Phys.*, 2008, 95, 465–492.

2. R. J. Abergel et al., *Health Phys.*, 2010, 99, 401–407.

3. R. J. Abergel et al., *Inorg. Chem.*, 2009, 48, 10868–10870.

4. M. Sturzbecher-Hoehne et al., *Dalton Trans.*, 2011, 40, 8340–8346.

5.M. Sturzbecher-Hoehne et al., in preparation.

6. M. Sturzbecher-Hoehne et al., *Radiochim. Acta*, 2013, in press.

7. M. Sturzbecher-Hoehne, D. K. Shuh, K. N. Raymond, and R. J. Abergel, in preparation.

3-42

Receptor recognition of transferrin bound to f-block metals: a segregation step in cellular acquisition of actinides

Manuel Sturzbecher-Hoehne[1], Gauthier Deblonde[1], Christophe Goujon[1], Anne Mason[2], Rebecca Abergel[1]

[1]Lawrence Berkeley National Laboratory, Berkeley, CA, USA, [2]University of Vermont, Burlington, VT, USA

Introduction Despite the general knowledge that actinides (An) and lanthanide (Ln) fission products pose great hazards for humans and can strongly bind to natural macromolecules, limited research has been directed to the characterization of transuranic actinide coordination chemistry in environmentally and biologically relevant species. Identifying these biological ligands and studying their properties as Ln/An complexes are critical to unravelling the mechanisms of uptake, transport and intracellular storage of toxic radioactive f-elements. Among the many biochemical targets for Ln and An ions, the mammalian iron transporter transferrin (Tf) is of importance and interest.[1] This protein shuttles iron as Fe(III) in the blood stream between sites of uptake, utilization and storage. The two iron-binding pockets of Tf are similar but not identical, each creating an octahedral environment suitable to stabilize Fe(III) and other metal ions.[2] Once bound to Tf, Fe(III) can be transported inside cells, through recognition by the cognate transferrin receptor (TfR). TfR is located on the extracellular surface of virtually all actively dividing cells and is able to bind apoTf and Fe_2Tf reversibly.[3] Complexes formed between Fe_2Tf and TfR undergo endocytosis and subsequently release iron inside cells through a pH-dependent mechanism.[4] Though tightly controlled for iron homeostasis, TfR-mediated endocytosis has also been discussed as a possible mechanism for effective cellular uptake of exogenous metal ions.[5–7] Probing the TfR recognition of Tf loaded with Ln or An ions is therefore crucial to understand the cellular acquisition pathways of such toxic metals and to potentially develop new preventive strategies against internal Ln and An contamination.

Results and Discussion

We developed a spectroscopic method based on size-exclusion high performance liquid chromatography (HPLC) that allows discrimination, at a micro-molar scale, between metal-free Tf, unbound receptor TfR, and the two receptor:metallo-protein complexes TfR:(M_2Tf) and TfR:(M_2Tf)$_2$ (Fig1. A). Hence, we are able to determine the two sequential dissociation constants K_{d1} and K_{d2} corresponding to the stepwise dissociation of M_2Tf by TfR for several metal ions, including alpha and neutron emitters: Fe(III), Ga(III), La(III), Nd(III), Gd(III), Yb(III), Lu(III), Th(IV), U(VI), Pu(IV) and Cm(III) (Fig 1. B). The thermodynamic constants obtained for each investigated receptor:metallo-Tf complex highlight the feasibility of Tf-mediated cellular acquisition of exogenous Ln and An metal ions.

The stability constants of the TfR:(MxTf)y adducts, under our experimental conditions, follow the order: Fe(III) >> Th(IV) ~ U(VI) ~ Cm(III) > Ln(III) ~ Ga(III) >>> Yb(III) ~ Pu(IV).[8] Based on these thermodynamic constants alone, metal ions that are readily taken up by the liver in vivo such as Th(IV), U(VI), and Cm(III), would be predicted to follow theTfR:Tf-mediated iron acquisition pathway for cellular incorporation.

Conclusion A size-exclusion HPLC method has been established to probe the binding of metal-substituted human Tf by the cognate receptor TfR, which allowed the determination of two dissociation constants. While the binding of a metal to human Tf mostly depends on the oxidation state, charge, and size of the metal ion, the recognition of M_2Tf by TfR seems to be driven by other factors including shape and conformation of the metal-bound Tf. This study confirms that even though a considerable portion of human Tf is unsaturated by Fe(III) and thus available to bind a large number of toxic metals, the receptor TfR appears to play a role in the translocation mechanism of exogenous metals by acting as an additional selective barrier for cellular entry. Additionally, these results highlight the necessity to establish solution chemistry parameters in order to elucidate in vivo biokinetic distribution patterns for Ln and An metals. Finally, the described physical chemistry approach could easily be implemented to probe other binding pairs and biological relevant complexes.

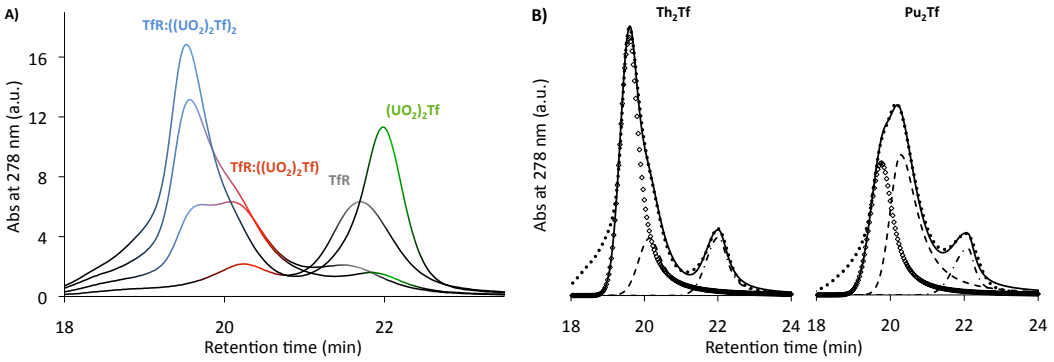

Figure 1. A) Evolution of chromatograms upon the addition of $(UO_2)_2Tf$ to TfR. [TfR] = 0.95 µM, $[NH_4HCO_3]$ = 100 mM, pH = 7.4, 25°C. Volume injected: 9 µL. **B)** Difference of TfR affinity for Th_2Tf (left) and Pu_2Tf (right). Chromatograms obtained for samples containing 0.95 µM TfR and 2.28 µM M_2Tf (100 mM NH_4HCO_3, pH = 7.4), and eluted at a 0.1 mL min-1 flow rate. Raw data are shown as dotted lines and fits as solid lines. Chromatograms were deconvoluted for the following species: $TfR:(M_2Tf)_2$ (~19.5 min, diamonds), $TfR:(M_2Tf)$ (~20.2 min, dashed line), M_2Tf (~22.1 min, dot-dashed line) to calculated the constants K_{d1} and K_{d2}.

Acknowledgement We thank Prof. Kenneth N. Raymond, Dr. David K. Shuh, Dr. Norman M. Edelstein, Dr. Guoxin Tian, and Dr. Petr Kuzmic for helpful discussions. Instrument acquisition and method development for the chromatography assays were supported by the National Institutes of Health (R.J.A., RAI087604Z); the experimental work on actinide-protein interactions was supported by the Director, Office of Science, of the U.S. Department of Energy under Contract No. DE-AC02-05CH11231, through a Laboratory Directed Research and Development program (R.J.A.), and by a U. S. Public Service Grant (A.B.M., R01 DK 21739).

References

1. D. M. Taylor, *J. Alloys Compd.*, 1998, 271-273, 6–10.

2. P. Aisen, M. Wessling-Resnick, and E. A. Leibold, *Curr. Opin. Chem. Biol.*, 1999, 3, 200–206.

3. H. Li, H. Sun, and Z. M. Qian, *Trends Pharmacol. Sci.*, 2002, 23, 206–209.

4. A. N. Steere, S. L. Byrne, N. D. Chasteen, and A. B. Mason, *Biochim. Biophys. Acta*, 2012, 1820, 326–333.

5. M. Sturzbecher-Hoehne, C. Goujon, G. J.-P. Deblonde, A. B. Mason, and R. J. Abergel, *J. Am. Chem. Soc.*, 2013, 135, 2676–2683.

6. M. P. Jensen, D. Gorman-Lewis, B. Aryal, T. Paunesku, S. Vogt, P. G. Rickert, S. Seifert, B. Lai, G. E. Woloschak, and L. Soderholm, *Nat. Chem. Biol.*, 2011, 7, 560–565.

7. C. Vidaud, S. Gourion-Arsiquaud, F. Rollin-Genetet, C. Torne-Celer, S. Plantevin, O. Pible, C. Berthomieu, and E. Quéméneur, *Biochemistry (Mosc.)*, 2007, 46, 2215–2226.

8. G. Deblonde, M. Sturzbecher-Hoehne, A. B. Mason, and R. J. Abergel, *Metallomics*, 2013, in press.

3-43

Actinide mixed oxide microspheres synthesis using Weak Acid Resin process: unconventional precursors for Minor Actinide Bearing Blanket fabrication

Picart Sebastien[1], Remy Elodie[1], Delahaye Thibaud[1], Bisel Isabelle[1], Dugne Olivier[1], Clavier Nicolas[2], Blanchart Philippe[3], Ayral André[4]

[1]CEA, Bagnols-sur-Cèze, France, [2]ICSM, Bagnols-sur-Cèze, France, [3]ENSCI, Limoges, France, [4]IEM, Montpellier, France

Alternative routes to powder metallurgy for the preparation of Minor Actinide Bearing Blankets pellets (MABB) are currently being assessed at CEA because it lowers the risks associated to dust dissemination during pellet fabrication [1]. New routes which produce oxide spherule precursor instead of oxide powder were developed and showed that it can simplify the process by avoiding complex and dusty steps such as milling and grinding [2]. One of them is called the "Weak Acid Resin" (WAR) route. It is based on the production of oxide microspheres from metal loaded ionic exchange resin beads and their subsequent transformation into oxide by heat treatment (Figure 1).

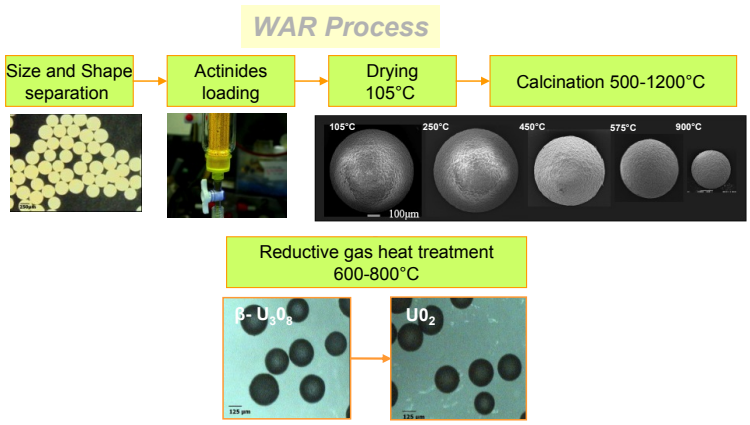

Figure 1: Modified WAR Process for uranium dioxide spherules synthesis

The original procedure developed at Oak Ridge National Laboratory was dedicated to the production of uranium carbide kernels for TRISO fuels from intimately mixed carbon and oxide precursors [3] and had been adapted at CEA Marcoule to the production of pure oxide based materials [4]. Its scientific feasibility was demonstrated for lanthanide [5] and actinide based materials in our laboratory [6]. This study describes the different steps of the process and the development of mixed oxide microspheres synthesis like mixed uranium-americium oxide microsphere as shown in Figure 2. It also focuses on the oxide spherules characterization and on their comparison to other precursors like powders obtained from oxalate precipitation or spherules obtained by sol-gel technology.

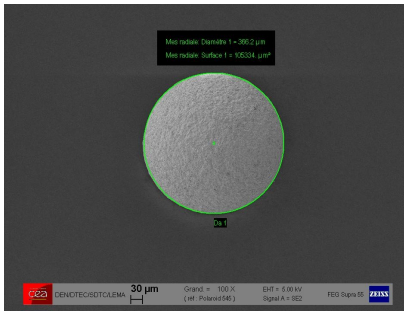

Figure 2: Mixed uranium-americium microsphere obtained by WAR process (Am content : 10 at% ;diameter 360 µm).

References

[1] F. Jorion, T. Delahaye, A. Gauthé, S. Picart, F. Lebreton, E. Remy,D. Horlait, International Conference on Fast Reactors and Related Fuel Cycles: Safe Technologies and Sustainable Scenarios (FR13) Paris, France 4-7 March 2013.

[2] E. Zimmer, C. Ganguly, J. Borchardt and H. Langen, Journal of Nuclear Materials 1988, 152, 169-177.

[3] G.W. Weber, R. L. Beaty and V. J. Tennery, ORNL, Nuclear Technology, 35, 217, (1977).

[4] S. Picart, H. Mokhtari and I. Jobelin, WO Patent 2010034716 (2010).

[5] E. Remy, S. Picart, S. Grandjean, T. Delahaye, N. Herlet, P. Allegri, O. Dugne, R. Podor, N. Clavier, P. Blanchart, A. Ayral, J. Eur. Cer. S., 32, 3199, (2012).

[6] S. Picart, H. Mokhtari and I. Jobelin, Actinides 2009, IOP Conference Series: Materials Science and Engineering, 9, 012025 (2010).

3-44

Thermodynamic evaluation of Np redox processes in dilute aqueous solutions at pH 4 – 10 under reducing conditions

David Fellhauer[1,3], Marcus Altmaier[1], Volker Neck[1], Xavier Gaona[1], Thierry Wiss[2], Markus Lagos[1], Jörg Runke[1,3], Thomas Fanghänel[2,3]

[1]Karlsruhe Institute of Technology, Institute for Nuclear Waste Disposal, Karlsruhe, Germany, [2]European Commission, JRC, Institute for Transuranium Elements, Karlsruhe, Germany, [3]Heidelberg University, Institute of Physical Chemistry, Heidelberg, Germany

One of the major characteristics of the early actinide elements (U to Am) in aqueous solution is their complex redox chemistry: up to four oxidation states can exist or even co-exist within the thermodynamic stability field of water. Due to the major differences existing between the aqueous chemistry of different An oxidation states, a quantitative understanding of An redox processes and the chemical factors influencing them is required. This is particular highly relevant in the context of safety assessment for nuclear waste disposal where reliable model calculations of An speciation and solubility are of fundamental importance. According to equilibrium thermodynamics the An oxidation state distribution and speciation is a function of pH value and redox potential pe (pe = 16.9 E_h for T = 25°C) and can therefore be calculated for a system with defined redox conditions (pe+pH).

In the present work we investigated if the redox behaviour of Np under reducing conditions can accurately be described in terms of equilibrium thermodynamics. Batch experiments in dilute aqueous solutions in presence of reducing agents at pH 4 – 10 were performed and the Np oxidation state distribution determined in the samples after long equilibration times were compared to the calculated equilibrium state (using data from NEA-TDB [2003GUI/FAN]). For the thermodynamic calculations the experimental (pe+pH)-values measured in the systems served as input parameters.

Experimental

The redox behaviour of ^{237}Np was systematically investigated as function of the redox potential (pe) and pH in 15 mL 0.1 M NaCl under Ar atmosphere at 22°C. The redox conditions (pe+pH) in the batch experiments were adjusted by additions of 0.01 M pH buffer to fix the pH between 4 and 10 (MES, PIPES, HEPES, TRIS or CHES) and 1-3 mM of chemically different organic or inorganic (homogenous and heterogeneous) reducing agents: hydroquinone, 9,10-anthraquinone / anthrahydroquinone-2,6-disulfonate (AQDS/AH_2QDS), $FeCl_2/FeCl_3$, synthetic magnetite, Fe powder, $Na_2S_2O_4$. The inactive matrix solutions were spiked with aliquots of a 3 mM $^{237}NpO_2^+$ stock solution to obtain $[Np]_{tot}$ = $(4\pm1)\cdot10^{-5}$ M (oversaturation approach). In four additional samples approx. 2 mg of $NpO_2\cdot xH_2O$(am) was added initially (undersaturation experiments; reducing agents: hydroquinone and $FeCl_2/FeCl_3$, respectively). The pH value, redox potential and aqueous Np concentration after 10kD (2 nm) ultrafiltration were determined as function of time (typically ~100 d; partly up to five years). Under the experimental pH conditions Np(V) is completely soluble whereas Np(IV) forms sparingly soluble $NpO_2\cdot xH_2O$(am) with a solubility of log [Np] = -9±1. The redox equilibrium Np(V)/Np(IV) can therefore be monitored by the concentration of dissolved Np in solution.

Results

a) Thermodynamics of the Np system:

The experimental (pe+pH)-values measured in the different samples are plotted into the pe-pH diagram in fig. 1. According to thermodynamic calculations with data from NEA-TDB [2003GUI/FAN], the experimental (pe+pH)-values are in the stability field of Np(IV), and $NpO_2\cdot xH_2O$(am) is the predominant Np compound expected in equilibrium. In presence of $NpO_2\cdot xH_2O$(am) as solubility limiting Np solid phase and for 4.5 < pH < 9.5, there are two equilibrium reactions that can thermodynamically control the Np concentration in solution:

$$\text{(a) } NpO_2\cdot xH_2O(am) \Leftrightarrow NpO_2^+ + e^- \text{ with } \log K^\circ_{IVam\_V} = \log [NpO_2^+] + \log \gamma_{NpO2+} - pe,$$

and

(b) $NpO_2 \cdot xH_2O(am) + (2\text{-}x)\ H_2O \Leftrightarrow Np(OH)_4(aq)$, with $\log K°_{s,0} = \log[Np(OH)_4(aq)] - (2\text{-}x) \log a_w$.

Under the experimental conditions of this work equilibrium (a) is relevant for pe = 6 to 2, i.e. in the region between the solid and dashed black borderlines in fig. 1, whereas equilibrium (b) is decisive for pe < 2 (below the dashed black borderline in fig. 1).

b) Comparison of experimental and calculated Np redox state distribution

In the samples with *AQDS/AH$_2$QDS*, *FeCl$_2$/FeCl$_3$* (pH > 6), *Fe powder* and *Na$_2$S$_2$O$_4$* (red symbols in fig. 1) the measured (pe+pH)-values are below the dashed borderline in fig. 1. Here, a complete reduction of Np(V) to Np(IV) is expected with (b) as the solubility limiting equilibrium reaction. The experimental observations are in agreement with the thermodynamic predictions: the initial Np(V) was quantitatively reduced to sparingly soluble $NpO_2 \cdot xH_2O(am)$ within maximum 200 d. The corresponding Np(IV) equilibrium concentrations were determined by high-resolution ICPMS (log [Np] = -9.5±0.5) which allows the quantification of a reliable value for log $K°_{s,4}$.

In the four systems with $NpO_2 \cdot xH_2O(am)$ as initial Np compound (undersaturation approach, blue points in fig. 1) the experimental redox conditions are inside or close to the (pe+pH)-region where equilibrium (a) controls the solubility of Np in solution. The samples were reacted for several years, and equilibrium states between solid $NpO_2 \cdot xH_2O(am)$ and aqueous NpO_2^+ were attained according to (a). The corresponding value for log $K°_{IVam\_V}$ was derived.

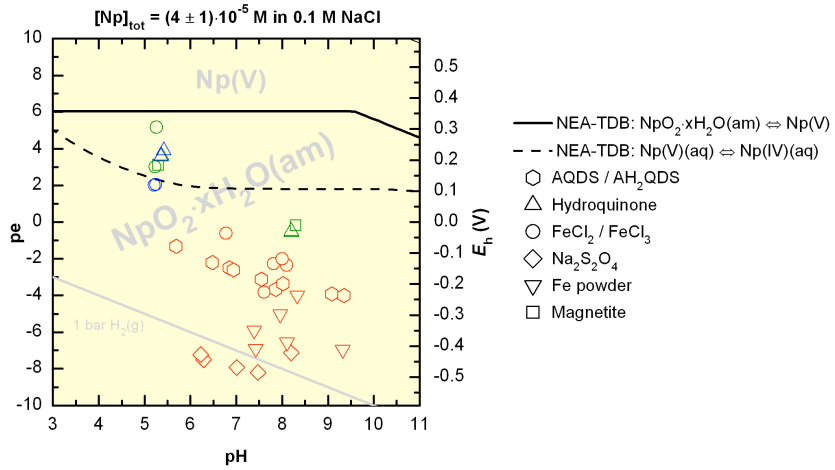

Fig. 1: Experimental (pe+pH)-values in the different Np redox samples. Blue and red symbols indicate samples where equilibrium (a) and (b) were attained, respectively. In samples marked with green symbols no equilibrium state has yet been reached due to very slow Np(V) reduction kinetics.

However, in some of the samples, discrepancies were found between predicted equilibrium state and experimental observations caused by very slow Np(V) reduction kinetics: even after 5 years the reduction of the initially added Np(V) by *hydroquinone* and commercial *magnetite* (green points in fig. 1) is still ongoing (the respective first-order reduction half-lives are 3 and 15 years), and the expected equilibrium level has not (yet) been reached.

Conclusions

The results of the present work clearly indicate that the behaviour of Np in aqueous systems under reducing conditions can accurately be described in terms of equilibrium thermodynamics with sparingly soluble amorphous $NpO_2 \cdot xH_2O(am)$ as the solubility controlling solid phase. Thermodynamic constants for the two decisive equilibrium reactions under these conditions were evaluated allowing a more precise quantification of the stability of $NpO_2 \cdot xH_2O(am)$. For some redox systems the equilibration between Np(V) and Np(IV) was found to be very slow indicating that for a comprehensive description of the aqueous Np redox behaviour the consideration of kinetic aspects might be necessary for certain scenarios.

3-45

Electronic Structure of Plutonium Dioxide

Yu.A. Teterin[1], K.I. Maslakov[1], M.V. Ryzhkov[2], A.Yu. Teterin[1], K.E. Ivanov[1], V.G. Petrov[3], D.A. Enina[3], S.N. Kalmykov[3]

[1]NRC Kurchatov Institute, Moscow, Russia, [2]Institute of Solid State Chemistry UD RAS, Ekaterinburg, Russia, [3]Lomonosov Moscow State University, Moscow, Russia

X-ray photoelectron spectroscopy (XPS) study of oxygen-containing actinides (An) compounds revealed that the peaks in the binding energy range 0 – 35 eV are several eV wide, which is often wider than the core peaks [1]. It contradicts the uncertainty principle $\Delta E \Delta \tau \approx \hbar$, where ΔE – natural width of the level from which an electron escaped, $\Delta \tau$ – hole lifetime. Since the hole lifetime decreases as the absolute energy of the atomic level increases, the XPS peak width for a certain level should decrease with the decreasing of the binding energy. But the observed XPS spectra for AnO_2 show an opposite trend [1]. That was the reason for theoretical and experimental studies of the low binding energy XPS structure nature in actinide oxides in the range 15 eV – 35 eV. As a result it was found that one of the reasons for such a XPS structure formation in actinide compounds is the formation of the outer (binding energies range 0 eV – 15 eV, OVMO) and the inner (binding energies range 15 eV – 35 eV, IVMO) valence molecular orbitals with the effective participation of the An6p and the O2s filled atomic shells.

The earlier experimental [1, 2, 3, 4, 5] and calculation [1, 2, 3, 6] results for PuO_2 allowed only qualitative interpretation of the low binding energy XPS spectra. In this work the XPS from

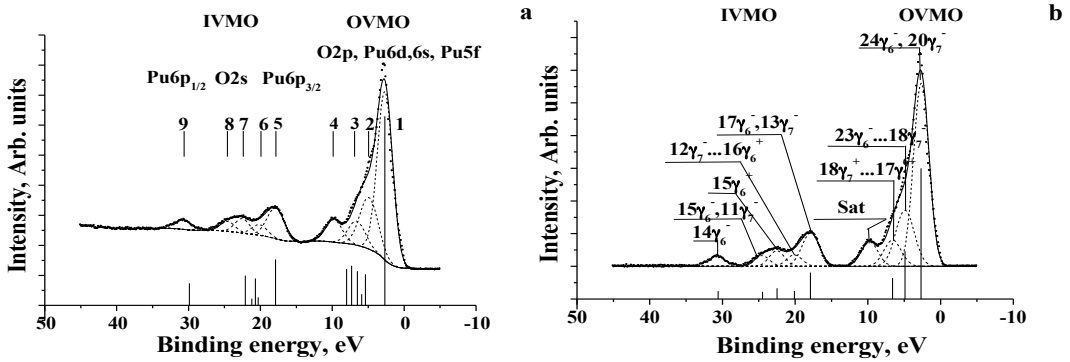

Fig. 1. Valence electrons XPS from PuO_2: a – XPS with the secondary scattered electrons background. Dashed lines show the decomposition into separate components, vertical bars show the RDVM calculated spectrum; b – XPS with background subtracted. Vertical bars show the expected correct spectrum.

PuO_2 layer on platinum substrate was acquired in the binding energy range 0 eV – 1250 eV. The valence band XPS structure in the binding energy range 0 eV – 35 eV was analyzed and interpreted taking into account the core XPS structure and the RDVM electronic structure calculation results (Fig. 1).

As a result it was theoretically shown and experimentally corroborated that chemical bond formation in PuO_2 results in appearance of the occupied Pu5f electronic states in the valence band. The atomic Pu6p orbitals were found to take a appreciable part in formation of both the inner valence and the outer valence (~0.3 Pu6p-electron) molecular orbitals (bands). The results of our investigation showed that the main role in the IVMO formation in PuO_2 was played by the $Pu6p_{3/2}$ and the O2s atomic orbitals of the neighboring plutonium and oxygen ions. The composition and the sequence order of the inner valence molecular orbitals in the energy range from 15 eV to 35 eV were determined and the valence electronic states densities in the range 0 eV - 35 eV in plutonium dioxide were calculated. These data allowed the quantitative scheme of molecular orbitals for PuO_2 (Fig. 2). This scheme is fundamental not only for understanding the chemical bonding nature in PuO_2, but also for interpretation the structure of other PuO_2 x-ray spectra.

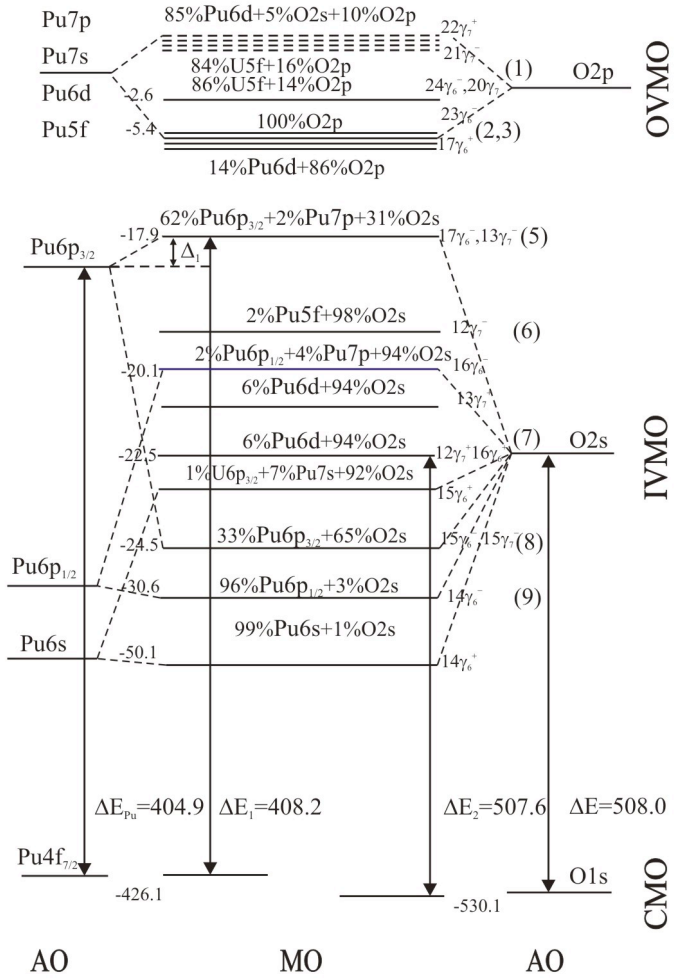

Fig. 2. MO scheme for PuO_2 built on the basis of theoretical and experimental data. Arrows show the experimentally measurable binding energy differences. Experimental binding energies (eV) are given to the left. Energy scale is not kept.

The work was supported by RFBR grant 13-03-00214-a.

References

[1] Yu.A. Teterin, A.Yu. Teterin. Russ. Chem. Rev. 2004. **73(6)**, 541.

[2] B.W. Veal, H. Diamond, H.R. Hoekstra. Phys. Rev. 1977. **15,** 2929.

[3] D. Courteix, J. Chayrouse, L. Heintz, R. Baptist, Solid State Commun. 1981, **39**(2), 209.

[4] M.T. Butterfield, T. Durakiewicz, E. Guziewicz et al, Surface Science. 2004, **571**, 74.

[5] T. Gouder, A. Seibert, L. Havela, J. Rebizant. Surface Science 601 (2007) L77 – L80.

[6] V.A. Gubanov, A. Rosen, D.E. Ellis. J. Phys. Chem. Solids. 1979. **40**, 17.

3-46

Chemical Bond Nature in Neptunium Dioxide

Yu.A. Teterin[1], K.I. Maslakov[1], M.V. Ryzhkov[2], A.Yu. Teterin[1], K.E. Ivanov[1], V.G. Petrov[3], D.A. Enina[3], S.N. Kalmykov[3]

[1]NRC Kurchatov Institute, Moscow, Russia, [2]Institute of Solid State Chemistry UD RAS, Ekaterinburg, Russia, [3]Lomonosov Moscow State University, Moscow, Russia

The outer (binding energy range 0 eV – 15 eV, OVMO) and the inner (binding energy range 15 eV – 35 eV, IVMO) valence molecular orbitals formation in actinide oxides results in the widening of the low binding energy x-ray photoelectron spectroscopy (XPS) lines and the additional structure appearance [1]. Since physical and chemical properties of any compounds are determined by their low binding energy valence electrons, formation of the inner valence molecular orbitals may affect the filling sequence of electronic levels influencing chemical and physical properties of compounds. The authors of [2] measured the low binding energy XPS spectrum for a NpO_2 thin layer on platinum substrate and the authors of [3] performed the non-relativistic calculations in the Xα-discrete variation approximation for neptunium dioxide.

This work presents reliable XPS data for a NpO_2 thin layer deposited on a platinum substrate, as well as from a bulk NpO_2 sample, acquired in the binding energy 0 eV – 1250 eV. The present data are compared with those of other authors [2, 4, 5]. The XPS data confirmed the presence of NpO_2 on the sample surface. The XPS structure in the binding energy range of 0 eV – 35 eV is interpreted and quantitatively analyzed taking into account the core XPS data and the self-consistent field relativistic discrete variation calculation results for the NpO_8^{12-} (D_{4h}) cluster reflecting the neptunium close environment in NpO_2.

The structure of the obtained spectra was compared to that of the photoelectron [4, 5] and x-ray photoelectron [2, 4, 5] spectra of NpO_2. As a result, it is theoretically shown and experimentally corroborated that chemical bond formation in NpO_2 results in appearance of the occupied Np5f electronic states in the valence band. The Np6p electrons are found to take a appreciable part in formation of not only the inner valence but also of the outer valence (~0.3 Np6p electron) molecular orbitals (bands). The results of our investigation showed that the main role in the IVMO formation in NpO_2 was played by the $Np6p_{3/2}$ and the O2s atomic orbitals of the neighboring neptunium and oxygen ions. The compositions and the sequence order of the inner valence molecular orbitals in the energy range of 15 eV – 35 eV have been determined, and the valence electronic states densities in the range 0 eV – 35 eV in neptunium dioxide was calculated. These data allowed the quantitative scheme of molecular orbitals for NpO_2. This scheme is fundamental for understanding the chemical bonding nature in NpO_2 and for interpretation of the structure of other NpO_2 X-ray spectra.

The work was supported by RFBR grant 13-03-00214-a.

References

[1] Yu.A. Teterin, A.Yu. Teterin. Russ. Chem. Rev. 2004. **73(6)**, 541.

[2] B.W. Veal, H. Diamond, H.R. Hoekstra. Phys. Rev. 1977. **15,** 2929.

[3] V.A. Gubanov, A. Rosen, D.E. Ellis. J. Phys. Chem. Solids. 1979. **40**, 17.

[4] J.R. Naegele, L. Manes: Actinides 1981, LBL–report 12441, p. 69 (1981).

[5] A. Seibert, T. Gouder, F. Huber. J. Nucl. Mater. **2009**, *389,* 470.

3-48

Structure and spectroscopic evidence of hexavalent neptunyl and plutonyl mono- and dinitrate complexes in aqueous nitric acid

Patric Lindqvist-Reis[1], Christos Apostolidis[2], Olaf Walter[2], Remi Marsac[1], Nidhu Lal Banik[1], Mikhail Yu. Skripkin[3], Jörg Rothe[1], Alfred Morgenstern[2], Rachel Eloirdi[2]

[1]Institut für Nukleare Entsorgung. Karlsruhe Institute of Technology, Karlsruhe, Germany, [2]Institute for Transuranium Elements, European Commission, Joint Research Centre, Karlsruhe, Germany, [3]Department of Chemistry, St. Petersburg State University, St. Petersburg, Russia

Neptunium and plutonium are the two radioactive elements succeeding uranium in the actinide series. Although they are not primeval in nature, large quantities of the elements have been generated in the nuclear industry, plutonium as fuel, neptunium as byproduct. In the PUREX process, spent nuclear fuel is dissolved in nitric acid, followed by liquid-liquid extraction ion-exchange steps for separation and recovery of usable uranium and plutonium, while neptunium is discarded. The predominant oxidation states of neptunium and plutonium in these systems strongly depend on the chemical environment. Although oxidation states from +3 to +7 are possible for neptunium and plutonium in aqueous solution (with the corresponding ionic species An^{3+}, An^{4+}, AnO_2^{+}, AnO_2^{2+}, AnO_4^{-}; An = Np, Pu), in these process solutions where the concentration of nitric acid is high, oxidation states of +4, +5, and +6 dominate. Despite that nitrate it is a weakly coordinating anion to metal ions in aqueous solution, at higher nitrate concentrations it forms inner-sphere complexes (contact ion pairs) with hexavalent uranyl, neptunyl, and plutonyl In the PUREX process solutions a fair amount of neptunyl- and plutonyl-nitrate complexes is therefore to be expected. Hence, basic knowledge about actinide speciation in aqueous nitrate solutions, including thermodynamic and structural characteristics, is necessary for optimization of such processes. In addition, systematic experimental studies along the series of hexavalent actinides are important to critically evaluate the concept of oxidation state analogy frequently used in actinide chemistry.

There are several spectroscopic studies published on uranyl-nitrate complexation in aqueous solution, but relatively few on the corresponding hexavalent neptunium and plutonium systems.[1-5] However, the agreement between the studies regarding the stoichiometry of the solution species at a given nitrate concentration is poor. For example, Ikeda-Ohno et al. found using EXAFS that UO_2^{2+} and NpO_2^{2+} were coordinated by three and two nitrate ions, respectively in 15 M HNO_3,[1-2] whereas Gaunt et al. concluded from their vis-NIR absorption and Raman studies that one nitrate ion was bound to PuO_2^{2+} in 15 M HNO_3.[3] These findings are in variance with two earlier vis-NIR absorption spectroscopic studies on NpO_2^{2+} and PuO_2^{2+} in nitric acid,[4-5] where it was concluded that the major complex in 15 M HNO_3 was a dinitrate complex.

Actinyl(VI)-nitrate complexes crystallizing from aqueous solution may have very different structures and stoichiometries depending on the nitrate concentration and the water activity. How these parameters control the crystal chemistry of plutonyl-nitrate complexes was discussed in a doctoral theses by Böhm.[6] We have made use of the synthesis schemes described in his thesis and sometimes modified them for obtaining single crystals of $[An^{VI}O_2(NO_3)_2(H_2O)_2]\cdot xH_2O$ (An = Np, Pu; x = 0, 1, 4). We here present the synthesis, X-ray crystal structures, NIR-vis absorption, IR and Raman spectra of these compounds and for $NH_4[Np^{VI}O_2(NO_3)_3]$. All these crystal structures, except that of $[PuO_2(NO_3)_2(H_2O)_2]\cdot H_2O$,[3] are new and have not been reported before.

An important question is whether the complexes present in the crystals also occur in solution. If so, under which conditions and to what extent? To find out, we compared the optical absorption and vibrational spectra of the above-mentioned compounds with those of the corresponding aqueous solutions, which we measured at different concentrations of HNO_3 between 0 and 14 M. Depending on the acid concentration, distributions of hydrated AnO_2^{2+}, $[AnO_2(NO_3)]^{+}$ and $[AnO_2(NO_3)_2]$ species were established, for which three distribution regions covering the whole nitric acid concentration range were identified. Differently from previous work,[3-5] small redshifts relative to the spectra of the non-complexed ions were observed in both the vis-NIR absorption spectra of the Np(VI) and Pu(VI) solutions at nitric acid concentrations between 4 and 10 M. We explain these shifts as being due to a likewise small increase in the ion's ligand-fields upon formation of a mononitrate complex. In contrast, the

large blue-shifts appearing above 10 M HNO_3 are consistent with the formation of dinitrate complexes with noticeably weaker ligand fields compared to the mononitrate complexes. This was confirmed by comparing with the vis-NIR absorption spectra of $[AnO_2(NO_3)_2(H_2O)_2]\cdot H_2O$. Thus, the assignment of the absorption bands corresponding to $[AnO_2(NO_3)]^+$ and $[AnO_2(NO_3)_2]$ species differs from those of previous investigators.[3-5]

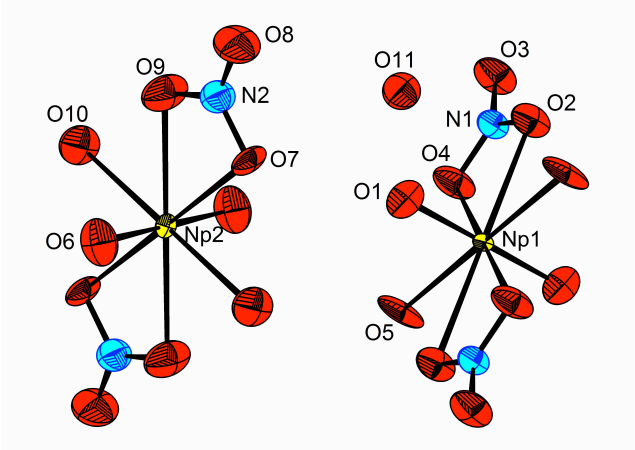

Figure 1. X-ray structure showing the two centrosymmetric $[NpO_2(NO_3)_2(H_2O)_2]$ entities and the lattice water molecule in $[NpO_2(NO_3)_2(H_2O)_2]\cdot H_2O$ (T = 173 K; hydrogen atoms are omitted; thermal ellipsoids are set at 90 % probability).

References

[1] A. Ikeda-Ohno, C. Hennig, A. Rossberg, H. Funke, A. C. Scheinost, G. Bernhard and T. Yaita, Inorg. Chem. 2008, 47, 8294.

[2] A. Ikeda-Ohno, C. Hennig, S. Tsushima, A. C. Scheinost, G. Bernhard and T. Yaita, Inorg. Chem. 2009, 48, 7201.

[3] A. J. Gaunt, I. May, M. P. Neu, S. D. Reilly and B. L. Scott, Inorg. Chem. 2011, 50, 4244.

[4] V. Y. Vasil'ev, N. N. Andreichuk and A. G. Rykov, *Soviet Radiochemistry* 1975, *17*, 21.

[5] V. Y. Vasil'ev, N. N. Andreichuk and A. G. Rykov, *Soviet Radiochemistry* 1975, *17*, 26.

[6] Böhm, M., 1992, *Zur Plutoniumchemie in wässriger Salpetersäure*, dissertation, Ludwig-Maximilians-Universität München, Germany (in German).

3-49

Raman Spectroscopic Study on Uranyl and Neptunyl Complexes in Concentrated Chloride Solutions

Toshiyuki Fujii[1], Akihiro Uehara[1], Yoshihiro Kitatsuji[2], Hajiumu Yamana[1]

[1]Research Reactor Institute, Kyoto University, Osaka, Japan, [2]Nuclear Science and Engineering Directorate, Japan Atomic Energy Agency, Ibaraki, Japan

Molten hydrate salts are highly concentrated electrolyte media with limited amount of water. In the melt, cations, anions, and water molecules contact each other continuously by forming a quasi-lattice structure. A solute actinide cation in the melt is surrounded by anions and water molecules which are contacted by cations of the matrix salt. The mean activity coefficient of salts is much larger than unity, while the activity coefficient of water is much smaller than unity. Chemical behavior of actinide ions in the molten hydrate salts are therefore of interest. Structural studies on uranyl complexes in highly concentrated chloride solutions have been performed by X-ray absorption fine structure (EXAFS) analysis [1]. The hydrated uranyl ion present in aqueous solutions is $UO_2(H_2O)_5^{2+}$, changed to $UO_2Cl_n(H_2O)_m^{2-n}$ (n + m = 4 or 5) with the increase of chloride concentration. The ligand exchange between hydrated water and Cl^- at the equatorial plane changes a bonding strength of the O=U=O axis. This can be observed in the Raman shift of symmetric stretching (v_1) frequency of UO_2^{2+} [3].

In the present study, we investigated the v_1 frequencies of uranyl and neptunyl in highly concentrated alkali chlorides (ACl) and alkaline earth chlorides ($AECl_2$) by Raman spectrometry. The v_1 frequency was also estimated by using *ab initio* methods. The ligand exchange reaction between hydrated water and Cl^- at the equatorial plane is discussed.

Weighed amount of ACl or $AECl_2$ was mixed with water for preparing various concentrations of chloride solutions. As a starting material, U_3O_8 was dissolved in 6 mol dm^{-3} (M) HCl. A portion of this solution was once dried by heating, and then the dried salt was dissolved in the chloride matrix. The concentration of U was 0.01 M. The sample was taken in a quartz cell and the cell was sealed. Raman spectra were measured by using a Raman spectrophotometer (NRS-3100, JASCO). A green laser with the wavelength of 531.9 nm was used at the output power of 57.6 mW. The measurement interval of a charge-coupled device (CCD) detector was set to be every 0.3 cm^{-1}. The operations of each 3-seconds measurement were accumulated by 25 times. The experimental temperature was 298 K. As a reference, 0.01 M U in 1 M HCl was analyzed. The v_1 frequency was observed at 870 cm^{-1}. This agreed with the literature value [3]. With the decrease of water content in the ACl and $AECl_2$ system, the v_1 frequency decreased to 849 cm^{-1}. This suggests that hydration water molecules at the equatorial plane of uranyl were substituted by Cl^- ions, which depressed the bonding strength of U=O. Half width of the v_1 peak increased with the decrease of water content. This suggests that $UO_2Cl_n(H_2O)_m^{2-n}$ species coexist in the concentrated chloride systems. Orbital geometries and vibrational frequencies of uranyl species were computed using the density functional theory (DFT). The v_1 frequency of $UO_2Cl_n(H_2O)_m^{2-n}$ showed smaller values compared with $UO_2(H_2O)_5^{2+}$. The calculation results support the experimental results obtained by Raman spectrometry.

Similar to the U case, 0.01 M Np in concentrated $CaCl_2$ was prepared. In order to analyze neptunyl of Np(VI), we used a nitric acid solution as the starting material. A portion of 1 M HNO_3 containing Np was dried by heating and then the dried salt was dissolved in $CaCl_2$ matrix. Since the concentration ratio of $[Cl^-/NO_3^-]$ is larger than 350, reaction of NO_3^- with neptunyl (and with Ca^{2+}) may be insignificant. Electronic absorption spectrum of the sample was measured, which suggested that Np(VI) and Np(V) coexist in the system. The Raman peaks were found in the range of 680 to 900 cm^{-1}. These are attributable to the v_1 vibrational modes of NpO_2^{2+} and NpO_2^+ complexes. Though it was less sensitive compared with the uranyl case, a Raman peak found at ~838 cm^{-1} shifted by changing water content of the system. The ligand exchange between hydrated water and Cl^- at the equatorial plane of neptunyl may have occurred.

[1] A. Uehara et al., NEA/NSC/DOC (2009) 15, and references therein.

[2] M. Åberg et al., Inorg. Chem., 22, 3986 (1983).

[3] C. Nguyen-Trung at al., Inorg. Chem., 31, 5280 (1992).

3-50

Development of a simplified soft-donor technique for trivalent actinide-lanthanide separations

Madeleine Langford Paden[1], Louise Natrajan[1], Clint Sharrad[1], Leigh Martin[2], Sarah Hendley[1]

[1]The University of Manchester, Manchester, UK, [2]Idaho National Laboratory, Idaho, USA

Nuclear waste reprocessing is essential to prevent the exhaustion of U^{n+} supplies and to reduce the radiotoxicity of the waste. Re-usable U^{n+} and Pu^{n+} present in nuclear waste can be separated from the fission products: Np^{n+}, Am^{3+} and Cm^{3+} and a mixture of Ln^{3+} ions. Np^{n+} can be extracted more easily as it has a variety of oxidation states, although separation of the minor actinides (MA^{3+}) from Ln^{3+} is difficult due to their chemical similarities. MA^{3+} ions are highly radiotoxic and it would be beneficial to transmutate them into shorter-lived radionuclides by neutron bombardment. However, Ln^{3+} ions are neutron scavengers and interfere with this process so must be removed first.

Solvent extraction (SX) is the separation of two or more species using two immiscible liquids and a complexing agent to selectively move only one species between phases. TALSPEAK (Trivalent Actinide Lanthanide Separation by Phosphorus reagent Extraction from Aqueous Komplexation)** is an effective SX method currently being developed in the US which utilises the preferential binding of holdback-complexant DTPA for MA^{3+} over Ln^{3+}. Benefits of the process include: it is resistant to irradiation, it allows the separation of MA^{3+} from Ln^{3+} without high acid and salt concentrations and it has been successfully performed on a pilot plant scale.

The use of amino acids as a combined buffer and soft donor is currently being investigated. If successful, this could eliminate the need for the separate complexant and lactate buffer, simplifying the process and allowing it to be carried out at lower pH, making it more efficient as more acidic conditions have been shown to increase the separation factor (SF). Eu^{3+} has been found to be preferentially extracted over Am^{3+} by the use of the amino acid alanine although, under current conditions, study has shown that SFs are higher when DTPA is used alongside the amino acid (SF 80.03 with DTPA/0.5M alanine). Amino acids (alanine, glycine and serine) have been shown to interact with Ln-DTPA complexes by luminescence spectroscopy (where Ln = Eu^{3+}, Tb^{3+} and Sm^{3+}). Emission and excitation data suggests there is fast exchange between bound and unbound amino acids, showing that there is an interaction between DTPA complex and the amino acid in the extraction process. Additionally, it has been found that other amino acids and lactate interact weakly with the metal ions and metal-DTPA complexes and are also in fast exchange between bound and unbound forms, indicated by luminescence spectroscopy and XAS. Analysis of Ln^{3+}/MA^{3+}-DTPA/amino acid complexes at different pH values in aqueous media and post-extraction into organic media is presently being carried out in order to understand the complex formation and separation mechanisms and to evaluate the potential of replacing the complexant with amino acids. Additional studies on the stability of Ln^{3+}/MA^{3+} complexes with amino acids are being conducted in collaboration with the Idaho National Laboratory and studies on the effect of irradiation on the extraction process are being conducted in collaboration with the Dalton Nuclear Institute. Our most recent results will be presented.

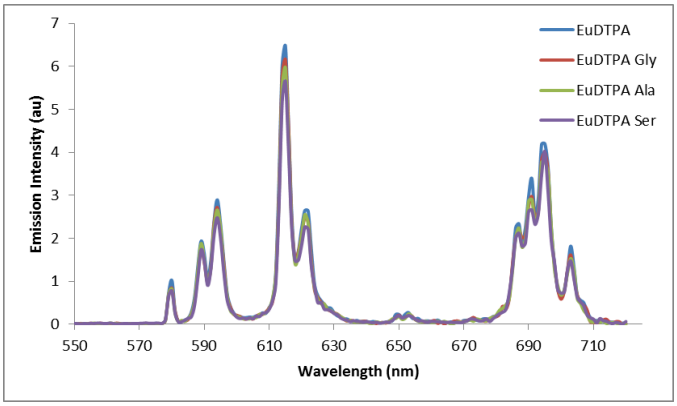

Figure 1: Emission spectra of EuDTPA with different amino acids in D2O at pD 3.6.

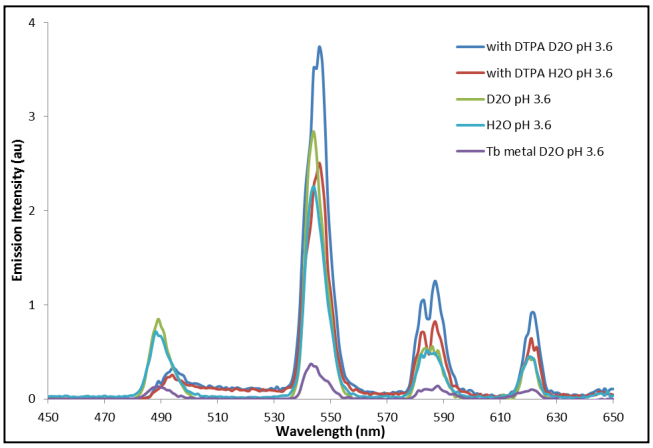

Figure 2: Emission spectra of Tb-Ala in H2O/D2O at different pH/pD values.

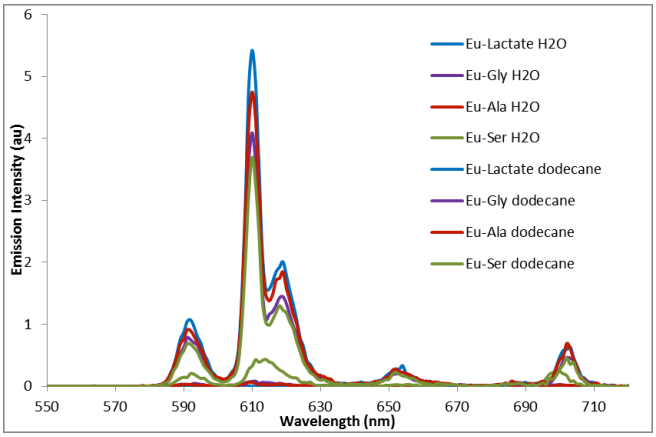

Figure 3: Emission spectra of Eu with different amino acids in D2O at pD 3.6.

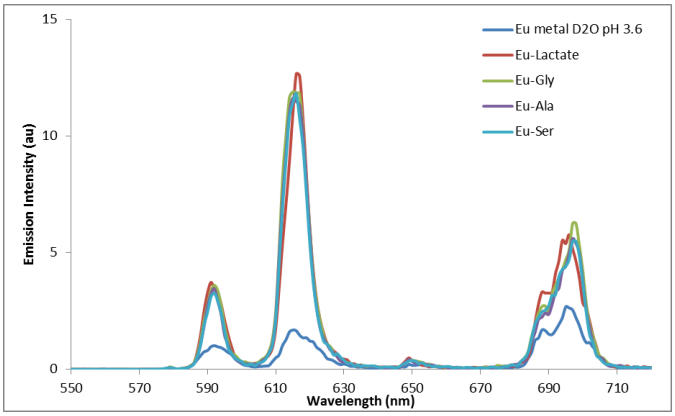

Figure 4: Emission spectra of Eu with different amino acids before and after extraction into dodecane with HDEHP from aqueous solution at pH 3.6.

3-51

Understanding molecular speciation of actinides in the PUREX process

Tamara Griffiths[1], Kate Tucker[1], Clint Sharrad[1], Francis Livens[1], Leigh Martin[2], Peter Kaden[3]

[1]University of Manchester, Manchester, UK, [2]Idaho National Laboratory, Idaho, USA, [3]Karlsruher Institut für Technologie, Institut für Nukleare Entsorgung, Karlsruhe, Germany

The PUREX process (Plutonium URanium EXtraction) is the most established technique for the processing of spent nuclear fuel. This liquid-liquid separation utilises 30 % tributyl phosphate (TBP) in kerosene to selectively extract hexavalent U and tetravalent Pu ions from commercial reactor fuel dissolved in nitric acid. The dissolved fuel also contains Np, which can exist as tetra-, penta- and hexavalent Np ions in aqueous nitric acid. Both Np^{IV} and $Np^{VI}O_2^{2+}$ ions can be extracted into the PUREX organic phase, however, the $Np^{V}O_2^{+}$ ion cannot extract. The minor actinides (*i.e.* Am^{III} and Cm^{III}) and the remainder of the fission products, including the trivalent lanthanides, are also not extracted by TBP, and remain in the acidic aqueous phase.

A molecular scale understanding of actinide speciation, in the organic phase of the PUREX process can assist in accurately describing the mechanism by which these separations occur. Further, this information may be of use in the development of novel separations techniques. In this presentation we will discuss the results of NMR and UV-vis spectroscopies, which probe the speciation of Np and Pu ions in PUREX extraction systems. ^{31}P-NMR spectra recorded for samples containing extracted Np and Pu ions in 30 % TBP/OK from $HNO_{3(aq)}$ show the presence of the $TBP.HNO_3$ solvate and extracted Np/Pu-TBP-nitrate species (Figure 1). UV-vis spectra recorded for extracted Np ions into 30 % TBP from $HNO_{3(aq)}$ show the presence of $Np^{VI}O_2^{2+}$ (570 nm), which then gradually converts to Np^{IV} (~700 nm) over time (Figure 2). The work has provided an insight into the Np/Pu-TBP-NO_3 complexes present in the organic phase, and it is envisaged that the information gained on actinide speciation in the organic phase could feed into quantitative models, which will be used to explore different options for fuel reprocessing.

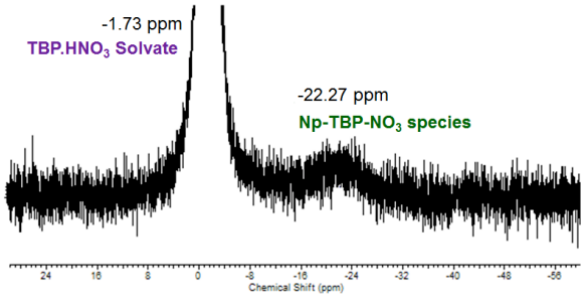

Figure 1: ^{31}P-NMR spectrum recorded for an organic phase sample of $Np^{VI}O_2^{2+}$ extracted into 30 % TBP/OK from 8 M aqueous nitric acid.

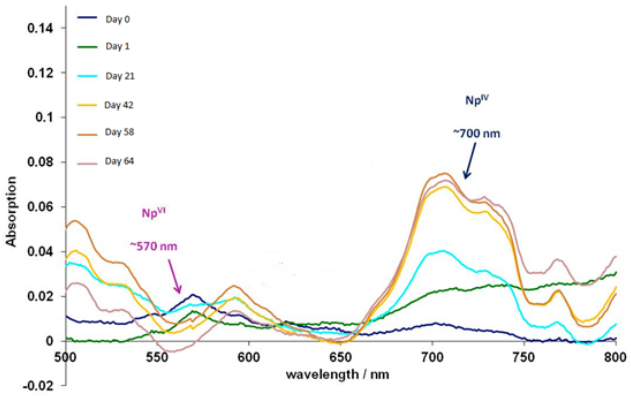

Figure 2: UV-vis spectrum recorded for an organic phase sample of Np extracted into 30 % TBP/OK from 8 M aqueous nitric acid (right).

3-52

In-situ XAFS analysis of electrochemical reduction of uranium (VI) in highly concentrated LiCl

Akihiro Uehara[1], Toshiyuki Fujii[1], Hajimu Yamana[1], Yoshihiro Okamoto[2]

[1]Research Reactor Institute, Kyoto University, Osaka, Japan, [2]Nuclear Science and Engineering Directorate, Japan Atomic Energy Agency, Ibaraki, Japan

Pyrochemical dry reprocessing of spent nuclear fuels has been developed. The pyrochemical reprocessing includes the dissolution of spent nuclear fuels in a molten salt medium and the selective recovery of actinides. Recently, room temperature ionic liquids were demonstrated into the electrochemical deposition of uranium instead of high temperature molten salts. On the other hand, coordination structure of actinide ions in highly concentrated electrolytes (14M LiCl, 6.9 M $CaCl_2$) has been studied since it is assumed that the water molecules in LiCl melts are strongly coordinated to lithium ion showing that this melt is a liquid with the properties of an ionic melt composed of bulky hydrated cations and chloride anions. According to X-ray absorption fine structure (XAFS) analyses, U(VI) species in 6.9 M $CaCl_2$ were estimated to be $UO_2Cl_2(H_2O)_2$ [1] which was distinctly different from $[UO_2(H_2O)_5]^{2+}$ in 0.1 M $HClO_4$. There are a few studies of the electrochemistry for the redox of UO_2^{2+} in the aqueous solution concentrated by the electrolytes [2,3]. Cohen [2] reported that the formation of UO_2^{+} in the aqueous solution highly concentrated by $CaCl_2$ and LiCl was identified absorption spectrophotometrically. He has also reported that uranium compounds were deposited on the cathode by electrolysis. Bansal et al. [3] reported that UO_2^{2+} was readily reduced to UO_2^{+}, and that was further reduced to UO_2 in the calcium nitrate tetrahydrate melt. However, the deposited compounds could not be identified since these compounds were very oxidative. In the present study, the coordination circumstance and the redox reaction of UO_2^{2+} in the highly concentrated LiCl solution were investigated by EXAFS analysis under the electrochemical operation. The mechanism of the reduction of UO_2^{2+} in LiCl is discussed by applying constant potential with XAFS measurement. The negative peak for the reduction of UO_2^{2+} in the cyclic voltammogram was observed at -0.1 V vs. silver|silver chloride electrode. Edge jump at the U L_{III}-absorption edge (E^0 = 17.15 keV) changed for the reduction of UO_2^{2+} by applying potential at -0.3 V for 6 hrs. It was found that UO_2 was formed at the working electrode after the reduction of UO_2^{2+}.

References

[1] A Uehara, et al., OECD-NEA 15(2009)197.

[2] D. Cohen, J. Inorg. Nucl. Chem. 32(1970)3525.

[3] NP Bansal et al., Electrochim. Acta 23(1978)1053, idem, Can. J. Chem. 59(1981)1515.

3-53

Selective recovery of actinides from An-Zr-fuel by electrorefining in molten LiCl-KCl

Roland Meier[1,2], Pavel Souček[1], Rikard Malmbeck[1], Claux Bennoit[1], Glatz Jean-Paul[1], Fanghaenel Thomas[1,2]

[1]European Commission, JRC Institute for Transuranium Elements, Karlsruhe, Germany, [2]Heidelberg University, Institute of Physical Chemistry, Heidelberg, Germany

The sustainable progress of nuclear power generation relies on a safe and secure management of radioactive waste and on implementing technologies using the advanced nuclear fuel cycle based on processes accomplishing the enhanced safety and security principles. To this aim, a pyrochemical electrorefining process for the recovery of actinides from metallic nuclear fuel based on An-Zr alloys in a molten salt media is investigated at ITU [1]. The process consists of anodic dissolution of the fuel to a molten salt bath and grouped selective electrochemical reduction of the actinides on solid Al cathodes in a form of An-Al alloys. It is advantageous to control the process in a way to avoid co-dissolution of Zr from the fuel in order to prevent consequent deposition of Zr metal together with actinides, which can negatively affect the quality of the product.

In the presented work, electrochemical behaviour of Zr during electrorefining of non-irradiated U-Pu-Zr alloy fuel was investigated in order to evaluate the amount of recovered actinides without anodic co-dissolution of Zr in dependency on the applied current density. Three anodic baskets made of Ta mesh were used in the same time and they were filled equally with a total mass of 2 g of U-Pu-Zr alloy (79 wt.% U, 19 wt.% Pu). The experiment consisted of three steps to assess different stages of the dissolution progress, each using one Al cathode. After each step, one basket was removed and the cathode was changed. Fig.1 (left) presents a principle of the process.

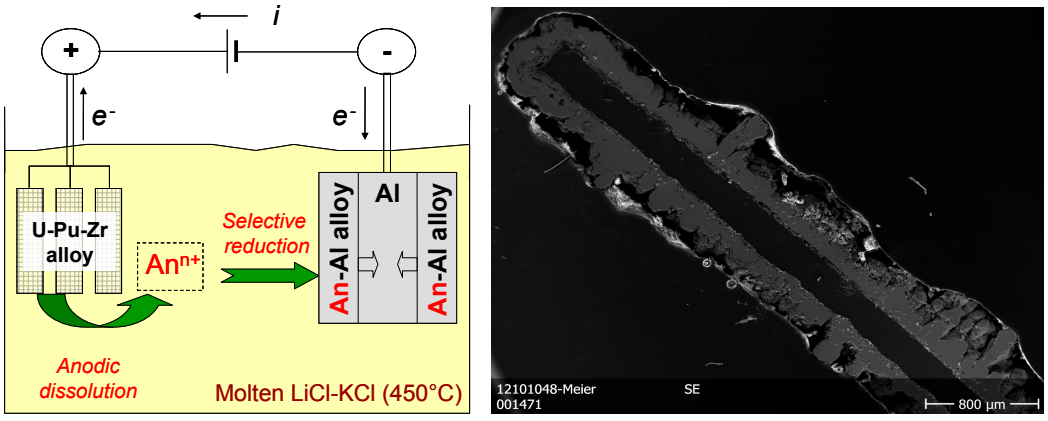

Fig. 1 Principal of the process (left); SEM micrograph of the cross section of electrode 3 (right).

The galvanostatic electrorefining was carried out with a constant current density of 20 mA/cm^2 and both electrodes potentials were monitored. In the first step, the electrorefining was stopped after dissolution of 70 % of the actinides from the alloy, assuming ideal current efficiency. This value was estimated as a presumptive limit of the alloy anodic oxidation without Zr co-dissolution. The next step was carried out up to the effective limit of selective actinides oxidation. A massive Zr dissolution was observed at the beginning of the third step, when the anodic cut-off potential was reached and exceeded. The selective oxidation was completed when 102 % of actinides were theoretically dissolved, which indicated that at the applied current density, almost all actinides can be dissolved without co-dissolution of Zr.

ICP-OES analyses of the anodic residues showed that after the second step, all Pu and the major part of U was really dissolved. On the other hand, the actinides dissolution was not fully achieved even after massive Zr oxidation proceeded, since a small portion of U was detected in the alloy after the last step. Due to very difficult dissolution of the anodic material, only qualitative analysis is available and a quantitative mass balance of the anodic residues was

not feasible. Dense, well adhered and homogeneously distributed deposits were obtained on all cathodes, as shown in the SEM micrograph of a cross section of the third cathode, Fig.1 (right). The ICP-OES analyses of the cathodes gave a molar ratio of U/Pu to Al of approximately 1/3 corresponding to the expected formation of $AnAl_3$ alloys. Adhered salt was distilled out prior to ICP-OES analysis.

The results of the ICP-OES analysis of the samples from the salt and the electrodes are given in Table.1. The values for Cl where calculated from the K and Li content. Only in the final stage of the experiment, a very small portion of Zr was detected in the salt. It agrees to the analyses of the deposits, where detectable Zr content was observed only for the last cathode.

Table 2 ICP-OES analysis of the salt and the electrodes, values for Cl where calculated from the Li and K content. Values are given in wt%.

	U	Pu	Zr	K	Li	Al	Cl
salt 1	1.38	0.32	< d.l.	25.76	6.76	< d.l.	57.73
salt 2	1.82	0.72	< d.l.	27.33	7.13	< d.l.	61.07
salt 3	0.97	0.39	< d.l.	26.13	6.88	< d.l.	58.66
salt 4	0.99	0.54	0.05	26.83	7.09	< d.l.	60.37
el. 1	54.38	7.06	< d.l.	< d.l.	< d.l.	23.04	< d.l.
el. 2	53.94	6.62	< d.l.	< d.l.	< d.l.	18.82	< d.l.
el. 3	49.97	5.02	0.89	< d.l.	< d.l.	21.16	< d.l.

Similar experiments with different current densities are planned in order to evaluate the maximum current density applicable for the process providing complete recovery of actinides without dissolution of Zr. For the recovery of the actinides from the An-Al alloys a chlorination process is under investigation [2].

References

[1] P. Souček, L. Cassayre, R. Malmbeck, E. Mendes, R. Jardin, and J.-P. Glatz, Radiochimica Acta 96:315 (2008).

[2] R. Meier, P. Souček, R. Malmbeck, and T. Fanghänel, Procedia Chemistry 7:785.

3-54

Actinide extraction and complexation properties of oxygen-nitrogen hetero donor ligand PTA

Tohru Kobayashi, Shinichi Suzuki, Hideaki Shiwaku, Tsuyoshi Yaita

Japan Atomic Energy Agency, 1-1-1 Koto, Sayo-cho, Sayo-gun, Hyogo, Japan

The development of extractant, which can efficiently separate actinides, is of increasing importance because it concerns establishment and simplification of separation techniques in nuclear fuel cycle and/or decontamination of radioactive waste. In particular, for the disposal of long-lived radionuclide, vitrification and deep geological storage is widely accepted as disposal strategy, and to avoid a risk of the long term storage, long-lived minor actinides such as trivalent actinides (An^{3+}) should be separated and transmuted into short-lived isotopes by neutron irradiation. However, the separation of An^{3+} from trivalent lanthanide (Ln^{3+}) is very difficult due to their similarity in chemical properties. Recently, the selective separations of An^{3+} over Ln^{3+} based on covalent bond formation were observed by some comparatively soft donor ligands such as aza-aromatic nitrogen ligands, but most nitrogen donor ligands are not effective for An^{3+} extraction in highly concentrated acidic conditions due to protonation of nitrogen atoms. Accordingly, the development of An^{3+} / Ln^{3+} separation reagent which shows effective separation even under acidic conditions is highly desirable.

To develop the new actinide separation reagent, which allows both high selectivity and extractability for minor actinides even under acidic condition, the combination of both nitrogen donor and oxygen donor which can strongly interact with actinides into one molecule has been proposed. Bearing this in mind, we designed and synthesized a novel tridentate ligand *N*-alkyl-*N*-phenyl-1,10-phenanthroline-2-carboxamide (PTA, Fig.1), composed by both phenanthroline moiety as comparatively soft donors and amide group as hard oxygen donor. As a result of extraction experiments, it was revealed that PTA can selectively extract Am^{3+} over Eu^{3+} even form highly concentrated nitric acidic solution. Furthemore, interestingly, the extraction behaviors drastically change by acid concentration of aqueous phase. In lower acidic condition, the extractabilities for Pu^{4+}, Am^{3+}, UO_2^{2+} and Ln^{3+} decrease with an increase in HNO_3 concentration. In contrast, in higher acidic condition, the extractabilities for Pu^{4+} and UO_2^{2+} increase with an increase of HNO_3 concentration, though the extractabilities for Am^{3+} and Eu^{3+} decrease (Fig.2). This result means that the extraction selectivity can be controlled by changing of acid concentration in aqueous phase. In this presentation, we will discuss the separation and complexation properties of PTA based on structural characters investigated by X-ray crystallography, X-ray absorption fine structure and spectroscopic titration method.

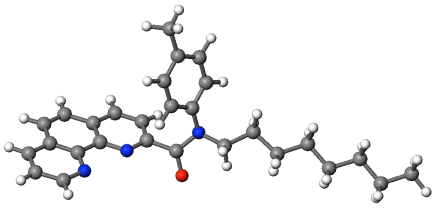

Fig.1 chemical structure of PTA

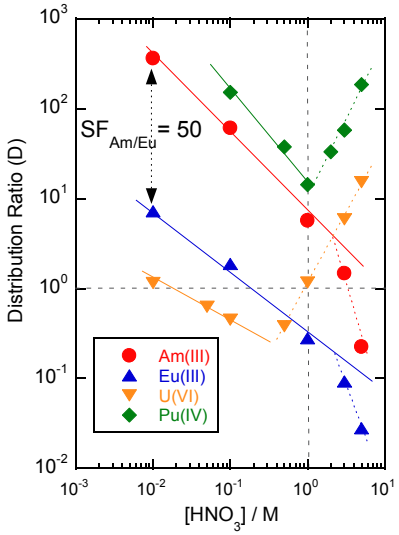

Fig.2 HNO_3 concentration dependence of actinides extraction by PTA

3-55

Formation of actinide(IV) carboxylate complexes in aqueous solution – the unexpected predominance of hexanuclear species

Christoph Hennig[1,5], Koichiro Takao[2], Shinobu Takao[3], Stephan Weiss[1], Werner Kraus[4], Franziska Emmerling[4], Andreas C. Scheinost[1,5]

[1]Helmholtz-Zentrum Dresden-Rossendorf, Institute of Resource Ecology, Dresden, Germany, [2]Department of Materials and Life Science, Seikei University, Tokyo, Japan, [3]Department of Engineering Science, University of Electro-Communications, Tokyo, Japan, [4]BAM Federal Institute for Materials Research and Testing, Berlin, Germany, [5]The Rossendorf Beamline at ESRF, Grenoble, France

Tetravalent actinides form strong complexes with carboxyl containing ligands. Such complexes play an important role in technological processes as well as biological and environmental systems. The aqueous chemistry of such complexes is therefore of wide interest. So far, most of the thermodynamic data of actinide(IV) carboxylates are estimated assuming mononuclear solution species (see for example [1]). We applied comprehensive spectroscopic studies (EXAFS, UV-Vis-NIR spectroscopy and X-ray diffraction) to estimate the complex structure of actinide(IV) carboxylates with different actinides (Th^{4+}, U^{4+} and Np^{4+}) and carboxylates ($RCOO^-$; R = H, CH_3, $CHR'NH_2$; R' = H, CH_3, CH_2SH) in aqueous solution and solid state [2-4]. These studies show clearly that in all of the investigated systems hexanuclear complexes appear, which become predominant with increasing metal and ligand concentration as well as increasing pH, and comprise finally often close to 100% of the species distribution. The aim of our studies was to investigate the complex structure, stability constants, and the mechanism of complex formation. Subsequently, as one example, the hexanuclear Th(IV) glycine system will be described in more detail.

Thermodynamic studies on the Th(IV) glycine complexes are rare. Sergeev et al. [5,6] determined an equilibrium constant of the 1:1 complex based on potentiometric titration data to log K = 8.90. Bismondo et al. [7] reinvestigated the system based on potentiomentic and calorimetric measurements and determined three formation constants (log K_1 = 2.55, log K_2 = 1.66 and log K_3 = 1.33). The authors of both studies assumed the formation of monomeric complexes in solution and excluded explicitly the potential formation of polymeric species. So far, no structural data of the Th(IV)-glycine species in solution are available. Furthermore, no crystal structures were determined which may provide at least hints on potential coordination of the species in solution.

The lack of information motivates a spectroscopic investigation of the Th(IV) glycine complexes. EXAFS spectra, shown in Figure 1, were recorded on samples in aqueous solution with 0.05 M Th(IV), 1 M glycine and pH values ranging from 0.5 to 3.2. The spectrum at pH 0.5 shows a single peak representing mononuclear complexes of $[Th(OH_2)_n]^{4+}$ and $Th(OH)_n^{(4-n)+}$ with $n \leq 2$. With increasing pH, the first peak in the Fourier transform becomes more asymmetric and finally splits. A second peak at $R+\Delta$ = 3.75 Å appears, and its intensity rises with increasing pH. This latter feature represents a Th-Th scattering interaction. The structure parameters indicate the appearance of a hexanuclear complex. This complex is stable until pH 3.2. At higher pH values precipitates a crystalline material. The EXAFS spectrum of this crystalline precipitate is identical with that of the solution at pH 3.2, indicating that the structure of the solution species remains preserved in the crystalline material. This fact allows a structure estimation of the solution species from structure parameters of the related crystal structure. This is a rare case, because other complexes show under similar conditions the tendency to polymerize during crystallization [4]. The crystalline precipitate was used for single structure analysis by X-ray diffraction (see for details [4]). A drawing of the crystal structure is shown in Figure 2.

The complex consists of a hexanuclear core with six Th(IV) atoms arranged at the corners of a nearly regular octahedron. Each of the eight faces of the octahedron is bridged by either a μ_3-O or a μ_3-OH, resulting in a total of four μ_3-O and four μ_3-OH per hexanuclear core. The twelve edges of the octahedron are bridged by the carboxylic group of the glycine ligands through a *syn-syn* coordination. The 12 COO^- groups of the glycine ligands compensate the charge of the $[Th_6(\mu_3\text{-}O)_4(\mu_3\text{-}OH)_4]^{12+}$ core. Of the twelve glycine ligands are six Gly^-, and six HGly ligands, whose positive charge is compensated by three NO_3^- and three ClO_4^- counter ions. The electron density distribution of the coordinated glycine ligands is different from the

free forms and influences the deprotonation behaviour of the gycine nitrogen. In the crystal structure appears an equimolar ratio of Gly^- and HGly at lower pH than that expected for the free ligand. It is likely that the solution species comprise a range of Gly^-/HGly variations. This is not the case for hexanuclear An(IV) complexes with $RCOO^-$; R = H and CH_3 [2,3]. We determined the formation constants of such hexanuclear complexes e.g. for Np(IV) with ligands of $RCOO^-$; R = H and CH_3 [3].

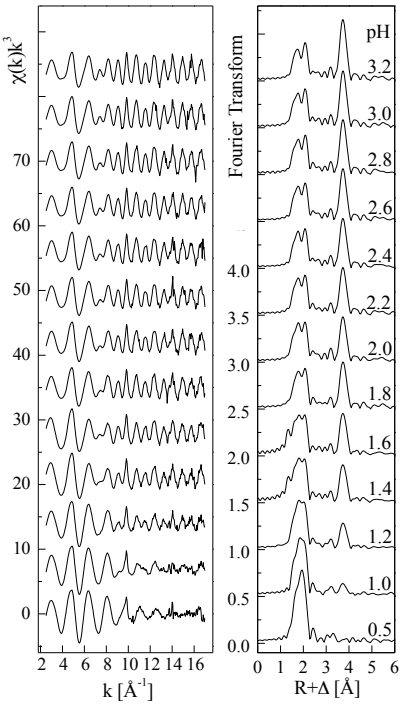

Figure 1: Th L_3-edge k^3-weighted EXAFS data (left) and the corresponding Fourier Transforms (right) of a sample series with 0.05 M Th(IV), 1 M glycine, pH range of 0.5-3.2.

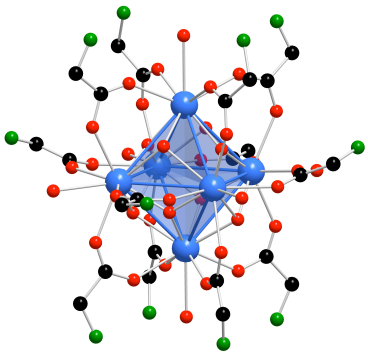

Figure 2: The $[Th_6(\mu_3\text{-}O)_4(\mu_3\text{-}OH)_4(H_2O)_6(Gly)_6(HGly)_6]^{6+}$ unit. Th – blue, O – red, C – black, N – green.

The appearance of hexanuclear complexes in aqueous solution corresponds with both, the onset of the An(IV) hydrolysis at the one hand, and the deprotonation of the carboxylic function at the other hand. This results in a competing reaction between hydrolysis and ligation. The hydrolysis results in a polymerization via oxo and hydroxo bonds, whereas the carboxylic function of the ligand results in the formation of 12 terminating chelate rings providing charge neutrality of the hexanuclear core and preventing further polymerization. Our studies indicate that future work on tetravalent actinide carboxylates in aqueous solution need consideration of the hexanuclear species.

References

[1] Casellato, U.; Vigato, P. A.; Vidali, M. *Coord. Chem. Rev.* **1978**, *26*, 85-159.

[2] Takao, S.; Takao, K.; Kraus, W.; Emmerling, F.; Scheinost, A.C.; Bernhard, G.; Hennig, C. *Eur. J. Inorg. Chem.* **2009**, 4771-4775.

[3] Takao, K.; Takao, S.; Scheinost, A.C.; Bernhard, G.; Hennig, C. *Inorg. Chem.* **2012**, *51*, 1336-1344.

[4] Hennig, C.; Takao, S.; Takao, K.; Weiss, S.; Kraus, W.; Emmerling, F.; Scheinost, A.C. *Dalton Trans.* **2012**, *41*, 12818-12823.

[5] Sergeev, G.M.; Korshunov, I.A. *Radiokhimija* **1973**, *15*, 619-622.

[6] Sergeev, G.M. *Radiokhimija* **1980**, *22*, 536-538.

[7] Bismondo, A.; Rizzo, L.; Tomat, G. *Inorg. Chim. Acta* **1983**, *74*, 21-24.

3-56

XAFS and solubility investigations of penta- and hexavalent actinides in dilute to concentrated salt brines

Jörg Rothe[1], Kathy Dardenne[1], David Fellhauer[1,2], Xavier Gaona Martinez[1], Marcus Altmaier[1], Thomas Fanghänel[2]

[1]Karlsruhe Institute of Technology, Institute for Nuclear Waste Disposal (INE), Karlsruhe, Germany, [2]JRC Institute for Transuranium Elements (ITU), Karlsruhe, Germany

For any reliable assessment of water intrusion scenarios into a projected underground nuclear waste repository, thorough understanding and thermodynamic description of the aquatic actinide (An) element chemistry are mandatory. In the case of rock salt as a possible host rock formation, waste matrix corrosion and dissolution will involve highly concentrated neutral to alkaline chloride solutions with Na^+ and Mg^{2+} as dominant cations. Additionally, Ca^{2+} dominated brines may be generated through corrosion of cementitious waste forms in $MgCl_2$ brines.

The chemistry of dissolved An cations in dilute aqueous solutions is largely controlled by complexation through hydroxide ligands (hydrolysis) and the solid-liquid equilibria forming between aqueous hydrolyzed species and binary oxyhydroxide phases (solubility). An behaviour in concentrated salt brines tends to be more complex, and the speciation schemes derived for dilute systems cannot be applied a priori. In particular, the formation of ternary M-An-OH aqueous species and solid phases has to be considered - as recently reported by our group (e.g., ternary M-An(V/VI)-OH solid phases with M = Na for Np(V) [1], M = Ca for U(VI) [2] and ternary Ca-An(III/IV)-OH aqueous complexes [3,4,5]). Therefore, detailed investigations of aquatic actinide chemistry and solubility at high ionic strength are mandatory for the development of realistic chemical models and sound safety assessment calculations for nuclear waste repositories in salt rock formations.

Synchrotron based X-ray Absorption Fine Structure (XAFS) techniques grant *in-situ* access to structural details of dissolved and solid An species, regardless of their degree of (crystalline) ordering. Hence, these techniques provide important key contributions to elucidate the relevant An equilibrium coordination environments prevailing in dilute to concentrated saline solutions. A comprehensive picture on penta- and hexavalent An species determining solid-liquid equilibria in a broad range of pH conditions and salt concentrations is required as basis for sound thermodynamic An solubility models. In this study, this goal is achieved by augmenting An L3-XAFS measurements performed at the INE-Beamline for actinide research at ANKA (KIT North Campus [6]) with batch solubility experiments, classical wet chemical analysis and laboratory techniques (e.g., XRD of solid An phases and UV-Vis spectroscopy of dissolved An species).

The focus of this presentation is on our systematic and comprehensive experimental program to study solubility, speciation and solid phase formation of Np(V), Np(VI) and Pu(VI) in dilute to concentrated $CaCl_2$ solutions under defined redox conditions. The unambiguous identification of a ternary Ca-Np(V)-OH species in alkaline $CaCl_2$ solutions by Np L3-EXAFS underpins that formation of this kind of compounds is not limited to tri- and tetravalent An cations, but also relevant for higher oxidation states, where An cations are generally present as ‘dioxo’ or ‘actinyl’ moieties. Furthermore, we identified a hitherto unknown ternary Np(V)-chloro-complex, $Ca[NpO_2Cl]^{2+}$, representing a new class of Ca^{2+}-stabilized actinyl complexes (in addition to the well-known Ca^{2+}-stabilized Ca-An-X species with X = OH^-, CO_3^{2-}), forming in concentrated $CaCl_2$ solution (4.5 M) for pH_m < 10 - cf. Np L3-EXAFS fit results in Fig. 1. Solubility and speciation of Np(V) under alkaline conditions in dilute to concentrated $CaCl_2$ solutions are determined by two solid phases, the metastable and highly disordered $CaNpO_2(OH)_{2.6}Cl_{0.4}{\cdot}2H_2O$ and the stable and well- ordered $Ca_{0.5}NpO_2(OH)_2{\cdot}1.3H_2O$ phase. In contrast to that, aqueous Np(VI) speciation under these conditions is controlled by equilibria with non-stoichiometric $Ca_xNpO_2(OH)_{2+2x}$ ‘neptunate’ phases (where x = 0.6 – 1.7 is increasing with the solution pH), characterized by a distorted ‘yl’ conformation with elongated axial and reduced equatorial Np(VI)-O bond distances.

The chemical behaviour of Pu(VI) in $CaCl_2$ solution observed in oversaturation experiments differs significantly from the behaviour of Np(VI) (this study) or that described in previous investigations of the corresponding U(VI)-system [2], where a fast equilibration of aqueous

and solid species was observed. Based on Pu L3-EXAFS results, the fact that Pu(VI) stayed in solution after rapid addition of hydroxide and solubility remains much higher compared to the U(VI)- and Np(VI)-systems, can be ascribed to the formation of metastable aqueous oligomeric Pu(VI)-species which only slowly transform into a more stable Ca-Pu(VI)-OH solid phase. With these results, once more the unique behaviour of aqueous Pu species, which cannot always be satisfactorily described by chemical analogues, is demonstrated.

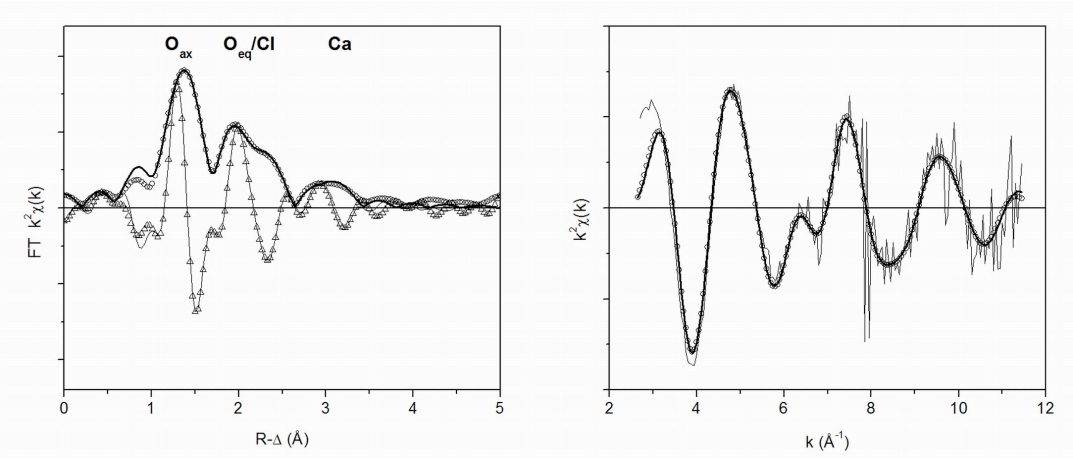

Fig. 1: Np L3-EXAFS fit results for aqueous $Ca[NpO_2Cl]^{2+}$ in (left) R- and (right) k-space (the k^2-weighted raw data is depicted as thin solid line).

References

[1] V. G. Petrov, X. Gaona, D. Fellhauer, K. Dardenne, J. Rothe, S. N. Kalmykov, M. Altmaier, Radiochim. Acta (2012), submitted.

[2] M. Altmaier, V. Neck, R. Müller, Th. Fanghänel, Abstract No. A1-3, Migration 2005 Conf., Avignon, France.

[3] M. Altmaier, V. Neck, Th. Fanghänel, Radiochim. Acta **96**, 541-550 (2008).

[4] V. Neck, M. Altmaier, Th. Rabung, J. Lützenkirchen, Th. Fanghänel, Pure Appl. Chem. **81**, 1555-1568 (2009).

[5] D. Fellhauer, V. Neck, M. Altmaier, J. Lützenkirchen, Th. Fanghänel, Radiochim. Acta **98**, 541-548 (2010).

[6] J. Rothe, S. Butorin, K. Dardenne, M. A. Denecke, B. Kienzler, M. Löble, V. Metz,

A. Seibert, M. Steppert, T. Vitova, C. Walther, H. Geckeis, Rev. Sci. Instrum. **83**, 043105 (2012).

3-58

Redox Mechanism of Nd(III) Ions in High Temperature LiCl-KCl Eutectic Observed by UV-Vis Absorption Spectroscopy in Combination of Electrolysis

Seung Park, Jong-Il Yun

KAIST, Daejeon, Republic of Korea

Knowledge of electrochemical and thermodynamic properties of fission products in high temperature molten salts is essential for the development of pyroprocessing of used nuclear fuel. Neodymium, one of the fission products, is a strong neutron-absorbing lanthanide element to be separated in the electrorefining and electrowinning process from used fuel. Up to now, reduction process of Nd(III) in chloride melt has been interpreted with two different processes [1]. One is the reduction directly from Nd(III) to Nd(0) [2], and the other is the two-step reduction from Nd(III) through Nd(II) to Nd(0) [3]. In the present work, the absorption spectroscopy and electrolysis were applied simultaneously to verify the mechanistic reduction process of Nd(III) ions in the LiCl-KCl molten salt.

All experiments were carried out at 773 K in argon atmosphere glove box (O_2, H_2O≤5 ppm). The furnace designed for spectroscopic measurement was installed at the bottom part of the glove box hermitically. We used anhydrous LiCl-KCl (44 wt% LiCl, Sigma Aldrich, 99.99 %) as the eutectic base and ultra-dry $NdCl_3$ (Alfa Aesar, 99.99 %) in a highly transmissible quartz cuvette cell. For electrolysis, tungsten wire (j=1.0 mm, Nilaco Co., ≥99.95 %) was used both as the working electrode and counter electrode. Silver wire (∅=1.0 mm, Sigma Aldrich, ≥99.99 %) in 1.0 wt% AgCl in LiCl-KCl eutectic was used as the reference electrode. Tungsten electrode was encapsulated in a home-made pyrex-filtered tube in order to prevent a cell contamination leached from the counter electrode material.

As shown in Fig. 1, the cyclic voltammogram of $NdCl_3$ in LiCl-KCl at 773 K obviously reveals two separate reduction steps of Nd(III)→Nd(II) and Nd(II)→Nd(0) observed at potential of -1.97 and -2.10 V, respectively.

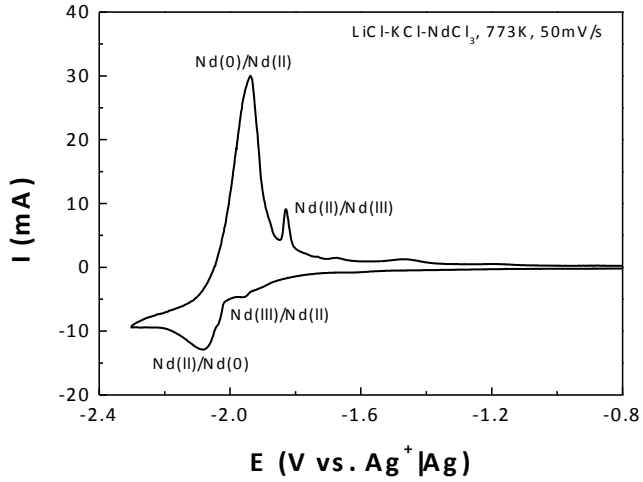

Fig. 1. Cyclic voltammogram of $NdCl_3$ in LiCl-KCl

For the verification of two-step reduction process, characteristic UV-Vis absorption spectroscopy was employed. The absorption spectrum for Nd(III) chlorides was recorded in open circuit, and its major absorption peak was seen at 589 nm. At cathodic electrolysis potential of -1.97 V for Nd(III)/Nd(II), a broad peak of Nd(II) around 502 nm was observed, whereas the absorption band height of Nd(III) was decreased. The absorption peaks of Nd(II) ions are in good agreement with those in literature [1]. After the applied cathodic potential becomes more negative than the Nd(lll)/Nd(0) potential, absorption bands of Nd(III) and Nd(II) gradually disappeared, and finally metallic Nd showing no characteristic absorption band was formed.

In summary, the reduction process of Nd(III) ions was confirmed as the two-step mechanism by simultaneous absorption measurements during electrolysis utilizing the pyrex-filtered counter electrode in the absence of any possible cell contamination. From the analysis of peak height of absorption spectrum of Nd(III) and Nd(II) while changing the applied potentials, it was obviously concluded that trivalent Nd ions are reduced first to divalent and then to the metallic Nd.

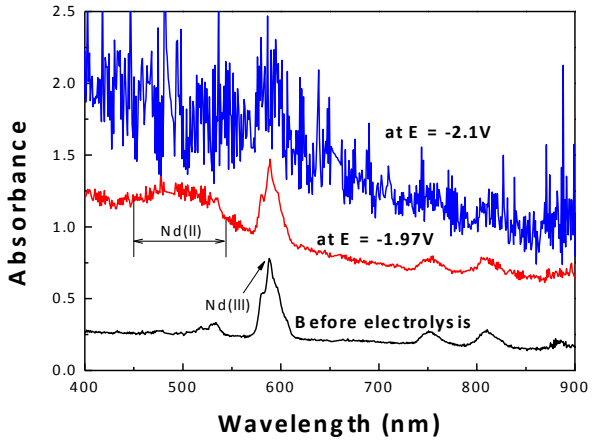

Fig. 2. Absorption spectra before electrolysis and during cathodic electrolysis potential of -1.97 V for Nd(lll)/Nd(ll) and -2.10 V for Nd(ll)/Nd(0)

References

[1] Kazuhito Fukusawa, et al. "Electrochemical Study of Neodymium Ions in Molten Chlorides" Zero-Carbon Energy Kyoto 2009. Springer Japan, 330-333 (2010)

[2] Hajimu Yamana, et al., “Electrochemically produced divalent neodymium in chloride melt”, J. Alloys Compd., **408-412**, 66-70 (2006)

[3] Yolanda Castrillejo, et al. "Solubilization of rare earth oxides in the eutectic LiCl–KCl mixture at 450^{o}C and in the equimolar $CaCl_2$–NaCl melt at 550^{o}C" Journal of Electroanalytical Chemistry, **545**, 141-157 (2003)

3-59

Investigation of Plutonium Trifluoride Solubility in Molten Fluorides

Alexander Maershin, Alexander Osipenko, Andrey Lizin

Research Institute of Atomic Reactors, Dimitrovgrad-10, Russia

Investigation of solubility of actinides and fission products in molten fluorides is of great urgency because of the potential application of these environments as a coolant and fuel in molten salt reactor systems. Moreover, such kind of data is required for the development of the partitioning processes for spent fuel and radioactive waste. The experimental data on the solubility of actinide trifluorides in molten salt systems supposed to be used as a fuel salt are so far lacking in literature.

The LiF-NaF-KF – FLINAK system with a low melting temperature is considered as a promising environment.

The paper describes the experimental data obtained on solubility of plutonium trifluoride in molten fluorides LiF-NaF-KF (FLINAK) in the temperature range from 550 to 700 ^{o}C. The solubility was studied using the isothermal saturation of the melt. The data obtained are of great urgency for further investigations, developments and design of the molten salt reactors.

3-60

Coordination Chemistry of Actinides with Hydroxamic Siderochelates

Alejandra Sornosa Ten, Pawel Jewula, Lé Vi Nguyen, Mélanie Bourdillon, Stéphane Brandès, Christine Stern, Jean-Claude Chambron, Michel Meyer

Institut de Chimie Moléculaire de l'Université de Bourgogne (ICMUB, DIJON, France

Siderophores are naturally occurring iron(III)-specific chelators, which are synthesized and excreted by most fungi and bacteria under iron-limiting growth conditions. Many siderophores contain anionic hydroxamate-like functional groups. The hard oxygen donors present in the hydroxamic acids exhibit high affinity for hard Lewis acids, like Fe^{3+}.

Under environmental conditions, actinides like plutonium(IV) or uranium(VI) are mainly found in case of accidental contamination as highly insoluble inorganic phases. As the concentration of hydroxamic siderophores in soils is typically in the range of 0.01–0.1 μM, recent studies have shown that these strong naturally occurring chelating agents increase the solubility, migration rate and bioavailability of plutonium. Indeed, the cyclic trishydroxamic acid desferrioxamine E (DFE) is able to solubilize $Pu(OH)_4$ by forming a highly stable $[Pu(DFE)(H_2O)_3]^+$ complex,[1] which is recognized by the outer-membrane iron-siderophore receptors and transported across the inner bacterial membrane.[2] It is therefore important to gain a deeper understanding of the interaction between actinide cations and this kind of ligands.

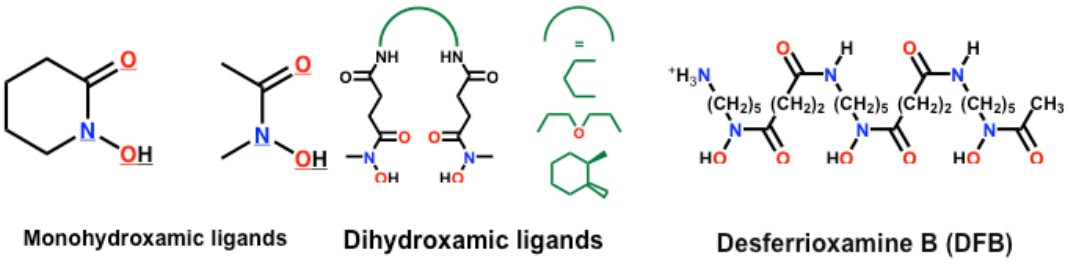

Figure 1 : Structural formulae of abiotic hydroxamic-based ligands and of the bacterial siderophore desferrioxamine B (DFB).

In this communication, we will describe the coordination properties of linear and cyclic hydroxamic acids, as well as of desferrioxamine B, an open chain analog of DFE, with respect to UO_2^{2+} (Figure 1). A combination of various spectroscopic techniques (UV–vis, RAMAN, and EXAFS) together with potentiometric titrations allowed us to unravel the speciation, to measure the binding constants, and to propose coordination schemes for the various complexes formed in solution. The protonation and complexation enthalpies have been determined by titration calorimetry.

[1] C. E. Ruggiero, M. P. Neu, J. H. Matonic, B. L. Scott, *Angew. Chem. Int. Ed*. **2000**, *39*, 1442.

[2] S. G. John, C. E. Ruggiero, L. E. Hersman, C. S. Tung, M. P. Neu, *Environ. Sci. Technol.* **2001**, *35*, 2942.

3-61

Investigation in field of partitioning of minor actinides and rare elements in chloride melt

Alexander Maershin, Alexander Osipenko, Mikhail Kormilitsyn

Research Institute of Atomic Reactors, Dimitrovgrad-10, Russia

Knowledge of the basic chemical and thermodynamic properties of actinides and fission products is necessary for creation the effective technological process of partitioning for pyrochemical reprocessing spent fuel. Electronic absorption spectroscopy can be applied for studying behavior of ions having f-electronic configuration in chloride melts. In the present work the electronic absorption spectroscopy was employed to study the reactions of minor actinides and rare elements containing chloride melts with oxygen species.

Spectrum of minor actinides Am(III) and Cm(III) complex were obtained in melt NaCl-2CsCl and melt 3LiCl-2KCl at different temperatures over argon atmosphere and different partial pressures of HCl/H_2O. Dependences of Am(III) and Cm(III) concentration on partial pressures of HCl/H_2O were obtained. From the experimental data dissociation constants of CmO^+, CmOCl, AmOCl were calculated.

Spectrum of Pr(III), Nd(III) and Sm(III) complex were obtained in melt 3LiCl-2KCl at 450^oC over argon atmosphere and different partial pressures of HCl/H_2O. Dependences of Pr(III), Nd(III) and Sm(III) concentration on partial pressures of HCl/H_2O were obtained. From the experimental data dissociation constants of praseodymium, neodymium and samarium oxy-compound were calculated.

Combined spectrum of Am(III) and Nd(III) complex were obtained at different concentration in melt 3LiCl-2KCl at 450^oC over argon atmosphere. Means of the electronic absorption spectroscopy for in-situ concentration monitoring to electrochemical separation of americium and neodymium with used liquid metal cathode was demonstrated.

3-62

Preparation, stabilization, spectroscopic, computational studies of tetravalent protactinium in aqueous solution

Nidhu Banik[1], Christian Marquardt[1], Marcus Altmaier[1], Clemens Walter[1], Jörg Rothe[1], Bernd Schimmelpfennig[1], Florent Réal[2], Valérie Vallet[2]

[1]Karlsruhe Institute of Technology (KIT), Institute for Nuclear Waste Disposal (INE), Karlsruhe, Germany, [2]University Lille1, CNRS, PhLAM Institute, Villeneuve d'Ascq, France

Whereas for the tetravalent actinide Th, U, Np, and Pu, an essential basic understanding of their chemistry in aquatic solution was achieved recently, this is not the case for the tetravalent protactinium. Pa(IV) with the simple electronic configuration, $5f^1$, in its ground state enables speciation by optical spectroscopy, and is also of interest for quantum chemical studies to probe the nature of the actinide-water chemical bonds across the series. However, due to constricted availability of Pa, the cascade of its α-emitting daughters, and the low redox potential only few studies have been performed in this field [1].

Our work aims at filling the gap in the understanding of aquatic chemistry of tetravalent actinides by unravelling the properties of Pa(IV) in various media combining not only complementary experimental methods, such as XAFS, TRLFS and UV-Vis spectroscopies, but also quantum chemical methods to explore the characteristic chemical behaviour of Pa(IV) and the neighbouring tetravalent ions.

A key step in the experimental work was to find a successful way of stabilizing protactinium in its tetravalent oxidation state for very long times. For the first time, we used a chemical reductant rongalite ($HOCH_2SO_2Na$) [2], for the preparation of Pa(IV) solutions. No complexation of rongalite with Pa(IV) was observed under strong acidic conditions.

It is known that Pa(IV) is easily oxidized in acids like HCl, H_2SO_4, and $HClO_4$. For stabilization experiments, the concentration of rongalite was fixed to 0.5 mmol/L. Three different acid solutions, at varying acidic strengths (0.1, 1.0, 2.0, 7.0 M), for three different Pa concentrations between $1 \cdot 10^{-5}$ and $1 \cdot 10^{-6}$ M, and with contact times of 1 to 165 hours, were investigated. After different contact times, the oxidation state of Pa was monitored by UV-VIS and TRFLS spectroscopies. We observed that Pa is oxidized more slowly in H_2SO_4 or HCl than in $HClO_4$. We found that the stabilization of Pa(IV) in aqueous solution to be possible up to several days depending on the acids and increasing with their concentration.

XAFS measurements were performed at the INE-Beamline for Actinide Research at ANKA. Measurements were performed using a specially designed sample cell suitable to keep redox sensitive samples stable in an inert gas atmosphere long enough to record EXAFS data under stable redox conditions. With this setup we were able, for the first time to record a XAFS spectrum of Pa(IV). Up to now only few Pa(V) but no Pa(IV)-XANES experiments have been reported in the literature. In Figure 1, the Pa L3-XANES spectrum of $Pa(IV)_{aq}$ is shown in comparison to the $Pa(V)_{aq}$ both in 1M HCl. As expected the white line maximum of the XANES of the $Pa(IV)_{aq}$ sample is located at markedly lower energy values compared to the pentavalent Pa.

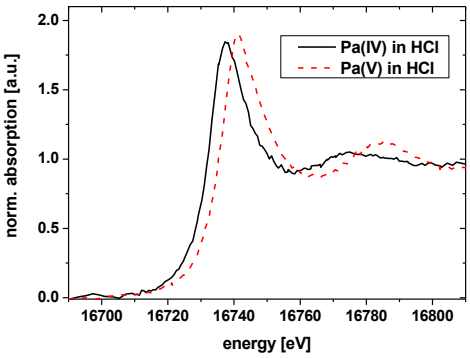

Figure 1. Pa L3-XANES spectra of Pa(IV) and Pa(V). The tetravalent Pa is prepared by rongalite (8.10-4 M) in HCl. [Pa] = 3.0.10-4 M. The spectra have been normalized with respect to their edge jump.

EXAFS measurements over a k range of 2.5 - 9.5 $Å^{-1}$ were performed to retrieve structural information of the first hydration shell surrounding the protactinium ions. For pH 0, good quality fits are achieved using a model of one oxygen shell of 11±2 atoms at 2.49 Å. Taking into account the intrinsic uncertainties of approximately 20% in the determination of the coordination numbers, our EXAFS data illustrate that Pa(IV) aqua ion distances fall into the expected trend from the progressively decreasing ionic radii. This trend is also confirmed by quantum chemical calculations for 8, 9 and 10 coordinated tetravalent actinide aqua ions. The geometries were optimized at the MP2 level of theory, followed by single-point calculations where multiconfigurational effects, spin-orbit coupling, and long-range solvent effects were accounted for. From the computed relative free energies, we can expect that 9 and 10 coordinated aqua ion may exist for Th, and Np, while 9-coordination is preferred for Pa, U, and Pu (See Figure 2).

The topology of the electronic density demonstrates that the An-water bond is predominantly ionic.

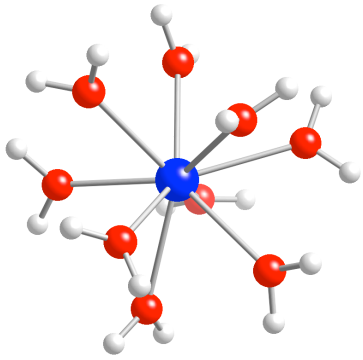

Figure 2. Perspective view of the 9-coordinated Pa(IV) aqua ion, computed at the MP2 level.

TRLFS measurements on Pa(IV) solutions were performed using a XeCl excimer laser for excitation. Emission spectra were recorded from 350 to 570 nm. Fluorescence life times of Pa(IV) species in different acid solutions are comparable to the literature [3]. Considerable improvement of the detection limit for Pa(IV) is possible by using TRLFS-OPO+SHG systems. Using this setup, Pa(IV) species are efficiently detected at the concentrations between $1.5.10^{-5}$ M and $5.0.10^{-7}$M. From the signal to noise ratio of the spectra we have derived a detection limit for Pa(IV) < $1.0.10^{-8}$ M.

The work reported here paves the way for further investigations of the speciation and complexation of tetravalent protactinium using a combined experimental method approach with TRLFS, XAFS, and UV-vis spectroscopy. The quantum chemical approaches help identifying the driving forces for the complexation through energetics and the analysis of chemical bond.

References

[1] R. Wilson, Nat. Chemistry 4, 586 (2012).

[2] A. D. Gel'man et al. Sov. J. At. Energy., **4**, 361 (1958).

[3] C. M. Marquardt et al. Radiochim. Acta, **92**, 445 (2004).

3-63

The Thermodynamics of Extraction of Lanthanides and Actinides by Solvating and Ion-Exchanging Ligands: A Comparative Study

Leigh Martin, Peter Zalupski, Travis Grimes

Idaho National Laboratory, Idaho Falls, Idaho, USA

In developing a sustainable "fully closed" nuclear fuel cycle, aqueous separations processes are necessary to remove the useful and transmutable actinides from the remainder of the fission and activation products in used nuclear fuel. As such it is likely that the actinides up to and including americium (and possibly curium) will be required to be removed from the used fuel that is currently stored in the US. The separation and transmutation of the actinides should lead to improvements in volume reduction and heat loading of the final waste forms sent to a geologic repository. Uranium, neptunium and plutonium can all be efficiently removed from dissolved nuclear fuel using existing co-extraction methodologies however, the isolation of americium and curium presents a significantly greater challenge.

The difficulty of isolation of the trivalent actinides from used nuclear fuel lies in their separation from the trivalent lanthanides. The similarity in chemical and physical properties of these two groups of *f*-elements has lead to some innovative methodologies for accomplishing the separation. Primarily liquid – liquid separations based on the use of soft donor atoms or utilizing the accessible higher oxidation states of americium have received the most attention. Regardless of the approach, the energy difference associated with a successful metal ion separation in a solvent extraction process is found to be relatively small. As such, paying careful attention to the thermodynamic properties of these systems (ΔG^o, ΔH^o and ΔS^o) assists in providing an insight into the driving forces behind the partitioning process and may also assist in the development of new liquid – liquid separations techniques.

Traditionally, the thermodynamic parameters ΔH, and ΔS for such biphasic reactions are measured indirectly using the van 't Hoff method. Despite this method giving a reasonable approximation, a more direct method of the heat of extraction may lead to more accurate results that are required to investigate the effects of the separations media on the extraction. Recent work has demonstrated the applicability of isothermal titration calorimetry for these types of direct ΔH measurements. To that end, the study of the direct measurement of the heat of extraction of americium, curium and the lanthanides by an ion exchanging extractant (e.g. HDEHP) and a solvating extractant has been highlighted as an area that could expand this field of research. By studying the thermochemistry of Am and Cm extraction from nitrate media by various organic phase extractants using a calorimetric approach and vant' Hoff analysis for comparative purposes, we have begun to further expand our thermodynamic understanding of these liquid-liquid extraction systems. Figure 1 and Table 1 summarize the results obtained from the HDEHP study. The results from the two methodologies used for the determination of the ΔH extraction will be compared and the challenges of thermochemical evaluation of liquid-liquid distributions will be summarized.

Figure 1. Thermodynamic parameters for the extraction of Ln^{3+}, Am^{3+} and Cm^{3+} by HDEHP in *n*-dodecane as a function of ionic radii. (ΔH and ΔG left axis, ΔS right axis.)

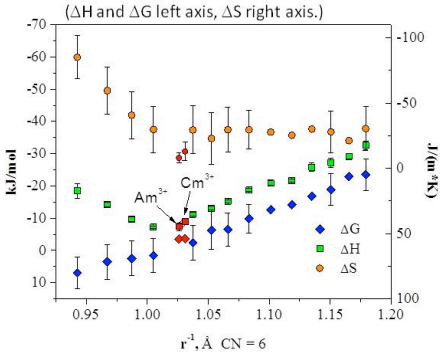

Table1. Thermodynamic parameters for the extraction of Am^{3+} and Cm^{3+} by HDEHP in *n*-dodecane.

Thermodynamic Parameter	Am(III)	Cm(III)
ΔH_{cal}, kJ mol^{-1}	-7.4 ± 1.2	-9.0 ± 1.0
ΔH_{extr}, kJ mol^{-1}	-5.8 ± 1.1	-7.2 ± 0.8
ΔG^a, kJ mol^{-1}	-3.56 ± 0.02	-3.63 ± 0.01
ΔS^b, J K^{-1} mol^{-1}	-8 ± 4	-12 ± 3

[a] determined using K_{ex} at 25ºC, [b] $\Delta S = (\Delta H_{extr} - \Delta G)/T$

3-64

Radiolysis of adsorbed water on actinides oxides surface: investigations on the surface state evolution by hydration

Jérémy Gaillard[1], Laurent Venault[1], Philippe Moisy[1], Jackie Vermeulen[1], Rachel Calvet[2], Nicolas Clavier[3]

[1]CEA Marcoule/DRCP, Bagnols sur Cèze, France, [2]b Université de Toulouse, Mines Albi, CNRS, Centre RAPSODEE, Albi, France, [3]ICSM-UMR5257, Bagnols sur Cèze, France

Several authors reported the radiolysis of adsorbed water on oxide compared to radiolysis of homogeneous liquid water. It has been shown that oxide surfaces can in some case either increase or inhibit formation of hydrogen due to water radiolysis[1]. Plutonium oxide and uranium oxide promotes the radiolysis of adsorbed water[2][3]. However, their ability to catalyze water decomposition seems different. The purpose of this study is to investigate the radiolysis of adsorbed water on a hybrid material with both uranium and plutonium atoms on the surface. The kinetics and the extent of the H_2 generation depends on several parameters as specific surface, relative humidity or dose rate[3] but appears to be also surface related since different surface states imply different kinetics. Thus the study of radiolysis of adsorbed water on actinides oxides leads to the study of the surface evolution during hydration. The inverse gas chromatography (IGC) and Raman spectroscopy are used to investigate the surface evolution under hydration. In a first step, these techniques are developed and tested on ceria as a surrogate for $(U,Pu)O_2$ surface before implementing on actinide oxides.

Radiolysis experiments consist in contacting $(U,Pu)O_2$ powder with argon atmosphere with a relative humidity equal to 80% in a closed vessel. In the figure 1, H_2 set 1 and H_2 set 2 shows an increase of H_2 concentration until the reach of a steady state at about 20 ppm g^{-1} (H_2 content is normalized by oxide weight). These experiments correspond of two successive experiments run in the exact same conditions. The presence of a steady state suggests equilibrium between generation and consumption of hydrogen An other experiment is run with the exact same conditions (argon with 80 % relative humidity) and with the same sample used for H_2 set 1 and H_2 set 2 except that the oxide was kept for 20 months in humid argon atmosphere (RH=60-80%). H_2 generation kinetics show a complete different behaviour without reaching of steady state during the first 900 hours (40 days). Kinetics is linear versus time. The H_2 generation is also more important leading to a content higher than 300 ppm g^{-1}.

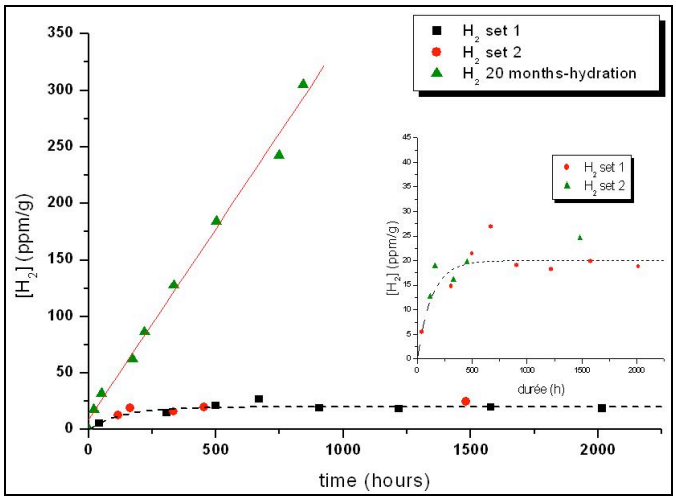

Figure 1: kinetics of H_2 generation by radiolysis of adsorbed water on $(U,Pu)O_2$

Thereby experimental results show a complete behaviour depending on whether oxide is freshly prepared or kept under hydration for a long period. Since these experiments in the same conditions, this observation must be explained by an evolution of the oxide sample itself under hydration. This evolution might be concentrated on the surface since it results from water adsorption. Besides pursuing radiolysis experiment, evolution of oxide surface under hydration is then investigated. Ceria surface is used as a surrogate for actinides oxide

surface. IGC is a physico-chemical method based on the adsorption of molecular probes to measure the dispersive component of the surface energy γ_s^d, monitoring the surface state. Ceria is analysed in a dry and a hydrated state. The measurement of γ_s^d shows an increase from 181 mJ m^{-2} to 232 mJ m^{-2} induced by hydration. This result attests of a surface evolution under hydration as suggested by radiolysis experiment. Raman spectrum on hydrated surface shows the apparition of an additional band at 484 cm^{-1} beside CeO_2 characteristic T_{2g} band (fluorite structure) (figure 3). Comparison with Raman spectra of cerium hydroxides and cerium oxides with specific preparation enables to attribute the additional band to the formation of surface hydroxide during surface hydration.

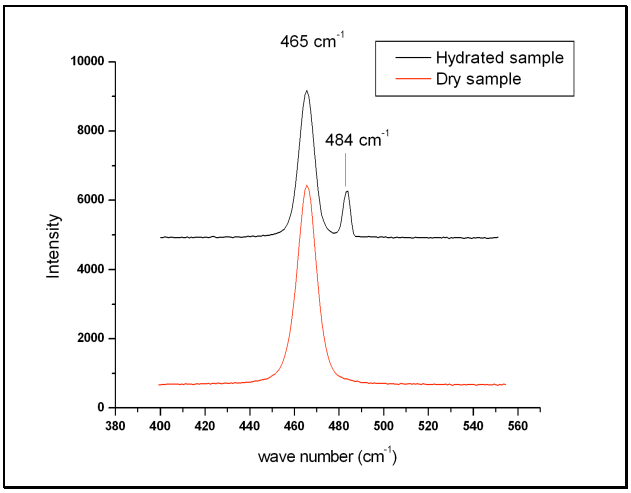

Figure 2 : Raman spectroscopy on dry and hydrated ceria sample

These results give interesting insights of the surface reactivity of actinides oxide toward water. Future work will be dedicated to the development of IGC on radioactive materials to study surface evolution upon hydration. Radiolysis experiments will be run on sample issued of different preparations to study the effect of different parameters on H_2 generation. The role of atmosphere humidity will be investigated as well.

References

[1] N. G. Petrik, A. B. Alexandrov, et A. I. Vall, *J. Phys. Chem. B*, vol. 105, 5935, 2001.

[2] J. A. LaVerne et L. Tandon, *J. Phys. Chem. B*, vol. 107, n° 49, 13623, 2003.

[3] M. V. Vladimirova et I. A. Kulikov, *Radiochemistry*, vol. 44, n° 1, 86, 2001.

3-65

Effect of a trivalent dopant, Gd^{3+}, on the reaction of $U_{1-y}Gd_yO_2$ and Cs_2O

Kim Jong-Goo, Jang Eun-Sil, Park Yang-Soon, Ha Yeong-Keong, Song Kyuseok

Korea Atomic Energy Research Institute, Daejeon, Republic of Korea

It was known that Cs compounds (Cs_2O, Cs_2CO_3 etc.) react on Uranium oxides to form Cs-U-O (cesium uranates) compounds. Cs-U-O compounds have become a matter of concern because those were observed at the periphery of irradiated nuclear fuels.

In this work, in order to investigate the effect of doped Ln^{3+} elements on the reaction between UO_2 and Cs_2O, Gd-doped stoichiometric UO_2's in various dopant contents (y= 0, 0.11, 0.22, 0.26 in $U_{1-y}Gd_yO_2$) were prepared, where Gd was chosen as a Ln^{3+} dopant.

Thermogravimetric analysis (TGA) for blended samples of Cs_2O and $U_{1-y}Gd_yO_2$ were performed in a temperature range of 30 ^oC to 1100 ^oC in a continuous argon flow, where calculated amounts of Cs_2O and $U_{1-y}Gd_yO_2$ were weighed to give Cs/U's (atom ratio) =2 in all the blended samples regardless of dopant contents, y.

Fig.1 shows thermogravimetric curves for the blended samples of Cs_2O and Gd-doped UO_2's and each thermogravimetric curves of the individual reactants UO_2 and Cs_2O are shown in Fig. 2.

Comparing the thermogravimetric curve for the blended sample of pure UO_2 and Cs_2O in Fig. 1 with those for the individual reactants UO_2 and Cs_2O in Fig. 2, the curve for only Cs_2O in Fig.2 shows large weight loss near 600 ^oC on the other hand that for the blended sample does now show any weight loss near 600 ^oC unlike Cs_2O in Fig. 2. From this, it can be inferred that Cs_2O in the blended sample was changed to other form of Cs by the reaction with UO_2, And the other form of Cs should be Cs-U-O which is stable near 600 ^oC.

Noticeable aspect in Fig.1 is that the curves for the doped UO_2 and Cs_2O show distinct weight losses compared to that of undoped UO_2 and Cs_2O and the extent of weight losses increased as the content of Gd increased. The weight losses for the curves of the doped UO_2 and Cs_2O could be thought to be caused from un-reacted Cs_2O species remaining in the blended samples, that is, the extent of reactions between doped UO_2 and Cs_2O could be lower than that of undoped UO_2 and Cs_2O and decreased as the content of Gd increased.

Considering that the Cs/U's of all the blended samples for $U_{1-y}Gd_yO_2$ and Cs_2O were same regardless of dopant contents, y, the extent of reactions between $U_{1-y}Gd_yO_2$ and Cs_2O should be influenced by the content of dopant, y. That is to say, the more dopant is, the more inhibition of the reaction between doped UO_2 and Cs_2O should be.

In order to identify the phase of samples after TGA, XRD measurements were carried out (Fig.3). As shown in Fig.3, for the sample of undoped UO_2 and Cs_2O two types of diffraction patterns were observed corresponding to cesium uranate phases of $Cs_2U_2O_7$ and $Cs_4U_5O_{17}$ and for the samples of doped UO_2 and Cs_2O the peak heights of cesium uranate phases decreased gradually as the content of Gd increased and the other hand diffraction patterns of fluorite corresponding to $U_{1-y}Gd_yO_2$ phases were observed and the peak heights increased gradually with increasing Gd content. The result of XRD means that the reaction of the undoped UO_2 and Cs_2O proceeded to consume all UO_2 and the other hand the reactions of the doped UO_2 and Cs_2O left more un-reacted UO_2 as the content of Gd increased. This XRD result supports the preceding inference from TGA that the more dopant is, the more inhibition of the reaction between doped UO_2 and Cs_2O is.

Cesium uranates dissolve well in an aqueous solution of approximately pH2, however UO_2 does not dissolve as well in this type of solution. The samples that were heated during the TGA measurement were treated using a pH2 solution to dissolve and separate the U ions from un-reacted UO_2. The amount of U ion, $U_{dissolved}$, that were dissolved in the pH2 solution were measured using ICP-AES and $U_{dissolved}$ / $U_{initial}$ ($U_{initial}$; the amount of U in $U_{1-y}Gd_yO_2$

initially added) were calculated (Table 1). $U_{dissolved}$ / $U_{initial}$ can be thought to be extent of cesium uranates formation through the reactions between $U_{1-y}Gd_yO_2$ and Cs_2O.

As shown in Table 1, the extent of cesium uranates formation decreased as the content of Gd increased.

From the experimental results, TGA, XRD and chemical analysis using ICP-AES, it was concluded that the reaction between doped UO_2 and Cs_2O is inhibited by doped Ln^{3+} ions, that is to say, the more dopant is, the more inhibition of the reaction is.

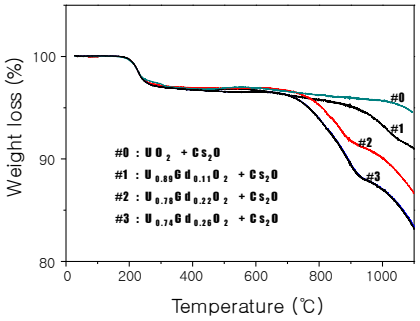

Fig. 1. Thermogravimetric curves for the mixtures of Cs_2O and $U_{1-y}Gd_yO_2$ (y=0, 0.11, 0.22, 0.26), where Cs/U atom ratios are 2 for all samples

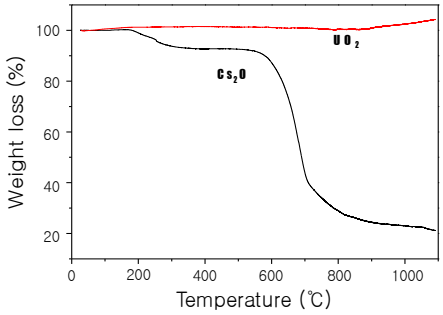

Fig. 2. Thermogravimetric curves for the sample of only Cs_2O and only UO_2

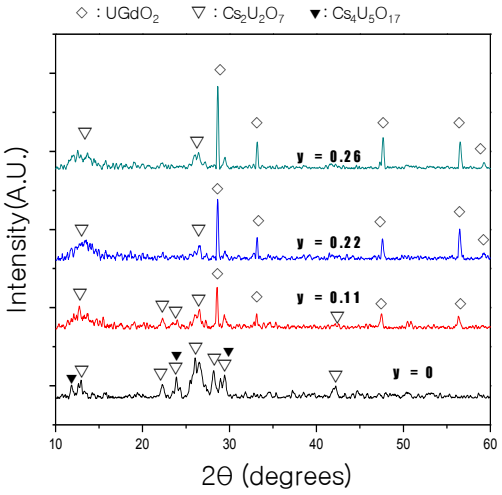

Fig. 3. XRD patterns depending on y after thermogravimetric measurements for the mixtures of $U_{1-y}Gd_yO_2$ and Cs_2O

Table. 1. Dissolved portions of U to initial amount of U ($U_{dissolved}/U_{ini}$) when treated by pH 2 solution after heating the samples of Cs/U=2

	Gd content (y) in $(U_{1-y}Gd_y)O_2$			
	0	0.11	0.22	0.26
$U_{dissolved}/U_{initial}$	0.95	0.84	0.65	0.63

3-66

Apparent Solubility of Thorium in the Presence of Humic Substances

Takayuki Sasaki, Yuka Matsuura, Taishi Kobayashi, Ikuji Takagi, Hirotake Moriyama

Kyoto University, Kyoto, Japan

The reaction of humic substances (HSs) with tetravalent actinide ions is competitive with the hydrolysis reaction in which the tetravalent ions form polynuclear, colloidal species and hydroxide precipitates, hence the resulting soluble species and solid phase compositions are determined by the balance of the hydrolysis and ligand-complexation reactions. In the previous study, the apparent solubility of thorium in the presence of organic ligand after filtration was investigated as a function of the proton concentration (pHc) [1]. In the presence of dicarboxylic acid such as succinic, glutaric, and adipic acids, few Th colloidal species larger than 2 nm were observed, and the solubility appeared to be controlled by thorium-OH-carboxylate solid phases. Th solubility in the presence of fumaric acid was similar to that in the presence of succinic acid, whereas no solid phase was observed in the presence of maleic acid under pHc 4 [1]. Thus, organic ligand having strong interaction with Th(IV) is thought to play an important role in the migration and a simple dicarboxylic acid which coordinates with a chelate configuration, can be considered as a model substance of humic substances in groundwater.

The present study focuses on the apparent solubility of Th-HS species. Size distributions of soluble species investigated by sequential filtration with different pore-sized filters, and solid precipitates analysed by elemental analysis. In the initial concentration of [HS]=5.3×10^{-3} eq/L and [Th]= 5.0×10^{-4} M at I = 1, over 90% Th species could be filtered out by 0.45 μm filter at the neutral pH region, and the apparent solubility obtained using 3 kDa NMWL filtration is much lower than that by 0.45 μm filter, indicating the coagulation and size distribution of HS complexes. At I = 0.1, on the other hand, the smaller species between 3 kDa and 0.45 μm filters are dominant species. The size increase of Th-HS complex might be caused by the higher concentration of Na^+ ion.

The weight percentages of carbon and hydrogen in the solid phases were determined by elemental analyser, and the Th and Na concentrations were measured using ICP-AES after dissolving the precipitates in a mixture of perchloric and nitric acids. With an increase of the initial [HS]/[Th] ratio in the solution, the carbon/thorium wt% in precipitates increased. Even in the excess of [Th] over [HS], the precipitate contains not only hydroxide ions but also HS molecule. The description of solubility-limiting solid phase and its solubility product may be affected by such stoichiometric proportion of the solid phase..

References

[1] T.Kobayashi, T.Sasaki, I.Takagi, H.Moriyama, ‘‘Solubility and solubility-limiting solid phase in M(IV)-OH-dicarboxylate ternary aqueous system,’’ J. Nucl. Sci. Technol., 48, 993 (2011).

3-67

Temperature Effect on the Solubility and Solid Phase Stability of Thorium Hydroxide

Taishi Kobayashi, Takayuki Sasaki, Ikuji Takagi, Hirotake Moriyama

Kyoto University, Kyoto, Japan

A prediction of solubility limit of tetravalent actinides (An(IV)) is required in safety assessment of geological disposal over a considerable time-span more than 100 thousands of years. An(IV) is easily hydrolyzed to form amorphous hydroxide ($An(IV)(OH)_4(am)$) which controls the solubility limit. It is suggested that, however, meta-stable $An(OH)_4(am)$ is potentially converted to crystalline oxide ($AnO_2(cr)$) during extremely long period of disposal or under an elevated temperature condition in the disposal site [1]. In the present study, we focused on the solubility and solid phase stability of thorium hydroxide after heating at 90°C in various pH and ionic strength. The apparent solubility was measured and the solid phase was analysed after a given heating period and the solubility product correlated to a particle size of the solid phase.

A Th perchlorate stock solution was diluted to prepare sample solutions, and pH value and ionic strength were adjusted by $HClO_4$/NaOH and $NaClO_4$, respectively. The sample solutions were then placed into an oven controlled at 90°C and kept for given periods. After aging at 90°C, the samples were cooled down to 25°C, and the proton concentration (pHc) was measured. The supernatant of the sample solution was filtered (3k - 100k Da filter, Millipore) and Th concentration determined by ICP-MS. The detection limit was about 10^{-8} M. The solid phase was separated by centrifugation, dried and analyzed using X-ray diffraction (XRD) measurement.

By heating at 90°C, the solubility decreased significantly in the acidic pH range within a few days and lower than those aged at room temperature [2]. In the XRD spectra of the solid phases, broad peaks corresponding to $ThO_2(cr)$ were observed, indicating the crystallization of the initial $Th(OH)_4(am)$. Based on the XRD spectra of the solid phase and the solubility, the particle size of the solid phase was estimated and the solubility products determined. The obtained solubility products and the particle size were discussed using the Schindler equation [3]. This work exemplifies the predicted transformation of amorphous phase into a thermodynamically more stable phase, and therefore less soluble solid of higher crystallinity due to processes at elevated temperature conditions.

References

[1] Rai, D., Moore, D. A., Oakes, C. S., Yui, M. Thermodynamic model for the solubility of thorium dioxide in the Na^+-Cl^--OH^--H_2O system at 23°C and 90°C. Radiochim. Acta 88, 297 (2000).

[2] Kobayashi, T., Sasaki, T., Takagi, I., Moriyama, H. Solubility of Thorium(IV) in the Presence of Oxalic and Malonic Acids. J. Sci. Nucl. Technol., 46, 1085 (2009).

[3] Schindler, P., Heterogeneous Equilibria Involving Oxides, Hydroxides, Carbonates, and Hydroxide Carbonates. Adv. Chem. Ser. 67, 196 (1967).

3-68

EXAFS investigation of substituent effect of the hybrid type PDA complexes for actinides and lanthanides separation.

Hideaki Shiwaku, Toru Kobayashi, Yoshihiro Okamoto, Shin-ichi Suzuki, Tsuyoshi Yaita

Japan Atomic Energy Agency, Sayo, Hyogo, Japan

The development of actinide ion recognition compound is a very important for treatment of radioactive wastes generated from nuclear reactor. It is well known that oxygen donor shows good affinity to hard metals like actinides and lanthanides, while nitrogen donor is possible to separate trivalent actinides from lanthanides through covalent interaction. On the other hand, the hybrid type ligand with both oxygen and nitrogen donor in same molecule is expected to be a new type ligand, which has both donor features. Thus, we developed the pyridinedicarboxyamide (PDA; shown in Fig.1), which can separate tri- and tetra-valent actinides efficiently from acidic solution [1-2]. In order to apply PDA to actual process, sufficient solubility to stable diluent like paraffinic solvent in addition to extractability of trivalent actinide would be requested. From the point of view, the relationship between structure of PDA and separation factor would possibly provide us key information for molecular design toward improvement of PDA derivatives. In our previous studies, MePhPDA (R_1=R_2=Methyl group, R_3=R_4=R_5=R_6=R_7=H) was regarded as starting material, and then straight alkyl chain was successively introduced into the position of methyl group. As a result, we found that changing the length of alkyl chain increased the solubility to paraffinic solvent; separation ability of traivalent actinides and lanthanides, however, did not simply correlated with length of alkyl chain.

On these previous studies, the lanthanide complex structures with these PDA derivatives were determined by EXAFS methods in order to clarify recognition mechanism. The PDA derivatives having alkyl chain of which carbon number was from 1 to 12 at R_1 and R_2 positions, respectively, were synthesized. The lanthanide complexes were prepared by mixing with PDA in methanol. Local structures around methanol were determined by EXAFS method. The EXAFS measurements were performed at the BL-27B station in the Photon Factory, KEK [3], and the BL11XU in SPring-8 [4]. The lanthanide L_{III} absorption edge spectra were measured in fluorescent mode by a 7-arrayed solid-state detector, while lanthanide K absorption edge spectra were measured in transmission method at SPring-8.

The relationship between Gd-N distance and carbon chain number is shown in Fig. 2. The plot against carbon chain number shows the minimum value at about 5. This V-shape tendency would be arising from combined effects of both increase in electrostatic interaction and steric hindrance. Generally, a decreasing tendency in bond distance along carbon chain number indicates an improvement of donor ability on nitrogen by increase in electron donation from alkyl chain. On the other hand, bulkiness of PDA interferes with complex formation, so that V-shape in the Fig. 2 could be observed.

These results suggest that suitable carbon number would be 6 from the standpoint of complex formation. This information will be helpful for improvement of molecular design technique. In this presentation, we will discuss about the other lanthanide complexes.

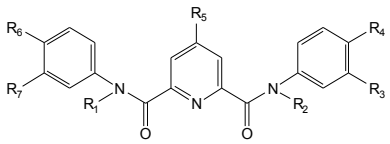

Fig.1 Structure of PDA

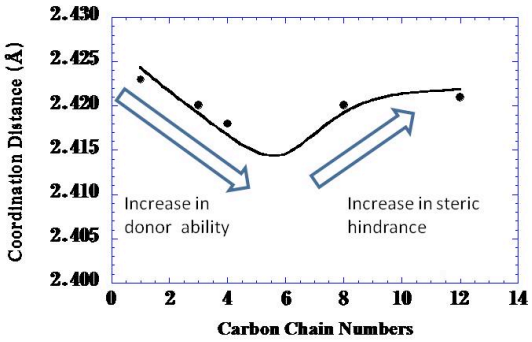

Fig.2 Relationship between coordination distance and Carbon chain numbers of substituent in a case of Gd-PDA complex.

References

[1] Shimada et al., *Sol. Ext. Res. Dev. Jap.,* **11**, 1-10 (2004); Shimada et al., *Sol. Extr. Ion Exch.,* **22**(2), 147-161, (2004)

[2] T. Yaita, et al., Physica Scripta, T115, 302 (2005).

[3] A part of XAFS measurement was performed under the approval of the Photon Factory, KEK Proposal No. 2007G675.

[4] A part of XAFS measurement was performed under the approval of the SPring-8 Proposal No. 2007A3504, 2007B3504, 2008A3504, 2008B3504, 2009A3504, 2009B3504, 2010A3504, 2010B3504, 2011A3504, 2011B3504.

3-69

Mathematical model for crystallization purification of uranyl nitrate hexahydrate in continuous crystallization column

Vladimir Kascheev, Olga Shmidt, Pavel Poluektov, Svetlana Tretyakova

Bochvar Institute (VNIINM), Moscow, Russia

Process of continuous isohydric uranyl nitrate hexahydrate (UNH) crystallization with co-current movement of UNH crystals and mother liquor in crystallization zone and counter-current movement of UNH crystals and washing solution in washing zone of crystallization column (Fig. 1) is investigated. Crystallization column operates continuously, and collection of purified crystals to the tank, drainage and product (wet UNH crystals) unloading are conducted in alternate-cyclic mode using two collectors [1].

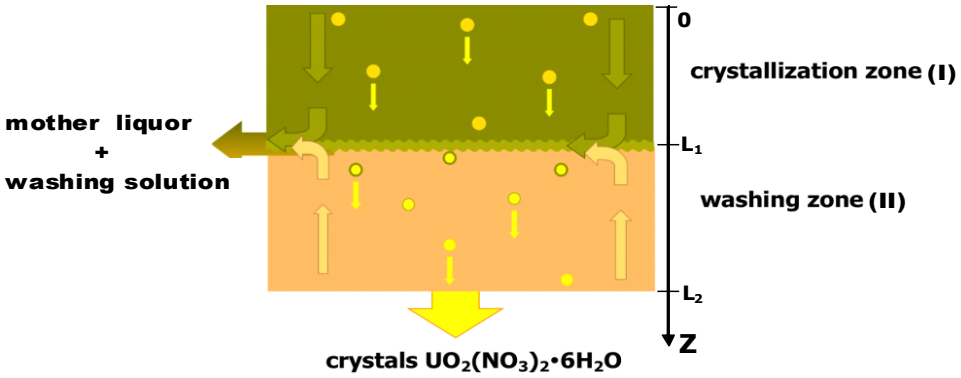

Figure 1 – Principal scheme of continuous crystallization process

Mother liquor (uranyl nitrate, nitric acid, water) containing fission products is injected to the zone I (crystallization zone). Cooling of zone I causes mother liquor splitting in two phases and precipitation of UNH crystals. Impurities remain in mother liquor. At the boundary of zones I and II mother liquor is removed from the column together with washing solution, which is injected to the apparatus at the bottom of zone II (washing zone) and flows up to the boundary of zones through displacement by sinking UNH crystals.

Mathematical model for column operation consists of three equation blocks describing the following aspects: conservation of matter during growth (dissolution) of crystals from liquid solution in crystallization (I) and washing (II) zones; regularities of growth (dissolution) of crystalline phase from oversaturated solution; temperature in zones I and II, which is regulated by temperature and flow of cooling liquid. There are two separated cooling circuits for zone I and II.

1) Equation of water conservation is written as:

$$u_l(z)\frac{d}{dx}\{[1-W(z)]C^V_{UNH}(z)\}+\beta u_s(z)\frac{d}{dx}W(z)=0, \qquad z>0;\ W(z=0)=0\,, \quad (1)$$

where:

$W(z)$ – volume fraction of crystaline phase in working volume of the apparatus; C^V_{UNH} – volume fraction of molecules, which form UNH crystals – uranyl nitrate and water (molecular ratio – 1:6); β – crystallization densifying factor (for UNH crystallization $\beta \approx 1{,}1$); $u_l(z)$ and $u_s(z)$ – dimensionless velocity of liquid and solid phase movement in working volume of the apparatus respectively. For zone I:

$$u_l(z)=1-AW^{\frac{4}{3}}(z)\left[\frac{\rho_s}{\rho_l(z)}-1\right], u_s(z)=1+AW^{\frac{2}{3}}(z)\left[1-W^{\frac{2}{3}}(z)\right]\left[\frac{\rho_s}{\rho_l(z)}-1\right],\ L_1>z>0;$$

$$u_l(z=0)=u_s(z=0)=1.$$

For zone II:

$$u_l(z) = -AW^{\frac{4}{3}}(z)\left[\frac{\rho_s}{\rho_l(z)} - 1\right], u_s(z) = AW^{\frac{2}{3}}(z)\left[1 - W^{\frac{2}{3}}(z)\right]\left[\frac{\rho_s}{\rho_l(z)} - 1\right], L_2 > z > L_1,$$

where:

$$A = \frac{2}{9}\frac{g}{\nu(T)V_0}\left(\frac{3}{4\pi n}\right)^{\frac{2}{3}};$$

g – free fall acceleration; $\nu(T)$- liquid phase viscosity (function of temperature); V_0- linear velocity of mother liquor at the apparatus inlet ($z = 0$); n- number of crystallization centers per unit of volume (it is assumed that number of crystallization centers is constant for each zone and does not change in time); ρ_s и $\rho_l(z)$ – density of crystalline and liquid phase respectively. Liquid phase density depends on components concentration, and therefore is changing with coordinate z.

2) Equation describing growth of cystalline phase from oversaturated solution is written as:

$$\frac{dR}{dt}(z) = k\left[C^V_{UNH}(z) - C^{V,Sat}_{UNH}(z)\right], t > 0, z > 0, \quad (2)$$

where:

k – UNH crystals growth rate characterizing value; $C^{V,Sat}_{UNH}$ – saturation concentration of UNH in liquid solution, depends on temperature and liquid phase content [2]; R- size (radius) of growing UNH crystals. Equation (2) can be transformed to:

$$\frac{d}{dz}\left[W^{\frac{1}{3}}(z)\right] = \left(\frac{4\pi n}{3}\right)^{\frac{1}{3}}\frac{k}{V_0 u_s(z)}\left[C^V_{UNH}(z) - C^{V,Sat}_{UNH}(z)\right]. \quad (2')$$

It should be noted, that stable crystallizer operation requires certain conditions at the boundary of zones I and II to be sustained, i.e.equal densities and temperatures of liquid phase on the both sides of boundary:

$$\rho_l(z = L_1 - 0) = \rho_l(z = L_1 + 0),\ T(z = L_1 - 0) = T(z = L_1 + 0). \quad (3)$$

Furthermore, crystalline phase changes movement velocity while passing boundary. It causes change of quantity of crystals per unit of volume in the zone II (n_{II}) against zone I (n_I), i.e.:

$$n_{II} = n_I\frac{u_s(z=L_1-0)}{u_s(z=L_1+0)},\ W(z = L_1 + 0) = W(z = L_1 - 0)\frac{u_s(z=L_1-0)}{u_s(z=L_1+0)}. \quad (4)$$

So, equations (1, 2') with system of expressions for calculation of temperature in working volume of the column and boundary conditions (3, 4) allow to calculate required working parameters ($W(z)$ and $T(z)$) and to optimize process of pricipitation by crystallization of UHN from mother liquor at different cooling modes in working zone of cristallizer.

References:

[1] Volk V.I., Vakhrushin A.Yu., Savenko V.P., Malysheva T.A., Arseenkov L.V. Russian patent №40905 «Apparatus for continuous crystallization and crystals unloading», registered 10.10.2004.

[2] Kogan V.B., Ogorodnikov S.K., Kafarov V.V. "*Ternary and multicomponent systems formed with inorganic substances*." Solubility reference book. vol. 1, pp. 268-273, Nauka, Leningrad, 1970.

3-70

Sulfurization behaviour of uranium and zirconium oxides with CS_2

Yuhei Fukuda, Akira Kirishima, Nobuaki Sato

Institute of Multidisciplinary Research for Advanced Materials, Tohoku University, Sendai, Japan

In March 2011, the loss of coolant accident occurred at Fukushima daiichi nuclear power plant due to the mega earthquake and the big tsunami. In the reactor, uranium fuel and a zircalloy cladding seemed to be melted by temperature rise in the core resulting in the formation of fuel debris. The fuel debris will be taken out within the next 20-25 years. Then the treatment for fuel debris should be considered. Especially, separation of uranium and zirconium oxides, which are the main component of the debris, is important. For the treatment of the above fuel debris, the sulphide process seems to be applicable [1]. The process consisted of three steps such as, 1) pulverization, 2) selective sulfurization, 3) selective dissolution. According to the previous research, UO_2 and U_3O_8 are sulfurized at 500^{o}C, but ZrO_2 is not sulfurized at 500^{o}C to 600 ^{o}C.The selective sulfurization may be possible between 500^{o}C to 600^{o}C.In this paper, sulfurization behaviour of uranium and zirconium oxides in the presence of CS_2 was examined by the heat treatment and the mechanochemical treatment techniques.

XRD results of the product by heat treatment are shown in Fig1. When the temperature was lower than 700^{o}C, the peaks of the products agreed well with those of a starting material, i.e. monoclinic ZrO_2. However, peaks of ZrOS and ZrS_2 appeared in the patter obtained at 800 ^{o}C [2]. Furthermore, those peaks became stronger at 1,000 ^{o}C. When of the mixture of UO_2 and ZrO_2 was treated by mechanochemical technique, the XRD results showed that a part of UO_2 dissolved in ZrO_2 forming the solid solution ($Zr_yU_{1-y}O_{2+x}$) Under the experimental conditions, formation of sulfide and oxysulfide were not observed. In summary, ZrOS and ZrS_2 were produced as a result of sulfurization by heat treatment at temperatures higher than 800 ^{o}C. On the other hand, the solid solution ($Zr_yU_{1-y}O_{2+x}$) was formed andUO_2 and ZrO_2 were not sulfurized by sulfurization using mechanochemical technique.

3-71

Nuclear Fallout Debris Formation and Fractionation in Aerodynamic Particles

Kiel Holliday[1], Mischa Monroe[2], Richard Gostic[1], John McClory[2], Ian Hutcheon[1]

[1]Lawrence Livermore National Lab, Livermore, CA, USA, [2]Air Force Institute of Technology, Dayton, OH, USA

Fallout samples from the immediate area around ground zero of a low yield, near surface nuclear test were collected. Samples were then sorted by size and a small subset of the particles was selected. Specifically, spherical glassy particles were isolated because they were found to have a higher quantity of residual fuel. These aerodynamic glasses represent a unique formation mechanism that can yield information about the nature of fallout debris. Additionally, because they represent a sample set that has a higher concentration of residual fuel, understanding the conditions from which they form may lead to the ability to select the highest forensic value samples from a nuclear event. Understanding the fractionation of nuclear fuel within fallout debris will also help in sample selection.

The study of fallout from historic nuclear tests has its advantages and challenges. The reduced radioactivity from fission products within a natural matrix makes them nearly impossible to detect by any method. The reduced radioactivity does, however, make sample handling easier and opens up the possibility of using advanced techniques that rely on the detection of induced x-rays and electrons. In this study, scanning electron microscopy coupled with energy dispersive spectroscopy is used to map out major element distributions, quantify transition regions between phases, and determine stoichiometries with a phase. This is then correlated with autoradiography mapping of the residual fuel so that it can be related to the composition of the matrix that it is in. X-ray absorption near edge spectroscopy and x-ray absorption fine structure was used to probe oxidation state and local environment of the fuel component. These results can be combined with traditional radiometric methods to achieve an understanding of how these aerodynamic particles are formed and the fractionation of the fuel component within them. An understanding of the mechanisms involved in fallout formation and fractionation is essential in predicting the most valuable forensics samples in an urban environment.

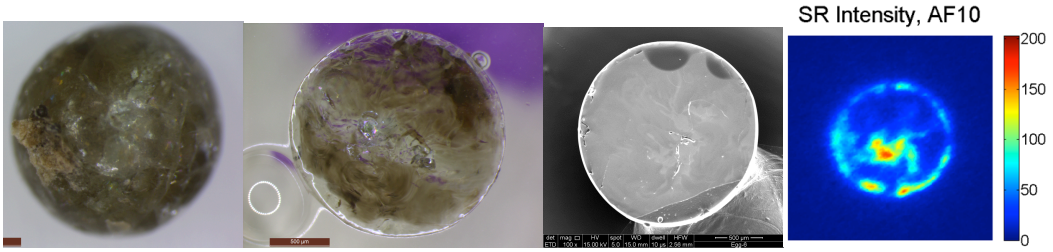

Figure 1: Aerodynamic fallout particle from near surface nuclear test by optical microscopy (top left); polished cross section of particle by optical microscopy (top right); polished cross section of particle by scanning electron microscopy (bottom left); autoradiography of polished particle (bottom right).

3-72

Complexation of actinides by the 1,4,7,10-tetraazacyclododecane-1,4,7,10-tetraacetic acid (DOTA)

Matthieu Audras, Laurence Berthon, Claude Berthon, Nicole Zorz, Dominique Guillaumont, Thomas Dumas, Philippe Moisy

CEA Marcoule, Bagnols-sur-Cèze, France

The poly-amino-carboxylate ligands form a promising family of f-element cations chelating agents. Due to the formation of strong complexes with actinides, these ligands could be used as hydrophilic complexants[(1)] in the actinide migration chemical process in geological environment and in actinide interaction with the human body in case of contamination. Amongst the poly-amino-carboxylate ligands, the DOTA macrocycle ligand (1,4,7,10-tetraazacyclododecane-tetraacetic acid, see Figure 1) is described as a powerful chelating agent with the lanthanides(III)[(2-4)] (log $\beta_1 \approx 25$ to 27[(5)]).

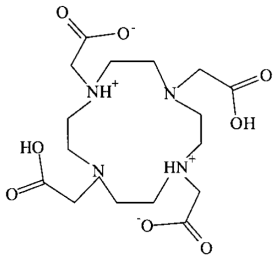

Figure 1: Developed formula of the DOTA molecule[(5)].

Solid state structures and coordination modes of the Ln-DOTA complexes are known for the whole lanthanide series[(6)]. Eight coordination sites are occupied by the N and O donor atoms and the ninth site is occupied by a water molecule. From a general standpoint, the stability constant rises across the lanthanide series as the M-N length drops due lanthanide contraction (reduced ionic radius and increasing effective charge). The reaction between Ln^{III} ions and DOTA is slow and occurs through the formation of intermediate species[(5)].First, the cation is bound to the four oxygen atoms of the carboxylate groups and to five water molecules. These species evolve rapidly: the lanthanide moves into the cavity to form $Ln(DOTA)(H_2O)^-$ in which the ion is bound to four nitrogen atoms, four carboxylate oxygen atoms and one water molecule.

The main goal of this work is to extend the investigations to the complexing behavior of DOTA with An^{III} and An^{IV} in aqueous solution. In order to achieve it our method will consist in a twofold approach, combining experimental data with modeling calculations. For this, the experiments will be based on the available knowledge on Ln-DOTA systems. Americium(III) has been selected, as being an An^{III} chemically close to Ln^{III}. Thorium(IV) and neptunium(IV) have been chosen to represent the An^{IV} series.

Besides the conventional analytical techniques (UV-Vis spectrophotometry, NMR and ESI-MS), the systems will be scanned with X-ray absorption spectroscopy (EXAFS) to determine the stoechiometry of the complexes, identify the ligand complexing sites and probe the coordination sphere of the cation. The experimental EXAFS spectra will be compared to models obtained thanks to quantum chemistry calculations.

The experiments proved complexation is occurring between DOTA and Am^{III} and showed that several species are at equilibrium in solution (see Figure 2a). We can infer from them Am^{III} behaves like lanthanides as a stable (1:1) complex is likely to form (see Figure 2b).

The differences in coordination mode regarding the An^{III}-DOTA and An^{IV}-DOTA systems will be analyzed: stoechiometry, participation of the complexing sites (N atom and/or COO^- functions) and distances to the metallic centre will be compared. The evolution over time of the formed species will be monitored as well.

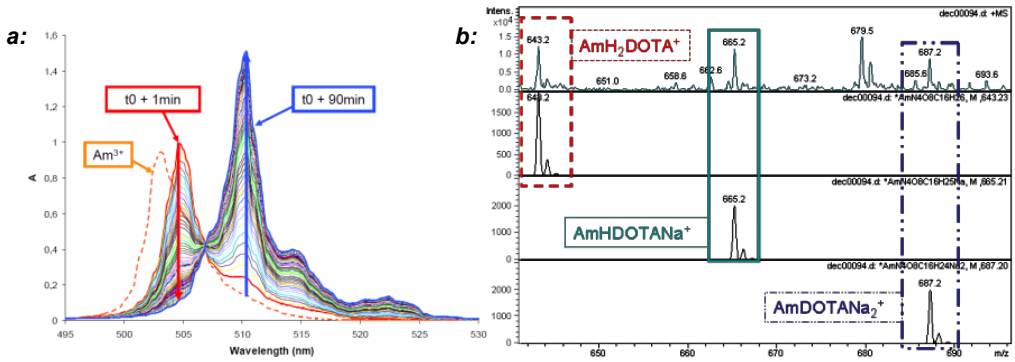

Figure 2: *a:* UV-Vis kinetic follow-up of the complexation of 2,5x10^{-3}M Am^{3+} by 0.2M DOTA in aqueous solution at pH = 3 and θ = 25°C. Dashed orange line: Am^{3+} in absence of DOTA. t_0: addition of the metal solution to the ligand solution.

b: ESI-MS spectrum 640-700 m/z zoom of an Am-DOTA system (top) and pattern simulations of the americium species. Composition: $Am(NO_3)_3$ – DOTA 10^{-3}M in 0.1M NaCl, diluted 100 times in H_2O/EtOH 50/50.

References

1. Choppin, G.R., Thakur, P. and Mathur, J.N. (2006) *Coordination Chemistry Reviews*, **250**, 936-947.

2. Cacheris, W.P., Nickle, S.K. and Sherry, A.D. (1987) *Inorg. Chem.*, **26**, 958-960.

3. Loncin, M.F., Desreux, J.F. and Merciny, E. (1986) *Inorg. Chem.*, **25**, 2646-2648.

4. Kumar, K., Jin, T.Z., Wang, X.Y., Desreux, J.F. and Tweedle, M.F. (1994) *Inorg. Chem.*, **33**, 3823-3829.

5. Moreau, J., Guillon, E., Pierrard, J.-C., Rimbault, J., Port, M. and Aplincourt, M. (2004) *Chemistry – A European Journal*, **10**, 5218-5232.

6. Viola-Villegas, N. and Doyle, R.P. (2009) *Coordination Chemistry Reviews*, **253**, 1906-1925.

3-73

Evidence for covalence in a *N*-donor complex of Americium(III)

Peter Kaden[1], Christian Adam[1,2], Björn B. Beele[1,2], Udo Müllich[1], Sascha Trumm[1], Andreas Geist[1], Petra J. Panak[1,2], Melissa A. Denecke[1]

[1]Karlsruhe Institute of Technology (KIT), Institute for Nuclear Waste Disposal (INE), Karlsruhe, Germany, [2]University of Heidelberg, Department of Physical Chemistry, Heidelberg, Germany

Partitioning and transmutation (P&T) is a strategy of reducing the long term radiotoxicity and heat load of spent nuclear fuel.[1] This involves separating the chemically similar lanthanides (Ln) from actinides (An) and converting the latter into shorter-lived fission products. Separation can be achieved by liquid-liquid extraction from nitric solutions using highly selective N-donor ligands, e.g., alkylated bis-triazinyl pyridines (BTP) in organic solvents. However, the molecular origin of the selectivity for actinide complexation in presence of lanthanides remains unclear. Our studies aim at understanding of the reasons for the observed selectivity, which in turn should allow design of improved extraction ligands or conditions.

NMR on paramagnetic compounds is a sensitive and versatile spectroscopic method that allows separation of the overall chemical shift into a part due to covalently transferred electron spin density (FERMI contact shift, FCS) and a distance- and angle-dependent part due to dipolar electron-nucleus spin coupling (pseudo contact shift, PCS). Thus, evaluation of FCS/PCS will allow evaluation of the share of covalence in metal-ligand bonds. Several methods for separation of FCS and PCS exist and have been successfully applied to lanthanide complexes.[2] However, most methods rely on calculated values such as spin expectation values, hyperfine coupling constants and ligand field parameters. All these values are still widely unknown for actinide compounds.

NMR investigations of an Am(*n*PrBTP)$_3^{3+}$ complex with a ^{15}N labelled ligand revealed large differences in ^{15}N chemical shift for coordinating N-atoms in comparison to both lanthanide(III) complexes and the free ligand. The temperature dependence of observed NMR chemical shifts for this complex indicates a weak paramagnetism. This fact and the observed large chemical shift for bound N-atoms allow us to conclude that metal-ligand bonding in the reported Am(III) N-donor complex has a larger share of covalence than in lanthanide complexes. This may account for the observed selectivity.

This work is supported by the German Federal Ministry of Education and Research (BMBF) under contract numbers 02NUK020A and 02NUK020D.

References

[1] M. Salvatores, G. Palmiotti, *Prog. Part. Nucl. Phys.* **2011**, *66*, 144-166.

[2] a) C. Piguet, C. F. G. C. Geraldes, in *Handbook on the Physics and Chemistry of Rare Earths, Vol. Volume 33* (Eds.: J. K.A. Gschneidner, J. C. G. Bünzli, V. K. Pecharsky), Elsevier, **2003**, pp. 353-463; b) C. F. G. C. Geraldes, S. Zhang, A. D. Sherry, *Inorg. Chim. Acta* **2004**, *357*, 381-395.

3-74

Towards stability rules of extractants involved in minor actinides partitioning processes: Study of TODGA degraded samples under different experimental conditions.

Hitos Galán[1], Ana Nuñéz[1], Amparo G. Espartero[1], Aritz Durana[2], Javier de Mendoza[2], Joaquín Cobos[1]

[1]Centro de Investigaciones Energéticas, Medioambientales y Tecnológicas (CIEMAT), Madrid, Spain, [2]Institute of Chemical Research of Catalonia (ICIQ), Tarragona, Spain

The new nuclear reactor concept under development will be able to re-use most of the U, Pu and minor actinides (MA: Am, Np, Cm). With this purpose it is necessary to develop suitable partitioning processes [1]. So far, TODGA (*N*,*N*,*N´*,*N´*-tetraoctyldiglycolamide, Figure 1) is considered one of the extractants with higher possibilities to be applied at industrial scale, since it has been demonstrated most of the requirements need for hydrometallurgical partitioning processes. In fact, most of processes for advanced fuel cycles developed in the framework of the European ACSEPT Project are based on TODGA, such as: DIAMEX [2], 1cycle-SANEX [3], and GANEX [4].

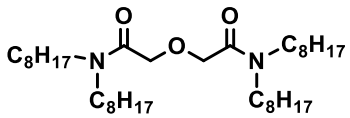

Figure 1.- Structure of the diglycolamide TODGA.

To evaluate the applicability of solvents for process development, it is necessary to demonstrate not only their good extraction properties, but also their degradation resistance, since the organic phase is in contact with highly radioactive solutions and high nitric acid concentrations. The solvent degradation leads to undesirable effects such as decrease of selectivity, third phase formation, etc. Therefore, it minimizes the regeneration of the used solvent, increasing the volume of the secondary waste products and the process cost. Most often, the new species generated have extracting properties that markedly differ from those of the original ligands.

In a previous work, a methodology for studying the stability of diglycolamides (DGA) as selective extractants of Am(III) and Eu(III) was set up, where is reported a completed characterization of irradiated samples by HPLC-MS [5]. This methodology has allowed us to explore the degradation from a structural point of view by identifying the nature of the sub-products formed during the irradiation and quantifying them.

Recently, that methodology has been applied to TODGA solvent to get a complete batch of data, and to explore how and why the experimental conditions can affect to the amounts and proportions of sub-products formed [6]. Applying this methodology we have been able to seen how modifying the experimental condition under study it is possible not only to characterize the degrade samples, but also, to get a better understanding about the stability rules. Furthermore it has been studied the influence of integrated dose, the dose rate, the use of different diluents and pre-treatments, particularly the influence of nitric acid in the media. Between others, those studies have shown a protective role of nitric acid on DGA compounds stability. Particularly in presence of high octanol proportion, where more amount of nitric acid is extracted after the pre-treatment, although it is known that the octanol increases the radiolytic and hydrolytic degradation.

Herein it is described the characterisation of TODGA degraded solvents under different experimental conditions to study its behaviour in more detail, and to know if the protection is due to the presence of protons or nitrates ions. Particularly, TODGA samples in (95:5)%vol TPH/octanol were irradiated with external ^{60}Co sources up to 1000 kGy (at a dose rate of 2.1 kGy/h) after a pre-treatment with different aqueous solutions using H_2O, HNO_3 (from 0.06M to

5M) and 3M solutions of $NaNO_3$, $HClO_4$ and $NaClO_4$. Irradiated TODGA and TODGA aging control samples were characterised by Am(III) and Eu(III) extraction assessment and the main degradation compounds have been analysed qualitatively and quantitatively by LC-MS, UV-diode and CG-MS.

Previous stability studies of different compounds concluded that the O-C bond is the weakest bond of the DGA molecule, and it is stabilized in nitric acid media. After the irradiation of TODGA samples contacted with H_2O, HNO_3, $NaNO_3$, $HClO_4$ and $NaClO_4$ solutions, TODGA concentration keeps higher in the samples pre-equilibrated with nitric acid. There are no relevant differences between samples pre-equilibrated with $NaNO_3$ and $NaClO_4$, and also for samples pre-equilibrated with H_2O. On the other hand, $HClO_4$ presence during the irradiation provokes a negative effect over TODGA stability, which is clearly reflected on the distribution coefficient $D_{M(III)}$ values. With regards to the main degradation fragments, it was found that in acid media the main fragment is always a 2-hydroxiacetamide. Meanwhile that situations change in samples which were not pre-equilibrated o pre-equilibrated with $NaNO_3$, $NaClO_4$ or H_2O, indicating again the stabilization of the O-C bond in DGA structure in acid media.

The quantitative data of TODGA stability study at different nitric acid concentrations indicated that the remaining TODGA concentration after the irradiation decreases as the nitric acid concentration in the organic phase reduces. Therefore, the high $D_{M(III)}$ values obtained for samples pre-equilibrated with high nitric acid concentration are due to both, a better extraction under these conditions and also a less degradation of TODGA. However, due to a change observed in the main fragments proportion it could be considered that when nitric acid concentration used is bellow 3M, it does not stabilize the O-C bond in TODGA structure and only acts as gamma irradiation scavenger. Therefore, it can be summarized that nitric acid shows a double protective effect: on one hand, provides a proactive effect on O-C bond due to acid media (H^+); and on the other hand, NO_3^- ions act probably as scavengers of gamma radiation.

Moreover, it has being studding TODGA degradation dependence on Eu(III) presence. The first results show that TODGA is less degraded against radiolysis when it is quantitatively complexed with Eu(III) and the hydrolytic degradation is enhanced, as well as occurs in presence of nitric acid.

This work has been developed under the framework of the European ACSEPT Project (VII-FP) and CIEMAT-ENRESA (ST-XXIV) collaboration agreement.

References

[1] Madic C. Overview of the Hydrometallurgical and Pyrometallurgical Processes Studied Worldwide for the Partitioning of High Active Nuclear Wastes. Proc. of OCDE-NEA 6th Information Exchange Meeting on P&T, Madrid: 2000, p. 53-64.

[2] Magnusson et al. Solvent Extr. Ion Exch. 2009; 27, 26.

[3] Wilden A., Schreinemachers C., Sypula M., Modolo G. Solvent Extr. Ion Exch. 2011; 29, 190.

[4] Brown J., McLachlan F., Sarsfield M., Taylor R., Modolo G., Wilden A. Solvent Extr. Ion Exch. 2012; 30, 127.

[5] Galán H, Murillo MT, Sedano R, Núñez A, Espartero AG, Prados P, de Mendoza J. Eur. J. Org. Chem. 2011; 3959-69.

[6] H.Galán, A. Núñez, A. G. Espartero, R. Sedano, A. Durana and J. de Mendoza. Procedia Chemistry 2012, 195-201.

3-75

Synthesis and Characterization of U-doped Zircon and Baddeleyite

V.G. Petrov, I.E. Vlasova, E.B. Furkina, M.V. Yevsunina, S.N. Kalmykov

Lomonosov Moscow State University, Moscow, Russia

Zircon mineral, $ZrSiO_4$, can contain actinides in its structure. Such structures are known to be highly chemical durable, high resistant to radiation damage, thus preventing release of the actinides. Zircon occurring in nature contains 0.06 wt.% of U in maximum. However, after Chernobyl accident one of the component of the “lavas” is stable U-bearing zirconium silicate with uranium content up to 12 wt.%. Furthermore, recently Pu-doped zircon-based ceramics with plutonium loading up to 10 wt.% were obtained. Thereby ceramics based on zircon $(Zr,An)SiO_4$ and baddeleyite $(Zr, An)O_2$ can be proposed as a nuclear waste matrix for immobilization of actinide (U, Pu, Am) [1-3].

The known methods to synthesize crystalline zirconium silicate usually require temperatures higher than 1300-1400°C that is not always economically acceptable. In this work we apply sol-gel technique accompanied with further sintering at 600, 900 and 1200°C to synthesize $Zr_{0.95}U_{0.05}SiO_4$ (that is equal to 8 wt.% U). Two methodologically different procedures were used: i) precipitation of U(VI)-Zr(IV) oxyhydroxides from uranyl and zirconoyl nitrate solution, hydrolysis of $Si(OC_2H_5)_4$ (TEOS), mixing of these two suspensions, hydrothermal treatment of the mixture at 100°C within 48 hours, drying, sintering at different temperatures; ii) simultaneous precipitation of U-Zr oxyhydroxides and TEOS hydrolysis in the same flask, further steps are the same as in “i)”.

All of the samples were characterized by scanning electron microscopy with energy dispersive X-ray spectroscopy (SEM-EDS) and X-ray diffraction analysis (XRD). It was found that all the phases after hydrothermal treatment have the same amorphous-like pattern and chemical composition close to stoichiometric. After sintering at 1200°C zircon and baddeleyite (monoclinic ZrO_2) phases were identified in samples prepared according to the both procedures. At lower temperatures (600 and 900°C) only tetragonal zirconium dioxide was observed for the “ii)” procedure and mostly baddeleyite for the “i)” procedure.

Chemical composition of all the samples was not uniform according to SEM-EDS. There were phases of pure Zr-U oxides and mixed Zr-U-Si oxides observed on elemental maps.

As a result of this work uranium was incorporated in two durable phases – baddeleyite and zircon which were obtained at temperatures lower than 1300°C. Further leaching and radiation tests will be performed to estimate suitability of such matrices for long-term actinide isolation.

This work was supported by RFBR grant 12-03-31548-a.

References

[1] R.C. Ewing. Proc. Natl. Acad. Sci. USA. 1999. **96**, 3432.

[2] L.M. Wang, S.X. Wang, R.C. Ewing. Philos. Mag. Lett. 2000. **80**, 341.

[3] B.E. Burakov, A.Ph. Smetannikov, E.B. Anderson, A.Yu. Alexeev. Mat. Res. Soc. Symp. Proc. 2006. **932**, 1017.g

3-76

Temperature and Ionic Strength Effects on Neptunium Speciation in Simplified Brine Systems

Donald Reed, Marian Borkowski, Michael Richmann, Jean-Francois Lucchini

Los Alamos National Lab, Carlsbad, NM, USA

Neptunium primarily exists in the environment in the Np(IV) and Np(V) oxidation state, although there are some high-pH (pH >12) conditions where Np(VI) is also stabilized. Under oxic conditions in near-neutral pH, $Np(V)O_2^+$ is the predominant species and is relatively mobile in the environment due to its high solubility and low tendency toward hydrolysis and complexation. Anaerobic microbial processes [1] and iron(0, II) will reduce neptunium to the Np(IV) oxidation state, which has an analogous environmental chemistry to Pu(IV), e.g., very strong hydrolysis, very strong tendency towards polymer/colloid formation, and low solubility. For this reason, Np(IV) will likely predominate under most anoxic conditions in brine or low ionic-strength groundwater.

In a long-term geologic repository setting, Np(V) can become an important contributor to release at long times (> 10, 000 years) under mildly oxidizing conditions. This increased importance is because it is very long-lived, its inventory builds up in time due to the decay of Am-241 in the wasteform, and it has a relatively high solubility and mobility over a wide pH range. In the USA, this potential release issue is mainly linked to repository concepts for the long-term disposal of high level waste (HLW) and spent fuel (SF) and not TRU nuclear waste disposal (e.g., the WIPP). In the WIPP, neptunium is not a key contributor to release due to its very low overall inventory in TRU waste (~ 10 Kg predicted for the entire waste inventory), the Am-241 inventory is also relatively low, and the timeframe for repository performance is only 10,000 years.

In this context, we are investigating the effects of temperature and ionic strength on the speciation of Np(V), and eventually Np(IV), to support the development of the safety case for an HLW/SF repository in salt should the low-probability event of brine inundation occur. This will also be supported in time with micro-calorimetric studies. Neptunium, for a number of reasons, is a model system to study and this will help form a strategy that will be extended to other multivalent actinides. Herein we report the progress we have made along this research path and present some initial data on the effects of temperature and ionic strength on the Np(V) aquo species, the complexation of Np(V) with borate, the complexation of Np(V) with carbonate and the modelling of the bio-associated of Np(V) with halophilic bacteria.

Experimental Approach: Neptunium-237 (~ 98% by mass) was purified by oxidation to Np(VI) in fuming perchloric acid, reduced to Np(V) by the addition of a few drops of 30% hydrogen peroxide, and precipitated as a carbonate solid by titration with sodium carbonate to ~ pH 7-8. This was then re-dissolved in the desired media (perchlorate, sodium chloride, or 0.1 M HCl) to make up the stock solutions.

The initial approach was to use absorption spectrometry to establish the speciation of neptunium. A Varian CARY 5000 spectrometer, equipped with a circulating water bath for temperature control (0 to 90^{o}C) was used to obtain temperature-specific spectra. These spectra were obtained in gas-tight cuvettes by temperature-equilibrating the reference and sample cuvette prior to obtaining a baseline correction and then spiking in the neptunium (typically 5-40 µL) to obtain the spectrum as function of complexation, ionic strength and temperature. Liquid scintillation counting (Beckman-Coulter LS6500 multipurpose scintillation counter) of the neptunium was done for each sample to correct for minor differences in neptunium concentration due to the pipetting. Lorentzian and gaussian fitting was done to model the absorption peaks and de-convolute the peaks and calculate λ_{max} and the half-height width of the spectra obtained. EQ3/6 and modified FITEQL approach was used to fit the biosorption data.

Spectroscopic Results: Data from four sets of experiments are reported: 1) the effect of ionic strength on the Np(V) aquo peak, 2) the effect of temperature on the Np(V) aquo peak, 3) Np(V)-borate complexation, and 4) Np(V) biosorption towards *Choromohalobacter sp*. (bacteria).

The Np(V) spectrum was obtained in perchloric and NaCl media up to ionic strengths of ~ 5 M. The effect of ionic strength in the perchlorate media is shown in Figure 1. Here a small blue shift was observed (~ 1.5 nm) as the ionic strength was increased. There was no significant change in the half-height peak width. In contrast, a red shift of ~ 2 nm was observed when spectra were obtained in NaCl media. This was interpreted as due to the formation of an Np(V)-Cl complex peak at 983 nm, that grows in with ionic strength.

The complexation of Np(V) with borate and carbonate led to new band formation that can be de-convoluted to determine the complex formation constants. Borate formed a 1:1 complex with Np(V) with a peak maximum at 985 nm (see Figure 2). Isobestic behavior was observed at fixed pH with variable borate concentration and at fixed borate concentration and variable pH indicating that a single species was being formed. The apparent formation constant for this complex was Log K_{app} = 2.11 ± 0.08.

The carbonate peak initially formed is at 991 nm ($NpO_2CO_3^-$) and a second species forms at 997 nm ($NpO_2(CO_3)_2^{3-}$). These two processes compete with each other and it is critical to maintain low concentrations of carbonate to investigate the borate complexation. In all cases, no evidence of hydrolysis was obtained until pH ~ 10 or higher [2].

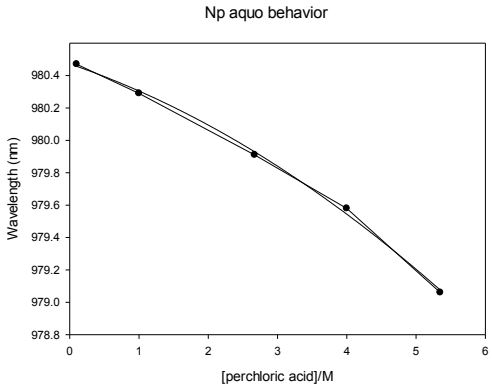

Fig. 1. Peak shift in the Np(V) aquo absorption band as a function of ionic strength in perchlorate media.

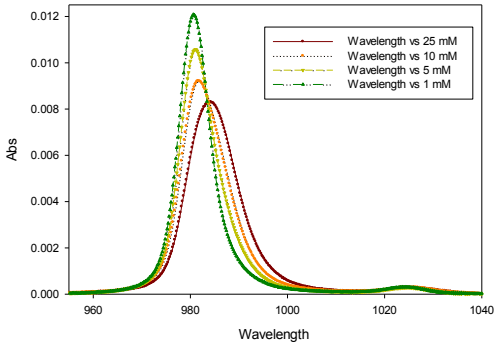

Fig. 2. Np(V) spectrum in the presence of varying concentrations of borate and pH ~ 8 showing an isobestic point.

The effect of temperature (20 – 90 ^{o}C) was established for Np(V) in 0.1 M HCl (no uncertainty in the speciation). The increase in temperature resulted in a steady blue shift in the absorption maximum (~ 2 nm) and a corresponding decrease in the line width. These changes, although small, are significant when de-convoluting the neptunium spectra at variable temperature given the very small spectral shifts observed in the complexes formed (e.g., chloride and borate). These data provide baseline spectra that are needed to evaluate the effects of temperature on complexation.

References

[1] Banaszak, J. E., S. M. Webb, B. E. Rittmann, J.-F. Gaillard, and D. T. Reed, “Fate of Neptunium in Anaerobic, Methanogenic Microcosm,” Scientific Basis for Nuclear Waste Management XXII”, 556 (1999) 1141-1149.

[2] Rao, L., T.G. Srinivasan, A.Y. Garnov, P. Zanonato, P.D. Bernardo and A. Bismondo, “Hydrolysis of Neptunium(V) at Variable Temperatures (10–85°C)”, Geochimica et Cosmochimica Acta, Vol. 68, No. 23, pp. 4821–4830, 2004

[3] Ams, D.A., J. S. Swanson, J. E. S. Szymanowski, J. B. Fein, M. Richmann, and D.T. Reed, “ The Effect of High Ionic Strength on Neptunium (V)Adsorption to a Halophilic Bacterium” accepted for publication in Geochimica et Cosmochimica Acta, 2013.

3-77

Scanning phase diagrams to discover new phases with original properties: Examples from U-T-Ge (T = Fe, Co, Ru) ternary systems.

Olivier Tougait[1], Mathieu Pasturel[1], David Berthebaud[1,4], Arnaud Soude[1], Thierry Roisnel[1], Margarida Henriques[2], Antonio Goncalves[2], Adam Pikul[3], Dariusz Kaczorowski[3]

[1]ICSR/CSM, UMR 6226, CNRS-Université de Rennes1, Rennes, France, [2]IST/ITN, Universidade Técnica de Lisboa, Sacavém, Portugal, [3]INTiBS PAN, Wroclaw, Poland, [4]CRISMAT, UMR CNRS 6508, Caen, France

Within the last years, new original physics of actinide-based compounds arose from the discovery of novel materials. This is particularly true for the high temperature superconductivity of $PuCoGa_5$ [1] (and subsequent members of this family). Also the intriguing coexistence of ferromagnetism and superconductivity in uranium germanides [2-4] stimulates many researches.

Our objective is the discovery of novel phases with original crystallographic, magnetic and/or (thermo)electrical properties, but also to understand the phase formation and solid-state equilibria within these systems, by systematic investigations of U-T-X (T = transition element; X = *p*-element) phase diagrams. Recently, we focused on U-T-Ge (T = Fe, Co, Ru) systems, evidencing the existence of more than 20 new phases.

Among the original behaviours encountered, we can mention (i) the complex crystal structure of $U_{34}T_{4-x}Ge_{33}$ (T = Fe, Co, Ru), (ii) the ferromagnetism of U_2Fe_3Ge despite unusually short U-U distances [5] or (iii) the existence of a solid solution on the ferromagnetic superconductor UCoGe influencing its magnetic properties.

The poster will present the 3 Gibbs diagrams of the previously mentioned U-T-Ge systems and significant results from each of them, in terms of crystal structures of ternary phases, magnetic or transport behaviours. Crystallographic and physical tendencies as a function of the transition metal will be highlighted.

References

[1] J. Sarrao, *et al.*, *Nature* **420**, 297 (2002).

[2] S. S. Saxena, *et al.*, *Nature* **406**, 587 (2000).

[3] D. Aoki, *et al.*, *Nature* **413**, 613 (2001).

[4] N. T. Huy, *et al.*, *Physical Review Letters* **99** (2007).

[5] M. S. Henriques, *et al.*, *Solid State Communications* **148**, 159 (2008).

3-78

Some progress made in f-element chalcogenide chemistry

Jean-Marie Babo, Peter C. Burns

University of Notre Dame, Notre Dame, IN, USA

Chalcogenide compounds continue to present great challenges for material and inorganic chemists. More new physical properties are reported as new structures are discovered. In addition, the introduction of some sulfide building blocks such as chalco-phosphate, chalco-germanate have generated from 0 to 3D structure brought structural diversity in f-element chalcogenide chemistry.[1-3] Very few chalcogenides with less common oxidation state have been reported. In the rare actinide cases, classic methods of characterization such as UV-vis, magnetism and bond lengths have not been always successful. Meanwhile, oxides comparatively to chalcogenides find their metals oxidation states much easily through those methods. For example, data of the UV-vis of uranium cations from +3 to +6 is accessible as well as those of some trans-uranium elements. Meanwhile UV-vis spectroscopy of chalcogenides have been mostly made for band-gap determination.[2,3] There is a need to publish those data, to bring the contrast and similarities. Here is a contribution as the absorption spectra of some ternary and quaternary thiophosphates of uranium(IV) with comparison to each other and to an oxide example.

References

[1] P. M. Picoli, K. D. Abney, J. D. Schoonover, P. K. Peter, *Inorg. Chem.* 2001, 40, 4871.

[2] K. Chondroudis, M. G. Kanatzidis, *J. Am. Chem. Soc.* 1997, 119, 2574.

[3] R. F. Hess, K. D. Abney, J. L. Burris, H. Dieter Hochheimer, P. K. Peter, *Inorg. Chem.* 2001, 40, 2851.

3-79

Heavy metal extraction using advanced PUREX style partitioning systems

Kate Tucker[1], Robin Taylor[2], Clint Sharrad[1], Tamara Griffiths[1], Sarah Heath[1], Peter Kaden[3]

[1]The University of Manchester, Manchester, UK, [2]National Nuclear Lab, Cumbria, UK, [3]Karlsruhe Institute of Technology, Karlsruhe, Germany

The PUREX (Plutonium URanium EXtraction) process utilises a 30% v/v tributyl phosphate extractant in a kerosene diluent for the selective removal of hexavalent uranium (U) and tetravalent plutonium (Pu) from spent nuclear fuel dissolved in nitric acid. The separation of uranium from spent nuclear fuel is likely to be imperative for the continued growth of nuclear fission power generation with the world's energy requirements. The removal of plutonium allows this to be used as a source of fuel in MOX (mixed oxide) or breeder reactors whilst also serving to reduce the radiotoxicity of the nuclear waste. However, some studies have indicated an improved extraction of some metals with the addition of chloride to the aqueous phase in these systems. Analysis of the effectiveness of these chloride containing systems can serve in the understanding of hybrid separation processes such as pyroprocesses that utilises a molten salt(s) to provide an initial separation of actinides from spent fuel followed by an aqueous process to polish the products e.g. MOLAQUA. In such a process it is almost certain that some carryover of chloride into the nitrate aqueous solution would occur and therefore an understanding of the effects of chloride ions and how they may modify the behaviour of actinides and lanthanides in the aqueous solvent extraction or oxalate precipitation processes is necessary. Further, understanding the role of chloride in aqueous based separation processes may be used to assist in the cleanup of chloride containing waste streams such as impure products remaining from pyroprocessing and chloride contaminated plutonium materials.

We have attempted to obtain a greater understanding of the fundamental chemistry of these chloride containing solvent extraction systems, by investigating extraction performance and speciation dependency on the ratio of hydrochloric to nitric acid concentrations and absolute acid concentrations in current and future extraction processes. It is hoped that this work will contribute to an overall model of the effect of chloride addition in nuclear separations technologies. Presented here is the use of advanced PUREX modifiers, tributyl phosphate (TBP), octanol and dihexyl octanamide (DHOA) in combination with various extractants N,N,N′,N′-tetraoctyl diglycolamide (TODGA), tetradodecyl diglycolamide (TDDDGA), tetraethyl diglycolamide (TEDGA) and tetraethylhexyl Diglycolamide (TEHDGA) for the extraction of U, Pu, Np, Am, Eu, Tc and Zr from HNO_3, HCl and mixed HNO_3 and HCl solutions. These systems will undergo analysis via numerous spectroscopic techniques including 31-P NMR, gamma, IR, UV/vis, SAXS and EXAFS.

3-80

Structural and Spectroscopic studies of Mononuclear Uranyl(VI) Complex Containing *O,O,N,N*-tetradentate ligand

Mohammad Azam, Saud Al-Resayes

King Saud University, Riyadh, Saudi Arabia

The actinide coordination chemistry has attracted considerable attention due to the development of nuclear technology for the production of electricity [1]. Complexes of actinide elements have been used due to their unique luminescent and magnetic properties, photostability, line like emission bands, diagnostic tools in biological sciences e.g., paramagnetic contrast agents in magnetic resonance imaging studies, second order non-linear optical chromophores as well as practical reprocessing of nuclear wastes [4-5].

Hereby, we describe the synthesis of tetradentate dianionic ligand 2,2'-(*1E,1'E*)-(2,2-dimethylpropane-1,3-dyl)bis(azanylylidene)bis(methanylylidene)diphenol and its complex with ($UO_2(CH_3COO)_2.2H_2O$) in 1:1 ratio in methanol. The new compounds have been characterized by elemental analysis ESI-Ms, UV-Vis, FT-IR, NMR, TGA and single crystal X-ray crystallography. X-Ray crystallography shows that geometry around uranium centre is distorted pentagonal bipyramidal with two imine nitrogen atoms, two phenolic oxygen atoms and a methanol molecule occupying fifth coordination site, together with two *trans* oxo groups.

References

[1] M.S. Bharara, K. Heflin, S. Tonks, K.L. Strawbridge, Anna E.V. Gorden, Dalton Trans., 2008, 2966-2973.

[2] J.P. Cross, M. Lauz, P.D. Badger, S. Petoud, J. Am. Chem. Soc. 126 (2004) 16278;

[3] S. Faulkner, S.J.A. Pope, B.P. Burton-Pye, Appl. Spectr. Rev 40 (2005) 1

[4] J.-C.G. Bünzli, G.R. Choppin, Lanthanide Probes in Life, Chemical, and Earth Sciences: Theory and Practice, Elsevier, Amsterdam, 1989

[5] C.E. Powell, M.G. Humphrey, Coord. Chem. Rev. 248 (2005) 725

3-92

New Ionic Liquid compounds for liquid/liquid extraction of actinides and other metallic ions

Dariia Ternova[1,2], Isabelle Billard[1], Valérie Mazan[1], Ali Ouadi[1], Stanislav Miroshnychenko[2], Vitaly Kalchenko[2]

[1]CNRS and Université de Strasbourg, Strasbourg, France, [2]Institute of organic chemistry, NAS of Ukraine, Kiev, Ukraine

Liquid-liquid extraction of actinides plays an important role in nuclear industry. In view of future waste reprocessing, new extracting agents and possibly new solvents are required. We focus on the study of Ionic liquids (ILs) as an alternative to traditional organic solvents because of their "greenness" and unique physicochemical properties, which allow unusual chemistry to occur. In particular, the possibility of their functionalization allows varying their chemical structure according to a specific task. Actually, grafting an extracting pattern onto the cationic part of an IL leads to very efficient extracting moieties for various actinides [1-3]. However, such a result may appear counter-intuitive, because one may wonder why a positively charged entity can interact strongly with a cation.

In order to better understand this point, new ILs with metallocomplexing fragments have been synthesized. The substances obtained are either cationic-extractants (IL-E(+)), based on positively charged imidazolium ring, or anionic-extractants (IL-E(-)) on the basis of tetrazolate ring, both containing a phosphine oxide group.

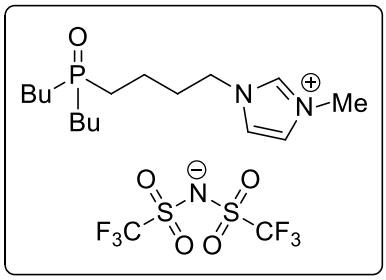

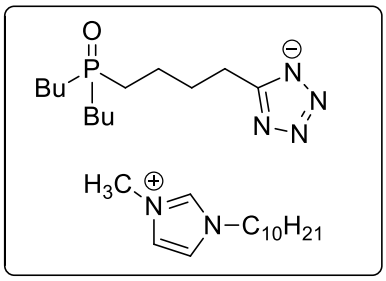

These task-specific ILs can behave as liquid phase and extracting agent. Liquid-liquid extraction of U(VI) has been studied in the solutions of these task-specific ILs in C_1C_nimTf_2N as a function of nitric acid concentration. Data are plotted in figs. 1 and 2.

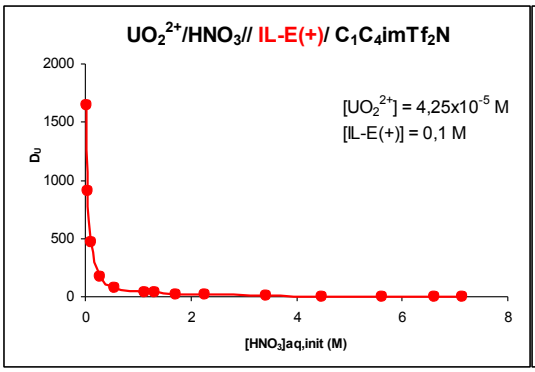

Figure 1

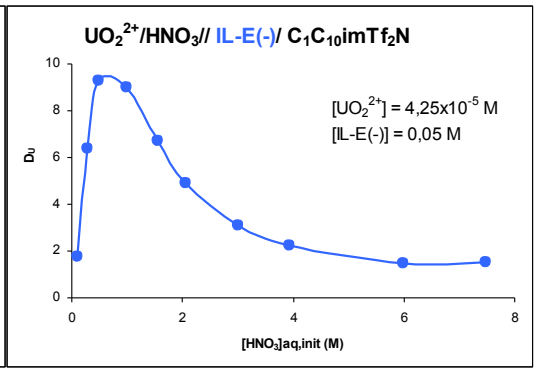

Figure 2

Under similar chemical conditions (metal and ligand concentrations) IL-E(+) appears to be more efficient than IL-E(-) for U(VI) extraction, with a maximum distribution ratio equal to ca. 1640 at (HNO_3) = 0.02 M, while the values of distribution ratio for IL-E(-) don't exceed ca. 9.3. However, above ca. HNO_3 = 3 M, IL-E(+) leads to a very limited distribution ratio (below 6.2). Another significant difference between the two extracting agents is the appearance of a

third phase at low nitric acid concentrations in the case of IL-E(-), which prevents reliable experiments. Despite these differences, both IL-E(+) and IL-E(-) do extract U(VI) from acidified aqueous solutions. Thereby, the charge of extracting moiety doesn't prevent extraction. However, owing to its specific chemical structure, IL-E(-) based on a tetrazolate anion cannot be considered as an universal representative for the IL-E(-) group of compounds: as a matter of fact, the tetrazolate part can be protonated and this could be the reason for the observed decrease in the distribution ratio as HNO_3 is increased: part of the H^+ solubilised in the IL phase may protonate the anion, giving rise to the neutral entity IL-E, which affinity towards U(VI) is possibly low.

As a preliminary conclusion to this work, it appears that the P=O group is an efficient U(VI) extracting pattern, irrespective of the charge of the skeleton on which it is grafted (IL-E(+) and IL-E(-)). As a perspective of this work, we will graft these P=O extracting patterns on calixarene-based ILs. It will help understanding the flexibility contribution to the extracting efficiency.

References

[1] Odinets, I.L., Sharova, E.V., Artyshin, O.I., Lyssenko, K.A., Nelyubina, Y.V., Myasoedova, G.V.,Molochnikova, N.P., Zakharchenro, E.A., 2010, Dalton Trans. 39, 4170

[2] Rout, A., Venkatesan, K.A., Srinivasan, T.G., Vasudeva Rao, P.R., 2012, Sep. & Puri. Tech. 97, 164

[3] Ouadi, A., Gadenne, B., Hesemann, P., Moreau, J.J.E., Billard, I., Gaillard, C., Mekki, S., Moutiers, G., 2006, Chem. Eur. J. 12, 3074

3-57

Preparation, phase composition, microstructure and electrochemical properties of UPd_3 and URu_3 in the solutions of nitric acid

Semen Zavarzin[1], Alexandre Maslennikov[2], Alexandre Osipenko[2], Alexandre Maershin[2], Irina Vlasova[3], Andrei Shiryaev[1]

[1]A.N. Frumkin Institute of Physical Chemistry and Electrochemistry of Russian Academy of Sciences, Moscow, Russia, [2]Open joint stock company State Scientific Research Institute of Atomic Reactors, Dimitrovgrad, Russia, [3]M.V. Lomonosov Mowcow State University, Chemistry Dept., Moscow, Russia

The intermetalic compounds (IMC) URu_3, UPd_3, $PuRu_3$ и $PuPd_3$ seem to be the most probable chemical state for the Ru subgroup metals formed during irradiation in FBR. The stability of these compounds is comparable with the stability of UN and PuN. Therefore in course of spent (U,Pu)N FBR fuel reprocessing, using electrorefining in chloride melts, 10 -5 % of Pu is retained in anodic slurry [1]. The quantitative recycling of plutonium during reprocessing requires thus the additional operation for its recovery from anodic slurry using aqueous techniques. To develop the efficient technique for the IMC dissolution in nitric acid the information on their corrosion and dissolution rate is required. The present paper deals with the development of the technique for the IMC URu_3, UPd3 preparation, characterization of the obtained compounds with X-ray diffraction and scanning electron microscopy (SEM) techniques and with a number of electrochemical tests, allowing to determine the IMC corrosion properties and dissolution rates in 0.5 – 6 M HNO_3.

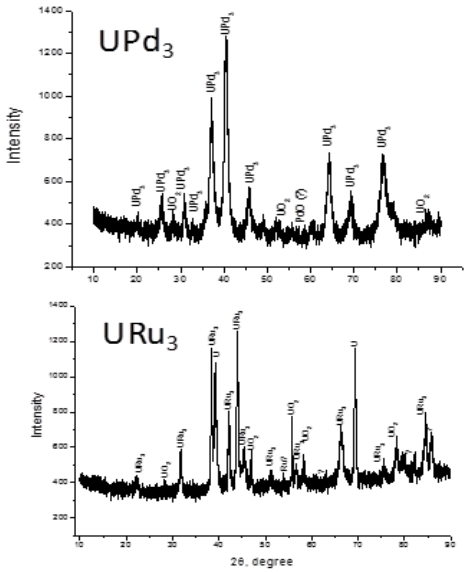

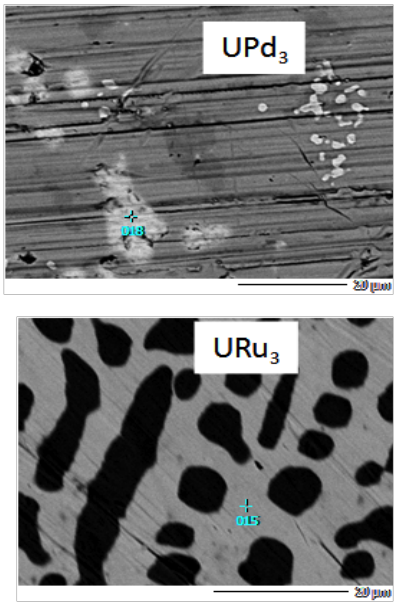

Fig. 1. X-ray diffraction patterns for the prepared UPd_3 and URu_3 samples.

Fig. 2. Surface microphotographs of UPd_3 and URu_3 samples.

Arc technique melting with inert tungsten electrode and cooled copper crucible were used to prepare the IMC URu_3, UPd_3. The melting was carried out in the high purity argon atmosphere. The prepared samples were characterized using X-ray diffraction (Fig. 1) and SEM (Fig.2) techniques. Analysis of X ray diffraction patterns of the IMC shown that UPd_3 and URu_3 appear to be the principal phases present in the samples. Insignificant impuritiy of UO_2 was found in both samples. The impurity of Ru metal was found in URu_3. The presented microphotographs of UPd_3 и URu_3 surfaces (Fig. 2) reveal high degree of homogeneity of principal phases. At UPd_3 photo the white spots corresponding to UO_2 impurity are easily seen. The presence of the Ru metal in the sample of URu_3 is proved by the SEM data. The appearance of this impurity, to our opinion, is due the slow rate of URu_3 formation in the melt and selective crystallization of small spherical particles of of Ru metal during the fast sample cooling. The data on the corrosion and dissolution of UPd_3 and URu_3 in 0.5 – 6.0 M HNO_3 were obtained for the first time by tracing linear voltammetry curves at the IMC samples as

the electrodes immersed in to the solution of HNO_3 with corresponding concentration. The data of corrosion tests on the IMC samples, calculated using Tafel equation [2] presented in the Table 1 indicate that the corrosion potentials, values of exchande currents (and correspondingly of IMC dissolution rates) increase with the increase of HNO_3 concentration. The most extensive increase of the mentioned parameters is observed when the HNO_3 concentration exceeds 2 M, proving the effect of autocatalytic reduction of NO_3^- ions at IMC surface on the IMC dissolution rates [3]. The dissolution rates of UPd_3 and URu_3 in the solutions, containing less than 4 M HNO_3, was found to be less, than 100 $mkg \cdot cm^{-2}h^{-1}$, proving

Table 1. Electrochemical characteristics of corrosion and dissolution of UPd_3 and URu_3 in solutions 0,5 – 6 моль/л HNO_3. Experimental conditions: Apparent surface contact – 0,23 cm^2, solution volume – 10 ml, dE/dt = 5 $mV \cdot s^{-1}$. T = 22±2°C

IMC	$[HNO_3]$, M	E^o, mV Ag/AgCl	i_o, $mA \cdot cm^{-2}$	β_a, mV	V_{diss}, $mg \cdot cm^{-2}h^{-1}$	E_{tr}, мВ Ag/AgCl
UPd_3	0.5	220	0.04±0.02	57	0.069±0.004	446
	1	241	0.10±0.03	74	0.17±0.04	511
	2	351	0,28±0.09	57	0.41±0.06	518
	4	534	2,8±0,2	66	4,9±0,1	545
	6	647	6,9±0,2	44	12,1±0,3	702
URu_3	0.5	325	0,05±0,02	190	0,09±0,04	1124
	1	267	0,02±0,01	147	0,03±0,02	1123
	2	239	0,01±0,01	125	0,02±0,01	1163
	4	648	0,45±0,09	125	0,8±0,1	1193
	6	698	2,5±0, 3	230	4,3±0,5	1203

that the IMC surface is passive in the range of potentials close to E^o. The values of Tafel slopes (E/Log(i)) observed at UPd_3 electrodes were 3 -4 times smaller in comparison with URu_3, proving that the passive film stability of the latter IMC surface is more stable. The increase of the HNO_3 concentration to 6 M results in the increase of the dissolution rate to 29 $mg \cdot cm^{-2}h^{-1}$ for UPd_3 and to 4.3 $mg \cdot cm^{-2}h^{-1}$ for URu_3. The indicated rate of the UPd_3 dissolution is achieved at 647 mV / Ag/AgCl, which is close to transpassivation potential at this electrode (Table 1). At the same time URu_3 surface stays in passive state up to the achievement of the potential, exceeding 1 V / Ag/AgCl. Thus, the dissolution of UPd_3 and URu_3 in HNO_3 based electrolutes with the rates, sufficient for the industrial application, is possible if the oxidation potential of the electrolyte exceeds 650 mV and 1200 mV / Ag/AgCl, correspondingly. The oxidative dissolution process may be realized by the introduction of strong oxidizing agent to the electrolyte or using the anodic dissolution of UPd_3 and URu_3. The latter process seems to have a number of technical restrictions associated with creation of reliable electric junction between the cell anode and the material to dissolve, as well as with the reduction of the dissolution current efficiency due to the water discharge at the anode surface at the potentials exceeding 1600 mV / Ag/AgCl.

References

H. Hayashiet al., Recent progress on the development of pyrochemical process of spent nitride fuels for ADS. / The 3rd International Pyroprocessing Research Conference (IPRC2010) November 29 – December 3, 2010, RIAR, Dimitrovgrad, Russia.

A. Bard, L.R. Faulkner. Electrochemical methods. Fundamentals and Applications. J.Wiley & Sons Sci. Publ. New-York, 2001, p. 92

P. Fauvet et al., Journal of Nuclear Materials 375 (2008) 52–64

ENVIRONMENTAL SCIENCE

PLENARY & INVITED

2-01

Radionuclide Biogeochemistry in the Nuclear Environmental Sciences.

Katherine Morris[1], Nicholas Bryan[1], Victoria Coker[1], Melissa Denecke[2], Gareth Law[1], Francis Livens[1], Jonathan Lloyd[1], Richard Pattrick[1], Sam Shaw[1], Pieter Bots[1], Diana Brookshaw[1], Timothy Marshall[1], Clare Thorpe[1], Adam Williamson[1]

[1]The University of Manchester, Manchester, M13 9PL, UK, [2]Karlsruhe Institute of Technology, Institut für Nukleare Entsorgung, Postfach 3640, 76021 Karlsruhe, Germany

Globally, there is a significant legacy of defunct nuclear plant and facilities; these represent some of the most hazardous sites in the world and their management is of critical concern. Additionally, many nations have now decided that the nuclear wastes that result from decommissioning these sites, and from operation of the nuclear fuel cycle, will be disposed of in deep geological disposal facilities. Underpinning any long-term strategy for management of these legacy facilities and nuclear wastes will be an understanding of the speciation and fate of radionuclides in these heterogeneous materials from their point of contamination through evolution in any disposal facility. Indeed, developing a mechanistic understanding of radionuclide behaviour in these complex systems is essential in developing strategies for long term management and/or remediation of contaminated land and in any performance assessment for nuclear waste disposal.

Biogeochemical processes can have a profound effect on the solubility of radionuclides in natural and engineered environments. The scope of these processes is significant with clear evidence that radionuclide solubility may be altered: (i) enzymatically via mediated redox reactions, (ii) by indirect redox reactions with, for example, Mn(II)- and Fe(II)-bearing minerals and biominerals, and (iii) for non-redox active species by incorporation reactions into new mineral systems formed as physicochemical conditions change. Understanding these reactions is important across radionuclide impacted environments from contaminated land where bioreduction and biomineralisation processes may be harnessed to control radionuclide mobility, through to radioactive waste disposal scenarios where there is a paucity of molecular scale information on mineralisation and bio-mineralisation processes and radionuclide behaviour under geological disposal facility relevant conditions.

Recent work exploring the behaviour of fission products and actinides will be discussed with a focus on mineralization / biomineralisation and reduction and reoxidation reactions, and their impact on radionuclide behaviour. The products of mineralisation in terms of bulk element cycles and biogeochemistry will be discussed in the context of radionuclide speciation and fate will be discussed. Specifically studies on bioreduction in sediments and examining strontium, technetium, uranium and neptunium behavior will be discussed in the wider context of contaminated land and geological disposal. Results show evidence for incorporation of strontium in systems forced to high pH. These results offer a new pathway for co-treatment of mobile contaminants in nuclear contaminated land systems where Sr-90 is often a significant and recalcitrant mobile contaminant and where redox active radionuclides such as Tc-99 and U-238 may be treated by bioreduction.

We also discuss more recent work on sediments from a high pH (pH > 10) old lime working environment (Buxton, UK) where we see robust development of bioreduction, ingrowth of the Fe(II)-bearing mineral magnetite (Figure 1), and observe concomitant reduction of radionuclides including uranium at pH 10 and above. We also discuss recent work on neptunium bioreduction in sediments and its relevance to metal reducing conditions and specifically its link to the manganese cycle.

In order to complement these experiments with complex sedimentary materials, a number of studies are ongoing using model microbe and / or mineral systems to probe the behavior of radionuclides. A system with biotite and chlorite, both iron containing silicates, will be discussed. The silicates have been exposed to the model Fe(III)-reducing microorganism *Geobacter* to increase the Fe(II) loading of the minerals. These “bio-primed” iron-silicates are then exposed to U(VI) and Np(V) and both mineral phases show increased reactivity of the uranium and neptunium after reaction with the Fe(III)-reducing pure culture. This implies that post Fe(III)-reduction these important mineral phases will be “primed” for radionuclide removal in a way that was previously unrecognised. In addition, recent work on actinide reactions with iron and manganese oxides across several model systems will be discussed. An abiotic study relevant to high pH conditions showing evidence for uranium incorporation during

transformation of ferrihydrite to hematite at high pH will be discussed (Figure 2). In addition, model pure culture bioreduction experiments with uranium doped ferrihydrite will be examined to elucidate the mechanisms of U(VI)-reduction at ambient pH. Finally, the first results from incorporation and redox cycling experiments with neptunium and model iron oxides will be presented.

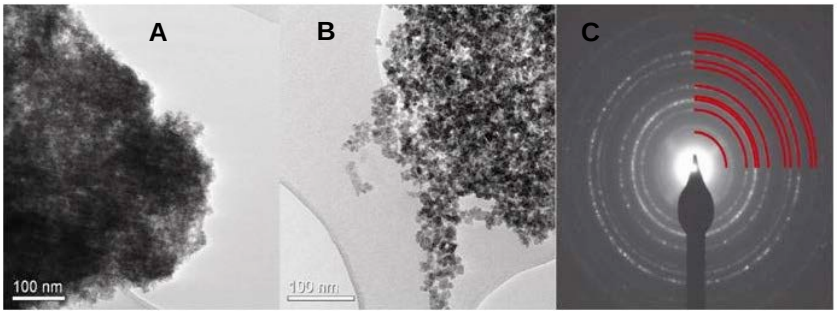

Figure 1. High resolution Transmission Electron Microscopy images of: (A) ferrihydrite; (B) biogenic “nano”-magnetite formed after bioreduction in Buxton sediments; and (C) the corresponding Selected Area Electron Diffraction (SAED) pattern for an individual magnetite crystallite overlain by the standard SAED pattern of magnetite.

Overall, several recent studies relevant to a range of environments including radioactively contaminated land and high pH conditions relevant to environments expected in geological disposal of cementitious waste forms will be discussed. The biogeochemical fate of radionuclides across these systems and in the sometimes "extreme" environments that these systems pose will be highlighted and the implications for radionuclide behavior discussed in the context of the nuclear environmental challenges that many nations face.

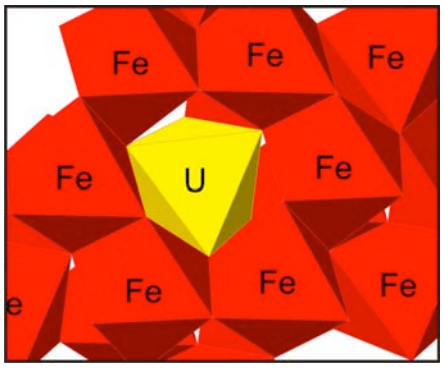

Figure 2. Conceptualisation of uranium incorporation into the iron-oxide phase hematite. Experiments with conversion of ferrihydrite to hematite in the presence of uranium suggest incorporation of the U(IV) into the mineral lattice.

1-04

The fate of trivalent actinides in clay based radioactive waste repositories

Maria do Sameiro Marques Fernandes, Rainer Dähn, Michael H. Bradbury, Bart Baeyens

Paul Scherrer Institut, Villigen PSI, Switzerland

The disposal of high level radioactive waste and spent fuel (HLW/SF) in deep geological repositories aims at isolating the radionuclides (RNs) from the biosphere for many hundreds of thousands of years. The sorption of RNs on mineral components of potential host rocks and backfill materials is a key process in retarding their migration. Clay minerals are major constituents in both the bentonite backfill material (montmorillonite), and, in argillaceous host rock formations such as Opalinus Clay (illite and illite/smectite mixed layers), currently being considered for a HLW/SF repository in Switzerland. Therefore it is critically important to develop an understanding of the uptake processes on clay minerals and to quantify and characterize them with the aim of strengthening the confidence in the safety case. Surface complexation models have been developed based on macroscopic sorption experiments to describe the sorption of RNs onto clay minerals under different geochemical conditions. However, robust and reliable modelling of the interaction between RNs and clay minerals also depends on a correct and consistent description of the surface complexes at the molecular scale.

Since actinides such as Am, Cm and Pu make a significant contribution to the radiotoxicity of HLW/SF, the aim of this study was to investigate the sorption tri-valent metals (Ln/An^{III}) on montmorillonite, illite and Opalinus clay by combining batch sorption experiments, surface complexation modeling, and the applying spectroscopic techniques.

The study consisted of two parts. Firstly, the sorption of Ln/An^{III} on montmorillonite and the influence of the geochemical in situ conditions, such as the presence of dissolved inorganic carbonate (DIC), was investigated. Since one of the predominant aqueous phase reactions of Ln/An^{III} is complexation with DIC, such complexes could potentially influence the actinide sorption and hence their migration rates. The sorption of Ln/An^{III} on montmorillonite in the absence and presence of DIC was investigated at low surface loadings ($\leq$ 8 mmol·kg^{-1}) by batch sorption experiments, Time-Resolved Laser Fluorescence Spectroscopy (TRLFS) and Extended X-ray Absorption Fine Structure (EXAFS) spectroscopy. The macroscopic sorption experiments showed that the presence of DIC (in equilibrium with atmospheric pCO_2 and in the presence of 20 mM $NaHCO_3$) led to a pronounced decrease of Ln/An^{III} uptake on montmorillonite at pH values above 7 (Fig. 1, symbols). However, modelling the data with a surface complexation sorption model [1] under the assumption that carbonate complexes did not sorb (Fig. 1, broken lines), clearly underestimated the experimental measurements.

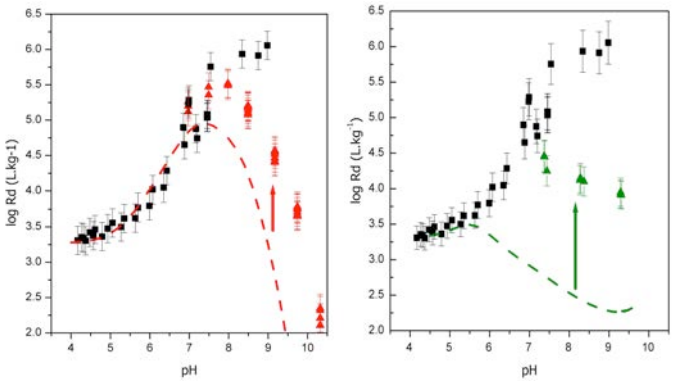

Fig. 1. Sorption of Eu^{III} on montmorillonite in the absence of DIC (■), in equilibrium with atmospheric pCO_2 (▲) and in 20 mM $NaHCO_3$ (▲). Modelling assuming Ln/An^{III} carbonate complexes do not sorb (---)(---).

A plausible explanation for this underestimation is the formation of ternary Ln/An^{III}–carbonate surface complexes. In order to verify this (or not), EXAFS and TRLFS were applied to Cm loaded montmorillonite. Differences in the Cm^{III} TRLFS spectra obtained for samples in the

absence and presence of 20 mM $NaHCO_3$ *i.e.* a red-shift of the excitation and emission spectra, as well as an increase in fluorescence lifetimes, showed unambiguously the influence of carbonate in the coordination environment of sorbed Cm^{III} (Fig. 2).

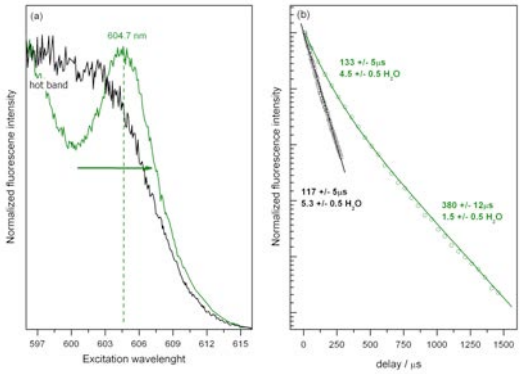

Fig. 2. a) Excitation spectra of the $^6D_{7/2} \rightarrow {}^8S_{7/2}$ transitions of Cm^{III} sorbed on montmorillonite in the absence of DIC (—) and in the presence of 20 mM $NaHCO_3$ (—) and b) the corresponding fluorescence decay profiles.

EXAFS measurements were carried out on Am/montmorillonite samples in the absence and presence of DIC. The radial structure functions (RSFs) of the Am loaded montmorillonite (≤ 3 mmol·kg^{-1}) in the absence (Am-Mont1) and presence (Am-MontC1) of DIC (pCO_2 ~$10^{-3.5}$ atm) clearly exhibit different features (Fig. 3). Am-L_{III} EXAFS spectra of Am-Mont1 showed Am-O and Am-Si/Al backscattering pairs, and clearly indicated inner sphere complexation at the clay surface. The EXAFS spectrum of the Am-MontC1 was consistent with the formation of a ternary Am^{III} carbonate complex at the montmorillonite surface, with 1 to 2 carbonate groups.

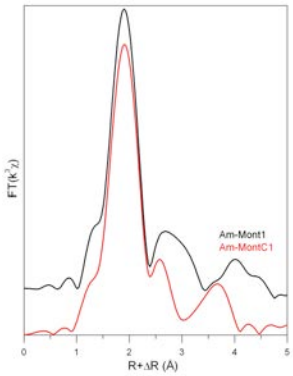

Fig. 3. RSFs of the experimental EXAFS spectra of Am^{III} sorbed on montmorillonite in the absence of DIC (—) and in equilibrium with atmospheric pCO_2 (—).

The second part of the study focused on the measurement of sorption isotherms of Ln/An^{III} on Opalinus clay. The data were modelled using the so called “bottom up” approach in which the main assumption is that the uptake of RNs in argillaceous rocks is dominated by 2:1 type clay minerals [2].

Sorption isotherms of Eu^{III} were measured on Opalinus clay samples in their respective equilibrium porewaters. Predictions of the sorption were made using the mechanistic sorption model developed for illite [3] scaled over the 2:1 type clay mineral weight content in the samples. Measurements and calculated values were in a good agreement.

The assumption that illite and illite/smectite mixed layers are the major sinks for Ln/An^{III} in Opalinus clay was investigated using EXAFS on illite and Opalinus clay samples prepared with low Am^{III} loadings (≤ 6.5 mmol·kg^{-1}). In both systems Am^{III} formed an inner-sphere complex indicated by the presence of Am-O and Am-Si/Al backscattering pairs. (Surface precipitation could be excluded.) Furthermore, the similarity between the RSFs obtained for Am^{III} sorbed on illite, and Am^{III} sorbed on Opalinus clay, unambiguously confirmed that sorption on illite is predominantly responsible for the uptake of Ln/An^{III} in a complex argillaceous rock system such as Opalinus clay (Fig. 4).

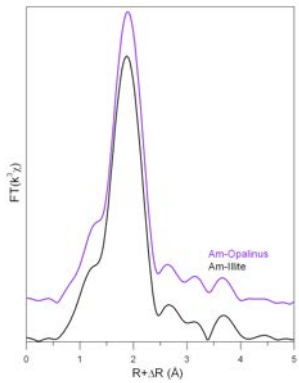

Fig. 4. RSFs of the experimental EXAFS spectra of Am^{III} sorbed on illite (—) and on Opalinus Clay (—).

References

[1] Bradbury & Baeyens (1997) *J. Contam. Hydrol.* 42, 141–163.

[2] Bradbury & Baeyens (2011) *Appl. Clay Sci.* 52, 27-33.

[3] Bradbury & Baeyens (2009) *Geochim. Cosmochim. Acta* 73, 1004-1013.

1-05

Solid solution-aqueous solution (SSAS) equilibria: experimental challenges and recent advances

Dirk Bosbach

Forschungszentrum Jülich, Jülich, Germany

Solid solutions are ubiquitous within the nuclear fuel cycle such as nuclear fuel (e.g. MOX), spent/used nuclear fuel, glassy & ceramic waste forms. These mixed compounds are typically produced at relative high temperatures (>1000°C) which promotes the mixing at molecular scales. Miscibility gaps as well as metastable states are limited in contrast to rather low (ambient) temperatures (< 100°C). During the evolution of a deep geological nuclear waste repository over extended periods of time (several hundred thousand years), the waste forms as well as EBS materials within the repository system may corrode and secondary phases will form at such low temperatures. Many radionuclides bind to these secondary phases via various distinct sorption reactions – including structural incorporation (solid solution formation) – thus controlling their availability in the mobile aqueous phase.

When assessing the long-term safety of a deep geological waste repository, the solubility of radionuclides is typically derived from solubility constants of pure compounds. However, In case the solubility of radionuclides is controlled by a solid solution, it may be significantly lower as compared to a pure compound. Therefore, SSAS may be quite important for defining the source-term for the near-field of a repository system when assessing its long-term safety.

Thermodynamic and structural concepts for solid solutions including actinides have been developed. However, in order to derive and apply thermodynamic data of mixed solid compounds under repository relevant conditions, various experimental challenges may need to be considered: (1) Do experimental SSAS data represent equilibrium conditions? Meta-stable states are quite common in low temperature aqueous environments and radionuclide uptake may be affected by kinetic effects. (2) Can we apply SSAS thermodynamic data to co-precipitation processes? In nature, compositional zoning in minerals indicate meta-stability.

Here, three selected SSAS systems will be presented: (1) Radiobarite, (2) An(III):Calcite and (3) An(III):clay/LDH Their specific experimental challenges and recent advances by combining controlled synthesis procedures near equilibrium with state of the art spectroscopic and computational approaches will be discussed.

2-02

Actinide Environmental Science Utilizing Soft X-ray Synchrotron Radiation

David Shuh[1], Tolek Tyliszczak[1], Stefan Minasian[1,2], Stosh Kozimor[2], Tsuyoshi Yaita[3], Shinichi Suzuki[3]

[1]Lawrence Berkeley National Laboratory, Berkeley, CA 94720, USA, [2]Los Alamos National Laboratory, Los Alamos, NM 87545, USA, [3]Japan Atomic Energy Agency, SPRing-8, Hyogo, 67-5148, Japan

The Molecular Environmental Sciences (MES) Beamline 11.0.2 scanning transmission x-ray microscope (STXM) at the Advanced Light Source (ALS) of Lawrence Berkeley National Laboratory is employed for soft x-ray synchrotron radiation investigations of actinide environmental science using small particles and thin sections of material.[1] The MES STXM can image and collect near-edge x-ray absorption spectroscopy (NEXAFS) spectra with a spatial resolution <25 nm from approximately 110 eV to 2000 eV. The ALS-MES STXM is downstream of an elliptical polarization undulator (EPU) that supplies a variable angle-included plane grating monochromator. Safety precautions for radioactive STXM investigations require encapsulation of the actinide materials between two thin (25 nm - 100 nm) silicon nitride windows and this is frequently accomplished by sealing two silicon nitride windows together with epoxy.[2,3] The actinide environmental science studies build on the fundamental actinide chemistry and materials sciences research that has been conducted at the MES STXM over the past several years.[2,4-7]

Some of the most contemporary issues in actinide environmental science concern the nature of the light atom interactions, oxidation state and speciation of the actinides, particle morphology, and elemental distributions/compositions within microscopic radioactive particles. STXM spectromicroscopy can be applied to the analysis of a wide range of materials for actinide environmental science by providing imaging and mapping at the nanoscale in a rapid, non-destructive manner with elemental, oxidation state, and chemical composition specificity. Additional benefits of STXM spectromicroscopy include the ability to examine the chemical nature and composition of the matrix that is hosting the small particles and the ability to interrogate environmental samples in a non-vacuum environment, thus permitting the use of "wet" and liquid samples. Soft x-ray STXM also provides a direct probe for light elements that are frequently difficult to fully quantify by traditional methods.[8] Most importantly, STXM enables analysis on any number of small particles, and can accommodate a variety of sample handling requirements to preserve sample integrity. As a first-in-line characterization tool, soft x-ray STXM complements destructive characterization methods, as it has done for extra-terrestrial particulate analyses that are then followed by destructive analysis techniques. STXM yields detailed chemical imaging at the nanometer length scale, thereby providing unique information to complement elemental, isotopic, chemical, and morphological data obtained from laboratory-based techniques.

The actinide $N_{4,5}$-edges are used both for spectromicroscopy purposes and to discriminate between oxidation states when possible (e.g., uranium(IV) dioxide, UO_2, vs. the uranyl(VI) ion, UO_2^{2+}). Light element edges are used to directly identify the chemical form of the actinides by characterizing the atoms coordinated to the actinide centers by ligand K-edge NEXAFS.[9] The K-edges of carbon, oxygen, fluorine, sodium, magnesium, aluminum, and silicon all reside in the soft x-ray energy regime, and are of particular utility for actinide environmental science. For instance, the oxygen K-edge has a unique feature for the UO_2^{2+} oxygen atoms and the edge energy and spectral profile shifts with changes in the coordinating environment observed for other uranium oxides, such as UO_2 or U_3O_8. There are additional elements of interest such as the transition metals, potassium, and calcium that can be probed at the $L_{2,3}$-edges, plus other constituents that can examined by the MES STXM with soft x-rays at the electron core levels shown in Figure 1. The chemical versatility of STXM and the spatial resolution capability permits effective identification of the chemical composition of matrix materials and enables the examination of actinides in complex multiphase environmental materials systems. Recent and current examples of actinide environmental science investigations using the MES STXM are briefly highlighted below.

The risk stemming from human exposure to actinides via the groundwater track has motivated numerous studies on the transport of actinides within geologic environments. However, the effects of waterborne organic matter on radionuclide mobility are still not completely

understood. The abilities of three humic acids (HAs - obtained from extraction of a peat soil) to co-transport U(VI) as UO_2^{2+} within water-saturated sand columns were studied by several complementary techniques. The strength of the HA effect on U mobility was positively correlated with the hydrophobicity of organic matter and NMR-detected content of alkyl carbon, which indicates the possible importance of hydrophobic organic matter in facilitating U transport. Consistently, the initial NEXAFS spectra collected by STXM spectromicroscopy show that U was enriched in micro areas of the HA that were composed of more aliphatic carbon.[10]

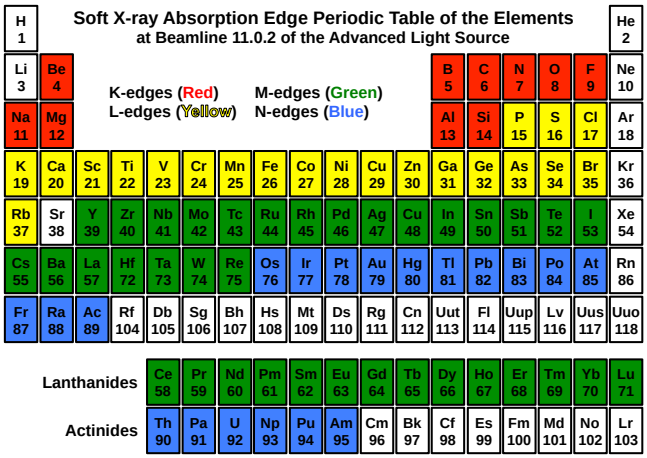

Figure 1. Generalized schematic of the x-ray absorption edges accessible at the Molecular Environmental Sciences Beamline 11.0.2 STXM at the Advanced Light Source.

An analytical application of STXM spectromicroscopy has been shown in Ref. 11, in which unknown impurities in NpO_2 particles were identified in a non-destructive manner to avoid the need for chemical processing and the generation of any transuranic mixed waste. STXM elemental maps and NEXAFS spectra of the small particles from the bulk powder material were used to identify the impurities (carbon and silicon) and their concentrations, which validated the results from another analytical spectroscopy (Figure 2). Additionally, the spectroscopic results also provided insight as to the chemical nature of the carbon and silicon species, which was used to trace the chemical history of the particulate materials.

The MES STXM is quite versatile (as illustrated in Figure 1) and can be applied to actinide-related environmental studies involving other radionuclides of importance, and to radionuclides in complex materials matrices. Foremost among the priorities is extension to new environmental materials systems and in particular, to glass and extended molecular structures that will build on our earlier fundamental studies and expertise in these materials systems. The utility of MES STXM spectromicroscopy for environmental science investigations of non-actinide radionuclides and matrixes is illustrated by preliminary characterization that has been performed on cesium in synthetic clay matrixes mirroring those from Fukushima, Japan as shown in Figure 3.[12]

The future prospects for soft x-ray synchrotron radiation STXM spectromicroscopy investigations in the fields of actinide and radionuclide environmental science are excellent, especially for the study of particulates and for the direct determination of light atom interactions with metal centers. The construction of new STXM end stations at increasingly capable soft x-ray beamlines will increase the availability of experimental time and coupled with constantly-improving instrument technical characteristics, will provide multiple, new scientific opportunities for actinide environmental science in the near future. Anticipated STXM enhancements in the near future include regular tomography, ptychography for true nanoscale spatial resolution, novel reaction cells for in-situ and in-operando chemistry, and fluorescence detection.[13] Lastly, synchrotron radiation-based STXM will establish a scientific foundation for future actinide environmental science activities based on x-ray instrumentation

that will emerge as new laboratory-based photon sources and new light source facilities become available.

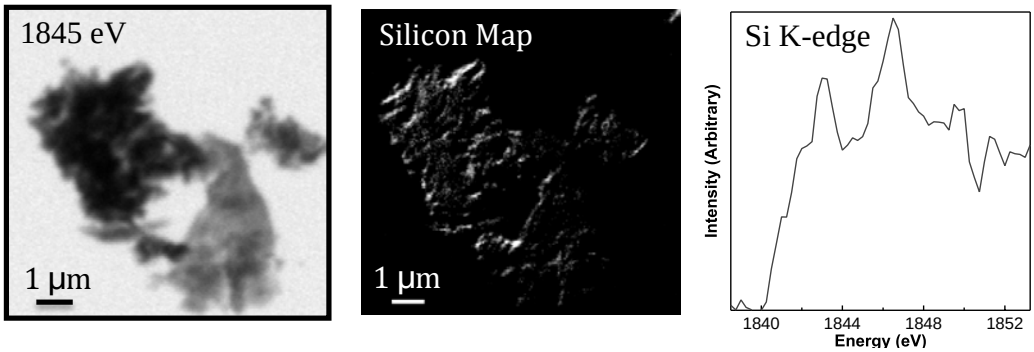

Figure 2. STXM normal x-ray image collected at 1846 eV (left) and a silicon elemental map (center) obtained from NpO_2 particles by the use of the Si K-edge with a gray scale contrast (white regions indicate areas of silicon contamination in the NpO_2 particles). From the Si K-edge NEXAFS spectral intensities (right), the content of Si in the NpO_2 can be determined.[11]

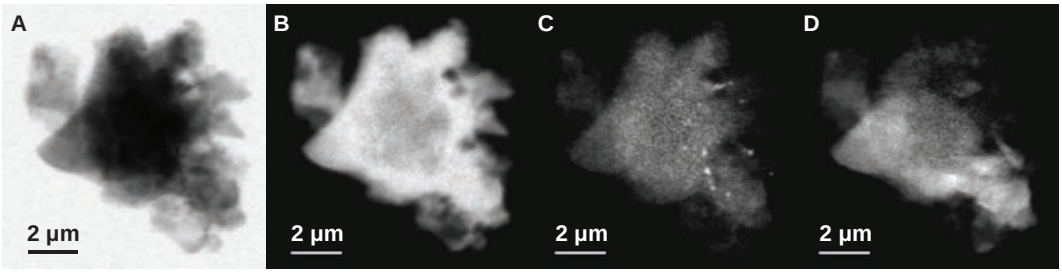

Figure 3. MES STXM data collected from a simulated and synthetically-prepared Fukushima clay (Sample 2) exposed to cesium. (A) normal x-ray image; (B) an oxygen elemental map obtained from the O K-edge; (C) an iron elemental map from the Fe L_3-edge; and (D) a cesium map enabled by the Cs M_5-edge. White regions in the elemental maps indicate areas of high elemental concentration within a standard image gray scale.[12]

References

[1] www.http://beamline1102.als.lbl.gov/

[2] H. Bluhm, K. Andersson, T. Araki, K. Benzerara, G. E. Brown, Jr., J. J. Dynes, S. Ghosal, H.-Ch. Hansen, J. C. Hemminger, A. P. Hitchcock, G. Ketteler, E. Kneedler, J. R. Lawrence, G. G. Leppard, J. Majzlam, B. S. Mun, S. C. B. Myneni, A. Nilsson, H. Ogasawara, D. F. Ogletree, K. Pecher, D. K. Shuh, M. Salmeron, B. Tonner, T. Tyliszczak, and T. H. Yoon, J. Electron Spectros. Rel. Phenom. **150**, 86-104 (2006).

[3] D. K. Shuh, "Scientific Capabilities of the Advanced Light Source for Radioactive Materials," in Speciation, Techniques and Facilities for Radioactive Materials at Synchrotron Light Sources, OECD NEA Workshop Proceedings, Karlsruhe, Germany, September (2006); OECD NEA **6288**, 125-134, (2007).

[4] H. J. Nilsson, T. Tyliszczak, R. E. Wilson, L. Werme, and D. K. Shuh, J. Anal. Bioanal. Chem. **383**, 41-47 (2005).

[5] H. J. Nilsson, T. Tyliszczak, R. E. Wilson, L. Werme, and D. K. Shuh, "Soft X-ray Spectromicroscopy of Actinide Particulates," in Recent Advances in Actinide Science, Ed. R. Alvarez, N. D. Bryan, and I. May, (Proc. Royal Soc. Chem.: Cambridge, U.K. 2006) pp. 56-58.

[6] P.-Anders Glans, G. Szigethy, D. Demoin, T. Tyliszczak, J. Xu, J. Guo, K. N. Raymond, and D. K. Shuh, Mater. Res. Soc. Symp. Proc. **1264**, BB06-05 (2010).

[7] R. Dähn, M. Vespa, T. Tyliszczak, E. Wieland, and D. K. Shuh, Environ. Sci. Technol. **45**, 2021-2027 (2011).

[8] S. G. Minasian, J. M. Keith, E. R. Batista, K. S. Boland, J. A. Bradley, S. R. Daly, D. Sokaras, S. A. Kozimor, W. W. Lukens, R. L. Martin, D. Nordlund, G. T. Seidler, D. K. Shuh, T. Tyliszczak, G. Wagner, T.-C. Weng, and P. Yang, J. Amer. Chem. Soc. **135**, 1864-1871 (2013).

[9] S. G. Minasian, S. A. Kozimor, D. K. Shuh, et. al., unpublished data, (2013).

[10] Y. Yang, J. E. Saiers, N. Xu, S. G. Minasian, T. Tyliszczak, S. A. Kozimor, D. K. Shuh, and M. O. Barnett, Environ. Sci. Technol. **46**, 5931-5938 (2012).

[11] C. T. Angell, T. H. Bray, R. Yee, R. Copping, P.-Anders Glans, T. Joshi, A. Klimenko, S. Korbly, W. D. Kulp, E. B. Norman, D. K. Shuh, E. Swanberg, G. A. Warren, and C. Wilson, Phys. Rev. C **82**, 054310 (2010).

[12] T. Yaita, S. Suzuki, S. G. Minasian, S. A. Kozimor, and D. K. Shuh, unpublished results (2013).

[13] A. P. Hitchcock, M. Orst, J. Wang, Y. S. Lu, and T. Tyliszczak, Environ. Sci. Technol. **46** 2821-2829 (2012).

2-03

Plutonium reactivity at the mineral/water interface

Moritz Schmidt[1], Karah Knope[2], Sang Soo Lee[2], Francesco Bellucci[2], Richard Wilson[2], Joanne Stubbs[3], Peter Eng[3], Paul Fenter[2], L. Soderholm[2]

[1]Karlsruhe Institute of Technology, Institute for Nuclear Waste Disposal, Karlsruhe, Germany, [2]Argonne National Laboratory, Chemical Sciences and Engineering, Argonne, IL, USA, [3]University of Chicago, Consortium for Advanced Radiation Sources, Chicago, IL, USA

Introduction

Reliable long-term predictions about the safety of a potential nuclear waste repository must be based on a sound, molecular-level comprehension of the geochemical behaviour of the radionuclides. Especially, their reactivity at the water/mineral interface will control their mobility and thus hazard potential. In order to be able to understand these processes analytical techniques that allow selectively probing the mineral/water interface and elucidating processes at the interface under *in situ* conditions are required. X-ray reflectivity techniques, such as crystal truncation rod (CTR) measurements and resonant-anomalous x-ray reflectivity (RAXR) have proven to be valuable tools for geochemical studies concerning reactions in the interfacial regime.[1]

Here we present a comprehensive study of the interactions, reactions, and structures of the actinides plutonium and thorium with the mineral muscovite. Muscovite is an alumina-silicate mineral from the mica family that exhibits a tetrahedron-octahedron-tetrahedron (TOT) layering, which is also a common structural motif in many clay minerals. However, muscovite grows into large single crystals with near-ideal surface cleavage parallel to the (001) basal plane, making an ideal model substance for x-ray reflectivity, as well as other surface studies. Plutonium is a major concern among the actinide elements, due to its high radiotoxicity and abundance in the nuclear waste. Plutonium geochemistry is complicated by the lack of natural analogues, as well as its complex aqueous chemistry and the accessibility of multiple redox states.

Results

In order to understand the complex behaviour of trivalent plutonium at the muscovite (001) surface we will present results of three recent studies. Firstly, the sorption of Th(IV) will be discussed as a strongly hydrated, hydrolysable actinide ion, while excluding any redox reactivity. CTR and RAXR data show that Th(IV) adsorbs as an extended outer sphere complex on the muscovite basal plane[2], i.e. an adsorbed complex sustaining two intact hydration shells.[3] In this adsorption state Th maintains a high degree of mobility close to the interface[2]. Supporting uptake measurements by alpha-spectrometry show that at high concentrations the adsorption of predominantly monomeric species is replaced by the formation and adsorption of thorium oligomers[2].

In a second part, the sorption behaviour of Pu(IV)-oxo-nanoparticles will be presented.[4] Pre-formed entities of well-defined, approx. 10Å sized $[Pu_{38}O_{56}]^{40+}$-nanoparticles adsorb strongly at the muscovite basal plane, forming one well-defined layer close to the interface as well as a second very large layer (>70Å) of aggregated nanoparticles. In the vicinity of the nanoparticles a distinct layering of counterions can be observed[4].

This data can subsequently be used to understand the more complex interfacial reactivity of trivalent plutonium. We will present evidence from CTR and RAXR, as well as AFM, alpha-spectrometry, and x-ray absorption spectroscopy (XAS), revealing a surface catalysed Pu(IV)-oxo-nanoparticle reaction, resulting in a structure very similar to what had been observed upon adsorption of pre-formed nanoparticles.

References

[1] P. Fenter, *Reviews in Mineralogy and Geochemistry* **2002**, *49*, 149-220.

[2] M. Schmidt et al., *Geochim. Cosmochim. Acta* **2012**, *88*, 66-76.

[3] S. S. Lee et al., *Langmuir* **2010**, *26*, 16647-16651.

[4] M. Schmidt et al., *Langmuir* **2012**, *28*, 2620-2627.

2-25

Isotopic Composition of Uranium and Activity Concentration of $^{134, 137}$Cs in Aerosol Samples Collected at 120 km from Fukushima before and after the Reactor Accidents

Taeko Shinonaga[1], Peter Steier[2], Markus Lagos[3], Takehisa Ohkura[4]

[1]Helmholtz Zentrum München, German Research Center for Environmental Health, Institute of Radiation Protection, Munich, Germany, [2]VERA Laboratory, Fakulität für Physik, Isotopenforschung, Universität Wien, Vienna, Austria, [3]Karlsruher Institut für Technologie (KIT), Institut für Nukleare Entsorgung, Karlsruhe, Germany, [4]Department of Radiation Protection, Nuclear Science Research Institute, Tokai Research and Development Center, Japan Atomic Energy Agency, Ibaraki, Japan

The recent catastrophic Tohoku Earthquake (moment magnitude 9.0) occurred on March 11, 2011 at 14 :46 (JST: UTC+9) generated huge tsunamis (>10 m) around the Pacific coast of the northeastern Japan and the tsunami hit the Fukushima Daiichi nuclear power plants (FDI-NPP). The first hydrogen explosion of the FDI-NPP_Unit 1 reactoroccurred on March 12, 2011, at 15:36 (JST), and Unit 3 reactor exposed on March 14, 2011 at 11:01 (JST). As results, a large amount of radioactive materials was released into the atmosphere. Following these catastrophes, the relating radioactive materials, mainly ^{131}I, ^{129m}Te, ^{132}Te, ^{134}Cs, ^{136}Cs and ^{137}Cs, in the environment were started to be analyzed.[1,2,3]. A high activity ratio of ^{241}Pu/$^{239+240}$Pu (>100) was found in soil and litter samples in a 20-30 km zone around the NPPs.[4] The data on actinides in aerosol samples is however rare compared with that on fission products.

To investigate the release of uranium (U) and radioactive cesium (Cs) in the atmosphere generated from the damaged reactors, we are analyzing isotopic compositions of U and activity concentration of ^{134}Cs and ^{137}Cs in the aerosol samples collected in Tokai, Japan (at 120 km south-southwest of the FDI-NPP) using accelerator mass spectrometry (AMS), sector-field inductively coupled plasma mass spectrometry (SF-ICPMS), and gamma spectrometry. The discussion on U in the atmosphere is focused on $n(^{236}U)/n(^{238}U)$ ratio measured by AMS, and $n(^{234}U)/n(^{238}U)$ and $n(^{235}U)/n(^{238}U)$ ratios measured by SF-ICPMS and AMS. Because the amount of natural uranium in aerosol samples as background is much smaller than that in, e.g., soil samples, it can be expected that the aerosol samples could be sensitive media to study non-natural U in the atmosphere.

Aerosol sampling system: The aerosol samples were collected with paper filter HE-40TA (Toyo Roshi Kaisha, Ltd.).[5]The active sampling area was 50 mm diameters and the flow rate of the sampling was 100 L/min. The sampling duration was typically 1 week and totally ca. 1000 m^3 aerosol was collected for each sample.

Gamma-ray measurements: The activity concentration of ^{134}Cs and ^{137}Cs was analyzed by gamma spectrometry. The results are shown in Figure 1. The activity concentration of ^{137}Cs before the accident was constantly below the detection limit ($8x10^{-6}$Bq m^{-3}), however high concentration (8 Bq m^{-3}) of ^{134}Cs and ^{137}Cs was detected after the accident, on March 15, 2011. The results show that the ratio of the activity concentration of ^{134}Cs and ^{137}Cs is 1:1, and both data lines in the figure are almost overlapping.

Uranium separation: Uranium in the filter samples was separated using commercially available ion exchange and ion chromatographic resins in nitrate system, and the second purification was performed in chloride system. The final fraction was prepared with $Fe(OH)_3$ co-precipitation for AMS measurements and was dissolved in 2% nitric acid for ICPMS measurements.

Measurements of ^{236}U by AMS: Isotopic ratio measurements of $n(^{236}U)/n(^{238}U)$ were performed by AMS with a tandem accelerator. Isotopic ratio detection limits $n(^{236}U)/n(^{238}U)$ of 10^{-13} can be achieved using this method.[6] The results are compared with the "natural background level" and the results of U isotopic ratios obtained by SF-ICPMS.

Measurements of uranium isotopic ratios by SF-ICPMS: The isotopic ratio of $n(^{234}U)/n(^{238}U)$ and $n(^{235}U)/n(^{238}U)$ was measured by SF-ICPMS. Non-natural U was found in the sample soon after the accident, and occasionally after that. The origin of the non-natural U is considered and discussed with the data on ^{236}U.

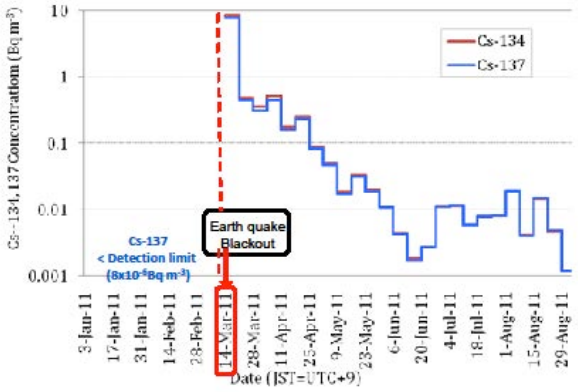

Figure 1 Activity concentration of ^{134}Cs and ^{137}Cs in aerosol samples before (^{137}Cs) and after the accident. The data lines of ^{134}Cs and ^{137}Cs are almost overlapping. The dotted line indicates the boundary line (11. March, 2011) before and after the accident.

Summary: Non-natural U was found in several aerosol samples collected after the FDI-NPP accident. The origin and the behavior of the non-natural U in the aerosol samples are verified using all data obtained in this study and literature values.

References

1 O. Masson, et al., *Environ. Sci. Technol., 2011*, **45**, 7670.
2 G.A. Wetherbee et al., *Environ. Sci. Technol., 2011*, **45**, 2574.
3 J.M. Schwantes et al., *Environ. Sci. Technol., 2012*, **46**, 8621.
4 J. Zheng et al. *SCIENTIFIC REPORTS, 2012*, 2:304.
5 N. Kinouchi et al., *Hokenbutsuri, 1995*, **30**, 309. (in Japanese, abstract in English)
6 P. Steier, et al., Nucl. Instrum. Methods. Phys., 2010, **44**, 1045.

2-26

Interaction of plutonium with magnetite under anoxic conditions: Reduction, surface complexation, and structural incorporation

Andreas C. Scheinost[1], Regina Kirsch[1], Thomas Dumas[1], David Fellhauer[2], Xavier Gaona[3], Marcus Altmaier[3]

[1]HZDR Inst. for Resource Ecology, Dresden, Germany, [2]JRC Inst. for Transuranium Elements, Karlsruhe, Germany, [3]KIT Inst. f. nukleare Entsorgung, Karlsruhe, Germany

For the redox-reactive fission products and actinides Se, Tc, U, and Np, it is assumed that the strongly reducing conditions in deep underground, anoxic nuclear waste repositories will reduce their mobility, since their lower-oxidation states commonly form solids of very low solubility. This is not necessarily the case for Pu, where the hexa- and pentavalent aquo-complexes prevalent at higher pe are replaced at lower pe by a tetravalent solid of low solubility, PuO_2, but also by a trivalent aquocomplex at lower pH (Fig. 1) [1, 2]. Since the predominance field of Pu(III)aq overlaps with that obtained for the Fe(II)/Fe(III) redox couple as aqueous species or in equilibrium with Fe(II)-bearing minerals [3], one should assume that Pu(III) exists under anoxic nuclear waste conditions, where Fe(II) sources are provided by corroding steel containers and Fe(II)-bearing clays used as confinement, as well as by geogenic minerals. Although some studies have previously reported on trivalent lanthanides, little is known on the retention mechanisms of the trivalent Pu aquo complex by minerals, with implications for the safety case of nuclear waste repositories.

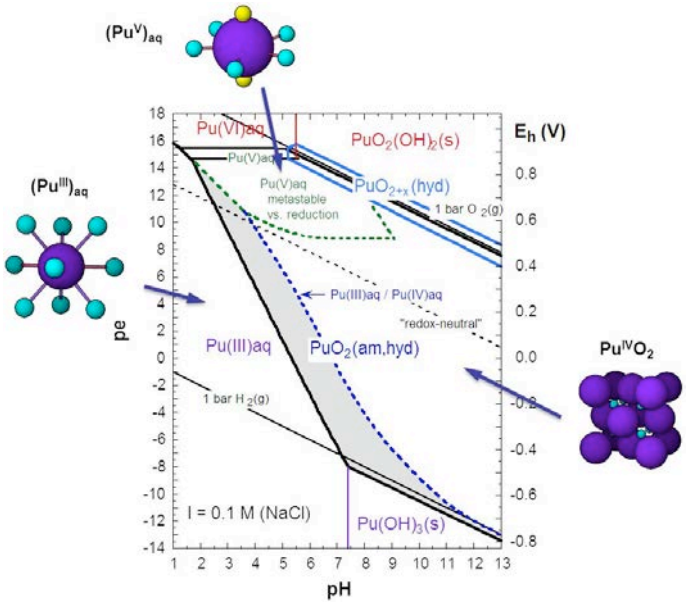

Fig. 1. Pe-pH predominance diagram for Pu calculated with thermodynamic data from NEA-TDB [5] and Neck et al. [2] for 0.1 M NaCl and $2x10^{-5}$ M Pu, along with ball-and-stick models of the most prevalent species.

Magnetite, $Fe^{III}_2Fe^{II}O_4$, is an important mineral in this context, since it forms by steel corrosion under anoxic conditions and is also prevalent as geogenic mineral. Especially as nano-particles and at close-to-stoichiometric Fe(II)/Fe(III) ratios of 0.5, it is a fast and efficient reducer of, e.g. Se, Tc, U, and Np [3, 4, 6]. The purpose of our studies was, therefore, to investigate the redox behaviour of Pu with nanoparticulate magnetite under strictly anoxic conditions.

We monitored the oxidation state of Pu with X-ray Absorption Near-Edge Structure (XANES) spectroscopy and used Extended X-ray Absorption Fine-Structure (EXAFS) spectroscopy to investigate the molecular structure around Pu in order to gain insight into the Pu uptake mechanism by magnetite. Pu-L_{III} edge XANES and EXAFS spectra were collected under

cryogenic conditions (15 K) in fluorescence mode using a 13-element high-purity Ge energy-dispersive detector at the Rossendorf Beamline at ESRF, Grenoble (France). Both sorption and coprecipitation experiments were conducted at the KIT-INE laboratories (Karlsruhe, Germany) using well characterized (UV-VIS), single-valent ^{242}Pu(V) and ^{242}Pu(III) stock solutions prepared electrochemically [7].

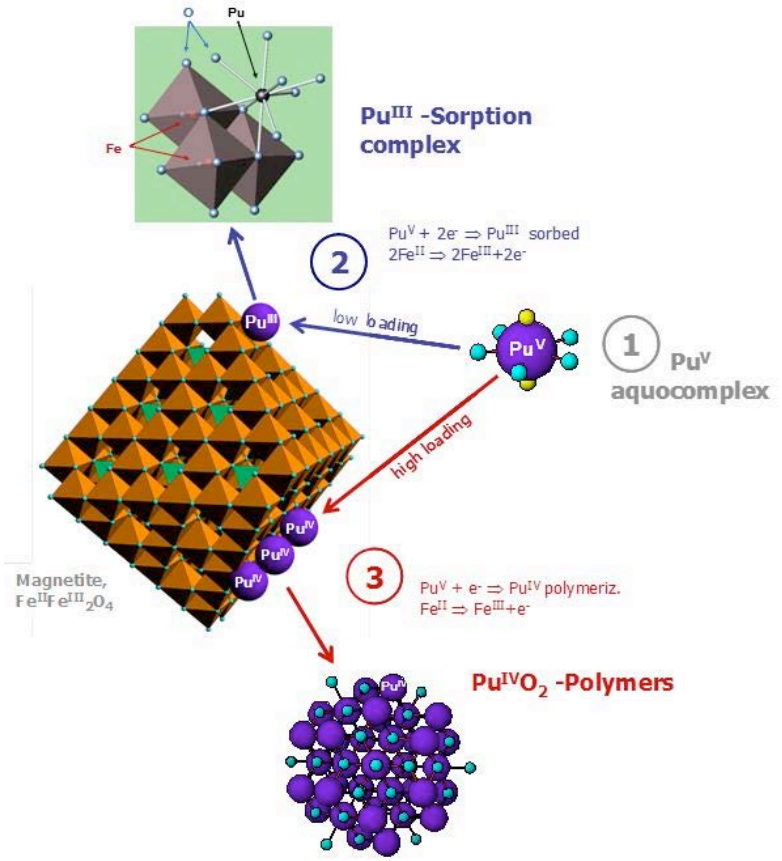

Fig. 2. Pu(V) uptake mechanisms by magnetite as depending on surface loading.

Pu sorption experiments to magnetite were conducted in the pH range 6-8 in 0.1 M NaCl and across an equilibration period between 1 and 8 months. Pu loadings varied between 30 and 75 nmol/m^2. Aqueous Pu concentrations dropped within 30 min. to values near or below the detection limit of LSC (10^{-9} M), hence uptake levels were at least 99.85%. In terms of oxidation state and molecular structure, there seems to be a clear distinction by surface loading. For all experiments with Pu loadings of 55 nmol/m^2 or lower, XANES showed that the final Pu oxidation state was always III. In order to elucidate the molecular structure, we employed FEFF-Monte Carlo simulations of the EXAFS spectra [8]. Plutonium was found to occupy a unique crystallographic position at the octahedrally terminated {111} faces constituting the predominant part of the magnetite surface. The nine-coordinated Pu(III) atom is sharing three oxygen atoms with the magnetite surface, forming a tridentate, trinuclear, triple edge-sharing surface complex (Fig. 2, 2) [7]. For the one sample with a Pu surface loading of 75 nmol/m^2, however, XANES showed a mixed oxidation state of 70% Pu(III) and 30% Pu(IV). Using a linear combination fit with the EXAFS spectra of the pure Pu(III) sorption complex and a PuO_2 reference, we could accurately reproduce the experimental EXAFS spectrum, and obtained also the 70/30 weight distribution already suggested by XANES [9]. Therefore, there exist two different reaction pathways as depicted in Fig. 2, one leading to formation of a tridentate Pu(III) surface complex at lower loading, and a second one leading to precipitation of PuO_2 polymers, at higher surface loading. This latter process is in line with previous work, where formation of PuO_2 was determined at the surface of Fe oxides [10]. In the absence of oxygen, the ultimate driving force for one or the other process may not be the surface loading, but instead the Pu solution activity and the competition of the two species for

Pu in solution. As long as the formation of the Pu(III) surface complex results in a Pu activity below the solubility of PuO_2, no PuO_2 is expected to precipitate. Due to Pu concentrations at or below the detection limit of the employed LSC method, this hypothesis could not be verified experimentally.

The 9-fold coordination of Pu(III) corresponds most likely to the tricapped prismatic structure of the early trivalent lanthanides, although the distal resolution of EXAFS was not sufficient to resolve this feature [11]. Although their ionic radii are about 1.4 times larger than that of Fe(III) (1.15-1.17 vs. 0.79 Å in six-fold coordination), trivalent lanthanides have been shown to substitute for Fe(III) in magnetite [12]. Thus Pu(III) with an ionic radius of 1.15 Å may also be able to become entrapped in the magnetite structure. This seems to be even more likely considering the already highly ordered structure of the surface complex. This structural uptake may proceed either by homogeneous coprecipiation of Pu with dissolved Fe, or by a heterogeneous surface process, where sorbed Pu(III) becomes entrapped after additional sorption of Fe(II) or by a recrystallization of the magnetite surface. The latter surface-driven processes were not observed within the duration of our longest sorption experiments (8 months), but cannot be excluded to happen during the geologic time-scales relevant because of the long half-lifes of Pu radionuclides. In order to simulate these processes we used a double approach, first a homogeneous coprecipitation, and second a Fe(II)-induced aging following the method of Boland et al. [13]. The Fe(II)-induced aging has been shown to be able to induce a substantial recrystallization of the solid phase, but can also be used as a model to simulate the entrapment of sorbed Pu by sorption of Fe. Two Pu loadings of 1000 and 3500 ppm were used for these experiments.

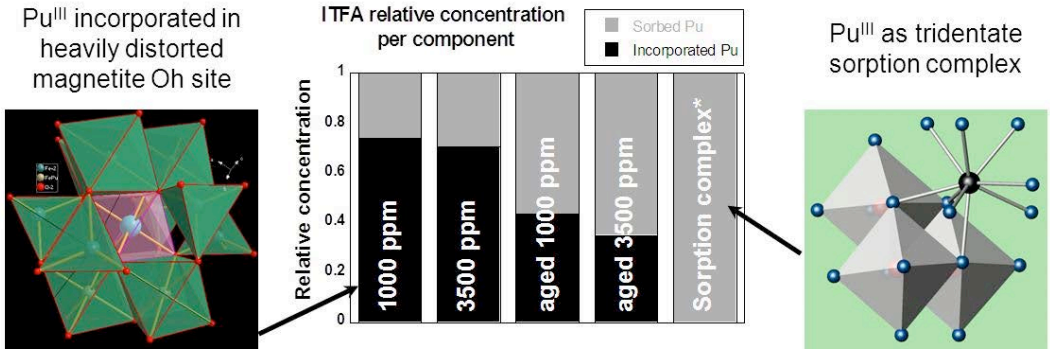

Fig. 3. Relative concentrations of Pu(III) incorporated by and sorbed to magnetite after initial coprecipitation and after aging.

UV-VIS spectroscopy showed an immediate reduction of Pu(V) to Pu(III) in the initial Fe(II)/Fe(III) chloride solution. After formation of the black magnetite precipitate, Pu(III) concentration in solution was below 10^{-9} M. XANES spectroscopy confirmed the trivalent oxidation state of solid phase-associated Pu. EXAFS spectroscopy was then used to investigate the molecular structure of incorporated Pu(III) in the fresh precipitate as well as after Fe(II)-induced aging. The EXAFS spectra revealed two different spectral components. The first component represents the tridentate Pu(III) sorption complex also observed during sorption experiments. The second component represents Pu(III) in a highly distorted magnetite Oh site. The proportion of the incorporated Pu(III) decreased from about 75% to 40% with Fe(II)-induced aging, while the proportion of sorbed Pu(III) increased correspondingly (Fig. 3) [14]. Our results suggest that Pu may be (partly) incorporated by magnetite through rapid coprecipitation processes, thereby confirming earlier results on lanthanide-doped magnetite. On the long term, however, there seems to be a tendency to expel Pu(III) from the structure. This observation is easily explained by an ionic radius 1.4 times larger than that of Fe(III) in magnetite, which makes its incorporation energetically unfavourable. Therefore, for understanding and modelling sorption processes affecting the migration of Pu from anoxic nuclear waste repositories, the tridentate Pu(III) surface complex is more relevant.

References

[1] Rai *et al.* (2002) *J. Sol. Chem.* **31**, 433-453.

[2] Neck *et al.* (2007) *C. R. Chim. (France)* **10**, 959-977.

[3] Kobayashi *et al.* (2013) *Radiochim. Acta*, in press.

[4] Scheinost *et al.* (2008) *J. Contam. Hydrol.* **102**, 228-245.

[5] Guillaumont *et al.* (2003) *Elsevier, Amsterdam*.

[6] Latta *et al.* (2012) *Environ. Sci. Technol.* **46**, 778-786.

[7] Kirsch *et al.* (2011) *Environ. Sci. Technol.* **45**, 7267–7274.

[8] Rossberg & Scheinost (2005) *Anal. Bioanal. Chem.* **383**, 56-66.

[9] Kirsch *et al.* (2013) manuscript in preparation.

[10] Romanchuk *et al.* (2011) *Radiochim. Acta* **99**, 137-144.

[11] Sobolev et al. (2011) *Phys. Status Solidi* **A 208**, 2293-2298.

[12] Moon *et al.* (2007) *Extremophiles* **11**, 859-867.

[13] Boland *et al.* (2011) *Environ. Sci. Technol.* **45**, 1327-1333.

[14] Dumas *et al.* (2013) manuscript in preparation.

4-22

Neptunium Biogeochemistry in Systems Representative of the Nuclear Legacy

Gareth Law[1], Clare Thorpe[1], Pieter Bots[1], Sam Shaw[1], Jon Lloyd[1], Francis Livens[1], Melissa Denecke[2], Jorg Rothe[2], Kathy Dardenne[2], Diana Brookshaw[1], Katherine Morris[0]

[1]The University of Manchester, Manchester, UK, [2]KIT-INE, Karlsruhe, Germany

Neptunium is a key risk-driving radionuclide in radioactive waste geological disposal and it is becoming increasingly apparent that microbially-mediated redox cycling is pertinant to geodisposal impacted environments [1]. In addition, Np (as NpO_2^+) is predicted to be the most mobile transuranic element in the shallow sub-surface at nuclear contaminated sites; however, when compared to other radionuclides, there is a paucity of information concerning neptunium's environmental behavior. This is particularly true when one considers: (i) the biogeochemical interactions of Np with the Mn and Fe cycles (ubiquitous elements implicated in actinide biogeochemical cycling [e.g. 2, 3]), and (ii) potential Np redox cycling under alkaline (pH > 10) conditions relevant to cementitious geological disposal facilities and their surrounding environments.

To further explore these relationships, in recent years we have characterised Np biogeochemical behaviour in a range of Fe and Mn dominated experimental systems, at both circumneutral pH and (in select systems) pH 10-13. This has included work with: bioreducing Mn-poor / Fe-rich sediment systems; Mn-rich sediment systems; synthetic Fe and Mn mineral systems (2-line ferrihydrite, goethite (αFeO(OH)), hematite (Fe_2O_3), magnetite (Fe_3O_4), vivianite ($Fe_3(PO_4)_2.8H_2O$), δMnO_2, tri-clinic birnessite and acid birnessite (Mn(III/IV)-oxides), hausmannite (Mn(II/III)oxide), and rhodochrosite ($MnCO_3$)); and Fe bearing silicates (biotite and chlorite) that had previously been exposed to model Fe-reducing microorganisms. In all cases, work was conducted at both low and high Np loadings (0.3 µM and 0.3 mM ^{237}Np, respectively), using freshly produced NpO_2^+ added to simulant groundwaters at concentrations below saturation. Thereafter, during a timecourse of sampling, aqueous Np was tracked by ICP-MS or LSA alongside any evolving stable element geochemistry. Soilds were also sampled under anaerobic conditions from select (0.3 mM ^{237}Np) systems for XAS analsysis. Here, EXAFS and XANES analysis were used to elucidate the Np-oxidation state and coordination environment, with data collected from the Np L_{III}-edge (17.610 keV) at ambient temperature in fluorescence mode by a 5 pixel solid-state detector (LEGe Canberra), using Ge(422) monochromator crystals on the ANKA Synchrotron INE beamline.

Taken together, data from these systems provides an unprecedented insight into the subtleties of Np biogeochemistry and highlights from each experiment will be presented. This will include:

- Results from microcosm experiments conducted with Mn-poor / Fe-rich sediments where Np removal from solution was accelerated comensurate with microbially mediated metal reduction (Mn(II) and Fe(II) ingrowth measurable) and XAS analysis of the sediments revealed reduction of Np(V) to insoluble Np(IV) [3]. Further, work with analogue sterilie sediments from this system indicated that Np(V) reduction was likely facilitated through abiotic reaction with Fe(II).
- Results from microcosm experiments conducted with Mn-rich sediments that underwent Mn reduction without measureable Fe(II) ingrowth, during which Np removal from solution was accelerated. Here, XAS analysis (Figure 1) revealed that Np(V) was wholly reduced to Np(IV) concomitant with Mn-reducing conditions although it was not clear whether reduction was directly (enzymatically) facilitated by the indigenious bacteria or whether a indirect, redox reaction dominated.
- Results from Fe and Mn pure-mineral systems conducted at circumneutral pH where Np reactivity varied considerably across the range of minerals with evidence for abiotic reduction in all Fe(II)-bearing systems and some evidence from Np(V) reduction in Mn(II/III)-bearing phases.
- Results from Fe mineral systems at pH 10 and 13 that showed a combination of sorption and potential incoporation of Np(V) or Np(IV) into Fe-mineral lattice sites dependant upon the system of study.

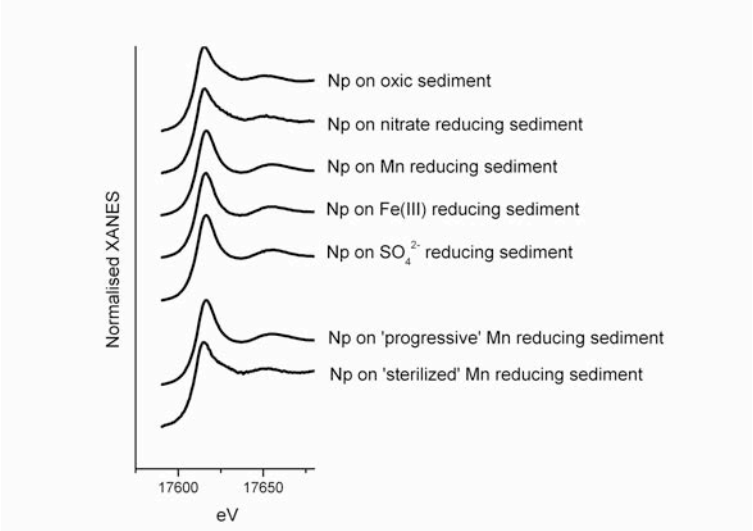

Figure 1. Np L_{III}–edge XANES spectra for Np amended sediments under different biological conditions. Spectra from oxic sediment, nitrate reducing sediment, and sterilized Mn-reduced sediment samples showed a Np(V) like multiple scattering resonance structure resulting from high energy scattering along the axial oxygens of the linear neptunyl moiety. Spectra from Mn reducing, Fe(III) reducing, sulfate reducing, and progressive Mn reducing sediment samples were more typical of Np(IV) XANES.

References

[1] T. Rizoulis, et al., Min. Mag. 26, 3621 (2012).

[2] G. T. W. Law, et al., Env. Sci. Tecnol. 44, 8924 (2010).

[3] B. A. Powell, et al., Env. Sci. Tecnol. 40, 3508 (2006).

4-23

Effect of organic acids on the adsorption and reduction of uranium(VI) by microorganisms

Toshihiko Ohnuki[1], Yoshinori Suzuki[2]

[1]Japan Atomic Energy Agency, Tokai, Ibaraki, Japan, [2]Tokyo University of Technology, Hachioji, Tokyo, Japan

The presence of actinides (ANs) in radioactive wastes is a major environmental concern due to their long radioactive half-lives, and its chemical toxicity. In order to estimate the mobility of ANs several studies examined its interactions with soils and subsoils composed of abiotic and biotic components, principally minerals and bacteria. Among the biotic components, several microorganisms have been shown to sorb ANs. The high capacity of microbial surfaces to bind ANs may affect the migration of ANs in the environment. Unfortunately, we have only limited knowledge of the role of microorganisms in the migration of ANs in the environment.

The radioactive wastes often include strong complexation reagents used as decontaminants, e.g. citric acid, nitrilotriacetic acid (NTA) and ethylenediaminetetraacetic acid (EDTA). Organic acids which form strong complex with U also exist in the environment. These organic acids can affect the sorption, precipitation and redox behavior of U by forming stable complexes. We have conducted the study of interaction of U(VI) with microorganisms in the presence of organic acids.

In the resting condition, U(VI) is adsorbed on the cell surface of microorganisms in the solution in the absence of organic acids. On the contrary, lower fractions of U(VI) was adsorbed on the cell surface in the solution containing organic acids. When U(VI) and lactic acid were supplied as a sole electron acceptor and a donor, respectively, under anaerobic condition at 30 °C at initial pH 7.0, *Shewanella putrefaciens* decreased the concentration of U in the solution up to approximately 10% within 24 hrs. SEM and XANES analysis indicated the formation of U(IV) precipitates around cell surface. In the presence of citrate, NTA, or EDTA, the concentrations of dissolved U scarcely changed. The UV-VIS spectra of the media showed that concentrations of U(VI) species decreased and those of U(IV) species increased with time. These results indicate that the presence of the strong complexation agents inhibit the biological reductive UO_2 precipitation by forming the soluble U(IV)-organic complexes The initial reduction rate of U(VI) in the citrate medium in which polynuclear U(VI)-citrate complex were formed was much slower than those in the NTA and EDTA media. Formation of the polynuclear complexes may be one of the reason for retardation of the U(VI) reduction by *S. putrefaciens*. Our results indicate that the presence of strong complexation reagents affect the chemical species of U(IV) and the reduction rate of U(VI).

ORAL

2-06

Sorption of uranium on lead hydroxyapatite

Karin Popa

'Alexandru Ioan Cuza' University, Iasi, Romania

Due to the extensive mining, milling, and enriching activities, important amounts of uranium were released into the environment [1]. With the decontamination purpose, the sorption capacity of lead hydrohyapatite [$Pb_{10}(PO_4)_6(OH)_2$] toward uranium was tested with the purpose of reducing the cost of the sorption process.

Lead hydroxyapatite is a highly-insoluble phase, with an important specific surface, which is easily produced as partially crystallised compound by direct precipitation from $PbCl_2$ and $(NH_4)_2HPO_4$ and subsequent heating of the gel at 110 ^oC. During the thermal treatment (110÷500 ^oC), the crystallinity increase, but the specific surface dramatically decrease (192±5 m^2/g and 45±3 m^2/g at 110 ^oC and 500 ^oC, respectively). This is why the product obtained at 110 ^oC was considered for further uranium sorption studies.

The sorption of the uranium from aqueous solution (pH = 5.65) was studied using a batch experiment by contacting 0.1 g solid phase with 100 ml uranium nitrate solution of $5 \cdot 10^{-6}$ M at pre-seated temperatures (4, 20, 40, and 60 ^oC) under continuous stirring.

Fluorimetric determination of uranium was performed by measuring the delayed fluorescence intensity of the uranyl ions (λ= 530 nm) excited by UV radiation in the residual solution. The method was validated in the measuring range 0.1-2.0 ppm by comparing the fluorimetric and the colorimetric results for the same solution (over 100 parallel determinations).

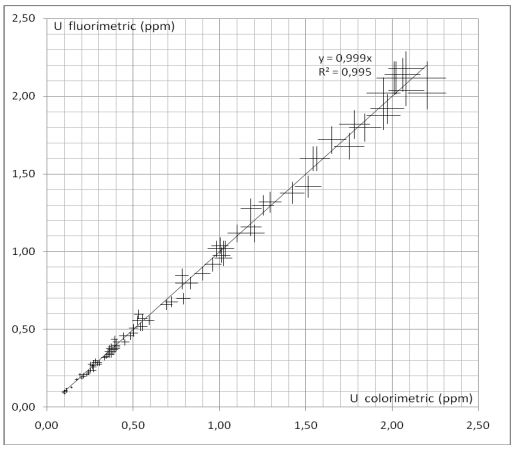

In order to assess the performance of the sorption process, the distribution coefficient was used: $K_d=[(C_i-C_t)/C_t]\cdot V/m$, where C_i and C_t represent the uranium concentrations in the initial solution and in the solution at time *t*, respectively, while the ratio *V/m* is the batch factor.

At all the studied temperatures, a rapid increase of K_d in the first minutes of contact can be observed and the equilibrium values are very fast attained ($K_{d,\ max}$ increase from 5,661 to18,833 ml/g, at 4 ^oC and 60 ^oC, respectively after one hour contact time). The sorption process is mostly due to the reactive surface of the lead hydrohyapatite, as in the case of calcium hydroxyapatite [2]. Although the maximum uptake capacity of lead hydrohyapatite is far lower than for other sorbents [3-5], this material is cheep and easily to obtained in any chemical unit. Moreover, this uranium concentration corresponds to the order of magnitude found in real cases, such as effluents resulted from mining, milling and reprocessing uranium facilities.

The thermodynamic parameters calculated for this sorption system are: ΔH^o = 15.96 kJ/mol, ΔS^o = 0.13 kJ/K·mol, and ΔG^o = - 19.87 kJ/mol (4 ^oC), ΔG^o = - 21.94 kJ/mol (20 ^oC), ΔG^o = - 24.53 kJ/mol (40 ^oC), and ΔG^o = - 27.12 kJ/mol (60 ^oC).

Retention of uranium from aqueous solution on lead hydroxyapatite would be of interest in further studies in view of concluding on the recycling performance of this sorbent. Also, the influence of competing ions would be of interest to be investigated.

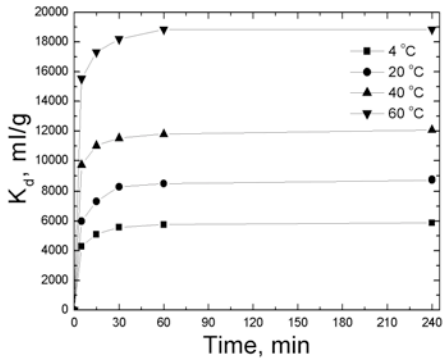

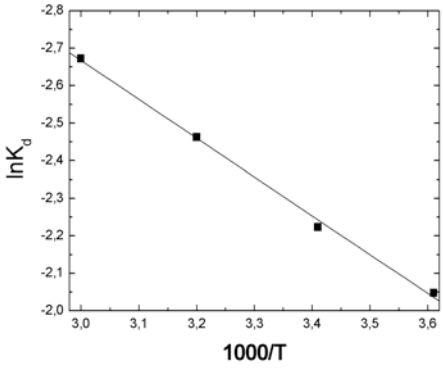

References:

[1] Sachs S, Bernhart G (2011) Influence of humic acids on the actinide migration in the environment: suitable humic acid model substances and their application in studies with uranium- a review. J. Radioanal. Nucl. Chem. 290(1): 17-29.

[2] Krestou A, Xenidis A, Panias D (2004) Mechanism of aqueous uranium(VI) uptake by hydroxyapatite. Miner. Eng. 17(3): 373-381.

[3] Jeanjean J, Rouchaud JC, Tran L, Fedoroff M (1995) Sorption of uranium and other heavy metals on hydroxyapatite. J. Radioanal. Nucl. Chem. 201(6): 529-539.

[4] Humelnicu D, Drochioiu G, Sturza MI, Cecal A, Popa K (2006) Kinetic and thermodynamic aspects of U(VI) and Th(IV) sorption on a zeolitic volcanic tuff. J. Radioanal. Nucl. Chem. 270(3): 637-640.

[5] Ulusoy U, Akkaya R (2009) Adsorptive features of polyacrylamide-apatite composite for Pb^{2+}, UO_2^{2+} and Th^{4+}. J. Hazard. Mater. 163(1): 98-108.

2-07

A TRLFS study on the sorption of Cm(III) on natural kaolinite – The role of mineral dissolution in alkaline kaolinite suspensions

Nina Huittinen[1], Thomas Rabung[2], Andreas Schnurr[2], Martti Hakanen[1], Jukka Lehto[1], Horst Geckeis[2]

[1]Laboratory of Radiochemistry, Department of Chemistry, University of Helsinki, Helsinki, Finland, [2]Institute for Nuclear Waste Disposal, Karlsruhe Institute of Technology, Karlsruhe, Germany

Sorption of radionuclides on mineral surfaces is regarded as one of the dominant retardation processes in the near and far-fields of nuclear waste repositories. As potential host-rock or buffer and backfill materials in these repositories, clay minerals play an important role as sorbent phases for mobilized radionuclides in the geosphere. Kaolinite, $Al_2Si_2O_5(OH)_4$, is one of the most abundant aluminosilicate minerals with a 1:1 layered structure of alternating aluminum hydroxide octahedral and silica tetrahedral sheets that share a common plane of oxygen atoms.

We have studied the sorption and speciation of trivalent curium on natural kaolinite from St. Austell (UK) with a special focus on explaining the curium speciation on the mineral surface under alkaline solution conditions (pH > 10). Time-resolved laser fluorescence spectroscopic (TRLFS) investigations were performed under argon atmosphere (O_2<1 ppm) using a constant curium concentration, ionic strength and mineral content of 2×10^{-7} M, 1 mM $NaClO_4$ and 0.25 g/l, respectively, throughout the study.

Deconvolution analysis of recorded TRLFS spectra over the investigated pH range 3-12 shows the presence of four curium complexes on the kaolinite surface in addition to the free curium aquo ion, $Cm(H_2O)_9^{3+}$, Figure 1.

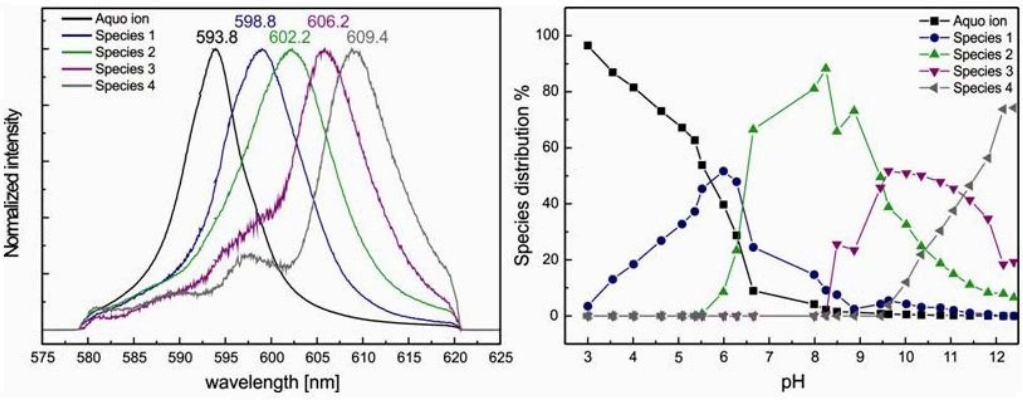

Figure 1. Pure component spectra (left) and the corresponding species distribution of Cm(III) sorption onto natural kaolinite (right) in 1 mM $NaClO_4$ derived by deconvolution of sum spectra [1].

Based on fluorescence lifetime data and the correlation of calculated curium solution complexes using the PhreeqC code [2] and spectroscopically derived Cm(III) surface complexes, species 1, 2, and 3 could be assigned to $>Cm(H_2O)_5^{2+}$, $>Cm(OH)(H_2O)_4^{+}$ and $>Cm(OH)_2(H_2O)_3$, respectively, on the kaolinite surface. Species 4, however, could not be assigned to the hydrolysis complex $>Cm(OH)_3(H_2O)_2^{-}$.

Due to the large bathochromic shift of the emission signal observed for species 4, we suggested that this curium species is formed through incorporation of curium by a precipitating aluminosiliceous phase of lower solubility than that of kaolinite, when the aluminium and silicon concentrations increase in solution upon kaolinite dissolution, Figure 2.

To confirm this hypothesis we performed oversaturation experiments, where excess amounts of aluminum, silicon, or a combination of both were added to alkaline kaolinite suspensions. Only silicon addition was found to influence the curium ligand-field under the experimental

conditions, Figure 3 (left), indicating an interaction of curium with dissolved/colloidal silicates that form in solution upon kaolinite mineral dissolution. In experiments with 10^{-3} M added silicon but no solid phase for curium attachment, only the hydrolysis species $Cm(OH)_2^+$ could be detected at pH 10 while no signal was obtained after increasing the pH to 11.5, Figure 3 (right). Thus, the formation of colloidal silicate species for the attachment of curium could be excluded and the observed species in alkaline kaolinite environments was assigned to a ternary kaolinite/curium/silicate complex forming between adsorbed curium at the mineral surface and dissolved silicates in solution.

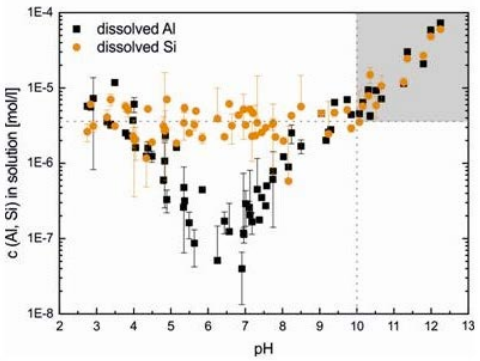

Figure 2. Concentrations of aluminum and silicon in 0.25 g/l kaolinite suspensions as a function of pH. Metal ion concentrations were determined with ICP-MS after equilibration times of at least 5 days.

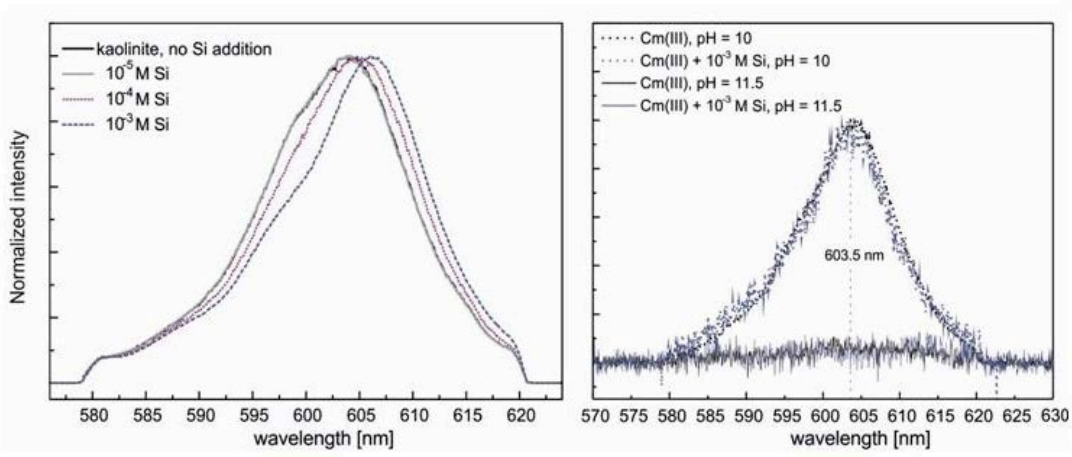

Figure 3. Left: Cm(III) emission spectra after addition of silicon to kaolinite suspensions at pH ~10. Right: Cm(III) emission spectra in the absence of kaolinite. No silicon addition (black spectra), 10^{-3} M silicon addition (blue spectra) [1].

A similar curium-silicate complex with identical spectroscopic features was also found in investigations with α-alumina as sorbent phase upon addition of silicon to the mineral suspensions, suggesting that silicon complexation with surface-bound curium is independent of the sorbent material.

References:

[1] Huittinen et al. (2012) New insight into Cm(III) interaction with kaolinite - influence of mineral dissolution. Geochim. Cosmochim. Acta 99, 100-109.

[2] Parkhurst and Appelo (1999) User's guide to PHREEQC (Version2) - A computer program for speciation, batch-reaction, one-dimensional transport, and inverse geochemical calculations. Water-Resources Investigations Report 99-4259, US Geological Survey, Denver, Colorado.

2-08

Identification of Np(V) sorption complexes at the hematite-water interface studied by in-situ ATR FT-IR spectroscopy

Katharina Müller, Annett Gröschel

Helmholtz-Zentrum Dresden-Rossendorf e.V., Institute of Resource Ecology, Dresden, Germany

Neptunium (Np) is one of the most important components of nuclear waste to consider for the long-term safety assessment of nuclear waste repositories, due to the increasing enrichment, the long half-life and the high toxicity of Np-237. Hence, great attention is attracted to its geochemistry [1]. Among the various geochemical reactions, the molecular processes occurring at the solid-water interface, e.g. sorption onto mineral phases, surface precipitation, and colloid formation strongly affect the migration behavior of the radioactive contaminant in the environment [2]. Thus, various components of geological materials, such as iron oxides and hydroxides play an important role in regulating the mobility of actinides in aquifers, due to their widespread environmental presence, high sorption capacity and tendency to form coatings on mineral surfaces [3]. In recent years, the sorption behavior of Np(V), the most relevant oxidation state under ambient conditions, onto iron oxides was mainly studied by macroscopic experiments [4]. For a better understanding of the molecular events occurring at the mineral's surfaces, ATR FT-IR spectroscopy is a useful tool for the in-situ identification of surface species [5]. In addition, time-resolved measurements provide kinetic information on the surface reactions.

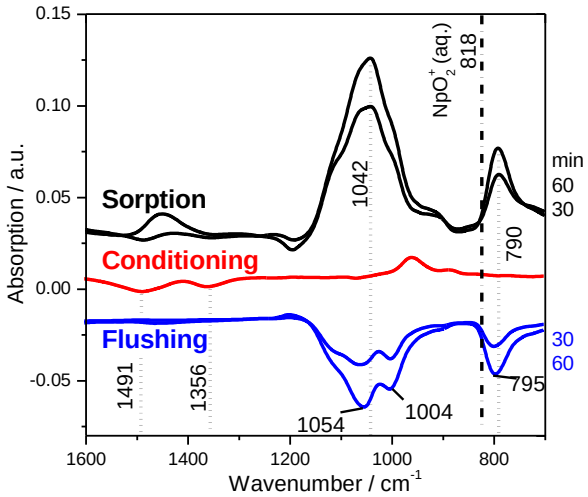

Fig. 1. ATR FT-IR spectra of 50 µM Np(V) sorbed onto α-Fe_2O_3 at pH 7.6, 0.1 M NaCl, D_2O, N_2. Values are in cm^{-1}.

In this work, Np(V) sorption on hematite is studied under a variety of environmentally relevant sorption conditions by in-situ ATR FT-IR spectroscopy [5]. The IR spectra obtained from the subsequent steps of the experiment, that is (1) conditioning, (2) sorption, and (3) flushing, are shown in Fig. 1.

The absence of significant bands below 1000 cm^{-1} in the conditioning spectrum demonstrates the stability of the stationary hematite film directly prepared on the ATR crystal's surface. The bands at 1491 and 1356 cm^{-1} represent the removal of carbonate by rinsing the hematite film, prepared in air with the CO_2 free solution. Upon Np(V) sorption, the band observed at 790 cm^{-1} is assigned to the antisymmetric stretching vibrational mode (v_3) of the neptunyl ion. The IR spectrum obtained from an aqueous solution at 50 µM Np(V), 0.1 M, pH 6 shows the absorption of $v_3(Np^VO_2)$ at 818 cm^{-1}. The red shift of v_3 to 790 cm^{-1} upon sorption can be assigned to an inner-sphere monomeric sorption complex, as previously reported for TiO_2, SiO_2 and ZnO [5]. The band at 1042 cm^{-1} is most probably due to surface modes of the mineral oxide provoked by the sorption processes and were already observed for interactions with

U(VI), Cs(I) and CO_3^{2-} [5]. In the flushing stage, a weakly bound species is released from the stationary phase, reflected by a negative band at 795 cm^{-1} in the respective spectra.

Additional experiments were performed at varied values of pH (5.6 – 12) and ionic strength (0.001 – 0.1) (Fig. 2). Upon increasing the pH from 5.6 to 8.6, no shifts of the bands at 1041 and 790 cm^{-1} are observed. But the intensities of these spectral features are considerably increased at higher pH values indicating an enhanced sorption capacity close to the IEP at pH 9.2. At pH > 10, the aqueous Np(V) speciation changes and NpO_2OH_{aq} is formed and distinctly changes the sorption behavior. The band of $v_3(Np^VO_2)$ is shifted to 773 cm^{-1}. The variation of ionic strength between 0.1 and 0.01 does not change the spectral characteristics. The higher intensities observed at 0.0001 M NaCl can be attributed to contributions of an outer-sphere complex which has to be verified by future experiments.

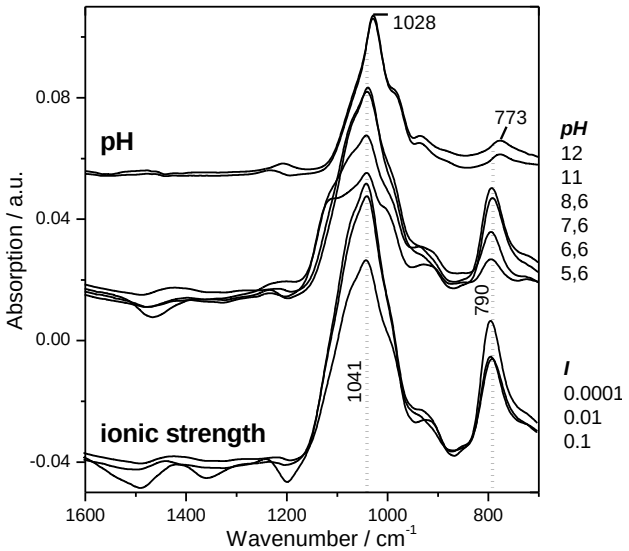

Fig. 2: ATR FT-IR spectra of 50 µM Np(V) sorbed onto α-Fe_2O_3 at a variation of pH (5.6-12) and ionic strength (0.1-0.0001). The other parameters remained constant: pH 7.6, 0.1 M NaCl, D_2O, N_2. Indicated values are in cm^{-1}.

In summary, the IR spectra evidence the formation of Np surface complexes on hematite which can be easily removed to a considerable extent by flushing with blank solution. From this behavior, the simultaneous formation of an inner-sphere species with contributions of an outer-sphere complex is suggested.

References

[1] Kaszuba, J. P. et al. (1999) *Environ. Sci. Technol.* **33**, 4427-4433.

[2] O'Day, P. A. (1999) *Reviews of Geophysics* **37**, 249-274.

[3] Tochiyama, O. et al. (1996) *Radiochim. Acta* **73**, 191-198.

[4] Brendler, V. et al. (2003) *Journal of Contaminant Hydrology* **61**, 281-291.

[5] Müller, K. et al. (2009) *Environ. Sci. Technol.* **43**, 7665-7670.

2-09

Characterisation of uranium minerals relevant to long term storage of spent nuclear fuel

Robert Baker[1], Aurora Walshe[1], Tonya Vitova[2]

[1]Trinity College, Dublin, Dublin, Ireland, [2]Karlsruhe Institute of Technology, Karlsruhe, Germany

The storage of spent nuclear fuel (SNF) in underground repositories means that the chemistry of uranium and the highly active Np, Pu, Am and Cm under the moist oxidising conditions must be well understood. The oxidation of UO_2 to UO_3 has been shown to go via a number of different phases, which can be oxyhydroxides of the type $[(UO_2)_8O_2(OH)_{12}]$ (Schoepite) or $[Ca(UO_2)_6O_4(OH)_6]\cdot 8H_2O$ (Bequerelite), silicate and phosphates of the type $[(UO_2)_2(SiO_4)]\cdot 2H_2O$ (Soddyite) or Autunite $(Ca[(UO_2)(PO_4)]_2.11H_2O)$. Interestingly these can react with H2O2, which is generated by radiolysis of water, to form unusual uranyl peroxides, studtite and metastudtite $[UO_2(\eta^2\text{-}O_2)(OH_2)_2]\cdot nH_2O$ (n = 2, 0). The incorporation of neptunium into these phases has been examined and rationalised on the basis of ion exchange or substitution of a NpO_2^+ fragment with a UO_2^{2+} fragment.

In this contribution we utilise solid-state cyclic voltammetry and potential controlled raman spectroscopy to measure the U(VI)/U(V) redox potential and show that studtite can oxidise Np(IV) to Np(V) whilst being itself reduced to UO_2 (Figure 1). This can therefore constitute a hitherto unknown mechanism for the release of Np into the near field environment. The colours of studtite and metastudtite are quite distinct and this is shown in a band gap difference of 0.7 eV, by just removing interstitial water molecules. We have utilised U L_3-edge EXAFS measurements to determine the solid state structure of metastudtite, as this is unknown experimentally. Upon removal of this water there is a significant phase change that involves a reordering of hydrogen bonding network. In addition we have used HR-XANES (High Resolution X-ray Absorption Near Edge Spectroscopy) to probe the local electronic environment of the uranium in studtite, metastudtite and schoepite (Figure 2). This technique allows the degree of 5f and 6d orbital participation to be directly measured and it validates recent computational work that shows that a peroxide group shows significant covalency in bonding to the uranium fragment.

We have expanded the electrochemical, absorption and vibrational spectroscopies to other uranium minerals that have relevance in geological storage. Compounds containing layers of uranyl oxyhydroxides with interstitial water, potassium and calcium ions, uranyl phosphates and carbonates have been explored to give a representative library of uranyl minerals. We will report on the variation of the U(VI)/U(V) redox potentials depending upon the coordination environment.

A reactivity pathway that has not been fully studies is the reactions of these minerals with other fission products such as iodide ion and ^{241}Am (in tracer studies), and the results will be presented.

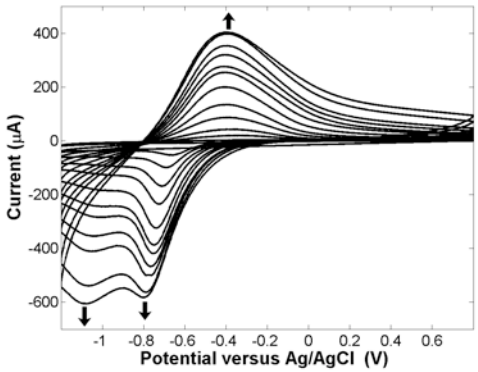

Figure 1. Solid-State voltammagram of studtite (LiClO4 as supporting electrolyte)

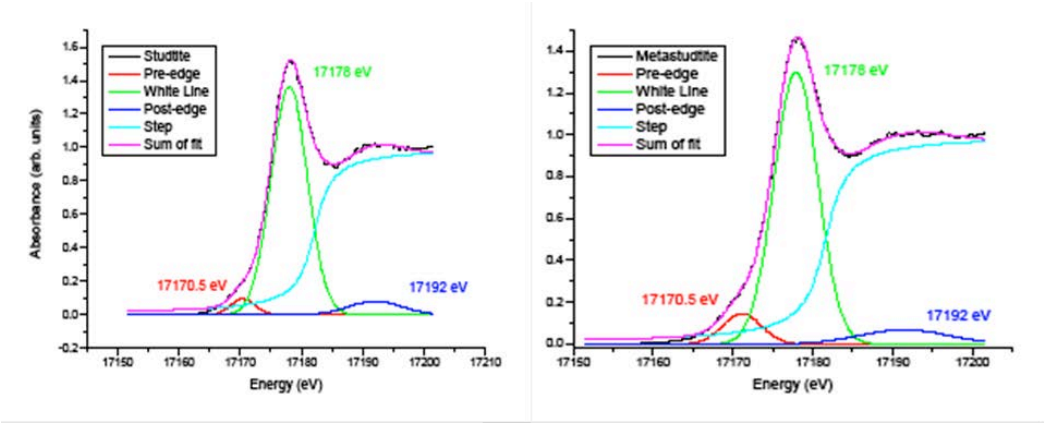

Figure 2. HR-XANES spectra of studtite and metastudtite

2-10

Determining the Biogeochemical Mechanisms that Control Plutonium Transport

Annie Kersting[1], Mavrik Zavarin[1], Brian Powell[2], Pihong Zhao[1], James Begg[1], Zurong Dai[1], Ben Jacobsen[1], Mark Boggs[1]

[1]Lawrence Livermore National Laboratory, Livermore, CA, USA, [2]Clemson University, Clemson, SC, USA

The mobility of plutonium (Pu) in the biosphere is a key environmental concern because of its severe toxicity and long half-life. In 2010, the global inventory of Pu was estimated at ~1900 metric tons with expected yearly increases of ~70-90 metric tons from the nuclear fuel industry [1]. Whether or not future US policy involves directly disposing or reprocessing the spent nuclear fuel, there is a need for an integrated strategy to expedite progress towards a safe permanent storage facility or facilities. Even optimistic estimates for recycling nuclear fuel and reducing the nuclear waste will still require a permanent storage facility.

Despite the critical need to understand the behavior of Pu in the surface and subsurface environments, scientists cannot yet reliably predict the biogeochemical conditions under which Pu will or will not migrate. Although several field studies have shown Pu to migrate associated with colloidal particles[2-4], other field studies suggest that colloidal transport may not be the dominant mechanism for Pu migration[5]. At high concentrations Pu can hydrolyze and form a Pu-oxide (PuO_2) colloid; yet their importance in the long-term fate and transport of Pu is even less well understood. Without a more complete conceptual understanding of the dominant biogeochemical processes that may inhibit or facilitate the Pu transport, we cannot adequately model its transport behavior.

Despite the gaps in our understanding, recent field and laboratory experiments are helping to shape a conceptual model of the behavior of Pu in the subsurface. In this presentation, I will summarize our current understanding of the dominant biogeochemical processes controlling Pu transport by discussing recent field and laboratory studies. Experimental studies will focus on 1) Pu behavior in ternary systems with both inorganic and organic phases, and 2) the stability of intrinsic Pu colloids in the presence of inorganic phases at both 25^{o}C and 80^{o}C. Results from both field and laboratory studies suggest that the fate and transport of Pu depends not only on the initial chemical forms, but the biogeochemistry and hydrology of the source location and subsequent transport pathways.

References

1. Albright, D.; Kramer, K., Global Stocks of Nuclear Explosive Material. *Bulletin Atomic Scientist* **2004**, 14-16.

2. Kersting, A. B.; Efurd, D. W.; Finnegan, D. L.; Rokop, D. J.; Smith, D. K.; Thompson, J. L., Migration of plutonium in ground water at the Nevada Test Site. *Nature* **1999,***397*, (6714), 56-59.

3. Novikov, A. P.; Kalmykov, S. N.; Utsunomiya, S.; Ewing, R. C.; Horreard, F.; Merkulov, A.; Clark, S. B.; Tkachev, V. V.; Myasoedov, B. F., Colloid transport of plutonium in the far-field of the Mayak Production Association, Russia. *Science* **2006,***314*, (5799), 638-641.

4. Santschi, P. H.; Roberts, K. A.; Guo, L. D., Organic Nature of Colloidal Actinides Transported in Surface Water Environments. *Environmental Science & Technology* **2002,***36*, (17), 3711-3719.

5. Zhao, P.; Zavarin, M.; Leif, R. N.; Powell, B. A.; Singleton, M. J.; Lindvall, R. E.; Kersting, A. B., Mobilization of actinides by dissolved organic compounds at the Nevada Test Site. *Appl Geochem* **2011,***26*, 308-318.

Lawrence Livermore National Laboratory under Contract DE-AC52-07NA27344.LLNL-JRNL-577472

2-11

Investigating the migration of trace levels of fallout plutonium and uranium in an ombrotrophic peat bog profile

Francesca Quinto[1], Erich Hrnecek[1], Michael Krachler[1], William Shotyk[2], Peter Steier[3], Stephan R. Winkler[3]

[1]European Commission Joint Research Centre, Institute for Transuranium Elements, P.O. Box 2340, 76125 Karlsruhe, Germany, [2]Department of Renewable Resources, University of Alberta, 839 General Services Building, Edmonton, AB, Canada T6G 2H1, Canada, [3]VERA Laboratory, Faculty of Physics, University of Vienna, Währinger Straße 17, A-1090 Vienna, Austria

Plutonium (^{239}Pu, ^{240}Pu, ^{241}Pu, ^{242}Pu) and uranium (^{234}U, ^{236}U, ^{238}U) isotopes were analysed in an ombrotrophic peat core from the Black Forest, Germany, representing the last 80 years of atmospheric deposition (AD 1917 to AD 1992). The reliable determination of these isotopes at levels of 10^7 atoms/g was possible using ultra-clean laboratory procedures and accelerator mass spectrometry (Steier *et al*., 2010).

Plutonium is detectable along the entire investigated peat core. The ^{240}Pu/^{239}Pu isotopic ratios are constant along the peat core with a mean value of 0.19 ± 0.02 (N = 32). This result is consistent with the acknowledged average ^{240}Pu/^{239}Pu isotopic ratio from global fallout in the Northern Hemisphere. The global fallout origin of plutonium (Kelley *et al*., 1999) is confirmed by the corresponding ^{241}Pu/^{239}Pu (0.0012 ± 0.0005) and ^{242}Pu/^{239}Pu (0.004 ± 0.001) isotopic ratios. The measurement of the isotopic vector of plutonium (^{239}Pu, ^{240}Pu, ^{241}Pu, ^{242}Pu) allowed the use of the ^{242}Pu/^{240}Pu isotopic ratio as an estimate of the initial ^{241}Pu/^{239}Pu isotopic ratio (Steier *et al*., 2013); in this way, it was possible to date the time of irradiation on the basis solely of plutonium isotopes. The date of plutonium irradiation (AD 1956 - AD 1964) was calculated and subsequently compared to the ^{210}Pb age of the peat layers. This comparison provided a confirmation that the global fallout derived plutonium is not fixed in the peat column, but has migrated downwards along the peat profile to layers preceding the nuclear age (Quinto *et al*., 2013a).

Similarly like plutonium, global fallout derived ^{236}U is identified along the investigated peat core. However, the maximum of ^{236}U is detected in correspondence to the age/depth layer of maximum stratospheric fallout (AD 1963). This finding constitutes the first observation of the ^{236}U bomb pulse in a terrestrial environment, which can be successfully used as an independent chronological marker complementing the ^{210}Pb dating of peat cores (Quinto *et al*., 2013b).

The identification of the plutonium and uranium isotopic composition characteristic of global fallout in peat layers pre-dating the period of atmospheric atom bomb testing (AD 1945 - AD 1980) is a clear evidence of the post-depositional migration of these elements downwards the peat profile. Comparing the abundances of the global fallout derived ^{236}U and ^{239}Pu along the peat core, the post depositional migration of plutonium clearly exceeds that of uranium (Quinto *et al*., 2013b). These findings can be useful to evaluate the risks associated to other kinds of nuclear contamination, like nuclear accidents and releases from nuclear facilities and nuclear waste disposal repositories. The results of the present study bring novel information on the behaviour of plutonium and uranium at femtograms and attograms levels directly *in situ* in an environmental scale experiment.

References

Steier P. et al., Nucl. Instr. and Meth. in Phys. Res., B, 2010, 268, 1045.

Kelley J. M. et al., Science of the Total Environment 1999, 237/238, 483.

Steier P. et al., Nucl. Instr. and Meth. in Phys. Res., B, 2013, 294, 160.

Quinto F. et al., Environ. Science: Processes & Impacts 2013a, 15, 839.

Quinto F. et al., Environ. Sci. & Techn. 2013b, DOI: 10.1021/es400026m.

2-27

Actinide Interactions with Ordered Mesoporous Carbon Materials

Heino Nitsche[1,2], Tashi Parsons-Moss[1,2], Harun Tüysüz[3], Jinxiu Wang[4], Deborah Wang[1,2], Stephen Jones[1,2], Daniel Olive[1], Erin Gantz[1,2], Dongyuan Zhao[4]

[1]University of California, Berkeley, Department of Chemistry, Berkeley, CA, USA, [2]Lawrence Berkeley National Laboratory, Nuclear Science Division, Berkeley, CA, USA, [3]Max-Planck-Institut für Kohlenforschung, Mülheim an der Ruhr, Germany, [4]Laboratory of Advanced Materials, Shanghai Key Laboratory of Molecular Catalysis and Innovative Materials, Department of Chemistry, Shanghai, China

Ordered mesoporous carbons (OMCs) are attractive as sorbents because of their extremely high surface areas and large pore volumes. We have explored Pu(VI) sorption interactions with three types of OMC materials, both as-synthesized and after chemical oxidation. The OMCs were characterized by nitrogen adsorption, scanning electron microscopy (SEM), transmission electron microscopy (TEM), Fourier transform infrared spectroscopy (FT-IR), and point-of-zero-charge determination via potentiometric titration and/or powder addition methods. Initial studies focused on comparison of Pu(VI) uptake by CMK-(carbon molecular sieves from KAIST) type mesoporous carbon with uptake by a commercial amorphous activated carbon. The CMK was synthesized via nanocasting by using cubic ordered mesoporous silica KIT-6 as a hard template. Oxidation of the CMK by treatment with nitric acid increased the density of oxygen-containing surface groups, especially –COOH, thus lowering the point of zero charge (PZC) of the material. Batch studies of all 3 materials with Pu(VI) solutions in a 0.1 M $NaClO_4$ matrix were performed to investigate pH dependence, sorption kinetics, Pu(VI) uptake capacities, competition with ethylenediaminetetraacetic acid (EDTA) in solution, Pu desorption and reusability. Both CMK materials demonstrated high Pu sorption from a wide range of pH environments, and greatly outperformed the activated carbon in terms of Pu(VI) uptake kinetics and capacity. Most batch experiments were done in pH 4 solutions. The Pu uptake from low-concentration solutions was faster for the oxidized CMK than for untreated CMK, but in more concentrated samples (~250 µM Pu), the Pu uptake kinetics and apparent capacity were the same for oxidized and untreated CMK. The 23-hour Pu(VI) uptake capacity of the CMK materials was measured to be at least 58 ± 5 mg ^{239}Pu per g CMK carbon, compared to 12 ± 5 mg ^{239}Pu per g activated carbon, as shown in Figure 1. The Pu interaction with the carbon surface was also probed via X-ray absorption spectroscopy (XAS) on the Pu LIII adsorption edge. Spectral fits of the X-ray absorption near-edge structure (XANES) data collected on both types of CMK samples showed that Pu(VI) was reduced to Pu(IV) at the carbon surface.

The promising results obtained with CMK prompted further investigation of actinide and lanthanide interactions with OMCs, but we have moved away from the fastidious nanocasting synthetic process, and expanded our studies to more pristine, robust and highly ordered OMCs. These include FDU-16-type (Fudan University OMC synthesized by evaporation-induced organic-organic self-assembly) and C-CS-type (Fudan University OMC synthesized by evaporation-induced organic-inorganic co-assembly into nanocomposites) carbons, and their oxidized counterparts. An oxidation method was adopted that uses acidic ammonium persulfate, which produces far more surface carboxyl groups than the nitric acid treatment. Figure 2 summarizes results of exploratory batch experiments that were performed with 10 µM Pu(VI), 0.1 M $NaClO_4$ solutions of various pH conditions, in contact with the different OMCs. Since oxidized C-CS showed the highest affinity for Pu(VI) sorption of all the OMCs, further investigations focused on comparison of pristine and oxidized C-CS. The oxidized C-CS shows very fast Pu(VI) uptake kinetics at all Pu concentrations, demonstrating that the surface functionalization exhibits more control over the batch kinetics than the pore structure or surface area. Batch experiments with C-CS and oxidized C-CS in perchlorate solutions ranging in ionic strength from 0.01 to 1.1 showed that ionic strength had no influence on Pu(VI) uptake in that range, indicating that sorption occurs via inner-sphere complexation. Batch interactions of C-CS and oxidized C-CS with Pu in different solution matrices are currently being investigated, as well as sorption of other species such as Eu(III) and Np(V). Preliminary data suggest that the sorption trends of Eu(III) to C-CS are quite different than those of Pu(VI), and sorption of Eu(III) seems more pH-dependent. Batch sorption and optical spectroscopy experiments reveal that OMCs can behave as powerful actinide reducing agents under certain conditions. The high affinity of mesoporous carbon for Pu(VI), and the

interesting redox chemistry at these carbon surfaces could be valuable for a variety of applications involving separation or sequestration of actinides.

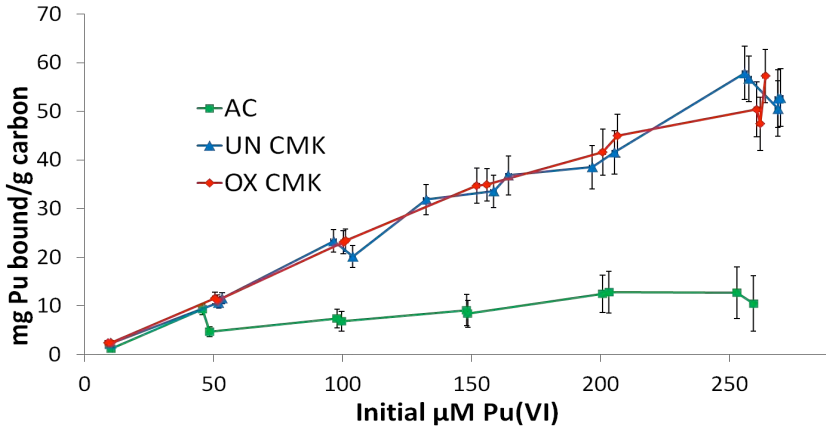

Figure 1: mg Pu bound per g carbon vs. initial µM Pu(VI) in batch samples of activated carbon, CMK, and oxidized CMK with approximately 1000 mL/g pH 4, 0.1 M NaClO4 solution. Sorption was measured after 23 hours contact. Lines are only to guide the eye, error bars represent 90% confidence.

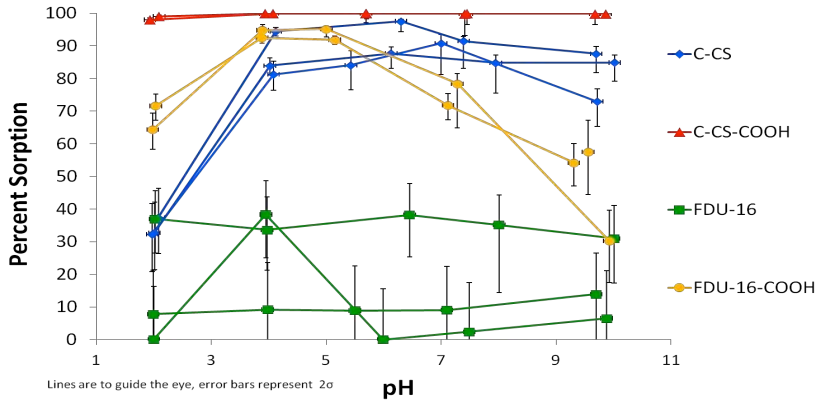

Figure 2: Percent sorption vs. solution pH in batch samples of several OMCs with approximately 1000 mL/g pH 4, 0.1 M NaClO4, 10 µM Pu (VI) solutions. Sorption was measured after 3 hours contact. Lines are only to guide the eye, error bars represent 90% confidence.

Acknowledgements. The majority of this work was supported by the US Department of Homeland Security Academic Research Initiative program. A portion of the work was supported by the National Nuclear Security Administration NNSC program. XAS measurements were carried out at the Stanford Synchrotron Radiation Lightsource, a directorate of SLAC National Accelerator Laboratory and an Office of Science User Facility operated for the U.S. Department of Energy Office of Science by Stanford University.

2-28

Actinide Colloids in High Ionic-Strength Media

Donald Reed, Marian Borkowski, Michael Richmann, Jean-Francois Lucchini, Danielle Cleveland

Los Alamos National Lab, Carlsbad, NM, USA

The Waste Isolation Pilot Plant (WIPP), located in South-Eastern New Mexico, has operated for over ten years as the only working TRU repository in the United States. It is the continuing success of this repository that is the basis of discussions to evaluate salt-based repository concepts for the permanent disposal of high level and spent fuel nuclear waste. In the WIPP safety case, colloidal actinide species are considered because they can contribute to the source term in the unlikely scenario of brine inundation.

The current WIPP colloid model [1] was based on an extensive literature review, some WIPP-specific experimental data, and some conservative simplifications that were extensively peer reviewed prior to the first license application. In this model, four types of colloids that could contribute to the actinide source term are identified: mineral, intrinsic, humic and microbial

The intrinsic and to a lesser extent the mineral colloidal actinide fraction was evaluated by examining size distribution of actinide/analog species in our WIPP-specific long-term solubility studies through sequential ultrafiltration and, in some cases, ultracentrifugation. Actinide/analog samples were consecutively filtered through different pore size filters (Fisher Amicon® ultrafilters). The following pore size filters were used: 0.45µm, 0.22µm, ~20nm (100kDa), ~10nm (30kDa), ~5nm (10kDa), and ~2.5nm (3kDa). That this approach did not impact the apparent actinide/analog concentrations was established by filtration of species known to be non-colloidal (see Fig. 1). A combination of extraction and ICP-MS analysis was used to establish the concentration and oxidation state of the actinide/analog.

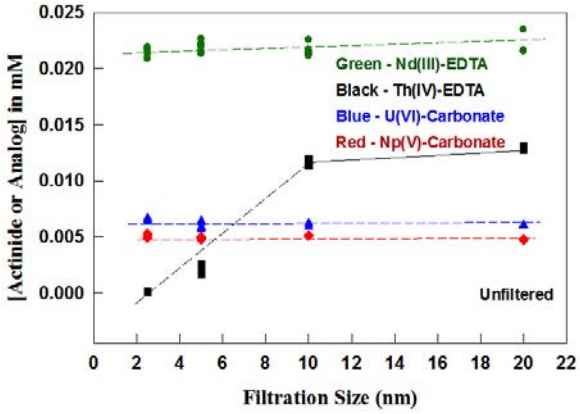

Fig. 1 Effect of the sequential filtration approach on dissolved actinide species in GWB brine at pC_{H+} ~ 9. For the Nd-EDTA, U-carbonate, and Np(V)-carbonate systems essentially full recovery of the actinide/analog was obtained. A significant filtration effect is noted for Th-EDTA in an analogous brine system where truly dissolved species were not expected.

In the sequential filtration studies, we observed <10 nm species in all cases investigated: specifically this is for the Nd(III), Pu(III), Th(IV) and U(VI) systems. The apparent colloidal fraction range from ~5% to ~ 80% of the aqueous fraction of the actinide and are roughly correlated with the oxidation state of the actinide. For the thorium system in particular, the total concentration and colloidal fraction decrease with time leading to concentrations that approach its predicted solubility in the brine system. For plutonium, which existed primarily in the Pu(III) oxidation state, significant association was observed with the colloidal iron present (typically > 20 nm in size). This, at the higher pH range investigated, also had a significant <10 nm fraction with a size distribution that varied with pH. In the absence of colloidal iron, there was essentially no evidence for Mg-derived mineral colloids in the brine. The results obtained are shown for the Nd^{3+} and Pu^{3+} brine systems investigated in Figure 2 and 3, respectively.

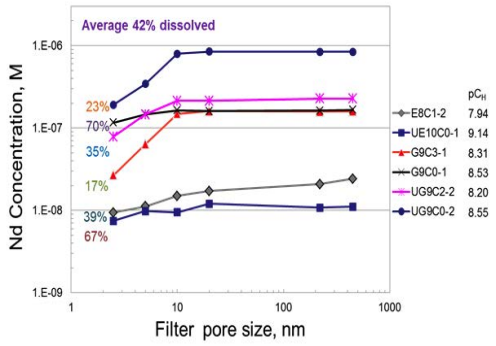

Fig. 2 Size distribution of Nd^{3+} for various brines and pH.

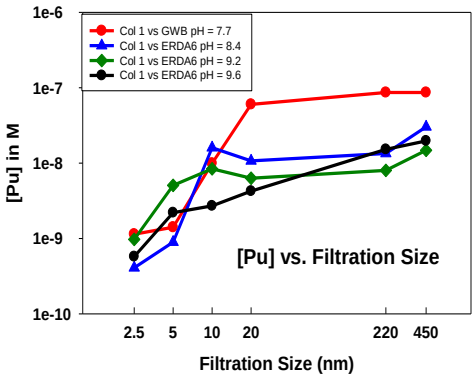

Fig. 3 Size distribution of Pu^{3+} for various brines and pH

The initial conclusions and observations that led to the current mineral colloid enhancement parameters were that only iron oxides, specifically goethite and magnetite, formed actinide mineral colloids in the systems investigated. There were no colloidal enhancements noted that could be attributed to the presence of Mg phases in our long-term studies. The plutonium experiments performed included iron and showed that the iron oxides generated due to anoxic corrosion in WIPP brine led to some mineral colloid formation. At the most repository-relevant pH (~ 9.5), a significant amount of Pu^{3+} was associated with the iron in solution corresponding to additional plutonium concentrations of 8.6×10^{-9} M to 2.3×10^{-8} M respectively. This is consistent with the 2.6×10^{-8} M that is currently in the WIPP model.

These observations, taken together, provide a more detailed description of the actinide source term and raise questions about the long-term stability, structure and equilibration of these nano-colloidal species. Accounting for the possible contribution of these species to the source term is important to the safety case for a salt-based repository, but these contributions, in the end, do not significantly impact predicted actinide release.

References

1. Compliance Certification Application for the Waste Isolation Pilot Plant, Appendix SOTERM. Title 40 CFR Part 191, Subparts B and C. Actinide Chemistry Source Term. 1996. United States Department of Energy/Waste Isolation Pilot Plant. Carlsbad Field Office; Carlsbad, NM.
2. Reed, D.T., J.S. Swanson, J.F. Lucchini, and M.K. Richmann, “Intrinsic, Mineral and Microbial Colloid Enhancement Parameters for the WIPP Actinide Source Term”, LANL report LCO-ACP-18, 2013.

4-24

^{237}Np Sorption by UO_2 Under Repository Conditions

Tatiana Kazakovskaya[1], Elena Zakharova[2]

[1]*Russian Federal Nuclear Center - VNIIEF, Sarov, Russia, 2Institute of Physical Chemistry and Electrochemistry RAS, Moscow, Russia*

The license application capacity of Yucca Mountain (YM) geologic repository is 77,000 tons of spent nuclear fuel (SNF) heavy metal. Since the atom percent burn-up of this fuel averages only ~4%, the remaining material is ~96% UO_2. Some key radionuclides may be sorbed by UO_2 and thereby may be retained by the SNF.

Early results of the sorption of neptunium (Np) on samples of uranium dioxide (UO_2), prepared several difference ways, have demonstrated that uranium oxides have a high potential for significantly attenuating movement of Np (see Fig. 1) [1].

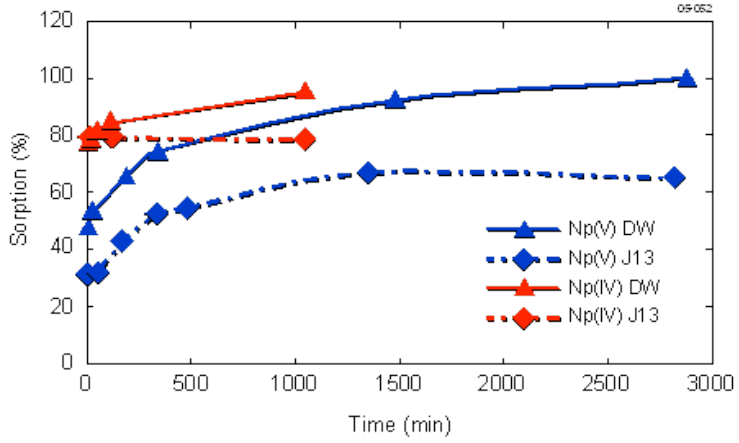

Fig. 1. Neptunium is Sorbed onto UO_2.

Russian experiments show that Np (V, IV) is strongly sorbed onto UO_2. In experiments, Np(IV) equilibrium is reached within two hours; Np(V) equilibrium is reached within 24 hours. The amount of Np(V) sorbed is determined by the degree of deprotonation of the OH-group surface. The Np(V) sorption onto UO_2 is practically irreversible. Sorption of Np(V) is accompanied with partial reduction of Np(V) to Np(IV). The sorption of Np(V) onto schoepite (the primary product of UO_2 corrosion) is less than the sorption of Np(V) onto UO_2 [2].

Retention of Np by UO_2 has important implications for the proposed YM high-level waste repository. By sorbing radionuclides on the UO_2 component of the SNF or on other chemical barriers, the sorption of UO_2 could have a large effect on the radiation dose from these elements at the YM site boundary (see Fig. 2). This work modifies a figure taken from ref. [3] by subtracting the Np and Np daughter contributions to total site boundary dose.

The primary contributor to long-term (>30,000 years) site boundary dose at YM geologic repository is ^{237}Np. Early experiments indicate that ^{237}Np is sorbed by UO_2. If this is confirmed, the long-term repository site boundary dose may be reduced by more than an order of magnitude.

There are caveats concerning this work. The solubility of UO_2 in deionized water and YM J-13 simulated water was determined by the U(VI) content in the surface layer, and by the O/U ratio. It was found that the solubility of UO_2 formed at lower temperatures (~700EC) is ten times higher than at higher temperatures (~800E). Fuel pellets are fired at even higher temperatures (~1200EC). It should also be noted that uranium colloid transport could be a means whereby neptunium and other sorbed radionuclides can be transported. Finally, these are screening experiments and do not yet meet YM quality assurance standards.

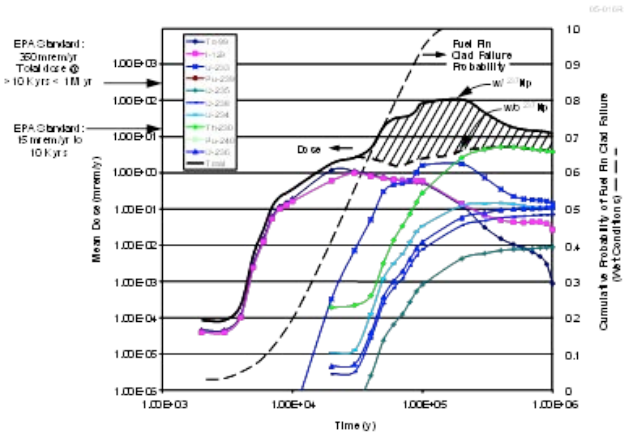

Fig. 2. The Contribution of ^{237}Np to YM Total Site Boundary Dose Calculations.

It should be noted in passing that other early Russian experimental results show that ^{99}Tc, the primary contributor to short-term site boundary dose, is also sorbed by UO_2. Furthermore, early experimental results show that UO_2 has filtration properties in which water flowing through UO_2 slows, then stops almost completely. Thus, contained UO_2, as in cladded UO_2, may have self-sealing properties.

References

1. T. V. Kazakovskaya, et al., “Sorption of Long-Lived Radioisotopes in Geological Repository Underground Waters by Depleted Uranium Oxides,” 10th International Conference on Environmental Remediation and Radioactive Waste Management, Glasgow, Scotland, September 4–8, 2005.

2. J. P. Kaszuba and W. H. Runge, “The aqueous geochemistry of neptunium: dynamic control of soluble concentrations with application to nuclear waste disposal”, Environmental Science Technology 33 (1999) 4427-4433

3. Figure 4-10, Scientific and Technical Priorities at Yucca Mountain, EPRI Report No. 1003335, December 2003.

POSTERS

3-17

The Hydrothermal Behavior of Depleted Uranium Oxides

Tatiana Kazakovskaya[1], Elena Zakharova[2], Vyacheslav Shapovalov[1]

[1]Russian Federal Nuclear center –All-Russia Scientific Institute of Experimental Physics, Sarov, Russia, [2]Institute of Physical and Electro- Chemistry, Russian Academy of Sciences, Moscow, Russia

Introduction

The development of nuclear power engineering is closely connected with the problem of high-level wastes (HLW) and spent nuclear fuel (SNF) storage or treatment. Eventually, all wastes are put into HLW and SNF repositories. One of the principal safety requirements of these repositories is to reduce the release of radionuclides on geological time scales. The system of multi-barrier shielding in SNF repositories will help to solve the problem of radionuclide seepage [ref. 1]. One of the most promising materials of such barriers is depleted uranium (DU), which is a residual product of the enrichment process to produce ^{235}U (used as nuclear fuel) from natural uranium. At present, over 1.2×10^6 tons of depleted uranium, with a ^{235}U content of 0.25-0.35 wt %, are accumulated in the world.

The transformations of uranium oxides (the basic SNF component) with ground waters under repository conditions are the key parameters to describe and forecast the main repository processes. Under ionizing radiance the temperatures in SNF repositories could reach 160 ^oC [ref. 1]. This work is devoted to hydrothermal tests of depleted uranium oxides.

Experimental aspects

Hydrothermal tests on depleted uranium oxide samples were carried out at high temperatures in solution, simulating Yucca Mountain ground water (J-13) and in deionized water (DW). The solid/liquid phase ratio in all cases was equal to 60 g/L. Teflon test-tubes with the prepared suspensions were placed into steel autoclaves and then treated under two temperatures: +70 ºC and +150 ºC.

Suspension aliquots were investigated to analyze solid phase changes and to detect uranium solubility. The time intervals were 1 week, 1, 1.5, 4, and 6 months. The solid phase analysis was done using X-ray phase analysis (RPA), X-ray photoelectron spectroscopy (RPES), and scanning electron microscopy (SEM) with energy dispersive X-ray spectrometry (EDX).

Results and Discussion

+70 ^oC . The RPA of UO_{2+x} samples demonstrated that at +70 $^\circ$C in J-13 solution during 6 months no new uranium phases are formed. The cubic lattice parameters (as compared with the initial sample) does not change, but we see an intensity decrease of the lines (222), (400), (331) and (420). At the same time, volume oxidation of UO_{2+x} is observed. The oxidation goes up to the formation of U_4O_9.

+150 ^oC. At + 150^{o}C such secondary phases of U(VI) as shoepite, mixed oxides of uranium, sodium and potassium $(Ca,Na,K)U_2O_7\cdot2H_2O$, together with compregnasite are formed. During 2.5 months no lattice changes and volume oxidation are observed. After 4-month exposure the lattice has changed.

The morphology investigation (SEM) of the samples exposed at hydrothermal conditions (+70 and +150 ^{o}C in J-13) during 6 months demonstrated that in both cases the secondary uranium phases are formed; but at 70 $^\circ$C the concentration of the surface new-formed phases is significantly lower than at 150°C. The needle crystals formed under these conditions may be detected as skupite [ref. 2]. This fact corresponds with the data of other methods. RPES analysis of the change of U(IV)/U(VI) ratio after hydrothermal leaching testified that there are two competitive processes: the volume oxidation and the formation of the secondary phases at the surface [ref. 3].

To evaluate the influence of temperature and carbonate-ions presence on the volume oxidation and the secondary phase formation, additional parallel experiments in DW were carried out. At room temperature, volume oxidation was detected neither in DW nor in J-13.

But it was demonstrated that carbonate-ions enlarge the rate of the secondary phase formation.

At high temperatures in DW the same processes as in J-13 solution occur: an intense volume oxidation at + 70 ^{o}C, and a slow volume oxidation with formation of secondary phases at + 150^{o}C. In DW the rate of secondary phase formation is lower than in J-13 solution.

Considering the experimental results one can conclude that the main factor, that determines the prior process, is not the solution composition, but the temperature. It seems that the kinetics of both process (the volume oxidation and the formation of the secondary phases) is the function of the temperature, which in the issue governs the oxidation mechanism of uranium under hydrothermal conditions [ref. 4].

It was found that particles of micron- ad nanosize had been formed in solution. Figure 1 shows the photograph of transparent Teflon test-tubes with suspensions. One can see that the color of the suspension treated at + 70 $^{\circ}$C is black (this color corresponds to uranium dioxide), while the color of suspension treated at +150 $^{\circ}$C becomes brown because of 6-valency uranium formation

Figure 1 – Samples of depleted uranium after 4-month tests in J-13 solution.

Conclusion

1. The hydrothermal tests of solid uranium dioxide testify that there are two competitive processes: the volume oxidation and the formation of the secondary phases at the surface.

2. The main factor, that determines the prior process, is not the solution composition, but the temperature. It appears that the kinetics of both process (the volume oxidation and the formation of the secondary phases) is a function of temperature.

References

1.Sokolova I.D., Shulga N.A. Project nacionalnogo khranilicha Yucca Mountain , Atomnaya technika zarubezhom , 2006, v. 10, pp. 3-12.

2.Uranium: Mineralogy, Geochemistry and the Environment edited by P. C. Burns and R. Finch. Reviews in Mineralogy, V. 38, Mineralogical Society of America, Washington, DC, 1999.

3 Clark S.B., Ewing R.C., Schaumloffel J.C., A method to predict free energies of formation of mineral phases in the U(VI)–SiO_2 –H_2O system, J. Alloys and Compounds 1998, V. 271–273, P. 189–193,

4. Kubatko K.-A., Helean K., Navrotsky A., Burns P.C., Thermodynamics of uranyl minerals: Enthalpies of formation of uranyl oxide hydrates, American Mineralogist 2006, V. 91, P. 658-666.

3-81

Chemiluminescence specroscopy of actinides and lanthanides in solutions

Igor Izosimov[1], Nikolai Firsin[2], Nikolai Gorshkov[2], Vladimir Mikhalev[2], Sergei Nekhoroshkov[2]

[1]Joint Institute for Nuclear Research, Dubna, Moscow region, Russia, [2]Khlopin Radium Institute, St. Petersburg, Russia

Of lanthanide or actinide properties analysis interest was to use advantages of luminescence procedure for detection of lanthanides and actinides having no self-luminescence, as an example, by initiation of luminescence of some agents through excitation of lanthanide or actinide element to be detected. An effort was made on initiation of luminol chemiluminescence through excitation of lanthanide and actinide ions with laser radiation [1,2]. The use of this type of chemiluminescence for detection of actinides is possible only in the case of selective excitation of chemiluminescence [2-4].

In this work the details of luminol chemiluminescence initiation through excitation of Sm(III), U(IV) and Pu(IV) ions with laser radiation are presented. Data on luminol chemiluminescence in solutions containing Sm(III), U(IV) and Pu(IV) are discussed. Chemiluminescence was induced by two-quanta excitation of lanthanide or actinide ions in the range of 4f or 5f electron transitions by the scheme *two steps-one color*, i.e. in irradiation of actinide-containing solution by one laser and by the scheme *two steps-two colors*, when a solution is irradiated by two lasers operating at different wavelengths. A multi-step scheme of chemiluminescence excitation makes this procedure not only highly sensitive but also highly selective procedure of detection of substances. Appropriate selectivity was reached in our experiments when chemiluminescence was initiated by transitions within 4f or 5f electron shell of lanthanide or actinide ions, which correspond to visible spectral range. Since the energy of one-quantum excitation in visible range is insufficient for initiation of luminol chemiluminescence, we selectively excited lanthanide or actinide ion by multi-quantum absorption of visible light. This fact allows using highly sensitive chemiluminescence procedure for selective detection of various valence lanthanide or actinide species in solutions based on individual features of their absorption spectra.

The experiments were performed on an installation involving a pulse nitrogen laser OBB 1010 with a pulse length of 1 ns and a pulse power of approximately 1.4 MW per a pulse and two tunable dye lasers OBB 1011 and OBB 1012 with a pulse length of 1 ns and 800 ps respectively. The pulse power 300 kW was reached for dye lasers. A delay time for luminescence registration was 2 μs. The spectra of chemiluminescence initiation as a result of excitation of Sm^{3+} ions with dye laser by using two steps-one color scheme (two photons absorbed during one laser pulse) is shown in fig.1. There is no complete similarity between the spectrum of chemiluminescence excitation and Sm^{3+} ions absorption spectrum. This experimental fact connected with the difference in the selection rule for single-quantum and multi-quantum absorption.

The spectrum of chemiluminescence excitation obtained in tuning of generation wavelength of the second laser (two steps-two colors scheme) is similar to the absorption spectrum of uranium (Fig. 2). The presence of absorption band of U(IV) in the range of retuning of the second laser results in appearance of a peak of luminol chemiluminescence. This fact undeniably confirms the selective mechanism of chemiluminescence excitation. Initiation of chemiluminescence as a result of excitation of Pu(IV) with two dye lasers was demonstrated for a solution containing CsF, luminol, and Pu(IV). A choice of solution composition was made based on an attempt to provide favorable conditions for observation of luminol chemiluminescence and to avoid formation of colloidal species of hydrolyzed Pu(IV). The spectrum of chemiluminescence excitation in both two steps-one color (Fig.3) and two steps-two colors (Fig.4) schemes correlated with absorption spectrum of Pu(IV). In both schemes we realized selective excitation of chemiluminescence and this selectivity is caused by the features of absorption spectra of Pu(IV) solutions.

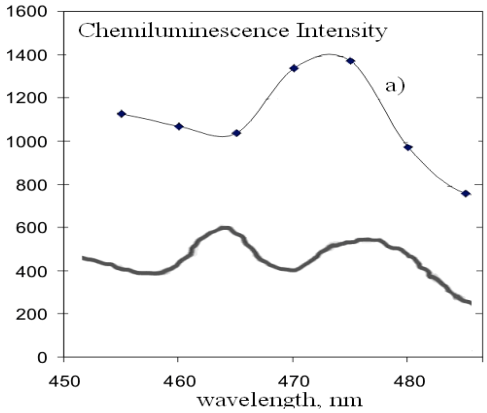

Fig.1. Two-steps one-color excitation of chemiluminescence. Excitation spectrum (a) of luminol chemiluminescence with dye laser in the range of absorption bands of Sm^{3+}. Chemiluminescence is detected at the wavelength of 460 nm. Absorption spectrum of Sm^{3+} is shown below.

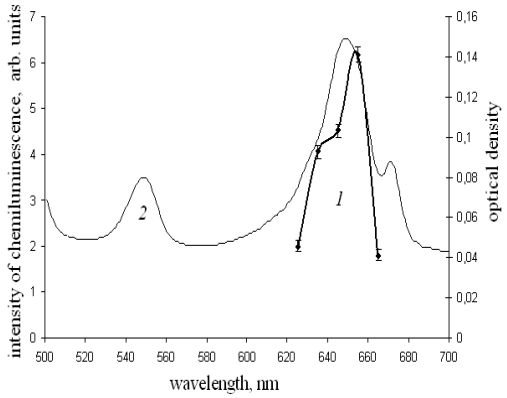

Fig.2. Two-steps two-colors excitation of chemiluminescence in solution luminol+U(IV)+HCl.(1). Chemiluminescence intensity dependence on the wavelength of laser radiation at the first excitation step. The wavelength of laser radiation at the second step was fixed at 500 nm. (2). Absorption spectrum of U(IV)+HCl solution.

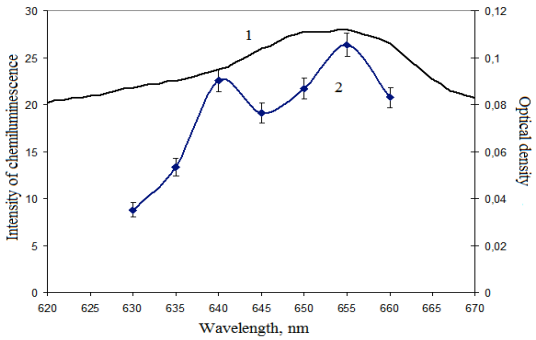

Fig.3. Spectrum of chemiluminescence excitation by the scheme two steps-one color in solution containing CsF, luminol, and Pu(IV) (*2*). Absorption spectrum of Pu(IV) (*1*).

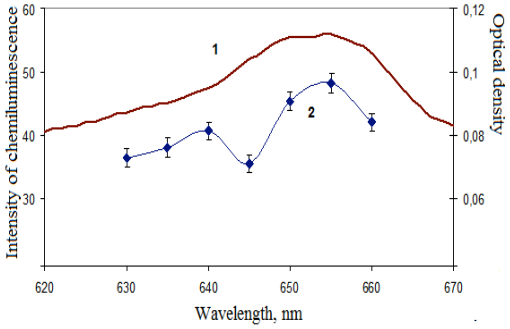

Fig.4. Spectrum of chemiluminescence excitation in CsF+luminol+Pu(IV) solution by the scheme two steps-two colors (*2*). Wavelength of laser radiation at the first excitation step was varied (*2*), the wavelength of laser radiation at the second step was fixed at 490 nm. Absorption spectrum of Pu(IV) (*1*).

References

[1]. Izosimov I.N., Gorshkov N.G., Mashirov L.G. *et al.*, Proc. Int. Conf. Actinides 2005, Manchester, UK, 2005, p.779.

[2]. Izosimov I.N., Phys. Part. Nucl., **38**, 177, 2007.

[3]. Izosimov I.N., Firsin N.G., Gorshkov N.G. *et al.*, Preprint of the Joint Institute for Nuclear Research, E6-2012-62, Dubna, 2012, 11 P.

[4]. Gorshkov N.G., Izosimov I.N., Mikhalev V.A. *et al.,* Radiochemistry, **6**, 525, 2012.

3-82

The fate of uranium and technetium during magnetite crystallisation at hyperalkaline pH

Timothy Marshall[1], Katherine Morris[1], Gareth Law[2], Frederick Mosselmans[3], Samuel Shaw[1]

[1]Research Centre for Radwaste and Decommissioning and Williamson Research Centre, School of Earth, Atmospheric and Environmental Sciences, The University of Manchester, Manchester, UK, [2]Centre for Radiochemistry Research and Research Centre for Radwaste and Decommissioning, School of Chemistry, The University of Manchester, Manchester, UK, [3]Diamond Light Source Ltd., Diamond House, Harwell Science and Innovation Campus, Didcot, Oxfordshire, UK

Geological disposal of legacy radioactive wastes stored at Earth's surface is now the predominant management pathway for these materials and is a task of importance for nuclear power generating countries. In many radioactive waste disposal scenarios, intermediate level wastes (ILW) are grouted and emplaced in a geological disposal facility (GDF) which will have cement present as a ubiquitous engineering material. Furthermore, cementitious materials have been considered as backfill for some GDF concepts. Therefore, post-closure leaching of cementitious materials in a GDF is expected to create hyperalkaline conditions in and around the repository, resulting in mineral alteration and crystallisation in the repository components and host rock. Iron within the host rock derived from the alkaline breakdown of Fe-bearing silicate minerals (e.g. biotite, chlorite), corrosion products formed within the repository, or iron flocs in the waste will form iron (oxyhydr)oxide minerals. The formation and re-crystallisation of these reactive minerals may sequester radionuclides through reduction to less soluble forms and/or incorporation into stable secondary iron oxide phases, therefore they may prove key to the fate of radionuclides in such environments [1, 2].

To evaluate the signficance of these processes, ferrihydrite was crystallised to magnetite (via addition of $Fe^{2+}_{(aq)}$) under CO_2-free, anoxic conditions in three synthetic cement leachates spiked with either U(VI) or Tc(VII). The leachates represent early (pH 13.1), middle (pH 12.5) and late (pH 10.5) stage cement evolution for a cementitious ILW GDF. After ageng, the headspace was flushed with CO_2-free air to reoxidise for 21 days. Parallel experiments were set up compare the radionuclide sorption behaviour onto pre-formed magnetite. These samples were allowed an equilbration period of 1 day prior to oxidation for 21 days. Solution samples were taken throughout to determine the partitioning of Tc/U between the solid and solution and X-ray Absorption Spectroscopy was used to characterise radionuclide associations with the solid phases after ageing and oxidation.

All U(VI) was removed from solution during magnetite formation, and analysis of the EXAFS spectra suggested U(IV) incorporation into the reduced mineral phase with some U(IV) surface species. Upon reoxidation, some U was remobilised to solution with variable levels of remobilisation seen in the different chemical treatments. Incorporated U appeared to be resistant to oxidation although surface species are oxidised to U(VI). Similarly, all Tc(VII) was removed from solution rapidly (minutes) upon addition of the $Fe^{2+}_{(aq)}$ with some oxidative remobilisation after 21 days and with differences in the remobilisation extent with chemical conditions. Very little variation was observed between the EXAFS at the different pH conditions, and only minor differences were observed between the reduced and oxidised samples even though significant remobilisation of Tc to solution had occured. Initial analysis of the EXAFS spectra show that a large fraction of the Tc is likely to be incorporated within the reduced mineral and that this phase may be resistant to reoxidation.

These data suggest that U and Tc can become reduced and immobilised within the lattice of stable iron oxide phases and that some fraction of the radionuclide is then recalcitrant to oxidative remobilisation. These data will be discussed in the context of the geochemical and spectroscopic data for these samples, and in terms of the wider significance of these processes in geological disposal and contaminated land.

References

[1] S. Kerisit, A.R. Felmy, and E.S. Ilton (2011). *Environ. Sci. and Technology* **45**; 2770.

[2] W. Um, H-S Chang, J.P Icenhower, W.W. Lukens, R.J, Serne, N.P. Qafoku, J.H. Westsik, Jr., E.C. Buck, and S.C. Smith (2011). *Environ. Sci. and Technology* **45**; 4904.

3-84

Biogeochemistry of uranium in the southern Baltic ecosystem

Alicja Borylo, Bogdan Skwarzec, Grzegorz Olszewski

University of Gdansk, Pomorskie, Poland

Introduction

Uranium is a radioactive and toxic metal, and it is a hazardous environmental pollutant. The principal source of uranium in the natural environment is the atmospheric precipitation of terrigenic material, soil resuspension, rock weathering, as well as river waters and fertilizers. On the other hand large amounts of uranium contents are produced by anthropogenic sources. The main contamination sources in the Baltic Sea waters are precipitation, river run-off and inflow from the North Sea.

Materials and methods

The analytical environmental samples include: sediment, organisms and surface water samples collected between 1997-2004 from the southern Baltic Sea, as well as phosphogypsum and surface water samples from area around the phosphogypsum stockpile in Wiślinka. The activities of ^{234}U and ^{238}U were measured using an alpha spectrometer. The accuracy of the analytical method and measure of precision was estimated to be below 2.4% and 3% respectively.

Results and discussion

Uranium in waters and sediments of the southern Baltic. The uranium content in the analyzed water samples and sediments of the southern Baltic were differentiated. The highest values were reported in the sediments taken from the Słupsk Bank and the Słupsk Narrow, while the smallest in the Bornholm Deep, what is probably connected with the information about the geological structure of the seabed. The concentration of uranium in sediments increases with depth of the sediment core, indicating the vertical diffusion processes of uranium from sediments to the bottom water through the intersticial water, and diagenetic changes occurring in the sediment material. The values of the activity ratio $^{234}U/^{238}U$ in the other analyzed sediments of the southern Baltic are in the range between 0.83 and 1.28. The small differences of the uranium content of the southern Baltic Sea surface and bottom waters were observed (3.69-6.11 $\mu g \cdot dm^{-3}$ and 1.81-3.81 $\mu g \cdot dm^{-3}$ respectively), while the values of the activity ratio $^{234}U/^{238}U$ range from 1.16 to 1.19 (Skwarzec et al., 2002).

Uranium in Baltic organisms. The source of uranium in the Baltic plants and animals is the sea water. The concentration of ^{238}U in the analyzed Baltic organisms ranged from 0.0112 $Bq \cdot kg^{-1}$ d.wt., in the muscle of fish, to 5.5 $Bq \cdot kg^{-1}$ d.wt.·in phytoplankton (Skwarzec et al., 2006). The ^{238}U concentration in Baltic zoobenthos ranged from 0.3 to 1.5 $Bq \cdot kg^{-1}$ d.wt., and the observed differences can be the result of the eating habits of the tested organisms. The values of uranium concentrations in phytoplankton organisms (0.45 $mg \cdot kg^{-1}$ d.wt.) are about 4 times higher than zooplankton organisms, where the concentration of this radionuclide was estimated at 0.11 $mg \cdot kg^{-1}$ d.wt., which indicates that uranium is easier and more eagerly accumulated by the phytoplankton (Skwarzec et al., 2004). Uranium concentrations in zoobenthos organisms ranged from 0.07 $mg \cdot kg^{-1}$ d.wt. and 0.12 $mg \cdot kg^{-1}$ d.wt., while the values of the activity ratio $^{234}U/^{238}U$ ranged from 1.04 to 1.39. The lowest concentrations of uranium were estimated for fish from the Baltic, while the values of the activity ratio $^{234}U/^{238}U$ were similar to other Baltic organisms (1.10-1.13). The average value of the activity ratio $^{234}U/^{238}U$ in the analyzed Baltic organisms is 1.15.

Uranium in marine birds. Uranium isotopes were determined in in the marine birds from the Polish area of the southern Baltic Sea among species permanently residing at the southern Baltic, species of wintering birds and species of migrating birds. The values of uranium concentration in whole organism are within the limits from 2.33 $mg \cdot kg^{-1}$ w.wt. in *A. tarda* to 18.08 $mg \cdot kg^{-1}$ w.wt. in *A. fuligula*. The concentration of uranium in organs and tissues of seabirds decreases in the series: rest of viscera> feathers> skin> liver> skeleton> muscles. The values of ratio $^{234}U/^{238}U$ in marine birds are between 0.90 and 1.23 (Boryło et al., 2010).

The inflow of uranium from catchment areas of the Vistula and Oder River. Analyzed concentrations of uranium isotopes ^{234}U and ^{238}U were very diverse. Higher uranium concentrations were found in the basin of the Vistula and Oder Rivers in the spring and the autumn, what is associated with the use of phosphate fertilizers in agriculture, increased underground and surface runoff of snowmelt water, while the smallest in the summer (Skwarzec et al., 2010a,b). The values of the activity ratio $^{234}U/^{238}U$ in rivers water ranged from 1.22 to 1.40. The isotopes ^{234}U and ^{238}U are not in radioactive equilibrium in the Vistula and Oder Rivers water and values this proportion are between 1.00 and 2.14.

The influence of the phosphogypsum stockpile in Wiślinka on the contamination of the southern Baltic ecosystem. The concentration of uranium in surface water samples collected near Wiślinka ranged widely between 0.05 $\mu g \cdot dm^{-3}$ and 430 $\mu g \cdot dm^{-1}$ (Boryło et al., 2009). The largest uranium concentration in analyzed water samples taken in the vicinity of the phosphogypsum waste heap indicates that uranium is lixiviated from phosphogypsum waste dump to retention reservoir and pumping station. The lower uranium concentration in surface water samples taken from the Martwa Wisła River shows that the migration and distribution of uranium radionuclides from the phosphogypsum waste heap to the Martwa Wisła River are rather slow. We observed that the values of the activity ratio $^{234}U/^{238}U$ in the water with immediate surroundings of waste heap were close to 1 and ranged between 1.00 and 1.10, while the in surface river water from the Martwa Wisła River were higher than one (1.10-1.20) (Boryło et al., 2009).The analysis of values of activity ratio $^{234}U/^{238}U$ in water samples from the Martwa Wisła River indicated that uranium is eluted from phosphogypsum waste and via river system is transported to the Bay of Gdańsk.

Conclusion

The area of the southern Baltic is characterised by high industrial and farming activities, contributing to the annual run-off from the Vistula and Oder Rivers. Moreover phosphatic fertilizers and phosphogypsum contain considerable amounts of uranium. The most important sources of uranium in waters of the southern Baltic are erosion of rock materials, leaching, wet and dry atmospheric fallout as well as human activities carried out in mining and agriculture.

Acknowledgments

The authors would like to thank the Ministry of Science and Higher Education for the financial support under grant DS/530-8120-4-D196-12.

References

1. Boryło A., Nowicki W., Skwarzec B., 2009. Isotopes of polonium ^{210}Po, uranium ^{234}U and ^{238}U for industrialized areas in Poland (Wiślinka), *Internat. J. Environ. Anal. Chem*, 89, 677-685.
2. Boryło A., Skwarzec B., Fabisiak J., 2010. Bioaccumulation of uranium ^{234}U and ^{238}U in marine birds, *J. Radioanal. Nucl. Chem*, 284, 165-172.
3. Skwarzec B., Boryło A., Strumińska D., 2002. Isotopes of ^{234}U and ^{238}U in water and sediments of the southern Baltic, *J. Environ. Radioactivity*, 61, 345-363.
4. Skwarzec B., Boryło A., Strumińska D.I., 2004. Activity disequilibrium between ^{234}U and ^{238}U isotopes in the southern Baltic, *Water, Air and Soil Pollution*, 159(1), 165-173.
5. Skwarzec B., Strumińska D.I., Boryło A., 2006. Radionuclides of iron (^{55}Fe), nickel (^{63}Ni), polonium (^{210}Po), uranium (^{234}U, ^{235}U, ^{238}U) and plutonium (^{238}Pu, $^{239+240}Pu$, ^{241}Pu) in Poland and Baltic Sea environment, *Nukleonika*, 51(Suppl.), 45-51.
6. Skwarzec B., Jahnz-Bielawska A., Boryło A., 2010a. The inflow of uranium ^{234}U and ^{238}U from the Vistula River catchment area to the Baltic Sea, *Radiochimica Acta*, 98, 367-375.
7. Skwarzec B., Tuszkowska A., Boryło A., 2010b. The inflow of uranium ^{234}U and ^{238}U from the Odra River catchment area to the Baltic Sea, *Oceanologia*, 52(4), 1-21.

3-85

The radiochemical contamination (^{234}U and ^{238}U) of zone around phosphogypsum waste heap in Wiślinka (northern Poland)

Grzegorz Olszewski, Alicja Borylo, Bogdan Skwarzec

University of Gdansk, Pomorskie, Poland

Introduction

One of significant components of the Vistula river delta in northern part of Poland (near Gdańsk) is phosphogypsum waste dump near Wiślinka village. The essence of radiotoxicity of phosphogypsum waste heap are natural alpha radioactive elements, which are leached by rains and bioaccumulated in plant and animal organisms. In the longer time they can cause the development of cancer disease (Skwarzec, 1995). The principal source of uranium in the natural environment is the atmospheric precipitation of terrigenic material, as well as fertilizers, phosphogypsum and other anthropogenic sources.

Materials and Methods

Phosphogypsum samples were collected in 1997 and 2007. The chosen species plants (ruderal, hygrophilous, edible plants and corn) were collected in 2008 and 2009. By comparison the same cultivated plants were collected in Luzino (near Wejherowo city) and Czapielsk (near Kolbudy city). The plants after collection were separated into green parts and root. The method of uranium (^{234}U, ^{238}U) determination in analyzed samples was based on procedures established by Skwarzec (1995; 1997; 2009).

Results and Discussion

Phosphogypsum is slightly enriched especially in ^{234}U and ^{238}U radionuclides and is connected with the phosphoric acid production technology and concentration of these radionuclides in phosphorites (Burnett at al., 1996). Among analyzed plants the highest concentrations of ^{234}U and ^{238}U were noticed for ruderal plants. Moreover higher ^{234}U and ^{238}U concentrations were measured in roots and lower in green parts of plants. The values of the activity ratio $^{234}U/^{238}U$ in analyzed plants ranged from 0.96±0.06 to 0.97±0.12 for ruderal plants and from 0.98±0.06 to 0.99±0.04 for hygrophilous plants and indicate that uranium in analyzed plants is of phosphogypsum origin. It is particularly important that the highest ^{234}U and ^{238}U concentrations were characterized for ruderal plants, which are covered with tomentose hairs. The higher activity of uranium in hygrophilous plants suggests that groundwater is a very important source of radionuclides to tissues and organs of these plants. The ratios of $^{234}U/^{238}U$ in analyzed hygrophilous plants were near one, which is consistent with their phosphogypsum character and are similar to values for water from the retention reservoir. The smaller ^{234}U and ^{238}U concentrations were noticed in edible plants. However, only in this group of plants the highest uranium concentrations were measured in green parts of the analyzed plants. As for the meadow, hygrophilous and ruderal plants the larger, pinnate and undulating surface of leaves of analyzed plants are convenient place for uranium deposition. This structure probably can retain phosphogypsum dust. The maximum ^{234}U and ^{238}U concentrations were measured in old leaves and those longer exposed to atmospheric fallout. It is suggested that the transfer of the analyzed radionuclides via the root system is rather negligible. The principal sources of uranium in analyzed edible plants are dry atmospheric fallout and precipitation, and soil resuspension process. Lower concentrations of ^{234}U and ^{238}U were observed in roots of analyzed edible plants. Despite having the same storage root system and the same tubers, plants accumulate varied amounts of radionuclides and this fact may be connected with e.g. turgidity of plants (determined by the water saturation) (Boryło and Skwarzec, 2011). Also the some herbaceous perennial flowering plants have a very shortened stem, which forms the so-called 'bulb' (Szafer et al., 1988). Thanks to this structure the water from atmospheric precipitation can flow downwards to the underground part of plant (Boryło and Skwarzec, 2011). The values of activity ratio $^{234}U/^{238}U$ are between 0.92±0.05 and 0.99±0.08 for edible vegetables, which were collected from private household II and from 0.96±0.10 to 0.99±0.09 for corn. The ^{234}U and ^{238}U concentrations in crop plants from phosphogypsum waste heap recorded in this study are generally higher than in control sites. The activity ratio $^{234}U/^{238}U$ in analyzed edible control plants is 1.02±0.09. On the basis of values of ^{234}U and ^{238}U concentrations in edible plants from phosphogypsum waste zone and uncontaminated area from Czapielsk and Luzino, it was calculated that radiochemical contaminations of vegetables from private household 6.4

and 3 times lower for ^{238}U in green parts and roots times higher in comparison to non-contaminated vegetables (control samples). The radionuclides activities in soil samples, which were collected around and from the slope of phosphogypsum waste heap, were much higher: from 87±5 to 342±11 Bq kg^{-1} wet wt for ^{238}U. The lower ^{234}U and ^{238}U radionuclides activities were estimated for soil samples from private household.

Conclusion

As a result of resuspention from the surface of phosphogypsum waste heap aerosols are emitted to near surroundings. Apart from atmospheric deposition, the plants can receive radionuclides from radioactive fallout and from the phosphogypsum fertilized soils. The obtained results of determinations of radionuclides in various environmental points indicate that the 300-meter buffer zone is not able to offset the negative influence of phosphogypsum waste heap on the surrounding environment.

Acknowledgments

The authors would like to thank the Ministry of Science and Higher Education for the financial support under grant DS/8120-4-0176-12, BW-538-8120-1470-11, BW-538-8120-1078-12 and UMO-2012/05/N/NZ7/00978. The publication is financed from European Social Fund in as a part of a project “Educators for the elite – integrated training program for PhD students, post-docs and professors as academic teachers at University of Gdansk” within the framework of Human Capital Operational Programme, Action 4.1.1, Improving the quality of educational offer of tertiary education institutions.

References

1. Boryło A, Skwarzec B. Bioaccumulation of polonium ^{210}Po and uranium (^{234}U, ^{238}U) in plants around phosphogypsum waste heap in Wislinka (northern Poland). Radioch Acta 2011; 99:1-13.

2. Boryło A, Skwarzec B, Olszewski G, The radiochemical contamination (^{210}Po and ^{238}U) of zone around phosphogypsum waste heap in Wiślinka. J of Environ Science and Health Part A 2012;47:675-687.

3. Burnett WC; Michael K; Schultz K; Hull CD. Radionuclide flow during the conversion of phosphogypsum to ammonium sulfate. J Environ Radioact 1996; 32(1-2): 33-51.

4. Skwarzec B. Polon, uran i pluton w ekosystemie południowego Bałtyku. Rozprawy i monografie 6. Sopot: Instytut Oceanologii PAN; 1995.

5. Skwarzec B. Radiochemical methods for the determination of polonium, radiolead, uranium and plutonium in environmental samples. Chem Anal 1997; 42:107.

6. Skwarzec B. Determination of radionuclides in aquatic environment. In: Analytical measurement in aquatic environments. Tylor&Francis: PE, 2009.

7. Szafer W, Kulczyński S, Pawłowski B. Rośliny polskie. Warszawa: PWN;1988.

3-86

^{241}Pu in the southern Baltic Sea

Dagmara Struminska-Parulska, Grzegorz Olszewski, Bogdan Skwarzec

University of Gdansk, Pomorskie, Poland

Most contamination studies have focused on alpha emitting plutonium isotopes so far. ^{241}Pu is less important in terms of its radiotoxicity than the α-emitting plutonium radionuclides ^{238,239,240}Pu but is quite significant because of its huge contribution to the whole plutonium fallout. Moreover β-emitting ^{241}Pu ($T_{1/2}$=14.35 years) decays to the long-living, highly radiotoxic α-emitting ^{241}Am ($T_{1/2}$=432.2 years) (Mussalo et al., 1980). The main sources of plutonium in the marine environment are nuclear weapon tests, satellites and civil nuclear power plant accidents (Aarkrog, 1991). Since 26 April 1986 there has been a new source of plutonium, namely the Chernobyl accident that should be taken into consideration (Skwarzec, 1995; Strumińska and Skwarzec, 2006). Our previous experiments on air samples indicated extreme increase of ^{241}Pu amount in atmospheric dust; in April 1986 and the activity of ^{241}Pu reached 3643 mBq g^{-1} dw (Strumińska and Skwarzec, 2006). The available information about the bioaccumulation and distribution of ^{241}Pu in the Baltic Sea ecosystem and Poland territory is still very limited. The main purpose of the present work was to complete the present knowledge and estimate the further levels of the Baltic Sea environment contamination.

The samples of water, plankton and fish from the southern Baltic (the Gulf of Gdańsk, the Słupsk Bank, the Bornholm Deep and the Pomeranian Bay) were collected from 1997 to 2001 and the concentrations of ^{241}Pu were measured using the indirect method (Skwarzec, 1997; Skwarzec et al., 2001; Strumińska and Skwarzec, 2006). The plutonium samples were remeasured 10 years later using an alpha spectrometer Alpha Analyst Canberra Packard and the determination of ^{241}Pu was done by measuring the increment in ^{241}Am from the decay of β-emitting ^{241}Pu (Skwarzec et al., 2001; Strumińska, 2003). All ^{241}Pu activities were calculated on the sampling time on the basis of formula by Strumińska and Skwarzec (2006). The accuracy and precision of the plutonium analysis were less than 7% (1.5-6.4%), estimated by analysis of the IAEA standard materials.

Seawater

The highest total ^{241}Pu concentration in seawater was found in the Słupsk Bank (3.35±0.17 mBq dm^{-3}) and this area had the highest concentration of ^{241}Pu connected to suspended matter as well (1.94±0.12 mBq dm^{-3}). High concentrations of ^{241}Pu in the central part of the southern Baltic Sea can be a result of Baltic water circulation. In the southern Baltic Sea basins, the circulation has forms of separate circulation cells; thanks to the Earth rotation (Corliolis effect) the seawater moves anticlockwise (Groenwald, 2003). The highest activity of ^{241}Pu in colloidal fraction was observed in the Gdańsk Bay. It is known the Vistula River carries a lot of plutonium; it is one of the biggest sources of plutonium in the southern Baltic (enriches the sea with 89.0 MBq of $^{239+240}$Pu annually) (Skwarzec et al., 2011). While $^{239+240}$Pu concentrations in the southern Baltic were increasing from the east to the west (Strumińska and Skwarzec, 2004), the total ^{241}Pu concentrations in seawater slightly increased from the west to the east. Obtained data showed increase of ^{241}Pu activities in comparison to our previous studies in May 1987 (Strumińska and Skwarzec, 2006). In water samples from the Gulf of Gdańsk and the Gdańsk Deep collected in 1999, the values of ^{241}Pu activities were almost 15 times higher. Despite all these years from the Chernobyl accident, the radiological effects are still observed in the environment and mean late plutonium inflow effect from Baltic catchment area.

Phyto- and zooplankton

The ^{241}Pu activity in phytoplankton sample from the Pomeranian Bay was 1.06±0.09 mBq g^{-1} dw. Within zooplankton samples the highest ^{241}Pu activity was found in samples from the central part of the southern Baltic (2.66±0.16 mBq g^{-1} dw) and from the Gdańsk Deep (2.64±0.70 mBq g^{-1} dw). In zooplankton samples, similar situation to seawater samples was noticed – the highest concentrations of ^{241}Pu were found in the central part of the southern Baltic Sea, and similarly to seawater it could be a result of Baltic water circulation.

Fish

Generally the data show significant differences in ^{241}Pu concentrations among all the species examined. The highest values of ^{241}Pu activities for whole organism were found in fish from *Perciformes:* benthic round goby (0.863±0.066 mBq g^{-1} ww) and pelagic perch (0.666±0.001 mBq g^{-1} ww). Both fish species feed on benthic invertebrates and small fish; especially round goby feeds mainly on blue mussel (*Mytilus trossulus*) and remobilizes heavy metals and radionuclides accumulated by these organisms (Kostrzewa et al., 2004). The lowest ^{241}Pu activity was found in flounder (0.104±0.009 mBq g^{-1} ww). The flounder is benthic fish but feeds on plankton and insects larvae when young and benthic invertebrates and small fish when adult. The differences in ^{241}Pu activity in the whole body in round goby and flounder could be caused by their diet. The plutonium was also non-uniformly distributed between the organs and tissues of the analyzed fish, especially pelagic herring and cod as well as benthic flounder. Most of ^{241}Pu in herring, cod and flounder was located in soft tissues. The tendency found during ^{241}Pu analysis agreed to our previous studies on $^{239+240}$Pu. The amount of plutonium in fish alimentary system confirms its role in plutonium intake. The participation of fish alimentary system in plutonium bioaccumulation depends on the organ function; the fish's feeding habits and its location in the Baltic Sea.

Radiation doses

It has been estimated that the yearly intake of ^{241}Pu via the consumption of Baltic fish by Poles (about 5 kg year^{-1}) equaled the intake of average value of 2.2 Bq per capita. According to muscles only (filet) the average consumption value decreased to 0.6 Bq. The annual individual effective dose values calculated on this basis (using the conversion factor given by the UNSCEAR (2000) – 4.8 nSv Bq^{-1} for ^{241}Pu) are 10.6 nSv per whole fish and 2.8 nSv according to muscles (filet). The total natural radiation exposure in Poland leads to an annual effective dose of 2.8 mSv (including ^{222}Rn) (Jagielak et al, 1997). This indicates the impact of the consumption of ^{241}Pu with Baltic fish on the annual effective dose for a statistical inhabitant of Poland is very small.

The authors would like to thank the Ministry of Science and Higher Education for the financial support under grant DS/8120-4-0176-12.

References

1. Aarkrog A. Environmental Science and Technology Department/Ecology Section. Risø National Laboratory, Roskilde, Denmark; 1991.
2. Groenwald M. Geografia morza. Gdańsk: Podkowa; 2003
3. Jagielak J, Biernacka M, Henschke A, Sosińska A. Radiologiczny Atlas Polski. Warszawa: PIOŚ, CLOR, PAA; 1997.
4. Kostrzewa J, Grabowski M, Zięba G. Polski. Arch Pol Fish 2004;12(2):21.
5. Mussalo H, Jaakkola T, Miettinen, JK. Health Phys 1980;39(2):245.
6. Skwarzec B. Polon, Rozprawy i monografie, IO PAN. Sopot; 1995.
7. Skwarzec B. Chem Anal (Warsaw) 1997;42:107.
8. Skwarzec B, Strumińska DI, Boryło A. Bioaccumulation and distribution of plutonium in fish from Gdansk Bay. J Environ Radioact 2001;55:167.
9. Skwarzec B, Jahnz-Bielawska A, Strumińska-Parulska DI. J Environ Radioact 2011;102:728.
10. Strumińska DI. PhD thesis. Gdańsk University, Faculty of Chemistry; 2003.
11. Strumińska DI, Skwarzec B. J Environ Radioact 2004;72:355.
12. Strumińska DI, Skwarzec B. J Radioanal Nucl Chem 2006;268(1):59.
13. Strumińska-Parulska DI, Skwarzec B. Oceanologia 2010;52(3):499.
14. UNSCEAR Sources and effects of ionizing radiation, Vol I: Sources, Appendix A 2000.

3-83

Purification and separation of U, Pu and Am isotopes in environmental samples by extraction chromatography for alpha-spectrometry analyses

Silvia Stoica, Cristian Dulama, Alexandru Toma, Cristina Ciocirlan, Relu Dobrin

Institute for Nuclear Research, Pitesti, Romania

Introduction

The measurement of radioactivity concentrations in soil and ocean sediments samples is an important tool for the monitoring of the environment. For this purpose, within our laboratory has been implemented a radiochemical procedure for the determination of alpha-emitting isotopes of uranium, plutonium and americium. The main steps of the procedure include leaching and dissolution of the sample, separation by extraction chromatography, source preparation and counting by alpha-spectrometry.

The analysis of environmental samples for low levels of uranium, plutonium, americium and other actinide elements is often hampered by sample-dependent problems involving the composition and/or mineralogy of specific samples. Relatively small samples (1-2 g of soil) are required to reach the extremely low detection limits occasionally mandated for environmental monitoring.

Experimental

The experiments were conducted using different environmental samples (soil and ocean sediments) in order to improve the purification and the separation of uranium, americium and plutonium with the perspective to optimize a routine procedure. ^{242}Pu and ^{243}Am and ^{232}U tracers were added to the sample for chemical recoveries monitoring, to correct the results and to improve precision.

To promote the release of radionuclides from solid environmental matrices such as geological materials the samples are leached and decomposed with mineral acids. Plutonium in these samples can be leached with acids such as HNO_3, hydrochloric acid and hydrogen peroxide. Most of the U in the terrestrial environment is contained in silicate minerals, which are often resistant to leaching with mineral acids other than hydrofluoric acid. Determination of U in terrestrial samples, therefore, requires an application of total sample decomposition in most cases.

Actinides were separated and purified by extraction chromatography with UTEVA and TRU resin, products of Eichrom Technologies. After separation, the actinides were co-precipitated with cerium fluoride, after minimum 30 minutes, the solution was filtered on a 0.1µm filter, which was dried then on a IR lamp and mounted on a stainless steel planchet.

Measurement of actinides was carried out by using a passivated implanted planar silicon (PIPS) detector with a typical resolution of 24 keV.

Fig. 1 shows the sequential separation procedure for U, Pu and Am isotopes using extraction chromatography.

Results and discussion

Results showed a constant chemical recovery and resolved peaks. To determine our laboratory performance (precision, accuracy and trueness of the method), IAEA soil samples were used as reference material. Therefore, the mean relative bias and the relative dispersion of the values were calculated for each analysis category of the present study. The values obtained are well within the acceptance criteria.

Alpha-energy measurements allowed us to find the minimum detectable activity (MDA) and the values are below 0,3 mBq/g for U and Pu isotopes and below 1 mBq/g for Am-241. The results in this work lead us to improve the purification and the separation of uranium, americium and plutonium with the perspective to optimize a routine procedure and offer a more rapid and effective surveillance tool.

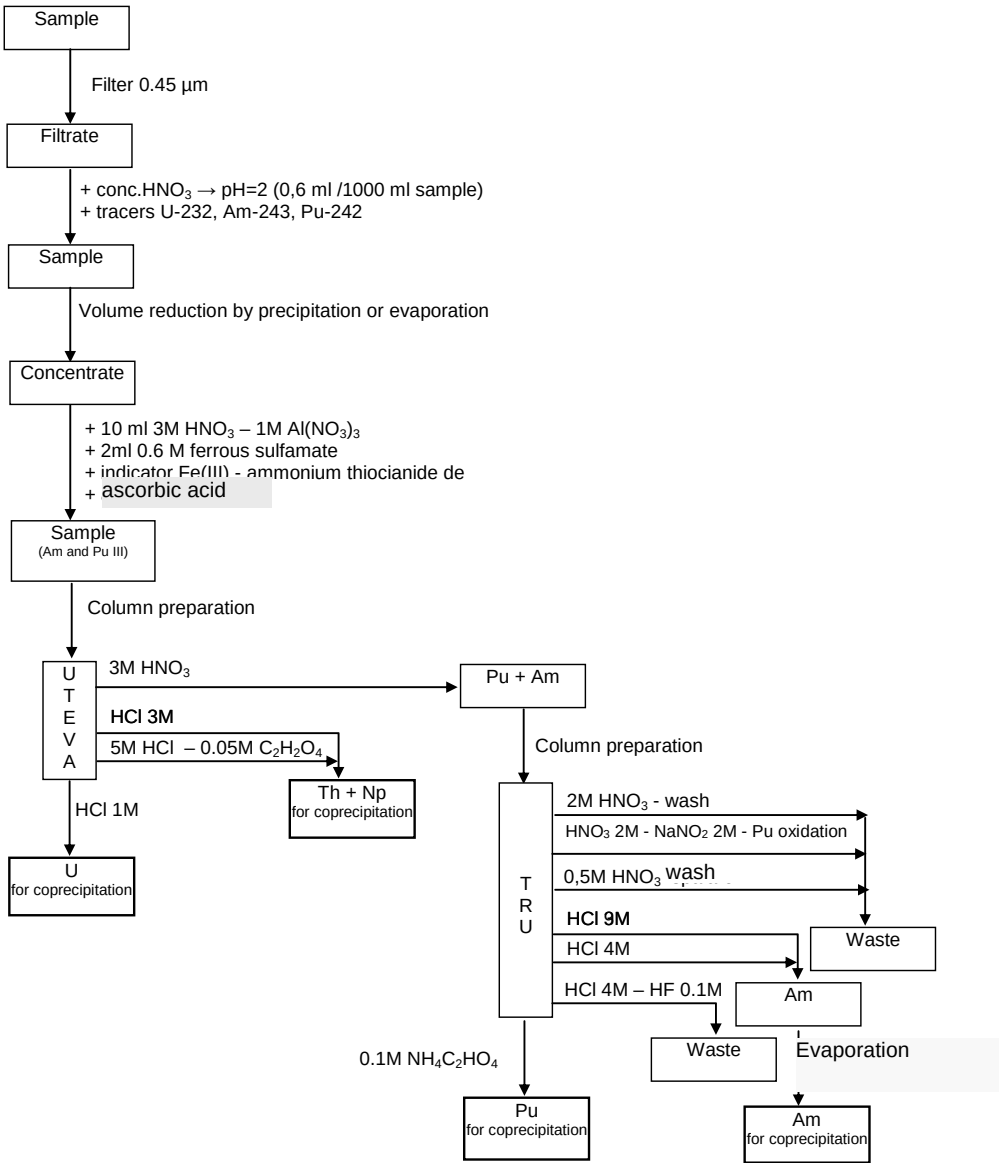

Fig. 1. Flow-chart of sequential separation procedure for actinide

By validating and implementing this method, Radiation Protection, Environment Protection and Civil Protection Laboratory within INR wishes to increase its technical capabilities and area of competence as notified laboratory. Also, to offer reliable results our laboratory participates annually to intercomparisons exercises and proficiency tests held by IAEA and ALMERA Network for radioactivity assessments of various environmental samples and reference material.

3-87

Study of the behaviors and the transfers of $^{238,239+240}$Pu and ^{241}Am in different natural compartments (soil, water, sediment)

Amélie Leclercq[1], Violaine Philippini[1], Christophe Den Auwer[1], Hervé Michel[1], Tiina-Leena Lavonen[1,2], Pier Lorenzo Solari[3], Samir Safi[4], Vittorio Barci[1], Geneviève Barci-Funel[1]

[1]Université de Nice-Sophia Antipolis, Institut de Chimie de Nice, UMR CNRS 7272, PCRE, Nice, Alpes Maritimes, France, [2]Laboratory of Radiochemistry, Falculty of Science, University of Helsinki, Helsinki, Finland, [3]Synchrotron SOLEIL, MARS beam line, Gif sur Yvette, France, [4]Université Paris Sud, Institut de Physique Nucléaire d'Orsay, Orsay, France

Nuclear weapon tests in the 60s and the Chernobyl nuclear power plant accident (1986) released non-negligible quantities of radionuclides (RNs) in the environment. This radioactive pollution has been studied since the 80s in south-east of France[1] and particularly in the "Parc national du Mercantour"[2]. The aim of this new investigation is to better understand the anthropogenic dispersion of contaminating RNs in natural environment. Thus, a non-anthropized catchment basin located in a wooded area at 1 742 m height in the "Boréon" mountain massif has been selected. Natural samples (soil, sediment, water) were collected in a mountain artificial water damming drainage basin.

The study was separated into two parts. In the first one, anthropogenic RNs ($^{238,239+240}$Pu and ^{241}Am) have been measured by alpha spectrometry in the three compartments (soil, water, sediment) after chemical separation and concentration in the laboratory. In the soil, the radioactive pollution stays near the surface. Furthermore, the isotopic ratios (^{238}Pu/$^{239+240}$Pu and ^{241}Am/$^{239+240}$Pu) demonstrate that $^{238,239+240}$Pu and ^{241}Am originate from the atmospheric nuclear weapon tests. In the lake sediments, direct deposits of the radioactive fallouts are detected in depth due to the effect of sedimentation causing RNs to leave the ground surface. The transfer between those two natural compartments demonstrates the importance of water as a transport vehicle and the prevalence of leaching compared to lixiviation. Leaching carries RNs from the drainage basin slopes, to the clearing and then to the sediment through the aqueous phase. In solid samples, RNs have a low mobility: ^{241}Am is the most movable isotope whereas $^{239+240}$Pu the less movable.

Due to the difficulties to model the dispersion of RNs in these compartments because of the intrinsic intricacy of natural media, a second step of this study has focused on simplified chemical systems using analogues. In order to go beyond the previous macroscopic description, the chemical reactivity of the RNs *versus* soil, water and sediment must be explored. Since the description of ^{241}Am in natural media is lacking data and since Am presents a much simpler RedOx chemistry than lighter actinides, we have selected it for the study of our semi-natural system. In addition, lanthanide analogues can be used to simulate Am behavior in simplified chemical systems[3]. Structural analysis of spiked water by X-ray absorption spectroscopy and time-resolved laser induced spectroscopy) have led to a better knowledge of Am behavior using Eu as an analog. In spiked water, the presence of two complexes, one inorganic $Eu(OH)CO_{3(aq)}$ and one organic with humic acids, has been proposed.

The combination of these two approaches improves the knowledge of the RNs behavior in natural compartments. In the future, inventory results related to sorption and structural analysis data on model systems may be integrated in geochemical models to predict the behaviors of RNs in case of a new accidental dispersion.

References

[1] Barci, G., Dalmasso, J., Ardisson G., *J. Radioanal. Nucl. Chem.* **1987**, 117, 337-46

[2] Rezzoug, S., *et al*., *J. Environ. Radioact.* **2006**, 85, 369-79

[3] Silva, R.J., *et al*., Chemical Thermodynamics of Americium, **1995,** Chemical Thermodynamics Series Volume 2

3-88

Sorption Characteristics of the Rocks Confining a Radioactive Waste Repository

Yulia Konevnik

IPHE RAS, Moscow, Russia

The radioactive waste (RW) possessing countries consider the possibility of the intermediate level radioactive waste disposal into the shallow repositories and the high level waste disposal into the deep ones located in the rock masses. The RW disposal safety is based on the created system of protective barriers that consists of both engineered barriers and natural ones, the latter being the repository confining rocks. Unlike the engineered barriers, the natural ones do not have the physical lifetime. The natural barrier capacity to function as a safety barrier depends on the geological and geochemical structure of the rock mass and its sorption properties with respect to different radionuclides.

In this work those characteristics are evaluated for samples taken in the “Eniseisky” area of the Nizhnekansky mountain group at the depth of 450-550 m at the RW repository location and from the location zone of the shutdown industrial uranium graphite reactor (IUGR). Currently the “Eniseisky” area is officially approved as the location for the RW ultimate disposal site under design.

The rock mass in the “Eniseisky” area is characterized as low fractured and consists of up to 80-90% by volume of the Archean biotite-plagioclase gneisses, differently altered. The gneisses contain the primary minerals, namely, plagioclase, quartz, biotite, muscovite; the secondary ones, namely, chlorite, albite, sericite, stellerite, epidote, calcite; supergene minerals, such as illite, kaolinite, montmorillonite, smectite as well as diabase up to 10% by volume. When drilling one of the wells a 7 cm thick crushed zone has been discovered at the depth of 250 m; the samples from the zone were studied in this work, too.

The sorption experiments were conducted with crushed rock samples of 0.1-0.25 mm fraction and the simulated surface and deep underground water of the composition analogous to that of the underground water in the repository location zone, under aerobic and anaerobic conditions.

For the investigated samples the distribution coefficient (K_d) values have been determined. For Pu(IV), Am(III), Cs(I) the K_d values are slightly higher than for Co(II) and Np(V). For Sr(II) and U(VI) the K_d values are lower; it is explained by the high mobility of those radionuclides in the geologic media. The retention factor (R) evaluation witnesses the fact that the distribution rate of the radionuclides investigated is by two-three orders of magnitude less than the underground water migration rate, just for strontium the distribution rate being less by merely one order of magnitude.

To evaluate the long-term radionuclide behavior in the geological medium the sorption experiments were performed with the rock samples previously contacted with the simulated underground water for over 2 years. For all the radionuclides studied the increase in the adsorbed radionuclide percentage with time has been observed. At that, the content of Pu and Am in the liquid phase came down below the detection limit, whereas the strontium concentration in the liquid phase decreased by a factor of 4. The neptunium concentration in the liquid phase was slightly reduced as well, neptunium being one of the most mobile long-lived radionuclides.

To investigate the adsorption reversibility and the strength of the radionuclide bond with the rock the adsorbed radionuclide speciation has been studied by the Tessier technique [1]. The percentage of radionuclides leached out with the underground water is no more than 5-10%, whereas the content of strongly fixed radionuclide species exceeds 50%. With time the percentage of the latter is gradually rising mainly on account of the increase in the quantity of the radionuclide bound to the iron-manganese oxides and to the residual fraction insoluble under the acidic treatment.

The most pronounced increase in the quantity of adsorbed radionuclide bound to the Fe/Mn oxide fraction was observed for Np. It was shown that the basic part of the adsorbed

neptunium is in the oxidation state of IV, whereas during the experiment both in the feed solution and in the liquid phase Np was detected in the oxidation state of V exclusively. From the data obtained the conclusion on the reduction of neptunium by the iron-bearing minerals contained in the rocks confining the RW repository under design has been made.

Thus, the rock mass will function as the anti-migration protective barrier with respect to the radionuclides contained in the solidified RW and irradiated graphite disposed of in the underground repository located in the rock mass even though the latter has the zones of higher permeability.

References

1. Tessier, A., Campbell, P.G.C., Bisson, M. Sequential extraction procedure for the speciation of particulate trace metals// Anal. Chem. 51 (1979). P. 844-851

3-89

Romanian perspective on the iron nano-particles utilization as remediators for radioactive polluted environment

Ioana-Carmen Popescu[1], Eugenia Panturu[1], Antoneta-Constantina Olteanu-Filcenco[1], Thomas Bleigh Scott[2], Richard Andrew Crane[2]

[1]R&D National Institute for Metals and Radioactive Resources, Bucharest, Romania, [2]Interface Analysis Centre, University of Bristol, Bristol, UK

The global energetic crisis has determined the development of nuclear fuel industry beside the green energy sources. Nuclear electric power represents a much more reliable energy supply then the green one, which doesn't work continuously. The main flaw of the nuclear power source is the environmental radioactive pollution, which represents a significant challenge for the entire scientific community due to its carcinogenic action. Water and air represents the main spreading "vehicles". This sensitive issue is solved by updated remediation technology. Ion exchange, solvent extraction, adsorption, biotechnologies and phytoremediation represent the main decontamination technologies used for wastewater treatment. Recently the iron nano-particles (INPs) have proven their strong remediation power of a relatively large variety of contaminants such as the chlorinated derivatives, heavy and radioactive metals. Due to their small size and high specific surface area the INPs are very reactive. They change the redox environmental conditions determining the metallic ion species' precipitation and immobilization on the reacted INPs' surface. The INP's may be used simple or embodied in different materials. The present contribution aims to point out the Romanian main achievements concerning the INPs' utilization as radioactive decontaminators of uranium-contaminated wastewater (mine water and water resulted from the uranium ore processing plant). Three research projects were achieved by our institute, one under the National Research Program and the other two in partneship with Interface Analysis Centre of University of Bristol as coordinators.

The first one represents the researches on the synthesis, characterization and decontamination capacities tests of the nanostructured zero-valent iron, which can be used for the radioactive contaminated water treatment from the uranium ore processing plant and it was funded by the Romanian National Authority for Scientific Research. There were synthesized two types of nanostructured iron namely: nanostructured zero-valent iron obtained by the boron hydride reducing method and nanostructured iron laid-down on the solid support -activated carbon Purolite resin type AG 20G and Purolite resin type C 160. The research for testing the decontamination capacity of the synthesized materials, which were added commercial resin Purolite ARSEN-Xnp impregnated with iron nanoparticles, have led to a decontamination capacity varied directly as the amount of nanostructured iron from the reactive material. Distribution coefficient values (for uranium) obtained after experiments are related both to the content of nano-iron material reagent and their adsorption properties. Utilization of these types of materials leads to a process with a decontamination efficiency of over 99.99% according to the environmental quality standards in the field of water policy.

The second one was achieved in partnership with the Interface Analysis Centre of University of Bristol and it was funded by NATO. There was studied the interaction of INPs with synthetic solutions containing U, Mo, Cr, Cu (10 ppm of each one) and with mine water respectively at various values of pH and on different types of INPs (simple and commerical ones). It is continued by a new project funded by Royal Society that studies the in-situ treatment of uranium-contaminated waters using iron nanoparticles.

3-90

New insights into uranyl interaction with proteins at physiological pH

Quentin Raffy, Isabelle Billard, Catherine Galindo, Mireille Del Nero, Rémi Barillon

Université de Strasbourg, IPHC, CNRS, UMR7178, 67037 Strasbourg, France

Introduction

Given uranium toxicity, comprehension of uranyl interaction with biological material of human relevance is of utmost importance, from the whole body scale to the molecular level. At the molecular level, uranium interaction with proteins has attracted a lot of attention, in particular the blood serum proteins Human Serum Albumin and Transferrin, which are likely to transport uranyl in the body and therefore to play a key role in its toxicity.[1-5]

It is well known that uranyl undergoes complex speciation at physiological pH, and can form complexes with serum small molecules such as carbonates, making the study of such systems rather intricate.

Results

We have studied protein-uranyl interaction while taking into account all known uranyl species that could exist at physiological pH. Bovine Serum Albumin (BSA) is well known to bind several metals, and shares similarities with Human Serum Albumin, which makes it a good candidate for a uranyl-binding protein model.

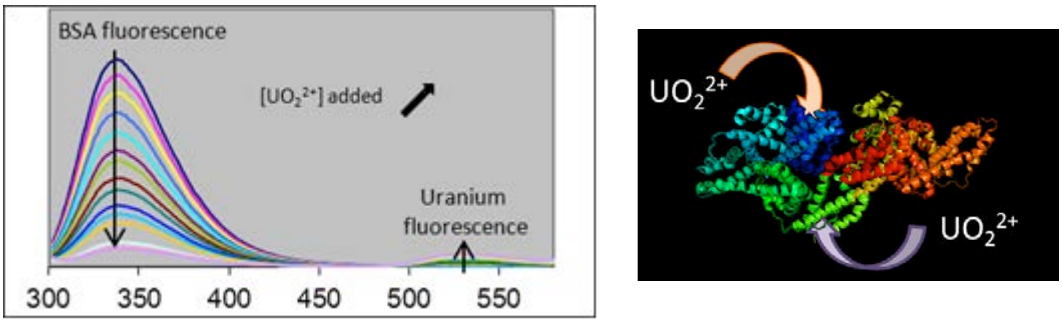

Figure 1: A. Change in fluorescence spectrum of BSA solution upon addition of uranyl solution. B. Schematic representation of UO_2^+/BSA complexation

The protein – uranyl interaction was followed by means of UV-Visible spectroscopy and fluorescence measurements (static and time-resolved). Strong fluorescence quenching of BSA was observed upon uranyl addition (cf. figure 1 A.). Addition of BSA to an uranyl solution also resulted in uranyl fluorescence quenching. The data obtained were treated using speciation software CHEAQS and home-made fitting program.

On this experimental basis, we propose a model, involving two successive complexations of several uranyl moieties, which is in very good agreement with the experimental data (figure 2). Our results allowed determination of the number of uranyl moieties complexed by the protein, as well as the corresponding equilibrium constants. Further experiments are in progress to determine the functional groups of the protein involved in the complexation.

The experimental protocol and data analysis can be applied to any protein containing enough fluorescent residues to measure the quenching induced by uranyl addition. Further studies with Human Serum Albumin will be conducted and compared to results obtained with other models taking into account or not the full speciation of uranyl.[2,6]

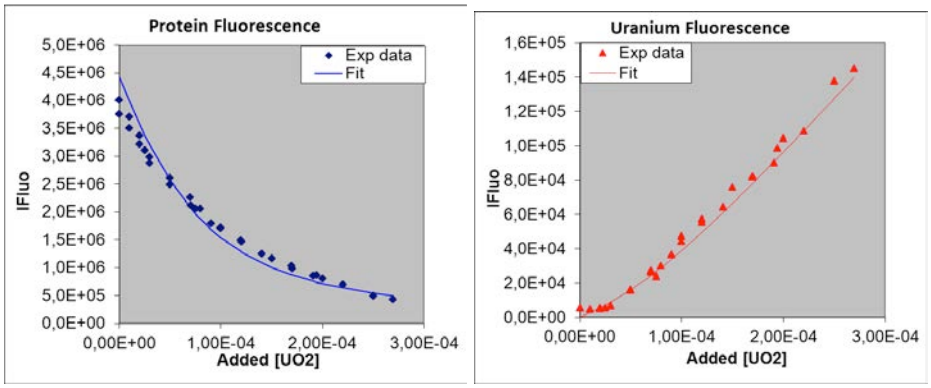

Figure 2: A. Evolution of the BSA fluorescence upon addition of uranyl. B. Evolution of the uranium fluorescence in the same experiment. Dots: Experimental data, plain line : fitted data

References

1 Michon J. *et al.*, *J. Fluoresc.*, **2010**, *20*, 581-590

2 Montavon G. *et al*., *J. Inorg Biochem,* **2009**, *103*, 1609-1616

3 Vidaud C. *et al.*, *Biochemistry*, **2007**, *46*, 2215-2226

4 Benavides-Garcia M.G., Balasubramanian K., *Chem. Res. Toxicol.* **2009**, *22*, 1613-1621

5 Hémadi *et al.*, *J. Phys. Chem. B*, **2011**, *115*, 4206-4215

6 Duff M.R.*et al*., *Angewandte Int. Ed.*, **2006**, *45*, 137-139

3-91

Uranium(VI) sorption on aluminium(hydr)oxides – inferring a functional relationship between sorption complex structures and physicochemical parameters by application of artificial neural networks

André Rossberg[1,2], Andreas C. Scheinost[1,2]

[1]Helmholtz-Zentrum Dresden-Rossendorf e.V. (HZDR), Dresden, Germany, [2]The Rossendorf Beamline at ESRF (ROBL)), Grenoble, France

Depending on physicochemical parameters (P) like pH, pCO2, surface area, surface loading, etc. structurally different U(VI)-aluminium(hydr)oxide sorption complexes are formed and are discussed in the literature. By using EXAFS and IR it was shown that edge sharing complexes, mono- and polynuclear ternary carbonato complexes, polynuclear corner and edge sharing complexes can be formed and that surface precipitation of schoepite occurs at higher U(VI) loadings. It cannot be excluded that depending on P several sorption complexes exist at the same time, hence the spectroscopic signal will be the weighted sum of the spectra of the mixed sorption complexes and therefore spectral mixtures are measured. In such case the structural analysis becomes problematic and can results in wrong interpretations. Therefore it would be desirable to have the possibility to un-mix the spectra into the spectra of the pure complexes and their fractions for each spectral mixture. The obvious advantage would be that the structural analysis is not anymore distorted and that the correlations of the resulting fractions of the sorption complexes with the parameter space P can be investigated. The latter aspect would bring an enormous benefit, because then the range of existence of the sorption complexes could be found directly and basing on spectroscopy.

Up to now the most powerful technique of choice to decompose spectral mixtures of coexisting sorption complexes is the factor analysis (FA) (1). However, the mathematical framework of FA does not allow the inclusion of other input than spectra and fractions, which is a strong drawback concerning the almost available additional information about P for each sample. Furthermore, if spectra from different series are included in the analysis and if the EXAFS spectra of the sorption systems are measured at the trace level, which is often the case, the experimental error can become too high for getting a reliable solution.

Artificial neural networks (ANN) can handle any kind of information. ANN's are commonly used for instance for text-, speech-, face- recognition, for prediction of time series like stock market prediction etc., hence for applications which need to infer a function from observations when a mathematical procedure will be too complicated or too expansive. Indeed, with the sorption systems one ends up in a similar situation that a function between the spectra and P exits, but that this function is obviously very complicated to find. A special kind of such ANN is the self-organizing map (SOM), invented by T. Kohonen in 1982 (2), which enables a representation of high dimensional data in a lower dimensional space, usually by mapping it onto a two-dimensional map. In this way SOM's were already used in spectroscopy for clustering and in order to find latent functional relationships between spectra and physicochemical parameters, but despite of the enormous advantages of SOM's it applications are still rare. However, up to now SOM's were not able to decompose spectral mixtures.

We modified the SOM algorithm so that for the first time also a SOM is able to decompose spectral mixtures into the spectra of the pure complexes, and their fractions like FA. Therefore the newly developed SOM brings the unique advantage that the range of existence of the sorption complexes can now be found basing on spectroscopy.

Concerning the decomposition of the spectral mixtures, we show that the robustness of the SOM against experimental error is higher when compared with FA. Results will be shown for theoretical chemical systems and for the EXAFS spectra of 30 samples of U(VI) sorbed on aluminium(hydr)oxides. For the latter example the SOM predicts the spectra of six acting sorption complexes together with their fractions for each sample. Moreover, due to the fact that the SOM infers a functional relationship between the spectra (sp) and the additionally included parameter space (simplified: sp = F(P), where P = pH, pCO2, surface area, surface loading, fractions of the sorption complexes) the ranges of existence of the sorption complexes can be deduced depending on P. Figure 1 shows an example for the correlation of three from the six identified sorption complexes with the pH. The result shows that as higher

the pH as higher the probability that polynuclear and ternary carbonato sorption complexes are formed and that at low pH formation of edge sharing sorption complexes is favoured.

Moreover, we show that for a given EXAFS spectrum of a sample and with the determined functional relationship, sp = F(P), the unknown fractions of the sorption complexes and the values of the parameter space P can be predicted. In turn, an EXAFS spectrum can be predicted for a given set of P. Instead of EXAFS spectra also spectra from other types of spectroscopy can be used. In sum, we think that due to the predictive feature and the large versatility SOM's might have in future strong impact on the understanding of the migration of radionuclides in the geosphere.

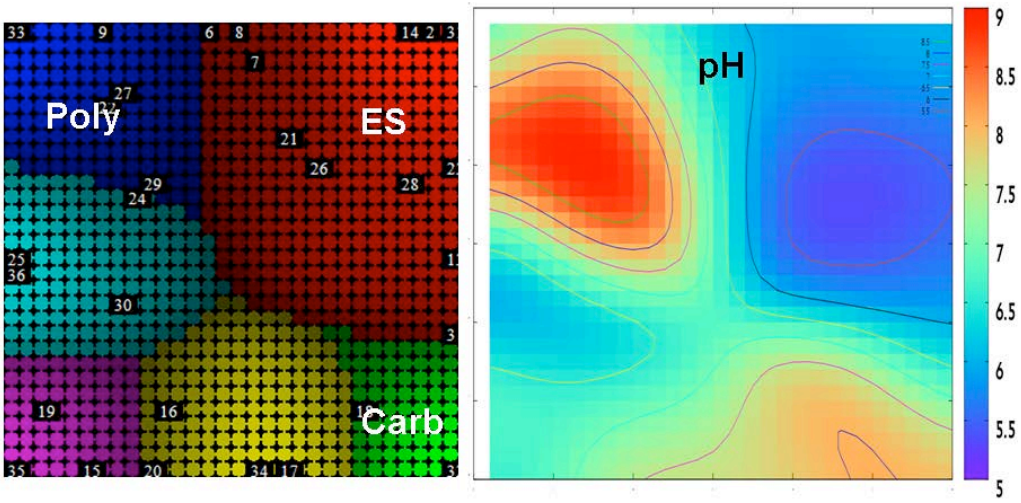

Figure 1. Example for the influence of the pH on the formation of polynuclear (Poly), edge-sharing (ES) and ternary carbonato (Carb) sorption complexes. Left: Self-organizing map after learning, each point (30x30) correspond to a neuron which contains a EXAFS spectrum and the values of the parameter space P (see definition of P in the text), each colour corresponds to one sorption complex, as darker the colour as more the complexes are mixed, small numbers are the identifier of the included samples at the determined positions (neurons), 31-36 are the pure sorption complexes. Right: Complementary map for the distribution of the pH.

References.

1. Rossberg, A.; Ulrich, K. U.; Weiss, S.; Tsushima, S.; Hiemstra, T.; Scheinost, A. C., Identification of Uranyl Surface Complexes on Ferrihydrite: Advanced EXAFS Data Analysis and CD-MUSIC Modeling. Environmental Science & Technology 2009, 43, (5), 1400-1406.

2. Kohonen, T., Self-organized Formation of Topologically correct Feature Maps. Biological Cybernetics 1982, 43, (1), 59-69.

MATERIALS SCIENCE

PLENARY & INVITED

4-01

Development Issues of Metal Fuels for Fast Reactors

Takanari Ogata

Central Research Institute of Electric Power Industry, Komae, Tokyo, Japan

Metal fuels utilizing U-Pu-Zr or U-Zr alloys were extensively developed in the Integral Fast Reactor program initiated in 1984 in Argonne National Laboratory. A wide variety of irradiation tests, in-pile transient tests, and out-of-pile heating tests in the program revealed the main features of steady-state irradiation behavior and transient performance of metal fuel, and demonstrated the high burnup potential up to about 20 at.% burnup. Increase in gas plenum pressure due to fission gas accumulation and cladding wastage due to fuel-cladding chemical interaction (FCCI) were identified as factors controlling metal fuel lifetime. Early commercial use may be possible as far as peak burnup is less than about 15 at.% and maximum cladding temperature is about 600^{o}C or lower. Remaining issues from an engineering viewpoint will be to confirm steady-state irradiation behavior of fuel pins with commercialized cladding materials of an improved high-temperature strength, and to demonstrate performance of high burnup fuel pins during unprotected transient events.

In recent years, corresponding to conceptual design studies of fast reactor cores for various needs, new metal fuel concepts have been explored aiming at further increase in fuel burnup, increase in maximum cladding temperature and application to minor actinide (MA) burner reactors. Barrier materials inside cladding wall (cladding liner) for suppressing FCCI and fission gas ventilation for reducing plenum gas pressure will be effective to increase the limits of maximum cladding temperature and/or fuel burnup. In a ~75% smear density metal fuel pin, at an axial position where local burnup exceeds more than approximately 10 at.%, incompressible volume increase of fuel slug due to non-gaseous fission product accumulation (solid FP swelling) starts to cause fuel-cladding mechanical interaction (FCMI). In order to attain peak burnup of higher than about 20 at.%, the fuel smear density may need to be optimized to mitigate FCMI. In the development of MA-bearing metal fuels, main interest is the influence of MA addition on FCCI. The issues in these new meal fuel concepts: (1) FCCI, (2) fission gas ventilation, and (3) FCMI, will be addressed by understanding of metal fuel irradiation behavior, as follows.

In FCCI during steady-state irradiation, cladding wastage by lanthanide fission products is dominant. The results of the out-of-pile tests with diffusion couples consisting of lanthanide alloys and Fe-base cladding materials indicated that the rate of the reaction between lanthanides and Fe-base alloys is much higher than the rate of FCCI observed in irradiated metal fuel pins. This suggests that FCCI during steady-state irradiation is controlled by radial migration of lanthanide fission products in a porous fuel slug. It is, therefore, important to identify a mechanism of the lanthanide migration. This is also useful for development of MA-bearing metal fuel since metallurgical behavior of MA is possibly similar to that of lanthanide elements. In the development of cladding liner, a key issue will be compatibility of liner materials and lanthanide elements.

Fission gas ventilation is not a new concept, and a similar ventilation device has been developed for a sodium-bond type control rod. This will be applicable to metal fuels after the behavior of volatile fission products such as cesium and iodine in a bond-sodium is understood and the performance of a ventilation device for metal fuels is demonstrated by irradiation tests.

For further increase in fuel burnup limit (higher than about 20 at.%), it is essential to evaluate FCMI based on better understanding of fuel slug swelling behavior. Fuel slug deformation under neutron irradiation is anisotropic; radial strain rate is more than two times larger than axial strain rate. A cross-section of an irradiated fuel slug exhibits a two or three-ring structure, and each ring (or annular region) shows a characteristic appearance. In the central gamma-phase region, spherical gas bubbles can be found. The pores in the low temperature peripheral region are characterized by a highly distorted configuration, which are associated with grain boundary tearing and cavitational void swelling. The intermediate zeta-phase region appears to be dense. When the fuel center-line temperature is lower than about 650^{o}C, the gamma-phase region is not formed, zeta-phase region occupies the central part of the slug, and the slug cross-section shows a two-ring structure. The ring structure seems to

be closely related to fuel constituent migration phenomenon; Zr is depleted in the zeta-phase region, and enriched in the central gamma-phase region and the low temperature peripheral region. In the isothermal diffusion in the U-Zr system, it is known that the diffusion flux of U is larger than that of Zr and Kirkendall voids are formed in the U side, which indicates remarkable vacancy flux exists. This suggests that fuel constituent migration may affect swelling behavior of the slug. However, the interrelation among anisotropic fuel slug deformation, characteristic ring structure and fuel constituent migration has not yet been explained well to date.

Estimation of solid FP swelling rate is also important in the FCMI evaluation. Two cases of the estimation were provided: ~1.5 vol.%/at.% at a maximum and ~1.2 vol.%/at.% as a most probable value. The difference of 0.3 vol.%/at.% is not small. The behavior of alkali and alkaline-earth fission products and the effect of radial migration of lanthanide fission products on solid FP swelling need to be quantitatively estimated.

For better understanding of metal fuel irradiation behavior, fuel alloy property data must be accumulated. For examples, the thermal conductivity and creep strain rate of U-Pu-Zr alloys have not been measured since 1970s. Fuel composition dependence on creep strain rate is not yet clarified.

Irradiation tests are planned for determining metal fuel performance limit and progress is expected in exploration of new metal fuel concepts for higher fuel performance. Basic study for better understanding of the irradiation behavior and accumulation of fuel alloy property data are important in order to support these research activities.

5-01

The high temperature behaviour of actinide fuels

Rudy Konings

European Commission, Joint Research Centre, Institute for Transuranium Elements, Karlsruhe, Germany

Actinide compounds and phases have been subject of extensive studies since the 1950s, particularly in view of their application in nuclear fuels. Since nuclear fuels operate at elevated temperature, in fast reactors even to a few hundreds of degrees below the melting temperature, a strong emphasis has been given to the (very) high temperature behaviour to understand the processes occurring during normal operation and accidental conditions in nuclear reactors. For obvious reasons, the past work has concentrated strongly on uranium and thorium fuels, and information on transuranium compounds and fuels is limited.

In addition to the radioactive nature of the materials, the high temperatures often complicate the work as a result of thermodynamically and kinetically driven chemical reactions, changing compositions (and valence states) or decomposition. High temperature studies of nuclear materials are thus far from trivial and can only be performed in a few laboratories worldwide. The Institute for Transuranium Elements has a long tradition in this field and has been working continuously on the improvement of the knowledge base on a wide variety of nuclear fuels. To reach this goal, systematic measurements have been combined with adaptation and innovation of experimental techniques aiming at generating relevant and new information. In this lecture a series of examples of recent achievements will be presented.

High-resolution Nuclear Magnetic Resonance Investigation into Chemical Shifts in UO_2 and ThO_2 and Ordering in Uranium-Thorium Oxide Solid Solutions.

Ian Farnan[1], Joseph Somers[2], Olivier Pauvert[2], Serge Fourcadot[2], Laura Martell[2], Kevin Boland[3], David Clark[3]

[1]University of Cambridge, Cambridge, UK, [2]EC-JRC-ITU, Eggenstein-Leopoldshafen, Germany, [3]Los Alamos National Laboratory, Los ALamos, NM, USA

High-resolution solid-state nuclear magnetic resonance (NMR) of polycrystalline ceramics, powders and amorphous materials requires rapid reorientation of the sample at angle of 54.7˚ (the 'magic' angle) to the applied magnetic field in order to remove anisotropic magnetic contributions the observed resonance. This is problematic for safe application to actinides because the rotation rates need to be of the order of the static line width and these can several tens of kHz (of the order of 100,000 to several million rpm). Several protocols have been developed recently for U/Th and transuranic containing materials where the required rotation rates required to narrow the lines, and produce high-resolution spectra, have been achieved. The results emerging are revealing very detailed atomic scale information on the chemical shifts of oxygens coordinated to different actinides and different numbers of actinides. These allow details of atomic ordering to be extracted from the high-resolution spectra of actinide oxides.

The paramagnetic susceptibility of the majority of actinide elements arising from unpaired 5f electrons creates particular problems for NMR spectroscopy. Strategies to overcome these effects that lead to the determination of the underlying chemical shift from the paramagnetic shift of the actinide will be discussed. The room temperature, static ^{17}O spin-lattice relaxation time (T_1) of UO_2 is invariant to rotation at high speed and the nutation behaviour of oxygen in mixed oxides (U/Th) under the applied radiofrequency fields is consistent with a more or less cubic environment for the oxygens bonded to more than one actinide in the fluorite structure. Application of his approach has led to unprecedented details of ordering in actinide oxide systems.

The approach is exemplified by a study of U/Th ordering in $(U/Th)O_2$. A series of $(U/Th)O_2$ oxides were prepared by mixing stoichiometric volumes of nitrate solutions, gelation with a polymer was followed by dispersion into ammonia solution to precipitate almost spherical beads of oxide. The beads were heated in 30% $^{17}O_2$ gas and finally annealed in Ar/H_2 to recover an oxygen 2.00 stoichiometry. These U/Th mixed oxides and end-members exhibit cubic lattice parameters, determined by X-ray diffraction, which follow Vegard's law very closely. Oxygen-17 MASNMR spectra of $Th_{0.95}U_{0.05}O_{2.00}$ sample resolve oxygen resonances due to tetrahedral OTh_4 and OTh_3U environments in the mixed oxide. The relative intensities of these peaks are consistent with a random distribution of U (and Th) in the first coordination sphere of oxygen. As the U content increases, magnetic susceptibility effects begin to dominate the spectra and it is increasingly difficult to resolve oxygens coordinated to two or more U. However, the OTh_4 peak remains well-resolved and the relative intensities are consistent with a random distribution of U in the oxygen first coordination sphere. Remarkable resolution is observed in a 1% U sample ($Th_{0.99}U_{0.01}O_{2.00}$), the OTh_3 site is resolved with the expected intensity for a random distribution, however, the OTh_4 site is split and the intensities of the two components of the OTh_4 resonance are consistent with a random distribution of U in the third coordination sphere of oxygen. This shows that an avoidance model for U-U is not operating, discrimination between a random distribution and an avoidance model is very difficult at low concentration.

1-78

Multiconfigurational Nature of 5f Orbitals in Uranium and Plutonium and Their Intermetallic Compounds

Corwin Booth

Lawrence Berkeley National Laboratory, Berkeley, CA, USA

The structural, electronic, and magnetic properties of U and Pu elements and intermetallics remain poorly understood despite decades of effort, and currently represent an important scientific frontier toward understanding matter. The last decade has seen great progress both due to the discovery of superconductivity in $PuCoGa_5$ and advances in theory that finally can explain fundamental ground state properties in elemental plutonium, such as the phonon dispersion curve, the non-magnetic ground state, and the volume difference between the α and δ phases. A new feature of the recent calculations is the presence not only of intermediate valence of the Pu 5f electrons, but of multiconfigurational ground states, where the different properties of the α and δ phases are primarily governed by the different relative weights of the $5f^4$, $5f^5$, and $5f^6$ electronic configurations. The usual method for measuring multiconfigurational states in the lanthanides is to measure the lanthanide L_{III}-edge x-ray absorption near-edge structure (XANES), a method that is severely limited for the actinides because the spectroscopic features are not well enough separated compared to the intrinsic resolution. Advances in resonant x-ray emission spectroscopy (RXES) have now allowed for spectra with sufficient resolution to resolve individual resonances associated with the various actinide valence states. Utilizing a new spectrometer at the Stanford Synchrotron Radiation Lightsource (SSRL), RXES data have been collected that show spectroscopic signatures of each of these configurations and their relative changes in various uranium and plutonium intermetallic compounds. In combination with conventional XANES spectra on related compounds, these data indicate such states may be ubiquitous in uranium and plutonium intermetallics, providing a new framework toward understanding properties ranging from heavy fermion behavior, superconductivity, and intermediate valence to mechanical and fundamental bonding behavior in these materials.

2-22

Experimental and atomistic modelling studies of nuclear fuel cycle materials

Greg Lumpkin[1], Rob Aughterson[1], Dan Gregg[1], Eugenia Kuo[1], Simon Middleburgh[1], Meng Qin[1], Massey de los Reyes[1], Gordon Thorogood[1], Yingjie Zhang[1], Zhaoming Zhang[1], Marc Robinson[2], Nigel Marks[2]

[1]ANSTO, Sydney, NSW, Australia, [2]Curtin University of Technology, Perth, WA, Australia

Advanced nuclear fuel cycles offer considerable promise for improvements in safety, performance, actinide management, and provide opportunities for associated methods of energy production (e.g., hydrogen based systems). In particular, by paying close attention to the actinides the new systems will benefit from additional fuel materials and reduced radio-toxicity in the wastes. These new reactor systems will also need new materials capable of performing under the extreme conditions imposed by temperature, radiation fields, and corrosive media. Here we present an update on studies of radiation damage in minerals and associated laboratory observations using ion irradiation of similar materials. Based on the available data, groups of potential actinide host phases are identified with intrinsic radiation tolerance due to recovery of damage on picosecond time scales (e.g., fluorite), those with longer term damage recovery (e.g., monazite), and many others wherein the kinetics are generally too slow for damage recovery on geological time scales. With regard to nuclear waste form materials, we briefly summarize the geochemical behaviour of Th-U minerals and related laboratory studies. Some of our latest results on brannerite (AB_2O_6) compounds are shown below (Figures 1-3).

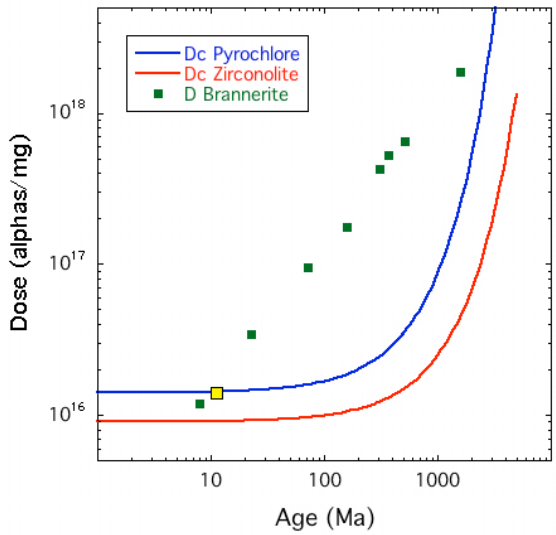

Figure 1 (left). Summary of radiation damage effects in natural brannerite in terms of alpha decay dose versus geological age. The critical dose for amorphization is about 1-2 x 10^{16} alphas/mg.

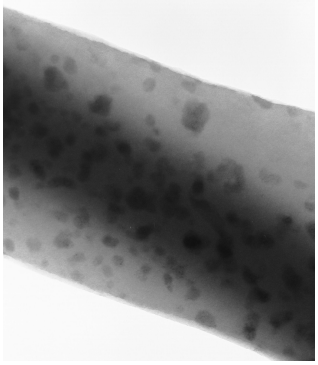

Figure 2 (right). TEM bright field image of amorphous natural brannerite containing abundant inclusions of uraninite. Width of image is approximately 500 nm.

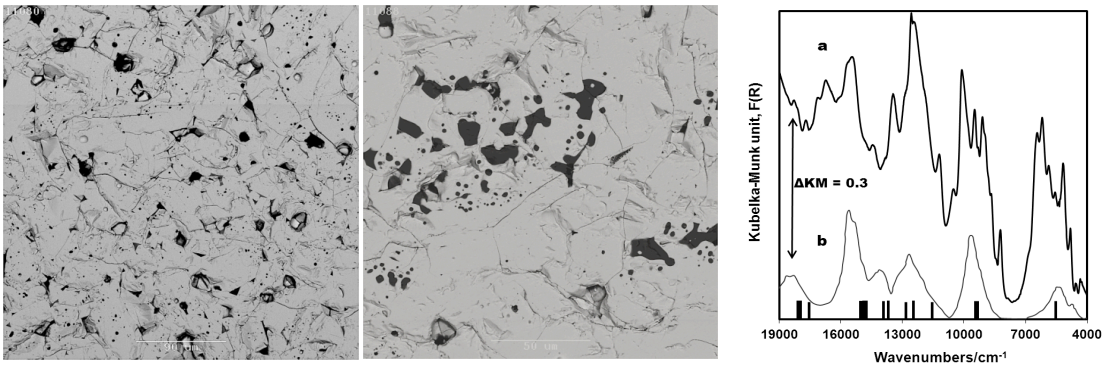

Figure 3. SEM images of synthetic thorutite $Y_{0.05}Th_{0.9}Pu_{0.}05Ti_2O_6$ (left) and $Th_{0.8}Pu_{0.2}Ti_2O_6$ (middle) showing near single phase structure with low porosity. DRS spectra of the Y-Pu sample and a reference spectrum (right) indicate Pu is predominantly tetravalent.

We have also conducted a range of experimental and atomistic modelling studies of nuclear materials relevant to fuel performance, the fundamentals of radiation tolerance in materials and the optimization of nuclear waste forms. This part of the presentation will touch upon some of the following studies: a) incorporation of excess oxygen and the development of additives for efficient sequestration of fission products in fuels, b) actinide and related compounds for inert matrix and waste form applications, c) studies of Tc compounds and the incorporation and decay of Tc to Ru in rutile, and d) fundamentals of radiation damage, including atomistic simulations of threshold displacement energies, mechanisms and energetics of defect formation and migration, and model materials for examining the effects of structure and bonding on radiation tolerance. Selected examples of our recent work on materials synthesis, characterization, and atomistic modelling are shown in Figures 4-7.

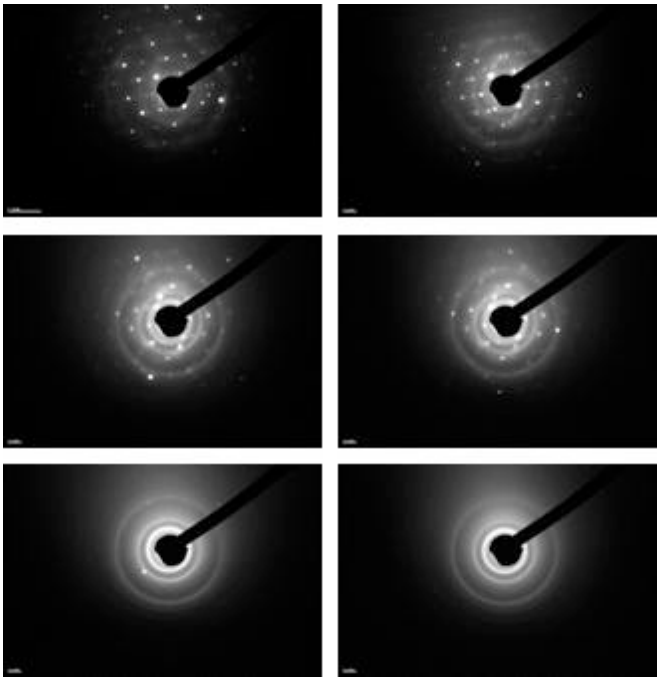

Figure 4 (left). Electron diffraction patterns of Ln_2TiO_5 with Ln = Sm/Yb, showing increasing development of amorphous fraction with increasing ion irradiation dose (1.0 MeV Kr ions, IVEM-Tandem Facility, ANL). In this figure, the dose increases from left to right and from top to bottom. The last two diffraction patterns in the sequence provide and estimate or “bracketing” value for the critical amorphisation dose.

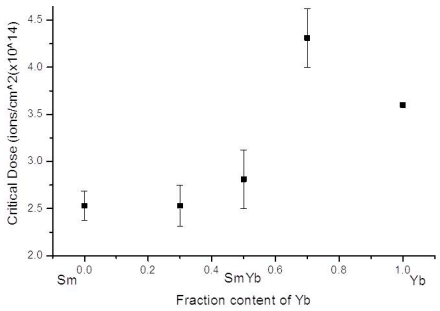

Figure 5 (right) Critical amorphization dose at room temperature of Ln_2TiO_5 with Ln = Sm/Yb showing variation of the critical dose for amorphization in this system. The two compounds with the lowest Yb contents are orthorhombic, the sample at x = 0.5 is hexagonal, and the two compounds with the highest Yb contents are cubic. This study illustrates a possible dependence between the critical dose for amorphization and structure type in this system, with the cubic compounds at high Yb content having the higher critical dose.

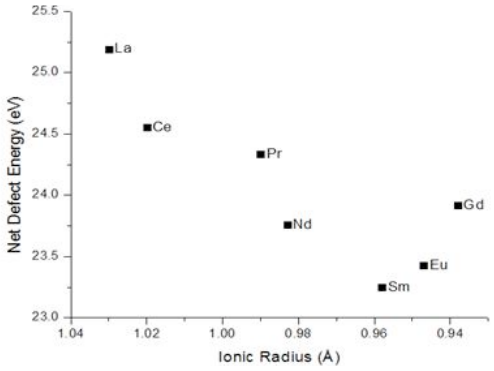

Figure 6. Atomistic simulation of the orthorhombic Ln_2TiO_5 compounds using empirical potentials. This figure shows the total Frenkel defect formation energy as a function of ionic radius of the Ln cation. Results indicate that the orthorhombic compounds are likely to show similar radiation tolerance upon irradiation.

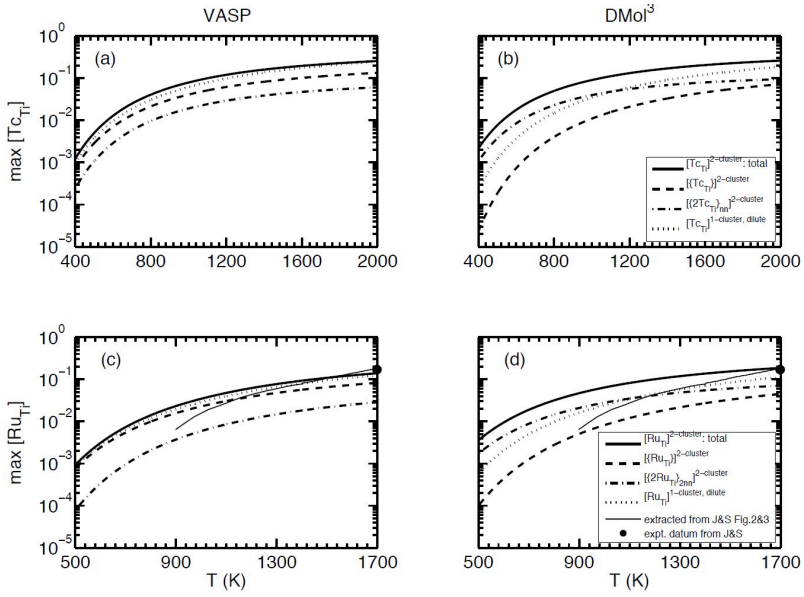

Figure 7. DFT calculations showing the predicted solubility of Tc in rutile (a, b) using two different simulation codes. Similar data are shown for Ru solubitily (c, d), in this case there are experimental data for this system and the results show good agreement with the calculations using both codes.

2-23

Keeping Actinide Reactivity Under Surveillance Using Optical Fingerprinting

Louise Natrajan[1], Sean Woodall[1], Adam Swinburne[1], Simon Randall[1], Kurt Smith[1], Katherine Morris[1], Nicholas Bryan[1], Andrew Kerridge[2], Robert Baker[3], Emtithal Hashem[3]

[1]The University of Manchester, Manchester, UK, [2]University College London, London, UK, [3]Trinity College Dublin, Dublin, Ireland

The UK in particular currently holds a substantial nuclear legacy arising from fission activities, with a large proportion of high activity wastes that pose a radiological threat to natural and engineered environments. In order to address these issues, we have begun a programme of work to establish a comprehensive understanding of the electronic properties and physical and chemical properties of the radioactive actinide metals using state of the art emission spectroscopic techniques. Our aim is to aid in the elucidation of migration pathways in material wasteforms as well as actinyl uptake and accumulation in the natural environment. Despite the importance of monitoring speciation, techniques for measuring actinide concentration and movement currently tend to be based on radiometric assay, which are destructive and provide limited information regarding oxidation state or chemical form. By contrast, time resolved emission spectroscopy, is a sensitive alternative technique to study the electronic properties of *f*-element compounds and can, in principal, be achieved remotely using fibre optic technology. Since the actinide ions uranium, plutonium and neptunium can co-exist in several oxidation states depending on the surrounding physical conditions, chemical behaviour is inherently linked to oxidation state. However, the speciation and environmental fate following biological and chemical induced redox processes remain to be fully explored and understood.

Our approach to this is to firstly use coordination chemistry to synthesise uranium compounds with ligands that model environmentally complexed species and use optical spectroscopy to understand and map both the chemical and physical behaviour of these species. We (and others) have recently established that U(IV) complexes are emissive and we will demonstrate that uranium in the +IV and +VI oxidation states can be detected simultaneously at relatively low concentrations. Time gating techniques enable the long lived uranyl(VI) species to be separated from the shorter lived uranium(IV) species. Furthermore, the form of the emission spectra of uranyl(VI) compounds are extremely sensitive to the nature of the ligand bound in the equatorial plane and the complex nuclearity (extent of aggregation), potentially giving a sensitive method of assessing the solution forms of uranium in environmental type conditions. We will next present our initial results on the coordination behaviour of neptunyl(V) and neptunyl(VI) ions with phosphine oxide based ligating agents and finally discuss how the optical properties of these model compounds can be applied to disproportionation reactions and redox events in solution. If time permits, we will present our initial results of adsorbed and incorporated uranium speciation in calcite materials as probed by emission spectroscopy.

2-29

First-principles modeling of nuclear fuels: strong 5f electron correlations and dispersive bonds

Emerson Vathonne[1], Michel Freyss[1], Marjorie Bertolus[1], Bernard Amadon[2]

[1]CEA, DEN, DEC, Centre de Cadarache, Saint-Paul-Lez-Durance, France, [2]CEA, DAM, DIF, DPTA, Arpajon, France

Much effort is still being put on the improvement of first-principles methods to study radiation effects in actinide-based nuclear materials. An accurate description of the electronic structure of the nuclear fuel material is required not only to get insight into elementary mechanisms of the material evolution at the atomic scale (*i.e.* atomic transport properties of point defects and fission products), but also to provide reliable structural and energetical data for the adjustment of parameters or potentials in empirical methods (classical molecular dynamics, kinetic Monte Carlo, etc.) at higher scales [1]. In particular, the importance of first-principles calculations within the multiscale modeling scheme of nuclear fuel materials is now widely recognised.

5f electron correlations: the DFT+DMFT method

On the one hand, the treatment within first-principles methods of the strong *5f* electron correlations in actinide compounds is still a challenge. Recently the DFT+U method [2] has supplanted the standard DFT (density functional theory) method in most of the first-principles studies of nuclear fuels such as uranium and plutonium oxides, carbides and nitrides. The DFT+U method enables a better treatment of the 5f electron strong correlations and a correct description of most of the material bulk properties. However, having DFT+U calculations converge to the ground-state of the system is tricky because the localization of the 5f electrons yielded by this method induces the existence of many local energy minima. To avoid that the DFT+U calculations remain trapped in such local minima, the OMC (occupation matrix control) method has been developed at CEA [3,4]. The DFT+U and OMC methods have in particular improved the confrontation of first-principles calculations to experiments for oxygen atomic diffusion in UO_2 [5]. This scheme is also used in the study of uranium and plutonium carbide fuels.

The DFT+DMFT method (DFT combined with dynamical mean field theory) [6] can further improve the modeling of strongly correlated materials such as UO_2. This method, which has been recently implemented in the ABINIT code [7], takes into account dynamical correlations and circumvents the issue of local energy minima. It also enables one to model with a limited number of atoms the paramagnetic character of the material such as displayed by UO_2 above 30 K, contrary to standard DFT or DFT+U. We will present the results obtained using the DFT+DMFT method in the Hubbard I approximation on the bulk properties of UO_2 and preliminary results on point defect formation energies. Even if the DFT+U method can describe satisfactorily a wide range of bulk properties of UO_2 (structural and elastic constants, non-collinear antiferromagnetic order), the DFT+DMFT method further improves the comparison to experimental data. In particular, as shown on the Figure 1, the DFT+DMFT density of states reproduces the uranium 5f peak below the Fermi level that was missed by the DFT+U method. The DFT+DMFT method, however, is still computationally too demanding to treat large supercells for the study of point defects or fission products in solids. But DFT+DMFT results obtained for few representative defect calculations in small supercells can be used as a benchmark for the evaluation of other less precise approximations, in particular DFT+U. We will present such a comparison for the formation energies of oxygen point defects in UO_2.

Van der Waals interactions and van der Waals density functional

On the second hand, further methodological improvements are required for the accurate treatment within the DFT framework of Van der Waals interactions which come into play for rare gas atoms, such as helium or the fission gases krypton and xenon. The DFT method (or DFT+U) within its standard local or semi-local LDA or GGA approximations do not describe the long-range van der Waals interactions (or dispersive interactions) and the improvement of DFT in this matter is an active field of research. Non-local correlation functionals, such as the

van der Waals density functional (vdW-DF) [9,10], have been recently developed and have shown success on a wide range of systems. Results will be reported on the assessment of these recent van der Waals functionals for the incorporation energies of rare gases in UO_2. The accuracy of DFT and the contribution of the van der Waals interactions to the incorporation energies of the rare gas atoms are discussed in the light of the electron density map analysis, as performed in a study of the bonding of rare gas atoms in small molecules [11].

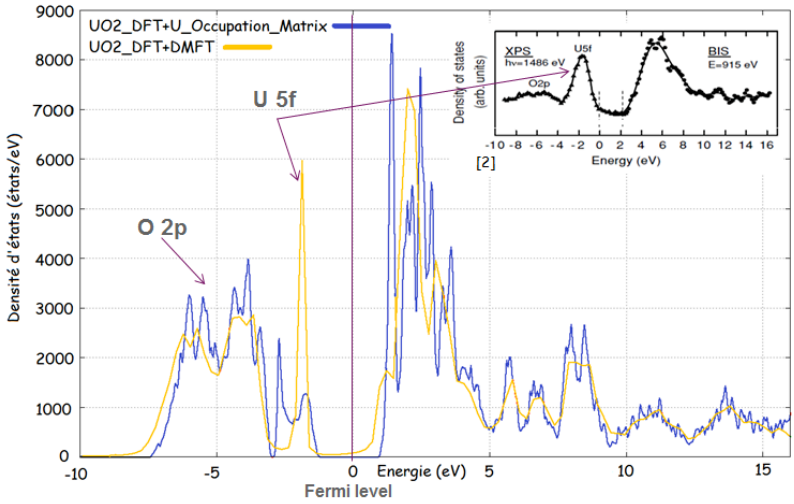

Figure 1: Density of states of UO_2 calculated with the DFT+U and DFT+DMFT methods, and comparison with BIS and XPS experimental spectra [8].

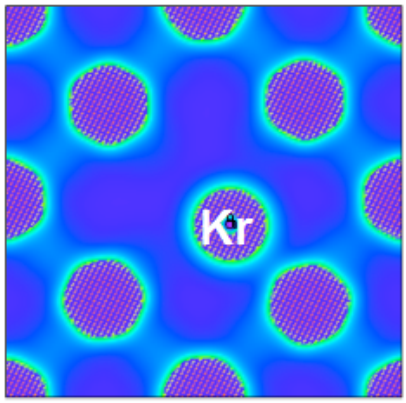

Figure 2: Electron density map of a krypton atom in a UO_2 Schottky defect.

References

[1] F-BRIDGE project (Basic Research for Innovative Fuel Design for GEN IV systems), project of the VII Framework Programme of the EC, http://www.f-bridge.eu/
[2] V. I. Anisimov, J. Zaanen, O. K. Andersen, Phys. Rev. B **44**, 943 (1991).
[3] B. Amadon, F. Jollet, M. Torrent, Phys. Rev. B **77**, 155104 (2008).
[4] G. Jomard, B. Amadon, F. Bottin, M. Torrent, Phys. Rev. B **78**, 075125 (2008).
[5] B. Dorado, P. Garcia, G. Carlot, C. Davoisne, M. Fraczkiewicz, B. Pasquet, M. Freyss, C. Valot, G. Baldinozzi, D. Siméone, M. Bertolus, Phys. Rev. B **83**, 035126 (2011).
[6] A. George, G. Kotliar, W. Krauth, M.J. Rozenburg, Rev. Mod. Phys. **68**, 13 (1996).
[7] B. Amadon, J. Phys.: Condens. Matter **24**, 075604 (2012).
[8] Y. Baer, J. Schoenes, Solid State Commun. **33**, 885 (1980).
[9] M. Dion et al., Phys. Rev. Lett. **72**, 246401 (2004).
[10] J. Klimeš, D. R. Bowler, A. Michaelides, J. Phys. Cond. Mat. **22**, 022201 (2010).
[11] M. Bertolus, M. Major, V. Brenner, Phys. Chem Chem. Phys. **14**, 553 (2012).

2-30

On the peculiarities of the DFT+U approach in the simulation of uranium dioxide

Matthias Krack

Paul Scherrer Institute, CH-5232 Villigen PSI, Switzerland

A reliable modelling of actinide materials is important as a complementary alternative to their experimental investigation, because experiments with such usually hazardous materials are difficult and costly. For the description of the chemical properties of actinide materials like uranium dioxide (UO_2), the simulation method has to include the electronic structure of the material explicitly and it has to provide a sufficient accuracy and predictive power for the given target material.

During recent decades density functional theory (DFT) has proven to be such a method for condensed phase systems. However, the accurate description of the strong correlation of the 5f electrons still poses a challenge for current density functionals and in fact a plain DFT method predicts UO_2 to be metallic. This problem is well-known and it occurs similarly for the 4f electrons of the lanthanides and the 3d electrons of the first-row transition metals. As a remedy Anisimov *et al.* [1] proposed the addition of a Hubbard-like U term to the DFT functional. This term introduces an energy penalty for the delocalised 5f electrons which "encourages" the 5f electrons to localise. In fact, this so-called DFT+U method shows the physically correct impact in the case of UO_2: a band gap is introduced and the antiferromagnetic state becomes lowest in energy in agreement with the experiment. Unfortunately, the DFT+U method creates also a manifold of possible localisation patterns for the 5f electrons at each uranium site which causes the occurrence of metastable states. Several recipes have been devised in the literature to tackle this problem, e.g. the occupation matrix control (OMC) [2], the U ramping method [3], the quasi-annealing method [4], and combined methods [5]. Their aim is to guarantee the convergence of the wavefunction optimisation to the electronic ground state for a given atomic configuration.

Basically, DFT relies only on the electronic density of the system and a potential multi-reference character of the underlying wavefunction, which is used to construct this density, is in principle not relevant, necessarily. However, DFT is implemented as Kohn-Sham DFT (KS-DFT) in most of the codes nowadays and thus the electronic density is constructed from a single set of KS spin orbitals. This causes difficulties in the automatic convergence to the true ground state density for UO_2 systems. It is needed to devise a proper set of initial KS orbitals which are then carefully converged.

Alternatively, more sophisticated methods like density mean-field theory (DMFT) [6] could be employed which do not rely on any empirical parameter like U. However, such methods are computationally much more expensive or even prohibitive for a simulation of the required model system sizes. Moreover, such methods often do not provide analytic energy gradients and thus the calculation of atomic forces is not yet feasible which disables any structural optimisations or molecular dynamics simulations. For this reason, one has still to resort to the DFT+U method currently using an empirically fixed U parameter in spite of any shortcomings of this approach if model systems has to be handled consisting of hundreds of atoms.

In this work cell optimisation of UO_2 bulk model systems consisting of at least 2 x 2 x 2 unit cells (96 atoms) are performed using the DFT+U implementation in the CP2K code (http://www.cp2k.org) [5]. CP2K employs a localised basis set of Gaussian-type orbital (GTO) functions for the description of the Hamiltonian. An auxiliary basis set of plane waves is used to expand the electronic density. A 1**k** antiferromagnetic structure is imposed and spin-orbit interactions are not considered explicitly. Scalar-relativistic norm-conserving Goedecker-Teter-Hutter pseudopotentials are employed for uranium and oxygen including 14 and 6 valence electrons, respectively. The selected orbital occupation matrix for each uranium atom is imposed for the first 5 iteration steps similar to the OMC method and then the wavefunction is converged without any constraint. Different effective U_{eff} values are used in the framework of the DFT+U approach proposed by Dudarev [7]. The 5f orbital occupations are obtained by projection based on a Mulliken population analysis. Such projections depend on the employed basis set and thus different methods might give different results for the same U_{eff} value. For this reason, several U_{eff} values are used to check for the impact of the empirical U_{eff} parameter.

Initially, the same 5f occupation pattern is adopted for each uranium site and all 21 possible occupation patterns are converged in a systematic manner followed by fully unconstrained cell optimisations, i.e. no symmetry constraint is imposed on the shape of the unit cell. A tight convergence criterion with a pressure tolerance of $\pm$1 bar is employed for the relaxed cell. All optimised cells stayed orthorhombic, but in most cases depending on the 5f orbital occupations the relaxed unit cell shows a tetragonal or even orthorhombic distortion, if the same 5f orbital occupation for each uranium atom is applied.

A mixed initial 5f orbital occupation for the alpha and the beta uranium atoms leads already to a lower energy and an almost cubic cell after relaxation. The energy difference and the shape of the corresponding relaxed electronic spin density are significant. Attempts to reach these states automatically using a U ramping method were not successful. As soon as any low energy 5f orbital occupation pattern is encountered, this state turns out to be stable during the entire cell relaxation. This observation implies that any annealing approach somehow "shaking" the nuclei to facilitate the convergence of the electronic structure to the ground state is rather unreliable, since the stability of the low-lying metastable states with respect to structural changes seems to be quite pronounced. Consequently, an initial 5f occupation pattern has to be guessed which is already quite close to the ground state. This poses a major technical problem for the simulation of defective systems or surfaces of actinide materials like UO_2.

References

[1] V. I. Anisimov *et al.*, Phys. Rev. B **44**, 943 (1991)

[2] B. Dorado *et al.*,, Phys. Rev. B **79**, 235125 (2009)

[3] B. Meredig *et al.*, Phys. Rev. B **82**, 195128 (2010)

[4] H. Y. Geng *et al.*, Phys. Rev. B **82**, 094106 (2010)

[5] J. Rabone and M. Krack, Comput. Mat. Sci. **71**, 157 (2013)

[6] G. Kotliar *et al.*, Rev. Mod. Phys. **78**, 865 (2006)

[7] S. L. Dudarev *et al.*, Philos. Mag. B **75**, 613 (1997)

4-02

Surface Science Study of Spent Fuel Corrosion Processes using Thin Film Model Systems

Thomas Gouder

EC-JRC-ITU, Karlsruhe, Germany

Surface science studies give valuable information on the mechanisms of corrosion processes of spent nuclear fuel. Corrosion is a surface process which proceeds via alteration of composition and structure of the topmost layers. It depends as well on the material properties (grain boundaries, defects, composition, etc) as on the environmental parameters (pH, oxidants, complexing agents, etc). Understanding the mechanisms of these reactions beyond simple rationalization is a difficult task, far from being completed. It requires decomposition of the complex process into simple chemical reaction steps, related to real surface and environmental parameters. This can be done by replacing the complex waste by simplified model systems, representative of the fuel, yet avoiding its high complexity ("single parameter studies").

An overview will be given on present and planned surface science facilities at ITU. Their goal is to combine a complete series of surface preparation, reaction and diagnostic tools in one single machine (Fig. 1). The tools are mounted on independent modules, which can be activated/deactivated/serviced on need. This gives a high flexibility and robustness in spite of the complexity of the machine. Special emphasis is given to the combination of spectroscopy techniques (XPS, UPS, TPD, HREELS, Kelvin probe) probing the average surface, and mapping techniques probing local reactivity aspects. To that purpose an AFM will be used for studying local reactivity under controlled atmosphere. It has a scanning electrochemical probe for in-situ electrochemistry studies. Thin film growth methods (sputter deposition, evaporation) are used to prepare fuel model systems. In particular reactive sputter co-deposition is a highly versatile method for preparing oxides, nitrides, carbides doped by supplementary inclusions. Samples with widely varying composition and oxidation state can thus be prepared in-situ. The methods are being used for studying e.g. the influence of fission products (e.g. the 4d transition metals forming the e-particles) on the redox potential, or to perform systematic studies of surface reactions of mixed oxides.

A recent example of a surprising surface reaction will be presented. We studied the surface interaction of PuO_2, UO_{2+x}, and U-Th and U-Pu mixed oxides (TOX and MOX) with ice. Ice was chosen to fix water in high concentrations to the surface under ultrahigh vacuum conditions. The study was motivated by the possible role of water in promoting further oxidation of PuO_2. To our surprise we found that in presence of UV light and ice, PuO_2 undergoes a fast surface reduction to Pu_2O_3, while UO_{2+x} (x = 0 to1) is also reduced, but to a lesser extent. In MOX, UO_{2+x} reduction is more pronounced, and this is directly related to the presence of Pu. A similar observation is made for TOX, where U reduction is also faster than in pure UO_{2+x}. Surface reduction is shown to be a true interfacial process, where the solid absorbs light and undergoes a photochemical reaction. It is not a simple surface reaction of the oxides with ice photolysis products.

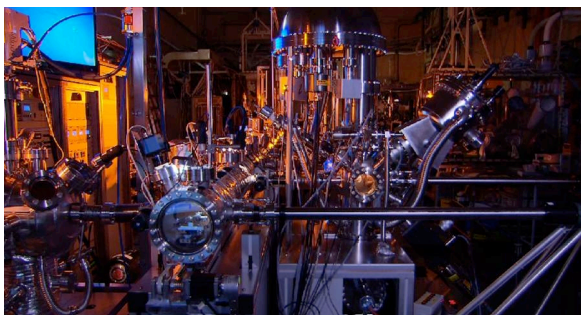

Fig. 1 Surface science lab station

4-03

Spectroscopic characteristics of U(VI)-lanthanide(III) complexes adsorbed onto a silica surface and U(VI)-carbonate complexes in aqueous solutions

Euo Chang Jung, Kyoung Kyun Park, Hee-Jung Im, Wansik Cha, Hye-Ryun Cho, Kwang-Wook Kim

Korea Atomic Energy Research Institute, Daejeon, Republic of Korea

The selective and sensitive detection of dioxouranium(VI) ion, U(VI), is required in various research fields related to the nuclear fuel cycle including the preparation of fuel, waste management, and environmental monitoring. The luminescence and Raman spectra of U(VI) have received considerable attention because analysis of the spectra is expected to provide information on the chemical speciation of U(VI) complexes. In this study, the spectroscopic characteristics of two types of uranium materials are investigated using TRLFS (time-resolved laser fluorescence spectroscopy) and Raman spectroscopy.

In the first part of this study, the characteristics of luminescence of U(VI)-lanthanide(III) complexes adsorbed onto a silica surface are discussed to understand the coadsorption behavior of U(VI) and lanthanide(III). The representative adsorption reactions in the experimental series are shown in Fig. 1. The adsorbed quantities of U(VI) and Eu(III) were calculated from the measured concentrations of U(VI) and Eu(III) in aqueous phase. The filled and empty circles denoted by the letters 'A' and 'B' in Fig. 1(a) represent the adsorbed quantities of U(VI) and Eu(IIII), respectively, on silica. U(VI) ions at a concentration of 2.4 μmol/g are almost completely removed from solution at pH 5.2-5.7 with a pH-adsorption edge of 3.7, while Eu(III) ions at the same concentration are completely removed at pH 6.8-7.0 with a pH-adsorption edge of 6.2. Here, the pH-adsorption edge is defined as the pH value at which the adsorbed quantity of metal ions is approximately 50% of the initial concentration. These results imply that the adsorption reaction on silica is stronger for U(VI) than for the Eu(III) ions. Thus, it is expected that the presence of adsorbed U(VI) on silica may reduce the adsorption of Eu(III) due to the marked competition between U(VI) and Eu(III) ions for the active sites on the silica surface. However, the data points depicted as square symbols, denoted by 'C' in Fig. 1(a), indicate the increased adsorption of Eu(III) in the presence of U(VI) ions. The pH-adsorption edge of 6.2 for Eu(III) alone shifted to 5.9 for Eu(III) with a U(VI) concentration of 200 μmol/g. Furthermore, it was observed that the pH-adsorption edge for Eu(III) shifted toward lower pH with increasing U(VI) metal concentration, as shown in Fig. 1(b). The reason for this phenomena can be understood by investigating the chemical interaction of the hydroxyl group of adsorbed U(VI) with Eu(III) to form surface complexes.

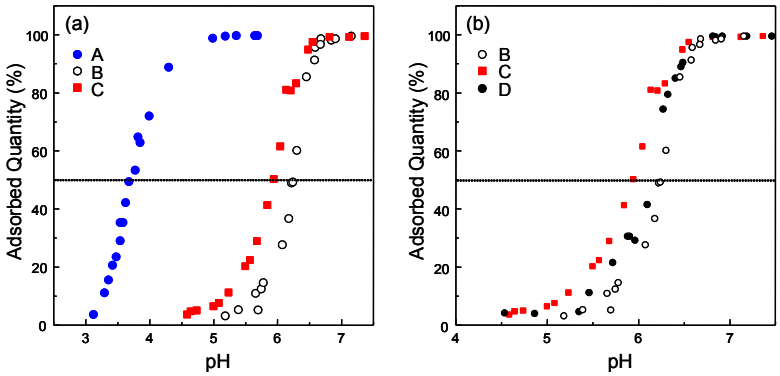

Fig. 1. A; U (2.4 μmol/g), B; Eu (2.4 μmol/g), C; Eu (2.4 μmol/g) + U (200 μmol/g), D; Eu (2.4 μmol/g) + U (24 μmol/g).

TRLFS was performed to verify the formation of the surface complexes. The representative luminescence spectrum for the coadsorbed U(VI) and Eu(III) on silica surface is shown in Fig. 2(a). The luminescence for Eu(III) is very weak at the excitation laser wavelength of 266 nm, as represented by the lower trace in Fig. 2(a). However, in the presence of coadsorbed U(VI),

the luminescence peaks of Eu(III) were found to be prominent at the excitation laser wavelength of 266 nm, as represented by the upper trace of Fig. 2(a), due to the energy transfer between U(VI) and Eu(III). The waveforms of the luminescence signals confirm that the energy transfer effect induces the quenching of luminescence intensity of U(VI) with the enhancement of the luminescence intensity of Eu(III). Fig. 2(b) shows the luminescence signal waveform recorded with a digital oscilloscope for U(VI) at 508 nm and Eu(III) at 702 nm. The origin of the X-axis indicates the time at which the pulsed laser beam is incident and laser-induced luminescence is generated. The luminescence signal waveform at 508 nm for adsorbed U(VI) on silica shows typical decay behavior with a lifetime of 225 ms (data not shown). The luminescence lifetime of U(VI) at 508 nm decreased from 225 ms to 40 ms with the coadsorbed Eu(III), depicted as a dotted line in Fig. 2(b). Moreover, the first rising part appears in the luminescence signal waveform of Eu(III) at 702 nm for the same sample. The rising time to arrive at the peak seems to be related to the luminescence lifetime (decay time) of U(VI). These results reflect the quenching effect of excited U(VI) ion by Eu(III) due to the energy transfer from the excited U(VI) to Eu(III). Based on these results, evidence is presented for the surface complex formation of ≡SiO-U(VI)-O(H)-Eu(III) species. The energy transfer effect is investigated for other lanthanide(III) and the results are discussed.

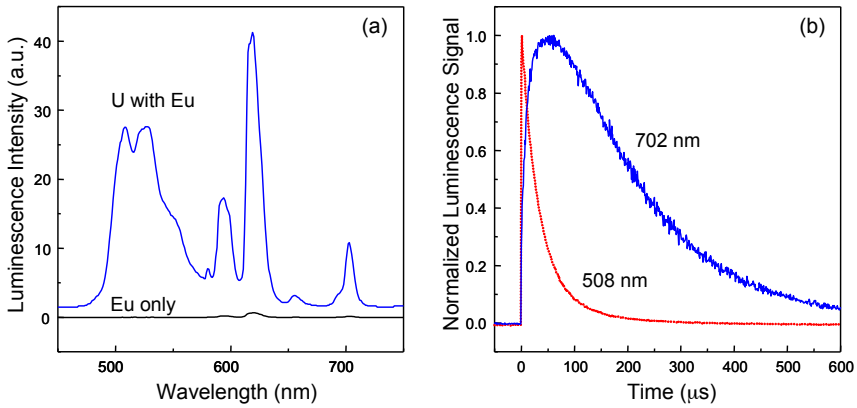

Fig. 2. (a) Luminescence spectra for U+Eu (6.25 μmol/g + 25 μmol/g, upper trace) and Eu (25 μmol/g, lower trace), (b) waveforms of luminescence signal for U+Eu at 508 nm and 702 nm.

In the second part, characteristics of the luminescence and Raman spectra of U(VI)-carbonate complexes in an aqueous solution are discussed to identify $UO_2(CO_3)_3^{4-}$, $Ca_2UO_2(CO_3)_3$(aq.) and $UO_2(O_2)(CO_3)_2^{4-}$. Uranyl tricarbonate ($UO_2(CO_3)_3^{4-}$) was chosen as a representative species of U(VI)-carbonate compound because few studies have addressed the luminescence characteristics of $UO_2(CO_3)_3^{4-}$. The existence of $UO_2(CO_3)_3^{4-}$ was first confirmed using Raman spectroscopy for several samples containing different concentrations of U(VI) and carbonate. Since then, TRLFS was performed for selected samples in which $UO_2(CO_3)_3^{4-}$ species exist as a major component.

The Raman spectrum of $UO_2(CO_3)_3^{4-}$, measured from the solution of $UO_2(ClO_4)_2$ (12.6 mM) + Na_2CO_3 (0.5 M), is shown in Fig. 3(a). A remarkable Raman peak at 811 cm^{-1} is observed with other Raman peaks at 934 and 1066 cm^{-1} for ClO_4^- and CO_3^{2-}, respectively. The dotted line in Fig. 3(b) represents the well-known luminescence spectrum of UO_2^{2+} (solution pH of 1). The luminescence peaks of selected samples having major components of $UO_2(CO_3)_3^{4-}$ were blue-shifted in wavelength compared to those of UO_2^{2+}, as illustrated by the solid lines in Fig. 3(b).

Because of the inner filter effect due to the strong absorption at the excitation wavelength of 266 nm, the luminescence intensities as a function of U concentration are not linear. Luminescence lifetimes of approximately 11 ns were measured for these samples. For the sample containing hydrogen carbonate and calcium ions on the order of a few tens of mg/L, a concentration similar to that in the groundwater taken from the Korea Atomic Energy Research Institute Underground Research Tunnel (KURT), the existence of $Ca_2UO_2(CO_3)_3$(aq.) species was confirmed using TRLFS. The luminescence characteristics of $UO_2(CO_3)_3^{4-}$ and $Ca_2UO_2(CO_3)_3$(aq.) were compared.

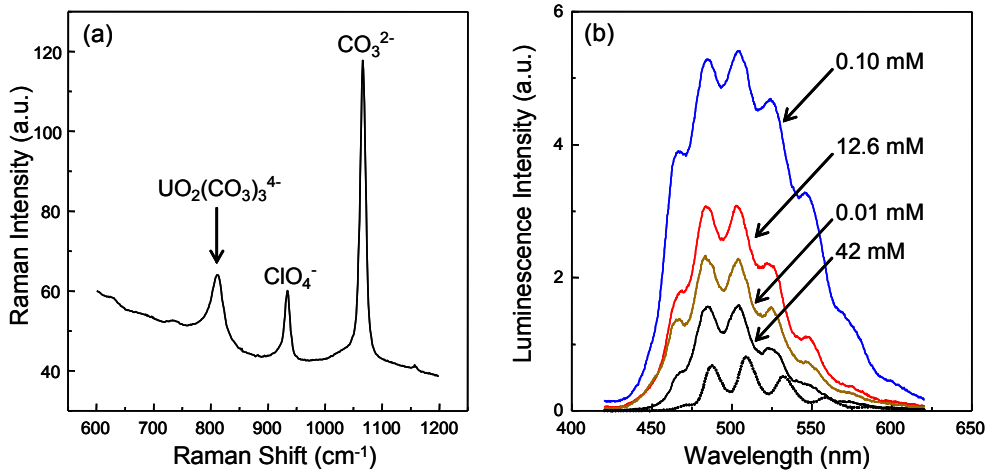

Fig. 3. (a) Raman spectrum of $UO_2(CO_3)_3^{4-}$ for $UO_2(ClO_4)_2$ (12.6 mM) + Na_2CO_3 (0.5 M) solution at pH of 11.4 (b) Luminescence spectra of $UO_2(CO_3)_3^{4-}$ for Na_2CO_3 (0.5 M) solutions with different concentrations of $UO_2(ClO_4)_2$. For the comparison purpose, the luminescence spectrum of UO_2^{2+} is also displayed, as a dotted line.

Finally, the chemical speciation of uranyl peroxocarbonate ($UO_2(O_2)(CO_3)_2^{4-}$) using Raman spectroscopy is discussed. This species is of interest in the recovery process of uranium from dirty UO_2 fuel scraps generated during nuclear fuel fabrication. Uranium is selectively dissolved to form this species, which has high solubility in a carbonate solution containing hydrogen peroxide. Uranium in a mixed solution of hydrogen peroxide and sodium carbonate can be precipitated as uranium peroxide when the solution is acidified to a pH of 2-3. Because of the instability of peroxide ion in alkaline conditions, $UO_2(O_2)(CO_3)_2^{4-}$ can decompose into $UO_2(CO_3)_3^{4-}$, which is stable in a carbonate solution. Thus, the chemical speciation of $UO_2(O_2)(CO_3)_2^{4-}$ and $UO_2(CO_3)_3^{4-}$ is necessary for the recovery process of uranium. In this part, the Raman spectra of the uranyl complex in the carbonate solution with hydrogen peroxide at different pH value are shown.

4-19

Uranyl speciation at the water / mineral interface: XPS; TRLFS and XAFS studies

Annick Froideval Zumbiehl[1], Mireille Del Nero[2], Rémi Barillon[2], Clotilde Gaillard[3], Klaus Lützenkirchen[4], Jean Hommet[5], Jean-Louis Hazemann[6]

[1]Paul Scherrer Institute, Nuclear Energy and Safety Research Department, Villigen, Switzerland, [2]Institut Pluridisciplinaire Hubert Curien, Département de Recherches Subatomiques, Strasbourg, France, [3]University of Lyon, Institut de Physique Nucléaire de Lyon, Villeurbanne, France, [4]European Commission Joint Research Centre, Institute for Transuranium Elements, Karlsruhe, Germany, [5]Centre National de la Recherche Scientifique, Laboratoire de Physique Corpusculaire, Caen, France, [6]Institut Néel, Grenoble, France

Uranium release in ground and drinking water is of concern at several U-contamined areas in the world. U mining and reprocessing has led to large amounts of U-rich soils, sediments or mill tailings, which are a local source for water contamination in specific environments. The uranyl ion is indeed complexed by many anions in ground waters and is potentially highly mobile.

The mobility of U(VI) may depend strongly on both mineral characteristics and on aqueous uranyl speciation. Detailed understanding of the respective roles of solution and surface parameters on the reactions at uranyl solution/mineral (quartz and Al-(hydr)oxide) interfaces is crucial to model accurately the behaviour of U in nature.

Spectroscopic investigations - X-ray photoelectron spectroscopy (XPS), extended X-ray absorption fine structure (EXAFS) and time-resolved laser-induced fluorescence spectroscopy (TRLFS) - of the uranyl chemistry at the 0.1 M $NaNO_3$ solution/mineral (quartz and aluminium hydroxide) interface have been conducted in order:

(i) to identify and to characterize the different uranyl surface species (mononuclear, polynuclear complexes and/or precipitates…), i.e. the coordination environments of sorbed/precipitated uranyl ions, and;

(ii) to investigate the influence of pH, initial uranyl aqueous concentration and hydroxyl ligand concentration on the uranyl surface speciation.

This study on the speciation of uranyl ions at the quartz surface (i) confirms the formation of uranyl polynuclear/oligomers on quartz from moderate (1 $\mu mol/m^2$) to high (26 $\mu mol/m^2$) uranyl surface concentrations and (ii) show that theses polynuclear species coexist with uranyl mononuclear surface species over a pH range ≈5-8.5 and a wide range of initial uranyl concentration of the solutions (10-100 μM). The uranyl concentration of these surface species depends on pH and on the initial uranyl aqueous concentration.

Hydrate (surface-) precipitates and/or adsorbed polynuclear species and monomeric uranyl surface complexes are formed on aluminium hydroxide. Uranyl mononuclear complexes are predominant at acidic pH, as well as uranyl in solution or on the surface. Besides mononuclear species, precipitates and/or adsorbed polynuclear species are predominantly formed at neutral pH values on aluminium hydroxide. A main contribution of our investigations is that precipitation and/or adsorption of polynuclear species seem to occur at low uranyl surface concentrations (0.01-0.4 $\mu mol/m^2$). The uranyl surface speciation is mainly dependent on the pH and the aluminol ligand concentration.

4-20

Dynamics and speciation in molten actinides fluorides

Catherine Bessada[1], Louis Maksoud[1], Vincent Sarou-Kanian[1], Haruaki Matsuura[2], Anne Laure Rollet[3], Christian Simon[3], Mathieu Salanne[3], Mathieu Gibilaro[4], Laurent Massot[4], Pierre Chamelot[4]

[1]CEMHTI CNRS, Orleans, France, [2]Tokyo Institute of Technology, Tokio, Japan, [3]PECSA CNRS UPMC, Paris, France, [4]LGC, Toulouse, France

Among the possible concepts of the Generation IV international forum, the molten salt reactor is of particular interest. Its main originality stands in the use of molten salts as both fuel and coolant and a possible online reprocessing with the extraction of fission products from the salt. The choice of the salt is of major importance and will influence the efficiency of this extraction. In particular, the separation of fission products from the molten salt will depend on their interactions with the other ions. Different mixtures have been proposed, such as NaF-ZrF_4-UF_4 or LiF-BeF_2-ZrF_4-UF_4, but LiF-ThF_4/UF_4 is now the reference system, with possible addition of CaF_2 or ZrF_4. Each element added will influence the thermochemical properties. It is thus very important to understand how the molten mixture is organised, and to characterize the different complexes involved in the molten phase.

The experimental study of such systems is difficult because of the combination of radioactive risks and molten fluorides corrosiveness. Our approach has been based first on a systematic study of AF-ZrF_4 (A= alkali cation) model system without radioactive element in a wide range of compositions. We have shown that the coupling of EXAFS and NMR experiments with molecular dynamics simulations was able to provide a quantitative description of such melts in situ at high temperature. The Zr^{4+} first solvation shell was shown to change importantly depending on the concentration (ZrF_4 content) and on the nature of the alkali [1,2].

If the NMR have already proved to be well suited for the light alkali cations (lithium, sodium, potassium, cesium…) and anions (fluorine and oxygen), and even for heavier nuclei such as lanthanum, yttrium and zirconium, X ray absorption becomes essential for rare earths and actinides nuclei study. Both techniques allow determining the coordination, the nature of neighbors and then to identify the ionic complexes formation in molten media providing specific developments of the cells because of the strong reactivity of molten fluorides at high temperature towards a great number of materials. For Actinides fluorides the addition of radioactive properties increases again the constraints and the experimental difficulties. A new cell has been specifically developed for EXAFS study in molten actinide fluorides, with a design based on multiple containers: starting from a pressed pellet of boron nitride mixed with the sample powder, put in between two boron nitride plates fixed by screws, and finally inserted in a closed BN cylinder with extremities refined up to 400 μm to allow X Rays transmission through the boron nitride itself.

In actinide fluorides-alkali fluorides molten mixtures, the point of view of the actinide cation described with the association of EXAFS experiments with Molecular Dynamics simulations, is improved by the ^{19}F HT NMR monitoring of the fluoride ion and its environment. The role of the anion is crucial because, depending on the composition of the salt, it may be considered as free fluorine or as fluorine connected with one or more actinide cations in highly concentrated mixtures. This connectivity will have a major effect on the transport properties or on the viscosity. On another hand, the local structure around the actinide cations will be described with the association of EXAFS experiments with Molecular Dynamics simulations.

New developments have been performed to improve the capability of these two techniques to describe more precisely the speciation in these melts. In NMR, the structural description obtained thanks to the evolution of the chemical shifts over the composition, or temperature is now extended with the description of the dynamics in such melts thanks to *Pulse Fields gradients NMR* (PFG NMR) technique developed in our laboratory (CEMHTI, CNRS Orleans), up to high temperature (1300°C) and specifically adapted for corrosive liquids [3]. The direct measurements of self-diffusion coefficients in the melts, allow describing the transport properties over a wide range of compositions and temperatures. The ionic complexes formed in the melts and their evolution depending on the composition strongly influence the mobility. It is then possible to visualize the melt starting from the free ions in diluted system, where the dynamics is governed mainly by the temperature, to the network like-liquids at higher

concentrations where the dynamics is directly governed by the complexes formation. From ^{19}F HT NMR data and MD calculations we can follow the increase of the number of bridging fluorines between complexes with the composition and inversely the decrease of free fluorines content.

Some recent results obtained in AF-ThF_4 and AF-UF_4 (A = alkali) melts will be presented.

Acknowledgments:

The research leading to these results has received funding from the project EVOL (Evaluation and Viability of Liquid Fuel Fast Reactor System) of the EURATOM FP7 under grant agreement n° 249696. The authors thank for their precious help B. Sitaud, P.L. Solari, D. Thiaudiere and S. Reguier from MARS and DIFFABS beam lines in SOLEIL synchrotron (France).

References

[1] C. Bessada, A. Rakhmatullin, A.-L. Rollet, J. Nucl. Mater. 360 (2007) 43-48.

[2] O. Pauvert, D. Zanghi, M. Salanne, C. Simon, A. Rakhmatullin, H. Matsuura, Y. Okamoto, F. Vivet, C. Bessada, J. Phys. Chem. B 114 (2010) 6472–6479.

[3] V. Sarou-Kanian, A.-L. Rollet, M. Salanne, C. Simon, C. Bessada, P. A. Madden, Phys. Chem. Chem. Phys. 11 (2009) 11501–11506.

ORAL

1-79

Charge distribution and local structure of $M_{0.80}Am_{0.20}O_{2\pm x}$ (M: Th, U and Pu).

Damien Prieur[1], Ursula Carvajal-Nunez[1], Marika Vespa[1], Tonya Vitova[2], Joseph Somers[1]

[1]European Commission, Joint Research Centre, Institute for Transuranium Elements, Karlsruhe, Germany, [2]Institut für Nukleare Entsorgung (INE), Karlsruhe, Germany

INTRODUCTION

Reduction of the long lived nuclear waste inventory can be achieved by partitioning of the long-lived heavy Minor Actinides (MA) from the nuclear waste for recycling and transmutation in fast neutron reactors[1]. Accordingly to this waste management strategy, dedicated assemblies with high Am contents in a host matrix are considered as promising transmutation fuels. At present, Am bearing oxide solid solutions are currently preferred as the structural properties of the fuels are key parameters for both reactor safety and performance. These essential irradiation-related aspects are also affected by the Oxygen to Metal ratio (O/M) which induces significant changes of the thermal and mechanical fuel properties. As the incorporation of Am in conventional oxide fuels (ThO_2, UO_2, PuO_2) would significantly affect both electronical and crystallographical properties of these materials, studying the charge of the metal atoms and the local geometric structure provides key experimental data to assess their use as transmutation blanket.

MATERIAL SYNTHESIS & EXPERIMENTAL APPROACH

At JRC-ITU, the Am bearing oxides are synthesized by coupling external gelation sol-gel and infiltration methods [2–4]. This process, overcoming the issue of dust, consists of the infiltration of Am nitrate solution into sol-gel produced porous beads. The infiltrated beads are then thermally treated to convert the Am nitrate to the oxide and are compacted into disks using a bi-directional press. The discs are then sintered in dedicated conditions. The charge distribution and the local structure of $M_{0.80}Am_{0.20}O_{2\pm x}$ (M= Th, U, Pu) were investigated by X-ray Absorption Spectroscopy (XAS) which allows probing cation valences and atomic local environments. XAS measurements were performed on powdered sample at the INE-Beamline at the Angströmquelle Karlsruhe synchrotron (ANKA, Germany) [5].

RESULTS & DISCUSSION

$M_{0.80}Am_{0.20}O_{2\pm x}$ samples were sintered during 8 hours at 1650°C in moisturized Ar-H_2 containing 2400 ppm of H_2O, corresponding to an oxygen potential of -384 kJ.mol^{-1}. In these sintering conditions, XRD and XAS results have shown that defective $Th(IV)_{0.80}Am(III)_{0.20}O_{1.90}$ and $U(IV)_{0.80}Am(III/IV)_{0.20}O_{1.93}$ fluorite solid solutions and a biphasic $Pu_{0.80}(IV)Am_{0.20}(III/IV)O_{2-x}$ material were achieved [2–4]. Different behaviours during sintering were observed depending on the host oxide matrix.

Firstly, the host cation (Th, U, Pu) remains tetravalent despite the employed reducing conditions. For Th, this result is expected as ThO_2 is reported as the only stable phase in the Th-O system [6]. Regarding the Pu cations, the presence of Pu(IV) is consistent with thermodynamical models which have foreseen that in the Pu-Am-O system the Am should be strictly trivalent before the reduction of Pu [7]. In contrast, however, other works suggest the oxidation of tetravalent to pentavalent U for $U_{0.80}Am_{0.20}O_{2\pm x}$ materials, [8–10].

Secondly, a pure Am(III) valence is achieved for the ThO_2 matrix while mixed Am(III/IV) valences are obtained with UO_2 and PuO_2, evidencing that the reduction of Am to Am(III) is enhanced in the ThO_2. It was found, however, that the $Pu_{0.80}(IV)Am_{0.20}(III/IV)O_{2-x}$ material is biphasic (both cubic) while Am bearing ThO_2 and UO_2 are single phase fluorite solid solutions. One can assume the structural stability of these latter materials is related to the lower oxygen potentials of UO_{2-x} and ThO_2 compared to PuO_{2-x} [6].

The structure of the studied samples has been fully characterized by assessing the interatomic distances, the coordination numbers and the Debye-Waller factor. Although direct comparison of these structural data is difficult due to the various O/M ratios, the presence of a

bimodal distribution of the distances in the first shell and an absence of local clustering around M and Am cations was identified.

$Pu_{0.80}(IV)Am_{0.20}(III/IV)O_{2-x}$ and $Th(IV)_{0.80}Am(III)_{0.20}O_{1.90}$ materials were post heat-treated under air at 800°C. This thermal treatment leads to the formation $Pu(IV)_{0.80}Am(III/IV)_{0.20}O_{1.98}$ and $Th(IV)_{0.80}Am(IV)_{0.20}O_{2.00}$ solid solutions, respectively[3,4]. As would be expected, the host cations (Th, Pu) remain tetravalent and Am is oxidized in both cases. However, for Th based materials, the oxidation of Am(III) to Am(IV) was complete while a mixed Am(III/IV) valence remains for the Pu bearing solid solution, under the same conditions. In addition to the difference of oxygen potential of Pu and Th oxides [6], this difference in the oxidation kinetics could be related to the original reduced materials, *i.e.* biphasic and single-phased for Am bearing PuO_2 and ThO_2 respectively. Nevertheless, 800°C is a sufficient temperature to ensure the phase transition from a two phases structure to a single phased solid solution. Furthermore, thermogravimetric measurements have shown that the transition from the defective $Th(+IV)_{0.80}Am(+III)_{0.20}O_{1.90}$ to the stoichiometric $Th(+IV)_{0.80}Am(+IV)_{0.20}O_{2.00}$ solid solution is achieved at 625°C [11].

A series of $(M,Am)O_{2\pm x}$ materials have been prepared at oxygen potentials of -384 $kJ.mol^{-1}$. All samples show a cubic structure. The majority cations (Th, U, Pu) remain tetravalent, while the Am is (III) in the Th material, and (III/IV) in the Pu material. This series will be completed shortly with a study of the Np equivalent.

ACKNOWLEDGEMENT

The authors gratefully acknowledge the members of the JRC-ITU and of the INE-beamline for their involvement in these projects.

REFERENCES

(1) Grouiller, J.-P.; Pillon, S.; De Saint Jean, C.; Varaine, F.; Leyval, L.; Vambenepe, G.; Carlier, B. *J. Nucl. Mater.* **2003**, *320*, 163.

(2) Vespa, M.; Rini, M.; Spino, J.; Vitova, T.; Somers, J. *J. Nucl. Mater.* **2012**, *421*, 80.

(3) Carvajal-Nunez, U.; Prieur, D.; Vitova, T.; Somers, J. *Inorg. Chem.* **2012**, *51*, 11762.

(4) Prieur, D.; Carvajal-Nunez, U.; Vitova, T.; Somers, J. *Eur. J. of Inorg. Chem.* **2012**, (accepted).

(5) Rothe, J.; Butorin, S.; Dardenne, K.; Denecke, M. A.; Kienzler, B.; Löble, M.; Metz, V.; Seibert, A.; Steppert, M.; Vitova, T.; Walther, C.; Geckeis, H. *Rev. Sci. Instrum.* **2012**, *83*.

(6) Guéneau, C.; Chartier, A.; Van Brutzel, L. In *Comprehensive Nuclear Materials*; Elsevier: Oxford, 2012; pp. 21–59.

(7) Osaka, M.; Kurosaki, K.; Yamanaka, S. *Journal of Nuclear Materials* **2006**, *357*, 69–76.

(8) Prieur, D.; Martin, P. M.; Jankowiak, A.; Gavilan, E.; Scheinost, A. C.; Herlet, N.; Dehaudt, P.; Blanchart, P. *Inorg. Chem.* **2011**, *50*, 12437–12445.

(9) Prieur, D.; Martin, P.; Lebreton, F.; Delahaye, T.; Banerjee, D.; Scheinost, A. C.; Jankowiak, A. *Journal of Nuclear Materials* **2013**, *434*, 7.

(10) Nishi, T.; Nakada, M.; Suzuki, C.; Shibata, H.; Okamoto, Y.; Akabori, M.; Hirata, M. *Journal of Nuclear Materials* **2011**, *418*, 311–312.

(11) Prieur, D.; Carvajal-Nunez, U.; Somers, J. *J. Nucl. Mater.* **2013**, *435*, 49–51.

2-24

Elastic Properties of Alpha Plutonium Measured Via Resonant Ultrasound Spectroscopy

Tarik Saleh, Adam Farrow, Franz Freibert

Los Alamos National Laboratory, Los Alamos, NM, USA

Cast pucks and rods of high density alpha plutonium were created as a part of R&D efforts at Los Alamos National Laboratories. The as-cast material was analyzed using a variety of characterization techniques, including immersion density, resonant ultrasound spectroscopy (RUS), dilatometry and quasi-static mechanical testing. This talk will present the elastic moduli of alpha plutonium alloys measured in the as-cast and thermally treated state. Over 30 samples from three separate castings were measured. Results are presented as a function of density, alloy content and age. Stress strain curves from quasi-static compression tests will be presented as well. This data will be compared to previous literature values and similar experiments done on older alpha material.

The 27 cylindrical samples of new (1-3 year old) alpha samples are the largest batch of similarly prepared samples for elastic moduli measurements. High quality repeatable data was measured across all samples. For these 27 samples (average density 19.58 g/cc) the average elastic moduli were as follows: Bulk Modulus = 51.23 GPa, Shear Modulus = 42.6 GPa. Standard of deviation of 1 GPa for bulk modulus and 0.3 GPa for shear modulus is reported, with a measurement RMS of 0.31%.

2-31

Thermodynamic stability of UO_2 surface by means of DFT+*U* calculations: interplay between polarity and overstoichiometry

François Bottin[1], Gérald Jomard[2], Grégory Geneste[1]

[1]CEA, DAM, DIF, Arpajon, France, [2]CEA, DEN, DEC, Saint-Paul-lez-Durance, France

These last years, a large number of theoretical works focused on uranium dioxide. The complex electronic structure of this compound is only captured by methods going beyond standard DFT calculations, such as the DFT+*U* framework [1] or calculations using hybrid functionals [2]. In particular, the occupation matrices of the *f* orbitals play a significant role [1,3,4] and a particular attention have to be paid in order to find the correct insulating ground state.

In this work we have computed the thermodynamic stability, as a function of the temperature and the oxygen partial pressure, of several surfaces for the three (110), (100) and (111) orientations of UO_2. If the first orientation is non-polar, the two last ones are polar and have a peculiar behaviour when the surface is non-stoichiometric. In particular, the electronic structure of these surfaces can be strongly modified with respect to the one obtained in the bulk. We have considered in this work seven terminations: the UO_2-(110), O-(100) and O-(111) which are stoichiometric, the U-(100) and U-(111) which are understroichiometric and finally, the O_2-(100) and O_2-(111) which are overstoichiometric.

All these calculations are performed using the electronic structure code ABINIT [5] on the massively parallel supercomputer TERA-100 (with a number of cores up to 2000) in the DFT+*U* framework. A fine tuning of all the relevant parameters involved in this approach have been made. In particular, for each orientation, the corresponding superbulk is computed (without any symmetry [1,3]) in order to obtain the correct occupation matrix of the *f* orbitals and check that the true ground state is in any case achieved.

The thermodynamic stability of these seven orientations-terminations is characterized by means of surface Grand potentials. For very low oxygen partial pressures we don't find any thermodynamically stable understoichiometric terminations and rather obtain, up to intermediary external conditions, a stoichiometric O-(111) termination. For oxygen rich chemical environments, we observe a peculiar feature: the overstoichiometric O_2-(100) and O_2-(111) terminations appear to be the most thermodynamically stable. The stability of these two terminations was not expected in view of both the polar character of these terminations and our study of PuO_2 surfaces [7]. For these two actinide dioxides we obtain strong surface electronic modifications, fulfilling the polarity compensation criterion and leading to a reduction of the actinide oxidation state in the outermost layers. But at odds with charge-transfer gap materials, for instance PuO_2, we do not observe any formation of open shell structures (“metallization”) at the O_2-(100) and O_2-(111) terminations of UO_2; the surface of this Mott-Hubbard gap materials still remains insulating.

In case of the strongly correlated oxide UO_2, this kind of polarity compensation, through a modification of the surface electronic structure, is found really competitive from a thermodynamic point of view, and becomes more efficient than the one operating through a modification of the surface stoichiometry. The ability of UO_2 polar surfaces to capture oxygen from external environments may be considered as a first step towards the overstoichiometry of the UO_2 compound.

References

[1] B. Dorado, B. Amadon, M. Freyss, and M. Bertolus (2009) Phys. Rev. B **79**, 235125.

[2] I.D. Prodan, G.E. Scuseria, and R.L. Martin (2007) Phys. Rev. B **76**, 033101.

[3] G. Jomard, B. Amadon, F. Bottin, and M. Torrent (2008) Phys. Rev. B **78**, 075125.

[4] J.-P. Crocombette, D. Torumba, and A. Chartier (2011) Phys. Rev. B **83**, 184107.

[5] X. Gonze et al. (2009) Comp. Phys. Comm. **180**, 2582-2615.

[6] F. Bottin, S. Leroux, A. Knyazev and G. Zerah (2008) Comput. Mater. Sci. **42**, 329.

[7] G. Jomard and F. Bottin (2011) Phys. Rev. B **84**, 195469.

2-32

Dissolution of innovative irradiated fuels: the case of HELIOS and CONFIRM

Gaël Ménard, Eva de Visser-Týnová

NRG, Petten, The Netherlands

The ASGARD project (European 7th Framework programme) focuses on research of advanced/novel nuclear fuels fabrication and their respective reprocessing issues for Generation IV reactors. Industrial solutions for reprocessing are nowadays based on the so-called PUREX process which represents therefore a guideline for the dissolution experiments.

A part of this project is dedicated to the dissolution of two High Flux Reactor Petten irradiated uranium-free fuels. The two fuel types under investigation are uranium-free nitride fuel, (Pu,Zr)N, and cermet fuel consisting of minor actinide oxide particles in a molybdenum matrix. These fuels have been irradiated in two former FP6 projects (respectively CONFIRM and EUROTRANS/HELIOS). The dissolution studies will be performed in the chemical cells of the Hot cells laboratories at NRG. The fuel pins were cut into thin disks of 5mm thickness for the dissolution experiments.

Figure 1: Pellet made from the CONFIRM experiment

The material from the CONFIRM pin, CONFIRM-30-U, $(Pu_{0.3}Zr_{0.7})N$, is a nitride fuel that has been developed for both their efficiency during irradiation (better thermo-conductivity) and their supposed easy-handling in the reprocessing stage. The material will then be dissolved in nitric acid of various concentration and, potentially, at different temperatures. The obtained solutions will be analysed: TIMS will be used to follow the kinetics of PuO_2 dissolution and gamma-spectrometry to control other nuclides dissolution rates over time. The given results will lead to a better understanding of the kinetics of dissolution of the material and to the process optimization.

The specific material of HELIOS pin 5, $Pu_{0.801}Am_{0.199}O_{2-x}$ (15.77 % vol)+ molybdenum matrix (84.23 %vol), presents a complex challenge for dissolution. Cer-Met fuels have been developed for their performance at high burn-up, though the reprocessing stage has not been inquired. The complexity of the fuel makes its reprocessing a challenge. To cope with this challenge, series of cold tests (pure molybdenum) and semi-warm tests (fresh PuO_2+Mo matrix pellets) have been conducted over the past year. The molybdenum matrix dissolution by acids leads often to precipitations of MoO_3, and molybdenum is insoluble at alkaline conditions. Based on the tests a three steps dissolution is proposed:

1) Dissolution in cold mild nitric acid (3M) to dissolve the inert matrix and avoid molybdenum precipitation

2) Alkaline washing step to remove the residual dissolved molybdenum

3) Dissolution of the PuO_2 with boiling concentrated nitric acid reinforced with the use of HF

Those experiments will also provide data on the behaviour of minor actinides during the reprocessing steps, with a special interest for americium. Preliminary results of dissolution studies of both irradiated fuels including the chemical analyses of the solutions will be presented and discussed in relation to reprocessing issues.

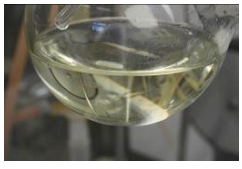

Figure 2: PuO_2 dissolved in HNO_3+HF (semi-warm)

3-06

Thermal conductivity measurement of $(Pu_{1-x},Am_x)O_2$ (x=0.03, 0.07)

Taku Matsumoto[1], Tatsumi Arima[1], Yaohiro Inagaki[1], Kazuya Idemitsu[1], Masato Kato[2], Kyoichi Morimoto[2], Masahiro Ogasawara[3]

[1]Kyushu university, Fukuoka, Japan, [2]Japan Atomic Energy Agency, Ibaraki, Japan, [3]Inspection development company, Ibaraki, Japan

1. Introduction

Development of minor actinide (MA) bearing MOX fuels has been conducted to reduce the amount of high level waste. In the development of such new type fuels, it is important to understand their physical properties. Because thermal conductivity is one of the important properties for the development, the effect of PuO_2 and AmO_2 content on the thermal conductivity of MOX was investigated. Although a few data of thermal conductivity of PuO_2 were reported previously, they differ widely. The data of Am-containing MOX were also reported, but the effect of Am was unclear due to the too low Am content. In the present work, thermal conductivity of $(Pu,Am)O_2$ was measured, and the effect of Am content was evaluated to contribute to analyze thermal conductivity of MA–bearing oxide fuels.

2. Experiment

In this study, two kinds of disc-like specimens $(Pu_{0.97},Am_{0.03})O_2$ and $(Pu_{0.93},Am_{0.07})O_2$ were prepared. The specimens were heated at 1123K for 5h in air to adjust O/M ratio to 2.00 and then measured by X-ray diffraction analysis. It was observed that both specimens had a single fcc phase, and lattice parameter corresponded to the values obtained from Vegard's law in the $PuO_{2.00}$ - $AmO_{2.00}$ system.

Thermal diffusivity was measured in the temperature range from 650K to 1450K in vacuum (about 10^{-3} Pa) with laser flash method. Measurement was carried out in both heating and cooling processes to confirm the change of the O/M ratio during the measurement. Post measurement specimens were also evaluated their O/M ratio by thermo-gravimetry.

Thermal conductivities were calculated from the following equation:

$$\lambda = \alpha \cdot \rho \cdot C_p \ldots(1)$$

where α is the thermal diffusivity, ρ is the density of specimen and C_p is the heat capacity at constant pressure. Density of specimens was measured by an immersion method to be 94~97% T.D. Densities at high temperatures were evaluated by thermal expansion data reviewed by Carbajo[1)].

Heat capacity was calculated by the Kopp-Neumann rule as follows,

$$C_p = (1-y)\times C_p(PuO_2) + y \times C_p(AmO_2) \ldots(2)$$

where $C_p(PuO_2)$ and $C_p(AmO_2)$ are the heat capacities of PuO_2 and AmO_2 respectively.

To compare the thermal conductivities of different porosities, the thermal conductivities were normalized to 100% theoretical density (T.D.) by the Maxwell-Eucken relationship.

3. Results and discussion

Measured thermal conductivities of $(Pu_{0.97}Am_{0.03})O_2$ and $(Pu_{0.93}Am_{0.07})O_2$ up to 1250K and 1450K were shown in Fig. 1. The thermal conductivities measured during cooling process from 1250K (Fig. 1 (a)) were a good agreement in those during heating. In this measurement, the O/M ratio was kept during heating and cooling process. On the other hand, the measured data during cooling process from 1450K (Fig. 1 (b)) were lower than those during heating. In this experiment, it was observed that final O/M ratio decreased from their initial value for both specimens. Especially, the $(Pu_{0.93}Am_{0.07})O_2$ was reduced to 1.968. This result suggests that the specimens kept the stoichiometric composition at temperatures less than 1250K.

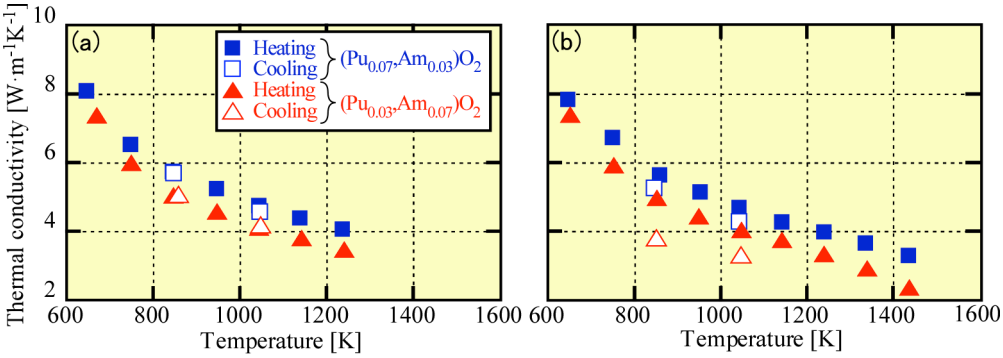

Fig. 1 The thermal conductivities of $(Pu_{0.97}Am_{0.03})O_2$ and $(Pu_{0.93}Am_{0.07})O_2$; (a) up to 1250K and (b) up to 1450K

The thermal conductivities of $(Pu_{0.97}Am_{0.03})O_{2.00}$ and $(Pu_{0.93}Am_{0.07})O_{2.00}$ up to 1250K (O/M=2.00) are shown in Fig. 2 as a function of temperature together with literature data for PuO_2 and UO_2. The data of Gibby[2] and Fukushima et al[3] are comparable. However, the data reported by Cozzo et al[4] is about 3 $Wm^{-1}K^{-1}$ higher than that by Gibby[2] and Fukushima et al[3] at 700K. Present data consisted with the literature data by Cozzo et al[4]. And thermal conductivity was slightly decreased with Am content.

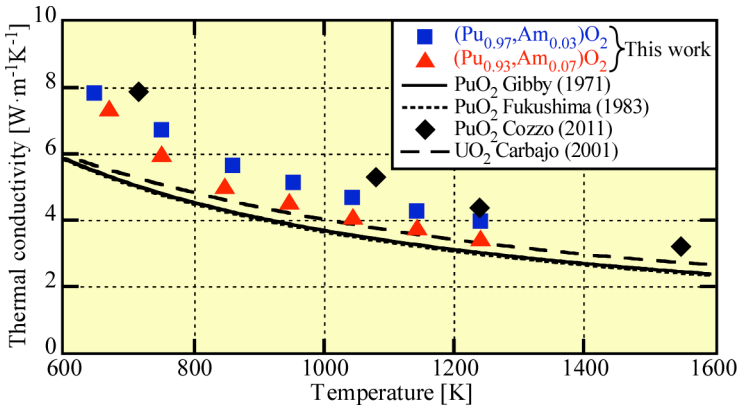

Fig. 2 The thermal conductivities of $(Pu_{0.97},Am_{0.03})O_2$ and $(Pu_{0.93},Am_{0.07})O_2$ (O/M=2.00)

4. Summary

The thermal conductivities of $(Pu_{1-x},Am_x)O_2$ (x=0.03, 0.07) were measured under 1250K. It consisted with the literature data by Cozzo. Increasing of Am content leads the thermal conductivities of $(Pu,Am)O_{2.00}$ slightly decreased. Above 1250K, decrease of thermal conductivity was observed due to the O/M ratio change during the measurement.

References

[1] J. J. Carbajo, et.al, *J. Nucl. Mater.*, **299** (2001) 181.

[2] R.L. Gibby, *J. Nucl. Mater.*, **38** (1971) 163.

[3] S. Fukushima, et.al, *J. Nucl. Mater.*, **114** (1983) 260.

[4] C. Cozzo, et.al, *J. Nucl. Mater.*, **416** (2011) 135.

3-07

Chemical Segregation of U-10wt.% Mo Fuel Foils During Simulated Bonding Cycles

Sven C. Vogel[1], Donald W. Brown[1], Maria Okuniewski[2]

[1]Los Alamos National Laboratory, Los Alamos, NM, USA, [2]Idaho National Laboratory, Idaho Falls, ID, USA

The mission of the Global Threat Reduction Initiative (GTRI) of the National Nuclear Security Administration in the U.S. DOE is to reduce and protect vulnerable nuclear and radiological material located at civilian sites worldwide by providing support for countries' own national programs. The GTRI Reactor Convert program converts research reactors from the use of highly enriched uranium to low enriched uranium. The baseline fuel for conversion of high performance research reactors is monolithic uranium-10wt.% molybdenum, encased in an aluminum cladding. During fabrication, the aluminum cladding is hot isostatic pressed so that it bonds to the rolled U10Mo foil. However, the final crystal structure of the U10Mo foil is dependent on the HIP'ing temperature and profile. The cubic γ phase is preferred for the fuel application and it is stable in U10Mo above ~560°C. However the fuel transforms to orthorhombic α (almost pure uranium), as well as meta-stable intermetallic γ, and γ' crystal structures if held at temperatures below this point.

Neutron diffraction data collected on the HIPPO instrument at LANSCE [1] from a post-HIP U7Mo sample has shown that the foil transforms in minutes into α-uranium and a supersaturated γ (bcc) phase when the HIP temperature is 520°C, which is much faster than seen in published time-temperature-transformation diagrams. To re-assess the published TTT diagram [2], we have performed in-situ neutron diffraction measurements on five rolled U10Mo foils while they were taken through a thermal cycle equivalent to the 520°C HIP procedure as well as several other temperatures (420, 460, 490, and 560°C). The phase and microstructural evolution is readily apparent in the diffraction data. Furthermore, the diffraction data also allows identification of intermetallic meta-stable phases as well as studies of the texture evolution. Our neutron diffraction data allows to uniquely establish the time-temperature-transformation (TTT) diagram without the need for quenching and with much more detail than e.g. dilatometry.

From lattice parameter measurements of the γ phase during the isothermal holding, we clearly observe redistribution of Mo atoms during the holding (Figure 1). Adapting a conversion for U-Mo lattice parameter to Mo concentration established by Sinha et al. [3], we can estimate the Mo concentration in the γ phase as a function of time. The resulting length changes obscure e.g. dilatometry measurements to assess the phase transformations as it is impossible to discriminate between length changes due to Mo partitioning and decomposition of the γ phase. From the texture data, we find that certain crystal orientations tend to preferentially transform, which could potentially be utilized to reduce the transformation rate (Figure 1).

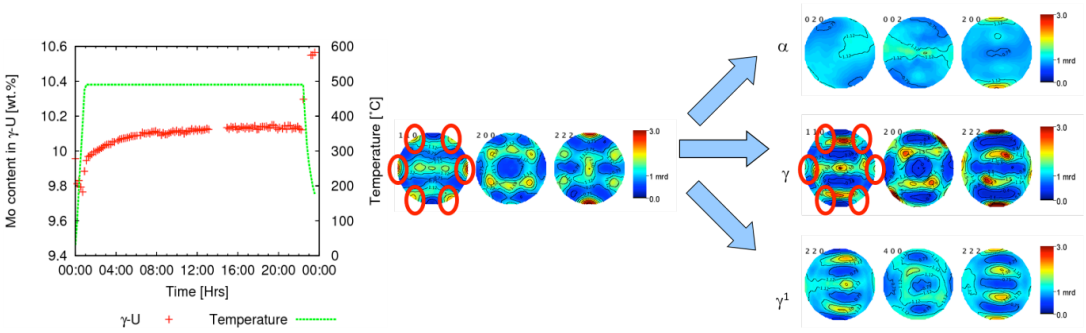

Figure 1: Left: Evolution of the Mo concentration, derived from the lattice parameter changes during isothermal holding at 490°C. The conversion from lattice parameter to Mo concentration by Sinha et al. [3] was determined for room temperature. We use our thermal expansion data to correct for thermal expansion, however, the influence of the Mo concentration on the lattice is likely different at room temperature and 490°C. The conversion of the first data point taken at room temperature is very close to the nominal composition, indicating reliability of the conversion at room temperature. The last data point, taken at

~180°C, results in a Mo concentration of ~10.55 wt%. It is therefore likely that the plateau observed during isothermal holding is closer to 10.6 wt%. Right: Pole figures of the initial g phase and the resulting α uranium and γ' phases as well as the residual γ phase after ~22 hrs annealing at 490°C. The areas in circles indicate crystal orientations that were populated in the pre-annealing material, but disappeared during the annealing, thus indicating a preference for these orientations to transform.

References

[1] H.-R. Wenk, L. Lutterotti, S. Vogel, “Texture analysis with the new HIPPO TOF diffractometer”, Nuclear Instruments and Methods in Physics Research A 515 (2003) 575–588.

[2] Repas, P., Goodenow, R., Hehemann, R., Transactions of the ASM, **57** (1964) 151.

[3] Sinha et al., J. Alloys and Compounds **491** (2010) 753.

3-08

Insight Into The Mechanism of Plutonium Hydride Formation

Patrick Allen, Long Dinh, William McLean, Scott McCall, Cheng Saw, John Haschke

Lawrence Livermore National Laboratory, Livermore, California, USA

SUMMARY: A general tenet in plutonium hydriding phenomenology is that hydrogen must diffuse through the PuO_2 layer to reach the oxide/Pu interface where nucleation starts and grows. However, since the solubility of hydrogen in PuO_2 is orders of magnitude smaller than that in Pu, the transport of enough hydrogen through the oxide barrier to start nucleation at the metal interface is unlikely, except through defects in the surface oxide such as cracks, impurity centers, lattice vacancies, Pu_2O_3 domains, and grain-boundaries, etc. Furthermore, experimental evidence reveals that, once reaching the oxide/metal interface, the majority of hydrogen taken out of the gas phase during the initial reaction time is simply incorporated into the Pu metal without chemical reaction while only a small fraction of the gas participates in the hydriding reaction at hydrogen saturated sites. Through a combination of pyrometry imaging, pressure drop measurement, thermal modeling, and FIB-SEM, we demonstrate that hydrogen diffusion and reaction are faster along grain-boundaries and that an inhomogeneous, intra-grain reaction, due to possible defects such as dislocations and localized phases, leads to the breaking up of the hydriding grains into smaller particles during reaction.

EXPERIMENTAL: Hydriding experiments were performed on Pu coupons cut from a sheet of PuO_2-coated polycrystalline delta-phase Ga alloy. During a typical hydriding experiment, the test specimen is mounted in a two-piece aluminum holder fitted with a pair of indium O-ring seals to prevent reactions at edge sites [1]. The mounted sample is placed in a vacuum chamber equipped with thermocouples, capacitance manometers, and sapphire windows for pyrometric imaging with an IR camera. To achieve the most consistent results, we initiate the reaction at a single site by removing the oxide layer at the center of each metal coupon [1]. Since hydrogen solubility in actinide oxides is many orders of magnitude less than that in pure metals [1, 3], the transport of hydrogen from the gas phase through the dioxide layer to the Pu metal is practically limited by hydrogen saturation in the dioxide layer (see Fig.1). Once a local hydriding spot forms, it can release heat and reduces the local PuO_2 to Pu_2O_3 promoting further corrosion [1,4-5]. The temperature evolution around the hydriding spot is compared against thermal modeling results performed with Comsol Multiphysics software [2], and microscopic structural information about the reaction zone is investigated with X-ray diffraction and FIB-SEM.

RESULTS & DISCUSSION: For the pyrometric imaging experiments during hydriding [6], it is observed that reaction preferentially initiates at the center site (see Fig. 2) upon pressurization of the evacuated reaction chamber with 10.5 mmol of research grade H_2 at room temperature. During the first 6 minutes of reaction, the temperature at the initial hydriding site increased by 5-6K. Growth of the initial site resulted in formation of a several-millimeter diameter site and attainment of the maximum ΔT (~60K) after 17 minutes. Heat-transfer thermal modelling of the hydriding reaction [2], using the advancing rate of the reaction front as measured by pyrometric imaging, reveals that the heat released during the first few minutes of the reaction is substantially less than that cited for PuH_2 formation [6]. This suggests the existence of a mixture of Pu and PuH_2 instead of a uniform PuH_2 reaction front, and depending on which reaction front (spherical or elliptical) is employed in modelling, only ~ 10% to 20% of H_2 removed from the gas phase reacted with Pu to form PuH_2. The additional H_2 absorbed by the Pu likely diffuses ahead of the observable reaction front to raise the hydrogen solubility in the sample under study and possibly started hydriding along grain boundaries where hydrogen saturation was reached.

Recent FIB-SEM measurements on a partially hydrided sample confirm the existence of hydrided regions along the grain boundaries ahead of the main hydriding reaction front [7]. In addition, the reaction front line seems to attack certain grains more preferentially than others along the same common grain boundary regions. Within the preferentially attacked grains, the intra-grain reaction front did not advance uniformly but exhibited a finger type of approach (see Fig. 3). Point dislocations can be readily formed in a radioactive environment and coalesce into line and/or pinned dislocations. These and other local variations inside the grains may be responsible for such an observed non-uniform, finger shape advancing

reaction front. In the case of line dislocation, the orientation toward or away from the grain boundaries may determine the probability of certain grains undergoing rapid reaction with hydrogen.

ACKNOWLEDGMENT: We would like to thank Robert Erler for excellent SEM support. This work performed under the auspices of the U.S. Department of Energy by Lawrence Livermore National Laboratory under Contract DE-AC52-07NA27344.

References

[1] L.N. Dinhet al., J. Nucl. Mater., **408** (2011),171.

[2] COMSOL Multiphysics version 4.2a, by COMSOL Inc., Stockhom, Sweden

[3] D. F. Sherman, D. R. Olander, J. Nucl. Mater. 166 (1989) 307.

[4] J. M. Haschke, T. H. Allen, L. A. Morales, Los Alamos Sci. 26 (2000) 252.

[5] J. M. Haschke, T. H. Allen, J. Alloys Compd. 320 (2000) 58.

[6] C. K. Saw et al., J. Nucl. Mater. 429 (2012), 128.

[7] L. N. Dinh et al., to be submitted.

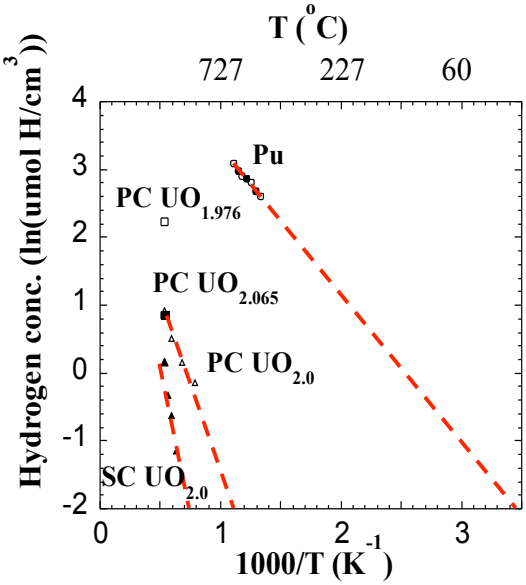

Fig.1: The hydrogen solubility in metal and oxide.

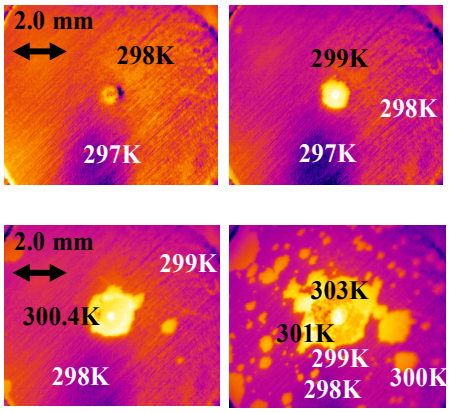

Fig.2: Pyrometric images of a growing hydriding spot.

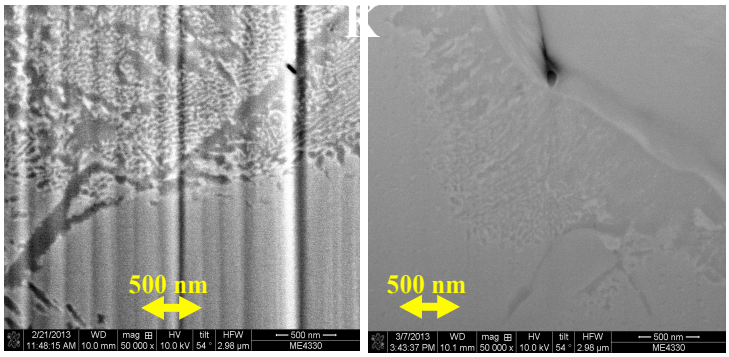

Fig.3: FIB-SEM images of hydrding trend at reaction front (left) and along a grain boundary ahead of the reaction front (right).

3-09

Ab initio study of defect production and migration in thoria

William Weber[1,2], Haiyan Xiao[1], Bin Liu[2], Yanwen Zhang[2,1]

[1]*University of Tennessee, Knoxville, TN, USA,* [2]*Oak Ridge National Laboratory, Oak Ridge, TN, USA*

Fluorite-structured thoria (ThO_2) is an important material for both technological and industrial applications. For example, thoria has been used as a solid-state electrolyte and has been proposed as an optical component material and laser host. Thorium is a fertile nuclear material, and ThO_2-based nuclear fuel containing fissile uranium or plutonium is attractive for advanced nuclear fuel cycles. Compared to UO_2-based fuels, ThO_2-based fuels show better thermo-physical properties and chemical stability, which ensures better in-pile performance. Thorium is widely distributed in nature, and it is 3 to 4 times more abundant than uranium. In addition, ThO_2 offers the promise of increased proliferation resistance, longer fuel cycles, higher burn-ups, and decreased production of minor actinides as nuclear wastes. Due to the importance of thoria for the nuclear industry in many countries, there has been increasing interest in theoretical calculations of radiation effects and defect properties. However, the dynamics of atomic processes in ThO_2 under irradiation are not yet well understood.

Table 1. Threshold displacement energies (eV) in ThO_2 [1].

	Th	O
[100]	53.5	17.5
[110]	48.5	30.0
[111]	61.5	>100
[112]	54.5	28.0

Ab initio molecular dynamics simulations of low energy recoil events in ThO_2 have been carried out to determine: 1) the threshold displacement energy, E_d, along specific crystallographic directions; 2) the role of charge transfer on the dynamics of the recoil process and defect production; and 3) the final defect configurations and charge redistribution [1]. These simulations reveal that charge transfer occurs during the dynamic displacement process, and the effective charge for the primary recoil atom varies significantly to overcome the energy barrier for defect formation. The calculated threshold displacement energies are summarized in Table 1. Charge redistribution leads to new defect configurations and charge states due to the delocalization of electrons on neighbouring atoms.

In addition, *ab initio* molecular dynamics has also been applied to investigate defect production and interactions from overlapping recoil events in thoria. Pre-existing defects from an initial cascade affect the pathways, energy barriers and damage end states associated with the dynamic processes that occur from overlapping recoil events. Electron transfer is found to play a role in the defect formation process for both single recoils and overlapping recoils.

An *ab initio* method has also been used to study the stability and migration of charged oxygen interstitials in ThO_2. The results reveal that oxygen interstitials are likely to lose electrons under *p*-type condition and gain electrons under *n*-type condition, behaving as donor and acceptor defects, respectively. For oxygen interstitials with charge states varying from 2- to 2+, the migration mechanism in ThO_2 is independent of the charge state, and the interstitialcy mechanism is preferred. The migration of O^+ and O^{2+} interstitials are more favourable, for which O-O split interstitials are observed at the “saddle point” as illustrated in Figure 1. The migration energy barriers for O^+ and O^{2+} in ThO_2 are on the order of 0.10 to

0.14 eV. These results provide new insights for further study of point defect behaviour in thoria.

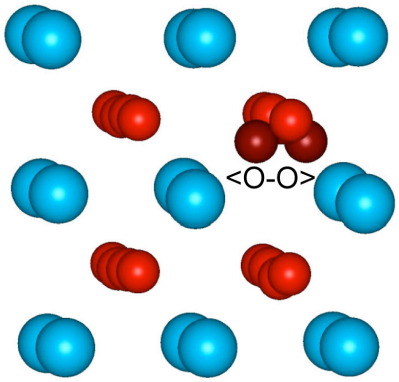

Figure 1. Schematic view of the optimized configuration for the "saddle point" in O^{+} migration in ThO_2.

This work was supported as part of the Materials Science of Actinides, an Energy Frontier Research Center funded by the Office of Basic Energy Sciences, U.S. Department of Energy.

References

1. H. Y. Xiao, Y. Zhang, and W. J. Weber, *Physical Review* **B 86** (2112) 054109.

3-10

DFT Investigation of Uranium Oxides and Defect Structures

Nick Brincat[1], Steve Parker[1], Geoff Allen[2], Mark Storr[3]

[1]University of Bath, Bath, UK, [2]Interface Analysis Centre, University of Bristol, Bristol, UK, [3]AWE, Aldermaston, UK

UO_2, the most common nuclear fuel material globally, is regularly oxidised during handling, storage and reactor operation. It is in fact the first in a complex family of oxides, initially based on the fluorite UO_2 unit cell (U_4O_9 and U_3O_7) but giving way to layered-type oxides as the O/U ratio increases (U_3O_8 and UO_3). Oxidation in UO_2 is known to occur via accumulation of point oxygen interstitials and defect aggregates such as Willis, cuboctahedral and split-interstitial clusters. The link between defect clusters and the U_4O_9 and U_3O_7 structures can be rationalised in terms of multiple Willis, cuboctahedral and split-interstitial clusters. Due to the difficulties with isolating the various oxides experimentally and the challenge of simulating such large systems a complete description of the UO_{2+x} system is still lacking.

In the present work we reproduce experimentally observed uranium oxide structures (UO_2, U_3O_8 and UO_3) using three different levels of DFT and considering non-collinear magnetism and spin-orbit coupling to predict their electronic and elastic properties to a high degree of accuracy. Extending these models to defective systems we now examine the stability of different defect clusters in UO_2 supercells. The formation energy of each cluster is calculated along with the variation of their concentrations with increasing the temperature. All interstitial clusters are found to be charge compensated by U^{5+} ions, suggesting this is the highest uranium oxidation state reached amongst the fluorite-based structure. Calculations show Willis and split di-interstitial clusters to have the most favourable formation energies per excess oxygen ion. Cuboctahedral clusters are shown to be most stable overall and are predicted to be present at higher concentration than any of the other defects.

4-06

Solid state phase transformation study on Pu-Ga alloys containing 0.18 to 0.63 wt.% Ga

Michael Ling, Nigel Park

AWE, Reading, UK

Many investigations have been carried out on the Pu metal and Pu-Ga alloys to explore phase equilibriums, phase transformation behaviours and structure/property relations previously, however, there still remain many outstanding problems. For example, transformation mechanisms are still not well understood in both the pure Pu metal and Pu-Ga alloys. The similarities and differences for the same type phase transformation occurred in pure Pu metal and in Pu-Ga alloy, effect of Ga concentration and starting condition of the Pu metal and Pu-Ga alloy on the transformation behaviours in different stages *etc.* are still not fully understood.

The current work presents the results of a study on effects of Ga concentration and starting condition of Pu-Ga alloys on their solid-state phase transformation behaviours in a set of Pu-Ga alloys containing 0.18 to 0.63 wt.% Ga under non-equilibrium conditions with a heating/cooling rate of 10°C/min in the temperature range of 25°C to 560°C by a dilatometry method. The characteristic dilation jumps and slopes shown in the dilatometry tracks during heating and cooling are ascribed to the known phase transformations in the Pu-Ga alloys (Fig.1). The rationale of such an ascription is discussed. The results show that Ga concentration and the starting condition of the Pu-Ga alloy have significant effects, as expected, showing as the variety of the onset and completion temperatures of a phase transformation. The results also suggest that the nature of as-cast α-phase is independent of the nominal Ga content in Pu-Ga alloys (Fig.2). The ε→δ transformation happens through two mechanisms when Ga <0.63 wt.%. Furthermore, the increase of thermal expansion coefficient of δ-phase with increasing Ga is also confirmed.

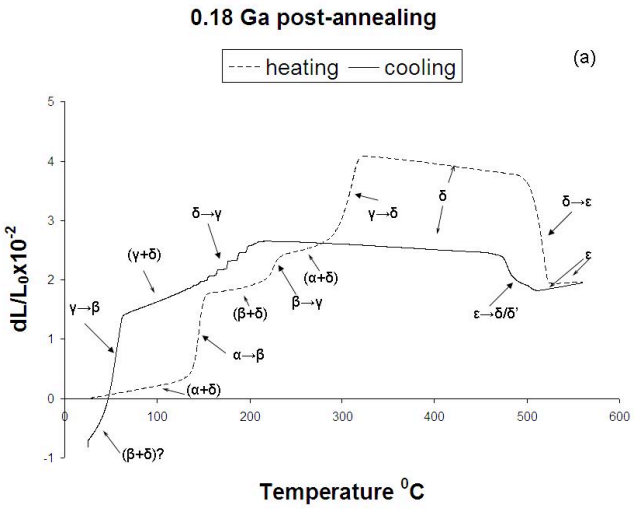

Fig.1 Dilatometry heating and cooling curves for post-annealed Pu-Ga alloy containing 0.18 wt % Ga heated from RT to 560 °C (ε-phase region) and cooled back to RT.

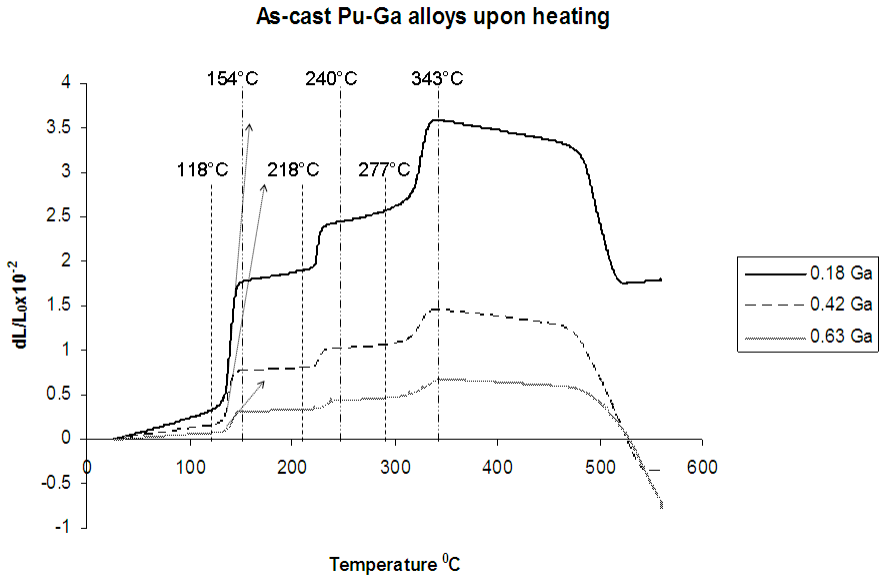

Fig.2 Dilatometry heating curves for as-cast Pu-0.18 wt.%Ga alloy, Pu-0.42 wt. %Ga alloy, Pu-0.63 wt.%Ga alloy heated from RT to 560 °C (ε-phase region).

4-07

Kinetic study of δ→α' isothermal martensitic transformation in PuGa 1at%

Fanny Lalire[1], Brice Ravat[1], Aurélien Perron[1], Benoit Oudot[1], Elisabeth Aeby-Gautier[2], Francois Delaunay[1]

[1]CEA, Is sur Tille, France, [2]École des Mines, Nancy, France

INTRODUCTION: δ-plutonium alloys are metastable and exhibit a martensitic transformation (δ→α' monoclinic structure) at low temperature. Moreover, the isothermal kinetics presents an unusual double-C Curve kinetics in the Time-Temperature-Transformation diagram [1]. Even if numerous theories were proposed, origins of these two distinct parts were not yet elucidated. Previous analyses of martensitic transformation kinetics in PuGa alloys [2,6] were performed on the basis of Avrami and Cohen-Kaufman models. In the present work, the phenomenological model developed by Pati and Cohen [7] in non-thermoelastic steels is used to study the isothermal martensitic transformation kinetics for PuGa 1 at.% alloy. This latter model seems indeed better adapted to describe plutonium alloys martensitic transformation since it allows a more precise description of the autocatalytic nucleation deduced from experimental nucleation rate and observed on optical micrographs.

EXPERIMENTAL DETAILS: Transformation kinetics were characterized on PuGa 1at.% alloy, that has been fully homogenized for 1000 hours at 733K. α' phase amount was determined from Rietveld refinement of X-ray diagrams recorded at different temperatures from -20°C to -190°C. Isothermal temperatures from -20°C to -90°C were directly reached with a temperature chamber (TTK 450 Anton Paar) allowing a fast cooling rate of -60°C/min which is coupled to a diffractometer (BRUKER AXS θ/θ D8 Advance) placed in glove box. Data at -190°C were obtained after liquid nitrogen quenching. Additional metallographic analyses were carried out to determine some parameters useful for Pati-Cohen model. Isothermal martensitic transformation was also studied during thermal cycling (from -20°C to 360°C) using XRD analyses, SEM analyses and optical micrographs.

THEORETICAL BASIS: Pati and Cohen developed an autocatalytic nucleation model to describe the isothermal martensitic transformation in a FeNiMn alloy using the following equation:

$$\frac{df}{dt} = \left[ni + f\left(p - \frac{1}{\overline{V}} \right) \right].(1-f).\upsilon.\exp\left(\frac{-\Delta W_a}{RT} \right).\left(\overline{V} + \frac{d\overline{V}}{d\ln N_v} \right)$$

The rate of transformation *df/dt* is expressed as a function of different parameters related to the evolution of embryos into martensite laths (initial embryos number per volume unity *ni*, lath mean volume $\overline{V}$, activated embryos number per volume unity Nv = f/$\overline{V}$), the autocatalytic factor p, the total nucleation free energy ΔW_a, the lattice vibration frequency υ and the isothermal transformation temperature T.

RESULTS AND DISCUSSION: Optical micrographs performed after isothermal holds at -20°C, -40°C and -190°C have revealed different α' morphologies between the two distinct parts of the TTT diagram. Indeed, a α' feather morphology was noticed at -20°C and -40°C. On the contrary, very thin parallel α' plates were formed at -190°C. A difference of accommodation mechanism (plastic then elastic) could explain the martensite morphology evolution versus the temperature. In these two cases, morphologies can be associated with an isothermal martensitic transformation controlled by an autocatalytic nucleation process.

Kinetics were thus studied in the framework of the Pati and Cohen formalism. All Pati-Cohen model parameters, excluding the single plate formation energetic barrier ΔW_a, were first assessed from PuGa 1at.% alloy optical micrographs. ΔW_a values were determined for each isothermal transformation temperatures from experimental kinetics data fitting. Results exhibit that incubation time and partial transformation are perfectly reproduced. Note that ΔW_a linearly decreases as transformation temperature decreases. A light break in slope is observed at -70°C which is the intermediary temperature between the two parts of the TTT diagram. To conclude, this work highlights that the Pati-Cohen model, which is based on the

phenomenon of autocatalytic nucleation, is well adapted to refine α' phase amount resulting from low temperature isothermal holding PuGa 1at% of a part of the TTT diagram.

In addition, the study of thermal cycling influence on isothermal martensitic transformations has revealed a progressive decrease of the maximum α' phase amount formed. Optical micrographs coupled to SEM analyses have showed a decrease in δ-grain size previously transformed in martensite.

References

[1] B. Oudot, K.J.M. Blobaum, M.A. Wall, A.J. Schwartz (2006) J. of Alloys and Comp., 1-6

[2] B. Ravat, C. Platteau, G. Texier, B. Oudot, F. Delaunay (2009) J. Nucl. Mater., 418-424

[3] K.J.M. Blobaum, J.R. Jeffries, A.J. Schwartz, H. Cynn, W. Yang, M.A. Wall, W.J. Evans (2011) J. Nucl. Mater., 1-7

[4] L. Kaufman, M. Cohen (1958) Progress in Metal Physics, **7**, 165-246

[5] P.E.A Turchi, L. Kaufman, Z.K. Liu, S. Zhou, Z-K Liu (2007) J. of Alloys and Comp., 28-35

[6] P.H. Adler, G.B. Olson, M.F. Stevens, G.F. Gallegos (1992) Acta Metal. Mater., **40**, 1073

[7] R. Pati, M. Cohen (1971) Acta Metallurgica, **19**, 1327-1332

4-08

The effects of thermal conditioning and recovery processes on the δ→γ phase transformation mechanisms in plutonium.

Sue Ennaceur

AWE, Reading, UK

The focus of this work has been directed towards gaining a greater understanding the behaviour of plutonium on cooling from the δ-phase. A number of studies by differential scanning calorimetry (DSC) and dilatometry on the d-phase (face centered cubic) to γ-phase (face centered orthorhombic) transformation have reported the remarkable behaviour of this transformation and have proposed a range of explanations for the mechanism based on the conditions examined [1,2,3].

The current DSC study, which has systematically examined a wide range of experimental conditions, shows new evidence indicating that the transformation is influenced by recovery processes that occur in the δ-phase. This work examines the influence of specimen condition, thermal conditioning and matrix recovery mechanisms on the δ→γ phase transformation in unalloyed plutonium and demonstrates that a complex balance is achieved between these processes to drive the reaction more towards one mechanism than another.

Depending on the specific thermal history and stability of a specimen the phase transformation may proceed via multi-staged or single peak athermal and isothermal mechanisms (Figs 1). The phase transformation pathway may also be induced to occur via sequential or mixed phase transformation routes or even by skipping a given phase to transform directly to a lower temperature phase (Fig 2).

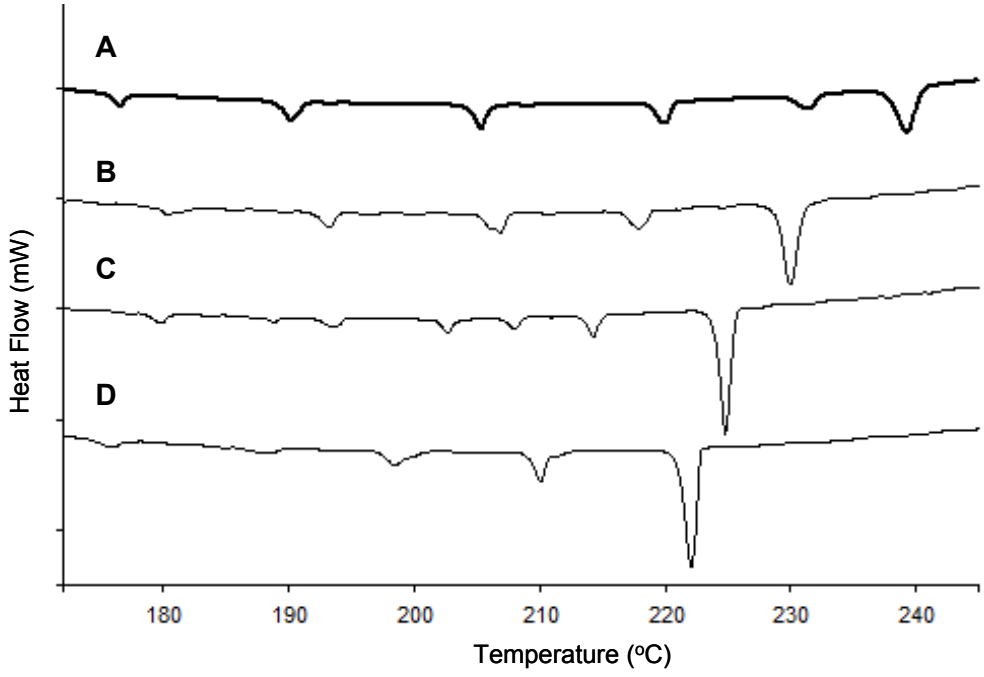

Figure 1. DSC thermograms for the δ→γ phase transformation on cooling from 450°C at a rate of 5°Cmin^{-1}: with no isothermal hold (A) and following isothermal holds of 1h (B), 12h (C) and 100h (D). (Ordinate axis (Heat flow): scale bars are separated by 10 mW).

Plutonium metal presents itself as a unique study case to investigate the complexities of phase transformation mechanisms. A non-alloyed system which has such an array of phase transformations with large differences in properties and within a relatively narrow temperature range provides a unique opportunity to examine the effects and influence of thermal conditioning on phase transformation mechanisms and in particular on the martensitic characteristics of a transformation.

This examination of the influence of specimen condition, thermal conditioning and matrix recovery mechanisms on the $\delta \rightarrow \gamma$ phase transformation in unalloyed plutonium show that a complex balance is achieved to drive the reaction more towards one mechanism than another. Unalloyed plutonium could therefore be used as a reference system to help understand the complex behaviour exhibited by dilute alloys of plutonium.

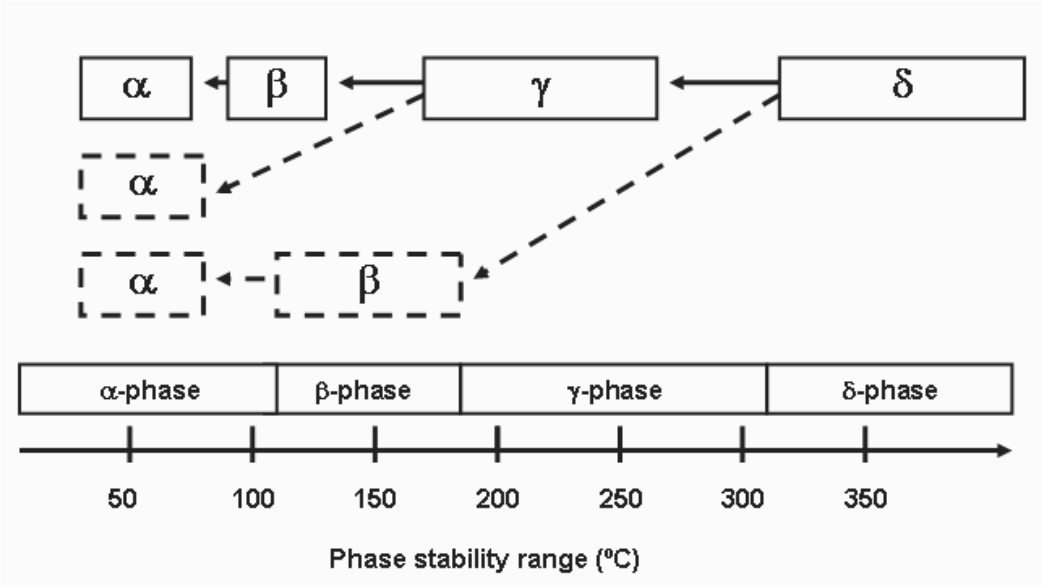

Figure 2. Diagram of sequential (bold lines) and mixed phase transformation (dashed lines) paths.

References

[1]. T.G. Zocco, D.S. Schwartz and J. Park, J. Nucl. Mater., **353,** (2006), 119.

[2]. R. Pascard, Plutonium 1960, E. Grison, W. B.H. Lord, R. D. Fowler (Eds),

Cleaver-Hume Press Ltd, 1960, 16.

[3]. B. Hocheid, A.Tanon and F. Miard, Acta Metallurgica, **13,** (1965) 144.

4-09

The unique solid-state NMR facility at JRC-ITU for the study of highly radioactive compounds

Laura Martel[1], Jean-Christophe Griveau[1], Chris Selfslag[1], Jacobus Boshoven[1], Olivier Pauvert[1], Ian Farnan[2], Joseph Somers[1]

[1]JRC-ITU, Karlsruhe, Germany, [2]University of Cambridge, Cambridge, UK

Magic angle spinning nuclear magnetic resonance (MAS-NMR) is a very powerful analytical technique for the study of the local structure in materials. Due to the difficulty of spinning radioactive powders at high speeds, only one experiment has been reported up to now on such compounds using MAS-NMR [1]. Recently, the Joint Researcher Centre-Institute for Transuranium Elements (JRC-ITU) in Karlsruhe (Germany) acquired a 9.4 T commercial NMR spectrometer dedicated for the study of actinides-bearing compounds. [Somers et al. *Rev. Sci. Instr.*, *accepted*] It has been integrated with a radioactive glovebox and a 1.3 mm commercial probe (rotation rates up to 70 kHz). Since June 2012 this unique apparatus permits the study of highly radioactive materials at very high spinning speed. The results of the first ^{17}O MAS-NMR investigation on highly radioactive actinide dioxides (Th, U, Np, Pu and Am) will be presented (Figure 1).

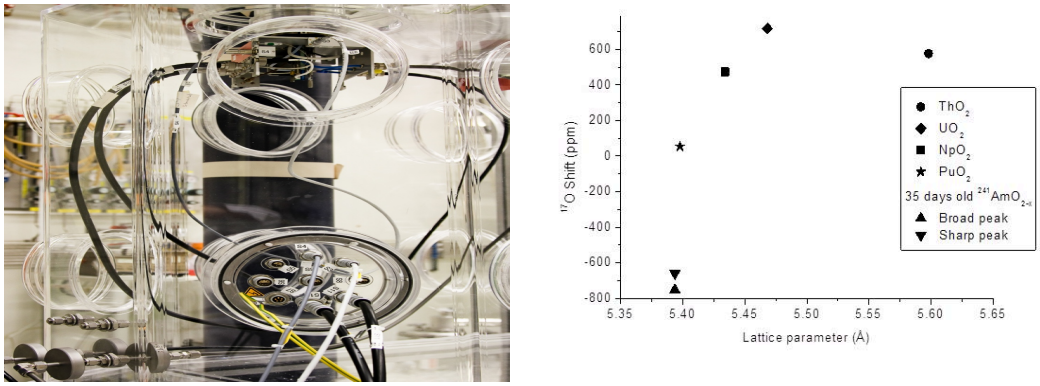

Figure 1: Left: The NMR facility for the study of highly radioactive compounds. Right: Evolution of the ^{17}O NMR signal as a function of the lattice parameter.

References

[1] I. Farnan et al. *Nature* **445** 190 (2007)

4-10

Raman spectroscopic characteristics of stoichiometric and non-stoichiometric uranium oxides

Gan Li, Wenhua Luo, Junbo Lv

China Academy of Engineering Physics, Mianyang, China

Introduction. Raman spectroscopy has been widely used to characterize uranium oxides providing information on the chemical structure or composition of a complex U-O system. Many works have been reported on the Raman spectra of stoichiometric uranium oxides such as UO_2 and U_3O_8, whereas the data of non-stoichiometric oxides are still rather scarce. In this work, Raman spectra of uranium oxides (UO_x) with various O/U ratios (x=2-2.67) were measured and their change with the oxygen content of the bulk was discussed with the aim of better identifying oxidation level of uranium dioxide samples in contact with air using this technique.

Experimental Procedures. A NETZSCH STA449C thermogravimetric analyzer was used to prepare the stoichiometric and non-stoichiometric uranium oxides. As-received α-U_3O_8 powder sample was cleaned by annealing under O_2 to 773 K for 4 h. UO_2 sample was prepared by reducing α-U_3O_8 with H_2 at 923 K for 12 h. β-U_3O_7 sample was prepared by the oxidation of UO_2 with O_2 at 473 K for 16 h. Samples of UO_x with various O/U ratios (x) ranging from 2 to 2.67 were prepared by heating UO_2 under O_2 at heating rate of 5 K/min up to 573 K for different times, followed by weighing to determine the gains by oxygen. The determined O/U ratios are 2.06, 2.11, 2.19, 2.32, 2.39, 2.51, 2.60 and 2.67.

X-ray diffraction (XRD) patterns of the prepared uranium oxide samples were measured by a Philips X'Pert PRO diffractometer using Cu-K_α radiation in order to get information on their structural changes depending on x. Raman spectra of these samples were collected with a Renishaw inVia Raman microscope. A 532 nm Nd-YAG laser was used as the excitation source, operated at low power to avoid oxidation of the sample surface during the measurements.

Results

a) Phase Characterization. As UO_2 powder is heated, the diffraction pattern of U_4O_9 phase begins to appear from x=2.06 to x=2.19, then another diffraction pattern of U_3O_7 phase appears from x=2.19 to x=2.33. Finally, at an O/U ratio greater than 2.33, the third diffraction pattern of U_3O_8 phase appears. The result indicates that the phase transition sequence is $UO_2 \rightarrow U_4O_9 \rightarrow U_3O_7 \rightarrow U_3O_8$, which supports the oxidation of UO_2 at low temperature is a three-step reaction [1] rather than a two-step reaction [2]: $UO_2 \rightarrow U_4O_9/U_3O_7 \rightarrow U_3O_8$.

b) Spectral description. Both measured Raman features of UO_2 at 445, 575 and 1150 cm^{-1} and those of α-U_3O_8 at 238, 336, 405, 480, 640, 750 and 800 cm^{-1} were found to be in good agreement with those reported in the literature [3,4]. For β-U_3O_7, a strong and broad peak at 465 cm^{-1} was observed, which is consistent with the results of Caculitan et al [5], rather than a small and very broad feature which could occur at approximately 410, 445 and 500 cm^{-1} reported by Allen et al [6].

For the non-stoichiometry UO_x ($x<2.33$), the spectra between 300 and 800 cm^{-1} were deconvoluted to four peaks at 445, 465, 575 and 630 cm^{-1}. The characteristic peak at 465 cm^{-1} of U_4O_9 and β-U_3O_7 appears from the O/U ratios higher than 2.06 and its intensity grows with increasing x, accompanied by a decrease in intensity of the 445 cm^{-1} peak. Meanwhile, the intensities of 575, 630 and 1150 cm^{-1} peaks decrease markedly together with the increasing intensity ratio of 630 to 575 cm^{-1} peaks, and almost absent at x=2.19. For $x>2.33$, the peak intensity of the U_3O_8 grows steadily to x=2.67 while that of the U_3O_7 decreases with increasing x. Based on these changes in spectral profile and corresponding XRD analysis results, the relationships between the various peaks and their relationships to lattice structure or oxygen content were discussed.

In order to determine the relationship between Raman signal strength and O/U ratio, the peak areas at 1150 cm^{-1} and 238 cm^{-1} were plotted against O/U ratio. A linear relationship in the range from x=2 to 2.11 and from x=2.39 to 2.67 between them was found, and this relationship, to some degree, can be used to evaluate the O/U ratios of air-oxidized uranium dioxide samples.

4-11

SIMS analysis of hydrogen and carbon co-precipitation in uranium and SEM/FIB analysis of its effect on surface reactions.

Patrick Allen, Ian Hutcheon, Jenny Matzel, Wigbert Siekhaus, Nick Teslich, Peter Weber

Lawrence Livermore National Laboratory, Livermore, CA, USA

Uranium metal typically contains carbon and hydrogen at concentrations above its solubility limit at room temperature [1]. While the distribution of carbides can easily be seen by optical or electron microscopy, the distribution of uranium hydride is not detectable by those techniques, not least because UH_3 is pyrophoric when exposed to air or moisture. To reveal the hydrogen distribution, we used the 30 keV caesium ion beam of a CSD Cameca NanoSIMS 50 to sputter 9 square areas of between 1600 and 12600 μm^2 to depths between 1 and 9 µm into a mechanically polished uranium surface and analysed hydrogen, carbon and oxygen secondary ions in its mass spectrometer, creating elemental distribution images with spatial resolution of 256x256 pixels. Elemental imaging was done after a depth greater than 500nm was reached to eliminate surface reaction products. Secondary electron images were also collected. Acquiring elemental images at a sequence of sputtering depth would enable three-dimensional characterization of the sample and its inclusions in future experiments. Secondary ion image processing was done using custom software (LIMAGE, L. Nittler, Carnegie Institution of Washington) that enables image alignment, ion ratio calculation and extraction of quantitative data. Quantification of absolute concentrations of H was estimated using published atom-per-atom relative sensitivity factors (RSFs) for H^- and C^- in silicon ($5x10^{23}$ and $5x10^{22}$ cm^{-3}; Wilson et al., 1989) with additional adjustments reflecting instrumental factors.

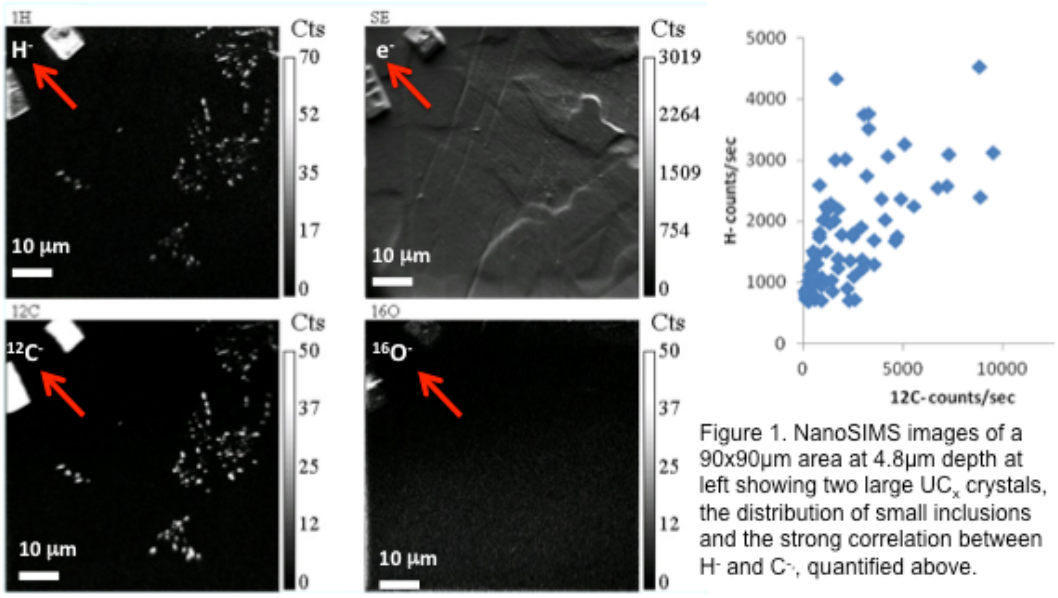

Figure 1. NanoSIMS images of a 90x90µm area at 4.8µm depth at left showing two large UC_x crystals, the distribution of small inclusions and the strong correlation between H^- and C^-, quantified above.

Secondary electron and ion images of H-, C-, O- in figure document the strong correlation between C- and H-, and the large number of small C-H- containing inclusions with an average number density of 2700/mm^2, consistent with the density UH_3 precipitates of ≤1µm expected at the sample's hydrogen content and the number of small surface reaction product "bumps" seen on polished surfaces [2].

The high H (highly reactive UH_3) concentration on the perimeter of carbide inclusions seen in figure 2 is a cause for prefe-rential corrosion seen there on an electro-polished surface exposed to H_2O in situ in an environmental SEM [3] and by us as a function of hydrogen content between "0" ppm and 1.8 ppm on surfaces of uranium [4] mechanically polished with diamond in a water slurry.

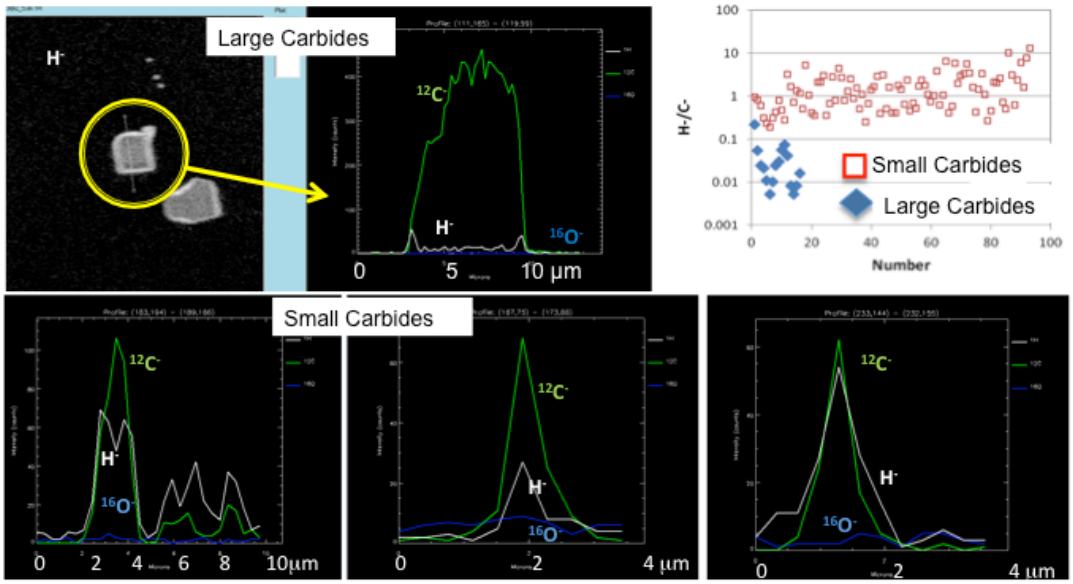

Figure 2. H^-, C^- and O^- line profiles across large (2 top left) and small (bottom) inclusions, and the H^-/C^- ratio of the interior of all inclusions analysed (top right). The average ratio $1H^-/12C^-$ of 16 large inclusions is .038 with a standard deviation (SD) of .053 and that of 93 small inclusions is 1.87 with an SD of 2.09. Large inclusions down to a size of 2µm (left image bottom) show higher H concentration at the perimeter.

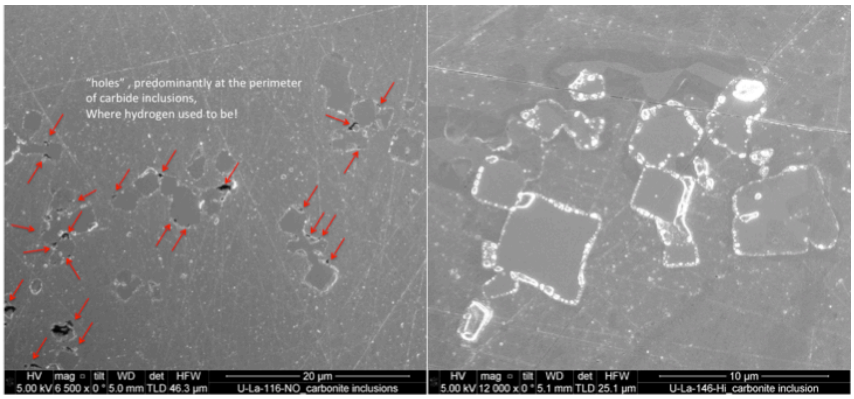

Figure 3. Reaction product formation on water polished uranium carbide perimeters as a function of hydrogen content. Left: "0" ppm (dehydrated @550 C in vacuum), right: 1.8 ppm.

Dehydrided uranium shows a multitude of holes on carbide perimeters (red arrows in left image, figure 3) while the right image with 1.8ppm H content at twice the magnification has no perimeter holes but substantial reaction product formation.

Summary: SIMS reveals that in uranium hydrogen always precipitates with carbon, and has a H/C ratio of .038±.053 within large (≥ 2µm) and of 1.87±2.09 within small carbon containing inclusions (~ 2700/mm^2, consistent with small surface blister formation). The large H/C ratio on large inclusion's perimeter is the likely cause of preferential reaction product formation on carbide edges.

References

[1] G. L. Powell, and J. B. Condon, Analytical Chemistry **45** (1973). [2] R. M. C. Harker, A.H., MRS 2012 Spring Meeting San Francisco (2012). [3] T. B. Scott *et al.*, Journal of Hazardous Materials **195** (2011).[4] Courtesy of E. Garlea, Y12 National Security Complex

4-21

Relative thermodynamic stability of radiation defect clusters and He bubbles in δ-Pu-Ga alloys and their interaction with preexisting extended defects

Alexey Karavaev, Vladimir Dremov, Gennady Ionov

Russian Federal Nuclear Center - Institute of Technical Physics, Snezhinsk, Chelyabinsk Region, Russia

During the past decades one of the most extensively studied material science problems is the degradation of material mechanical properties under effects of irradiation and radioactive materials physical properties changes due to self-irradiation known as radiation aging. The self-irradiation of Pu and its alloys results in the continuous production of radiogenic helium and Primary Radiation Defects (PRD) of crystal structure, their accumulation, diffusive migration, clustering etc. The microstructure (morphology) of the point defect clusters (i.e. equilibrium size of defect clusters, their shapes, the fraction of free and clustered defects) is the subject of great importance, since it has direct impact on the elastic-plastic properties of the material.

The present study is devoted to the investigations into the behaviour of PRD (vacancies) and He atoms produced as a result of α-decay of ^{239}Pu nuclei in the bulk of fcc δ - Pu-Ga alloys, their clasterization, forming of He bubbles and the interaction of the defect clusters with preexisting extended defects. While the dynamics of interstitial atoms in the fcc lattice of Pu-Ga alloys due to their high mobility is accessible for direct classical molecular dynamics (CMD) simulations even at low temperatures, characteristic times of migration of vacancies and He atoms are in the range from seconds to hours, which makes it impossible to model their diffusive dynamics in the lattice even using accelerated CMD. Instead in the present study we propose to investigate relative thermodynamic stability of metastable configurations of an ideal crystal with artificially introduced systems of defects of various morphologies using the Helmholtz free energy. For the investigations of relative thermodynamic stability of finite temperature systems it is insufficient to calculated and compare only the internal energies of different states. At the finite temperatures the entropy part of the Helmholtz free energy plays an important role. If one can calculate “absolute” values of free energy for different metastable states of a system for the same external conditions, it is possible to draw unambiguous conclusions about relative thermodynamic stability of those states for given conditions. Unfortunately the absolute values of free energy cannot be calculated in simple CMD simulations as an average of some quantity or expressed as a function of some averages. However, it is possible to evaluate the free energy values in the frames of CMD approach using so called Thermodynamic Integration Method (TIM) [1-3].

Previous CMD simulations [4] have shown that produced in the α-decay ^{235}U nuclei with the kinetic energy of 86 keV cause a displacement cascades and following amorphization (melting) of compact regions in the vicinities of the α-decays with sizes order of 8-10 nm containing 16,000-20,000 atoms. However, the crystalline structure of the damaged region almost completely recovers in nanosecond time scale. The residual defects after the re-crystallization are point defects – about 200 Frankel pairs. Interstitial atoms due to their high mobility [5] leave the cascade region rapidly. As a result after the fast stage (couple of nanoseconds) there is a localized in the vicinity of the α-decay depletion region with the size order of 10 nm containing about 200 vacancies. The other particles produced in the α-decays are α-particles with the energy about 5 MeV. They travel in the lattice of the fcc Pu-Ga alloys much further away from the vicinity of the α-decays and produce about 200 additional Frenkel pairs each. Losing kinetic energy the α-particles grab electrons and become He atoms, which accumulate in the bulk of the material with the age and tend to assemble in the form of bubbles [6] of characteristic sizes and He atom concentration (number of He atoms per vacancy site).

Within the scope of theoretical study into the radiation response of the δ-Pu-Ga alloys, we investigated the behaviour of compact vacancy clusters in the bulk of fcc Pu-Ga alloys, their interaction with the preexisting extended defects, namely, the edge dislocations, and performed CMD research into mechanisms which limit the growth of gas Helium bubbles. Specifically, we performed the CMD simulations to determine the solubility of He in the fcc δ-Pu-Ga lattice, the nature of the repulsive/attractive interaction of He bubbles with isolated He atoms in the lattice as dependent on the number of He atoms per vacancy site in the bubbles and their sizes.

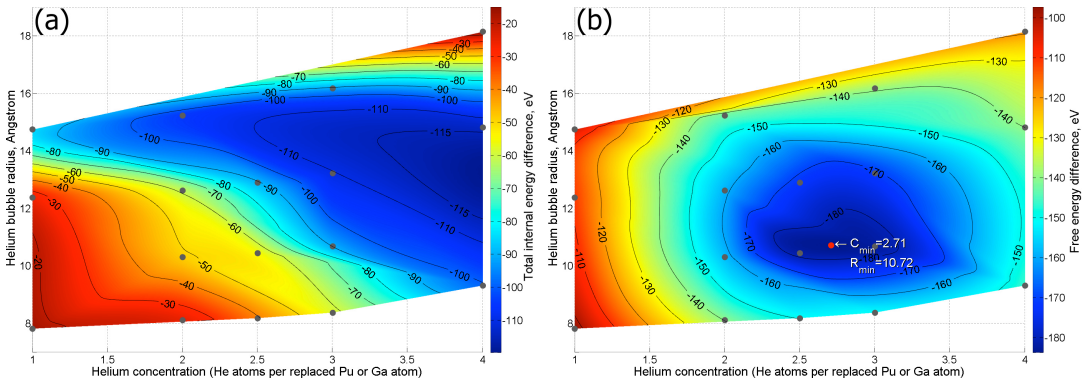

Figure 1. (a) – internal and (b) free energies differences of systems with all He atoms placed in bubbles and systems with bubbles and distributed He atoms as functions of He concentration and size of initial bubbles.

Helmholtz free energies of various metastable states were calculated using the TIM. Based on the calculations we drew conclusions about the relative thermodynamic stability of different configurations of defect clusters at the ambient conditions (conditions of storage):

- The configurations with the vacancies which are randomly uniformly distributed in the bulk of the fcc lattice appear far less favorable than the states with the compact vacancy clusters both in respect to internal energy and Helmholtz free energy. That is, vacancies in the fcc Pu-Ga lattice effectively attract one another.
- Two-dimensional vacancy clusters are less thermodynamically favorable then the three-dimensional compact ones.
- Of all the systems with pores of 200 vacancies considered, the configuration with “spherical” pore constructed by removing 200 atoms within a sphere of appropriated radius was found to have the lowest internal energy, while the lowest free energy has configuration with a spherical pore with the randomly distorted surface.
- Our calculations for Pu-Ga alloy demonstrated that configurations with spherically shaped pores with randomly distorted surfaces are thermodynamically more favorable than the configurations with stacking fault tetrahedra of corresponding sizes for all the “magic” vacancy cluster sizes from 15 up to 276 vacancies, unlike in other fcc metals like for example in Cu [7].
- Simulations of the interactions of isolated vacancies and vacancy clusters with edge dislocations indicated that both the isolated vacancies and vacancy clusters are effectively attracted by the edge dislocations that means that the latter are effective drains for the PRD.
- CMD calculations of the solubility of He in the lattice of fcc δ-Pu-Ga alloys were carried out and it was found that for all the parameters of He bubbles used (radius of He bubbles and He atom concentrations in them) the He bubbles does not dissolve in the lattice of fcc Pu-Ga alloys.
- A series of CMD simulations were carried out in order to investigate possible causes stopping He bubbles in the fcc lattice of Pu-Ga alloys from unlimited growing. It was demonstrated that surface of Helmholtz free energy of systems with He bubbles has minimum for the bubbles of radius R~1.1 nm and 2.7 He atoms per vacant site (See FIG. 1) which is very close to experimentally observed average equilibrium parameters of He bubbles in naturally aged material [6].
-

References

1. D. Frenkel and A.J.C. Laad. J. Chem. Phys., 81:3188 (1984).
2. D. Frenkel. “Free energy computation and first-order phase transitions,” in Molecular Dynamics Simulations of Statistical Mechanical Systems, XCVII (1986), Soc. Italiana di Fisica, Bologna, Italy.

3. D. Frenkel and B. Smit. “Understanding Molecular Simulations. From Algorithms to Applications”, Academic Press, San Diego (2002).
4. V.V. Dremov, F.A. Sapozhnikov, S.I. Samarin, D.G. Modestov, and N.E. Chizkova, J. Alloys Compd., v. 444&445, p. 197 (2007).
5. V.V. Dremov, A.V. Karavaev, S.I. Samarin, F.A. Sapozhnikov, M.A. Zocher, and D.L. Preston, J. Nucl. Mat, v. 385, pp. 79-82 (2009).
6. A.J. Schwartz, M.A. Wall, T.G. Zocco, and W.G. Walfer, Phyl. Mag., v. 85, pp. 479-488 (2005).
7. B.P. Uberuaga, R.G. Hoagland, A.F. Voter, and S.M. Valone, Phys. Rev. Lett., v. 99, p. 135501 (2007).

POSTERS

1-16

Influence of fluoride and oxide ions on the electrochemical behaviour of uranium in LiCl-KCl eutectic melt

Sergey Kuznetsov[1], Marcelle Gaune-Escard[2]

[1]Institute of Chemistry, Kola Science Centre RAS, Apatity, Russia, [2]Ecole Polytechnique U.M.R.-C.N.R.S. 6595, Marseille, France

Influence of fluoride and oxides ions on the electrochemical behaviour of UCl_4 and UCl_3 in LiCl-KCl eutectic melt was studied at 723-823 K by different electrochemical methods. Electroreduction of U(IV) in LiCl-KCl melt occurs via two successive steps involving transfer of one and three electrons:

$$U(IV) + e^- \rightarrow U(III) \quad (1)$$

$$U(III) + 3e^- \rightarrow U \quad (2)$$

The standard rate constants of charge transfer for the redox reaction were calculated from cyclic voltammetry data and for the discharge process using impedance spectroscopy method. The values of constants testify that redox process (1) proceeds quasi-reversibly, but the process of uranium electrodeposition (2) controlled by the rate of charge transfer.

The formal standard potentials of $E^*_{U(IV)/U(III)}$, $E^*_{U(IV)/U}$ and $E^*_{U(III)/U}$ were determined by different electrochemical methods and some thermodynamic properties of UCl_4 and UCl_3 dissolved in LiCl-KCl eutectic melt were calculated.

Additions of fluoride ions to the LiCl-KCl melt containing UCl_4 and UCl_3 did not lead to the change of electroreduction mechanism, but decreasing of standard rate constants of charge transfer and shifting to the negative region of formal standard potentials were observed.

Influence of oxide ions on electrochemical behaviour of LiCl-KCl-UCl_4 melt was studied too. After addition of Li_2O to the melt the heights of waves corresponding to electroreduction of uranium chloride complexes decreased and new two waves at more positive potentials appeared. Finally, at the O^{2-}/U(IV) certain ratio only these two waves remained on the voltammetric curve. The following chemical reaction proceeds in the melt:

$$3UCl_6^{2-} + 4O^{2-} \rightarrow 2UO_2^{2+} + U + 18Cl^- \quad (3)$$

and two waves observed on the voltammetric curve correspond to electroreduction of the uranyl-chloride complexes:

$$UO_2^{2+} + e^- \rightarrow UO_2^+ \quad (4)$$

$$UO_2^+ + e^- \rightarrow UO_2 \quad (5)$$

Using diagnostic criteria of cyclic voltammetry it was shown that electrode process (4) is complicated by following reaction of disproportionation.

1-17

Unalloyed uranium deformation curves under static and dynamic loading

Victor Pushkov, Margarita Andreeva, Alex Yurlov, Alex Kalmanov, Igor Shiberin

Russian Federal Nuclear Center – VNIIEF, Sarov, Russia

In [1] alongside with other investigations the authors studied the σ-ε curves of preliminary loaded uranium and U-6%Nb alloy. The pressure of preliminary loading was 5-45 GPa. However, to solve fundamental and applied problems it is necessary to know mechanical characteristics (in particular strain diagrams) for uranium, preliminary loaded by higher pressures up to pressures of phase transformations. The current work presents the survey of static and dynamic deformation curves of unalloyed uranium in its initial state and of that subjected to preliminary shock loading by the pressures 59-92 GPa.

1. Material and method of experiments.

For investigations wrought depleted uranium of technical purity with carbon content of ~0.05 weight% was used. Other major impurities were Fe, Si, Ni. Preliminary loading was performed by a shock-wave method at the impact with a plane impactor (V~2.0-2.8 km/s) against uranium disks (Ø60x10 mm) forming pressures σ_{xx} of 59, 75, 92 GPa in a loading wave. Samples for future tests were cut from retained disks.

Tests under static loading were performed using a standard tensile-testing machine 1958U-10-1 with the traverse speed 0.5 mm/min which corresponds to a strain rate $\dot{\varepsilon}$~10^{-3} s^{-1}. Tests under dynamic loading were performed using the SHPB method [1, 2] with the strain rate 950-1400 s^{-1}. Experimental set-up is given in Fig. 1. Rods of the EP strong steel of 16 mm diameter and 1500 mm length were used. The sizes of samples were Ø8x8 mm.

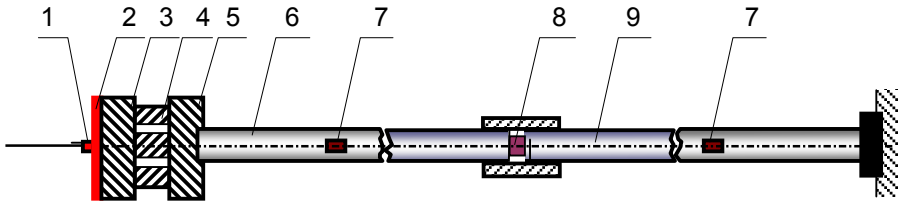

1,2 is HE; 3 is impactor; 4 is aluminum damper; 5 is connecter; 6 is loading rod; 7 are strain gauges; 8 is sample; 9 is support bar

Fig. 1 – Experimental setup for study of uranium compression curves

2. Investigation data.

Fig. 2 provides averaged σ–ε deformation curves, obtained under static compression of preliminary loaded uranium (P=59-92 GPa) as compared to the curve in its original state. Averaging was performed based on the results from 4-5 experiments.

As in experiments performed earlier [2], one can observe a significant strain hardening of unalloyed uranium. It follows from Fig. 2 that the average value of the yield strength $\sigma_{0,2ave}$= 462 MPa. Besides, as it is seen from Fig. 2, the curves for uranium loaded by the pressures 59 and 75 GPa practically do not differ from each other, and the $\sigma_{0,2ave}$ values are 844 and 835 GPa, respectively. For the pressure 92 GPa the value $\sigma_{0,2ave}$ is significantly lower and makes 500 MPa. This is only by ~8% higher than for uranium in its original state.

Fig. 3a presents σ-ε dynamic compression curves obtained for uranium loaded by the pressures 59 and 75 GPa. Fig. 3b presents σ-ε dynamic compression curves obtained for uranium loaded by the pressure 92 GPa. For the pressure 59 GPa the values $\sigma_{0,2}$ are 850-970 MPa with the strain rates $\dot{\varepsilon}$=950-1200 s^{-1}. This is close to the data for the pressure 75 GPa: the values $\sigma_{0,2}$ = 850-950 MPa with the strain rates $\dot{\varepsilon}$=970-1350 s^{-1} (see Fig. 3a).

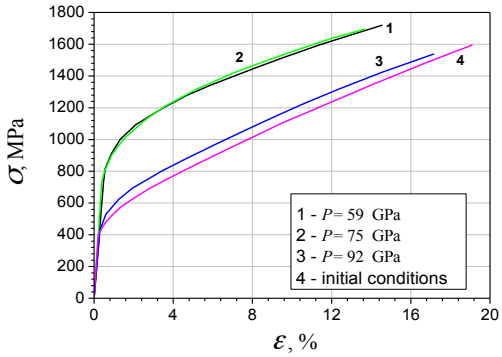

Fig. 2-Deformation curves of original uranium and preliminary loaded uranium under static compression, $\dot{\varepsilon}$~10^{-3} s^{-1}

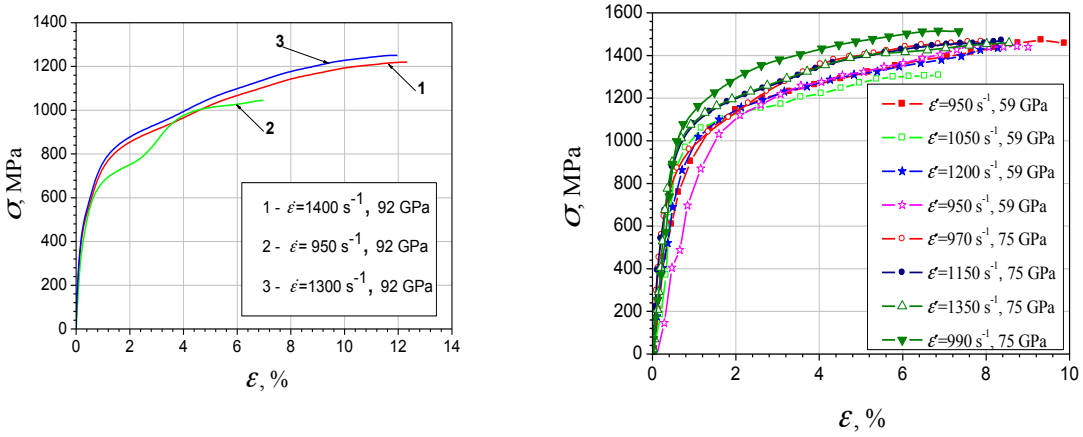

Fig. 3 –The strain curves of preliminary loaded uranium (P=59-75 GPa - (left), P=92 GPa - (right) under dynamic compression; $\dot{\varepsilon}$=950-1400 s^{-1}

Except for this, there is no significant difference in curves behavior after loading by the pressures 59 and 75 GPa (Fig. 3a). For the same pressures the given values $\sigma_{0,2}$ are higher by ~9% than those under static compression (Fig. 2 and Fig.3a). From curves of Fig.3b it follows that after preliminary uranium loading by shock-waves of 92 GPa of pressure, the yield strength values (with the strain rate $\dot{\varepsilon}$ =950-1400 c^{-1}) are only $\sigma_{0.2}$=540-600 MPa ($\sigma_{0,2ave}$=570 MPa), which is significantly lower, than after loading by the pressures 59 and 75 GPa. As opposed to uranium static compression loaded by the pressure 92 GPa, the set value $\sigma_{0,2ave}$ is by ~14% higher (Fig. 2 and Fig. 3b).

In conclusion, based on the test results the σ–ε curves were constructed, and comparative analysis of mechanical data was performed. Further investigations are necessary to reveal behavior features of preliminary loaded uranium.

References

1. Recent Dynamic Strength Testing of Uranium. Blumenthal W.R., Cerreta E.K., Dennis-Koller D., G.T. Gray III and Hixson R.S. 7th International Workshop on the Fundamental Properties of Plutonium. Russian Federal Nuclear Center –VNIIEF. Sarov. Russia. June 25th-29th. 2007.

2. V.A.Pushkov, A.P.Bol'shakov, G.A.Kvaskov, S.A.Novikov, V.A.Sinitsyn. Mechanical properties of uranium at quasi-static and shock-wave loading. Preprint, #54-97, Sarov, RFNC-VNIIEF, 1997.

1-18

The high temperature heat capacity of thorium-plutonium mixed oxides

Octavian S. Valu[1,2], Ondrej Benes[1], Rudy J.M. Konings[1,2], Joseph Somers[1]

[1]European Commission, Joint Research Centre, Institute for Transuranium Elements, Karlsruhe, Germany, [2]Delft University of Technology, Faculty of Applied Sciences, Delft, The Netherlands

Studies on oxides and mixed oxides of actinide elements such as thorium, uranium and plutonium are of great interest in nuclear industry since some of the oxides are used or are planned to be used as nuclear fuels in various types of reactors [1]. The thermodynamic properties such as enthalpy and heat capacity of these materials are needed for reactor design and safety calculations.

In the 1960s the thorium mixed oxide was introduced as potential fuel for fast and thermal reactors. It is known that thorium is about three times more abundant than uranium in the Earth's crust [2], thorium dioxide has the highest melting point of all oxides [3] and his thermal conductivity is higher than that of uranium dioxide [4]. The use of thorium-based fuel will produce less transuranium elements per unit of fission energy by using it in light water reactors (LWRs) as a fertile material to breed uranium.

Plutonium from reprocessing of LWR fuel can be used as an external start-up material into the thorium-based fuel since natural thorium, ^{232}Th, is not a fissile nuclide. (Th, Pu)O_2 can be used as a fuel in pressurized water reactors (PWRs) without making significant changes in the reactor system [5]. This type of fuel can be also effectively used to reduce the plutonium stockpiles by using a high plutonium consumption rate.

To understand the behaviour of the nuclear fuel during the irradiation, it is mandatory to have clear information about the thermodynamic properties of the "fresh" fuel material. The number of studies of the (Th,Pu)O_2 system is limited and therefore the heat capacity measurement of the system subject of this work.

Using a Setaram MDHTC, the enthalpy increments of (Th_{1-y},Pu_y)O_2 solid solutions, with y=0.03, 0.08, 0.30, 0.54 and 0.85 were measured in the temperature range 400 – 1800 K and the results of the heat capacity were derived.

We also measured pure ThO_2 and PuO_2 samples and compared them with literature data obtaining a good agreement. From that we conclude that our set-up allows us to measure the enthalpy increments precisely enough to predict the behaviour of the (Th, Pu)O_2 solid solution and to understand if the heat capacity of the solution follows ideal trend or if some excess parameters must be considered.

The C_P fit of the intermediate compositions was made by simultaneous linear regression taking into account the measured enthalpy data and the low temperature C_P values which at the first stage were estimated by the Neumann–Kopp rule. The preliminary results of the thus obtained C_P curves are close to ideal behaviour.

References

[1] C. Ganguly (1985) IAEA-TECDOC, **352**, 107-127

[2] D. R. Lide (2005) Handbook of Chemistry and Physics (86th version), CRC Press Inc.

[3] C. Ronchi, J. P. Hiernaut (1996) J. Alloy. Compd., **240**, 179-185

[4] J. Belle, R. M. Berman (1984) Technical Report DOE/NE-0060, Naval Reactors Office, United States Department of Energy

[5] Thorium-based nuclear fuel: current status and perspectives (1987) TECDOC-412, IAEA

1-20

Single and mixed f-elements sintered oxide pellets synthesis with tailored microstructures.

Elodie Remy[1], Sébastien Picart[1], Thibaud Delahaye[1], Isabelle Bisel[1], Olivier Dugne[1], Nicolas Clavier[2], Adila Azzou[3], Philippe Blanchart[4], André Ayral[5]

[1]CEA Marcoule, Bagnols sur Cèze/Gard, France, [2]ICSM UMR 5257 CEA-CNRS-UM2-ENSCM, Bagnols sur Cèze/Gard, France, [3]CRISMAT ENSICAEN, Caen/Calvados, France, [4]GEMH ENSCI, Limoges/Haute Vienne, France, [5]IEM UM2, Montpellier/Hérault, France

Transmutation of the long-lived radionuclides, such as americium, in sodium fast reactor is studied to reduce radiotoxicity and heat load of nuclear waste. The heterogeneous transmutation consists in the irradiation in fast neutron reactors of mixed oxide pellets containing uranium and 15 % of americium forming a homogeneous phase. Traditionally, those pellets are obtained through a metallurgic route involving several steps of blending, grinding uranium and americium oxide powders in order to synthesize a solid solution. Two types of pellets are under study, a dense microstructure and an open pore microstructure containing more than 8 % of open porosity. The latter is more appropriate to release helium gas produced during irradiation and to accommodate the swelling of the matrix due to alpha irradiation.

Our research project deals with the fabrication of $U_{1-y}Am_yO_{2\pm x}$ oxide pellets for the heterogeneous transmutation of Am and more specifically with the development of a powder-free process called CRMP (Calcined Resin Microspheres Pelletization) [1]. This dustless process consists in the synthesis of oxide microsphere precursors by the Weak Acid Resin (WAR) route [2] (cf. figure 1) and in their compaction and sintering for making ceramic pellets. The use of oxide spherules instead of powder eases transfer operation and avoids above all the handling of fine powders and significantly reduces the dissemination of highly-contaminating and irradiating dusts in the facility.

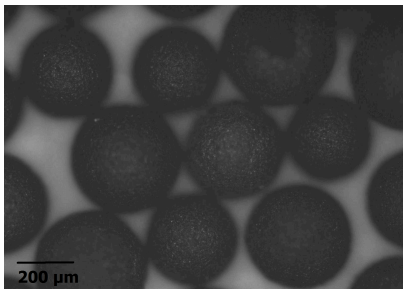

Figure 1 Mixed oxide $U_{0.90}Am_{0.10}O_{2\pm x}$ microspheres obtained by WAR process.

Currently, the compaction behaviour of oxide microspheres is examined through the optimization of Ce loaded resin mineralisation which impacts the oxide spherule mechanical behaviour and the green pellet microstructure.

Moreover, mixed oxide $UCeO_{2\pm x}$ and $UAmO_{2\pm x}$ microspheres have been synthesised and have been die-pressed into pellets and subsequently sintered. Dense pellets of 94 % TD of either $U_{1-x}Ce_xO_{2\pm x}$ ($10<x<30\%$) or $U_{0.90}Am_{0.10}O_{2\pm x}$ have been produced (cf. Figure 2). Final properties and microstructure of sintered pellets is discussed. Especially the formation of a solid solution associating uranium and cerium or americium is investigated by means of powder X-ray diffraction and dilatometric analysis.

This study also presents the use of CRMP process to synthesize pellets with tunable density [3]. In the case of UO_2 ceramics, dense or open-pore microstructures have been achieved (cf. figure 3) in agreement with the specifications of pellets which are designed for the heterogeneous transmutation of Am.

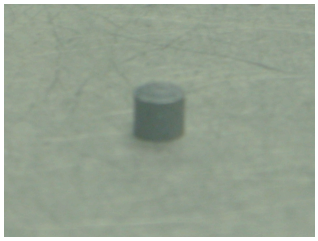

Figure 2 Dense pellet of $U_{0.90}Am_{0.10}O_2$ produced by the CRMP route.

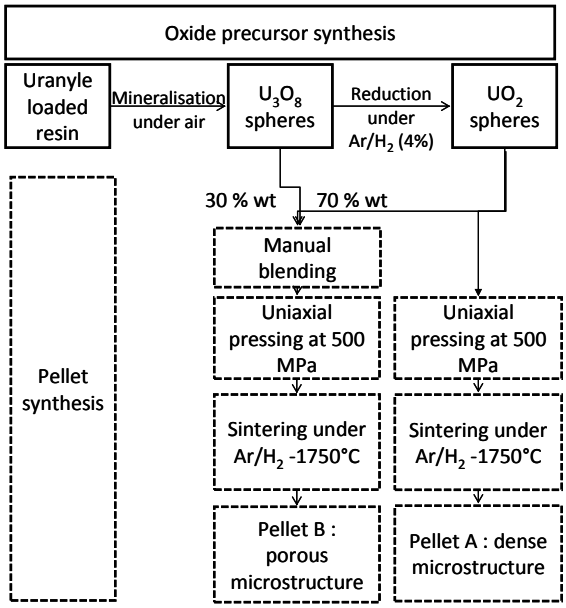

Figure 3 Synthesis of dense and porous pellets of UO_2 by using CRMP process.

References

[1] Remy E, Picart S and al. Calcined resin microsphere pelletization (CRMP): *A novel process for sintered metallic oxide pellets*. J. Eur. Ceram. Soc. 32 (2012) 3199-3209.

[2] Picart S, Ramiere I and al. *Experimental characterization and modelization of ion exchange kinetics for a carboxylic resin in infinite solution volume conditions application to monovalent–trivalent cations exchange*. J Phys Chem B.114 (2010)11027–38.

[3] Picart S, Remy E, Delahaye T. *Procédé de préparation d'un combustible nucléaire poreux*. French CEA patent FR 2979469 (2013).

1-21

MD simulation of the effect of self-irradiation upon static strength characteristics of materials

Vladimir Dremov, Gennady Ionov, Alexey Karavaev, Philipp Sapozhnikov

Russian Federal Nuclear Center - Institute of Technical Physics, Snezhinsk, Chelyabinsk region, Russia

Static strength characteristics are of great importance to structural and mechanical analyses. For structural materials, the characteristics such as elastic limit, strength limit, or plasticity (ultimate strain) are, unlike elastic moduli, very sensitive to the presence of impurities and defects in material under study. The direct Molecular Dynamics (MD) calculation of static characteristics is extremely difficult because the MD time scales do not exceed tens nanoseconds. This means that the direct modeling of compression or tension is done at rather high strain rates at which elastic limit and other mechanical characteristics are controlled by other microscopic processes.

Molecular dynamics simulations readily give dynamic strength characteristics at strain rates $>10^8$ 1/s. So, Dremov et al [V.V. Dremov, A.V. Karavaev, F.A. Sapozhnikov, M.A. Vorobyova, D.L. Preston, M.A. Zocher, J. Nucl. Mater., 414 (2011) 471–478] reported estimates for strength limit variations in model δ-PuGa alloys with different radiation defects under tension at strain rates 10^8-10^{11} 1/s. When strain rates are lower, the rate of relaxation processes dramatically decreases and the MD time scales (~ a few nanoseconds = 10^7 MD steps) are too short to the transition from elastic to plastic flow.

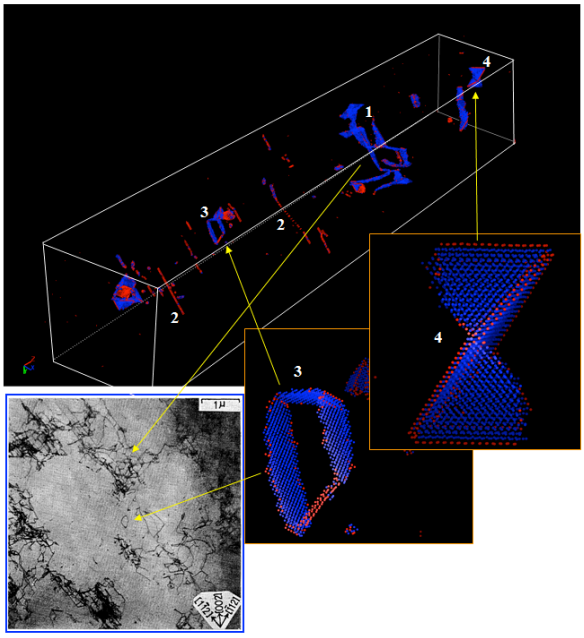

Fig.1 Equilibrium residual defects in a copper sample plastically deformed ε=Δl/l=4%. Figures show: edge dislocations (1); screw dislocations (2); dislocation loops (3); and stacking fault tetrahedra (4). Lower left: microphotograph of a copper sample plastically deformed ε=5% [Yoso Kawasaki, Journal of the Physical Society of Japan, 36 (1974), 142-148]

Here we propose a technique which allows the static yield stress to be obtained in MD simulations from the estimation of shear stress relaxation rate, which occur in the elastic-to-plastic transition, as a function of uniaxial deformation (applied stress). The technique is tested on copper and then applied to fcc δ-PuGa alloys whose strength characteristics tends to change most strongly with time due to self-irradiation. Calculated results are compared with experimental data for plutonium alloyed with different amounts of gallium and stored during different times.

The calculations are done in several steps. We first form a sample with arbitrary defects (see Fig. 1) and then determine the rate of shear stress relaxation that takes place due to dislocation structure transformation for different levels of load (see Fig. 2). Next, the extrapolation to zero relaxation rate gives the value of critical deformation which corresponds to static yield stress (see Fig. 3).

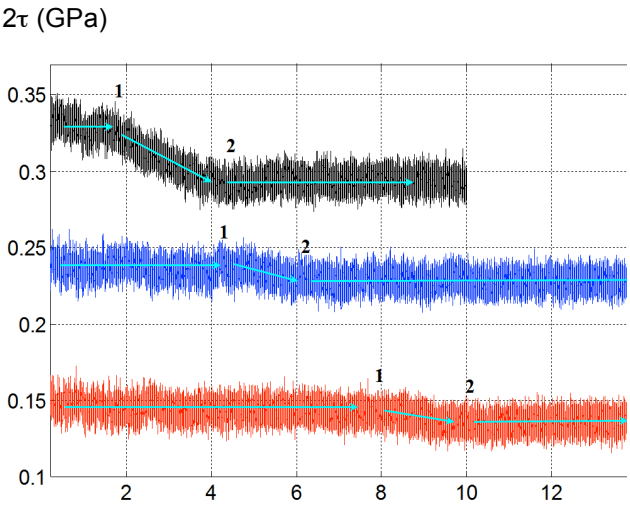

Fig. 2 PuGa alloy (3at.%Ga) Shear stress vs time during the relaxation at ε = 0.01 (black), 0.0075 (blue), and 0.005 (red)

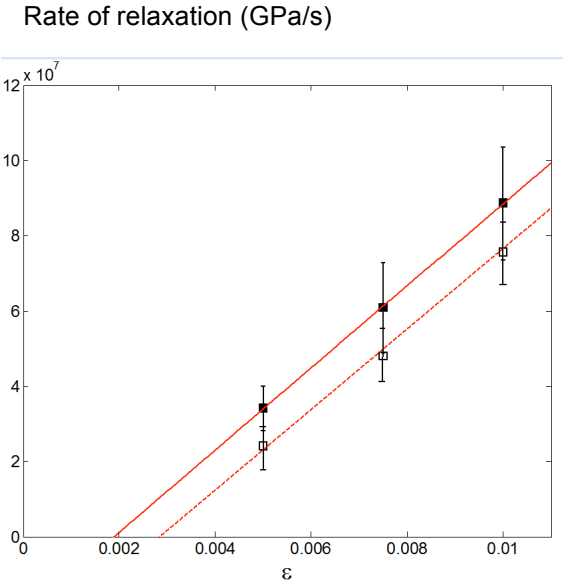

Fig. 3 PuGa alloy (3at.%Ga). Shear stress relaxation rate vs strain: MD calculations (black boxes) and their approximation (red line). Full black boxes and the solid red line show results for pure plutonium, and void boxes and red dashes are for samples with 0.3% primary radiation defects (vacancies).

Proceeding from the assumption that dislocation velocity linearly depends on applied stress (strain is proportional to strain at small stresses), calculated data were approximated by a straight line which crossed the strain axis at ε=0.2%. This strain at Young's modulus in direction [100] E'=42 GPa and Poisson's ratio 0.25 corresponds to yield stress 60 MPa which can be taken as static elastic limit, i.e., the stress below which dislocations stop moving.

To see how primary radiation defects influence the static yield stress, we did calculations for samples which additionally contain primary radiation defects with total concentration 0.3%. Figure 3 presents data on relaxation rate in presence of primary radiation defects. Their extrapolation to zero strain rate gives critical deformation ~0.3%, which is half as much against the value for defect-free samples.

1-22

Influence of Adding Niobium to Uranium on the Initial Kinetics of Hydriding

Ruiwen Li, Xiaolin Wang

China Academy of Engineering Physics, Mianyang,Sichuan, China

The reaction kinetics of U-H_2 has been shown to vary widely from study to study due to its dependence on a variety of factors. These factors that are apparently difficult to replicate or control include the surface characteristics of the uranium metal and the presence of gaseous impurity. Previous references showed that adding niobium to uranium can improve the anti-oxidation of U, and strengthen the mechanics properties of the metal. Yet, there is little information concerning the hydrogen corrosion of U-Nb alloy. In this work, the influence of alloying of uranium on the initial kinetics of hydriding was focused.

To study the behavior of hydrogen corrosion on U-2.5wt%Nb alloy, a gas-solid reaction system with an in-situ microscope was designed. The nucleation and growth of hydride of U-2.5wt%Nb alloy were continuously observed and recorded by a computer. The characteristic of hydride on Uranium and U-2.5wt%Nb were compared, the results showed that U-2.5Nb alloy is more susceptible to hydrogen corrosion than U. The growth rates of hydride on U-2.5wt%Nb were calculated by measuring the perimeter of hydride spots recorded by the in-situ microscope, seen in Fig.1. The reaction temperature dependency of growth rate of the hydride on U-2.5wt%Nb has been determined (seen in Fig.2), in the range 40-160°C, for pressure of 0.8×10^5Pa. An Arrhenius plot for *v* versus *T* yields activation energy of 24.34 kJ/mol for U-2.5wt%Nb alloy. A maximum velocity of hydride of U-2.5wt%Nb exists at the temperature of 125°C, and a thermodynamics reason for that was given.

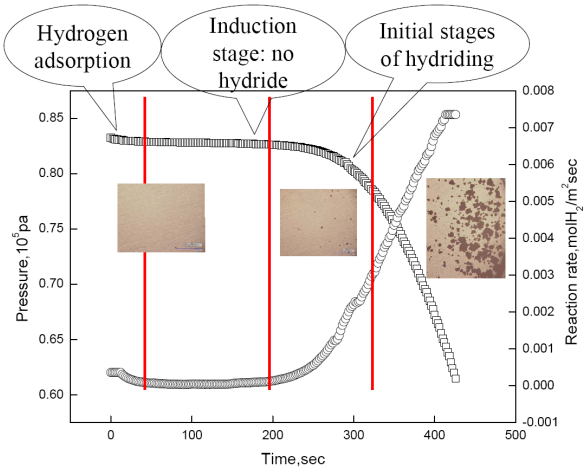

Fig.1 The initial kinetics of the reaction between H_2 and U-2.5wt%Nb: hydrogen pressure, reaction rate, and morphology, T=80°C, $P=0.83\times10^5$Pa

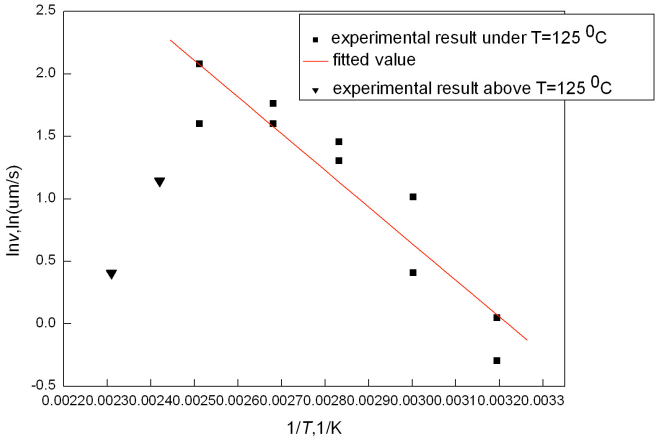

Fig.2 Growth rate dependence of reactive temperature

1-23

Microstructure-related hydride nucleation sites on aged U-0.79wt.% Ti alloy

Shi Peng, Wang Xiaolin, Li Fangfang, Li Ruiwen

China Academy of Engineering physics, Mianyang, Sichuan, China

The reaction of hydrogen with partially-decomposed U-0.79wt.% Ti alloy samples, which has been quenched in water and over-aged at 500 ^{o}C for 2h, have been studied by a hot stage microscope [1]. The hydride growth sites on the sample surfaces were studied using Laser Confocal Microscope. Enhanced hydrogen reactivity was observed in the decompostion area - particularly in the location of the grain boundaries of the mother γ phase - on sample surfaces. This is similar to the preferred hydriding on the grain boundaries of depleted uranium [2-4].

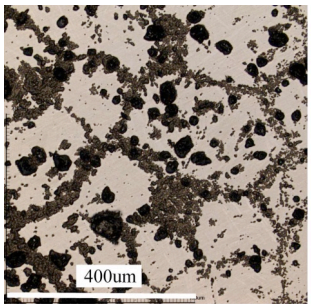

Fig. 1 The hydriding nucleation sites on the surface of 500 ^{o}C/2h aged U-0.79 wt.%Ti alloy

In the case of U-Ti alloy, the enhanced reactivity was found to be the result of the redistribution of titanium during the decomposition of α' phase into α+U_2Ti. Kelvin Force Probe results across the grain boundary of the mother phase demonstrates that the work function of α phase is higher than that of titanium-doped α' phase.

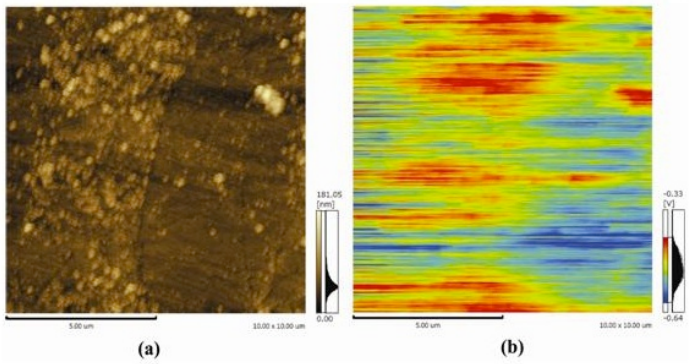

Fig. 2 AFM resuts taken at Kelvin Force Microscope (KFM) mode. (a) The morphology; (b) 2D work function of 500^{o}C/2h aged U-0.79Ti alloy. The scanned area was specially chosen to cross the grain boundary of the mother phase.

The results revealed that the doped titanium could reduce the hydriding reactivity and provided further evidence to support the assumption that the localized metal properties, including chemical makeup, microstructure and reactivity, are the determinants of initiation sites for hydriding of U-Ti alloy.

References

[1] Bloch J, Mintz M: IAEC - Annual Report 2001.

[2] Bingert J, Hanrahan R, Field R, Journal of Alloys and Compounds, 2004, 365 (1): 138-148.

[3] Scott T B, Allen G C, Findlay I, Philosophical Magazine, 2007, 87 (2): 177-187.

[4] Jones C P, Scott T B, Petherbridge J R, Solid State Ionics, 2013, 231 (0): 81-86.

1-24

Microstructure and corrosion resistance of Cr/CrN multilayer film prepared by magnetron sputtering on depleted uranium

Shengfa Zhu[1], Yanping Wu[1], Tianwei Liu[2], kai Tang[1], Qiang Wei[1]

[1]China Academy of Engineering and Physics, Mianyang, China, [2]Science and Technology on Surface Physics and Chemistry Laboratory, Mianyang, China

Depleted uranium (DU) has both military and civilian applications for its high-density. However, uranium is extremely apt to corrosion because of its high chemical activity, especially in salty, humid and high temperature environments. The corrosion of uranium can reduce the lifetime of components, while the corrosion products can release airborne particles that present environmental and health hazards. In order to reduce the corrosion, surface modifications and various coatings methods have been used to form environmentally friendly corrosion resistant coatings on the uranium. Cr/CrN multilayer coatings possess an unusual combination of mechanical and chemical properties, such as high fracture toughness, high cracking resistance, good corrosion resistance and high thermal and chemical stability. The aim of this work was to synthesize Cr/CrN multilayer films on the surface of uranium by unbalanced magnetron sputtering. The structure and corrosion resistance of the Cr/CrN film on uranium were investigated. The surface morphology and the depth profiles of elements were analyzed by SEM and Auger energy spectroscopy (AES), respectively. The corrosion behaviour of the samples was evaluated using potentiodynamic polarization curves.

The Cr, CrN layer, and Cr/CrN multilayer coatings were deposited on Si (100) wafer and depleted uranium (DU) samples (disk of Φ15mm×3 mm) in a unbalanced magnetron sputter (MFUMS) chamber. The base pressure was better than 5×10^{-4} Pa. The CrN film was prepared with N_2 gas introduced in the vacuum chamber; the deposition time was set to 2 min. Then a Cr film was deposited for 2 min without N_2 gas inlet. Thus alternative Cr and CrN layers were obtained by controlling the opening of N_2 gas valve.

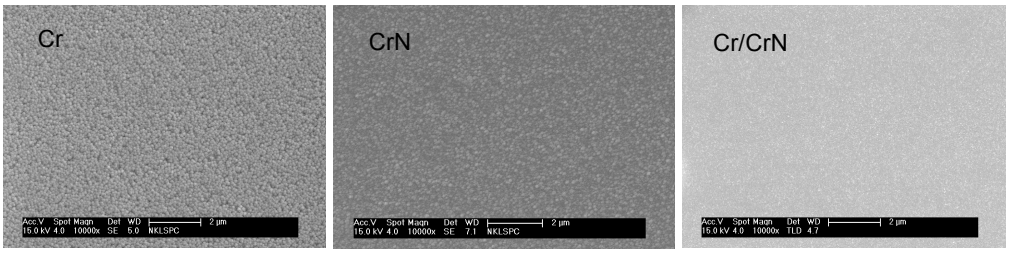

Fig. 1 Surface morphology of Cr, CrN, and Cr/CrN films

Fig. 1 shows the surface morphologies of Cr, CrN, and multilayered Cr/CrN films. The particle size of the Cr film was bigger than that of the CrN film. The microstructure of the CrN film was densely packed, with no voids or micro-cracks. Since the multilayer Cr/CrN film was composed of alternative Cr and CrN layers, a considerable amount of interface was formed between the Cr and the CrN films, which can effectively restrain the growth of columnar crystal. Thus the microstructure of the Cr/CrN multilayer film was uniform and compact.

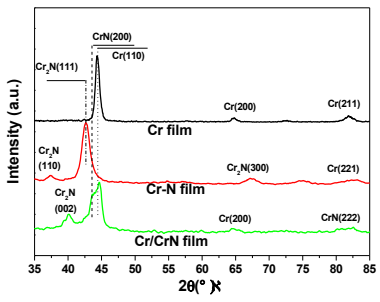

Fig.2 XRD patterns of Cr,CrN, and Cr/CrN multilayer film.

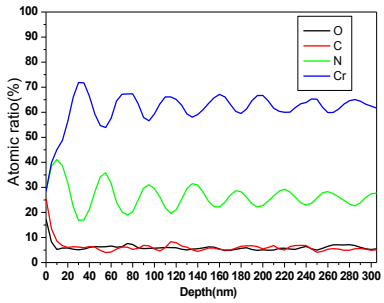

Fig.3 AES depth profiles of Cr,N,O, C elements in a Cr/CrN multilayer film.

XRD patterns are shown in Fig. 2. The single layer Cr film was mostly Cr with (110), (200), (211) orientations. The structure of the CrN film was mainly hcp-Cr_2N mixed with a little of Cr. The preferred orientation of Cr_2N was (111). The Cr/CrN multilayer film contained three phases, including fcc-Cr, hcp-Cr_2N and fcc-CrN.

The atomic ratio of Cr and N, as determined by the AES curves of Cr and N elements, showed periodical oscillations (Fig. 3). When the content of Cr reached the maximum value, the percentage of N is up to the minimum. The multilayer film had alternative Cr and CrN layers, the repeated period of Cr layer and CrN layer was about 40 nm. The high resolution Cr-2p XPS spectra for the Cr/CrN multilayer film show that the chromium peak is composed by four groups, corresponding to different chemical species: metallic chromium (Cr^0 , 574.43eV), chromium in nitrogen environment (Cr_2N and CrN, 574.98eV and 575.66eV respectively), and chromium oxides (Cr^{III}, 577.02eV). The N-1s XPS peak can be decomposed into two components, a peak at 397.5eV assigned to Cr_2N, and a peak at 396.9eV corresponding to CrN.

From Fig. 4, the corrosion potential of untreated DU was about -641 mV, as determined by extrapolation of the Tafel region. After the Cr film was deposited, the corrosion potential increased to about 350 mV, while the corrosion current density decreased significantly, the surface of Cr film exhibited a pseudo passivation behaviour and secondary passivation phenomenon. After deposition of the multilayer Cr/CrN, the corrosion potential of uranium increased to approximately 590 mV, and the corresponding current density decreased by about three orders of magnitude. Fig. 5 shows the SEM photographs of uranium and Cr/CrN multilayer films after polarization test. The surface of uranium produced corrosion holes (Fig. 5 left), while the Cr/CrN film possessed the higher corrosion resistance, the surface morphology exhibited no peeling off. There were only a small number of tiny cracks (Fig. 5 right).

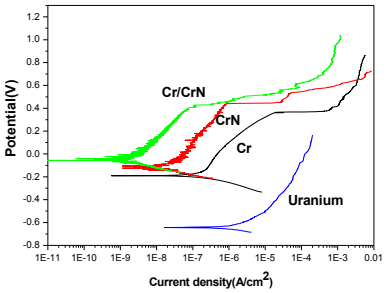

Fig. 4 Polarization curves of Cr, CrN, and Cr/CrN films

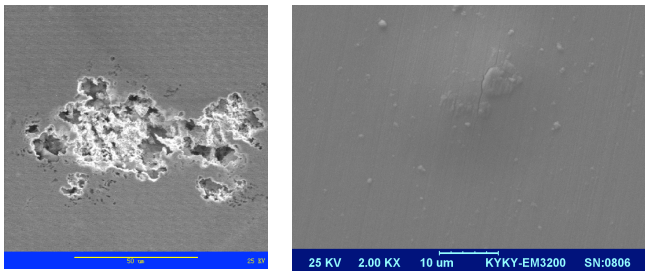

Fig. 5 SEM photographs of polarization test (left) uranium; (right) Cr/CrN films

Conclusion: Cr/CrN multilayer films were prepared on the surface of depleted uranium by unbalanced magnetron sputtering to improve its corrosion resistance. The multilayer film had alternative Cr and CrN layers in a different thickness, and had a perfect modulation structure with fine grain and good density. Not only chromium nitrides (Cr_2N and CrN) but also chromium oxides (Cr_2O_3) are detected. Metallic chromium is also found in films. The surface of Cr/CrN multilayer film exhibits a pseudo-passivation behaviour. Its corrosion potential increases to 590 mV and corrosion current density decreases three orders of magnitude. After polarization test, there are only a small number of tiny cracks. It is indicated that, after deposited Cr/CrN film by unbalanced magnetron sputtering, the corrosion resistance of depleted uranium is effectively improved.

1-25

Phase transformations in PuGa 1 at.% alloy: Elucidation of mechanisms of reversion process following martensitic transformation by coupling *in situ* experiments and CALPHAD-based calculations

Fanny Lalire, Brice Ravat, Aurélien Perron, Benoit Oudot, Francois Delaunay

CEA, Is sur Tille, France

At ambient pressure, plutonium metal has six different phases between room temperature and its relatively low melting point (640 °C). At room temperature, the thermodynamically stable phase of pure plutonium is the brittle α phase (monoclinic structure). However, the high-temperature δ–phase (face-centered cubic structure), which has the highest crystallographic symmetry but the lowest density and is stable from 315 to 457 °C, can be retained at room temperature by alloying plutonium with a few atomic percent of so-called "δ-phase stabilizing" elements such as Al, Am, Ce and Ga. Recently, US and Russian scientists concurred with each other in the view that the δ phase is metastable under ambient conditions, and that in Pu–Ga systems, this phase goes through an extremely slow eutectoid decomposition into α Pu and the intermetallic compound Pu_3Ga when cooled to temperatures below 100 °C; this process takes place over an estimated period of more than 10,000 years [1].

Furthermore, when the metastable δ phase of PuGa alloys with Ga contents lower than 3 at.% is cooled to subambient temperatures, a partial transformation into the martensitic α' phase occurs. The crystal structure of the α' phase is similar to that of the monoclinic α phase, consisting in a slightly expanded unit cell as a result of Ga atoms being trapped in the lattice (the prime here is used to indicate the presence of Ga atoms in the crystalline structure).

The reverse α'-to-δ transformation that is observed upon heating is particularly multifaceted in nature. Indeed, this process depends on the Ga content. In PuGa alloys with Ga contents greater than 1.7 at.%, the reverse transformation is direct. This direct α'-to-δ reversion occurs via a burst martensitic mode characterized by a series of endothermic spikes that correspond to a cascade of α' particles reverting to the δ phase [2]. In PuGa alloys with Ga contents close to 1 at.%, the reverse transformation has been found to be indirect before complete reversion to the δ phase, with the appearance of phases exhibiting body-centered monoclinic and face-centered orthorhombic crystalline structures that correspond respectively to the so-called β and γ structures of Pu [3]. However, the physics underpinning the behavior of Ga during this indirect reversion process remained unresolved.

The purpose of this work was to study PuGa 1 at.% alloy behavior from martensitic transformation to the whole reversion process. The relevant phase transformations were investigated as a function of temperature via *in situ* X-ray diffraction and dilatometry analyses carried out at low and high temperatures. The results show that the δ-to-α' martensitic transformation occurring at low temperatures is direct and does not involve any intermediate γ' phase. They also reveal that the reverse transformation of the two-phase δ + α' alloy during heating involves two competing modes, namely direct and indirect reversion. The latter is associated with a Ga diffusion process that governs the ratio between these reversion modes. The study demonstrates that the indirect reversion process consists in a Ga-enrichment of the remaining δ phase as well as the emergence of the β and γ phases of pure plutonium [4]. More precisely, specific isothermal experiments revealed the existence of two potential Ga diffusion paths during indirect reversion: (i) from the α' phase to the δ phase and (ii) from a new transient β' phase to the δ phase. Mechanisms of reverse transformation of PuGa 1 at.% alloy have been investigated in detail using CALPHAD-based simulations. This enables to focus on the thermodynamic and kinetic aspects of the competition between these two reversion modes, especially between direct reversion ($\alpha'_{1\,at.\%} \rightarrow \delta_{1\,at.\%}$) and the first step of indirect reversion ($\alpha'_{1\,at.\%} \rightarrow \beta_{pure\,Pu}(+\delta_e)$), whenever competition occurs [5]. Thermodynamic simulations indicated that both reversion modes were possible and that indirect reversion was more favorable. Finally, the ratio of direct to indirect reversion has been found to depend on three factors, namely heating rate, initial α' phase fraction and Ga content. All simulations

were confirmed experimentally and highlighted key aspects of reversion mechanisms. These newly revealed mechanisms have enabled in a PuGa 1 at.% alloy to fully understand the whole reversion process following martensitic transformation.

References

[1] S.S. Hecker, D.R. Harbur, T.G. Zocco, Prog. Mater. Sci. 49 (2004) 429−485.

[2] J.N. Mitchell, M. Stan, D.S. Schwartz, C.J. Boehlert, Metall. Mater. Trans. 35A (2004) 2267−2278.

[3] P. Deloffre, J.L. Truffier, A. Falanga, J. Alloys Compd. 271-273 (1998) 370−373.

[4] B. Ravat, B. Oudot, A. Perron, F. Lalire, F. Delaunay, Phase transformations in PuGa 1 at.% alloy: Study of whole reversion process following martensitic transformation, accepted J. Alloys Compd. 2013.

[5] A. Perron, B. Ravat, B. Oudot, F. Lalire, K. Mouturat, F. Delaunay, Phase transformations in PuGa 1 at.% alloy: Synergy between simulations and experiments to elucidate direct and indirect reversion competition, submitted to Acta Mater. 2013.

1-26

Corrosion of austenitic steels and their components in uranium-containing chloride melts

Alexandr Abramov, Ilya Polovov, Dmitriy Maltsev, Vladimir Volkovich, Oleg Rebrin

Ural Federal University, Ekaterinburg, Russia

Fused alkali halides can be used in prospective non-aqueous nuclear fuel reprocessing technologies as well as working media in active zones of molten salts nuclear reactors. However practical application of such technologies is hindered by the problem of finding suitable corrosion resistant materials working in contact with molten salts. From the economical point of view application of stainless steels as construction materials for the molten media is one of the most prospective ways. However, the mechanism of stainless steels corrosion in the fused halides has not been studied so far in sufficient detail to enable prediction of their behaviour.

Metallic iron, nickel, chromium, molybdenum and type AISI 316L and AISI 321 austenitic steels were chosen as the objects of our investigations. Corrosion tests were carried out in NaCl–KCl–UCl_3 (1 wt. % uranium) melts at 750 ºC. Duration of the corrosion tests was 30 h and several cylindrical samples of each studied material were used in every experiment. Corrosion rates of the metals and alloys were determined by gravimetric method. Average oxidation state of the dissolved metal species after the interaction with the melt was identified by electronic absorption spectroscopy. Surface of the corroded samples was examined by metallography (Olympus GX-71F), SEM (JSM 6490) and X-Ray microanalysis (Oxford Inca).

The rates of corrosion of studied metals in NaCl–KCl melt decrease in the following order: Cr > Fe > Ni > Mo (Table 1). This order correlates well with the formal standard electrode potentials of the studied metals in chloride melts thus indicating that the nature of the corrosion processes is electrochemical. Metallic molybdenum is the only corrosion resistant material in the uranium containing chloride melts and it can therefore be used as a construction material for the molten salt reactors.

Table1 – Formal standard electrode potentials of Fe, Cr, Ni and Mo and their corrosion rates in chloride melts at 750°C

Melt	Cr	Fe	Ni	Mo
	$E^{*}_{Me^{n+}/Me}$, V			
NaCl–KCl	*–1.59*	*–1.34*	*–0.97*	*–0.79*
	Corrosion rate, g/(m^2·h)			
NaCl–KCl	0.9	0.4	0.1	<0.01
NaCl–KCl–UCl_3	10.7	5.1	0.6	<0.01

It was found that the major products of stainless steel corrosion in the chloride melts are iron, chromium and manganese chloro-species. A spectroscopic study of the anodic dissolution of AISI321 and 316L stainless steels coupled with chemical analysis of the quenched melt samples revealed that the process always leads to the formation of $CrCl_4^{2-}$, $FeCl_4^{2-}$ and $MnCl_4^{2-}$ complex ions. The surface of the corroded samples of austenitic stainless steels was depleted in manganese and chromium and enriched in nickel and molybdenum.

After 30 h of exposure in NaCl–KCl–UCl_3 melts intergranular corrosion was noticed for all types of the austenitic steels. The degree of intergranular destruction of steels' surface in uranium containing molten salt is higher than in the pure NaCl–KCl equimolar melt.

In terms of intensity and depth of the corrosion layer in NaCl-KCl-UCl_3 the studied steels can be ranged in the order AISI 321 > AISI 316L. This sequence correlates well with the steels' carbon content. Occurrence of intergranular corrosion indicates chromium carbide formation along the grain boundaries of steels due to exposure to high temperatures (a so-called sensitization effect). As a result of sensitization chromium concentration at the grain boundaries decreases, and galvanic pairs between the chromium depleted regions and the carbide phases at the grain boundaries are formed (Fig. 1). Interaction of these galvanic pairs with studied melts leads to the destruction of chromium depleted regions. The obtained results show that austenitic stainless steels cannot be used as construction materials in NaCl–KCl based melts.

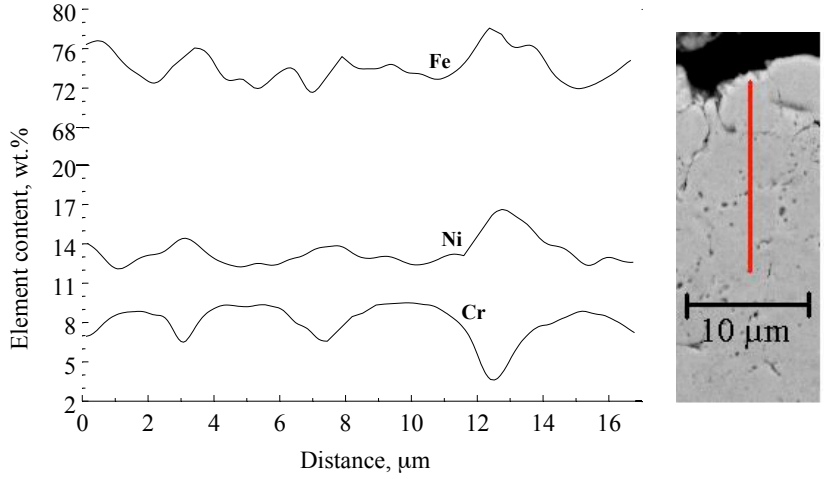

Fig. 1. Distribution of elements in AISI 321 sample along the line between the steel grains after 30 h contact with NaCl–KCl–UCl_3 melt at 750 °C (grain boundaries are situated at 3, 7 and 12 μm).

Financial support by the non-profit partnership on development of the international research and projects in the field of energetic «Global Energy» is gratefully acknowledged.

1-27

Interaction of prospective metallic construction materials with uranium-containing chloride melts

Robert Kamalov, Alexandr Bazhenov, Alexandr Abramov, Ilya Polovov, Dmitriy Maltsev, Vladimir Volkovich, Oleg Rebrin

Ural Federal University, Ekaterinburg, Russia

According to the technology roadmap for Generation IV nuclear energy systems molten salt reactors (MSR) with on-site uranium-thorium nuclear fuel cycle is one of six innovative reactor types. Practical realization of MSR relies on finding suitable construction materials stable in uranium- and thorium-containing salt melts.

The present work was aimed at studying corrosion performance of a number of prospective alloys in fused chlorides. Corrosion-resistant nickel-chromium-molybdenum alloys (Hastelloy N, Hastelloy G35 and Hastelloy C2000) and nickel-molybdenum alloy (Hastelloy B-3) were chosen for the study. Corrosion tests were performed in NaCl–KCl–UCl_3 (1 wt. % uranium) melts at 750 °C. Corrosion rates of the studied materials were determined after 30 h of exposure in the melt.

During exposure the studied materials were subjected to structural changes. Excessive intermetallic μ-phases were formed along the grain boundaries in nickel based alloys. Formation of excessive phases leads to the appearance of microgalvanic pairs resulting in subsequent dissolution of their anodic zones. After 30 h of exposure in NaCl–KCl–UCl_3 melt intergranular corrosion was noticed for all types of nickel-chromium-molybdenum alloys (Fig.1). In terms of intensity and depth of the corrosion layer the studied alloys can be ranged in the following order: Hastelloy G35 ≥ C2000 > Hastelloy N > Hastelloy B-3 (Table 1).

Table 1. Corrosion resistance of Hastelloys in NaCl–KCl–UCl_3 melts.

Alloy	Corrosion rate		Depth of corrosion layer, μm
	g/(m^2·h)	mm/year	
Hastelloy G35	0.19	0.18	16-18
Hastelloy C2000	0.15	0.16	30
Hastelloy N	0.06	0.06	14-17
Hastelloy B-3	0.03	0.02	—

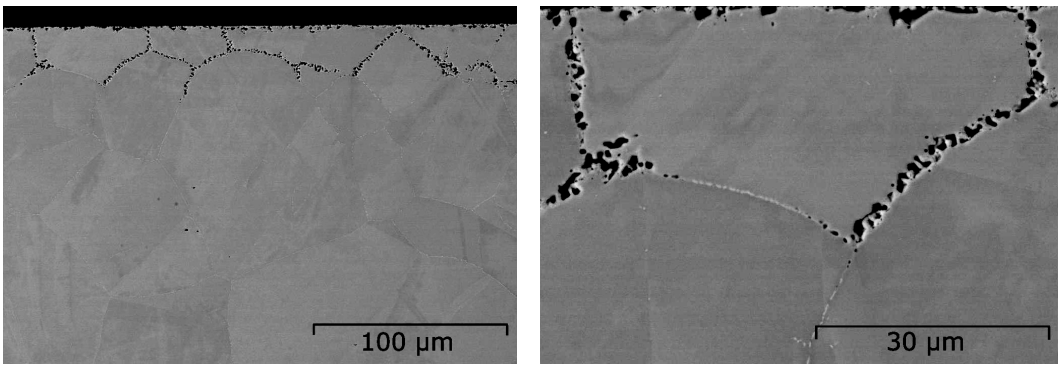

Figure 1. Microstructure of Hastelloy C2000 alloy after 30 h contact with NaCl–KCl–UCl_3 melt at 750 °C.

Low rate of corrosion of Hastelloy B-3 samples can be explained by the formation of a protective layer, enriched in molybdenum on the surface (Fig. 2a). The thickness of this layer is 1–2 μm. This passivation layer is formed by selective dissolution of nickel because more electronegative components of the alloys dissolve more actively. Hastelloy B-3 alloy is

corrosion resistant material in the uranium containing chloride melts and can therefore be considered as a prospective construction material for these media.

The surface of Hastelloy N was also enriched in molybdenum. However, this alloy is subjected to intergranular corrosion as the protective layer formed is not continuous (Fig.2b). This is due to differences in the chemical composition of the alloys. Hastelloy N contains 7.2 wt. % of chromium, which actively dissolves when the alloy is brought in contact with the chloride melt. Thus Hastelloy N cannot be used as a construction material.

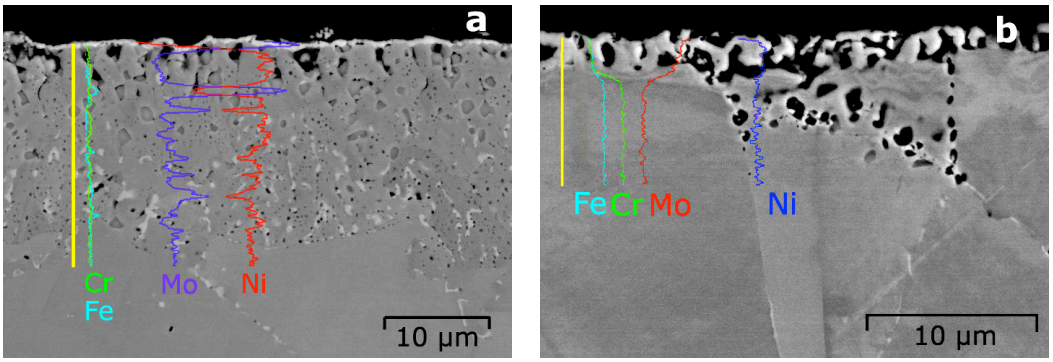

Figure 2. Distribution of elements from surface to bulk of Hastelloy B-3 (a) and Hastelloy N (b) alloy samples after 30 h exposure to NaCl–KCl–UCl_3 melt at 750 °C

Financial support by the OPTEC LLC is gratefully acknowledged.

1-28

Recent advances in the study of $U_{1-x}Am_xO_{2\pm\delta}$: solid solution formation, densification and structural properties

Florent Lebreton[1,4], Denis Horlait[1], Philippe M. Martin[2], Renaud C. Belin[3], Thibaud Delahaye[1], Philippe Blanchart[4]

[1]CEA, DEN, DTEC/SDTC/LEMA, Bagnols-sur-Cèze, France, [2]CEA, DEN, DEC/SESC/LLCC, Saint-Paul-lez-Durance, France, [3]CEA, DEN, DEC/SPUA/LMPC, Saint-Paul-lez-Durance, France, [4]GEMH/ENSCI, Limoges, France

To decrease the radiotoxicity and heat load of ultimate nuclear waste, incorporating the minor actinides (Am, Np, Cm) accumulated in spent fuels in fast neutron reactor assemblies for their transmutation is envisaged in the context of the GEN-IV forum. Among the several transmutation modes and associated fuels proposed (CERMET targets or homogeneous minor-actinide-bearing MOX fuels for instance) [1-3], interest in the heterogeneous transmutation of Am has risen in recent years, as evidenced by two recent experimental irradiations [4,5]. This mode consists of using $U_{1-x}Am_xO_{2\pm\delta}$ compounds as blanket fuels, i.e., destined for the periphery of the core, hence allowing x-values (Am/(U+Am) ratio) around 15 at.%. Limited information is available on these promising materials, so further research is required to evaluate the feasibility of transmutation deployment at an industrial scale. In this context, we report recently-performed studies on these materials, with emphasis on their fabrication (stages of $U_{1-x}Am_xO_{2\pm\delta}$ solid solution formation and densification by sintering) and structural characteristics.

The fabrication of $U_{1-x}Am_xO_{2\pm\delta}$, especially solid solution synthesis and densification, has been studied, mainly using dilatometry. Two processes for the fabrication of dense and homogeneous $U_{1-x}Am_xO_{2\pm\delta}$ pellets are investigated, namely:

- reactive sintering, for which $UO_{2+\delta}$ and $AmO_{2-\delta}$ are used as precursor powder and solid solution synthesis and densification must occur simultaneously [4]; and
- UMACS (uranium-americium conventional sintering), which uses a first thermal treatment dedicated to solid solution formation and a long grinding step to prepare a reactive and homogeneous powder used for sintering during a second thermal treatment [5].

Prior to dilatometric experiments, phenomena occurring in a $UO_{2+\delta}/AmO_{2-\delta}$ blend during solid solution synthesis were monitored by in-situ XRD (X-ray diffraction), under different atmospheres (neutral to reducing). As shown in Figure 1a, while $UO_{2+\delta}$ retains a fluorite structure, $AmO_{2-\delta}$ is fully or only partially reduced to hexagonal $Am^{+III}{}_2O_3$, depending on the atmosphere [6]. This reduction then strongly influences the solid solution formation, which begins around 1800 K. The comparison between the various atmospheres especially shows that the complete reduction of Am to the trivalent state is a key step for U/Am interdiffusion and consequently the achievement of a monophasic sample, as will be further described.

Solid solution formation also strongly affects pellet densification behaviour. This is notably observed during the reactive sintering of $UO_{2+\delta}/AmO_{2-\delta}$ pellets, for which the densification rate shows several stages of decrease associated with the solid solution synthesis [7].Interdiffusion between U and Am provokes the development of additional porosity through the Kirkendall effect, which impedes sintering and thus delays densification. In consequence, this process produces pellets with incomplete sintering, i.e., with densities limited to around 92%TD (theoretical density) [8]. This pitfall can, however, be overcome by dissociating solid solution synthesis and densification, like in the UMACS process. As pointed out in Figure 1b in the case of $U_{0.85}Am_{0.15}O_{2\pm\delta}$, the densification rate shows no decrease before high sintered densities (> 90%TD) are reached, despite a high sintering onset temperature.

The second part of this presentation will be dedicated to the structural study of mixed U-Am oxides. Little is known about such oxides with elevated americium contents. Recently, compounds with new compositions ranging from 15 to 50 at.%-Am were fabricated using the UMACS process [9]. As seen in Figure 2a, their densities decrease with Am content but remain superior to 93%TD up to 30 at.%-Am. Obtained compounds are, according to preliminary characterisation by XRD, monophasic when stored under an ambient, i.e.,

oxidising, atmosphere. Their lattice parameters under such conditions, reported in Figure 2b, seem to vary linearly with Am content up to 30 at.%, whereas values larger than expected are obtained for higher Am contents. All these values are far from those predicted by Vegard's law between UO_2 and AmO_2. This can be explained by the peculiar charge distribution in these mixed oxides, in which Am is completely trivalent, while U has a mixed +IV/+V oxidation state (at least up to 20 at.%) [10].

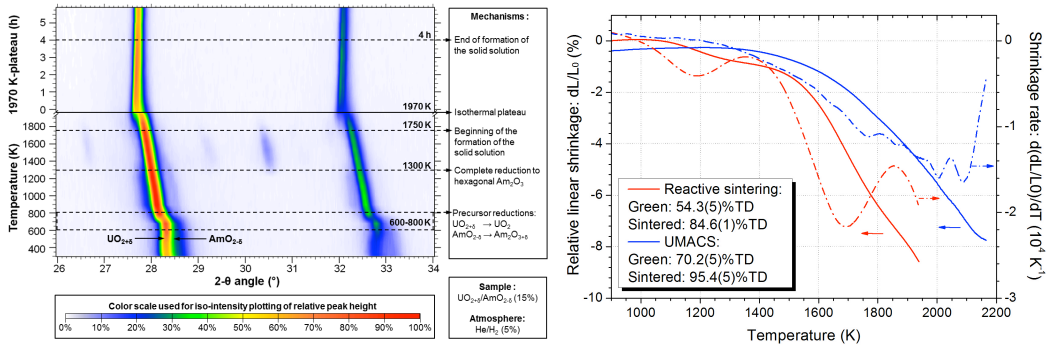

Figure 1 (a) Monitoring of the solid solution formation by in-situ XRD [6] and (b) densification of $U_{1-x}Am_xO_{2\pm\delta}$ pellets prepared by the reactive sintering or with the UMACS process (conventional sintering).

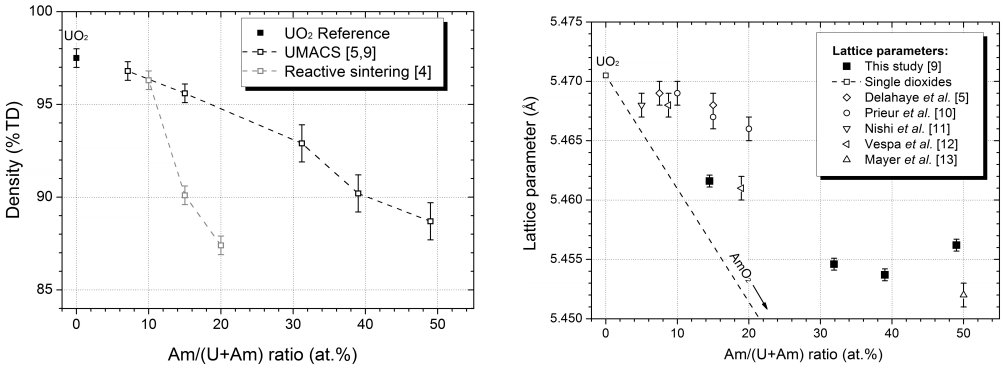

Figure 2 (a) Relative densities of 15 to 50 at.%-Am samples fabricated using the UMACS process [5,9] compared to those obtained with a reactive sintering [4], and (b) lattice parameters of obtained compounds [9], determined by XRD refinement, compared to other values reported in the literature [10-13].

After annealing under a reducing atmosphere, the oxidation of these compounds under ambient conditions was monitored using XRD. Obtained results point out the occurrence of peculiar phenomena for the highest Am-content samples, as biphasic materials are observed during the transition from a reduced to an oxidised state. Further details on this behaviour will be presented, with emphasis on the 50%-Am sample, as it was studied by in-situ XRD and XAS (X-ray absorption spectroscopy).

References

[1] M. Salvatores, *Prog. Nucl. Energy* **40** (2002) 375-402.

[2] R.J.M. Konings, K. Bakker *et al.*, *J. Nucl. Mater.* **274** (1999) 84-90.

[3] F. Lebreton, D. Prieur *et al.*, *J. Nucl. Mater.* **420** (2012) 13-217.

[4] D. Prieur, A. Jankowiak *et al.*, *J. Nucl. Mater.* **414** (2011) 503-7.

[5] T. Delahaye, F. Lebreton *et al.*, *J. Nucl. Mater.* **432** (2012) 305-12.

[6] F. Lebreton, R.C. Belin *et al.*, *Inorg. Chem.* **51** (2012) 9369-75.

[7] D. Horlait, A. Feledziak *et al.*, accepted in *J. Nucl. Mater.* (2013)

[8] M. Durazzo, A.M. Saliba-Silva *et al.*, *J. Nucl. Mater.* **433** (2013) 334-40.

[9] F. Lebreton, D. Horlait *et al.*, *J. Nucl. Mater.*, *In press*, accepted manuscript (2013).

[10] D. Prieur, P.M. Martin *et al.*, *Inorg. Chem.* **50** (2011) 12437-45.

[11] T. Nishi, M. Nakada *et al.*, *J. Nucl. Mater.* **418** (2011) 311-2.

[12] M. Vespa, M.Rini *et al.*, *J. Nucl. Mater.* **421** (2012) 80-8.

[13] K. Mayer, B. Kanellakopoulos *et al.*, *J. Alloy Compd.* **213/214** (1994) 456-9.

1-29

Thermal conductivities of $(U_{1-y}, Pu_y)O_{2.00}$ (y = 0.00-0.46)

Kyoichi Morimoto[1], Masahiro Ogasawara[2]

[1]Japan Atomic Energy Agency, Naka-gun, Ibaraki, Japan, [2]Inspection development company, Naka-gun, Ibaraki, Japan

1. Introduction. Plutonium and uranium mixed oxide (MOX) fuel has been developed for fast reactors (FRs). In general, concentration of Pu in a MOX fuel for FRs is up to 35 % in heavy metal. During irradiation, redistributions of heavy metal elements occur in fuel pellets by steep thermal gradient. Consequently Pu ratio of the total metal content (Pu-content) in pellets exceeds 40 % partially [1]. Thermal conductivity of nuclear fuel is one of the important physical properties for fuel design and performance analysis of nuclear fuels. Many studies discussing the influence of Pu-content on thermal conductivities have been conducted [2-6]. On the other hand, the disparity among these experimental results regarding the dependence of Pu-content on thermal conductivity is large and the researchers have different opinions about this dependence. In this study, the stoichiometric MOX specimens with different Pu-contents were prepared, and the dependence of Pu-content on thermal conductivities of them was investigated.

2. Experimental. The Pu-contents of the specimens prepared in this study were 2, 8, and 46 %. The thermal conductivities (λ) of these specimens were obtained from the thermal diffusivities (α), the heat capacities (C_p) and the densities (ρ) using the following equation, $\lambda = \alpha \cdot C_p \cdot \rho$. The thermal diffusivities were measured at temperatures up to about 1480 K with a laser flash apparatus. The heat capacities were calculated from those of UO_2 and PuO_2 by Kopp's law. The densities of specimens were measured by the immersion method. The thermal conductivities were normalized to those of 100 % theoretical density by the Maxwell-Eucken relationship [7]. The influence of Pu-content on thermal conductivity was evaluated systematically by the data in this study together with those in previous study [7].

3. Results and Discussion. Fig. 1 and Fig. 2 show the thermal conductivities as functions of temperature and Pu-content respectively. The data on UO_2 and 30%Pu-MOX were obtained in previous study [7]. It was shown that the thermal conductivities decreased monotonically with increasing Pu-content and its variation was small compared to that by O/M ratio change [8]. The difference of thermal conductivities between the specimens with high and low Pu-content decreased with increasing temperature.

4. Conclusions. In this study, the thermal conductivities of the stoichiometric MOX specimens containing from 2 to 46 % of Pu were obtained experimentally. In the Pu-content range less than 46 %, it was shown that the influence of Pu-content on thermal conductivities was small compared to that by O/M ratio change and its influence declined monotonically with increasing temperature.

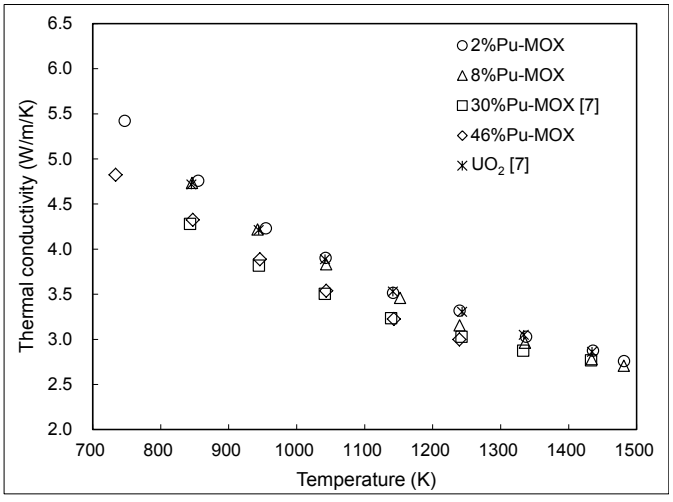

Fig. 1 Temperature dependence of thermal conductivities.

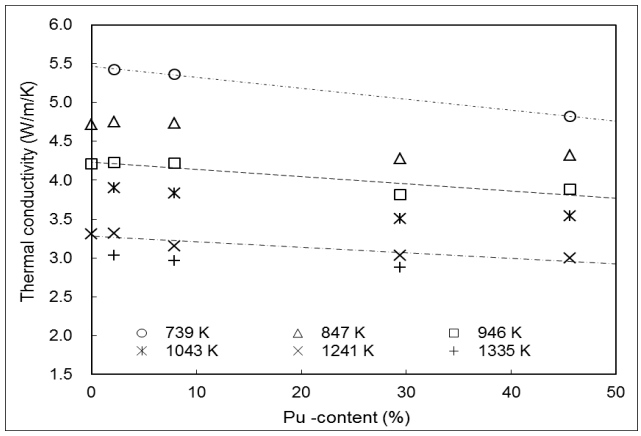

Fig. 2 Pu-content dependence of thermal conductivities.

References

[1] T. Ishii et al., J. Nucl. Mater., 294 (2001) pp.13-17

[2] R.L. Gibby, J. Nucl. Mater., 38 (1971) pp.163-177

[4] J.C. Weilbacher, CEA Report CEA-R-4572, France, 1974.

[3] C. Duriez, J. Nucl. Mater., 277 (2000) pp.143-158

[5] T. Arima et al., J. Alloys Compd., 400 (2005) pp.43-50

[6] S. Nichenko et al., J. Nucl. Mater., in press

[7] K. Morimoto et.al, J. Alloys and Comp., 452 (2008) 54–60

[8] K. Morimoto et.al, J. Nucl. Mater., 374 (2008) 378–385

1-30

Actinides oxalate compounds: structure directing role of the monovalent cations

Ana Gil-Martin[1], Bénédicte Arab-Chapelet[1], Murielle Rivenet[2], Philippe Martin[3], Andreas Scheinost[4], Isabelle Bisel[1], Stéphane Grandjean[5], Francis Abraham[2]

[1]Laboratoire de Conversion des Actinides et Radiolyse, CEA Marcoule DEN/DRCP/SERA, Bagnols sur Cèze, France, [2]UCCS, Equipe Chimie du Solide et Matériaux Nucléaires, Villeneuve d'Ascq, France, [3]Laboratoire des lois de comportement des Combustibles, DEN/DEC/SESC, Saint Paul lez Durance, France, [4]The Rossendorf Beamline at ESRF, Grenoble, France, [5]CEA Marcoule DEN/DRCP/DIR, Bagnols sur Cèze, France

The remarkably low solubility of f-element oxalates in acidic solution and the flexibility of the oxalate ligand lead to lanthanides and/or actinides-based solid oxalates which are particularly suitable to recover radioelements from nitric acid solutions. For example, oxalic precipitation of plutonium has become a major step during the reprocessing of the nuclear fuel at an industrial scale at the end of the PUREX process. It is used to recover plutonium from nitric acid solutions in order to convert this energetically valuable element into oxide further used for the MOX production.

Considering the actinide/lanthanide-oxalate systems, abundant different structures can be formed depending on the oxidation state of the f-element and on the synthesis conditions (presence of single-charged cation, temperature, pH…). These structures are built on various types of coordination spheres (i.e. distorded tri-capped trigonal prism for $Pu_2(C_2O_3)_3 \cdot 9H_2O$, bi-capped square anti-prism polyhedron for $U(C_2O_4)_2\ 2H_2O$ …) and different structural arrangement (mono, bi- or three-dimensional networks) leading to a large particle sizes range and variable . Considering morphologies (square plates, hexagonal prisms…), and shapes of the precipitated particles. Insertion of single-charged cations within the structural network forming double oxalate compounds further increases the number of crystallographic structures and morphology types which can be encountered that can be synthetized.

Among the monocharged cations present in double oxalate compounds, alkali cations or some nitrogen cations commonly used in nuclear field such as NH_4^+, $N_2H_5^+$, used to stabilize some actinides oxidation states, are listed. In mixed actinide (IV)-lanthanide/actinide (III) oxalates, the formation of An(IV)-Ln/An(III) solid solutions is based on the insertion of single-charged cations to ensure the charge balance during the partial substitution of the tetravalent cation by the trivalent one. The present work focuses on the influence of single-charged cations on the crystal structure and morphology of the mixed actinide (IV)-lanthanide/actinide (III) oxalate compounds. The impact of the single-charged cations mentioned above could be evidenced thanks to the combination of several structural (X-ray Absorption Spectroscopy, X-ray diffraction, Infrared spectroscopy…) and chemical analyses (ICP-AES, CHN elemental analysis).

A preliminary work was carried out on the Th^{IV}-Nd^{III} system. This study has demonstrated the inserted monocation influence on the crystallisation domains of oxalate compounds. Large ionic radii alkali such as Cs^+ for example tend to stabilize oxalate structures built on 10-fold coordinated metallic cations such as the hexagonal solid solution $M^+_{2+x}An^{IV}_{2-x}An^{III}_x(C_2O_4)_5 \cdot nH_2O$ on a large domain (Figure 1). On the contrary, when the single-charged cations available in solution are too small, the size of existence domain of the 10-fold oxalate compounds ($M^+_{2+x}An^{IV}_{2-x}An^{III}_x(C_2O_4)_5 \cdot nH_2O$) tend to decrease to benefit to 8-fold structures ($Th(C_2O_4)_2 \cdot nH_2O$).

Besides the grain size of the precipitated powders appears to be closely correlated to the nature of the single-charged cations which impact nucleation and crystal growth phenomena (Figure 2). Indeed, large monocations favour nucleation whereas small monocations promote crystal growth, the same result being obtained by increasing the Nd/(Th+Nd) ratio.

The structure directing effect of the monocation in the Th(IV)-Nd(III)-Rb(I) oxalates was probed by means of extended X-Ray Absorption Fine Structure analysis on the Rb K-edge. The results show that rubidium present in the channel of the hexagonal solid solution $(M^+)_{2+x}An^{IV}_{2-x}An^{III}_x(C_2O_4)_5 \cdot nH_2O$ is mainly coordinated to the oxygen atoms belonging to the water molecules of the hydration sphere (d(Rb-O)~2.9A) (Figure 3). There is no evidence by X-ray absorption that Rb could be coordinated to oxygen atoms of the oxalate ligands. The

structure directing effect should therefore be attributed to the hydrated cations rather than to the monovalent cations. These hydrated monocations are disordered in the hexagonal tunnels confirming the preliminary crystal X-ray diffraction results. These first results were followed by an experimental work on uranium and plutonium oxalate systems. The second part of this work confirms that the insertion of single-charged cations influences the structure and morphology of the An^{IV}- An^{III} oxalate precipitates.

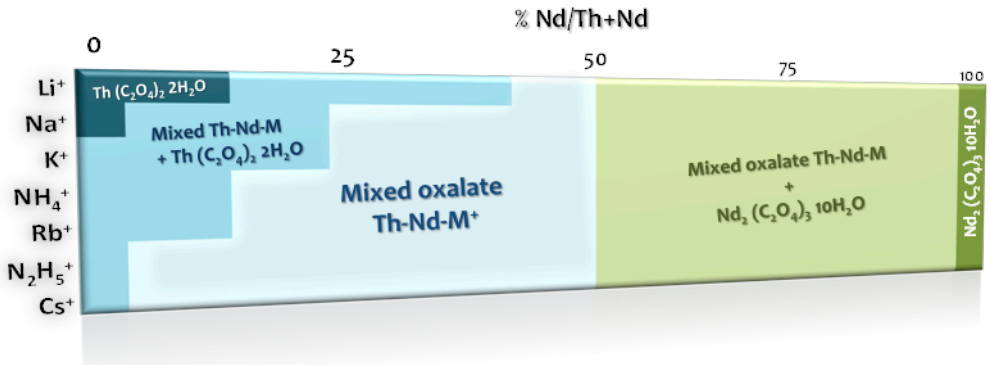

Figure 1. Existence domains M^{+}-Th^{IV}-Nd^{III} system phases

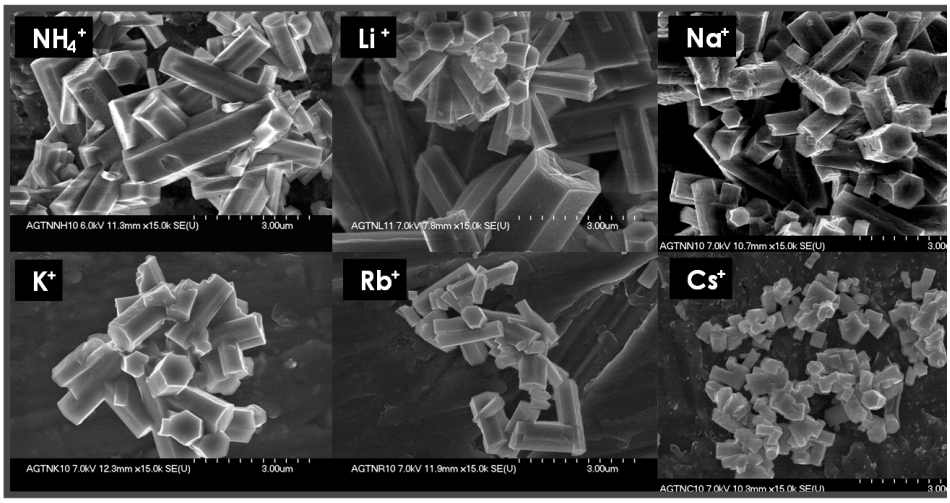

Figure 2. Influence of monovalent cation insertion on the grain size of mixed Th(IV)-Nd(III)-M(I) hexagonal oxalates

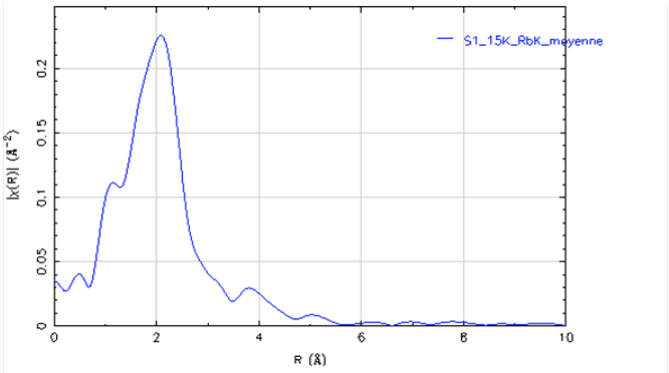

Figure 3. Rb K-edge K^3-weighted EXAFS spectra

1-31

Submicron and nanostructured uranium carbides prepared by electrospinning

Margarida S. Henriques[1], Adelaide Cruz[1], Joaquim Marcalo[1], Martina Kratochvílová[2], Ladislav Havela[2], Thierry Stora[3], Antonio P. Goncalves[1]

[1]IST/ITN, Technical University of Lisbon, CFMC-UL, 2686-953-Sacavém, Portugal, [2]Dept. Condensed Matter Physics, Faculty of Mathematics and Physics, Charles University, 121 16 Prague, Czech Republic, [3]CERN - European Organization for Nuclear Research, CH-1211 Genève 23, Switzerland

The CERN Isotope Separator On-Line Device, ISOLDE, is a facility dedicated to the production of radioactive ion beams used in studies of fundamental aspects in physics, materials science and medicine. The radioactive nuclides are produced by spallation, fission or fragmentation in a target, usually of uranium carbide (UCx), irradiated with a high-energy and high-intensity proton beam.

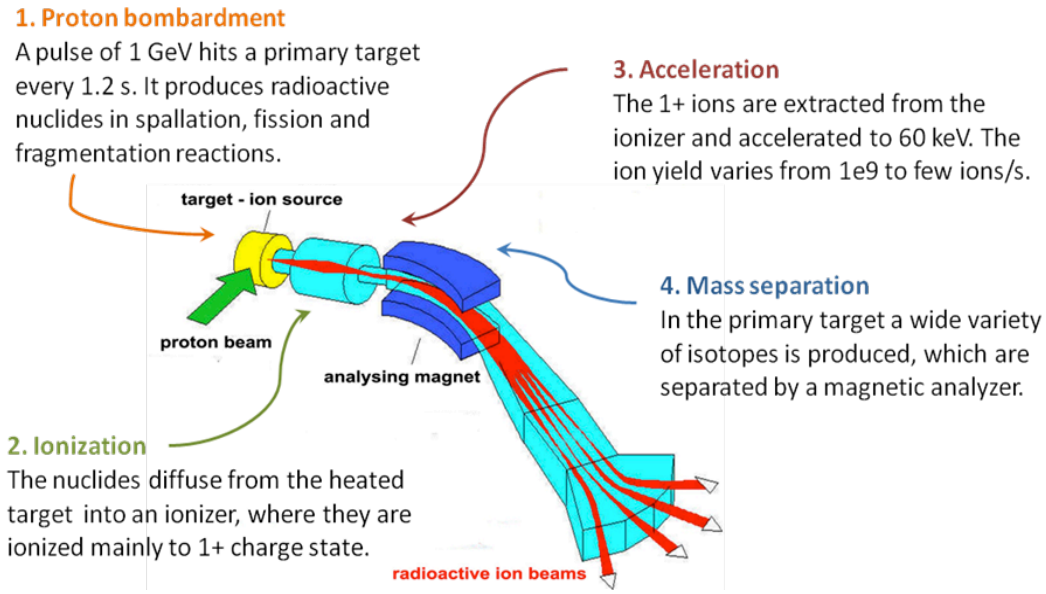

Figure 1. Production of radioactive ion beams at ISOLDE.

The products of the nuclear reactions first diffuse from the interior of the target to the surface and then evaporate from it. High ion diffusions and releases are therefore necessary conditions to obtain high intensity radioactive beams. Minimum delay times can be achieved for highly-permeable, low-density, open-structures operating at high temperatures [1]. It was recently proved that a significantly increase on the release and yields of exotic isotopes can be obtained on submicron and nanostructured porous materials [2]. The objective of this study is to produce submicron and nanostructured carbides of U to be tested at ISOLDE.

An exploratory work was first carried out with lanthanide (Ln) elements via electrospinning. Acetylacetonate lanthanides, $Ln(acac)_3$, were synthesized for Ln = Eu, Er and Yb and mixed with cellulose acetate. The solutions were then electrospun at positive voltages between 15 and 27 kV, a working distance of 10 cm, and flow rates of 1–5 ml/h. The dried electrospun materials (EM) were subsequently heat-treated at 700 and 800 °C in a flowing argon atmosphere. Scanning electron microscopy (SEM) observations of the EM show that, for the same ratio Ln/C = 4, the spinnability of the solutions is different for the different elements. Micrometric fibers are well formed for the case of Er, while for Eu the fibers are nanometric and exhibited many and large beads. In the case of the Yb no fibers are formed.

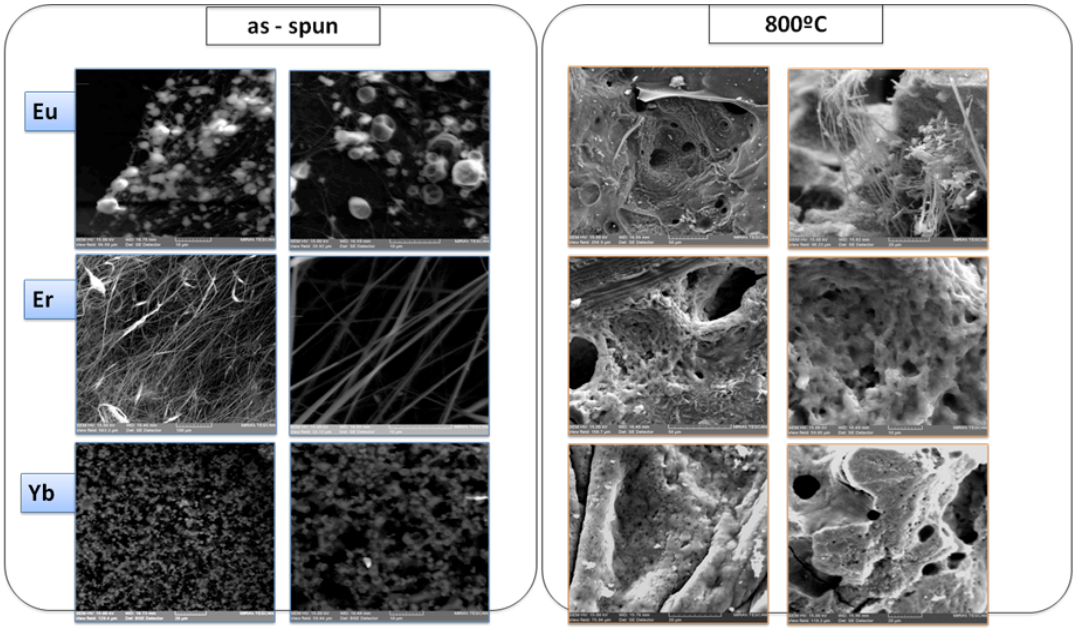

Figure 2. SEM images of the as-spun and heat-treated electrospun materials based on lathanides.

The heat treatment of the EM leads to the densification of the material and to the formation of highly porous samples, with an open porosity and large distribution of pore sizes. X-ray diffractionindicates the formation of LnC_2 for all the studied samples at both temperatures. The estimated average crystallite sizes were 13, 10 and <10 nm for ErC_2, EuC_2 and YbC_2, respectively. Preliminary results point to the possibility of shaping uranium carbides through the same type of precursors. The control over the solution parameters enables the tuning of porosity, surface/volume ratio and permeability of the final material. The results on the uranium materials will be presented and compared with the correspondent lanthanide ones.

References

[1] http://isolde.web.cern.ch/ISOLDE/;

[2] S Fernandes, PhD Thesis, CERN/EPFL (2010);

Acknowledgements

This work was partially supported by FCT, Portugal, under the contract CERN/FP/123588/2011 and the grant SFRH/BD/66161/2009 (M.S. Henriques).

1-32

Numerical Investigation of Interfacial Flow in a Molten Immiscible LiCl-KCl/Cd System

Kwangrag Kim, Jun-Bo Shim, Seungwoo Paek, In-Tae Kim

Korea Atomic Energy Research Institute, Daejeon, Republic of Korea

Agitation is one of the most common and important operations in the molten-salt electrochemical systems. Among these processes, an electrowinning system employing a molten-salt electrolyte and a liquid cadmium cathode has been proposed for the separation of uranium and transuranic elements from fission products. The use of a liquid cadmium cathode, which is the unique features of the process, provides hydro-dynamically a free surface electrode contacting with an immiscible molten-salt electrolyte. This free interface of immiscible liquids gives an electrode interface for carrying an electrical current and is inconstant depending on agitated conditions. A computational method to expect an effective area of the electrode surface in the molten-salt and liquid metal system is particularly interesting and challenging for an agitated operation frequently encountered in the electrowinning system. As a consequence, this study presents a new approach for studying the dynamics of two immiscible molten LiCl-KCl/Cd system, incompressible fluids in the presence of a free surface. The method is capable of tracking a contorting free surface as well as multiple fluid bodies which may be merging or splitting. A new concept of interface markers is introduced in order to enable the tracking of the interface of two (or more) immiscible fluids. An interface capturing scheme based on the volume-of-fluid (VOF) method are used for this approach. The governing equations using the Eulerian-Eulerian approach are solved for the volume fractions and the field variables of the multiphase in a computational fluid dynamics (CFD) platform. Details of the calculation of the velocity fields and free surface profiles which evolve in time are given. Representative simulation results are presented to illustrate the capabilities of this method for the molten LiCl-KCl/Cd system.

1-33

Persistence of the γ-phase in uranium-molybdenum alloy thin films

A M Adamska, T B Scott, R Springell

Interface Analysis Centre, University of Bristol, Bristol, UK

Uranium is a fundamental component of most nuclear fuels. Whilst early fission reactors were using natural uranium metal as fuel material, uranium dioxide (UO_2) became quickly the most diffused nuclear fuel. However, for the next generation of nuclear reactors, the use of metallic fuels is again an option because they offer a uranium density larger than the dioxides, and exhibit properties that promise to improve the fuel performance in terms of sustainability, reliability, and safety. Among uranium alloys, those with e.g. Nb, Mo or Zr are the most promising candidate materials.

Metallic uranium has three crystalline phases: α-, β-, and γ-phase. The α-phase is the room temperature (RT) form of uranium. It is orthorhombic with space group *Cmcm,* and unit cell parameters *a* = 2.854 Å, *b* = 5.87 Å, and *c* = 4.955 Å [1-2]. This phase is not a suitable fuel, because of its poor mechanical and thermal stability under typical reactor operating conditions [3-5]. The tetragonal β-phase of uranium exists between 668 and 775 °C [6]. The high-temperature (*T* > 775 °C) uranium γ-phase is more resistant to irradiation effects than the α-phase. It crystallizes in the body-centred cubic structure, with space group *Im*3*m* and cell parameter *a* = 3.524 Å. Although the γ-phase is not thermodynamically stable under preparation and irradiation conditions, it can be stabilized at RT by the addition of selected transition metals, such as Mo.

In the present study, series of poly- and single-crystal thin films of U-Mo have been grown both on glass and sapphire substrates, using UHV magnetron sputtering at T = 700 °C. In order to prevent oxidation, all U-alloys thin films were capped with a 20-50 nm thick protective layer of Mo or Nb. The crystal structure of the films has been investigated by means of X-Ray Diffraction (XRD) and Electron Backscattering Diffraction (EBSD). Energy-Dispersive X-ray (EDX) analysis was used to find the elemental composition of the materials. The thickness of the films was measured from cross-section analysis using Focused Ion Beam (FIB) and Scanning Electron Microscopy (SEM) techniques.

XRD and EBSD data indicate that for polycrystalline $U_{1-x}Mo_x$ alloys, the pure cubic uranium γ-phase exists for x ≥ 0.26 (12 wt.% Mo), see Fig. 1, whilst pure γ-U single crystals are formed for x ≥ 0.22 (10 wt.% Mo), see Fig. 2. However, a subtle phase stability difference between polycrystalline and single-crystal thin film systems may originate from the uncertainty of the experimental method used for the estimation of U and Mo composition for polycrystalline samples. Below 10 wt.% Mo concentration, the resulting thin film alloys exhibit a mixed α-γ uranium phase composition. To our knowledge this work represents the first report of epitaxially grown γ-U alloy thin films.

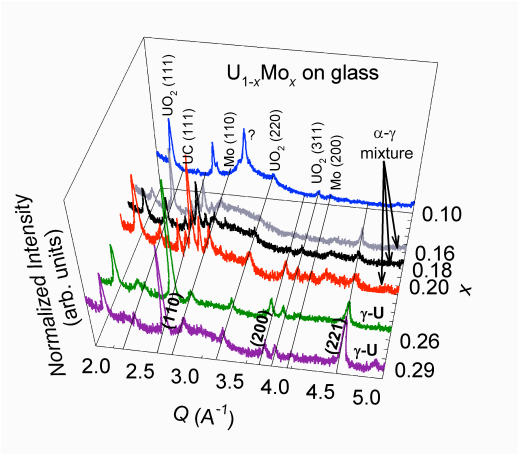

Fig. 1. XRD patterns of $U_{1-x}Mo_x$ alloy thin films deposited on glass at T = 700°C. Mo metal was used as a capping layer.

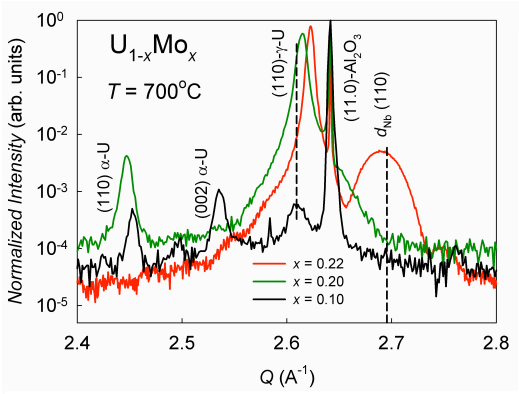

Fig. 2. XRD patterns close to the sapphire (11.0) peak for single-crystal $U_{1-x}Mo_x$ alloy thin films. Nb metal was used as a capping and buffer layer.

References

[1] C. S. Barrett et al., *Phys. Rev.* **129**, 625 (1963).

[2] G. H. Lander et al., *Acta Cryst.* **B26**, 129 (1970).

[3] A. N. Holden, *Physical Metallurgy of Uranium*, Addison-Wesley Pub. Co., USA, (1958).

[4] G. Ostberg et al., *J. Nucl. Mater.* **10 (4)**, 329 (1963).

[5] D. D. Keiser Jr et al., *J. Nucl. Mater.* **393**, 311 (2009).

[6] J. Donohue et al., *Acta. Cryst.* **B27**, 1740-1743 (1971).

1-34

Structure stability of the cubic γ-phase uranium molybdenum alloys

Ilya Tkach[1], Nhu-Tarnawska Hoa Kim-Ngan[2], Silvie Mašková[1], Ladislav Havela[1], Alexander Warren[3], Camilla Stitt[3], Tomhas Scott[3]

[1]Charles University, Prague, Czech Republic, [2]Pedagogical University, Krakow, Poland, [3]University of Bristol, Bristol, UK

We successfully prepared γ-U samples by Mo doping using splat cooling technique, which helps to stabilize the *bcc* structure to room temperature at low Mo levels. All samples were characterized by X-ray diffraction and electron microscopy. Samples with 15 at.% Mo exhibit a pure γ-phase (*bcc* structure), while with 11-12 at.% Mo show a stable γ^o-phase (tetragonal distorted γ-phase) [1]. Impurities of UC and UO_2 mostly segregated at the surface were observed in all samples. We performed phase stability investigation of γ-U as it is considered as a good candidate for low enriched nuclear fuel.

All samples were tested first for stability at ambient conditions. Our results indicate no visible changes on XRD of samples even after 1 year being exposed to air. Thermal stability of splat samples with 12 at.% Mo and 15 at.% Mo was tested by annealing at temperatures 500 °C and 800 °C. At annealing at 500 °C (Fig. 1 a, b), the α(021) reflection appeared after 4 h and increased after 10 h. At the same time the double peaks of initial γ^o-phase for sample with 12 at.% Mo transform into one broad peak of the γ-phase. With further increase of annealing time (72 h), the most intense γ-U peak γ(110) for both samples starts to split into double peaks of γ'-phase (known as U_2Mo) namely γ'(110) and γ'(103). So we can conclude that the γ-U splats are unstable at 500 °C and transform to the mixture of α and γ'-phase.

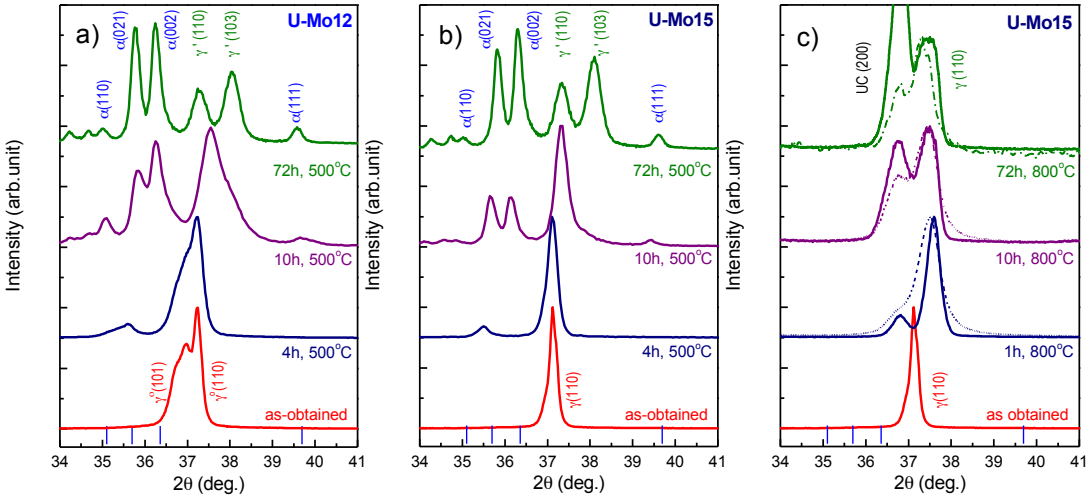

Fig.1. Comparison of (low-angle) XRD patterns of the U-12 at.% Mo and U-15 at.% Mo splat samples in the as-formed state (γ^o and γ respectively) with those upon annealing at 500 °C (a,b) and 800 °C (c) for different annealing times. The (blue) vertical ticks indicate the main reflections of the orthorhombic α-U structure.

When annealing at 800 °C for 4 h, the sample with 12 at.% Mo transforms from γ^o to γ. More annealing time only increases intensity of the UC peaks. Sample with 15 at.% Mo behaves in a similar way, preserving the γ-phase even for 144 h annealing (Fig.1 c). The annealing effect may be in the Mo homogenization.

Hydrogen absorption at room temperature was tested for pure-U splat and γ-phase alloys. While α-U sample quite easily forms β-UH_3 hydride, γ-U samples did not absorb hydrogen at ambient pressure. With increase of hydrogen pressure over 2.5 bar, γ-U samples start to form hydrides with hydrogen concentration 3 H/U atom. On the contrary to known crystalline β-UH_3, which is highly pyrophoric fine powder, our hydrides have the form of 1-5 mm long brittle

dark lamellas (Fig. 2), which are stable at air and have an amorphous structure (Fig. 3) with nanoscale grain size.

Such hydrides were tested by thermally stimulated desorption. Hydrogen release during heating is completed around 450 °C. The sample was characterised by room-temperature XRD after desorption at 800 °C, which indicates the γ-phase and UC, UO_2 impurities. XRD after desorption at 500 °C reveals a mixture of the γ- and α-phase with the same impurities. We can suggest that heating up to 800 °C can cause not only desorption but also phase transformation like during annealing (homogenisation of the γ-phase). On the other side, the desorption at 500 °C also cause transformation of the γ- into the α-phase.

We suggest that crushing the hydride and desorption of hydrogen at 800 °C can be used for the production of γ-phase U-Mo fine powders as alternative to centrifugal atomization [2].

Fig.2. The hydride $UH_3Mo_{0.18}$ (produced from U-15 at.% Mo splat) consists of elongated particles of 1-5 mm long, displayed on a millimetre grid.

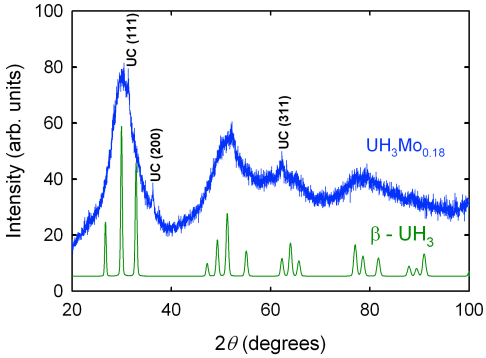

Fig.3. XRD pattern of hydride $UH_3Mo_{0.18}$ (produced from U-15 at.% Mo splat) shows amorphous structure with weak reflections of spurious UC.

Acknowledgements: This work was supported by the Czech Science Foundation under the grant No. P204/12/0285. Experiments were performed at MLTL (http://mltl.eu/), which is supported within the program of Czech Research Infrastructures (project no. LM2011025).

References

[1] I. Tkach, Nhu-T.H. Kim-Ngan, S. Mašková, M. Dzevenko, L. Havela, *J. Alloys Comp.* **101-109**, 534 (2012).

[2] K.H. Kim, D.B. Lee, C.K. Kim, G.E. Hofman, K.W. Paik, *J. Nucl. Mat.* **179-184,** 245 (1997).

1-35

German Joint Research Project on "Conditioning of long-lived Radionuclides in Ceramic Waste Forms" – An Introduction

Stefan Neumeier, Giuseppe Modolo, Dirk Bosbach

Forschungszentrum Jülich GmbH, Institute of Energy and Climate Research - IEK-6: Nuclear Waste Management, Jülich, Germany

The disposal of high level radioactive waste is one of the most pressing and demanding challenges of the 21st century. With respect to long-term safety aspects of geological disposal, the minor actinides (MA) such as Am, Cm and Np and long-lived fission products such as ^{35}Cl, ^{135}Cs, ^{79}Se, ^{90}Sr and ^{129}I may be of particular concern due to their long half-lives, their high radiotoxicity and mobility, respectively. Ceramic waste forms for the immobilisation of these radionuclides have been investigated extensively in the last decades since they seem to exhibit certain advantages compared to other waste forms (incl. borosilicate glasses and spent fuel) such as high loadings and chemical durability [1, 2]. Currently, most on-going nuclear waste management strategies mainly do not include ceramic waste forms. However, it is still important to study this option, e.g. with respect to specific waste streams and certain constraints regarding deep geological disposal.

In the present communication we report on the German Joint Research Project on "Fundamental studies on conditioning of long-lived radionuclides in ceramic waste forms" (funded by Federal Ministry of Education and Research (BMBF 2020+; FN: 02NUK021)) which started in October 2012 and has a duration of three years. The project is established with the overall objective to provide for an advanced understanding of the correlation between the material properties and the crystal structure of actinide containing ceramic waste forms with respect to long-term stability under conditions relevant to disposal in a deep geological repository. The research focuses on single phase ceramics such as monazite, zirconates/hafnates with pyrochlore structure and apatite for the immobilization of the MA and Iodine, respectively and includes:

1.) Development and optimization of synthesis routes suitable for immobilization of MA and Iodine into ceramic waste forms and the handling of radionuclides such as sol-gel route, hydrothermal synthesis and co-precipitation,

2.) structural and microstructural characterisation using state of the art spectroscopic (Raman, TRLFS, EXAFS), diffraction (powder and single crystal XRD) [3] and microscopic (SEM, FIB/TEM) techniques,

3.) determination of thermodynamic stability (calorimetry) and reactivity under conditions relevant to geological disposal, in particular with respect to leaching/corrosion in aqueous environments (static & dynamic dissolution experiments on powders and pellets) as well as

4.) studies on radiation damages (irradiation with α-particles and/or heavy ions, and incorporation of short-lived actinides such as ^{238}Pu, ^{241}Am or ^{244}Cm).

The project provides for experiments combined with atomistic modeling studies for an integration of the various results. Finally, a fundamental understanding of the long-term behaviour on the atomic scale will help to improve the scientific basis for the safety case of deep geological disposal concepts using ceramic materials.

The project is implemented by a consortium with 8 partners from research centres (FZ Juelich, KIT, HZDR/ROBL) which offer the ability to handle required amounts of actinides due to the infrastructure of the labs, universities (RWTH Aachen, Leibniz University of Hannover, Goethe University of Frankfurt) as well as industry (Brenk Systemplanung Aachen).

References

[1] G.R. Lumpkin: Ceramic waste forms for Actinides. Elements, 2006, 2, 365

[2] G. Deissmann, S. Neumeier, G. Modolo, D. Bosbach: Durability of potential plutonium waste forms under repository conditions. Mineral. Mag., 2012, 76(8), 38

[3] K. Holliday, S. Finkeldei, S. Neumeier, C. Walther, D. Bosbach, T. Stumpf: TRLFS of Eu^{3+} and Cm^{3+} doped $La_2Zr_2O_7$: A comparison of defect fluorite to pyrochlore structures. J. Nucl. Mater., 2013, 433, 479

1-36

Non-destructive studies of fuel rodlets by neutron resonance absorption radiography and thermal neutron radiography

Anton S. Tremsin[1], Sven C. Vogel[2], Michal Mocko[2], Mark A. M. Bourke[2], Vincent Yuan[2], Ron Nelson[2], Donald W. Brown[2], Bruce Feller[3]

[1]University of California at Berkeley, Berkeley, CA, USA, [2]Los Alamos National Laboratory, Los Alamos, NM, USA, [3]NOVA Scientific, Inc., Sturbridge, MA, USA

Many isotopes in nuclear materials exhibit strong peaks in neutron absorption cross sections in the epithermal energy range (1-1000 eV). These peaks (often referred to as resonances) occur at energies specific to particular isotopes, providing the means of isotope identification and concentration measurements [1]. The high penetration of epithermal neutrons through most materials is very useful for the studies where samples consist of heavy-Z elements and are opaque to X-rays and sometimes to thermal neutrons as well. The characterization of nuclear fuel elements in their cladding can benefit from the development of high resolution neutron resonance absorption imaging (NRAI), enabled by recently developed spatially-resolved neutron time-of-flight detectors [2]. In this technique the neutron transmission of the sample is measured as a function of spatial location and of neutron energy. In the region of the spectra that borders the resonance energy for a particular isotope, the reduction in transmission can be used to acquire an image revealing the 2-dimensional distribution of that isotope within the sample. Provided that the energy of every transmitted neutron is measured by the detector used and the irradiated sample possesses neutron absorption resonances, then isotope-specific maps can be acquired simultaneously for several isotopes, even in the case where samples are opaque or have very similar transmission for thermal neutrons and X-rays or where only low concentrations of particular isotopes are present (<0.1 atom% in some cases). Ultimately, such radiographs can be utilized to measure isotope concentration and can be combined to produce three-dimensional distributions using tomographic methods.

We present the proof-of-principle NRAI and transmission Bragg edge imaging performed at Flight Path 5 (FP5) at the LANSCE pulsed neutron source of Los Alamos National Laboratory [3]. A set of urania mockup fuel rodlets with intentionally introduced defects was investigated. The maps of elemental composition of rodlets containing urania and tungsten were obtained simultaneously by the resonance absorption imaging with spatial resolution better than ~200 μm, while the voids and cracks were revealed by the transmission images obtained with the thermal and cold neutrons. Our proof-of-principle experiments demonstrate that simultaneous acquisition of resonance and Bragg edge spectra enables concurrent mapping of isotope distributions, imaging of cracks and voids as well as measurements of some crystallographic parameters of fuel rodlets and its cladding. The energy-dispersive neutron radiography results are compared with X-ray and proton radiography characterizations of the same rodlets [4].

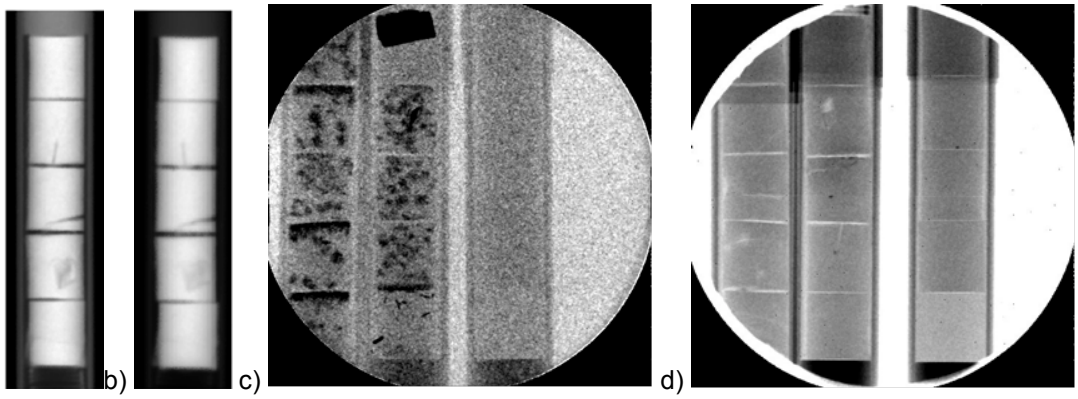

Figure 1. Comparison of proton radiograph (a) and X-ray radiograph (b) of the same set of pellets as well as energy-dispersive neutron radiographs viewed at a neutron energy of a tungsten absorption resonance (c), darkening the locations with tungsten in the beam, and neutron radiograph averaged over the thermal neutron energies from the same measurement, showing density variations. The absolute dimensions of the pellets are the same for all cases, however, different pins where used for (a), (b) and (c), (d).

References

[1] W. E. Lamb, Jr., "Capture of Neutrons by Atoms in a Crystal", Physical Review 55, pp. 190-197 (1939).

[2] A.S. Tremsin, J.B. McPhate, J.V. Vallerga, O.H.W. Siegmund, W. Kockelmann, E.M. Schooneveld, N.J. Rhodes, W. B. Feller, "High Resolution Neutron Resonance Absorption Imaging at a Pulsed Neutron Beamline", IEEE Trans. Nucl. Sci. 59, pp. 3272-3277 (2012).

[3] A.S. Tremsin, S.C. Vogel, M. Mocko, M.A.M. Bourke, V. Yuan, R. Nelson, D.W. Brown, B. Feller, “Non-destructive studies of fuel rodlets by neutron resonance absorption radiography and thermal neutron radiography”, submitted to J. Nucl. Mat. (2013).

[4] C. L. Morris, M. Bourke, D. Byler, C. F. Chen, G. Hogan , J. F. Hunter, K. Kwiatkowski, F. G.Mariam, K. Mcclellan, F. Merrill, D. J. Morley, A. Saunders, “Qualitative Comparison of Bremsstrahlung X-rays and 800 MeV Protons for Tomography of Urania Fuel Pellets”, Rev. Sci. Instrum. 84, 023902 (2013).

1-37

Phase transformation inhibition in Pu-1.9 at.% Ga

Jason Jeffries, J. Bradley, Mark Wall

Lawrence Livermore National Laboratory, Livermore, CA, USA

While the metastable, retained δ-phase of Pu-1.9 at.% Ga is generally the observed phase of this system at room temperature, decreasing temperature will elicit a martensitic phase transformation to the α'-phase, which has a nearly 18% smaller lattice volume than the δ-phase. This phase transformation is characterized by uncommon kinetics, but it also shows a strong sensitivity to previous heat treatment schedules. If a specimen of Pu-1.9 at.% Ga is cycled through the δ–α' transformation and α'-δ reversion without a sufficient high-temperature annealing treatment, then the volume fraction of the α'-phase formed on cooling will rapidly decrease with increased cycling. A simple hypothesis to explain this behaviour is that the δ–α' transformation produces significant lattice defects, dislocations, or strains that are retained even through the α'-δ reversion process. In this scenario, subsequent transformations would then occur in a field of increasing dislocation density, which is presumed to be detrimental to the δ–α' transformation. However, no detailed experimental investigations exist to quantify any detailed behaviour or existence of these putative transformation-inhibiting defects. Here we report experiments using differential scanning calorimetry and transmission electron microscopy that reveal some of the effects of annealing that overcome this phase transformation inhibition. We will discuss likely candidates for phase transformation inhibition as well as their potential relationships with Pu aging.

1-38

X-ray diffraction study of the eutectoid decomposition of γ-U(Mo) powder produced by magnesiothermic reduction.

Guillaume Champion[1,2], Mathieu Pasturel[1], Xavière Iltis[2], Olivier Tougait[1]

[1]ICSR/CSM, UMR 6226, CNRS-Université de Rennes1, Rennes, France, [2]CEA, DEN, DEC, Saint Paul Lez Durance, France

Because of their high uranium density and good irradiation stability, powder of γU(xMo) alloys, (7 < x < 9 wt % Mo) with the high temperature *bcc*-form of uranium are considered as the most promising candidates for the fuel conversion of research and test reactors. Post irradiation examinations experiments pointed out, among other [1, 2], (i) a major role of the decomposition reaction, γU(xMo) → U_2Mo + αU occurring below the eutectoid temperature at about 585°C, on the fission gases behaviors and fuel-matrix interactions, mainly, and (ii) the influence of the microstructures of γ-U(Mo) particles associated to their fabrication process; atomization or grinding. Current research work aims to prepare U(Mo) particles that would meet the requirements for nuclear uses through the development of an innovative route for powder production. We propose a new method of producing γ-U(Mo) particles by using a solid state "chemical reduction-agglomeration" based on the Kroll's process [3]. This alternative process consists in the reduction of uranium dioxide by magnesium in presence of Mo in a sealed Mo crucible heated at temperatures ranging from 750-1100°C for dwell periods ranging from 12 to 48 hours. An appropriate quenching allows to retain the high temperature *bcc*-form γU(Mo). The side products are easily removed by a soaking into a diluted hydrochloric acid solution under sonication. The agglomerates have a typical size in the range 20-100 µm, with an irregular shape. They display even at the periphery equiaxed grains with homogeneous distribution of Mo. In-situ and ex-situ X-ray diffraction experiments were carried out to probe the γ destabilization and phase stability at about 450°C. Our results are compared to the available time-temperature-transformation diagrams for U(xMo) alloys.

References

[1] A. Leenaers et al., *J. Nucl. Mater.* **2011**, *412*, 41.

[2] S. Van den Berghe *et al*., *J. Nucl. Mater.* **2008**, *375*, 340.

[3] G. Champion *et al*., Adv. Eng. Mater., **2013**, 15, 257.

1-39

Selective Actinides Separation Process by Amide Based New Ligands

Shinichi Suzuki, Tohru Kobayashi, Tsuyoshi Yaita, Hideaki Shiwaku

Japan Atomic Energy Agency, Tokai, Ibaraki, Japan

The synthesis and extraction of major actinide (U and Pu) with branched *N,N*-di-alkyl monoamide (BAMA) were carried out. These amide compounds which have branched alkyl substitute and oxygen donor in a molecule are developed as extractants for uranium isolation [1]. Furthermore, *N*-alkyl-*N*-phenyl-1,10-phenanthroline- 2-carboxamide (PTA) are newly developed as extractant for trivalent actinide and lanthanides. These PTA ligands contain two aza-aromatic donors and an oxygen donor in a molecule [2]. The typical BAMA and PTA compounds are shown in figure 1.

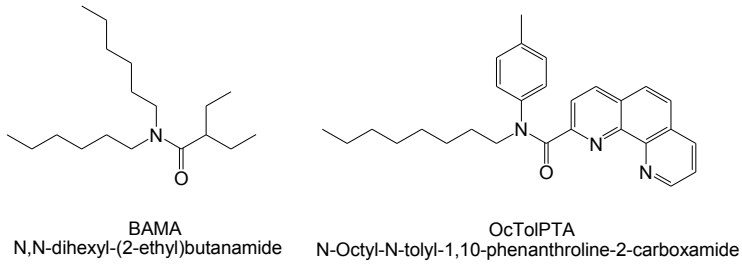

BAMA
N,N-dihexyl-(2-ethyl)butanamide

OcTolPTA
N-Octyl-N-tolyl-1,10-phenanthroline-2-carboxamide

Figure 1 Amide based new ligands investigated in this study.

The main concept of all actinide(An) recovery process is to recover and stock all An and to dispose only fission products (PGM group, lanthanide, etc). The main purpose of this solvent extraction technique using amide based compounds is selective separation of Uranium(VI) BAMA and group separation of Pu-Np-Am-Cm with PTA for FBR and LWR spent fuel treatment.

Since BAMA occurs the steric hindrance on the complexation with metal cations, BAMA can be used to separate An(VI) from An(IV). In this study, we synthesized more than fifth kinds of BAMA for U(IV) isolation. Furthermore we evaluated third phase formation with these BAMA and radiolysis of several kinds of BAMA with gamma-ray irradiation.

In this present process, PTA had important role for all TRU recovery under acidic condition from high level liquid waste. The nitrogen donor ligands like phenanthroline (PHEN) could effectively extract An(III) from Ln(III) with pH solution. However PHEN showed protonation in acidic solution.

To extract An(III) from Ln(III) even high acidic solution, we develop the combination of both nitrogen and oxygen donors has been proposed, which would allow both high extractability and high selectivity for An(III) and An(IV). Based on this concept, we designed and synthesized a novel tridentate ligand, N-alkyl-N-phenyl-1,10-phenanthroline-2-carboxamide (PTA), which exhibits high extractability and selectivity for Am(III) over Eu(III) under acidic condition.

In this presentation, we will show the extraction properties of BAMA and PTA for actinide and fission products in acidic solutions, and the structural property with EXAFS study. In addition, new all actinide recovery process will be also proposed.

References

[1] S. Suzuki, et.al.,*OECD/NEA publication,* NEA6420, III, 150-155 (2010)

[2] T. Kobayashi, et.al., *Sep.Sci.Tech*., 45: 16, 2431-2436(2010)

1-40

Densification of uranium carbide pellets: Preliminary result of spark plasma sintering and comparison with conventional sintering techniques

Olivier Tougait[1], Matthieu Peniel[1], Mathieu Pasturel[1], Odile Merdrignac-Conanec[1], Christophe Lau[2], Sandrine Tusseau-Nenez[2]

[1]ICSR/CSM, UMR 6226, CNRS-Université de Rennes1, Rennes, France, [2]IPN-O, Pôle ALTO, Orsay, France

The binary uranium-carbon phase diagram comprises three intermediate phases (UC, U_2C_3 and UC_2) showing high melting / decomposition points, high thermal conductivity, lack of phase-transformations at temperatures of practical relevance, and good stability under irradiation, which allow their use under extreme conditions. Therefore, uranium carbides are important materials in nuclear R&D projects, either as possible fuel for the Generation IV gas fast reactor (GFR-He), or as target materials at ISOL facilities of the third generation.

The microstructure of nuclear materials plays a major role in determining the working performance. Even for a given composition, changes in microstructure (morphology and grain size, amount of phases, size and distribution of porosity, etc.) result in markedly different behavior. Regarding the next generation of ISOL-facilities, the effective density (i.e. the bulk including only closed porosity) of the target should be as high as possible, in order to make best use of the primary beam. However, for fast and efficient release of the products, a large amount of open pores is needed. Therefore, the optimization of the target yield can only result from a compromise between the density and the porosity.

Spark Plasma Sintering (SPS) combines simultaneously the application of pressure and electric current directly on the sample. Joule heating provides high heating rates and short processing times. Some recent studies [1] show the possibility of using the SPS technique to obtain nanocomposite materials that we are considering to apply for the fabrication of innovative uranium carbide targets.

The present report consists of a parametric study of the synthesis and sintering of uranium carbides (UC and UC_2), and their effects on the microstructure of the final objects. The synthesis of powders of UC and UC_2 was conducted by carboreduction reaction of UO_2 in presence of carbon graphite, in molar ratios between 1:3 and 1:6 at high temperature. The temperature of treatment and their dwell periods range between 1 500 and 1 900 °C and 1 to 30 h, respectively. The samples were analyzed by scanning electron microscopy (SEM) and X-ray diffraction (XRD). The microstructural parameters have been extracted from the diffractograms by Rietveld method and measurement of particle size and specific surface area. The sintering of the pellets was conducted by pressureless heat-treatments ranging from 1 500 to 1 900 °C for 2 h, by hot-pressing under load up to 120 MPa at 1600 °C for 2 h, and by SPS for fast sintering. The microstructure of the densified pellets was analyzed by XRD and SEM. The open porosity was evaluated by combining He pycnometry and geometrical method.

[1] G.D. Zhan *et al.*, Nature Materials, 2 (2003) 38.

1-41

High-temperature experimental study on the U-Mo-C system

Matthieu Peniel, Mathieu Pasturel, Olivier Tougait

Insitut des Sciences Chimiques de Rennes, Rennes, France

Solid phase equilibriums and determination of the isothermal sections of the U-Mo-C diagram, at 1000°C and 1400°C have been recently reported, but this study leaves the solid-liquid relations unresolved. However, this study confirms the formation of two ternary phases: $UMoC_2$ (*Pnma)* and $U_2Mo_2C_3$, (*C2/m)*; and nine binary compounds: UC (*Fm-3m*), α-UC_2 (*I4/mmm*), β-UC_2 (*Fm-3m*), U_2C_3 (*I-43d*), MoC (*P-6m2*), β''-Mo_2C, β-Mo_2C (*P63/mmc*), β'-Mo_2C (Pbcn) and U_2Mo. Regarding the solid-liquid transformations, previous works [2, 3, 4] have established several pseudo binary eutectic points (along the lines $UMoC_2$- β-Mo_2C, $U_2Mo_2C_3$-Mo, $UMoC_2$-Mo, $UMoC_2$-C, UC_2-$UMoC_2$, UC-$UMoC_2$ and UC-$U_2Mo_2C_3$), two ternary eutectics (in the ternary regions $UMoC_2$-C-UC_2 and $UMoC_2$-C $MoC_{0.7}$), one binary peritectic (along UC-γ-U(Mo)) and one ternary peritectic forming the reaction UC + Mo ↔ $U_2Mo_2C_3$ + liq. at 1830°C. Ugajin et al. [3] also reported the congruent melting of $UMoC_2$ at 2350°C. In these studies, however, the temperature range available was limited to 2000°C, calling for further investigation at higher temperatures. Also, the compositions of some of these invariant points are either lacking or estimated from a similar system (U-W-C), and the temperature of the peritectic decomposition of $U_2Mo_2C_3$ is roughly estimated as "above 2200°C".

The present study deals with the solidus and liquidus surfaces, as well as the relevant invariant points in the system. A series of samples with various compositions, prepared by arc-melting, were characterized by thermal analysis using two different methods. Low temperatures events were studied using Differential Thermal Analysis from room temperature to 1600°C. Higher temperature thermal arrests were studied from the cooling curves recorded with an infra-red pyrometer measuring the 800-2500°C range. The pyrometer was calibrated by measuring the melting points of selected metals (Cu, U, Ni, Co, Fe, Cr, Nb). The measurement error was thus established as ±20°C.

The crystallographic composition of the samples was checked by XRD measurements, while elemental analysis and microstructural study were performed using SEM imagery coupled to EDS analyses.

The results of this study establish the peritectic formation of $U_2Mo_2C_3$ at 2290°C, and the temperature and composition of the eutectic points mentioned in the literature. The melting temperature of $UMoC_2$ was found to be slightly higher than previously reported (at 2450°C). It was also found that a previously unreported eutectic valley exists in the three-phase field UC-UC_2-$UMoC_2$.The full results of this study will be presented, along with the solidification behaviour of the U-Mo-C system.

References

[1] M. Peniel, H. El Bekkachi, O. Tougait, M. Pasturel,H. Noël; *Sol. St. Phen., 194 (2013) 26-30.*

[2] W. Chubb, D.L. Keller, Batelle Memorial Intitute Report BMI-1685. (1964).

[3] M. Ugajin, J. Abe, M. Kurihara, *J. Nucl. Sci Tech., 12 (1975) 560-566.*

[4] H. Holleck, *J. Nucl. Mater.*, *124 (1984) 129-146.*

1-42

Pyrochlore – a promising host phase for actinide immobilisation

Sarah Finkeldei[1], Kiel Holliday[2,4], Eva de Visser-Týnová[3], Felix Brandt[1], Stefan Neumeier[1], Giuseppe Modolo[1], Thorsten Stumpf[4], Dirk Bosbach[1]

[1]Forschungszentrum Jülich GmbH, Institut für Energie- und Klimaforschung - IEK-6, Jülich, Germany, [2]Lawrence Livermore National Laboratory, Livermore, USA, [3]NRG, Petten, The Netherlands, [4]KIT, Institut für Nukleare Entsorgung, Karlsruhe, Germany

Zirconate based pyrochlores are very promising host phases for the minor actinides (MA = Np, Am, Cm) and plutonium as they are highly durable against aqueous alteration and radiation damages [1,2]. Pyrochlores are chemically very flexible structures with the general formula $A_2B_2X_6Y$, which are known to form solid solutions. Here, we have focused on ZrO_2 based pyrochlores with A = La, Nd, Eu, Pu, Cm; B = Zr; X = O; Y = O.

Based on a wet chemical synthesis route, which was developed using non-radioactive surrogates, the solid solution formation of zirconia based pyrochlores with Pu and Cm was studied. A simultaneous co-precipitation of the Nd-, Zr- and Pu-hydroxides was applied to yield highly homogeneous pyrochlores. The crystallisation of the $(Nd,Pu)_2Zr_2O_7$ pyrochlore solid solution was carried out during a sintering step under reducing conditions. Several samples with a Pu concentration of 5 mol% or 10 mol% were synthesised. Powder X-ray diffraction (XRD) measurements showed a systematic shift of the reflexes of the pyrochlore with the different Pu contents, indicating the structural uptake of Pu. However, the presence of additional PuO_2 could not be excluded by XRD measurements. Furthermore, scanning electron microscopy (SEM) was carried out on a $Nd_{1.9}Pu_{0.1}Zr_2O_7$ pellet. The SEM images and energy-dispersive X-ray spectroscopy (EDX) confirmed a homogeneous distribution of Pu within the whole pellet.

An insight into the structural environment of MA within the pyrochlore was obtained using time resolved laser fluorescence spectroscopy (TRLFS) [3]. Fluorescence spectra were obtained by UV and direct excitation of Cm and Eu doped $La_2Zr_2O_7$. The observed splitting of the major species after direct excitation indicates the presence of Cm or Eu at the A position of the pyrochlore crystal structure. The maximum splitting of the $^5D_0 \rightarrow {}^7F_{1,2}$ transition for the minor species in the pyrochlore structure is caused by disordered vacancies in the nearby environment of the A position, which are typical for the defect fluorite structure. Zirconia based pyrochlores are known to transform to the defect fluorite structure due to radiation damage. In future studies, the distinction of the defect fluorite and pyrochlore environment may allow the quantification of radiation damages in zirconia based pyrochlores via TRLFS.

References

[1] R.C. Ewing, *C. R. Geosci.*, **343** (2011) 219-229. [2] G.R. Lumpkin, *Elements*, **2** (2006) 365-372. [3] K.S. Holliday, *et al.*, (2013) *J. Nucl. Mater.* **433**, 479-485.

1-43

XRD monitoring of α self-irradiation effects in $U_{1-x}Am_xO_{2\pm\delta}$ mixed-oxides

Denis Horlait[1], Florent Lebreton[1], Thibaud Delahaye[1], Roussel Pascal[2]

[1]CEA, Bagnols-sur-cèze, France, [2]Unité de Catalyse et de Chimie du Solide, Villeneuve d'Ascq, France

The microstructural evolution of several $U_{1-x}Am_xO_{2\pm\delta}$ ($0 < x \leq 0.5$) fluorite solid solutions due to ^{241}Am α-decay were studied with the help of X-ray diffraction, after performing an initial heat treatment under a reducing atmosphere. The variations of lattice parameter, crystallite size and microstrain were determined as a function of the cumulated dose (i.e., as a function of time and x). For the very first self irradiation times, a decrease of the cell volume was unexpectedly determined and corresponds to an initial oxidation of all the samples. Then the unit cell is found to expand with a rate directly proportional to the Am amount and reaches a maximum value of 0.8-0.9% volume relative increase after a time inversely proportional to the sample activity. For the considered experiment time (over a year) and the cumulated dose (over 10^{18} $\alpha.g^{-1}$), the fluorite structure was found to be maintained, though consequent diminutions of the diffraction lines relative intensities of $U_{0.925}Am_{0.075}O_{2\pm\delta}$ and $U_{0.85}Am_{0.15}O_{2\pm\delta}$ have been noted.

1-44

Electronic Structure of Actinide Surface Reactions and Complexes

Krishnan Balasubramanian, Patrick Allen, William McLean II

Lawrence Livermore National Lab, Physical & Life Sciences Directorate,, Livermore CA 94551, USA

This presentation will focus on reactions at actinide surfaces with emphasis on actinide catalysis. Surface and interfacial reactions of actinide materials are critical to understanding of corrosion of these materials. Moreover, 5f-element catalysis is a topic of considerable interest in recent years. Our high-level relativistic computational studies reveal that reactions of molecules such as H_2 at actinide surfaces and interfaces depend on the electronic and topological nature of the surfaces. Computational studies show that whereas UO_2 surface layers are passivating for the reactions toward H_2, this is not the case with U_2O_3 surfaces which are highly catalytically active in promoting the hydriding reactions. The vacancies in U_2O_3 and likewise in the corresponding Pu oxides play an important role in promoting hydriding reactions, as the sites adjacent to the vacant sites are strongly reactive with the H_2 molecule. Our computational studies also provide significant new insight into the role of elemental impurities such as Si, W, Fe,C, Rh, S, C etc., in catalytic activity of uranium material toward H_2 gas. Our computed Laplacians derived from relativistic computations appear to provide significant new insight into the catalytic activities, as shown In Fig. 1.

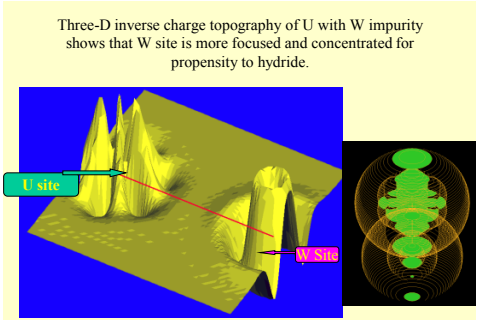

Fig 1 Laplacian Plots of Charge Densities provide insight into catalytic activity of uranium material in the presence of W impurity.

Relativistic computations provide insight into propagation of hydriding reactions, once a site reacts with H_2 molecule forming UH_3. As see from Fig 2, this site acts as a catalytic site for further reactions toward H_2. This presentation will also highlight the role of different impurities, and other surface and interfacial features on actinide hydriding reactions. The dramatic contrast between the catalytic activity of UO_2 versus U_2O_3 is explained with insights derived from charge densities and vacancies in these surface layers.

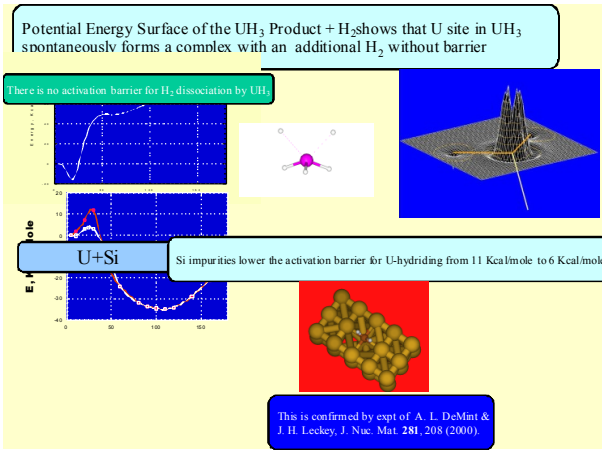

Fig 2 Computational Insights into UH_3 + H_2 reaction and the role of Si elemental Impurity in Hydriding Reactions.

PHYSICS

PLENARY & INVITED

1-01

Signature of Strong Correlations in Actinides and its Compounds: A Dynamical Mean Field Theory Perspective

Gabriel Kotliar

Center for Materials Theory, Department of Physics and Astronomy, Rutgers University, Piscatway, NJ 08854, USA

Plutonium is a unique element, poised at the edge of a localization delocalization transition. Its compounds exhibit remarkable phenomena, ranging from insulating behaviour with a topologically non-trivial band structure in PuB_6 [1] to high temperature superconductivity $PuCoGa_5$ [2]. In the last decade a new paradigm for understanding, modelling and predicting physical properties of these materials has emerged based on realistic implementations of dynamical mean field theory (DMFT) concepts [3, 8,9]. This theory treats the wave (band-like) and the (particle-like) multiconfigurational multiplet aspects of the f-electrons on the same footing. This theory accounts for the volume of δ-Pu in a paramagnetic configuration [6] and predicted its phonon spectra [7].

In DMFT, an underlying self-consistent impurity model can be used to reconstruct local observables of a material. An illustrative example is the valence histogram, describing the weight of each atomic configuration in the ground state of the solid. This important concept, and the resulting prediction for Pu can now be probed experimentally using resonant XES [5] and neutron form factor measurements [11].

There are now many applications by many groups which have extended the reach of this approach to many actinide based compounds. We will review the basis of the DMFT approach and compare some results with selected experiments on 5f electron system. We will conclude with some new directions to face the challenge for material design in this field [10].

References

[1] XY Deng K Haule and G Kotliar preprint (2013).

[2] J. L. Sarrao et al., Nature **420**, 297 (2002)

[3] A. Georges, G. Kotliar, W. Krauth, and M. Rozenberg, Rev. of Mod. Phys. **68**, 13-125 (1996).

[4] Per Soderlind, G. Kotliar, K. Haule, P. Oppeneer, and D. Guillaumont, MRS Bulletin **35** , 883, (2010).

[5] C.H. Booth, Y. Jiang, D. L.Wang, J. N. Mitchell, P. H. Tobash, E. D. Bauer, M. A.Wall, P. G. Allen, D. Sokaras, D. Nordlund, T.-C. Weng, M. A. Torrez, and J. L. Sarrao PNAS **109**, 10205-10209 (2012)

[6] J. H. Shim, K. Haule, and G. Kotliar, Science **318**, 1615-1617 (2007).

[7] X. Dai, S. Y. Savrasov, G. Kotliar, A. Migliori, H. Ledbetter, and E. Abrahams, Science Mag. **300**, 953-955 (2003).

[8] Advances in Physics, **56** (6), 829-926 (2007)

[9] G. Kotliar, S. Savrasov, K. Haule, V. Oudovenko, O. Parcollet, and C. Marianetti, Rev. of Mod. Phys. **78**, 000865 (2006).

[10] Z. P. Yin, Xiaoyu Deng, K. Basu, Q. Yin, G. Kotliar, arXiv:1303.3322 (2013).

[11] M. E. Pezzoli, K. Haule, and G. Kotliar, Phys. Rev. Lett. **106**, 016403 (2011).

2-18

Recent Developments in $PuMGa_5$ and $PuMIn_5$ (M=Co, Rh) Heavy Fermion Superconductors

Eric Bauer

Los Alamos National Lab, Los Alamos, NM, USA

The discovery of superconductivity in $PuCoGa_5$ with a transition temperature of T_c = 18.5 K [1] and its superconducting cousin $PuRhGa_5$ (T_c=8.7 K) [2] has generated renewed interest in Pu-based intermetallic compounds. These $PuMGa_5$ materials belong to the same family of tetragonal $CeMIn_5$ (M=Co, Rh, Ir) heavy fermion superconductors. A variety of measurements have firmly established that the $CeMIn_5$ compounds are unconventional *d*-wave superconductors, most probably mediated by antiferromagnetic spin fluctuations. The physical properties of two new members of this "115" family of superconductors, $PuRhIn_5$ and $PuCoIn_5$, are very similar to those of $CeMIn_5$, shedding new light on the origin on superconductivity in these $PuMIn_5$ materials. In this talk, I will describe what we have learned about this growing family of "Pu115" heavy fermion superconductors over the last decade.

References

[1] J. L. Sarrao et al., Nature **420**, 297 (2002).

[2] F. Wastin et al., J. Phys.: Condens. Matter **15** S2279 (2003).

1-02

Elementary excitations in Uranium Dioxide: Unravelling the tangle

Paolo Santini[1], Stefano Carretta[1], Giuseppe Amoretti[1], Roberto Caciuffo[2], Nicola Magnani[6], Arno Hiess[5], Louis-Pierre Regnault[4], Gerry Lander[3]

[1]Dipartimento di Fisica e Scienze della Terra, Università di Parma, Parma, Italy, [2]European Commission, JRC, Institute for Transuranium Elements, Karlsruhe, Germany, [3]Institut Max von Laue-Paul Langevin, Grenoble, France, [4]SPSMS-CEA/UJF, Grenoble, France, [5]European Spallation Source, Lund, Sweden, [6]KIT, Institute of Nanotechnology, Karlsruhe, Germany

Uranium dioxide is one of the most investigated actinide compounds and it has long been considered an archetype for multi-k ordering and magnetoelastic phenomena. In spite of this, the nature of elementary excitations in its antiferromagnetic phase has been debated since their first investigations by inelastic neutron scattering (INS) [1]. These experiments evidenced well-defined magnetic and vibrational modes whose complex dispersion relations indicated large mutual interactions with resulting hybrid magnon-phonon modes. Subsequent INS experiments [2], including measurements with neutron polarization analysis, provided a detailed picture of the low-energy dynamics. The most astonishing aspect is the presence of qualitative features in the dispersion relations which cannot be explained in terms of any theory based on magnons and phonons. In particular, an entire optical branch of excitations observed in INS should simply not be there and its nature has been unknown for several decades (see Fig. 1).

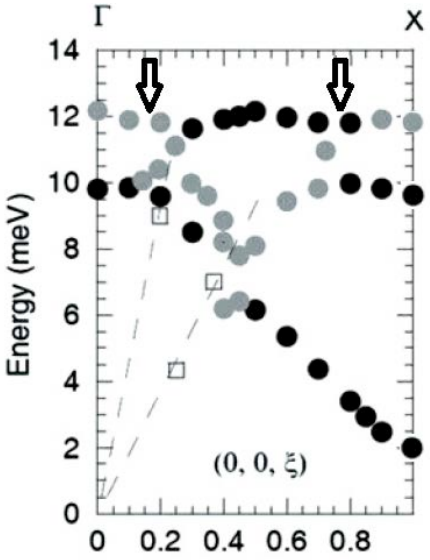

Fig, 1: INS results for elementary excitations in the low-temperature phase of UO_2 along the Γ-X crystallographic direction of the cubic lattice.

Grey symbols indicate qualitatively smaller INS intensity than black symbols. Broken lines and open squares indicate acoustic phonon branches measured at 270 K.

The optical branch indicated by arrows has remained unexplained for a long time. We have demonstrated that this branch and several other anomalous features observed in INS spectra are associated to a new, peculiar type of elementary excitations corresponding to quadrupolar waves (QWs) [3]. These represent a distortion of the charge density distribution of U ions which propagates in the lattice through two-ion quadrupolar couplings. While such exotic collective excitations are expected to be relatively common in systems with active orbital degrees of freedom, they are usually experimentally difficult to access and UO_2 represents the first compound where direct measurements exist. Indeed, since the energy-scale of bare QWs in UO_2 is close to that of bare magnons and phonons, hybridization between these different dynamical modes occurs. Thus, QWs carry along spin and lattice fluctuations. Even a small degree of mixing makes QWs visible in INS as neutrons are scattered by their magnetic or phonon components.

The identification and modelling of these collective excitations sheds light onto the scarcely known world of multipolar two-ion interactions, the nature and form of which usually remain elusive. Indeed, static properties are typically affected by only a few of the many possible microscopic couplings between active quadupoles/multipoles. In particular, when quadrupoles are order parameters in a phase transition, the relative importance of phonons (Jahn-Teller) and exchange (electronic) mechanisms in the phase transition cannot be inferred from static properties. Conversely, in the dynamics, many active multipoles and the detailed microscopic interactions among them play a role, and much more information can be extracted by modelling experimental data on multipolar dynamics, in much the same way as the detailed form of spin exchange couplings can be extracted by modelling spin-wave spectra.

UO_2 undergoes a first-order phase transition at 30.8 K to an ordered structure corresponding to a triple-**k** arrangement of spins and electric quadrupoles. We have calculated the dynamics in this phase by the random phase approximation (RPA) [3], explicitly including spins, quadrupoles and phonons as active dynamical degrees of freedom. It is important that the whole set of phonons (including high-energy optical ones) is considered and realistically modelled (a rigid-ion model was adopted) as even strongly off-resonant phonons qualitatively influence the low-energy dynamics. The Hamiltonian

$$H = H_{SS} + H_{QQ} + H_P + H_{ME} \qquad (1)$$

is the sum of terms corresponding to superexchange dipole-dipole (H_{SS}) and quadrupole-quadrupole (H_{QQ}) interactions, free phonons (H_P), and magnetoelastic phonon-quadrupole couplings (H_{ME}). Dynamical susceptibilities are calculated in RPA by considering fluctuations around the four-sublattice configuration of the triple-k structure. The RPA system is solved numerically and the INS cross section is then obtained from the absorptive part of the dynamical magnetic susceptibility. Within this approximation, phonons act as a transmitting medium for effective two-ion quadrupolar couplings, which can be described in terms of a long-range retarded interaction. This acts in concurrence with superexchange two-ion quadrupolar couplings to propagate quadrupolar fluctuations.

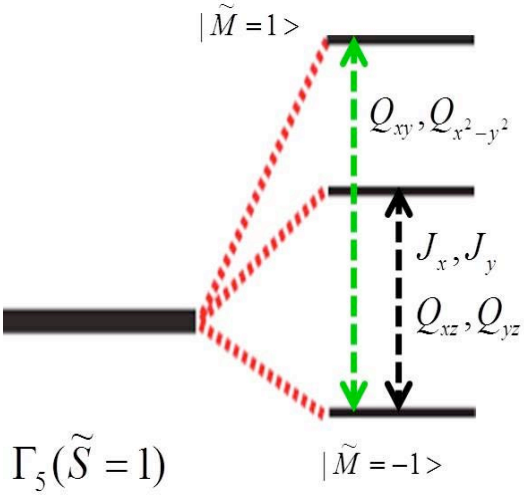

Fig. 2 : splitting of the crystal-field triplet ground state in the ordered phase. One transition is magnetoquadrupolar, the other is purely quadrupolar. Involved quadrupoles are labelled by their symmetry.

The Γ_5 triplet ground multiplet of UO_2 (pseudo-spin s=1) splits in the ordered phase into three singlets (Fig. 2), which result in two classes of excitations at low temperature: magnetoquadrupolar ($\Delta M=1$) and purely quadrupolar ($\Delta M=2$). The propagation of these single-ion excitations by the Hamiltonian Eq. (1) yields optical and acoustical spin-wave and quadrupolar branches, but their character is not pure as these branches mix with one another and all mix with phonons. The degree of mixing strongly depends on the wavevector.

The calculations provide a satisfactory interpretation of INS data (Fig. 3). In particular, the branch indicated by arrows in Fig. 1 corresponds to mostly quadrupolar-optical excitations, whereas other excitations correspond to optical and acoustical spin-waves. Mixing with phonons causes spectacular anticrossings involving all types of electronic excitations. Interestingly, the model predicts the existence of a quadrupolar-acoustical (QA) branch which

had never been observed in INS experiments. Indeed, its mixing with spin-wave modes being tiny, its magnetic INS cross-section is very small (the QA branch is barely visible in Fig. 3).

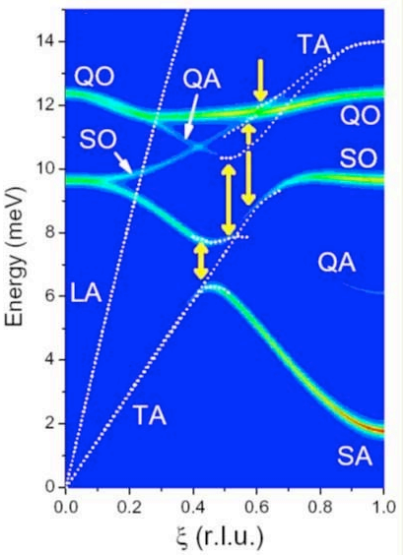

Fig. 3: dipolar magnetic INS cross-section along ΓX calculated by the present model. Dashed white lines show modes with large phonon component and vibrational INS cross section. Arrows indicate anticrossings involving transverse-acoustical phonons on the one hand, and spin-wave and quadrupolar branches on the other hand. In correspondence of these anticrossings, elementary excitations have half phonon character and half electronic character.

The presence of these hidden elementary excitations can be indirectly proved by exploiting the predicted huge anticrossing between QA and phonon modes (second arrow from the left in Fig. 3). For reduced wavevectors close to 0.6, the mixing is maximal and results in two modes

$$\psi_1 \approx \frac{1}{\sqrt{2}}(\mathrm{QA}+\mathrm{TA}) \quad \psi_2 \approx \frac{1}{\sqrt{2}}(\mathrm{QA}-\mathrm{TA})$$

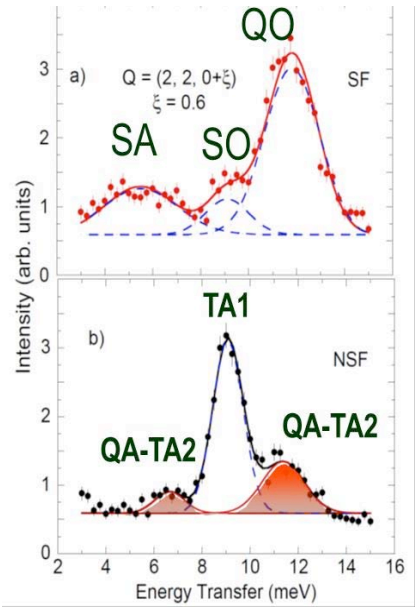

This implies that two peaks in the vibrational INS cross-section should be present in an energy-window where a single peak (bare TA phonon) would be expected.

In order to confirm these theoretical predictions we have performed new INS experiments targeting mixed electron-phonon modes along ΓX [4]. Triple-axis spectrometers have been used to compare neutron scattering intensities in different polarization channels and at equivalent points in different Brillouin zones. In this way, magnetic and phonon characters in excitations have been unambiguously identified.

Fig. 4: Constant-Q energy scan recorded at Q = (2,2,0) + (0,0,0.6) (P||Q; T = 2K). (a) Neutron counts in the spin-flip (SF) channel; individual components of the spectrum are shown by dashed lines. (b) Non-spin-flip (NSF) neutron counts. The central peak at ~9 meV is a transverse acoustic phonon, whereas the weaker peaks at ~ 6.6 meV and ~ 11.4 meV correspond to mixed phonon-quadrupolar acoustic modes.

These experiments have revealed the presence of two additional modes with vibrational character for reduced wavevectors close to 0.6, thus confirming the prediction of the model of a hidden quadrupolar-acoustical branch.

The behaviour of elementary excitations resulting from these recent as well as from previous INS experiments poses strict constraints on the form of the Hamiltonian in Eq. (1). In particular, we can unequivocally quantify the role of Jahn-Teller and superexchange mechanisms in the behaviour of quadrupolar degrees of freedom. Surprisingly (in view of the large anticrossings involving phonons) it turns out that as far as the static quadrupolar order is concerned, superexchange plays the leading role (Fig. 5).

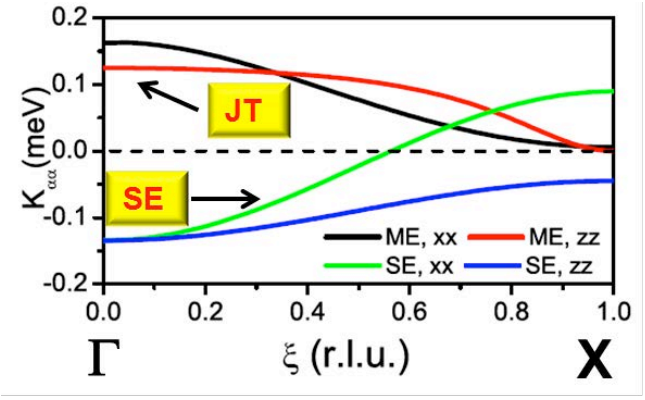

Fig. 5: Fourier transform along ΓX (**q** along z) of static quadrupole-quadrupole couplings arising from superexchange (SE) and Jahn-Teller (JT) interactions. The quadrupole labels are x="yz" y="xz" z="xy". For instance, "xx" means an interaction involving a pair of yz quadrupoles.

In fact, at the wavevector describing this ordering [X-point] Jahn-Teller interactions appear to be nearly vanishing and hence the order is stabilized by superexchange quadrupolar interactions alone. However, Jahn-Teller interactions are important both in the dynamics away from X and in static properties near Γ (macroscopic quadrupolar response).

To conclude, elementary excitations in UO_2 are a tangle of modes with hybrid spin, quadrupole and phonon character. These modes result from a complex interplay between superexchange and magnetoelastic interactions, and their modelling provides an exceedingly detailed picture of the role of quadrupoles in the physical properties. A similar complex role is expected in other systems with unquenched orbital degrees of freedom, notably in actinide compounds with high symmetry. However, additional complications (e.g., conduction electrons or lack of mixing with visible modes) may render the identification of elementary excitations and their theoretical modelling more problematic than in UO_2.

[1] G. Dolling and R. A. Cowley, Phys. Rev. Lett. 16, 683 (1966); R. A. Cowley and G. Dolling, Phys. Rev. 167, 464 (1968).

[2] W. J. L. Buyers and T. M. Holden, in Handbook on the Physics and Chemistry of the Actinides, Vol. 2, edited by A. J. Freeman and G. H. Lander (Elsevier, Amsterdam, 1985);

R. Caciuffo, G. Amoretti, P. Santini, G. H. Lander, J. Kulda, and P. de V. Du Plessis, Phys. Rev. B 59, 13892 (1999); E. Blackburn, R. Caciuffo, N. Magnani, P. Santini, P. J. Brown, M. Enderle, and G. H. Lander, Phys. Rev. B 72, 184411 (2005).

[3] S. Carretta, P. Santini, R. Caciuffo, and G. Amoretti, Phys. Rev. Lett. 105, 167201 (2010).

[4] R. Caciuffo, P. Santini, S. Carretta, G. Amoretti, A. Hiess,, N. Magnani, L.-P. Regnault, and G. H. Lander, Phys. Rev. B 84, 104409 (2011).

1-03

Vibrational properties of the light actinides

Johann Bouchet

CEA, Bruyeres-le-Chatel, France

Despite general interest in f -electron elements, details about their phonon-dispersion relationships are very limited. Experimentally, this fact is due to the great difficulty of realizing such experiments. The usual technique for the study of phonons, based on neutrons scattering, needs crystals large enough and isotopes with a small neutron absorption cross section. Lanthanides and actinides hardly fulfil these two conditions, not to mention the radioactivity of some of them. But recently, a new hope has emerged with several works, using inelastic x-ray scattering, mostly on U [1,2] and Pu [3]. Nevertheless all this experimental issues show that theoretical works are needed to tackle the f electrons systems elastic properties. Unfortunately these calculations are far from being straightforward [4]. Theoretically, the most important problem comes from the difficulty to treat correctly the f-electrons and the relativistic effects needed in such heavy materials. Here we apply the Density functional Perturbation Theory (DFPT) implemented in the ABINIT package to study the phonon spectrum of Th [5], Pa and U [6]. We have also investigated the effect of pressure on the elastic constants of Th, Pa, U and Np. We show how several of the Born stability criteria are violated at the phase transitions occurring in light actinides.

In the α-U phase there are remarkable phonon anomalies in the [100] direction [7], see figure 1. At low temperature (T_0 = 43 K) a phase transition takes place to a new complicated structure (α_1-U), which is described as a charge-density wave (CDW). Uranium is the only element discovered so far to exhibit such a phase transition at ambient pressure. As a function of pressure the CDW disappears at ~1.5 GPa, and, at the same pressure, the superconducting temperature reaches a maximum of ~2 K, and then decreases with further pressure. Using DFPT we calculate the electron-phonon coupling, the phonon linewidth and their evolution in pressure to discuss the interplay of charge-density waves and superconductivity in uranium [8]. The CDW has a strong impact on the elastic properties of uranium[9]. Here we have measured the equation of state of uranium compressed in a DAC up to 60 GPa, with X-ray diffraction, at 298K and 20K (below the CDW transition). The most hydrostatic pressure transmitting medium in this conditions, helium, has been used for these experiments in order to obtain reference EoS parameters (in particular, bulk modulus) suitable for comparison with ab initio calculations. In addition, elastic constants have been calculated for the α_1-U structure at 0K. Using the quasi-harmonic approximation, the temperature effect on α-U lattice parameters and bulk modulus, see figure 2, have been calculated in order to generate an ab initio based 298 K

P−V compression curve. The predictive character of DFT-GGA for the physical properties of uranium is discussed.

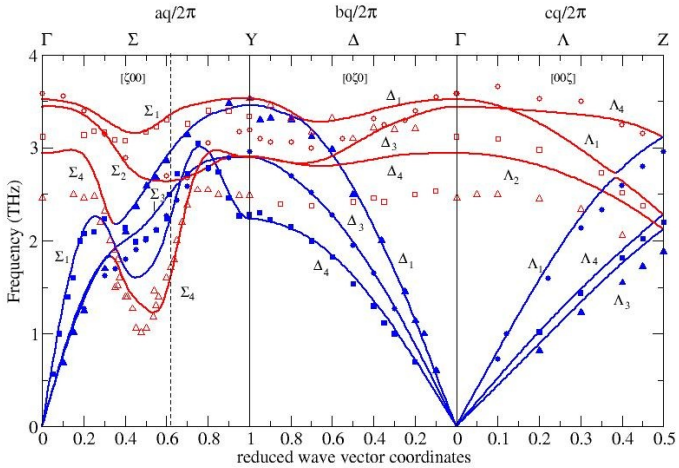

Figure 1. Calculated phonon-dispersion curves for α-U at the lattice parameter corresponding to static equilibrium. Experimental neutron-scattering data are denoted by symbols.

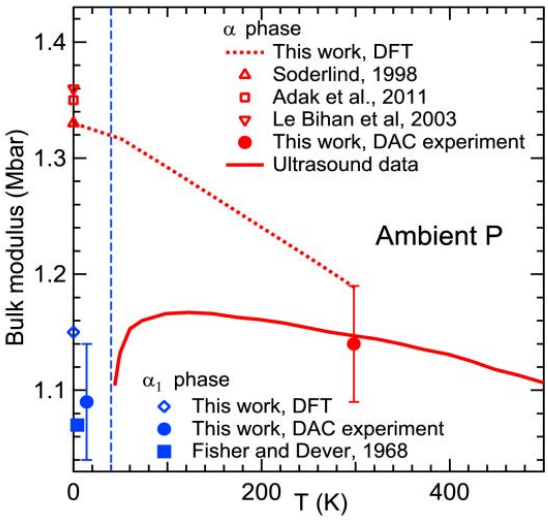

Fig 2. Variation of the bulk modulus of α-U and α_1-Uwith temperature at ambient pressure. Closed symbols and solid lines correspond to experimental data; open symbols and dashed line correspond to theoretical predictions. Ultrasound data for α-U are from Ref. 9. The vertical dashed line delimits the stability domains of α-U and α_1-U.

[1] M.E Manley et al. Phys. Rev. Lett. 86, 3076 (2001).

[2] M.E Manley et al.Phys. Rev. B 67, 052302 (2002).

[3] J. Wong et al. Science 301, 1078 (2003).

[4] X. Dai et al. Science 300, 953 (2003).

[5] J. Bouchet, F. Jollet and G. Zerah Phys Rev B, 74 (2006).
[6] J. Bouchet Phys Rev B, 77 (2008)

[7] W. P. Crummett et al., Phys. Rev. B 19, 6028 (1979)

[8] S. Raymond et al., Phys. Rev. Letter, 107, 136401 (2011)

[9] E. S. Fisher and D. Dever, Phys. Rev. 170, 607 (1968).

1-83

Spins, electrons and broken symmetries: realizations of two channel Kondo physics

Rebecca Flint

Massachusetts Institute of Technology, Cambridge, MA, USA

Actinide heavy fermion materials provide a rich playground to study exotic states ranging from heavy Fermi liquids to hidden order to unconventional superconductivity. The larger 5f orbitals lead to more mixed valency than their rare-earth cousins, with correspondingly higher temperature scales. In this talk, I will review two open problems in actinide physics – hidden order in URu_2Si_2[1] and the emergence of superconductivity out of a Curie paramagnetic state in $NpPd_5Al_2$ [2] and related materials, and argue that these two different broken symmetry states have a common origin in two-channel Kondo physics [3-6].

Introduction

Heavy fermion materials contain two species of electrons: nearly free conduction electrons and strongly interacting f-electrons that are localized at high temperatures. The Kondo effect is an antiferromagnetic interaction through which the conduction electrons screen the local moments to form Kondo singlets, giving rise to a heavy Fermi liquid. Equivalently, the Kondo effect is a hybridization between the two types of electrons. In the *single-channel* Kondo effect, this hybridization is generated by valence fluctuations of the f-ion from a ground state doublet to an excited singlet state, as shown in Fig 1(a). As the excited singlet carries no quantum numbers, it breaks no symmetries and the Kondo effect develops as a crossover. This process is captured in the single-channel Anderson model,

$$H = \sum_{\mathbf{k}} \epsilon_{\mathbf{k}} c^\dagger_{\mathbf{k}} c_{\mathbf{k}} + V \sum_j \left(c^\dagger_j |0\rangle\langle\sigma| + H.c. \right) + \sum_j \epsilon_f |\sigma\rangle\langle\sigma| \qquad 1)$$

where |0> and |σ> represent the empty (excited) and singly-occupied (ground) states of the f-ion. We solve this model by introducing a slave boson, *b* to represent the excited singlet and a pseudo-fermion, f_σ to represent the doublet [7]. The development of a coherent Kondo effect is then captured by the development of <b> at the Kondo temperature, T_K, which decreases the valence, n_f= 1-<b>^{2}. While the mean-field theory mistakenly captures this effect as a phase transition, gauge fluctuations restore its crossover nature.

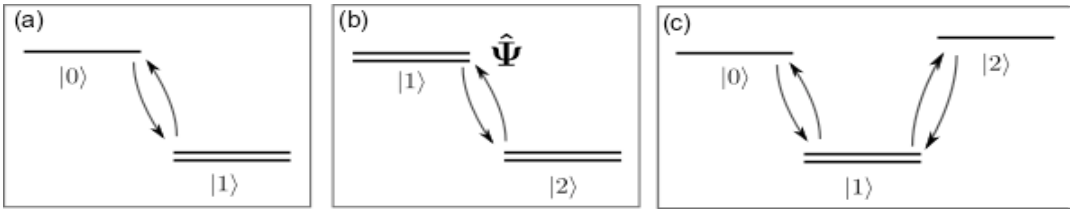

Figure 1: (a) The usual Kondo effect involves virtual valence fluctuations between a Kramers doublet and an excited singlet state (b) Hastatic order involves a non-Kramers doublet fluctuating to an excited Kramers doublet. (c) Composite pairing arises when the Kramers doublet fluctuates to two excited singlets whose charge differs by two.

However, if the excited state is a doublet, which carries a quantum number, the development of Kondo coherence breaks a real symmetry and develops as a phase transition. There are two possibilities, depending on the number of f-electrons in the ground state. Ions with an even number of f-electrons will have a *non-Kramers doublet* ground state – one that can be split by lowering the crystal symmetry, while odd numbers of f-electrons have a *Kramers doublet* protected by time-reversal symmetry. As valence fluctuations involve one electron, a non-Kramers doublet must fluctuate to an excited Kramers doublet with a magnetic quantum number, as shown in Fig 1(b), and the development of hybridization breaks time-reversal symmetry. The resulting state is not conventional magnetic order, although it does involve a

tiny magnetic moment. Instead, it is a *spinorial hybridization* that we have named *hastatic order* [4]. The other possibility is a ground state Kramers doublet, with two excited states that differ by charge 2*e*, as shown in Fig 1(c). If these excited states have similar energies, these form a pseudo-doublet that carries a charge quantum number. The two channel Kondo effect then breaks U(1) charge conjugation symmetry to form a *composite pair superconductor*[5].

Non-Kramers ground state: *Hastatic Order*

The problem of hidden order in URu_2Si_2 is one of the oldest in condensed matter. At high temperatures, URu_2Si_2 looks like a typical heavy fermion material with Ising moments. However, at T_{HO} = 17.5K, it undergoes a mean-field-like phase transition involving nearly one-third of the spin entropy [1]. The order parameter developing at this phase transition has eluded identification for over 27 years, leading to the name “hidden order” [8].

There is currently no consensus on the relevance of itinerant and local physics in URu_2Si_2, or even on the dominant valence of the uranium ion, with various probes suggesting either $5f^2$ or $5f^3$ [9-11]. However, the large magnetic anisotropy seen both in the high temperature susceptibility and in dHvA measurements at low temperatures [12] is difficult to reconcile with a Kramers doublet ground state. The possible non-Kramers doublet [13],

$$|\Gamma_5 \pm\rangle = a|J=4, J_z = \pm 3\rangle + b|J=4, J_z = \mp 1\rangle \qquad 2)$$

Is Ising-like for all *a* and *b,* while the $5f^3$Kramers doublets are Ising-like only for certain values [4]. Therefore, we take the URu_2Si_2 ground state to be a non-Kramers doublet.

Several recent experiments hint that the hidden order is a type of hybridization – STM experiments find that the hybridization gap and the band bending develop at T_{HO}[14,15]; pump-probe optical measurements that find the quasiparticle lifetime increasing sharply below T_{HO} [16]; and dHvA finds that the heavy quasiparticles at low temperatures have a strong Ising anisotropy inherited from the f-electrons[12]. These results indicate that the hidden order is a hybridization between Ising (non-Kramers) f-electrons and (inherently Kramers-like) conduction electrons. The valence fluctuation term capturing this hybridization is,

$$H = V_{\sigma\alpha}|\mathbf{k}\sigma\rangle\langle\alpha| + H.c.$$

where |kσ> represents a conduction electron with spin σ and momentum **k**, |α> represents a Γ_5 state with pseudo-spin α and $V_{\sigma\alpha}$ the hybridization between them. The key difference between Kramers and non-Kramers states is their behavior under double-time-reversal symmetry. Kramers states pick up a negative sign, $|\mathbf{k}\sigma\rangle \xrightarrow{\theta^2} -|\mathbf{k}\sigma\rangle$, while non-Kramers states are left invariant, $|\alpha\rangle \xrightarrow{\theta^2} +|\alpha\rangle$. Since the Hamiltonian is trivially invariant under double-time-reversal, $V_{\sigma\alpha}$ must invert under double-time-reversal, $V_{\sigma\alpha} \xrightarrow{\theta^2} -V_{\sigma\alpha}$, and so $V_{\sigma\alpha}$ transforms like a *spinor*, breaking both single and double-time-reversal. In other words, $V_{\sigma\alpha}$ mixes a half-integer spin state with an integer spin state and must itself carry a half-integer spin. It is this spinorial hybridization that characterizes hastatic order[4].

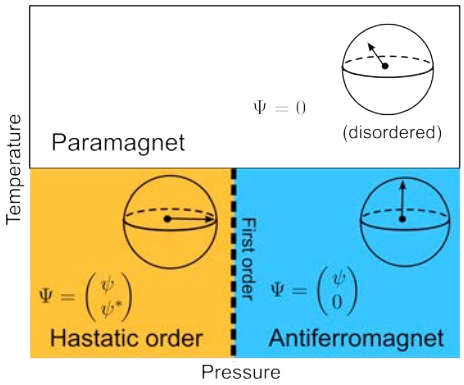

Figure 2: Hastatic phase diagram: the hastatic spinor is disordered in the paramagnet, points in the basal plane in hastatic order and along the c-axis in the antiferromagnet.

When this hastatic spinor orders, it develops not only a magnitude, the usual Kondo effect, but also selects a direction in spin space, breaking both time-reversal and spin-rotation symmetries. If the spinor points along the magnetic c-axis, the resulting state is an

antiferromagnet – actually a *hastatic antiferromagnet* where the large f-electron magnetic moments develop as a consequence of the hybridization, not magnetic ordering (although this state is indistinguishable from a conventional antiferromagnet). If the hastatic spinor instead points in the basal plane, the resulting state has no large moments and strongly resembles the hidden order. This state is *hastatic order*. As hastatic order is related to antiferromagnetism by a rotation, there is a first-order 'spin-flop' transition between the two (Fig. 2).

Hastatic order has several other experimental consequences. As the non-Kramers doublet is protected by tetragonal and time-reversal symmetries, the hybridization breaks both. Broken time-reversal symmetry leads to a staggered basal plane conduction electron moment whose magnitude is limited by T_K/D, where D is the conduction electron bandwidth. Broken tetragonal symmetry has already been found, both as the development of a nonzero χ_{xy} [17] and as a small orthorhombic distortion [18], but only in small crystals.

Kramers ground state: Composite Pair Superconductivity

Composite pairing is generated by the two-channel Kondo effect with two different charges [3,5]. The one-channel Kondo effect forms a Kondo resonance as electrons scatter off the local moments; the second channel allows that resonance to itself resonate between electron and hole channels, creating a condensate of pairs. The involvement of the local moments means that these are *composite pairs*, $\langle c^\dagger_{1\downarrow} c^\dagger_{2\downarrow} S_+ \rangle$ which combine a triplet pair of conduction electrons in two orthogonal symmetries (1 and 2) with a local spin flip to make a charge 2*e* singlet. The particular symmetries of the two channels (determined by crystal fields) determine the symmetry of the pair – for the Ce 115s it is a d_{x2-y2}-like. These singlet, d-wave composite pairs have all the symmetries of a magnetic pair and so the two mechanisms can work in tandem to raise T_c, as shown in the phase diagram of Fig. 3(b) [27]. The presence of a second mechanism in Ce (where $4f^1$ fluctuates to both $4f^0$ and $4f^2$), but not in Yb (where $4f^{13}$ only fluctuates to $4f^{14}$) naturally explains the dearth of Yb superconductors. The second mechanism also explains the two domes in the Ce 115s.

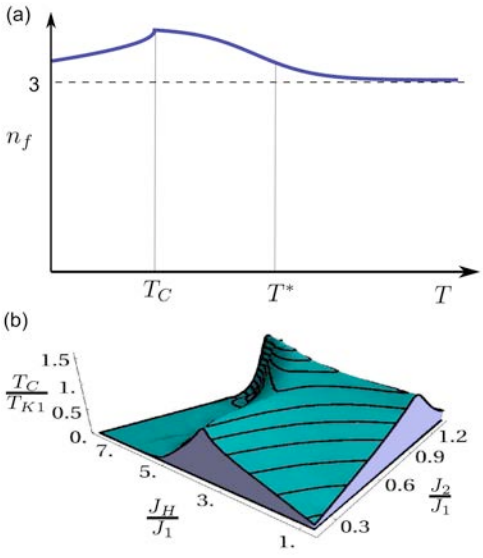

Figure 3: (a) Expected $n_f(T)$ behavior in $NpPd_5Al_2$. (b) Magnetic pairing (favored by the magnetic coupling J_H) and composite pairing (strongest when the two Kondo couplings, J_1 and J_2 are nearly equal) work together to increase T_c.

But if composite and magnetic pairs are identical from a symmetry perspective, how can we tell them apart? There are two key differences – first, composite pairing is a *local* phenomena, taking place mainly within the unit cell, and as such it should be far more robust to disorder on the rare earth sites (which disturb only a single unit cell) than to disorder on the In sites (which disturb multiple unit cells). Secondly, composite pairing is a version of the Kondo effect and so it affects the charge of the f-ion, both as valence and as higher multipole moments of the charge distribution [6]. The valence, $n_f(T)$ changes smoothly through T*, but composite pairing develops at a phase transition and so leads to a sharp kink at T_c. The f-valence can be measured by core-level x-ray spectroscopy in the Ce 115s and the Mössbauer isomer shift in $NpPd_5Al_2$ [28]. Similarly, as the electron and hole channels involve different f-electron orbitals, the composite pair condensate carries a quadrupole moment. This moment also develops sharply at T_c and can be measured with NQR. We estimated the NQR frequency shift to be 5 kHz/K [6], and a shift of this magnitude has been observed in both $CeCoIn_5$ and $PuCoIn_5$[29]. This result is suggestive, but not conclusive. By contrast, $n_f(T)$ provides a conclusive test for composite pairing: in

$NpPd_5Al_2$, the Np^{4+} valence will increase smoothly with decreasing temperature as the ($5f^3 \rightarrow 5f^4$) fluctuations turn on, but then kink sharply downwards at T_c as the ($5f^3 \rightarrow 5f^2$) fluctuations turn on (see Fig. 3(a)). This would be a 'smoking gun' signature of composite pairing.

Conclusions

While hidden order and superconductivity do not initially appear related, they can both be explained by two-channel Kondo physics, where the development of Kondo coherence breaks the symmetry of an excited doublet or pseudo-doublet at a phase transition. For hastatic order, this symmetry is time-reversal, while for composite pairing it is U(1) charge conjugation. The two phases have similar condensation entropies coming from their two-channel Kondo origin, $S \approx \frac{1}{2} R \ln 2$ and similar field dependence as field splits both ground state doublets. In fact, both URu_2Si_2 and $CeCoIn_5$ exhibit quantum critical points at or near their upper critical fields. Variations of the same theme should be relevant in other Pr and U compounds with different doublets, as initially proposed in UBe_{13} for the quadrupolar Γ_3 [30,31]. Another extension is superconductivity in systems like Fig 1(b), but with the ground state and excited doublets switched, as seems likely in UBe_{13}.

References

[1] T.T.M. Palstra et al. Phys. Rev. Lett. 55, 2727 (1985).

[2] D. Aoki et al., J. Phys. Soc. Jpn., 76, 063701 (2008).

[3] P. Coleman, A. M. Tsvelik, N. Andrei and H. Y. Kee, Phys. Rev. B 60, 3608(1999).

[4] P. Chandra, P. Coleman and R. Flint, Nature 493, 621 (2013).

[5] R. Flint, M. Dzero, and P. Coleman, Nature Physics 4, 643 (2008).

[7] P. Coleman, Phys. Rev. B 28, 5255 (1983).

[6] R. Flint, A. Nevidomskyy and P. Coleman, Phys. Rev. B 84, 064514 (2011).

[8] J. A. Mydosh and P. M. Oppeneer, Rev. Mod. Phys. 83, 1301 (2011).

[9] C. Broholm et al, Phys. Rev B 43, 12809 (1991).

[10] J.-G. Park, K. A. McEwen, M. J. Bull, Phys. Rev. B 66, 094502 (2002).

[11] J.R. Jeffries et al., Phys. Rev. B 82, 033103 (2010).

[12] M. M. Altarawneh et al. Phys. Rev. Lett. 108, 066407 (2012).

[13] H. Amitsuka and T. Sakakibara, J. Phys. Soc. Japan 63, 736 (1994).

[14] A.R. Schmidt et al.Nature 465, 570–576 (2010).

[15] P. Aynajian et al, Proc. Natl Acad. Sci. USA 107, 10383–10388 (2010).

[16] G.L. Dakovski et al, Phys. Rev. B 84, 161103(R) (2011).

[17] R. Okazaki. et al. Science 331, 439–442 (2011).

[18] Private communication from Y. Matsuda

[19] H. Hegger et al, Phys. Rev. Lett. 84, 4986(2000).

[20] J. L. Sarrao et al., Nature (London) 420, 297 (2002).

[21] E. D. Bauer et al, J. Phys.: Condens. Matter 24 052206 (2012).

[22] J.L. Sarrao, J. D. Thompson, J. Phys. Soc. Jap. 76, 051013(2007).

[23] J. P. Paglione et al, Nat. Phys. 3, 703 (2007); L. Shu et al, PRL. 106, 156403 (2011).

[24] S. Nakatsuji et al, Nature Physics4, 603 - 607 (2008).

[25] N. D. Mathur et al, Nat. 394, 39 (1998); K. Miyake, S. Schmitt-Rink & C. M. Varma, PRB 34, 6554 (1986); D. J. Scalapino, E. Loh& J. E. Hirsch,PRB 34, 8190 (1986); M. T. Béal-Monod, C. Bourbonnais, & V.J. Emery, PRB. 34, 7716 (1986).

[26] P.H. Frings et al. J. Magn. Magn. Mater. 31, 240 (1983).

[27] R. Flint and P. Coleman, Phys. Rev. Lett. 105, 246404 (2010).

[28] K Gofryk et al, Phys. Rev. B 79, 134525 (2009).

[29] Private communication from H. Yasuoka and G. Kotroulakis

[30] H. R. Ott et al, Phys. Rev. Lett. 50, 1595 (1983).

[31] D.L. Cox, Physica C 15, 1642 (1988).

1-84

Field reentrant superconductivity and Fermi surface instabilities in uranium ferromagnets

Dai Aoki[1,2]

[1]CEA-Grenoble, Grenoble, France, [2]IMR, Tohoku University, Oarai, Japan

We review our recent advances on ferromagnetic superconductors, UGe_2 [1], URhGe [2] and UCoGe [3], where the superconductivity (SC) peacefully coexists with ferromagnetism (FM), forming the spin-triplet state of Cooper pairs. Thanks to a variety of ferromagnetic ordered moments M_0 between three ferromagnetic superconductors, (UGe_2: 1.5 μ_B, URhGe: 0.4 μ_B, UCoGe: 0.05 m_B), striking new phenomena as well as fundamental long-standing issue associated with itinerant ferromagnetism start to be clarified [4].

We focus on the field-reinforced superconductivity, magnetic fluctuations and Fermi surface instabilities. When the field is applied along the hard-magnetization axis (b-axis) in UCoGe and URhGe, the temperature dependence of the upper critical field H_{c2} shows the unusual S-shaped or field-reentrant behaviour [5,6], while for the field along easy-magnetization axis, H_{c2} at 0K remains at the small value close to the Pauli limit. Strong Ising-type magnetic fluctuations are clearly demonstrated by the anisotropic field-dependent effective mass detected by the resistivity, specific heat, magnetization measurements. A paradox is that URhGe shows a spin-reorientation with a step-like magnetization curve at 12T with the first-order transition where the field-reentrant superconductivity appears, while no anomaly is detected in magnetization on UCoGe, but resistivity, thermopower, Hall effect indicate the anomaly around 14T. In UCoGe, not only the magnetic fluctuation but also the associated Fermi surface instabilities play a important role for the field-reinforced superconductivity, forming the spin-triplet state [7]. The similarity with a low-carrier superconductor URu_2Si_2 is discussed.

References

[1] S.S. Saxena, et al.: Nature 406 (2000) 587.

[2] D. Aoki, et al.: Nature 413 (2001) 613.

[3] N.T. Huy, et al.: Phys. Rev. Lett. 99 (2007) 067006.

[4] D. Aoki and J. Flouquet: J. Phys. Soc. Jpn. 81 (2012) 011003.

[5] F. Levy, et al.: Science 1343 (2005) 309.

[6] D. Aoki, et al.: J. Phys. Soc. Jpn. 78 (2009) 113709.

[7] D. Aoki, et al.: J. Phys. Soc. Jpn. 80 (2011) 013705

2-19

5f electron correlations and core level photoelectron spectra of actinide compounds

Gertrud Zwicknagl

TU Braunschweig, Braunschweig, Germany

Actinide-based intermetallic compounds exhibit highly complex phases with unusual phenomena at low temperatures [1]. Prominent examples are the formation of heavy fermions, unconventional superconductivity, unusual magnetism, "hidden order" as well as their co-existence. The anomalies observed in numerous observables originate from the strongly correlated electrons in the partially filled 5f shells of the actinide ions. The electronic properties of actinide compounds are determined by the competition between the tendency towards delocalization of the 5f electrons via hybridization with extended conduction electrons and the tendency towards localization reflected in the formation of local moments.

The central focus of the present study are the core level spectra of actinide compounds. The key idea is to exploit the different screening behavior of localized and itinerant electrons to decide whether and to which extent the 5f-states can be considered as localized (atomic-like)

or itinerant (band-like). The theoretical work has been motivated by recent experiments [2] which showed that the core level spectra of U compounds exhibit rich structures with a wide yet systematic variation from compound to compound.

A comprehensive microscopic understanding of the spectral line shapes is still missing. Ejima et al. [3] analyzed the core-level spectra of various U compounds within the

Kotani-Toyozawa (KT) model [4] assuming two different final states. Okada[5], on the other hand, emphasizes the necessity to include several final state configurations and to account for 5f-5f-exchange effects.

In the present paper, we calculate the core level spectra of actinide intermetallics adopting the Gunnarsson-Schönhammer (GS) [6] ansatz. As the core level spectral line shapes are essentially determined by the local electronic structure in the immediate vicinity of the actinide sites impurity models should be appropriate. The central focus are multiplet effects which are fully accounted for by diagonalization of the Coulomb matrices for the various configurations. The influence of intra-atomic correlations can be seen by comparing the resulting spectral line shapes to those obtained from an averaged Coulomb repulsion.

For a microscopic description, we adopt the single-impurity Anderson-like model

$$H = H_f + H_{band} + H_{hyb} + H_c + H_{cf}$$

where the three components H_f, H_{band}, and H_{hyb} describe the 5f states, the conduction electrons and the mixing or hybridization between the two, respectively. The dynamics of the core level and its interaction with the f-states are accounted for by H_c and H_{cf}. Let us first discuss H_f which describes the 5f electrons. It is given by

$$H_f = \varepsilon_f \sum_{jz} f^\dagger_{jz} f_{jz} + H_{f\,Coul}$$

where the orbital energy ε_f determines the f-valence of the ground state of the isolated ion. The usual fermionic operators $f^\dagger_{jz}(f_{jz})$ create (annihilate) an electron in the 5f-state with total angular momentum j=5/2 and z-projection j_z. Considering the fact that the spin-orbit splitting is large we neglect contributions from the excited spin-orbit multiplet j=7/2 and adopt the j-j-coupling scheme. The local Coulomb repulsion is then given in terms of the Coulomb matrix elements which can be expressed in terms of the usual Clebsch-Gordan coefficients and the Coulomb parameters U_J. The intra-atomic correlations which are the focus of interest in the present paper involve the anisotropic parts of the Coulomb interaction which are (usually) not screened and hence retain their atomic values. As we expect the anisotropic Coulomb parameters to be rather robust with respect to changes in the chemical composition or to pressure we use fixed values for the differences U_4-U_0=-3.79eV, U_2-U_0=-2.72 eV which were

determined from an ab initio calculation for UPt_3 [7]. For the present calculations, we adjust the isotropic part of the Coulomb interaction so as to reproduce an averaged repulsion <U>=2.5 eV. A similar value was used to quantitatively analyze Th spectra [8,9] and in the model calculations [5]. The resulting Coulomb parameters are $U_0$5=5.68eV, U_2=2.96eV and U_4=1.89eV.

The weakly correlated conduction bands are described by

$$H_{band} = \sum_{n\mathbf{k}\sigma} \varepsilon(n\mathbf{k}) c_\sigma^\dagger(n\mathbf{k}) c_\sigma(n\mathbf{k})$$

where $c_\sigma^\dagger(n\mathbf{k})$ $(c_\sigma(n\mathbf{k}))$ creates (annihilates) a conduction electron in a state with band index n, wave vector **k** and spin projection s whose energy is denoted by $\varepsilon(n\mathbf{k})$. Finally the coupling between the two subsystems involves the hybridization matrix elements

$V_{jz\ s}$ (n**k**). When analyzing a specific material, realistic conduction bands and hybridization matrix elements can be deduced via Down-Folding from standard band structure calculations based on Density Functional Theory (DFT). For the model studies presented here we use typical values for the averaged hybridization strengths. We neglect the band index and keep only those conduction electron degrees of freedom which couple to the impurity [6,10] assuming an energy-independent (anisotropic) hybridization parameters V_{jz}.

The dynamics of the core level is described by

$$H_c = \varepsilon_c nc = \varepsilon_c F\dagger F$$

where $F\dagger(F)$ creates (annihilates) a 4f-state at the actinide site. The core level interacts with the 5f-states through

$$H_{cf} = -U_{fc}(1 - n_c)\sum_{jz} n_{fjz}$$

We choose U_{fc}=5.4eV and e_c=388eV.

The central quantity to be considered here is the core level photoemission current. Within the sudden approximation, the latter is directly related to the core spectrum

$$\rho_c(\omega) = -\frac{1}{\pi}\lim_{\eta\to 0}\mathrm{Im}\ g_c(\omega + i\eta)$$

which can be calculated from the expectation value of the resolvent

$$g_c(z) = \left\langle \Psi_0 \middle| F\dagger\left(\mathrm{z} - \mathrm{E}_0(\mathrm{N}) + H\right)^{-1} F \middle| \Psi_0 \right\rangle$$

Here E_0 (N) and denote the energy and wave function Y of the N-particle ground state.

The core spectra are calculated by Exact Diagonalization of the Molecular Model

(MM) [11,12] also referred to as Zero Band Width Anderson Model [13] which provides a basis for qualitatively understanding the anomalous properties of Ce and Yb compounds. The simplifying assumptions underlying the model can be justified since the occupied band width of the conduction states is comparable to or smaller than the average Coulomb interaction. The ansatz is supported by the fact that the ground state properties predicted by the MM agree well with those obtained from a variational ansatz for finite band width. For a detailled comparison see [14]. The properties chosen for discussion include ground state energy,

the 5f-valence, the relative weights of the $5f^n$-configurations as well as the (anisotropic) orbital-dependent renormalization of the hybridization[15]. The results [16] indicate that (a) a careful description of the intra-atomic correlations is important and (b) the orbital-selective renormalization of the bare hybridization in the ground state should be reflected in the line shapes.

We first demonstrate the influence of Coulomb correlations on the core hole spectral line shapes for fixed isotropic hybridization. We include also the reference calculation at fixed 5f-count assuming uncorrelated 5f-states which hybridize with uncorrelated conduction states. In the spirit of the Density Functional Theory (DFT) the 5f-level position at fixed hybridization is chosen so as to reproduce the given 5f-valence [12]. The spectra for uncorrelated 5f-electrons exhibit many lines corresponding to the presence of many different configurations in the mean-field ground state (see e. g. [17]). The weights of the lines reflect the probabilities for the various configurations which are essentially given by combinatorics in the uncorrelated state. It can be seen that the spectra are narrowed by the Coulomb repulsion. This reflects the suppression of charge fluctuations. Intra-atomic correlations which are included by keeping only the diagonal matrix elements of the Coulomb matrices and finally by diagonalizing the full Coulomb matrices remove degeneracies and affect the relative weights of the lines. In a second step, we allow for anisotropic hybridization where the intra-atomic correlations may strongly reduce subdominant channels. Our results confirm that the anisotropic orbital-selective renormalization of the hybridization should be reflected in the spectral line shapes.

It is tempting to speculate that the conjectured “dual” character of the 5f electrons [18] could be tested by analyzing the fine structure of core level spectra. The central hypothesis of the dual nature model is that the low-energy properties of many U-based heavy fermion compounds can be described assuming band-like delocalized 5f-derived quasi-particles which co-exist with localized 5f moments. This simplified picture reflects the orbital-selective renormalization of the hybridization. It has been shown that the dual model allows for a quantitative description of the renormalized quasi-particles - the heavy fermions - in UPd_2Al_3 and UPt_3 [19,20].

To allow for a more quantitative analysis, the calculations are extended in several respects. It is of particular importance to include effects which tend to broaden the actual spectra. First and foremost, a realistic description of the conduction electrons, i. e., their DOS and their hybridization with the U 5f-states is included by using information from standard ab-initio electronic structure calculations. Second, the description of intra-atomic correlations will be generalized by using intermediate coupling. Finally, shake-up processes as described by the KT theory are accounted for.

References

[1] P. Thalmeier and G. Zwicknagl, in: Handbook on the Physics and Chemistry of Rare Earth, volume 34, pages 135--287, (Elsevier B. V., 2005)

[2] Shin-ichi Fujimori et al., J. Phys. Soc. Jpn. **81**, 014703 (2011)

[3] T. Ejima et al., Phys. Ref. B **53**, 1806 (1996)

[4] Akio Kotani and Yukata Toyozawa,J. Phys. Soc. Jpn. **35**, 1073 (1973); **37**, 912 (1974)

[5] Kozo Okada, J. Phys. Soc. Jpn. **68**, 752(1998)

[6] O. Gunnarsson and K. Schönhammer, Phys. Rev. B **28**, 4315 (1983)

[7] G. Zwicknagl et al., Phys. Rev. B **65**, 081103(R) (2002)

[8] O. Gunnarsson et al., Phys. Rev. B **32**, 5499 (1985)

[9] D. D. Sarma, et al., , Z. Phys. B - Condensed Matter **63**, 305 (1986)

[10] A. Bringer and H. Lustfeld, Z. Phys. B - Condensed Matter **28**, 213 (1977);

H. Lustfeld and A. Bringer, Solid State Commun. **28**, 119 (1978)

[11] Peter Fulde, Joachim Keller, and Gertrud Zwicknagl, in: Solid State Physics Vol. **41**, edited by F. Seitz, D. Turnbull, and H. Ehrenreich (Academic Press, New York, 1988);

[12] Erich Runge and Gertrud Zwicknagl, Ann. Phys. **5**, 333 (1996)

[13] A. C. Hewson, The Kondo Problem to Heavy Fermions, (Cambridge University Press, 1993)

[14] Gertrud Zwicknagl, Mat. Res. Soc. Symp. Proc. Vol. 1444 (2012)

[15] E. Runge et al., Phys. Rev. B **69**, 155110 (2004); D. V. Efremov et al., Phys. Rev. B **69**, 115114 (2004)

[16] Gertrud Zwicknagl, Phys. Status Solidi B **250**, 634 (2013)

[17] J. Hubbard, Proc. Roy. Soc. **A276**, 238 (1963)

[18] A. Grauel et al., Phys. Rev. B **46**, 5818 (1992); Andrei Galatanu et al., J. Phys. Soc. Jpn., **74**, 1582 (2005); A. Hiess et al., Physica B, Condensed Matter **378**, 748 (2006); N. K. Sato et al., Nature, **410**, 340 (2001)

[19] G. Zwicknagl et al., Phys. Rev. B **65**, 081103(R), (2002); Phys. Rev. B**68** , 052508 (2004)

[20] G. Zwicknagl and P. Fulde, J. Phys. Condens. Matter **15**, S1911 (2003); P. Fulde, P. Thalmeier, and G. Zwicknagl, in: Solid State Physics Vol. **60**, edited by Henry Ehrenreich, Frans Spaepen, (Academic Press, New York, 2006)

2-20

Diverse nature of 5*f* electrons in cage-compounds UT_2Zn_{20} and UT_2Al_{20}

Przemyslaw Swatek, Dariusz Kaczorowski

Institute of Low Temperature and Structure Research, Polish Academy of Sciences, Wroclaw, Poland

For more than half a century, uranium-based intermetallics have continuously attracted much scientific interest for their unusual physical properties. A point of controversy that despite many efforts has not been unambiguously solved until now is the nature of the 5*f* electronic states, which are responsible for magnetism in these materials. It is generally believed that in uranium intermetallics the 5*f* electrons are essentially itinerant, with the only fairly well-established exception being UPd_3 [1] Nevertheless, for several compounds, including heavy-fermion superconductors UPt_3 and UPd_2Al_3, one observed some features of the localized behavior, which accompany their predominantly itinerant electron characteristics [2]. Therefore, a theory of the dual character of the 5*f* electrons was formulated [3], which successfully accounted for most of the experimental data.

The apparent scarcity of uranium-based materials where the 5*f* electrons can be treated as purely localized makes the search for such systems very appealing. Recently, an important discovery in this field was reported in the literature [4,5], namely that of the localized magnetism in the compounds UCo_2Zn_{20} and URh_2Zn_{20}. The two phases belong to a family of Zn-rich ternaries RT_2Zn_{20}, well known for their spectacular physical properties when *R* is a rare-earth atom (*T* stands for a *d*-electron transition metal) [6-9]. The localized character of the 5*f* electrons in these compounds might be a consequence of expected negligible direct *f*-*f* magnetic exchange interactions (the shortest U-U distance is about 6 Å) and very weak *f* - ligand hybridization (the uranium atoms are located in a cage-like nearly-spherical polyhedron made by sixteen Zn atoms with closed outer electronic shells). Both phases, UCo_2Zn_{20} and URh_2Zn_{20}, were characterized in Refs. 4 and 5 as heavy-fermion compounds with paramagnetic ground states, and their properties were interpreted in terms of the Anderson impurity model in the single-ion Kondo limit. Moreover, an ionic-like electronic configuration of the uranium atoms was supported by the crystalline electric field effects recognized in the experimental data.

Contrary to the *localized* paramagnetic behavior claimed for UCo_2Zn_{20} and URh_2Zn_{20}, the isostructural compound UIr_2Zn_{20} was found by the same researchers to be an *itinerant* heavy-fermion system that orders ferromagnetically at 2.1 K [4,10]. Interestingly, the transition to the long-range ordered region was established to have a first-order character. Another member of the UT_2Zn_{20} family with *itinerant* 5*f* electrons is the compound URu_2Zn_{20}, which was recently characterized as a paramagnetic heavy-fermion material with strong effect of antiferromagnetic spin fluctuations [11].

In contrast to the UT_2Zn_{20} ternaries, the isostructural Al-based counterparts UT_2Al_{20} (*T* = Ti, V, Nb, Ta) were found to exhibit Pauli paramagnetism with strongly *delocalized* 5*f* electrons [12]. Fairly surprisingly in this context, for UCr_2Al_{20} a ferromagnetic-like behavior was reported to set in below 180 K [13]. Also in UMn_2Al_{20} a ferromagnetic order was encountered, yet at much lower temperature of 17.5 K [14]. Most unexpectedly, the onset of a long-range ferromagnetic state, clearly evident in the magnetization data, was not observed in the temperature variations of the specific heat and the electrical resistivity of the compound. This unusual behavior was interpreted in Ref. 14 within two different pictures: *local-moment* magnetism induced in a singlet-triplet system or small-moment *itinerant* ferromagnetism. In both scenarios, the magnetism in UMn_2Al_{20} was associated with the uranium atom sublattice.

The intriguing findings of the entirely different nature of the 5*f* electronic states in the closely related compounds motivated us to undertake our own investigation on the UT_2Zn_{20} and UT_2Al_{20} ternaries [15-20]. Our research was performed on high-quality single-crystalline specimens, which were studied in broad ranges of temperature (down to 350 mK) and magnetic field strength (up to 9 T) by means of comprehensive magnetic, electrical transport and thermodynamic measurements. The main focus was at elucidating the actual nature of the 5*f* electrons in the entire series of these intermetallics. Remarkably, our results differ in several key aspects from those reported in the literature.

First of all, according to our results, all the UT_2Zn_{20} exhibit *itinerant* character of the 5*f* states [15,17,18]. They are heavy-fermion materials with moderately enhanced electronic specific heat [170-400 mJ/(mol K^2)] and pronounced Kondo lattice effect. All of them remain paramagnetic down to 350 mK. However, an increasing tendency for magnetic ordering along the series $UFe_2Zn_{20} \rightarrow URu_2Zn_{20} \rightarrow UOs_2Zn_{20} \rightarrow UCo_2Zn_{20} \rightarrow URh_2Zn_{20} \rightarrow UIr_2Zn_{20}$ may be anticipated from the calculated values of the Wilson ratio. The studied single crystal of UIr_2Zn_{20} was found paramagnetic down to the lowest temperatures studied, at odds with the ferromagnetic behavior reported in Refs. 4 and 10. The intriguing features of the Co-, Rh- and Ir-bearing phases are broad maxima observed at low temperatures in the temperature variations of the magnetic susceptibility and the specific heat over temperature ratio [15,18]. These anomalies likely arise due to spin fluctuations (antiferromagnetic correlations localized in *k*-space) in the systems of itinerant 5*f* electrons. Within the proposed scenario, the maxima manifest metamagnetic-like transitions, similar to those observed before for archetypal paramagnetic heavy-fermion compounds like $CeRu_2Si_2$ [21] and UPt_3 [22], and recently also for the Yb-based ternaries YbT_2Zn_{20} (*T* = Co, Rh, Ir) [23], isostructural counterparts to UT_2Zn_{20}. The absence of such features in UFe_2Zn_{20} and URu_2Zn_{20} [15,17] can be rationalized by considering the effect of *f–d* hybridization that is likely much stronger in these two compounds than in UCo_2Zn_{20}, URh_2Zn_{20} and UIr_2Zn_{20} because of larger numbers of d holes in the electronic shells of the transition metal ligands.

As regards UCr_2Al_{20}, the compound was established to be a Pauli paramagnet with moderately enhanced magnetic susceptibility and electronic contribution to the specific heat, arising primarily due to the 3*d* electronic shell of chromium [19]. For UMn_2Al_{20}, our bulk magnetic measurements and polarized neutron diffraction experiments [20], corroborated the ferromagnetic ordering in this compound that sets in below T_C = 17.5 K, as reported in Ref. 14. However, at odds with the previous presumptions, the magnetic properties of this material have been established to arise due to the presence of magnetic moments on the manganese-atom sites, while the uranium-atom sublattice remains nonmagnetic. Actually, the uranium contribution to the magnetism of UMn_2Al_{20} seems reflected just in an enhanced temperature-independent magnetic susceptibility, which is of the order of magnitude of the Pauli paramagnetism observed for UCr_2Al_{20} [19] and the other UT_2Al_{20} aluminides with *T* = Ti, Nb, and Ta [12].

References

[1] Y. Baer, H. Ott, and K. Andres, Solid State Commun. **36**, 387 (1980).

[2] T. Takahashi, N. Sato, T. Yokoya, A. Chainani, T. Morimoto, and T. Komatsubara, J. Phys. Soc. Jpn. **65**, 156 (1996).

[3] G. Zwicknagl and P. Fulde, J. Phys. Condens. Matter **15**, S1911 (2003).

[4] E. Bauer, J. Thompson, J. Sarrao, andM. Hundley, J. Magn. Magn. Mater. **310**, 449 (2007).

[5] E. D. Bauer, C. Wang, V. R. Fanelli, J. M. Lawrence, E. A. Goremychkin, N. R. de Souza, F. Ronning, J. D. Thompson, A. V. Silhanek, V. Vildosola *et al.*, Phys. Rev. B **78**, 115120 (2008).

[6] M. S. Torikachvili, S. Jia, E. D. Mun, S. T. Hannahs, R. C. Black, W. K. Neils, D. Martien, S. L. Bud'ko, and P. C. Canfield, Proc. Natl. Acad. Sci. USA **104**, 9960 (2007).

[7] S. Jia, S. L. Bud'ko, G. D. Samolyuk, and P. C. Canfield, Nat. Phys. **3**, 334 (2007).

[8] S. Jia, Ni Ni, G. D. Samolyuk, A. Safa-Sefat, K. Dennis, H. Ko, G. J. Miller, S. L. Bud'ko, and P. C. Canfield, Phys. Rev. B **77**, 104408 (2008).

[9] S. Jia, Ni Ni, S. L. Bud'ko, and P. C. Canfield, Phys. Rev. B **80**, 104403 (2009).

[10] E. D. Bauer, A. D. Christianson, J. S. Gardner, V. A. Sidorov, J. D. Thompson, J. L. Sarrao, and M. F. Hundley, Phys. Rev. B **74**, 155118 (2006).

[11] C. H. Wang, A. D. Christianson, J. M. Lawrence, E. D. Bauer, E. A. Goremychkin, A. I. Kolesnikov, F. Trouw, F. Ronning, J. D. Thompson, M. D. Lumsden, Ni Ni, E. D. Mun, S. Jia, P. C. Canfield, Y. Qiu, and J. R. D. Copley, Phys. Rev. B **82**, 184407 (2010).

[12] S. Niemann, and W. Jeitschko, J. Solid State Chem. **114**, 337 (1995).

[13] K. Okuda, S. Noguchi, Y. Nakazawa, and M. Ishikawa, J. Phys. Soc. Jpn. **58**, 4296 (1989).

[14] C. H. Wang, J. M. Lawrence, E. D. Bauer, K. Kothapalli, J. S. Gardner, F. Ronning, K. Gofryk, J. D. Thompson, H. Nakotte, and F. Trouw, Phys. Rev. B **82**, 094406 (2010).

[15]P. Swatek and D. Kaczorowski, J. Phys. Soc. Jpn. **80**, SA106 (2011).

[16] M. Daszkiewicz, P. Swatek, and D. Kaczorowski, J. Alloys Compd. **517**, 26 (2012).

[17] P. Swatek, and D. Kaczorowski, J. Phys.: Condensed Matter **23**, 466001 (2011).

[18] P. Swatek, M. Daszkiewicz, and D. Kaczorowski, Phys. Rev. B **85**, 094426 (2012).

[19] P. Swatek and D. Kaczorowski, J. Solid State Chem. **191**, 191 (2012).

[20] P. Wisniewski, P. Swatek, A. Gukasov, and D. Kaczorowski, Phys. Rev. B **86**, 054438 (2012).

[21] P. Haen, J. Flouquet, F. Lapierre, and P. Lejay, J. Low Temp. Phys. **67**, 391 (1987).

[22] P. H. Frings and J. J. M. Franse, Phys. Rev. B **31**, 4355 (1985).

[23] Y. Hirose,M. Toda, S. Yoshiuchi, S. Yasui, K. Sugiyama, F. Honda, M. Hagiwara, K. Kindo, R. Settai, and Y. Onuki, J. Phys.: Conf. Ser. **273**, 012003 (2011).

3-97

Observation of ^{239}Pu NMR in $PuO_{2-\delta}$ – Facts and Perspective –

Hiroshi Yasuoka, Geogios Koutroulakis, Scott Richmond, Kirk Veirs, Eric Bauer, Joe Thompson, Jarvinen Gordon, David Clark

Los Alamos National Laboratory, Los Alamos, NM, USA

In actinide compounds, Nuclear Magnetic Resonance (NMR) studies have been forced to limit their scope to nuclei associated with ligand atoms. The only exception of direct observation of NMR in actinide nuclei is that of ^{235}U NMR in UO2. There have been extensive efforts to realize NMR in actinide compounds since the electronic properties of these materials are predominantly governed by the actinide atom itself.

We report the first observation of NMR signal on the ^{239}Pu nucleus in any material. Our ^{239}Pu NMR measurements were performed on plutonium dioxide, PuO_2, for a wide range of external magnetic field values (Ho = 3 ~ 8T) at a temperature of T = 4K. By mapping the external field dependence of the measured resonance frequency, we determined the nuclear gyromagnetic ratio to be $^{239}\gamma_n(PuO_2)$ = 2.856 ± 0.001 MHz/T. Assuming a free ion value for the Pu^{4+} hyperfine coupling constant, we estimated a 'bare' value of $^{239}\gamma_n$ = 2.29 MHz/T for the ^{239}Pu nucleus, hence a nuclear magnetic moment of $\mu_n = 0.15\mu_N$ (where μ_N is the nuclear magneton). Our findings put an end to a fifty-year long search for Pu NMR and open potentially a new horizon for the solid state physics, nuclear materials science and complex chemistry in Pu compounds. In this talk, we will also discuss the NMR/NQR work relented to Pu based superconductors and chemical complexes.

3-98

High quality single crystal growth and electronic state investigation of actinide intermetallic compounds

Yoshinori Haga

Japan Atomic Energy Agency, Tokai, Ibaraki, Japan

Recent progress in high quality single crystal growth and experimental investigation on electronic states of actinide intermetallic compounds will be reviewed. Among them, the tetragonal $HoCoGa_5$-type compounds are well known for their unconventional superconductivity and magnetic orderings. In particular, we focus on the magnetic ground state and its relationship to average atomic radius of actinide atom. On the other hand, $ThCr_2Si_2$-type compounds are attracting attentions because of unusual behavior. The occurrence of the hidden-order state in URu_2Si_2 and superconductivity coexisting with it are extensively studied using an extremely high quality single crystal. Finally discovery of new intermetallic actinide compounds will be mentioned. As an example, an allotrope was found in $NpGa_3$ by utilizing low-temperature crystal growth using Ga flux. All these characteristics are closely related to 5f electronic states responding to physical or chemical environments.

4-25

Magnetic circular dichroism with x-rays and electrons

Jan Rusz

Department of Physics and Astronomy, Uppsala University, Uppsala, Sweden

X-ray magnetic circular dichroism (XMCD; [1]) is today an established experimental probe of atom-specific magnetic properties. In XMCD experiment a photon of well-defined energy is absorbed by an atom with a probability that is proportional to the number available unoccupied states with an energy that allows fulfilling the energy conservation. The energy E of photon is absorbed and an electron inside the sample is excited from an occupied state to an unoccupied state with energy difference equal to E. These transitions are modulated by energy-dependent dipole matrix elements, which reflect the selection rules in the excitation process. Thanks to these dipole matrix elements a deeper insight into the local electronic structure can be gained by tuning the polarization of the beam of photons. Specifically, using the circularly polarized photons one can probe magnetic properties of atoms by measuring a difference of the x-ray absorption for right-handed and left-handed circularly polarized photons. This effect relies on spin-orbital splitting of the initial states, e.g., in actinides the 3d electrons split into $3d_{3/2}$ and $3d_{5/2}$ and transitions from these to unoccupied 5f final states gives rise to M_4 and M_5 absorption edges. Second condition to observe XMCD is naturally a magnetic moment in the studies electron shell. In the case of $M_{4,5}$ edges in actinides, we study the magnetism of 5f electrons. An essential element for the success of XMCD are so called sum rules [2,3], which relate the energy-integrals of the XMCD spectra to the local magnetic moments – the spin and orbital angular momenta, respectively.

We will review our recent results of measurements and simulations of XMCD spectra on Np and Pu-based Laves phases, such as $NpAl_2$, $NpFe_2$, $NpOs_2$ and $PuFe_2$ [4]. Electronic structure calculations of XMCD and their comparison to experimental data provide means to probe for the most likely scenario of the description of electronic structure. Our calculations are based on density functional theory using static LSDA+*U* method. While a good match is obtained for the shape of the XMCD spectra, the local magnetic moments obtained by theory are not in satisfactory agreement with experimental ones. More sophisticated dynamical models might provide a better match for the electronic structure of these strongly correlated materials.

Recently, a new experimental method has been developed that is closely related to XMCD. It was named electron magnetic circular (or chiral) dichroism (EMCD) and it is measured with a transmission electron microscope (TEM) instead of a synchrotron beam-line. We will review the short history of this method starting from its proposal in 2003 [5], first experimental proof-of-the-concept in 2006 [6], formulation of the theory [7] and sum rules [8,9] in 2007 to the present state-of-the-art and early applications, for example [10,11]. Despite many efforts, EMCD is still in its development phase, particularly from the point of view of quantitative studies. On the other hand, qualitative EMCD experiments have reached resolutions below 2nm [12].

The main advantages of the EMCD, when compared to XMCD, are costs, availability and lateral resolution. Even a state-of-the-art TEM is a device considerably cheaper than a synchrotron beam-line and as such it can be available locally to a research group. The resolution of TEM reaches routinely sub-nanometer resolution (although for EMCD effect this range is yet to be accomplished). TEM is also a very versatile instrument that combines diffraction experiments, elemental analysis, local electronic structure studies via electron energy loss spectroscopy and now also magnetism.

At present, the major disadvantage is low signal to noise ratio. Optimization of the strength of EMCD signal leads to a requirement of single-crystalline specimen oriented in specific Bragg condition. A further complication then arises from the dynamical diffraction effects, which can be rather complex, rendering the optimal sample orientation and detector position system specific. Fortunately, these effects are well described by state-of-the-art theories. Needless to say, for EMCD experiments on crystalline specimen theory plays an indispensable role for its capability to predict an optimal experimental geometry.

The basic principle of EMCD is in fact very similar to XMCD. A probe particle – an electron in the case of EMCD – interacts inelastically with an atom in the sample. As a result, an electron in the sample is excited into an unoccupied level. The interaction between the two electrons happens via an exchange of virtual photon. An EMCD experiment focuses on optimization of the measurement conditions in such a way that we preferentially generate transitions with certain handedness of circular polarization of the virtual photon. As for XMCD, also in EMCD we need to measure at least two spectra, from which a difference is related to the magnetic signal. It has been shown experimentally that x-ray absorption spectroscopy and electron energy loss spectroscopy provides analogic insight into the electronic structure. This analogy extends also for the EMCD.

In the case of TEM measurements the intensity of the core-level edges drops down rapidly with the energy of such transitions. Therefore, in order to study the 5*f* electron shell in actinides, it would be optimal to probe the $N_{4,5}$ edges, i.e., 4*d*->5*f* transitions. The energy of corresponding transitions is of the order of 700-800eV. It is similar to the $L_{2,3}$ edges of transition metals measured in the EMCD literature.

As an outlook, we suggest that EMCD can become a valuable complementary tool to probe magnetic properties of actinides. Going beyond EMCD, TEM measurements are not limited to dipole transitions. In fact the non-dipole transitions can constitute a substantial contribution to the electron energy loss spectra, leaving also a specific trace in the diffraction plane [13]. This may allow detection of quadrupole, octupole or higher order multipole transitions – adding to the already high versatility of the TEM.

References

[1] J. L. Erskine, E. A. Stern, Phys. Rev. B **12**, 5016 (1975)

[2] B. T. Thole, P. Carra, F. Sette, and G. van der Laan, Phys. Rev. Lett. **68**, 1943 (1992).

[3] P. Carra, B. T. Thole, M. Altarelli, and X. Wang, Phys. Rev. Lett. **70**, 694 (1993).

[4] F. Wilhelm, R. Eloirdi, J. Rusz, R. Springell, E. Colineau, J.-C. Griveau, P. M. Oppeneer, R. Caciuffo, A. Rogalev, G. H. Lander, arXiv:1303.2496 [cond-mat.str-el].

[5] C. Hebert, P. Schattschneider, Ultramicroscopy **96**, 463 (2003)

[6] P. Schattschneider, S. Rubino, C. Hebert, J. Rusz, J. Kunes, P. Novak, E. Carlino, M. Fabrizioli, G. Panaccione and G. Rossi, Nature **441**, 486 (2006).

[7] J. Rusz, S. Rubino, and P. Schattschneider, Phys. Rev. B **75**, 214425 (2007)

[8] J. Rusz, O. Eriksson, P. Novak, P. M. Oppeneer, Phys. Rev. B **76**, 060408(R) (2007).

[9] L. Calmels, F. Houdellier, B. Warot-Fonrose, C. Gatel, M. J. Hÿtch, V. Serin, E. Snoeck, and P. Schattschneider, Phys. Rev. B **76**, 060409(R) (2007).

[10] Z. H. Zhang, X. F. Wang, J. B. Xu, S. Muller, C. Ronning, and Q. Li, Nature Nanotech. **4**, 523 (2009).

[11] Z.Q. Wang, X.Y. Zhong, R. Yu, Z.Y. Cheng, and J. Zhu, Nature Comm. **4**, 1395 (2013).

[12] P. Schattschneider, M. Stoeger-Pollach, S. Rubino, M. Sperl, Ch. Hurm, J. Zweck, and J. Rusz, Phys. Rev. B **78**, 104413 (2008).

[13] J. Rusz, S. Rubino, O. Eriksson, P. M. Oppeneer, K. Leifer, Phys. Rev. B **84**, 064444 (2011).

4-26

Fundamental magnetic interaction in actinide-based nanomagnets

Nicola Magnani

Institute of Nanotechnology, Karlsruhe Institute of Technology (INT-KIT), Karlsruhe, Germany

A single-molecule magnet (SMM) is a zero-dimensional complex which can retain all or part of its magnetization *M* for a long period of time after the external magnetic field *H* used to magnetize it is removed. Under these conditions, the *M*(*H*) curve for each single molecule displays an hysteresis cycle similar to that of a bulk permanent magnet; however, instead of the coercivity associated with domain-wall motion in a three-dimensional structure, the hysteresis of a SMM arises from the slow relaxation which results from bistable magnetic configurations at the molecular level. In other words, once the external field is reversed or removed, the fast direct transition between the non-equilibrium magnetized state and the ground state is forbidden and a different, usually thermally-activated pathway must be followed (Fig. 1), which can become long at low temperatures.

The crystal-field potential describes the splitting of electronic levels due to the ligands which surround the magnetic ion in question and, together with exchange interaction, is the main responsible for providing the anisotropy barrier which results in slow magnetic relaxation. The combined effect of crystal field and spin-orbit coupling determines the splitting of the lowest-energy term, and consequently the nature of the electronic ground state.

For 3*d* systems the crystal field is stronger than the spin-orbit coupling, and it usually selects an orbital singlet ground manifold within the lowest-energy *LS* term; in this situation the orbital moment is effectively quenched and the spin-orbit interaction is not active to first order, therefore the magnetic ion can be regarded as having a pure spin moment. During the first decade of SMM research, the main strategy to improve the anisotropy barrier (and therefore figures of merit such as the blocking temperature) was to increase the total spin of the molecule by increasing the number of magnetic centers as well as their individual spins; this implied sticking with transition metals of the 3*d* group since the radial extension of their unfilled electronic shell is very large, which in turn usually translates to a strong magnetic exchange. The anisotropy itself, though, is generally not very favorable for this class of elements, since spin-only moments are not affected by the crystal-field potential (the main source of magnetic anisotropy in good-performance bulk permanent magnets).

Rare earths, on the other hand, conserve the orbital degrees of freedom due to the fact that the electronic repulsion (which maximizes the spin and orbital atomic moment as stated by the first and the second Hund's rules) is much larger than the crystal field; in addition, the spin-orbit interaction maintains the spin and orbital components parallel in the ground multiplet, therefore maximizing the magnitude of the total moment J. It is therefore not surprising that the effective barrier which was measured for the first lanthanide-based SMM to be reported, $[Pc_2Tb]^-\cdot TBA^+$ (Pc = phthalocyanine dianion; TBA = $N[C_4H_9]_4$) [1], was larger than for any 3*d*-based SMM to date. This complex is made by a single Tb center "sandwiched" between two Pc rings, hence the definition of "single-ion magnet" (SIM) was coined.

The first actinide-based complex for which slow magnetic relaxation was reported is the trivalent-uranium-based SIM $U(Ph_2BPz_2)_3$ [2]. The zero-field peaks in the Im(χ) curves only amount to a very small fraction of the total susceptibility and clear deviations from linearity in the Arrhenius plot indicate that the possible cause are direct relaxation processes due to the transverse ligand-field terms; nevertheless, the effective relaxation barrier U_{eff} = 20 cm^{-1} and the lifetime $\tau_0 = 1\times10^{-9}$ s extracted from the ac susceptibility measurements by fitting the linear part with an Arrhenius-type law are comparable with those of several typical SMMs. Shortly thereafter, the same group published a thorough investigation of the closely related dihydrobispyrazolylborate complex $U(H_2BPz_2)_3$, which has a lower anisotropy barrier but displays two distinct and well-resolved relaxation domains visible in the Cole-Cole plot [3].

In order to reduce the direct tunneling processes which are apparently hindering slow relaxation, several groups reported experiments on the organometallic cyclooctatetraenyl (COT) sandwiches belonging to the actinocene family. The neutral uranocene $U(COT)_2$ displays a D_{8h} local symmetry at the magnetic site and its ligand-field Hamiltonian for 5*f* electron is therefore purely axial; however, it contains U(IV), which is a non-Kramers ion and

has the tendency to prefer a non-magnetic singlet ground state. To maintain the favourable $5f^3$ configuration of trivalent uranium, the magnetic behavior of its anionic analog, i.e. of a $K[U(COT)_2]$ complex, was probed instead. However, ac measurements did not detect a sizeable relaxation barrier, the most likely cause being a lowering of the local symmetry at the uranium site caused by the influence on the K^+ cation on the molecular structure of the complex, giving rise to transverse crystal-field terms which lead in turn to fast direct relaxation processes. We therefore turned our attention to the next member of the actinocene row, $Np(COT)_2$ or neptunocene [4], since the latter maintains its D_{8h} symmetry while displaying a formal $5f^3$ configuration on its tetravalent neptunium site and a $|M_J \pm 5/2\rangle$ Kramers' doublet ground state; moreover, dc susceptibility measurements suggest that the lower excited states may be about 1400 cm^{-1} above the ground doublet, which could translate into a huge energy barrier against magnetic relaxation in absence of other effective channels. However, even in this case only a small ac peak is observed without any static external magnetic field, although 0.5 tesla are enough to make this behavior change completely. Even if no ligand-field transverse terms are present, in fact, the electronic ground-state doublet can interact with the nuclear moment of ^{237}Np via the hyperfine interaction, and this gives rise to several crossing points which are expected to provide very fast relaxation pathways in a way similar to quantum tunnelling of the magnetization. Under a 7 tesla magnetic field the Zeeman splitting of the electronic doublet is for most orientations so large that the hyperfine coupling becomes ineffective; indeed, the Arrhenius curve for this field is linear and practically vertical. As a result of these peculiar magnetic properties, the measured magnetization curve for neptunocene displays partial hysteresis starting from saturation as soon as the magnetic field is decreased, but immediately closes back to the original curve at lower fields as soon as the fast relaxation kicks in (Fig. 2).

Together with anisotropy, magnetic exchange is an essential feature of transition-metal SMMs because it combines the relatively low spin-only moments of several *3d* ions into a "giant spin" ground state, which can make quantum tunneling processes very unfavourable in a sufficiently axial anisotropy. In contrast, as discussed above, most of the research results on lanthanoid-based complexes focused on single-ion magnets, where the required large moment is generated by the unquenched orbital contribution (which is parallel to the spin in heavy rare earths). One must also consider that the radial extension of the unfilled 4f shell of lanthanoid ions is much smaller with respect to the open 3d shell of transition metals, so the strength of superexchange interaction is expected to be much smaller in the former case; in fact, when it is present either its effect are restricted to low temperatures or another ingredient such as an active radical is required to enhance it [5,6]. The 5f shell of actinoid ions is considered to be close to a crossover in this respect, due to a radial extension which is much larger than for lanthanoids but at the same time retains most features of localized electrons as opposed to the largely itinerant nature typical of transition metals. It is therefore natural to wonder if this can somehow be used to realize actinide-based SMMs with improved properties. Whereas the dinuclear U(III) complexes with slow magnetic relaxation reported so far tend to display negligible superexchange interaction [7], we have recently found a large magnetic coupling in a U(V)-based dimetallic with a very short U-U distance [8]. Some high-symmetry U(V) compounds have also proven extremely useful in estimating the f-electron contribution to bonding [9], which of course plays a crucial role in determining the magnetic exchange [6]; this is especially important in view of the fact that a U(V)-based complex has recently been reported to display SIM properties despite its relatively low magnetic moment [10].

The only molecule amongst those reported so far which displays both slow magnetic relaxation at zero field and sizeable intramolecular superexchange interaction and whose magnetic centers are all actinide ions is the heterovalent Np-based trimetallic $\{Np^{VI}O_2Cl_2\}\{Np^{V}O_2Cl(thf)_3\}_2$ [11]. The ground states on each magnetic center of this triangle-shaped complex are determined by the axial ligand field, but clear signs of superexchange coupling are visible in the dc susceptibility curves below 20 K (Fig. 3). The dominant superexchange interaction is an antiferromagnetic coupling between the two Np^{V}-Np^{VI} pairs (J_{ex} = -10.8 K), while the interaction between the two Np^{V} centers is much smaller (of the order of 0.5 K). Interestingly, this peculiar configuration seems to give rise to an effective ferromagnetic coupling (the upturn in the χT curve); the reason why this happens is that the

Np^{V} ions carry a much larger ground-state moment than Np^{VI}, so that the dominant AF interaction actually favors a “parallel” alignment of their two spins. Nevertheless, the effective barrier U_{eff} = 140 K extracted from the Arrhenius law is larger than the superexchange splitting and therefore points toward a basically single-ion origin of the slow relaxation, involving Orbach processes. In the foreseeable future, actinide-based SMM research will likely increasingly involve heterometallic 3d-5f [12] or 4f-5f [13] systems, following the very interesting properties of some 3d-4f complexes [14].

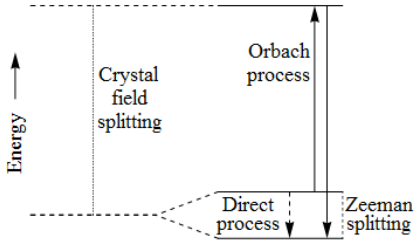

Fig. 1: Scheme of the main mechanism leading to slow relaxation in f-electron-based complexes. The axial part of the crystal-field potential isolates a ground-state doublet with a large M_J value so that under a Zeeman splitting the direct relaxation process (dashed arrow) is forbidden. Instead, the magnetization can relax through a thermally-activated Orbach process, following the path indicated by full arrows: excited crystal-field states are populated by the absorption of phonons with the right energy, until the system reaches a level which is connected to the ground state by an allowed transition. Direct processes are the equivalent of quantum tunnelling of the magnetization in 3d-metal clusters, and when they are strictly forbidden the observed energy barrier U_{eff} is at least as large as the splitting between the ground and the lowest excited crystal-field levels.

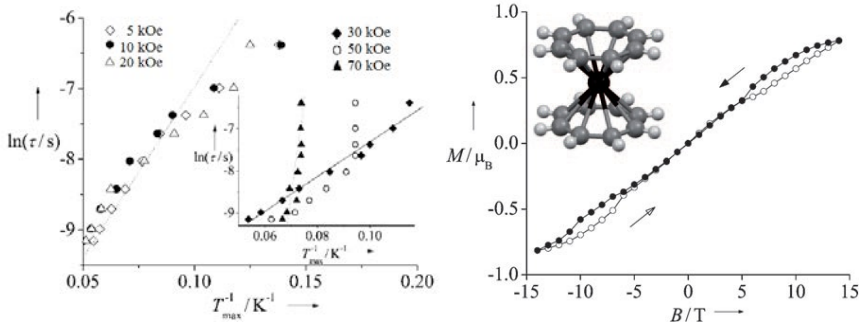

Fig. 2: Magnetic properties of neptunocene (from [4]). Left panel: Arrhenius plots obtained from the imaginary part of the ac susceptibility measured for different values of the applied dc magnetic field. Right panel: magnetization curves measured at 1.8 K on increasing and decreasing the field (see arrows).

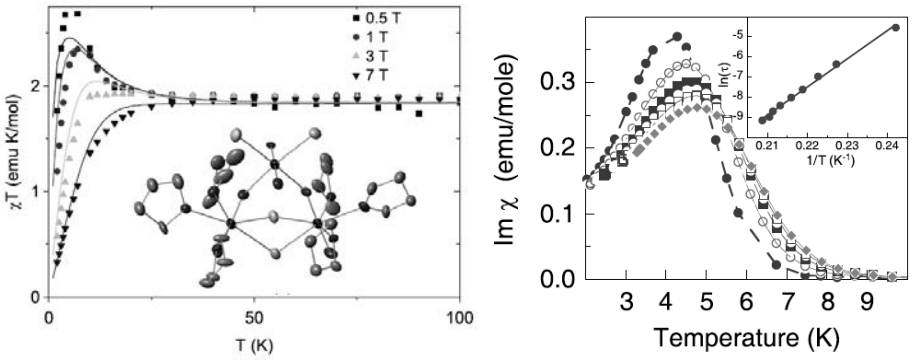

Fig. 3: Magnetic properties of the Np-based heterovalent trimetallic triangle $\{Np^{VI}O_2Cl_2\}\{Np^{V}O_2Cl(thf)_3\}_2$ (from [11]). Left panel: dc susceptibility measured for different values of the applied field. Right panel: imaginary part of the ac susceptibility in absence of applied dc field. The corresponding Arrhenius plot is shown in the inset.

References

[1] N. Ishikawa, M. Sugita, T. Ishikawa, S. Koshihara, Y. Kaizu, J. Am. Chem. Soc. 125, 8694 (2003).

[2] J. D. Rinehart and J. Long, J. Am. Chem. Soc. 131, 12558 (2009).

[3] J. D. Rinehart, K. R. Meihaus and J. R. Long, J. Am. Chem. Soc. 132, 7572 (2010).

[4] N. Magnani, C. Apostolidis, A. Morgenstern, E. Colineau, J.-C. Griveau, H. Bolvin, O. Walter and R. Caciuffo, Angew. Chem. Int. Ed. 50, 1696 (2011).

[5] J. D. Rinehart, M. Fang, W. J. Evans and J. R. Long, Nat. Chem. 3, 538 (2011).

[6] W. W. Lukens, N. Magnani and C. H. Booth, Inorg. Chem. 51, 10105 (2012).

[7] D. P. Mills, F. Moro, J. McMaster, J. van Slageren, W. Lewis, A. J. Blake and S. T. Liddle, Nat. Chem. 3, 454 (2011).

[8] P. L. Arnold, G. M. Jones, S. O. Odoh, G. Schreckenbach, N. Magnani and J. B. Love, Nat. Chem. 4, 221 (2012).

[9] L. A. Seaman, G. Wu, N. Edelstein, W. W. Lukens, N. Magnani and T. W. Hayton, J. Am. Chem. Soc. 134, 4931 (2012).

[10] D. M. King, F. Tuna, J. McMaster, W. Lewis, A. J. Blake, E. J. L. McInnes and S. T. Liddle, Angew. Chem. Int. Ed.. doi: 10.1002/anie.201301007 (2013).

[11] N. Magnani, E. Colineau, R. Eloirdi, J.-C. Griveau, R. Caciuffo, S. M. Cornet, I. May, C. A. Sharrad, D. Collison and R. E. P. Winpenny, Phys. Rev. Lett. 104, 197202 (2010).

[12] V. Mougel, L. Chatelain, J. Pécaut, R. Caciuffo, E. Colineau, J.-C. Griveau and M. Mazzanti, Nat. Chem. 4, 1011 (2012).

[13] P. L. Arnold, E. Hollis, G. S. Nichol, J. B. Love, J.-C. Griveau, R. Caciuffo, N. Magnani, L. Maron, L. Castro, A. Yahia, S. O. Odoh and G. Schreckenbach, J. Am. Chem. Soc. 135, 3841 (2013).

[14] J. Rinck, G. Novitchi, W. Van den Heuvel, L. Ungur, Y. Lan, W. Wernsdorfer, C. E. Anson, L. F. Chibotaru and A. K. Powell, Angew. Chem. Int. Ed. 49, 7583 (2010).

5-02

Structural investigations of actinides with advanced X-ray spectroscopy techniques

Tonya Vitova

Karlsruhe Institute of Technology, Karlsruhe, Germany

Electronic Structure. High-energy resolution X-ray absorption/emission spectroscopy (HR-XAS/HR-XES) and inelastic X-ray scattering (IXS) are emerging as effective tools for investigations of actinide (An) and lanthanide (Ln) electronic structures with high impact on fundamentally important debates such as on the level of localization/delocalization of An and Ln valence electronic states and their hybridization with ligand orbitals [1-6]. New spectroscopic observations aid to evaluate theoretical approaches for calculations of absorption/emission spectra of excited systems. For example, experimental U L_3 edge high-energy resolution X-ray absorption near edge structure (L_3-HR-XANES) and L_3 edge valence-band resonant inelastic X-ray scattering (L_3-VB-RIXS) spectra of the U mineral schroeckingerite, as well as U L_3-HR-XANES, uranium f and d density of states (f/d-DOS) calculated with the *ab initio* multiple scattering FEFF9.5 code [7] are plotted in Figure 1. In order to calculate the correct energy position of the pre-edge structure present in the experimental spectrum at about -8 eV, it is necessary to include electronic transitions to U 5f states and to mix the U f-DOS in the self-consistent field loop for calculation of scattering potentials. Since this peak was previously not observed, the U f states were fixed as part of the core, atomic-like electronic states in the FEFF calculations of L_3-HR-XANES and DOS spectra. As a result, the 5f states appeared localized giving wrong conclusions about the nature of the metal-ligand bonding. The L_3-VB-RIXS spectrum measured at an excitation energy 17176 eV, the maximum of the most intense absorption resonance at about 0 eV in Figure 1 (white line, WL), shows a remarkably similar shape to the occupied d-DOS evolving as a sensitive indicator for d states contribution in the valence band [8].

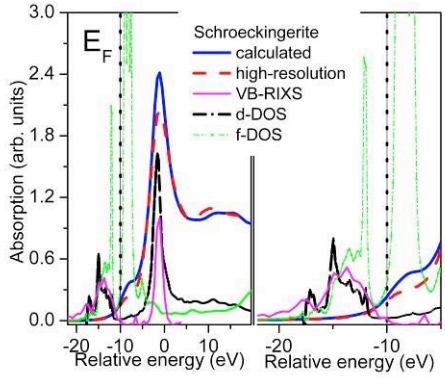

Figure 1: Experimental U L_3-HR-XANES, VB-RIXS and calculated U L_3-HR-XANES and U f- and d-DOS of schroeckingerite.

We will discuss electronic structural differences between $[Pu(C_{23}N_7H_{31})_3](CF_3SO_3)_3$ ($[Pu(BTP)_3](OTf)_3$) and $[Ln(C_{23}N_7H_{31})_3](CF_3SO_3)_3$ ($[Ln(BTP)_3](OTf)_3$) complexes in relation to the greater binding affinity of the N-donor ligand BTP to An compared to Ln. This molecule is of potential use in the so called Partitioning & Transmutation strategy for reduction the radiotoxicity of spent nuclear fuel [9]. The ($[Pu(BTP)_3](OTf)_3$) and ($[Ln(BTP)_3](OTf)_3$) electronic structures are probed by L_3-HR-XANES and N K-edge spectroscopy techniques. The relative energy positions and transition probabilities for $2p_{5/2}\rightarrow 4f/5f$, $2p_{5/2}\rightarrow 5d/6d$ and $1s\rightarrow 2p$ electronic transitions are determined. The 4f/5f and 5d/6d level of participation in bonding with the BTP molecule is evaluated by comparing experimental results with theoretical calculations with the FEFF9.5 and TD-DFT calculations employing the ORCA software package.

Speciation. The high sensitivity of HR-XAS/HR-XES to different oxidation states [1] and local coordination atomic environments compared to standard XAS/XES techniques facilitate detection of An/Ln species in environmentally relevant redox sensitive systems. Figure 2 shows comparison of simulated spectra 90% U^{VI} and 10% U^{IV} measured in standard transmission mode U L_3-XANES (INE-Beamline, ANKA, Karslruhe) and U L_3/M_4-HR-XANES (ID26-beamline, ESRF, Grenoble). The standard and high-energy resolution L_3 edge simulated spectra do not change significantly from the U^{VI} spectra. However, the M_4 edge spectrum exhibits an intensive additional feature A characteristic for U^{IV} (Fig. 2, right). This example demonstrates the potential of the U M_4-HR-XANES for investigations of minor oxidation states in oxidation-state mixtures.

We will present comparative L_3/M_4-HR-XANES and L_3-VB-RIXS investigations on various uranium minerals and L_3-HR-XANES uranium sorbed on magnetite compared to maghemite nanoparticles. The energy positions and intensities of the pre-edge, WL and multiple scattering resonances are compared and discussed as characterisation tools for bonding distances and local atomic environment.

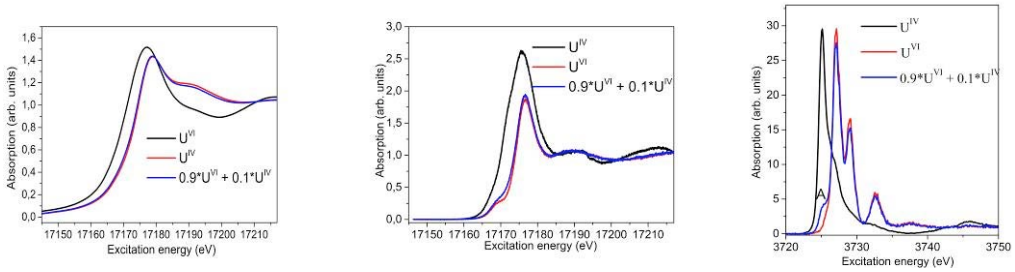

Figure 2: (left) U transmission mode L_3-XANES, (middle) L_3-HR-XANES, (right) M_4-HR-XANES of U^{IV} (UO_2), U^{VI} (meta-schoepite) and a linear combination of 90% U^{VI} and 10% U^{IV} reference spectra.

Low-energy absorption edges. Non-resonant inelastic X-ray scattering (NIXS) utilizes high penetration hard X-rays (6-20 keV), facilitating the use of double containment concepts for measurements of low-energy absorption edges of atoms in radioactive systems [2, 10-13]. For example, Fig. 3 shows a U $O_{4,5}$ measurement of metallic α-U sputtered on a Al_2O_3 substrate and covered by a Nb layer with thicknesses 1000 Å (α-U), 1000 mm (Al_2O_3) and 500 Å (Nb). The penetration depth of the X-rays in the sample is varied by changing the angle α (Fig. 3) between the incident X-ray beam and the surface of the sample. As a result, the signal of either the Al L_3-XANES (Fig. 3, top) or the α-U $O_{4,5}$-XANES (Fig. 3, bottom) is enhanced. The NIXS measurement is performed at momentum transfer q=9.88 $Å^{-1}$ enhancing the oscillatory strength for multipolar transitions with rank 3 and 5, as previously reported [2, 13]. The well resolved multiplet structure at high q compared to the broad standard U $O_{4,5}$ XANES dominated by a giant resonance for dipole transitions (q=1) (not shown) makes this technique appealing for many applications. The main disadvantage of the technique is the low cross section of the scattering process requiring high-photon flux (10^{12}-10^{13} ph/s) and multiple analyser crystal arrays. Rapid developments in instrumentation have led to the current design of 100 analyser crystal spectrometers at ESRF (Grenoble, France) and PETRAIII (Hamburg, Germany). These state-of-the-art instruments will allow, e.g., investigations of K edges of low Z elements (O, C, N) of liquids with a few mmol/l concentrations.

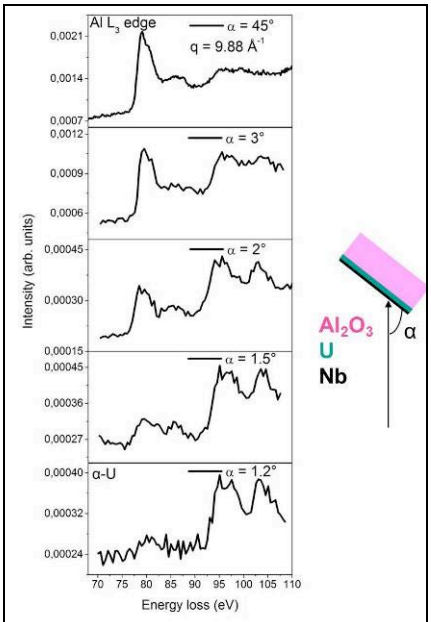

Figure 3: NIXS spectra of a layered sample, schematically shown, for different gracing incidence angles α between the X-ray beam and the surface of the sample.

Instrumentation. HR-XAS/HR-XES and IXS have become established as standard speciation characterization techniques. The required spectrometers with an array of crystals (up to 100) based on Rowland/von Hamos geometry are currently in operation or under commissioning at various synchrotrons [14-16]. However, investigations of transuranium elements in solid/liquid phase or in-situ conditions are still challenging due to missing infrastructure necessary for complying with safety rules for handling radioactive materials. We have recently built and commissioned a five analyser crystal spectrometer (multi-analyser crystal spectrometer, MAC-spectrometer) currently

operating at 90° scattering, vertical plane Rowland circle geometry at the INE-Beamline for actinide research at the ANKA synchrotron radiation facility, Karlsruhe (Fig. 4) [17]. The design of the instrument is adapted from the operational spectrometer at the ID26-beamline, ESRF [14]. The MAC-spectrometer will be installed in 2015 in the controlled laboratory hutch of the wiggler beamline for catalysis and actinide research (CAT-ACT-Beamline) currently under construction. In addition to an extended energy range (3-60 keV), the CAT-ACT-Beamline will provide up to two orders of magnitude higher photon flux compared to the INE-Beamline. These two experimental stations are located in close proximity to the Institute for Nuclear Waste Disposal (INE) allowing fast (about 15 minutes) transportation of samples simplifying investigations of sensitive sample systems.

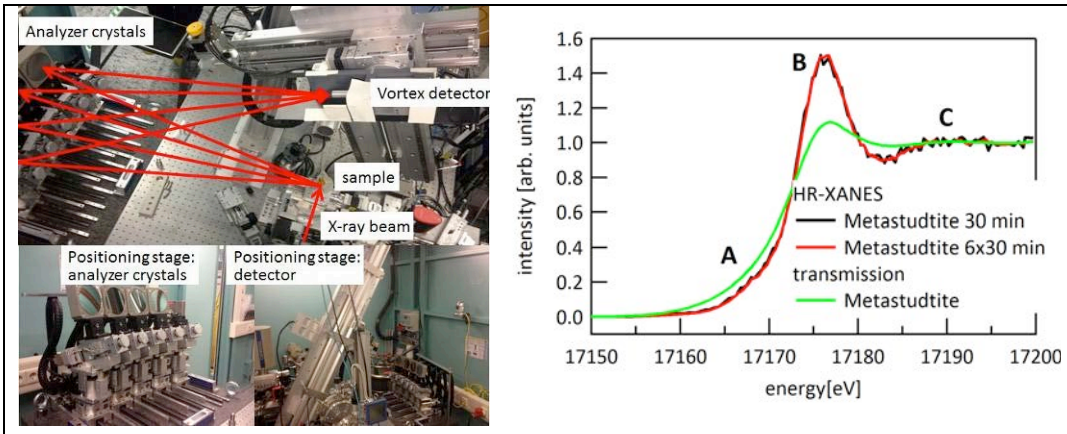

Figure 4: (left) The MAC-Spectrometer installed at the INE-Beamline: a) sample, analyser crystals and detector during experiments; positioning stages of the b) five analyser crystals and c) the detector. (right) Example of a U L_3-edge HR-XANES measurement of metastudtite.

Figure 4 (right) shows U L_3-edge HR-XANES spectra of the U mineral metastudtite measured 30 or 180 minutes compared to a simultaneously recorded transmission mode spectrum. The HR-XANES spectra demonstrate comparable energy resolution to the spectra measured at the ID26-beamline (Fig. 1). The incident X-ray beam was monochromatized using a Ge(422) double crystal monochromator. The emitted U $L\alpha_1$ fluorescence was diffracted by four Ge(777) analyzer crystals at 77.5° Bragg angle and focused on a SDD Vortex. The MAC-spectrometer will be equipped in 2013 with a He-environment reducing the X-ray absorption by air, thereby facilitating actinide M-edge HR-XAS/XES experiments.

Acknowledgments:

The work is performed in collaboration with Christos Apostolidis, Robert Baker, Sergei Butorin, Roberto Caciuffo, Melissa Denecke, Andreas Geist, Jörg Göttlicher, Florian Huber, Kristina Kvashnina, Gerrit van der Laan, Gerry Lander, Patric Lindqvist-Reis, Peter Nagel, Ivan Pidchenko, Tim Prüßmann, Jörg Rothe, Thorsten Schäfer, Bernd Schimmelpfennig, Stefan Schuppler, Laura Simonelli and Olaf Walter within the Helmholtz Young Investigators Grant VH-NG-734.

References

1. Vitova, T., et al., *High energy resolution x-ray absorption spectroscopy study of uranium in varying valence states.* Physical Review B, 2010. **82**(23): p. 235118.

2. Caciuffo, R., et al., *Uranium 5d-5f electric-multipole transitions probed by nonresonant inelastic x-ray scattering.* Physical Review B, 2010. **81**(19): p. 195104.

3. Kvashnina, K.O., S.M. Butorin, and P. Glatzel, *Direct study of the f-electron configuration in lanthanide systems.* Journal of Analytical Atomic Spectrometry, 2011. **26**(6): p. 1265-1272.

4. Denecke, M.A., et al., *Highly resolved synchrotron-based investigations related to nuclear waste disposal.* Actinides and Nuclear Energy Materials, 2012. **1444**: p. 269-280.

5. Butorin, S.M., *Resonant inelastic X-ray scattering as a probe of optical scale excitations in strongly electron-correlated systems: quasi-localized view.* Journal of Electron Spectroscopy and Related Phenomena, 2000. **110**(1-3): p. 213-233.

6. Kotani, A., et al., *Single Impurity Anderson Model versus Density Functional Theory for Describing Ce L-3 X-Ray Absorption Spectra of CeFe2: Resolution of a Recent Controversy.* Physical Review Letters, 2012. **108**(3): p. 036403.

7. Kas, J.J., et al., *Real-space Green's function approach to resonant inelastic x-ray scattering.* Physical Review B, 2011. **83**(23): p. 235114.

8. Glatzel, P., et al., *In situ characterization of the 5d density of states of Pt nanoparticles upon adsorption of CO.* Journal of the American Chemical Society, 2010. **132**(8): p. 2555-7.

9. Panak, P.J. and A. Geist, *Complexation and Extraction of Trivalent Actinides and Lanthanides by Triazinylpyridine N-Donor Ligands.* Chemical Reviews, 2013. **113**(2): p. 1199-1236.

10. Bradley, J.A., et al., *Experimental and Theoretical Comparison of the O K-Edge Nonresonant Inelastic X-ray Scattering and X-ray Absorption Spectra of NaReO4.* Journal of the American Chemical Society, 2010. **132**(39): p. 13914-13921.

11. Bradley, J.A., et al., *Probing electronic correlations in actinide materials using multipolar transitions.* Physical Review B, 2010. **81**(19): p. 193104.

12. Pylkkanen, T., et al., *Universal Signature of Hydrogen Bonding in the Oxygen K-Edge Spectrum of Alcohols.* Journal of Physical Chemistry B, 2010. **114**(41): p. 13076-13083.

13. van der Laan, G., *Nonresonant inelastic x-ray scattering from actinides and rare earths.* Physical Review B, 2012. **86**(3): p. 035138.

14. Glatzel, P. and U. Bergmann, *High resolution 1s core hole X-ray spectroscopy in 3d transition metal complexes - electronic and structural information.* Coordination Chemistry Reviews, 2005. **249**(1-2): p. 65-95.

15. Fister, T.T., et al., *Multielement spectrometer for efficient measurement of the momentum transfer dependence of inelastic x-ray scattering.* Review of Scientific Instruments, 2006. **77**(6): p. 063901.

16. Sokaras, D., et al., *A high resolution and large solid angle x-ray Raman spectroscopy end-station at the Stanford Synchrotron Radiation Lightsource.* Review of Scientific Instruments, 2012. **83**(4): p. 043112.

17. Rothe, J., et al., *The INE-Beamline for actinide science at ANKA.* Review of Scientific Instruments, 2012. **83**(4): p. 043105.

5-03

Soft X-ray Spectroscopy of the Actinides

J. G. Tobin

Lawrence Livermore Natl Lab, Livermore, CA, USA

We are developing and utilizing several variants of soft X-ray spectroscopy as probes of actinide electronic structure [1]. Perhaps the most demanding and powerful actinide spectroscopy is that using soft x-ray and VUV photons. Because of the relatively low energy and fairly small sampling depths of these photons and the corresponding electrons, it is necessary to use un-encapsulated samples with highly cleaned and well-prepared surfaces. This causes a myriad of sample containment problems for these radioactive materials. Despite these hindrances and difficulties, the soft-x-ray and ultra-violet spectroscopy of the actinides can provide an amazing level of detailed information, particularly having to do with 5f electronic structure.

For example, we have used a combined X-ray Photoelectron Spectroscopy (XPS) [2], X-ray Absorption Spectroscopy (XAS) [3,4], and Bremstralung Isochromat Spectroscopy [3,5] study to provide the most refined and definitive picture of the unoccupied electronic structure of uranium dioxide (Figure 1).

As part of the development and utilization of Resonant Inverse Photoelectron Spectroscopy (RIPES) and X-Ray Emission Spectroscopy (XES), we performed calibration experiments upon CeOxide [5] and compared them to earlier XAS results [6] (Figure 2).

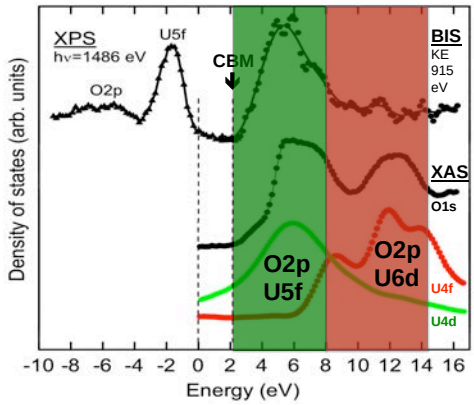

Figure 1

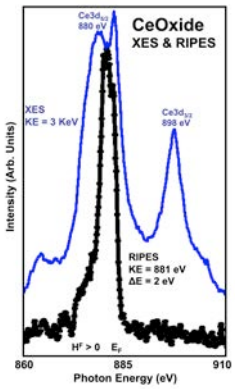

Figure 2

Figure 1. A summary of our earlier results for XPS, BIS and XAS of UO_2 is shown here. The green region represents the part of the UDOS dominated by U5f and O2p states and the red area is that dominated by the U6d and O2p states. CBM is conduction band minimum. UDOS is Unoccupied Density of States.

Figure 2. The XES and RIPES of Ce Oxide.[5] Our sample consisted of a thin layer of Ce Oxide lying above Ce metal. Under conditions such as these, thin layers, composed of materials that would normally be insulating in the bulk, can continue to exhibit a Fermi edge, owing to the thinness of the film and the underlying conductor. The XES spectrum resolves two components in the Ce3d 5/2 region, assigned to the underlying Ce metal and the near surface Ce Oxide thin film. The RIPES resonance occurs under the Ce Oxide component.

While the Ce Oxide RIPES displayed a very strong resonance and only weak dispersion, the uranium dioxide sample exhibited a weaker resonance, strong dispersion and a unique satellite structure in the RIPES, as shown in Figure 3 [7]. The satellite structure in the RIPES and XES is driven by the separation of the Unoccupied Density of States (UDOS) of UO_2 into 5f and 6d components, as illustrated in Figure 1.

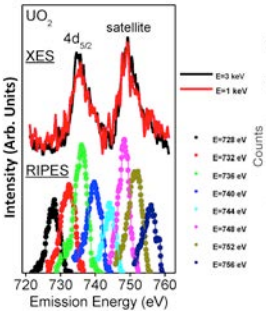

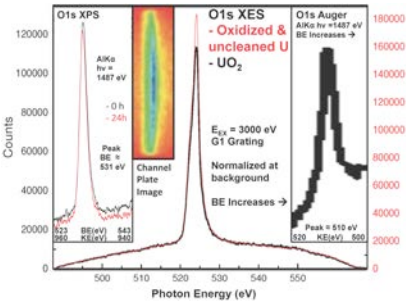

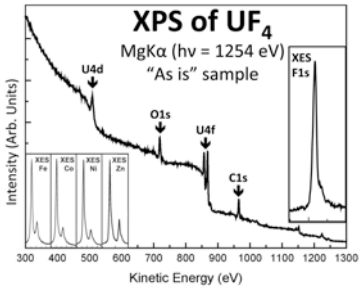

Figure 3 **Figure 4** **Figure 5**

Figure 3. (Left) The RIPES and XES of UO_2 is presented here. The XES is shown in the upper part of the figure and the RIPES in the lower part of the figure. Backgrounds have been subtracted. The legend denotes the energy of the excitation, i.e. the incoming electrons. The horizontal scale on the bottom is the energy of the outgoing photons. The resolution band-pass was 2 eV. Note that the satellite is as large as the main peak.

Figure 4 (middle), O1s spectra: XES, Auger (right inset), XPS (left inset) and the channel plate image (central inset).

Figure 5 (right) XPS and XES of the "as is" UF_4. Note the presence of multiple contaminant peaks in the XPS (e.g. O1s near KE = 720 eV and the C1s near KE = 970 eV) and the relatively poor signal to noise (e.g., the U4d doublet near KE = 500 eV and the U 4f near KE = 870 eV). The F1s XPS peak, which should be near KE = 550 eV, is not easily observable. Alternatively, the F1s XES peak shown in the rightmost inset over a 30 eV range, is sharp and exhibits good signal to noise. In the series of insets to the left, 30 eV wide scans of the Fe, Ni, Co and Zn 2p XES are shown, used for calibration.

One of our present directions of research is the development of XES as a means to probe "as is" samples. By "as is," it is meant that the sample is used without any *in vacuo* cleaning. Examples are shown in Figures 4 and 5 [8].

We also use variants of soft X-ray spectroscopy, such as XAS [9], BIS [9] and resonant photoemission [10], to experimentally cross-calibrate the cluster calculations that we are pursuing with our colleagues from Russia [9,10]. Examples of our results are shown below. The central atom (Pu1 site) is the most bulk-like.

Future work includes plans for the return to the utilization of spin-resolved photoelectron spectroscopy for probing electron correlation in actinides [11,12].

Lawrence Livermore National Laboratory is operated by Lawrence Livermore National Security, LLC, for the U.S. Department of Energy, National Nuclear Security Administration under Contract DE-AC52-07NA27344. This work was supported by the DOE Office of Science, Office of Basic Energy Science, Division of Materials Science and Engineering.

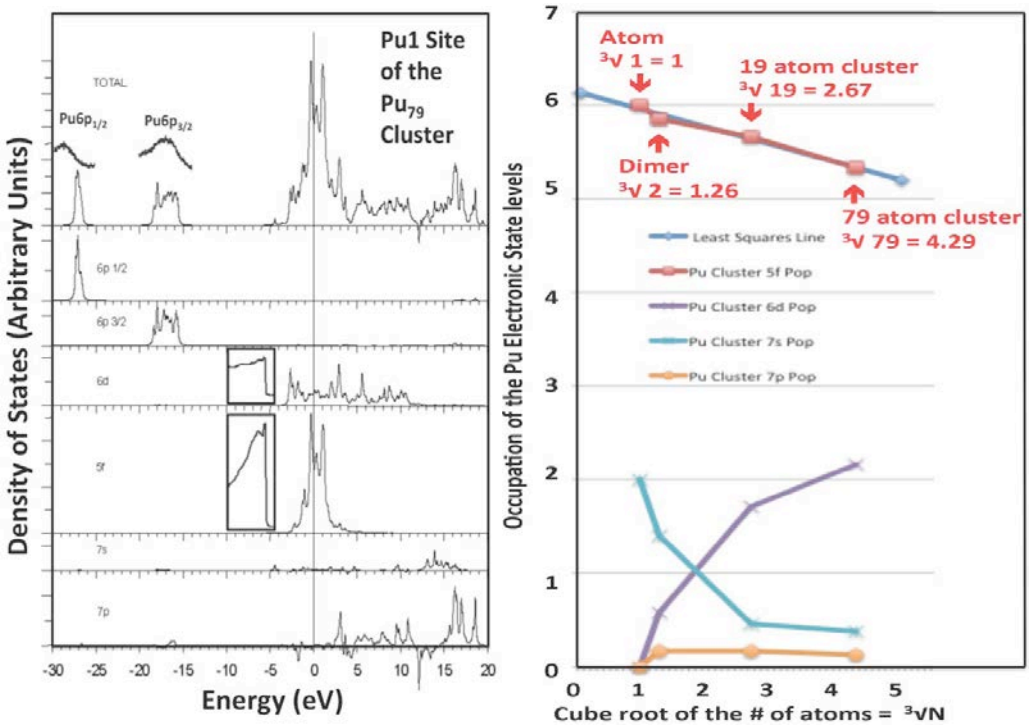

Figure 6. (Left) Total and partial densities of states for the central atom Pu1 of a Pu_{79} cluster. (light lines) Spectroscopic results from a bulk Pu sample are also shown here (heavy lines in insets). The spectroscopic data are representative of experimental DOS estimates, although skewed by cross-sectional effects. The two 6p experimental peaks, taken at the Cooper Minimum with hv = 225 eV, are shown at their measured binding energies, vertically offset above the total spectrum. The near Fermi edge region, collected on resonance at hv = 125 eV to strongly emphasize the 5f character, is shown in the inset, horizontally offset from the calculated 5f peak. Similarly, the near Fermi edge region, collected at anti-resonance at hv = 100 eV to strongly emphasize the 6d character, is shown in the inset, horizontally offset from the calculated 6d peak. The unphysical negative values of 7p partial DOS are due to the use of diffuse basis functions. [10]

Figure 7. (Right) Plot of Pu 5f, 6d, 7s and 7p average occupations versus the cube root of the number of Pu atoms. ($^3\sqrt{N}$) For an atom with N = 1, $^3\sqrt{N}$ = 1; For a dimer with N = 2, $^3\sqrt{N}$ = 1.26;For Pu_{19} cluster with N = 19, $^3\sqrt{N}$ = 2.67;For a Pu_{79} cluster with N = 79, $^3\sqrt{N}$ = 4.2. Also shown is the least squares fitted line for the 5f occupations. Note the linear relationship for the 5f occupations. [10]

References

1. S.-W. Yu,J. G. Tobin, and B. W. Chung, Rev. Sci. Instr. **82**,093903 (2011).
2. S.-W. Yu and J.G. Tobin, , J. Vac Sci. Tech. **A 29**, 021008 (2011).
3. S.-W. Yu et al., Phys. Rev. B **83**, 165102 (2011).
4. S.-W. Yu et al., J. Vac. Sci. Tech. A. **30**, 011402 (2012).
5. J.G. Tobin et al., Phys. Rev. B **83**, 085104 (2011).
6. J.G. Tobin et al., J. Vac. Sci. Tech. **A 29,** 031504 (2011).
7. J.G. Tobin and S.-W. Yu, Phys. Rev. Lett, **107**, 167406 (2011).
8. S.-W. Yu and J.G. Tobin, J. Electr. Spectr. Rel. Phen., in press, 2013.
9. J.G. Tobin et al., J. Vac. Sci. Tech. A. **31**, 013001 (2013).
10. M.V. Ryzhkov et al., Int. J. of Quantum Chemistry, doi: 10.1002/qua.24417 (2013).
11. J.G. Tobin et al., EPL **77**, 17004 (2007).
12. S.W. Yu, J.G. Tobin, and P. Söderlind**,** J. Phys. Cond. Matter **20**, 422202 (2008), Fast Track Communication.

ORAL

1-06

Emergent Fermi liquid physics in actinides within an intermediate coupling model

Tanmoy Das

Los Alamos National Laboratory, Los Alamos, NM, USA

Understanding and modeling correlated electronic spectra has remained a constant theme of research for decades. We have relatively better modeling capabilities for systems residing either in the weakly or strongly correlated regimes. However, the intermediate coupling regime poses a challenge since both the Fermi-liquid or dynamical mean-field theories are inadequate here. Over the last few years, we have been working on developing a computational scheme for this problem. Our intermediate coupling model is based on materials-specific band structure, from which self-energy correction is computed via a self-consistent approach including full momentum dependent dynamical correlations. In this talk, I will present results for several representative actinide compounds in the Pu-115, and U-115 families, and others. A common feature of intermediate coupling scenario is that the self-energy splits the electronic structure into low-energy coherent states (emergent Fermi liquid state), and high-energy localized state (residual Mott state), yielding a coexistence of itinerant and localized states. The resulting electronic fingerprint reveals a universal 'S' or waterfall shape in the dispersion, and a peak-dip-hump feature in the density of states. The results suggest a generic route for formulating the correlated Fermi-liquid physics from which a unified theory of unconventional superconductivity may emerge.

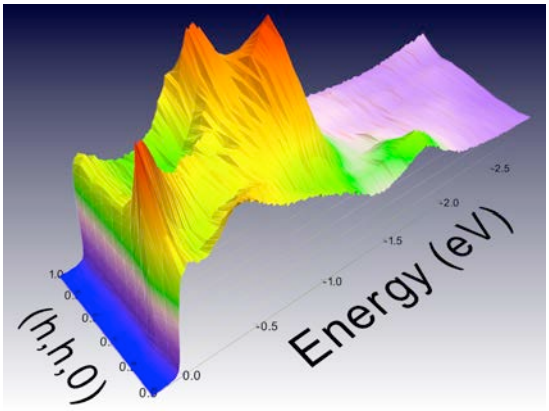

Figure: 3D rendering of the single-electron spectral weight for a representative actinide compound UCoGa5. The momentum dependence of the spectral weight `hot-spots' represents that the system resides in the intermediate coupling regime. The sharp peak at the Fermi level clearly marks the emergence of Fermi-liquid low-energy spectra, despite the presence of localized 'hump' feature at high-energy.

References

[1] Das, Zhu, Graf, Phys. Rev. Lett. **108**, 017001 (2012).

[2] Das, Durakiewicz, Zhou, Joyce, Sarrao, Graf, Phys. Rev. X **2**, 041012 (2012).

1-07

Unified character of correlation effects in unconventional Pu-based superconductors and δ-Pu

Alexander Shick[1], Jindrich Kolorenc[1], Jan Rusz[2,1], Peter Oppeneer[2], Alexander Lichtenstein[3], Mikhail Katsnelson[4], Roberto Caciuffo[5]

[1]Institute of Physics, ASCR, Prague, Czech Republic, [2]Uppsala University, Uppsala, Sweden, [3]University of Hamburg, Hamburg, Germany, [4]Radboud University Nijmegen, Nijmegen, The Netherlands, [5]European Commission, Joint Research Centre, Institute for Transuranium Elements, Karlsruhe, Germany

$PuCoGa_5$, discovered in 2002, has the highest critical temperature of 18.5 K among heavy-fermion superconductors [1], that is one order of magnitude higher than for typical heavy-fermion compounds. Spin and charge valence fluctuations may have an important role in mediation of the superconducting phase in the Pu-115 family of 5f-electron heavy-fermion superconductors. Specific character of the coupling mechanism remains uncovered. Very recent point-contact spectroscopy experiments [2] show that the paired superconducting electrons have wavefunction with the d-wave symmetry.

In this work we address electron correlation effects in $PuCoGa_5$ and $PuCoIn_5$ materials making use of a combination of the local density approximation (LDA) with an exact diagonalization (ED) of the Anderson impurity model [3]. The band structure obtained by the relativistic version of the full-potential linearized augmented plane wave method (FP-LAPW) is extended to account for the f-orbital atomic multiplets and their hybridization with the conduction bands. We show that the unconventional character of superconductivity in the Pu-115 compounds and the unusual physical properties of delta-Pu, in particular the unexpected absence of magnetism, may have a common origin in the intermediate-valence nature of the Pu 5f-electron ground state. In all three compounds the Pu atoms exhibit a $5f^5$-$5f^6$ intermediate-valence ground state, with a partial delocalization of the $5f^5$ multiplet. The local 5f magnetic moment is compensated by a moment in the surrounding cloud of conduction electrons. In the case of $PuCoGa_5$ and d-Pu the compensation is complete and the Anderson impurity grounds state is a non-magnetic singlet. On the other hand, for $PuCoIn_5$, the compensation is partial and the Pu ground state is magnetic. On the basis of these results, we discuss the role of spin and charge fluctuations for Cooper pairing, and the nature of the unconventional d-wave superconducting state in $PuCoGa_5$ and $PuCoIn_5$.

References

[1] J. L. Sarrao, L. A. Morales, J. D. Tompson, B. L. Scott, G. R. Stewart, F. Wastin, J. Rebizant, P. Boulet, E. Colineau, and G. H. Lander, Nature **420**, 297 (2002).

[2] D. Daghero,M. Tortello, G.A. Ummarino, J.-C. Griveau, E. Colineau, R. Eloirdi, A. B. Shick, J. Kolorenc, A. I. Lichtenstein, and R. Caciuffo, Nature Comm. **3**, 1785 (2012).

[3] A. B. Shick, J. Kolorenc, J. Rusz, P. M. Oppeneer, A. I. Lichtenstein, M. I. Katsnelson, and R. Caciuffo, Phys. Rev. **B** 87, 020505 (2013).

1-08

Photoemission imaging of 3-dimensional Fermi surface pairing at the hidden order phase transition in URu_2Si_2

Peter M. Oppeneer[1], Jian-Qiao Meng[2], John A. Mydosh[3], Peter S. Riseborough[4], Krzysztof Gofryk[2], John J. Joyce[2], Eric D. Bauer[2], Yinwan Li[5], Tomasz Durakiewicz[2]

[1]Uppsala University, Uppsala, Sweden, [2]Los Alamos National Laboratory, Los Alamos, NM, USA, [3]Leiden University, Leiden, The Netherlands, [4]Temple University, Philadelphia, PA, USA, [5]Wolfram Research Inc., Champaign, IL, USA

The 2nd order phase transition occurring in URu_2Si_2 at T=17.5K from a heavy fermion state to an unknown, or "hidden order" phase has drawn much scientific attention. In spite of 25 years of intensive research, the physics underlying the hidden order (HO) phase transition has escaped unveiling (see [1] for a recent review). Angular resolved photoemission spectroscopy (ARPES) in the hidden order phase, in combination with density-functional theory (DFT) based calculations, can form an ideal tool to investigate momentum-dependent changes of the Fermi surface topology.

We report first our results of full-potential, relativistic density-functional theory calculations. We show that there exist two Fermi surface (FS) sheets that exhibit unusually strong nesting at the antiferromagnetic wavevector, $\mathbf{Q}_0$=(0, 0, 1). The corresponding energy dispersions fulfill specific relations on eight FS hotspot lines on the Fermi surface. The spin-orbital characters of the involved 5f states are however distinct, j_z=± 5/2 vs. j_z=±3/2, and therefore the occurring degenerate Dirac crossings are symmetry protected in the nonmagnetic normal state. However, pairing of electrons in these two FSs can commence through interaction via a quasiparticle at wavevector $\mathbf{Q}_0$ in addition to an exchange of longitudinal angular momentum Δj_z=±1. Dynamical symmetry breaking through an Ising-like spin-orbital excitation mode at $\mathbf{Q}_0$ could induce such hybridization of the two FS states, causing substantial FS gapping [2].

Second, to analyze the predicted Fermi surface, we have performed ARPES experiments probing deep into the HO state of URu_2Si_2, utilizing tunable photon energies with sufficient energy and momentum resolution to detect the near-Fermi surface behaviour. Our ARPES results reveal: (i) the full itinerancy of the 5f electrons; (ii) the crucial three-dimensional k-space nature of the Fermi surface and its critical nesting vectors, in good comparison with DFT calculations, and (iii) the existence of hot-spot lines and Fermi surface pairing, leading to Fermi surface gapping in the hidden order phase. The Fermi surface in the HO appears to be symmetry-broken with respect to the body-centered translational vector, leading to a down-folding to a simple tetragonal Brillouin zone. Areas in k-space where quasiparticle intensity is removed in the HO transition are identified.

The measured Fermi surface cross-sections in the k_x-k_y plane (at k_z=0) obtained by ARPES are shown in Figure 1. The cross-sections at the Fermi energy (E_F) are given in panel a, and overlain with the DFT-computed cross-sections. There is a good agreement between measured FS cross-sections and the DFT cross-sections computed for the antiferromagnetic phase (panel d). This highlights the regions in the Brillouin zone where electronic intensity has been removed through FS gapping in the HO state, which is here identified to happen along the Γ to M high-symmetry line.

Our ARPES study of the near-Fermi surface behavior in URu_2Si_2 provides furthermore evidence that the FS has a strong 3D topology, showing good agreement with DFT calculations. Enhanced quasiparticle intensities indicate an essential pairing of FS states, particularly occurring at hot-spot lines. The HO transition is found to be characterized by a strongly momentum dependent FS reconstruction. The occurring FS removal and associated quasiparticle states appear as a signature of pairing of FS states on different parts of the Fermi surface that are joined by nesting vectors.

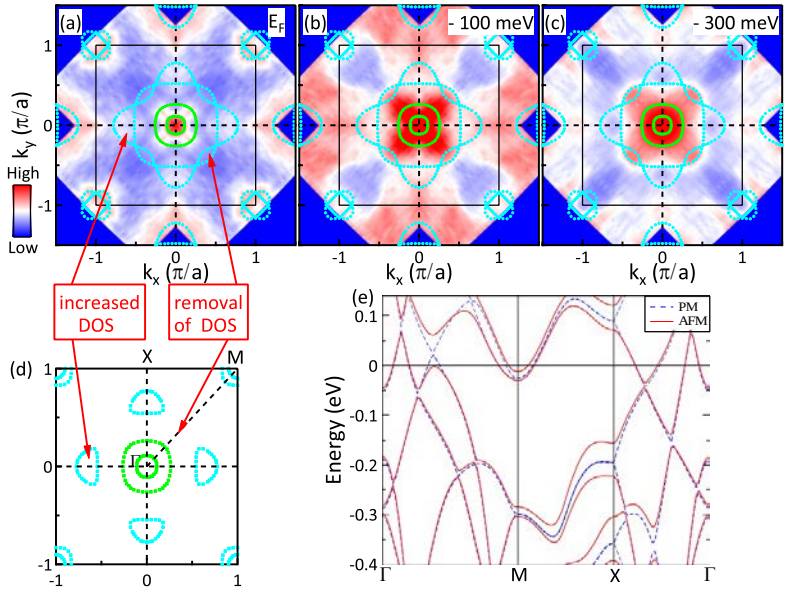

Figure 1. ARPES Fermi surface mapping in the k_x – k_y plane (at k_z=0) of URu_2Si_2 in the HO state. a-c: constant energy contours at the Fermi energy (E_F), and at 100 meV and 300 meV below E_F. Calculated DFT cross-sections are shown in light blue for the nonmagnetic phase (panels a-c) and for the antiferromagnetic phase in panel d. The corresponding DFT band dispersions are given in panel e.

Refernces

[1] J. A. Mydosh and P. M. Oppeneer, Rev. Mod. Phys. 83, 1301 (2011).

[2] P. M. Oppeneer, S. Elgazzar, J. Rusz, Q. Feng, T. Durakiewicz, and J. A. Mydosh, Phys. Rev. B 84, 241102 (2011).

1-09

Detection of a finite 5*f* orbital magnetic moment in Curium metal using XMCD

Fabrice Wilhelm[1], Rachel Eloirdi[2], Ross Springell[3], Eric Colineau[2], Jean-Christpohe Griveau[2], Roberto Caciuffo[2], Andrei Rogalev[1], Gerard H. Lander[2]

[1]European Synchrotron Radiation Facility, Grenoble, France, [2]European Commission, Joint Research Centre, Institute for Transuranium Elements, Karlsruhe, Germany, [3]Royal Commission for the Exhibition of 1851 Research Fellow, Interface Analysis Centre, University of Bristol, Bristol, UK

The precise configuration of the spin and orbital moments in the actinides is a matter of controversy [1, 2]. This is particularly true in the center of the series, around Pu – Am – Cm, when the exchange interaction is increasing with the number of 5*f* electrons, but the spin-orbit interaction is strong and the moments may not be totally localised, i.e. bandwidth also plays a role. Cm lies at the center of the actinide (5*f*) series and if it is like Gd it should have a $^8S_{7/2}$ spectroscopic state, i.e. with no 5*f* orbital magnetic moment. Recent EELS measurements have been interpreted to suggest that, because of the large spin-orbit coupling, Cm follows intermediate coupling with a small, but finite, orbital moment [3]. If an finite orbital moment exists, the total moment will then be < 7 μ_B and be about 6 μ_B, which appears in contradiction to earlier results deduced from the susceptibility [4]. However, the latter study used samples of ~ 1 µg, so there are some uncertainties. We have performed x-ray magnetic circular dichroism (XMCD) experiments on Curium metal (~1mg) to detect the existence of small 5*f* orbital magnetic moment contribution. XMCD have been carried out at the $M_{5,4}$-edges of Curium at 30K and 70K under an applied magnetic field of 17T. We found that the branching ratio which provides the angular part of the 5f spin-orbit interaction is around ~0.70 in good agreement with EELS [3]. Based on atomic multiplet theory, our results confirm that intermediate coupling best describes the coupling between the spin and orbital components of the ground state. Further, we found the existence of a finite 5*f* orbital magnetic moment, which is about 10% of total moment in Curium.

References

[1] K. T. Moore & G. van der Laan, Rev. Mod. Phys. **81**, 235 (2009).

[2] J. H. Shim, K. Haule, & G. Kotliar, Nature, **446**, 513 (2007).

[3] K. T. Moore *et al.,* Phys. Rev. Lett. **98,** 236402 (2007).

[4] P. G. Huray & S. E. Nave, in “Handbook of the Physics & Chemistry of the Actinides: eds. A. J. Freeman & G. H. Lander, Elsevier, 1987, Vol. 5 p. 311 et seq.

1-10

Unconventional superconductivity in Transuranium compounds: 10 years of research at ITU

Jean-Christophe Griveau[1], Krzysztof Gofryk[2], Eric Colineau[1], Eric D. Bauer[2], Paul Tobash[2], Rachel Eloirdi[1], Tomasz Klimczuk[3], Jean Rebizant[1], Richard G. Haire[4], Roberto Caciuffo[0]

[1]Institute of Transuranium, Karlsruhe, Germany, [2]Los Alamos National Laboratory, Los Alamos, USA, [3]Faculty of Applied Physics and Mathematics, Gdansk, Poland, [4]Oak Ridge National Laboratory, Oak Ridge, USA

Concerning condensed matter physics in uranium and transuranium compounds, the last decade has been full of surprises compared to the last half century. Indeed, these last 10 years have led to the discovery of a multitude of systems based of *5f* electrons with astonishing properties, especially from the point of view of interplay between magnetism and superconductivity. Ferromagnetic superconducting systems, predicted long time ago [1,2], have been observed experimentally, first under pressure, for UGe_2 [3] and then at ambient pressure for URhGe [4] and UCoGe [5], which are simultaneously superconducting (T_c = 0.80, 0.25 and 0.22 K respectively) and ferromagnetic (T_C= 52, 9.5 and 2.9 K, respectively). In the Transuranium systems, the first big shock came with the observation of superconductivity in $PuCoGa_5$ with a surprising T_c = 18.6 K [6], one scale above all other heavy fermion superconductors based on *5f* electrons. This is still a record in all the *f*-electrons systems. Other systems based on Pu ($PuRhGa_5$ [7], $PuCoIn_5$ and $PuRhIn_5$ [8]) or Np ($NpPd_5Al_2$ [9] (the only neptunium based superconductor) have been reported which can be related to other "known" classes of intermetallics systems such as heavy fermions superconductors with magnetic ground state. Up to now, only $PuCoGa_5$ remains definitely difficult to associate to one class.

However it is important to stress that the efforts on superconductivity studies in actinides have started much longer before, with the study of uranium metal and the key role of the Charge Density wave anomaly reported [10]. Other actinides such as Pa have been considered but the main difficulty was to get them pure enough for a basic study. A definitive answer on the superconducting properties of Pa has been realised only when very pure Pa metal was prepared at ITU [11] and first measurements below 1 K have been performed in the framework of collaboration between ITU and LANL [12], reporting T_c~0.4 K. Works on actinides metal preparation [13] lead also to the possibility to study the basic properties such as the heat capacity [14] of americium metal (^{243}Am). The nature of superconductivity of americium has been widely considered as puzzling. Am presenting challenging features, such as scarcity, radio-activity and a huge self heating, this gives to its low superconducting transition temperature T_c~0.8 K a challenging aspect. Positioned just after Pu, at the *5f*-volume cell Mott transition associated to the *5f* localisation, americium is extremely sensitive to pressure and a complex structure diagram under pressure has been reported. A huge effort has been initiated at ITU to understand the link between structure and superconductivity especially when trying to access the very low temperature range below 1 K. This work lead to observe exotic phenomena such as a huge increase of critical field associated to the variations of T_c variation and the probable change of type of superconductivity from Type I to Type II [15].

Numerous systems have been examined at ITU in the last decades also, based on the analogy of structure or properties of existing Rare Earths superconductor's counterparts. The last family explored being the "1-1-1-1" [16] family, but as in the simple substitution cases such as NpRhGe or PuRhGe [17] (for URhGe), none of these attempts have led to the discovery of new superconductors. From this point of view, only the "1-1-5" family with in particular $PuCoGa_5$ and recently, $PuCoIn_5$ ($CeCoIn_5$) and the "1-5-2" family with $NpPd_5A_{l2}$ [18] ($CePd_5Al_2$ [19]) have shown superconductivity in both the rare-earth and Transuranium analogues.

Future studies should be addressed to examine the basic properties of transplutonium elements such as Cm, Bk, and Cf as elements or as a part of compounds (alloys or oxides). These studies should be considered as a benefit to our basic knowledge and to the support to nuclear applications as these materials are present in irradiated fuels and constitute to the main problematic of nuclear wastes management.

References

[1] Layzer, A., and D. Fay, 1971, Int. J. Magn. **1**, 135.

[2] Fay, D., and J. Appel, 1980, Phys. Rev. B **22**, 3173.

[3] Saxena, S. S., et al. 2000, Nature (London) **406**, 587.

[4] Aoki, D., A. Huxley, E. Ressouche, D. Braithwaite, J. Flouquet, J.-P. Brison, E. Lhotel, and C. Paulsen, 2001, Nature (London) **413**, 613.

[5] Huy, N. T., D. E. de Nijs, Y. K. Huang, and A. de Visser, 2008, Phys. Rev. Lett. **100**, 077002.

[6] Sarrao, J. L., L. A. Morales, J. D. Thompson, B. L. Scott, G. R. Stewart, F. Wastin, J. Rebizant, P. Boulet, E. Colineau, and G. H. Lander, 2002, Nature (London) **420**, 297.

[7] Wastin, F., P. Boulet, J. Rebizant, E. Colineau, and G. H. Lander, 2003, J. Phys.: Condens. Matter **15**, S2279.

[8] E. D. Bauer, M. M. Altarawneh, P. H. Tobash, K. Gofryk, O. E. Ayala-Valenzuela, J. N. Mitchell, R. D. McDonald, C.H. Mielke, F. Ronning, J.-C. Griveau, E. Colineau, R. Eloirdi, R. Caciuffo, B. L. Scott, O. Janka, S. M. Kauzlarich and J. D. Thompson J. Phys.: Condens. Matter (2012) **24**, 052206.

[9] Aoki, D., Y. Haga, T. D. Matsuma, N. Tateiwa, S. Ikeda, Y. Homma, H. Sakai, Y. Shiokawa, E. Yamamoto, A. Nakamura, R. Settai, and Y. Onuki, 2007, J. Phys. Soc. Jpn. **76**, 063701.

[10] J. A. Lee, P. W. Sutcliffe, K. Mendelssohn, Phys. Lett. (1969), **30A**, 106.

[11] J. Bohet and W. M. Müller, Journal of Less Comm Metals, (1978) **57**, 185.

[12] J. L. Smith, J.-C. Spirlet, W. M. Müller, Science (1979) **205**, 189.

[13] J.-C. Spirlet and W.M. Müller, Journal of Less Comm Metals, **31** (1973) 35.

[14] R.O.A. Hall, M.J. Mortimer, D.L. McElroy, W. Müller, JC Spirlet, Transplutonium 1975 Eds Müller, R. Lindner, 139.

[15] J.-C. Griveau, J. Rebizant, G. H. Lander and G. Kotliar, Phys. Rev. Lett. (2005) **94**, 097002.

[16] T. Klimczuk, H. C. Walker, R. Springell, A. B. Shick, A. H. Hill, P. Gaczynski, K. Gofryk, S. A. J. Kimber, C. Ritter, E. Colineau, J.-C. Griveau, D. Bouexiere, R. Eloirdi, R. J. Cava, and R. Caciuffo, Phys. Rev. B, (2012) **85**, 174506.

[17] E. Colineau, J. P. Sanchez, F. Wastin, P. Javorsky, E. Riffaud, Y. Homma, P. Boulet and J. Rebizant, J. Phys.: Condens. Matter **20** (2008) 255234.

[18] Griveau, J.-C., K. Gofryk, and J. Rebizant, 2008, Phys. Rev. **B** 77, 212502.

[19] F. Honda, R. Settai, D. Aoki, Y. Haga, T. D. Matsuda, N. Tateiwa, S. Ikeda, Y. Homma, H. Sakai, Y. Shiokawa, E. Yamamoto, A. Nakamura, and Y. O¯ nuki, J. Phys. Soc. Jpn. 77, Suppl. **A** 339 (2008).

1-85

Possible Pseudogap Phase in the Cubic Superconductor UBe_{13}

Astrid Schneidewind[1], Arno Hiess[2,3], Oliver Stockert[4], Philipp Geselbracht[5], Paul Steffens[3], Zachary Fisk[6]

[1]JCNS, Forschungzentrum Jülich at Maier-Leibnitz-Zentrum, Garching, Germany, [2]European Spallation Source ESS AB, Lund, Sweden, [3]Institut Laue – Langevin, Grenoble, France, [4]MPI-CPfS, Dresden, Germany, [5]TU München, Maier-Leibnitz-Zentrum, Garching, Germany, [6]University of California, Irvine, USA

Unconventional superconductivity, as observed in several Cerium-based and actinide superconductors, has been discussed to be originated by antiferromagnetic fluctuations for a long time [1]. Experimental findings on changes of antiferromagnetic (AF) spin dynamics at the superconducting phase transition support this scenario in antiferromagnetic ordered compounds and in systems located in vicinity to antiferromagnetic quantum criticality [2]. Inelastic neutron scattering is the particular important tool to appreciate this interrelation of magnetism and superconductivity since studying the microscopic spin dynamics in momentum and energy space.

The most investigated actinide superconductor, UPd_2Al_3 (T_N = 14 K, T_c = 2 K), reveals an unusually complex spin dynamics [3] but significant changes are observed only at the AF zone center on entering the superconducting state by changing temperature or magnetic field [4]. Similar behaviour is observed for the Cerium-based superconductors. All these systems show a layered crystal structure, as well as copper-based superconductors and pnictides.

Here we present a study on UBe_{13}, which is an actinide-based, heavy-fermion superconductor (T_c = 0.85 K, γ > 1J/molK^2) with cubic crystal structure. No long-range magnetic order is observed but longitudinally polarized spin dynamics building up below T ~ 50K [8].

A large single crystal UBe_{13} (T_c = 0.85 K) has been investigated by high-resolution cold neutron three-axis spectroscopy on PANDA at FRM2, Germany, and IN14 at ILL, France.

The energy dependence of the normal state response can be modeled superimposing a quasi-elastic (QE) contribution with a Lorentzian line-shape and an inelastic contribution. The QE signal is consistent with fluctuations established in previous experiments on powder samples and linked to anomalies in the specific heat, from which a Kondo temperature T_K = 20 K has been deduced. The inelastic contribution shows a maximum at ΔE = 0.55 meV probably related with the observed Schottky-like anomaly in bulk measurements around T = 2 K. Our data taken in the superconducting state show a shift of spectral weight to higher energies with respect to the normal state, which indicates the opening of a *superconducting* gap is reflected in the *spin* dynamics. The observed shift in UBe_{13} coincides with the inelastic contribution already present in the normal state, similar to the observation of a pseudogap pahse in under-doped copper-based high-T_c-superconductors.

Looking at the $U_{1-x}Th_xBe_{13}$ phase diagram, the temperature of this T = 2 K Schottly-like anomaly decreases with doping. This resembles the copper-based high-T_c superconductors, for which the pseudogap temperature decreases with doping. The anomaly vanishes at the concentration with highest T_c. With such a scenario in mind, we are currently investigating the energy scales of optimally doped $U_{1-x}Th_xBe_{13}$ with x = 0.035. Preliminary INS results will be presented and compared to our findings for the pure UBe_{13} compound.

References

[1] K. Miyake et al. Phys. Rev. B 34 6554 (1986), D.J. Scalapinoet al, Phys. Rev. B 34 8190 (1986), P. Monthoux et al. Nature 450 1177 (2007)

[2] O. Stockert et al., Nature Physics 7, 119-124 (2011), C. Stock et al., Phys. Rev. Lett. 100 (2008) 087001, N. Metoki et al., PRL 80 (‘98) 5417; N. Bernhoeft et al., PRL 81 (‘98) 4244;

[3] A. Hiess et al., J. Phys. Cond. Matt. 18 (2006) R437

[4] S. Coad et al., Physica B 276-278 (‘00) 764; A. Hiess et al., PRB 66 (‘02) 64531

1-86

The increase of the Curie temperature of UGa_2 at high pressure

A.V. Kolomiets[1,2], J. Prchal[2], J.-C. Griveau[3], L. Havela[2], A.V. Andreev[4]

[1]Department of Physics, Lviv Polytechnic National University, 12 Bandera Str., Lviv, Ukraine, [2]Department of Condensed Matter Physics, Charles University, Ke Karlovu 5, 121 16 Prague, Czech Republic, [3]European Commission, Joint Research Centre, Institute for Transuranium Elements, Postfach 2340, Karlsruhe, Germany, [4]Institute of Physics, ASCR, Na Slovance 2, 182 21 Prague, Czech Republic

UGa_2 is a convenient model system for the investigation of the 5*f*-magnetism. It has the hexagonal crystal structure of the AlB_2 type and orders ferromagnetically at T_C = 126 K in a collinear ferromagnetic structure [1-3]. Despite the simplicity of the crystal and magnetic structures UGa_2 has several rather unusual features. Firstly, its high T_C coexists with the high degree of the 5*f* localization, which can be deduced from the large U-U spacing ($d_{U\text{-}U}$ = 4.01 Å), the uranium magnetic moments of μ_U = 3 μ_B/U obtained from the neutron diffraction, and the pronounced magnetocrystalline anisotropy. There is also an uncertainty about the 5*f* configuration: $5f^2$, $5f^3$, and even itinerant 5*f* were suggested by different authors [1,4-7]. The focus of the present work is the investigation of the 5*f* states by high-pressure resistivity and high-temperature susceptibility experiments. All measurements were performed on the parts of the same single crystal pulled by the Czochralski method in a tri-arc equipment.

The resistivity curves of UGa_2 for the ***i*** // ***a***-axis and ***i*** // ***c***-axis have similar shapes: $\rho(T)$ increases with the increasing temperature till approximately the Curie temperature, around which it comes through the broad maximum, and then decreases slightly all the way up to the room temperature. The room-temperature resistivity for the ***i*** // ***c*** exceeds 280 μOhm*cm and for the *a*-axis it is about twice lower. These values are incompatible with the simple electron-phonon scattering expected for the case of the purely localized or delocalized 5*f* states. Moreover, they are close to or even exceed the maximum resistivity of 200 μOhm*cm expected for metallic systems.

The $\rho(T)$ shape in UGa_2 is convenient for the determination of the Curie temperature: the steep drop in resistivity just below the broad maximum, which corresponds to the T_C, can be determined by derivation even at high pressures when the anomaly gets broadened. The ***i*** //***c*** setup was used in high-pressure studies as the anomaly at T_C is more pronounced than for ***i***//***a***.

The application of external pressure lowers the slope of the $\rho(T)$ curve below the T_C and broadens as the anomaly accompanying the FM ordering (Figs. 1,2). Still the position of the T_C can be traced unambiguously up to p = 15.2 GPa, which was the highest pressure achieved in the current experiment. The Curie temperature increases monotonously with increasing pressure till p = 14.2 GPa where it reaches 154 K, and then drops rapidly to 147 K at 15.2 GPa (Fig. 2).

The increase of pressure also has a dramatic effect on the conduction electron scattering particularly in the magnetically disordered state. The room temperature resistivity decreases by the factor of 3 at p = 15.2 GPa compared to the ambient pressure. Also between 11.9 GPa and 15.0 GPa the metallic character of the resistivity is recovered, and even though at p = 15.0 GPa the $\rho(T)$ slopes still differ below and above T_C, the resistivity increases with increase of temperature in the whole temperature range.

The low-T resistivity of UGa_2 is dominated by the electron-magnon scattering with the magnon gap Δ of about 65 K and 50 K for the *a*- and *c*-axis, respectively. The gap width can be associated with magnetic anisotropy within the basal plane. Its value for ***i***//***c*** was found increasing up to 90 K at p = 8 GPa and then again decreases down to 50 K at p = 15.2 GPa.

Susceptibility measurements at ambient pressure were performed up to T = 650 K in order to investigate the possible effect of the CEF excitations and spin fluctuations. A broad anomaly was observed on $\chi(T)$ around 320 K, on both sides of which the magnetic susceptibility can be described by the Curie-Weiss law with different effective moments.

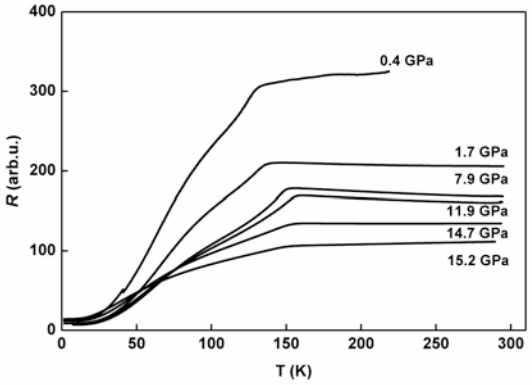

Fig. 1. Pressure effect on the resistivity of UGa_2 for ***i*//*c***.

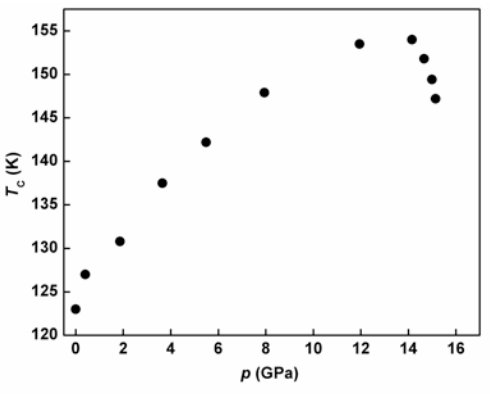

Fig. 2. Variation of the Curie temperature of UGa_2 with pressure.

The results presented above can be interpreted within a two-band model, in which the exchange interaction between the localized states is strengthened by applied pressure reaching a maximum, behind which the hybridization becomes destructive to U moments. The results indicate that UGa_2 represents indeed a special case of intermediate 5*f* delocalization with a strong pressure increase of T_C, which cannot happen neither in the 5*f* localized or 5*f* band limits. This gives restrictions to applicability of conventional DTF-type calculations.

Acknowledgements: This work was supported by the Czech Science foundation under the grant no. P204/10/0330. Participation in the European Commission JRC-ITU Actinide User Laboratory program through the support of the European Community-Access to Research Infrastructures action of the Improving Human Potential Programme (IHP), contract RITA-CT-2006-026176, is acknowledged

References

[1] R. Ballou et al. *J. Phys. Colloques* 43 (1982) C7.

[2] A. Andreev et al. *J. Phys. Colloques* 40 (1979) C4.

[3] A. C. Lawson et al. *J. Magn. Magn. Mater.* 50 (1985) 83.

[4] M. Divis et al. *Phys. Rev. B* 53 (1996) 9658.

[5] R. J. Radwanski and N.H.Kim-Ngan, *J. Magn. Magn. Mater.* 140-144 (1995) 1373.

[6] B. Reihl et al. *Phys. Rev. B* 32 (1985) 3530.

[7] T. Honma et al. *J. Phys. Soc. Japan* 69 (2000) 2647.

2-21

Amorphous 5*f* ferromagnet with high T_C: UH_3Mo_x

Ladislav Havela[1], Ilya Tkach[1], Zdenek Matej[1], Silvie Mašková[1], N.-T.H. Kim-Ngan[2], Alexander V. Andreev[3]

[1]Faculty of Mathematics and Physics, Charles University, Prague, Czech Republic, [2]Institute of Physics, Pedagogical University, Krakow, Poland, [3]Institute of Physics, Academy of Sciences, Prague, Czech Republic

Uranium metal in the *bcc* form (γ-U) can be obtained at low temperatures by combined action of Mo doping and fast cooling. By the splat cooling technique we succeeded to obtain pure *bcc* phase (or its tetragonally distorted derivative) for as low as 11 at.% Mo [1]. This phase has a robust superconducting ground state. It is also more stable against oxidation than α-U and and we found that it also resists hydrogen absorption at ambient pressure. Certain H absorption can be forced at elevated H pressures. The amount of H absorbed corresponds to UH_3Mo_x.The product is not fine powder as for UH_3, but retains its bulk nature. Very broad XRD peaks point to amorphisation – the structure corresponds to UH_3 but the grain size is below 1 nm.

The material was subjected to low-temperature studies of electrical resistivity, magnetic susceptibility and heat capacity. All indicate a link to well known features of β-UH_3, ferromagnet with T_C = 175 K and spontaneous moment $\mu_s \approx 0.9$ μ_B/U [2]. The presence of Mo and/or structural disorder lead surprisingly to enhancement of both paramaters to $\mu_s \approx 1.0$ μ_B/U and T_C = 200 K for $UH_3Mo_{0.18}$. A striking feature is very high coercivity, reaching $\mu_0 H_c$ = 3.7 T at low temperatures, which can be associated with random distribution of high anisotropy. A link to β-UH_3 is also revealed by the similar value of the Sommerfeld coefficient γ = 29 mJ/mol K^2 for $UH_3Mo_{0.18}$. On the other hand, electrical resistivity has a weakly negative slope known from the U-Mo alloys, with an anomaly at 200 K superimposed. Absolute values exceeding 1000 μΩcm indicate a semi-metallic nature. Variations of parameters with Mo concentration are subject of current study and will be reported.

The newly synthesized hydride represents a new class of material – amorphous 5*f* ferromagnet with high T_C. Deviations from crystallinity at U compounds studied so far always led to the suppression of magnetic order [e.g. 3]. We conjecture that the reason for different behaviour of U hydrides is that despite a certain increase of the mean U-U spacing (which can enhance T_C, as T_C of UH_3 is stronly sensitive to compression [2]) it remains in the range of ferro coupling between neighbours. Magnetic moments are therefore not exposed to competing F-AF interactions.

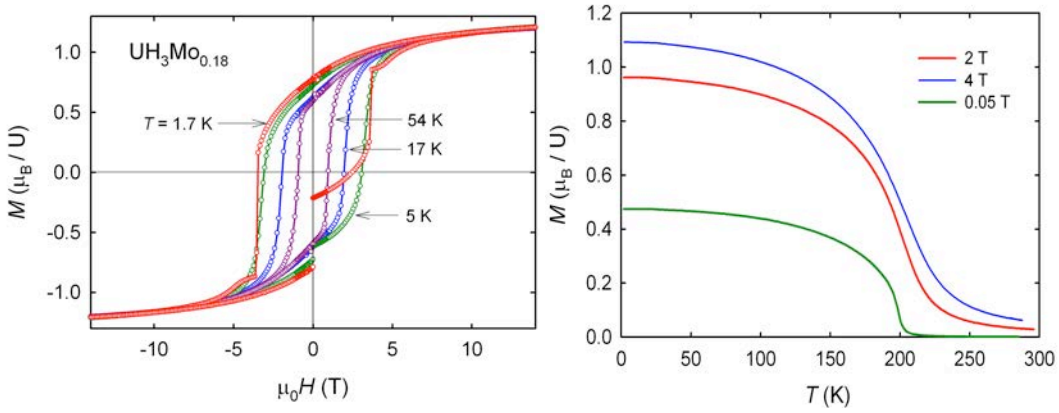

Fig.1: Hysteresis loops of $UH_3Mo_{0.18}$ at selected temperatures (from 1.7 to 54 K) -left- and temperature dependence of magnetisation in various fields - right.

Acknowledgements: This work was supported by the Czech Science Foundation under the grant No. P204/12/0285. Experiments were performed at MLTL (http://mltl.eu/), which is supported within the program of Czech Research Infrastructures (project no. LM2011025).

References

[1] I. Tkach et al., J. Alloys Comp. 534 (2012) 101.

[2] A.V. Andreev et al., J. Alloys Comp. 267 (1998) 32.

[3] L. Havela et al., J. Alloys Comp. 408-412 (2006) 1320.

3-93

The UCoGe ferromagnetic superconductor: results from HRTEM studies

Antonio P. Goncalves[1], Margarida S. Henriques[1], Elsa B. Lopes[1], Laura C.J. Pereira[1], Arne Janssen[2], Thierry Wiss[2], Silva Maskova[3], Jan Prokleska[3], Ladislav Havela[3]

[1]IST/ITN, Technical University of Lisbon, CFMC-UL, 2686-953-Sacavém, Portugal, [2]European Commission, Joint Research Centre, Institute for Transuranium Elements, D-76125 Karlsruhe, Germany, [3]Dept. Condensed Matter Physics, Faculty of Mathematics and Physics, Charles University, 121 16 Prague, Czech Republic

In BCS theory of superconductivity ferromagnetic order prevents the pairing of electrons in a singlet state [1]. The discovery of coexistence of superconductivity and ferromagnetism in UGe_2, URhGe and UCoGe [2-4] raised the question on the existence of new mechanisms of superconductivity formation. In UCoGe the superconductivity seems to occur at the border of the weak ferromagnetic ordering, the attraction between the electrons being mediated by critical magnetic fluctuations. Doping experiments showed the resistance of superconductivity to small variations in composition, but the UCoGe physical properties were also found to be extremely sensitive to the sample history [4-6]. We undertook a survey trying to relate the bulk magnetic and superconductiing properties with the microstructure details, as revealed by high-resolution transmission electron microscopy (HRTEM) using UCoGe samples subjected to different types of heat treatment.

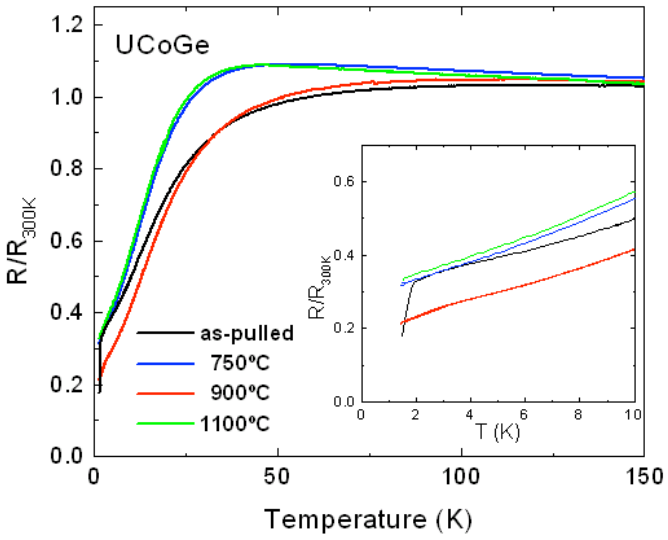

Figure. 1. Electrical resistivity ratio versus temperature of the UCoGe pulled material submitted to different heat treatments. Inset shows the low temperature details of the curves.

The study was undertook on the material pulled by the Czochralski method from a melt of a nominal composition 1.01U:1Co:1Ge. The compositional homogeneity of the as-pulled material was confirmed by microanalysis. The as-pulled material was cut in four pieces and three of them were submitted to heat treatments at 750ºC, 900ºC and 1100ºC, respectively. Powder XRD indicated the TiNiSi-type structure for all the four pieces, but the lattice parameters differ somewhat. The largest unit cell was found for the 900ºC sample. The minimum electrical resistivity and maximum residual resistivity ratio were also observed in the 900ºC sample (~5.5). The other materials present residual resistivity ratios more than 40% lower (Figure 1). The heat capacity and magnetic susceptibility measurements indicate ferromagnetism for all samples, the Curie temperature slightly decreasing on the heat treated materials.

The HRTEM characterization was made using pieces extracted from the same materials used in the bulk properties study. The as-pulled material shows a large number of Moire fringes, which reflect the high degree of defects observed at higher magnefications, as disorder, stacking faults and misalignments. The increase of the annealing temperature decreases the number of such defects. The material heat-treated at 750ºC still shows regions with HRTEM images similar to the as-pulled, arise with other regions with a high degree of long-range order and regions where the appearance of nano-domains can be seen. The 900ºC sample has a very high number of nano-domains (with 4-10 nm typical diameters), which is most probably related with its higher unit cell parameters and residual resistivity ratio value. The 1100ºC material shows no nano-domains and a high degree of long-range order.

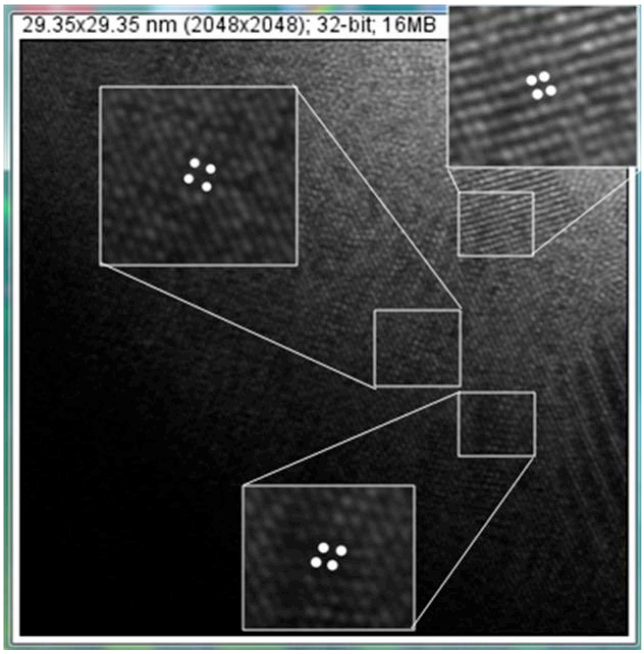

Fig. 2. HRTEM image of the UCoGe as-pulled material, evidencing the large number of defects.

Acknowledgments

This work was partially supported by the ACTINET-I3 project with Contract Number 232631, by FCT, Portugal, under the contract No. CERN/FP/123588/2011, and by the FCT-ASCR 2012 bilateral collaboration between Portugal and the Czech Republic. M.S.H. would also like to acknowledge the SFRH/BD/66161/2009 support.

References

[1] N. F. Berk, J. R. Schiefferm, Phys. Rev. Lett. 17 (1966) 433

[2] S.S. Saxena et al., Nature 406 (2000) 587

[3] D. Aoki et al., Nature 413 (2001) 613

[4] N.T. Huy et al., Phys. Rev. Lett. 99 (2007) 067006

[5] N.T. Huy, D.E. de Nijs, Y.K. Huang, A. de Visser, Phys. Rev. Lett. 100(2008) 077002

[6] D.E. de Nijs, N. T. Huy, A. de Visser, Phys. Rev. B 77 (2008) 140506(R)

3-94

New Uranium Heavy Fermion Antiferromagnet, γ>400 mJ/UmolK^2

Greg Stewart, Jungsoo Kim

Physics University of Florida, Gainesville, Florida, USA

We report the specific heat, 0.4 – 10 K, and the magnetic susceptibility, 2-300 K, of a new heavy Fermion antiferromagnet, T_N = 2.5 K. In addition to the second order magnetic phase transition, there is another transition clearly visible at 5 K in the specific heat (see Fig. 1) but not in the magnetic susceptibility, χ (see Fig. 2). Due to the lack of a signature in χ and the approximate field *independence* of the specific heat of this second transition at 5 K, we suggest that it is a structural phase transition as seen, e. g., in the A-15 superconductor (T_c≈17 K) V_3Si at 20 K[1].

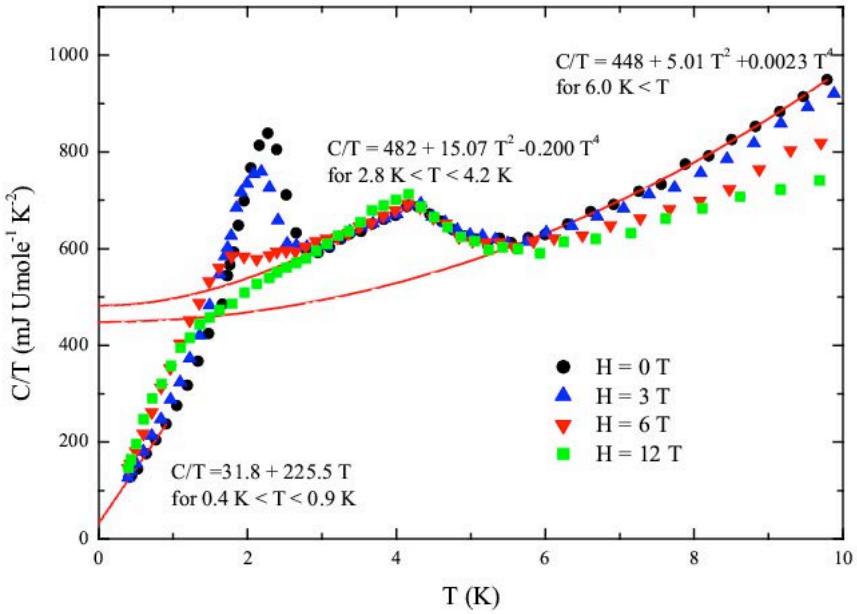

Figure1: Specific heat divided by temperature, C/T, vs temperature of a new uranium based heavy Fermion compound between 0.4 and 10 K, in zero and applied magnetic field. Fits shown are to the zero field data. Note the field independence of the transition at 5 K. The fit to the data above 5 K results in γ≈450 mJ/UmolK^2. The gapping of the Fermi surface by the magnetic order in the present system leaves a much smaller fraction of the T>T_N γ remaining than observed in the other two constant-γ heavy Fermion antiferromagnets U_2Zn_{17} and UCd_{11}[2-3], where γ(T→0) is about 30-35% of γ(T>T_N).

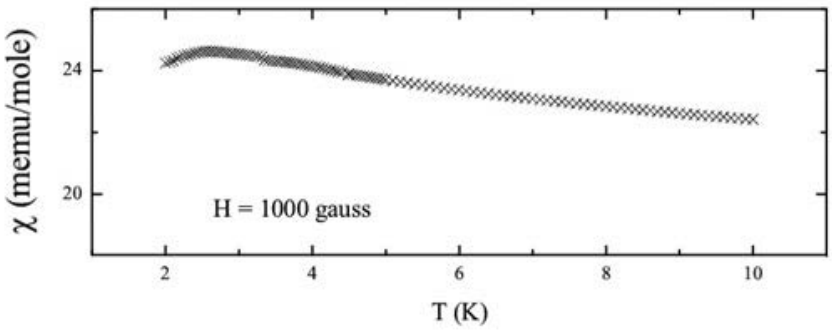

Figure 2: Low temperature dc magnetic susceptibility of a new uranium based heavy Fermion compound showing the antiferromagnetic transition at around 2.5 K and no indication of a magnetic anomaly around 5 K.

In comparing this discovery with previous magnetic Uranium-based heavy Fermion systems, the present work presents the first temperature-independent γ value* over 250 mJ/UmolK^2 since the antiferromagnets U_2Zn_{17} (T_N=9.7 K, γ=535 mJ/UmolK^2, χ(4 K)≈12 memu/Umol) and UCd_{11} (T_N=5.0 K, γ=840 mJ/UmolK^2, χ(4 K)≈38 memu/Umol) were discovered[2-3] in 1984. Other Uranium-based systems discovered since 1984 with large temperature-independent γ's include systems where magnetism coexists with superconductivity, e. g. UPd_2Al_3 (γ≈150 mJ/UmolK^2)[4] and URhGe (γ=164 mJ/UmolK^2)[5-6], magnets, e. g. UMn_2Al_{19} (γ≈250 mJ/UmolK^2)[7] and UCu_5In (γ≈240 mJ/UmolK^2)[8], and systems where no ordering is present, e. g. U_4RhGa_{12} (γ=140 mJ/UmolK^2)[9].

Resolving the possible question of coexistence of superconductivity with magnetism, as was found[6] in URhGe with better quality samples, must await refinement of sample quality and/or measurement to lower temperatures in the present system.

*as distinct from non-Fermi liquid materials where C/T is not the constant γ but rather diverges logarithmically as $T \rightarrow 0$

References

1. C. C. Huang, et al., Solid State Comm. 33, 581 (1980).
2. H. R. Ott, et al., Phys. Rev. Lett. 52, 1551 (1984).
3. Z. Fisk, et al., Phys. Rev. B 30, 6360 (1984).
4. C. Geibel, et al., Z. Phys. B 84, 1 (1991).
5. I. H. Hagmusa, et al., Physica B 281-282, 223 (2000).
6. D. Aoki, et al., Nature 413, 613 (2001).
7. C. H. Wang, et al., Phys. Rev. B 82, 094406 (2010).
8. D. Kaczorowski, et al., Phys. Rev. B 63, 144401 (2001).
9. R. Jardin, et al., J. Alloys and Comp. 432, 39 (2007).

5-06

Study of the phase equilibria in the Na-U-O, Na-Pu-O and Na-Np-O systems, and application to the safety of Sodium cooled Fast Reactors.

Anna Louise Smith[1,2], Philippe Raison[1], Emmanuelle Suard[4], Laura Martel[1], Joseph Somers[1], Jean-Yves Colle[1], Ondrej Benes[1], Christos Apostolidis[1], Gilles Wallez[5], Ian Farnan[3], Anthony Cheetham[2], Rudy Konings[1]

[1]Institute for Transuranium Elements, Karlsruhe, Germany, [2]Department of Materials Science and Metallurgy, University of Cambridge, Cambridge, UK, [3]Department of Earth Sciences, University of Cambridge, Cambridge, UK, [4]Institut Laue Langevin, Grenoble, France, [5]Laboratoire de Chimie de la matière condensée, UPMC, Chimie ParisTech, Paris, France

Operating in a closed fuel cycle and with a fast neutron spectrum, Sodium cooled Fast Reactors (SFRs) were considered as a promising option for the next generation of nuclear reactors by the International Generation IV Forum. SFRs present a high energy production yield, and sodium is particularly interesting as a metallic coolant because of its high heat capacity preventing overheating. One significant safety concern regarding these types of reactors comes from the potential interaction of the sodium metallic coolant with the fuel in case of a breach of the stainless steel cladding [1-3]. $(U_{1-x}Pu_x)O_2$ mixed oxide fuels are considered as a reference for such reactors as substantial experience has already been gained in terms of fabrication, reactor operation, reprocessing, and risk assessment. Past experimental work carried in the 1980s has shown however, that the interaction between sodium liquid and urania-plutonia solid solutions, leads to the formation of $Na_3(U_{1-x}Pu_x)O_4$ in the temperature range of the fuel during operation, at the boundary between cladding and fuel [4]. Moreover, the latter product is of lower density, and with less than half the thermal conductivity relative to the mixed oxide [1-3]. With such properties, one can anticipate local swelling and temperature increase in the fuel pin, potentially inducing further cladding failure, restraining the flow of coolant within a sub-assembly of fuel pins, or resulting in a contamination of the primary coolant with plutonium, minor actinides or highly radioactive fission products.

Despite many studies carried out on the fuel sodium reaction product given its technological importance, its crystal structure remains a subject of controversy [5]. The plutonium concentration in the MOX fuel being typically of the order of 20 wt%, the compounds Na_3UO_4 and $Na_3(U_{1-x}Pu_x)O_4$ are expected to be isostructural and have similar thermomechanical and thermodynamic properties [4]. The discrepancy regarding the crystal structure of Na_3UO_4 was therefore resolved in the present work. The product was shown to be isostructural with Na_3BiO_4, i.e. monoclinic with the space group P2/c using X-Ray diffraction coupled to neutron diffraction carried out at the Institut Laue Langevin (Grenoble). ^{23}Na Magic Angle Spinning Nuclear Magnetic Resonance was also performed on the compound, which confirmed the crystal structure with the existence of three different sites for sodium. The coefficients of thermal expansion were finally estimated in the temperature range 298 to 1073 K along the three directions: $\alpha_a(T) = 29.47.10^{-6}\ K^{-1}$, $\alpha_b(T) = 19.51.10^{-6}\ K^{-1}$, $\alpha_c(T) = 19.03.10^{-6}\ K^{-1}$. Those values are quite large compared to uranium oxide ($\alpha(T) = 10.8\times10^{-6}\ K^{-1}$), meaning that local swelling would be a real issue in the event of a clad breach.

One main goal of the Generation IV systems is sustainability through the optimization of uranium resources, and through the minimization and management of nuclear waste [6]. The long-term storage of high-level radioactive waste, especially of the long lived actinides (Np, Am, Cm) generated during the irradiation process in conventional nuclear, is a subject of primary concern for the nuclear industry with respect to the public. One solution to reduce the waste's radiotoxicity is hence to recover the long-lived isotopes (Np, Am, Cm) from the spent fuel and re-irradiate them in the fast reactors to transmute them in less -radioactive elements with shorter half-lives [7-8]. The use of advanced oxide fuels, i.e. (U, Pu, Np, Am, Cm)O_2 in SFRs will however introduce a very complex chemistry for which many data are still missing. The Na-U-O system has been extensively reviewed in the literature in terms of crystal structures [9], magnetic [10], spectroscopic [11] and thermodynamic properties [12]. The potential products of reaction are numerous: (Na_2UO_4, Na_4UO_5, $Na_2U_2O_7$, $NaUO_3$, Na_3UO_4, $Na_{11}U_5O_{16}$, Na_4UO_4), although some crystal structures and chemical compositions are still questioned. The data available on the Na-Pu-O and Na-Np-O systems is much more limited. Keller and his co-workers appear as the pioneers of the studies on the interaction of minor

actinides with alkali metals [13]. But a number of uncertainties remain about the phases, explored in the 1960s with the Debye-Scherrer method [14], while the thermodynamic data is almost non-existent [15]. As part of our program of research at the Institute for Transuranium Elements, we are currently re-investigating the crystal structures, thermomechanical and thermodynamic properties of the phases forming in the Na-U-O, Na-Pu-O and Na-Np-O ternary phase diagrams [16]. Such studies are of primary importance for the safety assessment and thermodynamic modelling of the system in accidental conditions. At the conference, we shall present our most recent results, including room temperature and high temperature X-Ray diffraction studies, Mössbauer spectroscopy for the determination of the oxidation state of the neptunium in the sodium neptunates, ^{23}Na Magic Angle Spinning Nuclear Magnetic Resonance for the structural characterization, drop calorimetry, PPMS and Knudsen effusion cell mass spectrometry [17] for the thermodynamic investigation of the various compounds.

[1] M. Housseau *et al.*, In *Panel Proceedings Series*, page 349 (IAEA, Vienna, 1974)

[2] P.E. Blackburn and W.K. Hubbard, In *Proceedings of Conference on Fast Reactor Fuel Element Technology*, R. Farmakes (Ed.), page 479 (Amer. Nucl. Soc., Hinsdale, Illinois, 1972).

[3] M. Housseau *et al.*, Report CEA-N-1588. 1973

[4] M.G. Adamson *et al.*, J. Nucl. Mater. 97 (1981) 203-212

[5] R. Lorenzelli *et al.*, J. Nucl. Mater. 130 (1985) 298-315

[6] A technology Roadmap for Generation IV Nuclear Energy Systems. Issued by the U.S. DOE Nuclear Energy Research Advisory Committee and the Generation IV International Forum (2002)

[7] L. Koch, J. Less-Common Met. 122 (1986) 371-382

[8] C.T. Walker and G. Nicolaou, J. Nucl. Mater. 218 (1995) 129-138

[9] S. Pillon, Etude des diagrammes de phases U-O-Na, Pu-O-Na et U,Pu-O-Na. PhD thesis, Univ. Du langudoc, (1989)

[10] S. Van den Berghe *et al.*, J. Solid State Chem. 177 (2004) 2231-2236

[11] V.A. Volkovich *et al.*, Vib. Spectrosc. 17 (1998) 83-91

[12] I. Grenthe *et al.*, *Chemical Thermodynamics of Uranium*. Issy-les-Moulineaux (France), OECD edition, (2004)

[13] C. Keller *et al.*, J. Inorg. Nucl. Chem. 27 (1965) 1225-1232

[14] L.R. Morss *et al.*, J. Alloy. Compd. 203 (1994) 289-295

[15] R.J. Lemire *et al.*, Chemical Thermodynamics of Neptunium and Plutonium. Elsevier Science B.V., Issy-les-Moulineaux (France), OECD edition (2001)

[16] A.L. Smith *et al*., J. Nucl. Mater. 413 (2010) 114-121

[17] A.L. Smith *et al*., J. Chem. Thermodyn. (2013) 132-141

5-07

Impact of hydrogen absorption on onset of magnetism in $U_2(Ni_{1-x}Fe_x)_2Sn$

Silvie Maskova[1], Ladislav Havela[1], Aleksandre Kolomiets[1,2], Khrystyna Miliyanchuk[3], Alexander V. Andreev[4], Heinz Nakotte[5], Joe Peterson[5]

[1]Department of Condensed Matter Physics, Charles University, Prague, Czech Republic, [2]Department of Physics, Lviv Polytechnic National University, Lviv, Ukraine, [3]Faculty of Chemistry, Ivan Franko National University, Lviv, Ukraine, [4]Institute of Physics, ASCR, Prague, Czech Republic, [5]Department of Physics, New Mexico State University, Las Cruces, USA

Polycrystals $U_2(Ni_{1-x}Fe_x)_2Sn$ and their hydrides were prepared so as to investigate the character and stability of magnetism in U_2Ni_2Sn (antiferromagnet with T_N = 26 K). Hydrogen absorption in U_2Ni_2Sn leads to stronger magnetic interactions ($U_2Ni_2SnH_{1.8}$ has T_N = 87 K [1]). The other terminal phase, U_2Fe_2Sn, does not show any long-range magnetic order and for this compound no hydrogenation studies have been published to date. A rapid suppression of antiferromagnetic order with increasing Fe concentration is evidenced by the reduction of T_N observed e.g. in C/T (fig.1). For $U_2(Ni_{0.8}Fe_{0.2})_2Sn$ the magnetic order is lost and the low-temperature C/T reveals behavior that is reminiscent of non-Fermi-liquid scaling. The Sommerfeld coefficient γ, which measures the electronic contribution to the specific heat, increases with increasing Fe concentration (fig. 2). It reaches a maximum value of ≈ 430 mJ/mol.K^2 for $U_2(Ni_{0.8}Fe_{0.2})_2Sn$. With further increment of Fe concentration, γ decreases again. Magnetic susceptibility stays temperature dependent with increasing Fe concentration but all attributes of Curie-Weiss behavior are lost.

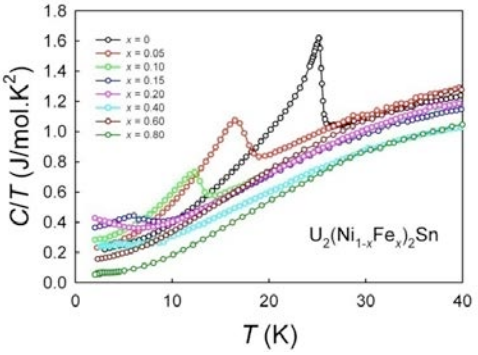

Fig. 1. Temperature dependence of the specific heat (in the C/T vs. T representation) for $U_2(Ni_{1-x}Fe_x)_2Sn$.

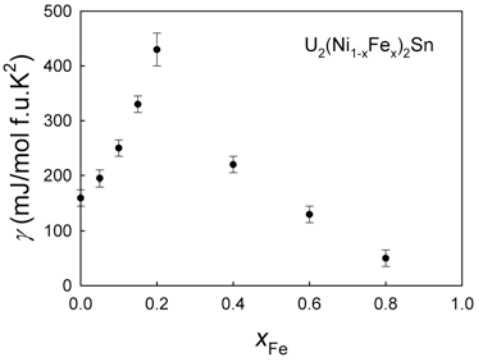

Fig. 2. Concentration dependence of Sommerfeld coefficient of specific heat of $U_2(Ni_{1-x}Fe_x)_2Sn$.

The hydrogen absorption of approx. 2 H/f.u. in AF compounds on the Ni rich side leads to an increase of the Néel temperature (fig. 3), nevertheless the ordering temperature also rapidly decreases with increasing Fe concentration. Antiferromagnetic order disappears at approximately the same Fe concentration as in the case of parent alloys. It seems that the lattice expansion upon hydrogenation in the $U_2(Ni_{1-x}Fe_x)_2Sn$ has only little influence on magnetic properties around x ≈ 0.2. The hydrogenation of Fe-rich alloys leads to an unexpected development of ferromagnetic order between x = 0.23 and 0.8 (T_C = 38 K at x = 0.6).

We can assume that a quantum critical point has been observed in $U_2(Ni_{1-x}Fe_x)_2Sn$ around 20% Fe. The behaviour resembles U_2Co_2Sn [2]. For the hydrides a weak ferromagnetism develops on the Fe rich side, extending almost up to $U_2Fe_2SnH_{1.7}$. This leads to an unusual situation as a parent quantum critical point appears as a singularity between two types of magnetic order. An attempt has been made to understand the variations in the context of strongly non-linear variations of different types of $d_{U\text{-}U}$.

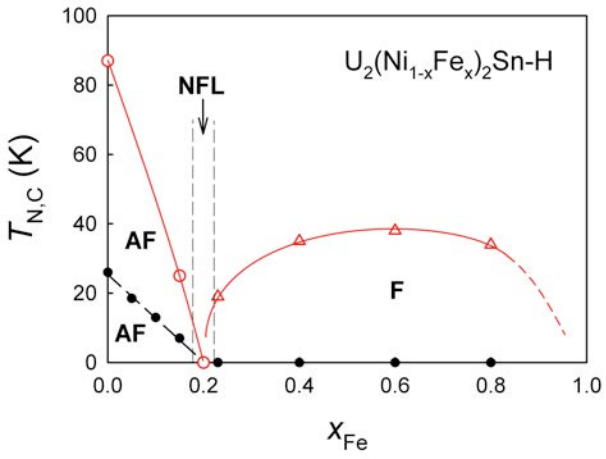

Fig. 3. Magnetic phase diagram of $U_2(Ni_{1-x}Fe_x)_2Sn$ and their hydrides (circles denote the Néel temperature, triangles the Curie temperature). Black full symbols correspond to parent compounds, red open symbols to the hydrides.

Acknowledgement

This work was supported by the Grant Agency of the Czech Republic under the grants No. 204/12/0285 and 204/10/0330. Experiments were performed at MLTL (http://mltl.eu/), which is supported within the program of Czech Research Infrastructures (project no. LM2011025).

References

[1] K. Miliyanchuk, L. Havela, A.V. Kolomiets, S. Danis, L.C.J. Pereira, A.P. Gonçalves, Physica B 378-380, 983 (2006).

[2] J. S. Kim, J. Alwood, S. A. Getty, F. Sharifi, and G. R. Stewart, Phys. Rev. B 62, 6986 (2000).

5-08

Density Functional Study of CO Adsorption on Pu (100) Surface

Wenhua Luo, Daqiao Meng, Gan Li, Huchi Chen

China Academy of Engineering Physics, Mianyang,Sichuan, China

The adsorption of CO molecules on Pu (100) surface is investigated using the generalized gradient approximation (GGA) of spin-polarized density functional theory (DFT) with RPBE functional. Several possible adsorption configurations considered here (see Table 1), the O-down adsorption is less stable than the C-down adsorption which is found to be strong chemisorption. The stability of adsorption configuration of CO is fourfold tilted > fourfold vertical > twofold vertical > onefold. A CO molecule of the most stable configuration is tilted relative to the surface normal by 56.5°. In this case, the CO bond is elongated to 1.37 Å and the adsorption energy is 31.6 kcal/mol. Mulliken charge distribution analysis indicates that the interaction of Pu with CO mainly takes place in the first layer with the other three layers being only slightly affected. Density of states (DOS) analysis indicates that the interaction between Pu atom and CO molecule results mainly from the contribution of hybridized molecular orbital of CO molecule and hybridized orbital of surface Pu atoms, and adsorptions of CO push the top of 5f band deeper away from the Fermi level, indicating further bonding by the 5f orbitals might be less probable. A similar calculation performed for the C and O atoms indicates that the adsorption at the fourfold site is the most stable among various configurations, with adsorption energies of 164.6 and 170.5 kcal/mol, respectively. Finally, the barriers for dissociation of CO bound in a fourfold site have been calculated to be 6.5 kcal/mol, indicating that the dissociation of a CO molecule can takes place even in the low-temperature regime.

Table 1 The optimized geometrical and energy parameters for CO/Pu (100) system

configuration		φ^{a} / °	$r_{C\text{-}O}$ / Å	$r_{Pu\text{-}C}{}^{b}$ / Å	$r_{Pu\text{-}O}{}^{b}$ / Å	$h_{X\text{-}surf}{}^{c}$ / Å	E_{abs} / eV
onefold	O-down	0	1.138	4.646	3.508	3.508	0.291
	C- down	0	1.161	2.437	3.598	2.437	1.012
twofold vertical	O-down	0	1.137	5.557	4.483	4.173	0.288
	C-down	0	1.177	2.562	3.547	1.969	1.077
fourfold vertical	O-down	0	1.137	5.818	4.797	4.199	0.286
	C-down	0	1.198	2.777	3.579	1.529	1.176
fourfold tilted	C-down	56.47	1.372	2.383	2.321	0.776	1.371
CO (isolated)			1.136				

a: φ represents the angle between the C-O bond and the normal vector to the surface.

b: *r* represents the shortest distance of the C or O atom to the Pu atoms in the first layer.

c: *h* represents the height of the C or O atom in CO above the surface.

POSTERS

1-45

On Relationship Between Thermodynamic and Dynamic Properties of Light Actinides

Alexander Uchaev, Nadezda Selchenkova, Elena Kosheleva, Valery Punin

Russian Federal Nuclear Center – VNIIEF, Sarov, Russia

Earlier it was shown [1-3], that the dynamic failure process was a phase transition similar to the second order phase transition and percolation transition, when connectivity appeared in the failure centers cascade, changing the body continuity that was characterized by a density variable - susceptibility, related to failure centers density. This process is non - linear [1]. In non-linear dissipative media under high-intense action a number of degrees of freedom decreases. This means, that the system undergoes a self-arrangement of non-equilibrium system structural elements, characterized by large-scale correlations. Such transitions are also called kinetic phase transitions. Earlier it was also demonstrated that the dynamic failure process occurred at specific time-amplitude values of depression wave, moreover the critical value of absorbed energy, leading to failure, correlated to a thermodynamic enthalpy potential [2].

The above-said grounds the possibility for introducing the efficient failure temperature T_{eff}, as a property of dynamic failure process, in the wide longevity ranges $t \sim 10^{-6} \div 10^{-10}$ s. Effective failure temperature T_{eff}, as well as Debay temperature θ_D, melting temperature T_{melt} are quantitative characteristics, in the given case - percolation phase transition characteristics.

Let's note that dissipative structures being developed on different time-scale levels by Le Chatelier principle resist to the external high-intense action and determine the time boundary of maintaining functional metal properties under extreme conditions [3].

For the first time for actinides (Th, U, Np, Pu) there have been specified efficient temperatures T_{eff}, which are quantitative characteristics of the dynamic failure process. $T_{eff}(t)$ specifies the atom energy in a cell in the mode of mass depression wave velocity, which while developing a pulsed negative pressure, causes the dynamic failure phenomenon.

References

1. R.I.Il'kaev, V.T.Punin, A.Ya.Uchaev, N.I.Selchenkova, L.A.Platonova, Ye.V.Kosheleva, A.S.Konkin. Physical nature of metals longevity in the dynamic failure phenomenon //Nuclear physics and engineering. 2010, vol. 1, № 2, p.99-103.

2. R.I.Il'kaev, A.Ya.Uchaev, S.A.Novikov, N.I.Zavada, L.A.Platonova, N.I.Selchenkova. Universal metals properties in the dynamic failure phenomenon. // Academy for Sciences Reports, 2002, vol. 384, № 3, P. 328-333.

3. Uchaev A.Ya., Punin V.T., Selchenkova N.I., Kosheleva E.V. On synergetic and athermic processes in the dynamic destructive phenomena. Zababakhin scientific lectures: Collection of proceedings of XI International Conference, 16-20 April 2012. – RFNC – VNIITF, Snezhinsk. RFNC-VNIITF's publishing house, 2012. P.198-199.

1-46

Physical properties of UBeGe and ThBeGe intermetallic compounds

Roman Gumeniuk, Andreas Leithe-Jasper, Walter Schnelle, Michael Nicklas, Ulrich Burkhardt, Horst Borrmann, Yuri Grin

MPI CPfS, Dresden, Germany

In the past decades the U-containing ternary compounds with 1:1:1 and binaries with 1:2 stoichiometries were object of numerous studies. Among them, the orthorhombic germanide UGe_2 is of special interest. Being a ferromagnet with a pretty high T_C = 52 K, it becomes superconducting under pressures of 1.0–1.6 GPa [1, 2]. The dual behavior of the U 5*f* electrons plays in such cases the most important role and often is not well understood. Here we report on the crystal structure and physical properties of the new ternary germanides ThBeGe and UBeGe.

Samples of UBeGe and ThBeGe were prepared by arc melting of pieces of U (99.9 wt. %), Th (99.7 wt. %), Be (99.9 wt. %) and Ge (99.999 wt. %) elements. The resulting ingots were placed in Al_2O_3 crucibles, sealed in tantalum tubes, and annealed at 900 °C for 240 hours. Powder X-ray diffraction (XRD) of the products was performed on a HUBER G670 imaging plate Guinier camera with Cu$K_{\alpha 1}$ radiation (λ = 1.540598 Å). Lattice parameters refinement by least squares fitting, crystal structure solution from X-ray powder diffraction pattern and refinement have been done using the program package *WinCSD* [3]. The scalar-relativistic electronic structures of all compounds were calculated using the full-potential FPLO code (version 9.01-35) [4]. The magnetization of the samples was measured in a SQUID magnetometer (MPMS XL-7, Quantum Design). The heat capacity and electrical resistivity measurements were performed with a relaxation-type calorimeter (PPMS, Quantum Design).

Both UBeGe (a = 3.8948(1) Å, c = 8.1536(1) Å, R_I = 0.076, R_P = 0.103) and ThBeGe (a = 3.9659(1) Å, c = 8.5343(2) Å, R_I = 0.065, R_P = 0.095) crystallize with ZrBeSi structure type (space group $P6_3/mmc$) [5], which belongs to the family of the derivatives of the AlB_2 prototype. The observed U-U contacts in the UBeGe are of 3.8948(1) Å, thus being well above the Hill limit (3.5 Å) suggesting a rather localized nature of U 5*f* electrons.

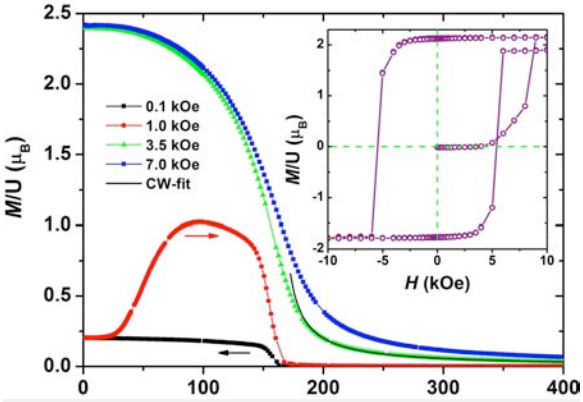

Fig. 1. Temperature dependence of magnetization of UBeGe in different magnetic fields together with Curie-Weiss fit (black line). Inset: magnetization isotherms at 1.8 K.

The temperature dependence of the magnetization (Fig. 1) shows UBeGe to order ferromagnetically at T_C = 157 K. The low fields measurements indicate a rather low anisotropy The experimentally determined saturation moment of 2.43 μ_B/U-atom at 7T agrees well with the theoretically calculated one (LSDA+U) of 2.1 μ_B/U-atom. The magnetization loop at 1.8 K is pronounced rectangular with a large coercive field of ≈ 0.55 T (inset to Fig. 1). In the paramagnetic range Curie-Weiss behaviour with μ_{eff} = 3.2 μ_B and θ_P = 160 K is observed, in agreement with strong ferromagnetic interactions. Electrical resistivity and specific heat capacity show strong second-order type anomalies at T_C. All these findings would indicate a well localized character of U 5*f* electrons, which was already expected from the crystal structure.

Theoretical (LDA) calculations predict ThBeGe to be a simple metallic system with low density of states at the Fermi level, $N(E_F)$ = 0.6 states eV^{-1} $f.u.^{-1}$. The DOS at EF is mostly due to the mixing of Th 6*d*, Be 2*p* and Ge 4*p* states.

The electrical resistivity, $\rho(T)$, of polycrystalline pieces of ThBeGe increases with increasing temperature in the whole measured temperature range. The room-temperature resistivity $\rho_{(300\ K)}$ of ThBeGe of 173 μΩ cm together with the ρ_0 of 89 μΩ cm indicates fair quality of the investigated specimen (RRR = 1.9).

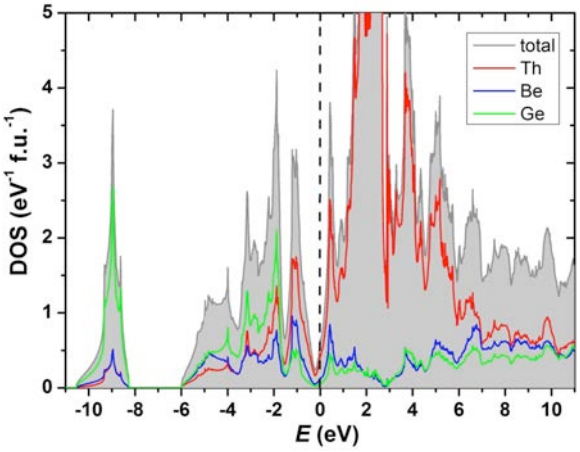

Fig. 2. Electronic structure of ThBeGe.

The Sommerfeld coefficient γ = 1.1 mJ mol^{-1} K^{-2} of the low temperature specific heat (1.8 - 8 K) of ThBeGe indicates a low DOS at the Fermi level of ≈ 0.5 states eV^{-1} f.u.$^{-1}$, which is in excellent agreement with the theoretical calculations.

In conclusion we synthesized two new intermetallics representatives UBeGe and ThBeGe crystallizing with ZrBeSi type of structure. UBeGe is a ferromagnet with T_C = 157 K and with a large coercive field of ≈ 0.55 T. Analysis of the crystal structure as well as studied physical properties show rather localized character of the U 5*f* electrons in this compound. ThBeGe is a simple metallic germanide with low density of states at the Fermi, which was confirmed by theoretical calculations and measurements of electrical resistivity and specific heat.

[1] A. Huxley, I. Sheikin, E. Ressouche, N. Kernavanois, D. Braithwaite, R. Calemczuk, J. Flouquet, Phys. Rev. B **63**, 144519 (2001).

[2] R. Troc, Z. Gajek, and A. Pikul, Phys. Rev. B **86**, 224403 (2012).

[3] L. Akselrud, P. Zavalii, Y. Grin, V. Pecharsky, B. Baumgartner, E. Wölfel, Mater. Sci. For. **335**, 133 (1993).

[4] K. Koepernik, H. Rosner, Phys. Rev. B **59**, 1743 (1999).

[5] J. Nielsen, N.C. Baenziger, Acta *Crystallogr.* **7**, 132 (1954).

1-47

On the possibility of predicting the dynamic properties of light actinides

Elena Kosheleva, Alexander Uchaev, Valery Punin, Nadezda Selchenkova

Russian Federal Nuclear Center- VNIIEF, Sarov, Russia

According to literature data light actinides, for example, such as Th, U, Np, Pu can be used as energy nuclear materials [1, 2]. Consequently, acute is knowledge of light actinides behavior under extreme conditions at high-intense external action. This is related to abnormal operation modes of high-intense power facilities. A high-intense pulsed heat-up of a condensed media can lead to the medium wave motion, developing a negative pressure. At definite amplitude of external action in local regions there can arise dynamic destructive processes, in this case an element or a facility unit loses its functional properties.

Results of studies conducted earlier have shown that condensed media, involving metals, reveal universal synergetic attributes of relaxation of strongly non-equilibrium states through destructive processes. In its turn, dynamic destructive processes in condensed media on different time-scale levels are of cooperative character. This is conditioned by fractal nature of dissipative structure ensembles, arising as a result of high-intense action onto the condensed media, their percolation properties, non-equilibrium system transitions from one time-scale level onto another one, obeying a concentration criterion as well as by the fact that a state probability of the system is not proportional to the distribution Boltzmann function [3-5]. Quantitative characteristic of relaxation processes is a generalized susceptibilityχ. In case of mechanical systems the role of generalized susceptibility χ is played by compressibility *K,* related to a density variable – the density of failure centers [3, 4].

The unique mechanism of the dynamic failure process (the loss of the body connectivity through clustering of failure centers cascade), the unique order parameter (final density *N(t)* of failure centers) and equal space dimension, where the process goes on, specify the possibility for predicting of light actinide dynamic properties.

Based upon the earlier determined relationship $P^{\gamma}(t) \cdot t = \text{const}$ ($\gamma = 3{,}8$, *P(t)* - pressure, leading to failure), which is true for the process of the dynamic metals failure with different z in the longevity range $t \sim 10^{-6} \div 10^{-10}$ s, as well as on the basis of determined scaling ratios of accumulating dissipative structure cascade on different time-scale levels (starting from the nano-level and up to the macro-level), light actinides' behavior under extreme conditions have been predicted.

References

1. Physical encyclopedia / the chief editor A.M. Prokhorov. M.: The Great Russian Encyclopedia. The chief editor A.M. Prokhorov, V. 3. 1992. P. 327.

2. Physical encyclopedia / the chief editor A.M. Prokhorov. M.: The Great Russian Encyclopedia. V. 5. 1998. P. 148.

3. R.I.Il'kaev, V.T.Punin, A.Ya.Uchaev, N.I.Selchenkova, L.A.Platonova, E.V.Kosheleva, A.S.Konkin. Physical nature of metals longevity in the dynamic failure phenomenon //Nuclear Physics and Engineering, 2010, vol. 1, № 2. - P. 99-103.

4. Uchaev A.Ya., Punin V.T., Selchenkova N.I., Kosheleva E.V. On synergetic and athermic processes in the dynamic destructive phenomena. Zababakhin scientific lectures: Collection of report abstracts of XI International Conference, 16-20 April 2012. – RFNC – VNIITF, Snezhinsk. - P.198-199

5. R.I.Il'kaev, V.T.Punin, A.Ya.Uchaev, S.A.Novikov, E.V.Kosheleva, L.A.Platonova, N.I.Selchenkova, N.A.Yukina. Time regularities of metals dynamic failure, conditioned by hierarchy properties of dissipative structures – a failure centers cascade // Academy for Sciences Reports, 2003, vol. 393, № 3. - P. 326-331.

1-48

Physical nature of light actinides longevity in the dynamic failure phenomenon

Nadezda Selchenkova, Alexander Uchaev, Valery Punin, Elena Kosheleva

Russian Federal Nuclear Center – VNIIEF, Sarov, Russia

It is known that a number of actinides are nuclear energy materials that can be used in pulsed research facilities, where they are subject to high-intense action [1, 2]. As a rule, relaxation of strongly non-equilibrium states is accompanied by destructive processes [3, 4]. In papers [3, 5] it is shown, that from a self-similarity property of damageability accumulation there results a bond between the amplitude of critical pressure $P(t)$ and the material longevity *t*, defined as

$$P(t)^{\gamma} t = const,$$

where $\gamma \approx 3{,}8$. This very condition specifies the ability for simulating the dynamic failure process under laboratory conditions when scaling the real time process [3]. The longevity is composed of the waiting time of failure centers occurrence $t_{wt.}$ and the time of clustering of failure centers cascade $t_{c.}$, when connectivity in the failure centers system, and a percolation cluster arise.

In papers [2, 4] it was shown that $t_{wt.} >> t_{c.}$ Due to this correlation, $t_{wt.}$ time determination evaluates the time boundary of maintaining the functional properties of metals under extreme conditions. In case of mechanical systems the role of generalized susceptibility χ is played by compressibility *K,* related to a density variable – the density of failure centers $N(t) = \int J(t)dt$ [4, 6]. The centers formation rate *J(t)* of a number of studied metals, as the research results show, presented in paper [4], have similar values. It was applied R/S analysis [7] for determination Hearst index of failure centers distribution in the failure surface of metallic Pu [8], subject to shock-wave effect and the failure surfaces of copper and steel samples, affected by a thermal shock. Hearst index H_{Pu} = 0,7, H_{Cu} = 0,66, H_{Fe} = 0,65 possess similar values, what justifies to the similarity of failure processes in the mentioned samples.

It is demonstrated, that the physical nature of light actinides longevity, placed in the extreme conditions (thermal shock action) in the range of non-equilibrium states $t \sim 10^{-6} – 10^{-10}$ s is determined by the time of formation of critical concentration of failure centers cascade (changing the body connectivity) which are a percolation cluster. The unique mechanism of the dynamic failure process (the loss of the body connectivity through clustering of failure centers cascade), the unique order parameter (final density *N(t)* of failure centers) and similar space dimension, where the process is going on, specify the physical nature of metals longevity, involving fissile materials.

References

1. Physical encyclopaedia / Chief Editor A.M. Prokhorov. M.: The Great Russian Encyclopaedia. V. 3. 1992. P. 327.
2. Physical encyclopaedia / Chief Editor A.M. Prokhorov. M.: The Great Russian Encyclopaedia. V. 5. 1998. P. 148.
3. R.I.Ilkaev, V.T.Punin, A.Ya.Uchaev, S.A.Novikov, E.V.Kosheleva, L.A.Platonova, N.I.Selchenkova, N.A.Yukina. Time regularities of the process of metals dynamic failure, conditioned by hierarchy properties of dissipative structures – failure centers cascade. // Academy for Sciences Reports, 2003, vol. 393, № 3. - P. 326-331.
4. R.I.Ilkaev, V.T.Punin, A.Ya.Uchaev, N.I.Selchenkova, L.A.Platonova, E.V.Kosheleva, A.S.Konkin. Physical nature of metals longevity in the dynamic failure phenomenon //Nuclear Physics and Engineering. 2010, vol. 1, № 2, p.99-103.
5. R.I.Ilkaev, A.Ya.Uchaev, S. A. Novikov, N.I. Zavada, L.A.Platonova, N.I.Selchenkova. Universal properties of metals in the dynamic failure phenomenon. // Academy for Sciences Reports, 2002, vol. 384, № 3, P. 328-333.

1-19

Ab initio prediction of surface stability of fluorite materials and experimental verification

Pablo Maldonado[1], José R. A. Godinho[2], Lena Z. Evins[3], Peter M. Oppeneer[1]

[1]Department of Physics and Astronomy, Uppsala University, Uppsala, Sweden, [2]Department of Geological Sciences, Stockholm University, Stockholm, Sweden, [3]Swedish Nuclear Fuel and Waste Management Co., Stockholm, Sweden

Understanding the surface properties and surface reactivity of materials with the fluorite-type structure, such as UO_2, ThO_2 and PuO_2 is crucial for achieving comprehensive knowledge of then long-term dissolution and alteration of spent nuclear fuel. In this context, CaF_2 and CeO_2 are used as surrogates to UO_2 in dissolution experiments.

Utilizing first-principle simulations [based on density functional theory (DFT) corrected for on-site Coulomb interactions (DFT+U)] we develop a model to explain the experimental stability in solution of materials having the fluorite structure, such as CaF_2 and CeO_2. It is shown that the stability of a surface is mainly dependent on its atomic structure and the presence of sites where atoms are deficiently bonded. Using as reference planes the surfaces with low surface formation energies, viz. (111), (100) and (110), our results reveal the relation between the surface energy of any Miller-indexed plane and the surface energy of those reference planes, being dependent on the fluorite surface structure only. Therefore they follow the same trend for CaF_2 and CeO_2. Comparison with experimental results shows a correlation between the trends of dry surface energies and surface stabilities during dissolution of both CaF_2 and CeO_2. Even though the chemical processes of dissolution of CeO_2 and CaF_2 are different. A further computation of ThO_2 and UO_2 surfaces has been made to verify the results on actinide surfaces.

Furthermore, we have studied the adsorption energies and the coverage-dependent adsorption energies of water on the (111) surface of CeO_2 and UO_2. *Ab initio* molecular dynamics (AIMD) simulations have been performed to probe the configurational space of the adsorbed water molecules starting from different initial atomic configuration. A DFT+U calculation was performed using the lowest-energy structures along with molecular dynamics simulations for the computation of the adsorption energies. The energy barrier of the dissociative adsorption of one water molecule in both systems is computed.

To appear in J. Phys. Chem. C (2013) DOI: http://pubs.acs.org/doi/abs/10.1021/jp312645f

The research leading to these results has received funding from the European Atomic Energy Community's Seventh Framework Programme (FP7/2007-2011) under grant agreement No. 269903.

1-49

Magnetization of U_2Fe_3Ge and $U_3Fe_4Ge_4$ under external pressure

Alexander Andreev[1], Zdenek Arnold[1], Denis Gorbunov[1,2], Margarida Henriques[3], Ladislav Havela[2], Antonio Gonçalves[3]

[1]Institute of Physics ASCR, Prague, Czech Republic, [2]Dept. Condensed Matter Physics, Charles University, Prague, Czech Republic, [3]Instituto Superior Técnico, Sacavém, Portugal

We present results of magnetization study of two intermetallic compounds of the U-Fe-Ge ternary system, U_2Fe_3Ge and $U_3Fe_4Ge_4$, under high hydrostatic pressure. The magnetization was measured using SQUID magnetometer in fields up to 7 T at ambient and elevated (up to 0.9 GPa) pressure along the easy magnetization axis of single crystals.

U_2Fe_3Ge crystallizes in the hexagonal Mg_2Cu_3Si structure, an ordered variant of the hexagonal $MgZn_2$ Laves phase, and orders ferromagnetically at Curie temperature T_C = 55 K. Magnetic moments lie in the basal plane with the spontaneous magnetic moment M_s of 1.0 μ_B/f.u. at T = 2 K. The anisotropy field along the *c*-axis is 10 T at T = 2 K. No anisotropy within the basal plane was detected [1]. $U_3Fe_4Ge_4$ crystallizes in the orthorhombic $Gd_3Cu_4Ge_4$ structure type and is a ferromagnet with M_s of 1.2 μ_B/f.u. at T = 2 K and T_C = 18 K. The easy-magnetization direction is the-*a* axis, anisotropy fields along the *b*-and *c*-axis are 40 and 60 T, respectively, at T = 2 K [2]. Ordered magnetism is associated with uranium sublattice in both cases. It dominance in the magnetism follows from the ^{57}Fe Mössbauer spectroscopy study suggesting very low or even zero Fe moments.

The magnetization measurements at high hydrostatic pressure up to 0.9 GPa were performed on single crystalline samples in a SQUID magnetometer using a miniature piston-cylinder CuBe pressure cell. The cell was filled with a mixture of mineral oils as a pressure transmitting medium. The pressure was determined at low temperatures using the known pressure dependence of the critical temperature of the superconducting state of the Pb sensor placed inside the cell. The studies were performed in magnetic fields up to 7 T in the temperature range from 2 K to 50 K.

In both compounds, M_s and T_C are very sensitive to the external pressure. Figure 1 demonstrates the decrease of magnetization under pressure. Figure 2 shows the pressure dependence of M_s and T_C. Critical pressure of suppression of the ordered magnetism is estimated as 3-4 GPa. Whereas T_C decreases with pressure with approximately the same rate ~25%/GPa, M_s changes much faster in U_2Fe_3Ge (33%/GPa) than in $U_3Fe_4Ge_4$ (13%/GPa). Such high values of pressure derivatives point to mostly itinerant character of 5*f* electrons in the compounds. Nevertheless, we can conclude that degree of localization is higher in $U_3Fe_4Ge_4$ that generally correlates with much higher magnetic anisotropy of this compound compared to the Laves phase U_2Fe_3Ge with very low U-U spacing. So far we cannot relate the pressure effects with a true volume compression for both compounds, as the bulk modulus (130 GPa) has been studied only for U_2Fe_3Ge.

Acknowledgements: This work was supported by the Czech Science Foundation under the grant No. P204/12/0150. Experiments were performed at MLTL (http://mltl.eu/), which is supported within the program of Czech Research Infrastructures (project no. LM2011025).

References

[1] M.S. Henriques, D.I. Gorbunov, J.C. Waerenborgh, L. Havela, A.B. Shick, M. Diviš, A.V. Andreev, A.P. Gonçalves, J. Phys.: Condensed Matter 25 (2013) Art. No. 066010.

[2] M.S. Henriques, D.I. Gorbunov, J.C. Waerenborgh, L. Havela, A.V. Andreev, Y. Skourski, A.P. Gonçalves, J. Alloys Comp. 555 (2013) 304.

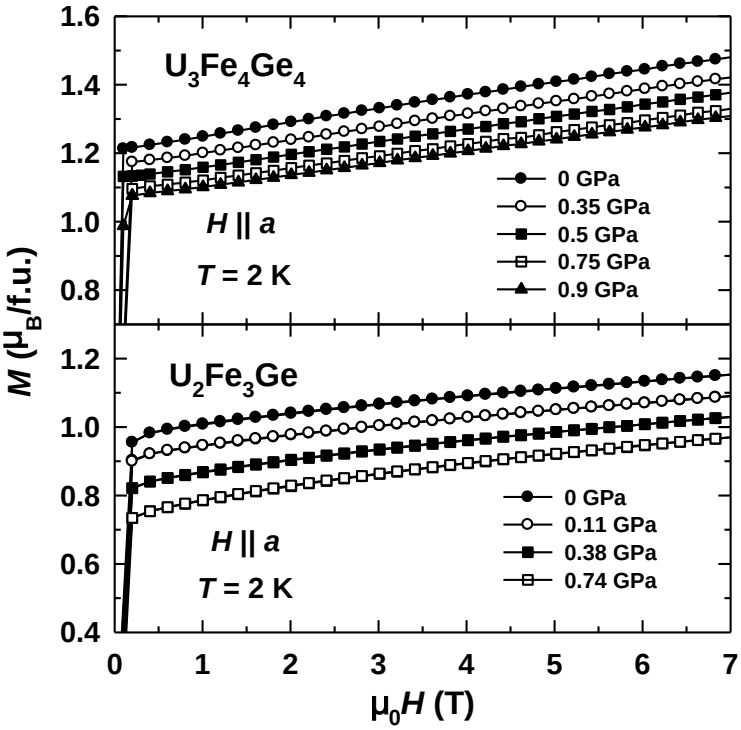

Fig. 1. Magnetization curves at different pressure at T = 2 K in field applied along the easy axis of the $U_3Fe_4Ge_4$ and U_2Fe_3Ge single crystals.

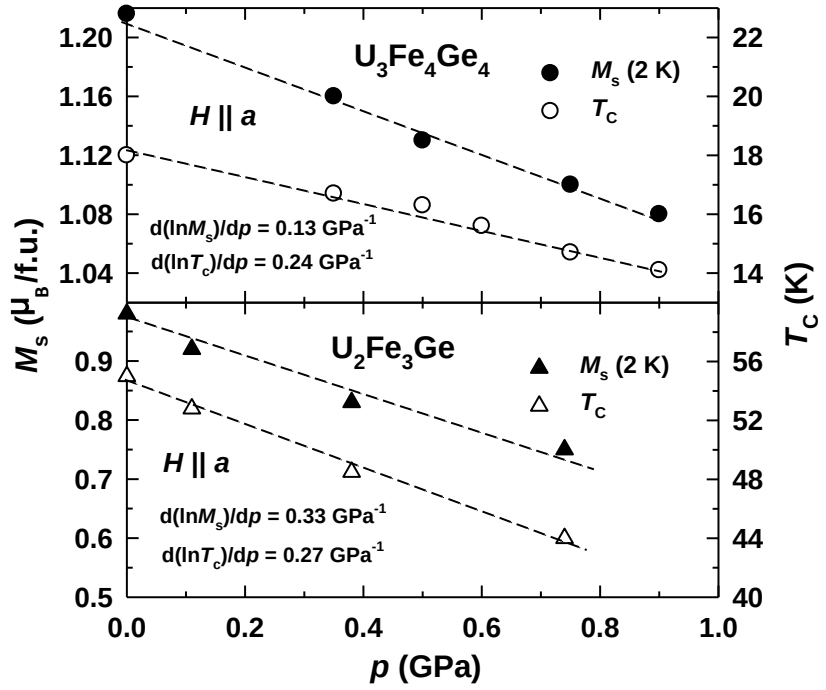

Fig. 2. Pressure dependence of M_s (at T = 2 K) and T_C of $U_3Fe_4Ge_4$ and U_2Fe_3Ge.

1-50

Electronic structure and Fermi surface of paramagnetic and antiferromagnetic UPt_2Si_2

Saad Elgazar[1], Jan Rusz[2], Peter Oppeneer[2], John Mydosh[3]

[1]Dept. of Physics, Johannesburg, South Africa, [2]DMT, Uppsala, Sweden, [3]Dept. of Physics, Leiden, Norway

We report density functional theory-based calculations of the electronic structure and Fermi surface properties of the intermetallic uranium compound UPt_2Si_2, which orders antiferromagnetically at T_N = 32 K with a total magnetic moment of $2\mu_B$ /U-atom and exhibits a moderate mass enhancement in the specific-heat coefficient. Our investigation is carried out using relativistic, full-potential band-structure methods within the framework of the local spin density approximation (LSDA), the LSDA with orbital polarization correction (LSDA + OPC), and the LSDA supplemented with an additional Hubbard U (LSDA+U). We find that the LSDA + OPC scheme predicts the total magnetic moment in best agreement with experiment; from this we infer that the 5f electrons in UPt_2Si_2 are orbitally polarized, mostly itinerant, and exhibit only a slight tendency toward localization. Our total energy calculations predict UPt_2Si_2 to form in the $CaBe_2Si_2$ (P4/nmm) structure, in contrast to URu_2Si_2 ($ThCr_2Si_2$: I4/mmm). The theoretical Fermi surfaces are also studied for the nonmagnetic and antiferromagnetic phases with the employed computational schemes and are found to be quasi-two-dimensional. At the antiferromagnetic transition, the Fermi surface is found to become more two-dimensional with small regions of gapping.

1-51

First-principles calculation of intrinsic and defective properties of UO_2 and ThO_2

Han Han, Cheng Cheng, Ping Huai

Shanghai Institute of Applied Physics, Chinese Academy of Sciences, Shanghai, China

The coated particle fuel is originally designed for the high temperature gas-cooled reactor. Recently, several new high temperature reactor concepts have been developed. For instance, Fluoride Salt Cooled High Temperature Reactor use a liquid salt coolant combined with high temperature gas-cooled reactor fuels. Small modular Advanced High Temperature Reactor is a new small modular fluoride salt cooled reactor concept developed at Oak Ridge National Laboratory. The Thorium Molten Salt Reactor (TMSR) in China has also proposed a concept design based on pebble-bed fluoride salt cooled reactor with thorium-uranium alternate once-through fuel cycle. In the history of coated-particle fuel, the Tristructural Isotropic (TRISO) fuel is one of the most reliable candidates, which has a uranium oxycarbide kernel coated with a series of layers that act as the cladding. The inner pyro-carbon layer is designed to accept gaseous fission products and attenuate fission product recoils. The SiC layer's function is to contain metallic fission products and provide structural support for the fuel particle. The outer pyro-carbon layer serves as a structural component and protects the SiC layer during compacting. These coated particle fuels have highly robust safety characteristics, with the ability to retain fission products up to temperatures of 1600°C or more. U, Th and Pu fuels have been experimentally used in form of oxides, carbides and nitrides in TRISO particles. The behaviour of nuclear fuel in reactor is very complicated due to their neutronics properties as well as thermo mechanical strength, chemical stability, microstructure, and defects. It is very important to understand these material properties from microscopic picture.

The complicated bonding nature of 5f-orbital leads to unique electronic structure of actinide compounds [1-2]. For instance, typical oxidation states of actinides range from 3 to 6 for uranium and 3 to 7 for neptunium and plutonium [3]. In this paper, the properties of intrinsic/defective uranium and thorium dioxide are studied by using the density functional theory in the generalized gradient approximation. A small lattice distortion is found due to the magnetic ordering of ground state of UO_2 (as illustrated in Figure 1(a)). The lattice constant c_0 (parallel to the spin) is different from the other two constants a_0 and b_0. Strong correlation also plays an important role in UO_2. The Hubbard U correction method has been introduced to describe the correlation. The lattice constants are found to be a_0=5.41 Å, and c_0=5.42Å without U. By taking into account the Hubbard U correction, the lattice constants are increased to a_0=5.57 Å, and c_0=5.50 Å. We have also checked the total phonon density of states in case of the small lattice distortion, which was obtained by minimizing the total energy of the electronic structure calculations. The phonon spectrums for antimagnetic UO_2 and diamagnetic ThO_2 are obtained by density function perturbation theory. The dispersion curves of the distorted UO_2 crystal has been shown in Fig. 1(b) with the LO-TO splitting. The U-dependence of the phonon density of states is found to be very weak, which is consistent with the theoretical assumption that excited-state properties of the electronic states should not affect ground-state materials properties very much. The properties of UO_2 and ThO_2 with defects have also been investigated, and will be discussed in detail in the conference.

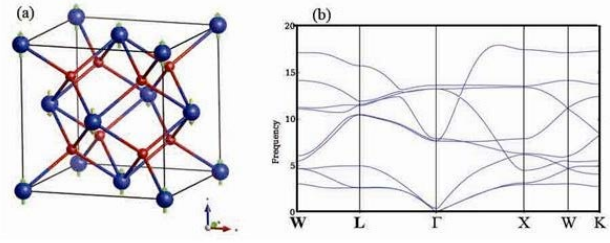

Figure 1 (a) The structure and magnetic ordering of ground state of UO_2. (b) The phonon dispersion curves of antimagnetic UO_2. The LO-TO splitting effect and Hubbard U correction are both concerned.

References

[1] G. Schreckenbach, G. Shamov, Acc. Chem. Res. 43, 19 (2010).
[2] Kevin T. Moore, Rev. Mol. Phys. 81, 235-298 (2009).
[3] N. Kaltsoyannis, P. Scott, The f Elements, Oxford University Press: New York, 1999.

1-52

Simulations of incipient damage and nanovoids in plutonium during alpha-decay

Boris Nadykto, Sergey Sokolov, Alexander Panov, Alexey Samodolov

Russian Federal Nuclear Center - VNIIEF, Sarov, Russia

Alpha-decay of ^{239}Pu produces a 5.2 MeV alpha-particle (nucleus of helium atom) and an 86 keV recoil atom (^{235}U). Damage in the material is mostly associated with the influence of the recoil atom. In [1], transmission electron microscopy of Pu-Ga metal alloy at room temperature revealed the formation of ~1.4 nm diameter sites (voids or bubbles) unoccupied by metal atoms. In [2], Jeffries et al made an attempt to establish the growth mechanism of nanoformations interpreted by the authors as helium bubbles. They concluded that the growth is attributed to the migration and coalescence of such nanoformations rather than to helium diffusion into this space and its gradual expansion.

The mechanism of bubble development at room temperature remains open. Coalescence of point defects and clusters into bubbles is disputable, because the rate of diffusion of Pu atoms is extremely low at such temperatures. According to [2], the bubbles do not grow with temperature up to 325 ^{o}C, whereas the diffusion coefficient increases significantly as compared with its value at room temperature.

In [3], the growth of initial defects in the bulk due to the influence of the recoil atom is simulated using a macroscopic model of shock impact produced by the recoil atom on the surrounding material. The moving atom of uranium is treated as a solid sphere having the same equation of state as the macroscopic material. The U atom slows down, because its momentum is transferred to a large number of surrounding Pu atoms. As a result, pressure behind the shock front decreases.

In this model, nano-voids can form directly as a result of initial damage produced by the recoil atom without nucleation. Material vaporization behind the shock front occurs at a thermal energy exceeding the heat of vaporization. Due to high thermal pressure, the density of the material drops below the initial density. The subsequent fast cooling results in the formation of free volume. Another route for the formation of initial free volume in the delta-alloy of Pu is associated with the known delta→alpha′ transformation under compression [4].

Simulations were done using the TIM-2D code [5], [6], intended for 2D continuum mechanics simulations on unstructured Lagrange meshes. The mesh is composed of arbitrary non-self-intersecting polygons with a variable number of vertices. Heat transfer is calculated using an implicit scheme obtained by differential projection of difference operators [7]. The numerical technique for motion calculations in the elastoplastic approximation [8] is based on the Wilkins method.

The recoil atom (from U) was simulated as a rigid sphere with a radius of 0.18 nm and initial velocity of 2.7 10^{7} cm/s. The simulations were done both for alpha-Pu, and for Pu-Ga alloys with different content of Ga. Compression of the alpha-phase corresponds to a bulk modulus of 50 GPa. Elastic compression of delta-Pu corresponds to a bulk modulus of 30 GPa. According to [4], the delta→alpha′ transformation manifests itself in a very flat compression region, which begins at a lower pressure for alloys with a lower Ga content. In the simulations, such compression was assumed to continue up to the intersection with the compression curve of the alpha-phase.

In the paper, we compare the size of the developing lower-density Pu region (voids), and the path of the recoil atom in alpha-Pu and in two Pu-Ga alloys containing 1.0 and 3.5 at.% Ga. As an example, Fig. 1 shows variations in the lower-density Pu region behind the shock front produced by the recoil atom in the delta-alloy of Pu-3.5 at.% Ga. The spherical region having a radius of 3.3 nm has a density of ~2 g/cm^3. The radius of a similar region in the alpha-phase is ~ 3% smaller.

The path of the recoil atom is 9 nm for the delta-alloy and 7.5 nm for alpha-Pu. The distance traveled by the recoil atom as a function of time is shown in Fig. 2. Damage simulations for a material initially having a 0.7 nm radius free volume display almost no effect on the size of incipient damage area. Damage simulations were also done for a material containing a 0.7 nm radius He bubble with He density of 0.6 g/cm^3.

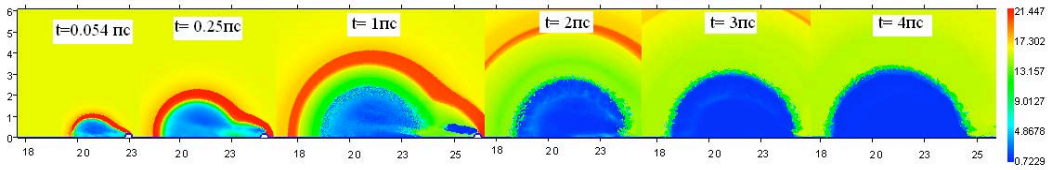

Figure 1 – Pu density distribution behind the shock front produced by the recoil atom in Ga-alloyed δ -Pu

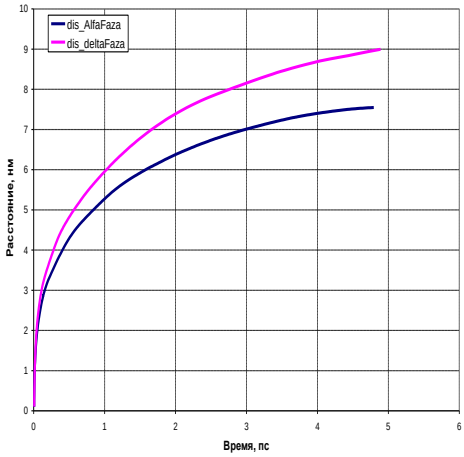

Figure 2 – Distance traveled by the recoil atom in alpha-Pu and Ga-alloyed delta-Pu as a function of time

Pu cooling to 500-600 K with the heat conductivity parameters typical of Pu macrosamples is reached in 5-6 ps. After such cooling, one can expect low-density Pu to condense on a wall of a nearly spherical void. We make an attempt to simulate the void relaxation considering the surface tension of Pu, its strength and viscosity.

References

1. A. Schwartz, M.Wall, T. Zocco, W. Wolfer. Phil. Mag. 85, 479-488 (2005).

2. J.R. Jeffries, M.A. Wall, K.T. Moore, A.J. Schwartz. Journal of Nuclear Materials. 410 (2011). 84-88.

3. B.A. Nadykto, O.B. Nadykto. In Ageing Studies and Lifetime Extension of Materials. Edited by. L.G. Mallinson. 415-417, 183-189 (2000).

4. S.S. Hecker, D.R. Harbur, T.G. Zocco. Prog. Mater. Sci. **49** (1-3), 429-485 (2004).

5. S.S. Sokolov, A.A. Voropinov, I.G. Novikov, A.I. Panov et al. // Voprosy Atomnoi Nauki i Tekhniki. Ser. Mathematical Modeling of Physical Processes. 2006. No. 4. pp. 29-44.

6. I.G. Novikov, A.I. Panov, S.S. Sokolov // Journal of Computational Mathematics and MAthematica Physics of RAS. 2005. V. 45. No. 9. Pp. 1487-1500.

7. S.S. Sokolov // Voprosy Atomnoi Nauki i Tekhniki. Ser. Mathematical Modeling of Physical Processes. 2004. No.4. pp. 62-80.

8. A.I. Panov. Ibid. 2004. №4. pp. 27-40.

1-53

Thermal and elastic properties of actinides on the example of americium and curium: a self-consistent thermodynamic approach

Anton Filanovich, Alexander Povzner, Varvara Oskina

Ural Federal University, Ekaterinburg, Russia

In order to understand the nature of unusual properties of actinides, especially of such important from the practical point of view as U and Pu, one has to understand the whole trend of properties change in the series of actinides. Am and Cm, which follow Pu in the actinide series, are of great scientific interest not only from the fundamental point of view, but also for practical purposes. E.g., recently it was suggested to use the blends of Am and Cm for radioisotope heat-source production [1], Am presents interest in its utilization in the perspective mixed-oxide fuels [2].

Despite the evident importance of Am and Cm investigations, extremely small amount of the experimental data on the thermal and elastic properties of these metals is available as compared e.g. with Pu. While the heat capacity and thermal expansion of Am has been reported in rather old papers [3,4], in the case of Cm such data is not available at all. Temperature dependencies of the elastic moduli of Am and Cm are also not studied – the experimental data are limited to the values at T~300 K. Therefore modelling of the properties of Am and Cm is necessary.

In the present study in terms of the self-consistent thermodynamic model [5], which enables to account for the effect of phonon anharmonicity, we have calculated the temperature dependencies of thermal and elastic properties of Am and Cm in the temperature range from 0 to 1300 K. We utilize the data on the electronic heat capacity of Am and Cm obtained in the previously carried out self-consistent calculation of the electronic structure and magnetic susceptibility in framework of the approach [6], which combines the ab initio calculations in the LDA+U+SO method with the generalized spin-fluctuation s(p)df-model.

The calculations of electronic heat capacity, based on the calculations of magnetic susceptibility, revealed that in Cm despite the very large magnetic susceptibility the amplitude of spin fluctuations is low, hence the renormalization of electronic heat capacity associated with many-electron effects is negligibly small. However, in case of Am this renormalization rather strongly affects the temperature dependence of its electronic heat capacity – see the inset to the Fig. 1.

In assessing the thermodynamic parameters of Am, we proceeded from the condition of the best agreement between the calculated total heat capacity of Am and the available experimental data – see Fig. 1. Since in the case of Cm no experimental data is available, we proceeded from the assumption that the lattice heat capacity of Cm should have temperature dependence similar to the lattice heat capacity of isostructural analog of Cm in the lanthanide series, i.e. gadolinium. Due to the fact that the Fermi energy of Cm is located at the minimum of the densities of states, the “one-electron” electronic heat capacity of Cm is small. Therefore, as one can see from Fig. 1, the total heat capacity of Cm is almost identical to the lattice (phonon) contribution. The lattice contribution C_{ph} to the heat capacity at low temperatures is smaller in case of Am than Cm owing to the higher Debye temperature of Am (see inset to Fig. 2). However, at elevated temperatures C_{ph} of Am starts exceeding C_{ph} of Cm, which can be explained by stronger phonon anharmonicity in the case of Am. This along with larger electronic heat capacity of Am leads to that at high temperatures the total heat capacity of Am essentially exceeds the total heat capacity of Cm.

In Fig. 2 we show the results of our calculations of the bulk modulus B(T) of Am and Cm in comparison with the experimental data, which is available only at the ambient temperature. One can see that the values of B(T) of both metals are comparable, however Am exhibits stronger temperature dependence of the bulk modulus.

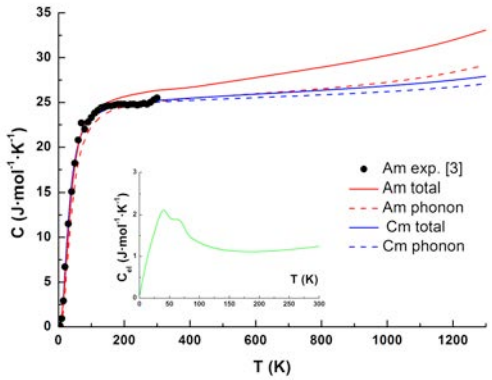

Fig. 1. Temperature dependencies of the molar heat capacity of americium and curium; the inset shows the electronic heat capacity of Am.

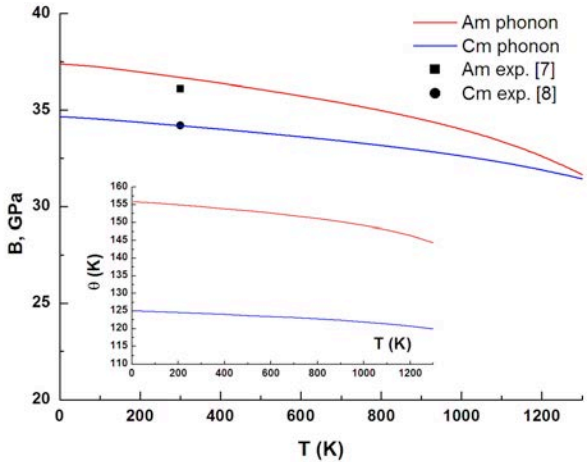

Fig. 2. Temperature dependence of the bulk modulus of americium and curium; inset shows the Debye temperature of Am and Cm.

In addition to the properties considered here, in the present work we also present the results of the carried out calculations of the temperature dependencies of coefficient of thermal expansion and density of Am and Cm. The effect of the phonon anharmonicity on the considered properties is discussed.

References

[1]O'Brien R.C., Katalenich J.A. // J. Propulsion And Power. 2011. V. 27, I. 5. P. 1131

[2]Kurosaki K., Adachi J., et al. // J. Nucl. Sci. Technol. 2006. V. 43, N. 10. P. 1224

[3]Hall R.O.A., Lee J.A., Mortimer M.J., et al. // J. Low Temp. Phys. 1980. V. 41. P. 397

[4]McWhan D.B., Cunningham B.B. et al. // J. Inorg. Nucl. Chem. 1962. V. 24. P. 1025.

[5]Filanovich A.N., Povzner A.A. // J. Nucl. Mat. 2013. V. 437, I. 1-3. P. 102.

[6]Volkov A.G., Povzner A.A., Filanovich A.N. // J Supercond. Nov Magn. 2013. V. 1. DOI 10.1007/s10948-012-1935-0

[7]Stephens D.R., Stromberg H.D., Lilley E.M. // J. Phys. Chem. Solids. 1968.V. 29. P. 815

[8] Troc, R., Suski, W.: 3.1.1.1 Atomic properties. SpringerMaterials - The Landolt-Börnstein Database / Wijn, H.P.J. (ed.). DOI: 10.1007/10008848_1

1-65

Production of Super Heavy Plutonium Isotopes for Basic Research

Stanislav Vesnovskii[2], Lev Kazakov[1], Alexey Kupriyanov[1], Evgeny Romanov[1], Valery Tarasov[1]

[1]JSC "State Scientific Centre - Research Institute of Atomic Reactors, Dimitrovgrad, Russia, [2]RFNC–VNIIEF, Sarov, Russia

Owing to optimal nuclear-physical features, the heavy plutonium isotopes ^{242}Pu and ^{244}Pu are considered as the most suitable for comparative study of internal atomic layers by neutron diffraction analysis as well as the investigation of basic physical properties of 5f- metals.

The unique neutron and physical characteristics of the research reactor SM allow accumulating plutonium isotope mixture where ^{242}Pu percentage is 94-96%. There are shown the optimal irradiation conditions to minimize final percentage of ^{241}Pu isotope that is vitally important for increasing the efficiency of further electromagnetic separation.

Production of quite large amount of the ^{244}Pu isotope is limited by the too short half- life of the parent ^{243}Pu ($T_{1/2} \approx 5$ hrs). It is shown that using the highest neutron flux irradiation position of the SM reactor (central neutron trap) for a two-year irradiation, it is possible to accumulate plutonium with ^{244}Pu percentage amounting to about 20% and a ^{244}Pu yield about 5-10mg/g Pu.

A further increase of ^{244}Pu percentage is possible with the use of mass - separator of S-2 RENC-VNIIEF model. The operational parameters of the mass-separator and procedures of radiochemical separation of scattered material as well as plutonium purification allow producing up to 1g of plutonium with enrichment above 99 %.

1-54

Microscopic theory of the insulating electronic ground states of actinides dioxides AnO_2 (with An = U, Np, Pu, Am and Cm)

Michi-To Suzuki[1,2], Nicola Magnani[3], Peter M. Oppeneer[1]

[1]Japan Atomic Energy Agency, Chiba, Japan, [2]Uppsala University, Uppsala, Sweden, [3]Lawrence Berkeley National Laboratory, Berkeley, CA, USA

The electronic ground states of the actinide dioxides AnO2 (with An=U, Np, Pu, Am, and Cm) are investigated employing first-principles calculations within the framework of the local density approximation +U (LDA+U) approach, implemented in a full-potential linearized augmented plane wave scheme. A systematic analysis of the An-5f states is performed which provides intuitive connections between the electronic structures and the local crystalline fields working on the 5f states in the AnO2 series. Particularly the mechanisms leading to the experimentally observed insulating ground states are investigated. These are found to arise from the strong spin-orbit and Coulomb interactions of the 5f orbitals. However, as a result of the different 5f configurations, these interactions work in distinctly different ways for each of the AnO2 compounds.

In agreement with experimental observations, the nonmagnetic states of plutonium and curium dioxide are computed to be insulating, whereas those of uranium, neptunium, and americium dioxides require symmetry breaking to reproduce the insulator ground states, a condition which is met with magnetic phase transitions. We show that the occupancy of the An-f orbitals is closely connected to each of the appearing insulating mechanisms. We furthermore investigate the detailed constitution of multipolar moments for transverse 3q magnetic ordered states in UO2 and longitudinal 3q high-rank multipolar ordered states in NpO2 [1] and AmO2.

The self-consistently computed charge distributions around the actinide ion of non-magnetic PuO_2 and CmO_2 are shown in Figure 1, while the computed charge and spin distributions around the actinide ion in UO_2, NpO_2 and AmO_2 are shown in Figure 2. The distribution of spin-moments (denoted by the color) is plotted as projection on the (111) axis, which is the local threefold rotational axis at the An sites.

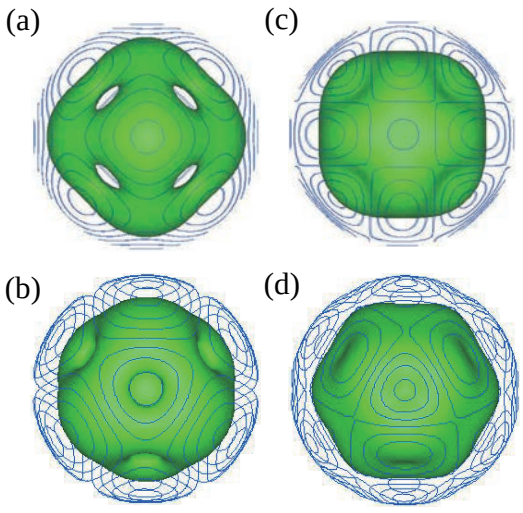

Figure 1. Computed non-magnetic charge distributions of the An 5f electrons in PuO_2 (a and b) and CmO_2 (c and d). Top panels are viewed from the (100) direction, bottom panels from the (111) direction. The calculations were made with the LDA+U approach (with U=4 eV and J=0).

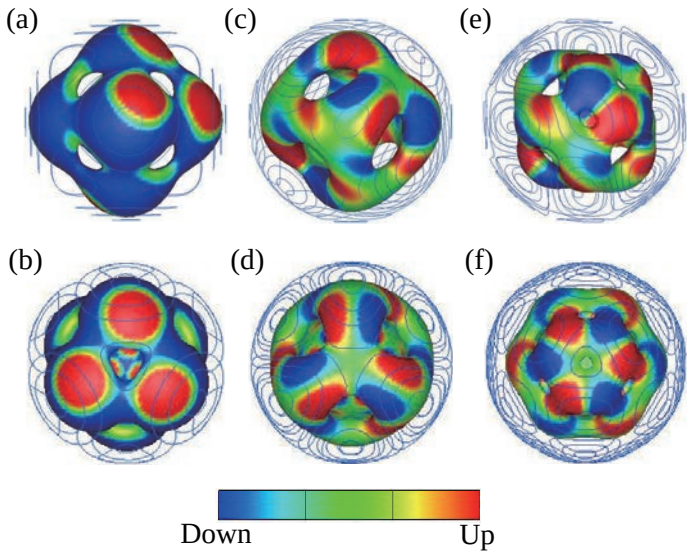

Figure 2. Charge and spin distributions of the An 5f electrons at the An site: a and b: UO_2, c and d: NpO_2, and e and f: AmO_2. The top panels are viewed along the (100) direction, the bottom panels along the (111) direction, illustrating the (111) threefold symmetry axis.

Acknowledgment. This work has been supported by the EU-FP7 project “Redupp”, by the JPSJ KAKENHI and the JAEA, by SKB and by VR.

References

[1] M.-T. Suzuki, N. Magnani, and P. M. Oppeneer, Phys. Rev. B 82, 241103(R) (2010).

1-55

^{119}Sn Mössbauer spectroscopy of 3d-, 4f- and U-intermetallic compounds

Vasily Krylov

Skobeltsyn Institute of Nuclear Physics, Moscow State University, Moscow, Russia

The results of Mössbauer spectroscopy (MS) investigation of the magnetic hyperfine fields (HFs) on ^{119}Sn probe nuclei for the different groups of the intermetallic compounds based on the 3d-, 4f-elements and uranium are presented in this work. The observed regularities of the spin density formation on the nuclei of nonmagnetic tin atoms reflect the specific features of the magnetic 3d-3d, 4f-4f, 3d-4f, and 5f-5f exchange interactions. It has been shown that the mechanisms of electron polarization on ^{119}Sn nuclei are significantly different for the following groups of the compounds.

1. The compounds TFe_2 (T=Sc, Ti, Y, Zr, Lu, Hf, U) with cubic $MgCu_2$-type and hexagonal $MgZn_2$-type Laves structures are ferromagnets (FM) except for $TiFe_2$ that is an antiferromagnetic (AFM). The Fe-Fe magnetic exchange interaction is responsible for magnetic ordering of the TFe_2 compounds. In the FM compounds TFe_2, the HFs for ^{119}Sn atoms localized on T-sites (HF = B_1) are positive and proportional to the Fe magnetic moments: $B_1=A_1\times\mu_{Fe}$, where A_1=28 T/μ_B is the hyperfine coupling constant. The HF B_1 reaches the value of about 50 T for ^{119}Sn in $ZrFe_2$[1)]. The HFs for ^{119}Sn atoms localized on Fe-sites (HF = B_2) are negative: $B_2=A_2\times\mu_{Fe}$, where A_2=−3.8 T/μ_B.

2. In the ordered alloys of rare earth metals (RE) with p-metals, the HFs for ^{119}Sn atoms occur due to 4f-4f indirect magnetic interaction and reach the values of 40 T. Systematics of the HFs for ^{119}Sn in the FM and AFM binary Gd - X compounds (X is a p-metal) of different compositions and crystalline structures are presented in this work. The HF values on ^{119}Sn nuclei in $REAl_2$ и REGa FM compounds are proportional to the spin magnetic moment of RE ions[2)].

3. Huge HFs reaching to 56 T have been found for ^{119}Sn atoms localized on RE-sites of RE-3d compounds (3d are Fe, Co and Mn atoms with the localized magnetic moments)[1)]. This value is the maximum of the known HF values for ^{119}Sn atoms in the metallic magnets. It has been shown that the HFs are created due to two additive contributions of RE- and 3d-magnetic sublattices[3)]. The temperature dependencies of the HFs for ^{119}Sn atoms localized on RE- and 3d-sites of $REFe_2$, $RECo_2$, $RECo_5$ compounds, are directly related to the temperature changes of 4f-4f, 3d-4f and 3d-3d exchange interactions.

4. The selectivity of the magnetic hyperfine interaction for ^{119}Sn atoms to the certain 3d-3d or 4f-4f magnetic exchange interactions of the ternary RE-based intermetallic compounds has been observed. The HFs on ^{119}Sn nuclei localized in Si sites of GdMnSi and GdCoSi ferrimagnetic compounds are induced only by Gd magnetic moments. The contributions of Mn and Co magnetic moments to the HF are equal to zero[4)]. On the contrary, the HFs for ^{119}Sn atoms localized in Ge-positions of $REMn_2Ge_2$ compounds are formed only by the Mn-magnetic moments.

5. The HFs on ^{119}Sn nuclei in UTM (T is a d-metal, M is a p-metal) compounds with ZrNiAl-type crystal structure are proportional to the full magnetic moment of U-ions: B = A × μ_U, where A= 6.5(4) T/μ_B. The HFs are formed by the nearest U-ions and reach of 10 T[5)]. The results of ^{119}Sn MS study on UPdSn, UCuSn, UAuSn, UNiSn, UCuGe[6)], UGa_3, UIn_3, UPb_3, UGa_2, UGe_2, USn_2[7)] compounds indicate a strong anisotropy of the magnetic hyperfine interaction and magnetic exchange interaction caused by the significant nonsphericity of 5f-electron shell of uranium ion.

Among the 3d-, 4f-, and U-magnetic moments, the ability to create a spin polarization on the ^{119}Sn nuclei is the largest for 3d-moments (in equivalent of the unit magnetic moment) and this one is the smallest for the unit magnetic moment of RE-ions.

References

1) V.I. Krylov *et al.*, J. Magn. Magn. Mater., **305** (2006) 1.
2) N.N. Delyagin *et al.*, J. Magn. Magn. Mater., **308** (2007) 74.
3) N.N. Delyagin *et al.*, J. Phys.: Condens. Matter., **19** (2007) 086205.
4) N.N. Delyagin *et al.*, Phys. Stat. Sol. (b), **131** (1985) 555.
5) V.I. Krylov, J. Appl. Phys., **109** (2011) 07E140.
6) V.I. Krylov *et al.*, J. Alloys. Comp., **347** (2002) 36.
7) V.I. Krylov *et al.*, J. Alloys. Comp., **343** (2002) 33.

1-56

The role of transition metals (TM) on the structure symmetry of Al-TM-Ac alloys (Ac= actinides and lanthanides)

Avraham I Bram[1,2], Arie Venkert[3], Louisa Meshi[1,2]

[1]*Department of Materials Engineering, Ben-Gurion University of the Negev, Beer-Sheva, Israel*[2] ,*Ilse Katz institute for nanotechnology, Ben Gurion University of the Negev, Beer-Sheva, Israel*[3] ,*Nuclear Research Center-Negev, Beer-Sheva, Israel*

One of the theories developed for the prediction of the stability of the structure of alluminides containing transition metals was proposed by Kiv et al [1]. The suggested theory claims that phase transform to more stable phase with higher symmetry when the effective charge of the transition metal and electronegativity of the neighbours of the transition metal atom increase. Therefore, the stability and the symmetry of the structure are a function only of the atomic content especially the type of the transition metal. This theory explained the stability of phases in terms of the coordination compounds and based on the chemical bonds theories [2]. Those theories suggest that the degenerated energy levels of d-orbital in transition metal atoms split under the influence of the field of surrounding atoms. The distance between the splitted levels is the factor which may control the stability of the structure [3]. The greater the distance between the splitted levels, the structure is more stable. The splitted levels affect the electronegativity of the neighbours of the transition metal atom and the effective charge of the transition metal. The structure symmetry is explained by Jahn-Teller effect [4].

The aim of this work is to examine experimentally the suggested theory by the characterization of the Al-TM-Ac system. We chose Thorium (z=90) to represent the actinides and lanthanides and Vanadium (z=23), Iron (z=26) and Nickel (z=28) to represent the transition metals. Alloys with different transition metal were prepared with the same 87at%Al-8at%TM-4at%Th composition by arc melting. Then, the samples were homogenized in the resistance furnace for 3 weeks at different temperatures according to the alloys composition. Characterization of the phase content was performed by using scanning and transmission electron microscopy (SEM and TEM) and X-ray powder diffraction method. The composition of the phases was analyzed by Energy Dispersive X-ray Spectroscopy (EDS).

Several new phases were revealed during the research: $Al_{11}Th_3$, $Al_{20}V_2Th$ and $Al_{10}Ni_2Th$. We confirm that the Kiv theory is valid only for phases having the same stoichiometric composition.

References

[1] A.E. Kiv, V.I. Ezersky, M.M. Talianker, Mater. Sci. and Engineering A352, 2003, 100.

[2] S. Sugano, Y. Tanabe, H. Kamimura, Multiplets of Transition Metal Ions in Crystals, Academic Press, New York, London, 1970, 331.

[3] D.A. Brown, W.J. Chambers, N.J. Fitzpatrick, Inorg. Chem. Acta. Rev. 6, 1972, 1013.

[4] H.A. Jahn, E. Teller, Proc. R. Soc. A161, 1937, 220.

1-57

The screening effect of magnetic exchange interaction in the U- and Gd-based intermetallic compounds

Vasily Krylov[1], Vladimir Sechovský[2], Alexander Andreev[3]

[1]Skobeltsyn Institute of Nuclear Physics, Moscow State University, Moscow, Russia, [2]DSMP, Faculty of Mathematic and Physics, Charles University in Prague, Prague, Czech Republic, [3]Institute of Physics ASCR,, Prague, Czech Republic

The Mössbauer spectroscopy (MS) studies of uranium and rare earth (RE)-based intermetallics shown that the magnetic hyperfine fields (B_{hf}) on the ^{119}Sn nucleus is induced by the magnetic moments of the nearest uranium or RE ions.

The non-collinear antiferromagnets compounds UCuGe and UCuSn with competing exchange interactions crystallize in hexagonal SrPtSb-type and orthorhombic $P2_1cn$ structure, respectively. In these compounds, uranium magnetic moments are equal to about 2.0 μ_B and are ordered below T_N =62(2) K [1, 2]. The influence of vacancies on the B_{hf} at the ^{119}Sn nuclei in UCuGe compound has been investigated by MS at [3].

For the whole region of x, the ^{119}Sn Mössbauer spectra of $UCuGe_{1-x}Sn_x$ compounds (x=0.01 – 1.0) represent a superposition of two magnetic sextets with two sets of hyperfine parameters. Two subspectra with significantly different values of the B_{hf}, B_1 and B_2, correspond to the two local magnetic states: low-field (LF) and high-field (HF). The obtained data lead to the conclusion that the LF-component corresponds to the ^{119}Sn atoms which interact only with the three nearest uranium magnetic moments. The magnetic exchange of this group of ^{119}Sn atoms with the other three more distant uranium moments is shielded by the Cu-layer and does not contribute to B_1. The HF-component B_2 corresponds to other group of ^{119}Sn atoms which have a magnetic exchange with all six uranium ions around the tin atoms. The structural (Ge-Cu) and (Sn-Cu) defects or vacancies in Cu-layers of the $UCuGe_{1-x}Sn_x$ compounds lead to disruption of the shielding Cu-layer and creation of bonds of the Sn atoms with all the six uranium ions.

B_1 decreases monotonously from 6.3 T to 5.4 T with increasing x whereas B_2 increases from 9.8 T to 11.7 T. The temperature dependences of magnetic hyperfine fields B_1 and B_2 are also different. B_1 decreases with increasing temperature and droops to zero at the magnetic ordering temperatures of parent compounds, T_{N1} =61(1) K. The hyperfine field B_2 droops to zero at higher temperature T_{N2} which increases from 70 K at x=0.01 to 83 K at x=1.

The screening effect of magnetic exchange interaction by Ge(Sn) and Cu layers has been found using the ^{119}Sn MS also in the $U(Ge_{1-x}Sn_x)_2$ (x=0.01 – 1.0) and $UCu_{2-x}Sn_2$ (x=0.0 – 1.0) compounds, respectively.

In the ferromagnetic (FM) and antiferromagnetic (AFM) Gd – X (X is a p-element) compounds, the averaged contribution of each uncompensated Gd moment to the B_{hf} on the ^{119}Sn nucleus is equal to ΔB= – 4.5 (5) T. In Gd-Cu and Gd-Ag compounds, GdCu, $GdCu_5$, $GdCu_4Pd$, $GdCu_4Ag$, $Gd_3Ag_4Sn_4$ [4], and $Gd_3Cu_4Ge_4$, the B_{hf} values on ^{119}Sn nuclei extrapolated to 0 K can be expressed as $B_{hf} = \Delta B \times N$, where ΔB = – 4.7(2) T/μ_{Gd} is a contribution of each Gd-moment to B_{hf}, and N is the number of uncompensated Gd magnetic moment in the nearest neighborhood of tin atoms.

In the AFM GdCuSn, GdAgSn, and GdCuGe compounds crystallizing in the hexagonal GaGeLi-type of structure, the hexagonal layers of atoms Gd, Cu(Ag) and Sn(Ge) alternate in the sequence Gd-Sn(Ge)-Cu(Ag)-Gd along the c axis. The tin atoms are surrounded by six atoms of Gd (3Gd atoms are located in the lower layer and 3Gd ones in the more distant upper layer).

The MS on the ^{119}Sn nuclei in GdCuSn compound was studied in [5]. It has been suggested that the compound has a collinear AFM structure with the propagation vector [1/2, 0, 0].

We have found that B_{hf} on the ^{119}Sn nuclei in GdCuSn and GdAgSn is oriented along the c-axis. The B_{hf} values at 5 K are equal to 5.31(1) T and 5.04(2) T, respectively. These values correspond to the contribution of only one Gd magnetic moment to the B_{hf} on ^{119}Sn nuclei. It

is possible if only the three nearest Gd magnetic moments are involved in the magnetic exchange with the Sn atoms, the contributions from two of them mutually compensate. The three more distant Gd moments are shielded by a Cu-layer. Therefore they do not contribute to the hyperfine field on the ^{119}Sn nuclei. The Cu-vacancies and partial Cu-Ge disorder in the compound GdCuGe lead to penetration of the magnetic exchange from three more distant Gd atoms through the Cu-layer. Therefore for the part of the ^{119}Sn nuclei in GdCuGe, B_{hf} is formed by two uncompensated Gd magnetic moments and reaches of 10 T.

Conclusions:

1. The MS investigation of B_{hf} on the ^{119}Sn probe nuclei in uranium and RE-based compounds have shown that in the compounds with layered crystal structure the screening effect of the magnetic exchange interaction by layers of p-or s, d-nonmagnetic atoms is observed.

2. In magnetically ordered compounds This effect can lead to the appearance of selected layers, free of magnetic exchange and of transferred (induced by this exchange) electron polarization.

3. The presence of the vacancies in the shielding layer can lead to a creation of new magnetic bonds between the components of the alloy. This in turn leads to a significant change in magnetic properties of a compound and coexistence of two (or more) local magnetic states with different temperatures of local magnetic ordering.

References

[1]. J. Leciejewicz, A. Szytuta, A. Zygmunt, J. Magn. Magn. Mater. **97** (1991) 219

[2]. H. Nakotte et al., J. Appl. Phys. **79** (1996) 6408

[3]. V.I. Krylov et al., J. Alloys Comp. **347** (2002) 36

[4]. C.J. Voyer et al., J. Phys. Condens. Matter. **19** (156209), (2007) 10

[5]. D. Bialic, R. Kruk, R. Kmieć, K. Tomala, J. Alloys and Comp. **257** (1997) 49

1-58

Studies on the $UFeC_2$ uranium carbide

Margarida S. Henriques[1], Yuriy Verbovitskiy[1], Ladislav Havela[2], Antonio P. Goncalves[1]

[1]IST/ITN, Technical University of Lisbon, CFMC-UL, 2686-953-Sacavém, Portugal, [2]Dept. Condensed Matter Physics, Faculty of Mathematics and Physics, Charles University, 121 16 Prague, Czech Republic

Ternary systems of actinides (An) with transition elements and carbon have been subject to numerous investigations due their importance in nuclear technology. Within this field, renewed attention is now being paid to actinide carbide-based compounds as strong candidates for fuels in nuclear plants of the Generation IV. Some of the advantages of U carbides when compared with UO_2 are the lack of phase transformations at practical temperatures, dimensional stability under irradiation, higher fissile metal density, melting point and thermal conductivity.

The U-Fe-C system was first investigated to provide a background for the description of the interaction between carbide fuels and steel canning materials [1]. Several studies on pseudo-binary and isothermal sections of the ternary phase diagram at 1050 [2] and 1400ºC [1] have been reported. The compound with composition $UFeC_2$ was found to be formed by a peritectic reaction in the section UC_2-Fe [3] and later it was suggested (from powder X-ray data and) to be isostructural with $UCoC_2$ [4]. No physical properties studies have been made on $UFeC_2$ up to the starting of this work. Here we present the investigation of $UFeC_2$ in terms of structure, magnetism and specific heat.

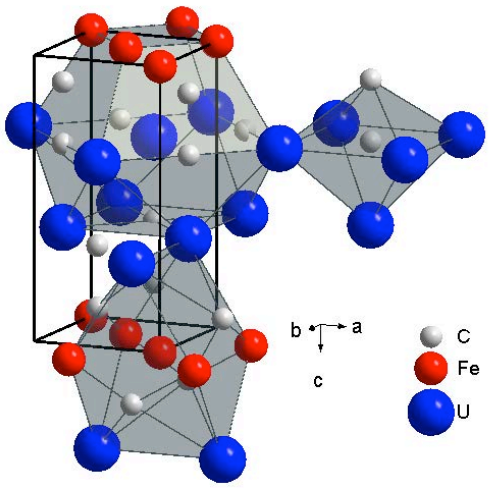

Figure 1. Unit cell and near-neighbor environments for $UFeC_2$.

The $UFeC_2$ crystal structure determination, from XRD single crystal data, indicates that this compound crystallizes in the tetragonal P4/nmm ($UCoC_2$- structure type), with lattice parameters, a = 3.4846(6) Å and c = 7.380(6) Å, in good agreement with the previous reported results [4]. In $UFeC_2$ the minimum U-U distance is ~3.27Å, well below the Hill limit, hinting an absence of magnetic transitions in this compound. Magnetization measurements show that $UFeC_2$ is a Pauli paramagnet down to 2 K, with $\chi = 1.75 \times 10^{-8}$ m^3/mol. Specific heat measurements confirm that no magnetic transition exists down to 2 K and allow the estimation of the electronic contribution, γ = 11 mJ/mol K. All the results point to a fully delocalized system.

Acknowledgments

This work was partially supported by FCT, Portugal, under the contract CERN/FP/123588/2011 and the grant SFRH/BD/66161/2009 (M.S. Henriques).

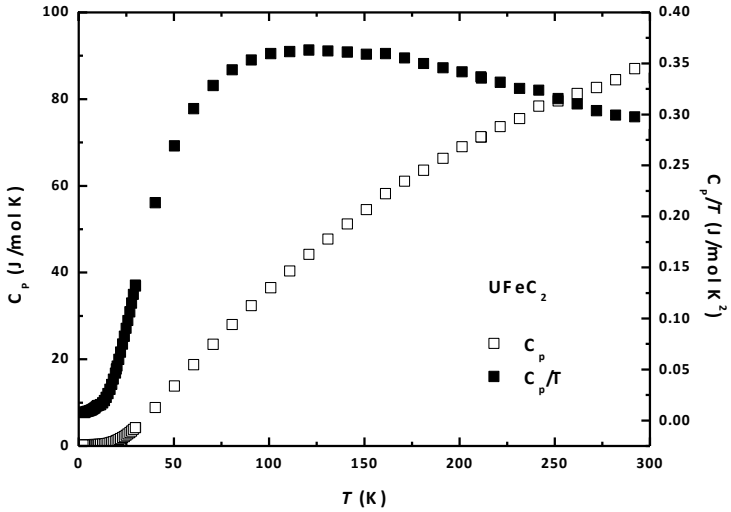

Figure 2. Specific heat as a function of temperature of $UFeC_2$.

References

[1] V. Kuznetsov, ‘Uranium- Iron- Carbon’, Springer 2008

[2] Z.M. Alekseyeva, Metally 5 (1992) 151

[3] P. Baldock et al., J. Nucl. Mater. 4 (1961) 322

[4] M.H. Gerss, W. Jeitschko, Mater. Res. Bull. 21 (1986) 209

1-74

Structural, Electronic and Magnetic Properties of $NpNi_5$

Amir Hen[1,2], Eric Colineau[1], Rachel Eloirdi[1], Jean - Christophe Griveau[1], Itzhak Halevy[3,4], Itzhak Orion[2], Roberto Caciuffo[1]

[1]Institute for Transuranium Elements, Postfach 2340, D-76125 Karlsruhe, Germany, [2]Ben Gurion University, IL84105 Beer-Sheva, Israel, [3]Nuclear Research Center Negev, P.O. Box 9001, IL84190 Beer-Sheva, Israel, [4]California Institute of Technology, W. M. Keck Laboratory 138-78, Pasadena, California 91125, USA

The physical properties of binary actinides and transition metal alloys are of great importance for the safety assessment of nuclear fuels. Since transition metals are major components of the cladding material of fuel rods (stainless steel, HT-9 etc.), the physical properties of those compounds formed by accidental fuel-cladding interactions could have limiting factors on the fabrication, life time operation and disposal of nuclear fuels. Binary compound of the form ReT_5 (Re = rare earth, T = Transition metal) has been in the focus of interest mainly because of their magnetic properties (small Re to T stoichiometric ratio, large spontaneous magnetization and high Curie temperature) and their ability to store large amount of hydrogen per formula unit (f. u.)

Reported in 1997 [1], $NpNi_5$ was synthesized and identified to have hexagonal (D_2d) $CaCu_5$ crystallographic structure, with room-temperature lattice parameters a = 8.3107(1) Å and c = 8.1058(1) Å. In the present study, $NpNi_5$ has been synthesized and characterized by means of powder x-Ray diffraction (Fig. 1 left panel), Superconducting Quantum Interference Device magnetometry (SQUID, Fig. 1 right panel), ^{237}Np Mössbauer spectroscopy [2] (Fig. 2 left panel) and specific heat measurements (Fig. 2 right panel).

Magnetization curves indicate that $NpNi_5$ is a ferromagnet (T_C ~ 16 K), fit of the paramagnetic part to the Curie–Weiss law (C~1.7 emu·K/mol, θ_P ~ 14.6 K) gives an effective moment μ_{eff} ~ 3.7 μ_B per f.u. – no magnetization hysteresis was observed. The isomer shift ($\delta_{IS} \approx$ -11.1 mm/s vs. $NpAl_2$) observed in Mössbauer spectra suggests a tetravalent Np state, but considering the influence of conduction electrons we determine a Np^{3+} ($5f^4$ configuration) oxidation state. The hyperfine field determined by fitting of the spectra (~439T) gives an ordered moment at the Np site μ_{Np} ~ 2 μ_B per Np ion (1 μ_B = 215 T [3]). The magnetic transition is clearly visible in the temperature dependence of the specific heat, and a magnetic phase diagram as a function of temperature and external magnetic field was generated.

In this communication we will present the results obtained and discuss them in the light of theoretical considerations.

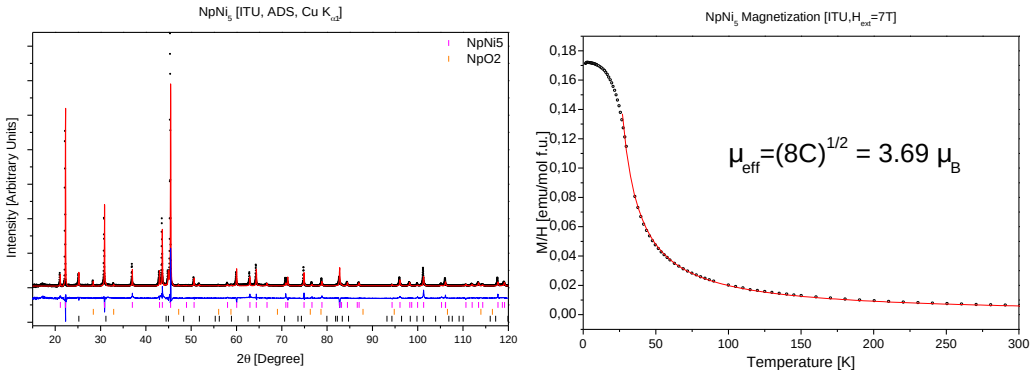

Fig. 1 Left: Powder x-ray diffraction pattern of $NpNi_5$, black dot – measured data, red line – fitted profile, blue line – difference profile, vertical tick – angular position of Bragg peaks. Right: Temperature dependence of the magnetic susceptibility, red line – fit to the Curie-Weiss law.

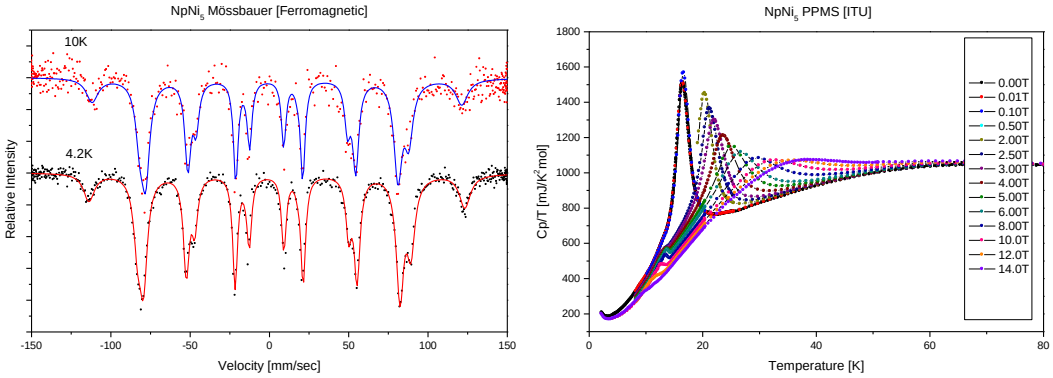

Fig. 2 Left: Mössbauer spectra taken in the ferromagnetic region, dots – measured data, lines – fits of hyperfine fields to the measured data, spectrum is composed of one hyperfine field as expected from the crystallography. Right: Normalized heat capacity as a function of temperature in various external magnetic fields.

Acknowledgements

The high purity Np metals required for the fabrication of the compound were made available through a loan agreement between Lawrence Livermore National Laboratory and ITU, in the frame of a collaboration involving LLNL, Los Alamos National Laboratory and the US Department of Energy.

References

[1] M. Akabori et al., Journal of Alloys and Compounds 257 (1997) 268-272.

[2] R.L. Mössbauer., Zeitschrift für Physik, Bd. **151**, S. 124-143 (1958).

[3] B. D. Dunlap and G. M. Kalvius, in Handbook on the Physics and Chemistry of the Actinides, edited by A. J. Freeman and G. H. Lander (North-Holland, Amsterdam, 1985), Vol. 2, p. 329.

1-60

Proposal for thermo-mechanical property correlations of MOX bearing minor actinides fuels

Sara Perez-Martin, Michael Schikorr

Karlsruhe Institute of Technology, Karlsruhe, Germany

In this work we have studied thermo-mechanical properties of actinide oxides and mixtures oxides. We have reviewed the literature for results of experimental studies as well as model descriptions for thermal properties in order to propose new correlations for thermal conductivity, linear expansion and heat capacity for MOX fuel bearing minor actinides.

Based on individual actinide oxide experimental and model results we have parameterized the thermal conductivity for minor actinides (MA) oxides using approximately the same functional relationship as Philipponneau (Ref. 1) did for MOX fuel:

$$\lambda = \left(\frac{1}{A + BT} + CT^3 \right) \alpha \;\; ; \;\; A(x,\tau) = a_1 \left(x + a_2 \right)^{a_5} - a_3 + a_4 \tau$$

Porosity effect is considered according to Maxwell-Eucken equation:

$$\lambda = \lambda_0 \alpha ; \; \alpha(p) = \frac{1-p}{1+2p}$$

Bruggeman's procedure (Ref. 2) has been used to estimate the MA-MOX mixture thermal conductivity assuming that MA are inclusions in the MOX matrix:

$$1 - \%MA = \left(\frac{\lambda_{MA} - \lambda_{MA-MOX}}{\lambda_{MA} - \lambda_{MOX}} \right) * \left(\frac{\lambda_{MOX}}{\lambda_{MA-MOX}} \right)^{\left(\frac{1}{3}\right)}$$

where %MA is the fraction of MA in the fuel mixture (i.e. 0.05), λ_{MOX} is the MOX fuel thermal conductivity (Philipponneau proposed correlation), λ_{MA} is the thermal conductivity of MA-mixture and $\lambda_{MA\text{-}MOX}$ is the thermal conductivity of the final oxide fuel MA-MOX mixture. In the following figure the thermal conductivity correlations of individual oxides (Am-O, Cm-O and MOX) and for the 5%MA-MOX mixture fuel are plotted.

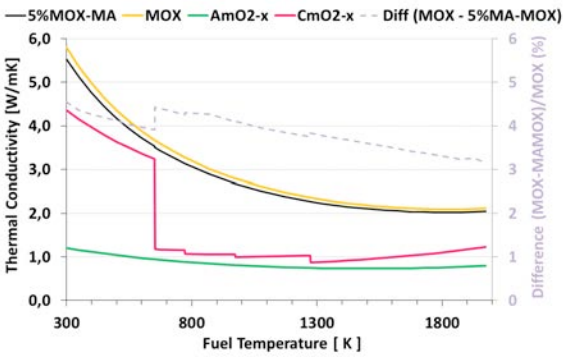

Albeles' procedure (Ref. 3) for solid solutions has been also studied in this work for estimating the thermal conductivity of mixtures oxides. No major differences have been found for 5-10% MA in MOX fuel between solid solution (Abeles) and inclusions (Bruggeman) mixtures.

Heat capacity and linear expansion, unlike thermal conductivity, do not depend strongly on burn-up, O/M ratio or porosity. Therefore only the fuel temperature dependency is considered. A simplified average procedure to obtain the MA-MOX mixture heat capacity and linear expansion is used. In the following figures heat capacity and linear expansion of individual oxides (Am-O, Cm-O, Np-O and MOX) and 5%MA-MOX fuel mixture are plotted.

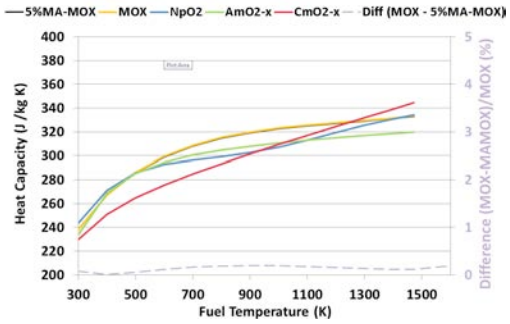

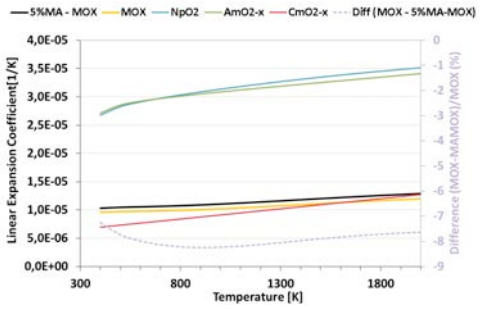

We have used the average of the individual actinide oxide melting temperatures as a first approximation to estimate the melting temperature of the 5%MA-MOX mixture. The value is 3003 K which is marginally smaller than MOX melting temperature (~ 3050 K). Individual oxide melting temperatures are: UO_2 3120 K, PuO_2 2674 K, NpO_2 2836 K, Am_2O_3 2481K and Cm_2O_3 2543 K.

We have also reviewed the liquidus and solidus temperature correlations used in SAS-SFR code. According to latest experimental results solidus and liquidus temperature correlations should be reviewed due to the fact that melting temperature measurements using rhenium capsules give higher values than measurements made with tungsten capsules. The reason is that a liquid phase of tungsten and plutonium oxide appears in the mixed oxide during melting and this liquid phase was found to have an effect on the measurement of melting point. This fact has an important effect in MOX melting temperatures with Pu enrichment higher than 20% and consequently in MA-MOX melting temperature values.

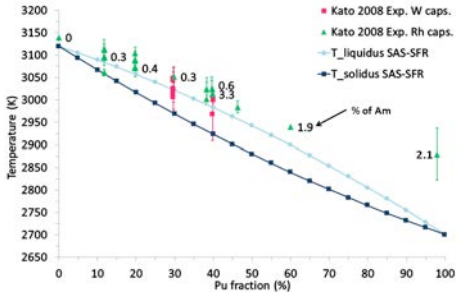

More details about the experimental data used in this work as well as the proposed correlations validation will be presented in the talk.

References:

1. Y. Philipponneau, Journal of Nuclear Materials 188 (1992) 194-197

2. .E. Lemehov, V.P. Sobolev, M. Verwerft. Journal of Nuclear Materials 416 (2011) 179–191

3. B. Abeles, Physical Review Vol. 131 Nr 1 1963 1906-1911

1-61

Structure and magnetism in $U_2Ni_{21}B_6$, $(U,Nb)_2Ni_{21}B_6$ and $(U,Nb)_3Ni_{20}B_6$

Alessia Provino[1,2], Amitava Bhattacharya[3], Sudesh K. Dhar[3], Cristina Bernini[2], Marcella Pani[1,2], Flavio Gatti[4], Pietro Manfrinetti[1,2]

[1]Department of Chemistry, University of Genova, Genova, Italy, [2]CNR-SPIN, Genova, Italy, [3]Condensed Matter Physics & Material Science, Tata Institute of Fundamental Research, Mumbai, India, [4]Department of Physics and INFN, University of Genova, Genova, Italy

We have investigated the magnetic behaviour of $U_2Ni_{21}B_6$ and the substituted $U_{2-x}Nb_xNi_{21}B_6$ and $Nb_{3-x}U_xNi_{20}B_6$ which crystallize in the cubic $W_2Cr_{21}C_6$ and $Mg_3Ni_{20}B_6$ crystal structures (both ternary derivatives of C_6Cr_{23}-type [1]). In the ternary compounds the unit cell offers one site for U atoms (8*c*) and three not equivalent-symmetry sites for Ni atoms (4*a*, 32*f*, 48*h*). The substitution of U by Nb seems to lead to a change in the crystal structure towards the $Mg_3Ni_{20}B_6$-type, where also the atomic site 4*a* becomes occupied by Nb.

$U_2Ni_{21}B_6$ shows Pauli paramagnetic behaviour, with a low temperature susceptibility of 2.1×10^{-3} emu/mol derived from the magnetization versus field plot at 2 K. Our results are in agreement with the recently reported result in literature on $U_2T_{21}B_6$ (T = Ni and Co) [2], where an itinerant non-magnetic state of U-5*f* electrons is postulated (Figure 1). The magnetization data also indicate that Ni 3*d* band in $U_2Ni_{21}B_6$ is filled and devoid of a magnetic moment. On the other hand, the susceptibility of $Nb_2Ni_{21}B_6$, measured in a field of 100 Oe, decreases monotonically from 300 K, χ(300 K) = 3.6 emu/mol, down to the lowest temperature of 1.8 K. The in-field magnetization at 300 K shows a typical ferromagnetic behaviour with a saturation magnetization of nearly 0.5 μ_B/f.u., which increases to 0.6 μ_B/f.u. at 1.8 K (Figure 2). Assuming the magnetization is uniformly distributed over Ni ions, the results imply a very low moment of 0.03 μ_B/Ni in the ground state. The magnetization data thus identify $Nb_2Ni_{21}B_6$ as a weak itinerant ferromagnet with a Curie temperature > 300 K. Results from crystallographic and magnetic investigation will be presented.

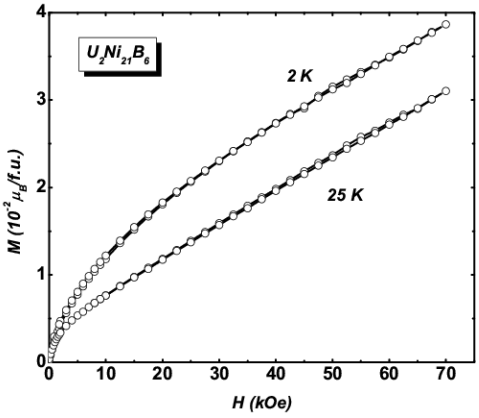

Figure 1. In-field magnetization at 2 and 25 K of $U_2Ni_{21}B_6$

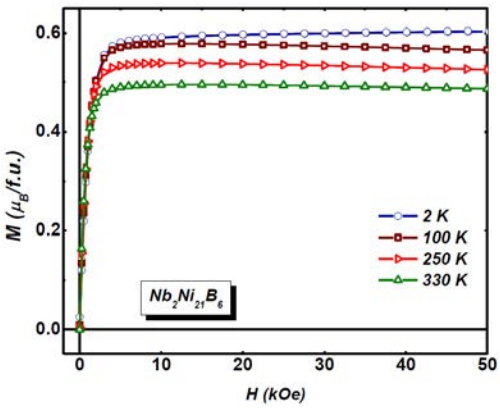

Figure 2. In-field magnetization at 2, 100, 250 and 330 K of $Nb_2Ni_{21}B_6$

References

[1] P. Villars, K. Cenzual, Pearson's Crystal Data - Crystal Structure Database for Inorganic Compounds, Release 2010/11, ASM International, Materials Park, Ohio, USA.

[2] J. Kitagawa, M. Ishikawa, *Solid State Commun.* **153** (2013) 76.

1-62

Vibrational Properties of Uranium Hydride and Uranium Deuteride

Alice I. Smith, Luke L. Daemen, Joe R. Wermer, Jeffery Aguiar, Bogdan Mihaila, Roland K. Schulze

Los Alamos National Laboratory, Los Alamos, NM, USA

Due to their incomplete 5f shell, actinides and their compounds exhibit interesting electrical and magnetic properties. Among those, the U-H system presented great interest for the nuclear industry, for more than sixty years. Most studies focused on the stoichiometric and near-stoichiometric UH_3, in relation to the nuclear fission investigations, and to the possibility of being a hydrogen storage system. Two crystalline modifications of uranium trihydride have been characterized and are denoted α-UH_3 and β-UH_3[1]. The discovery of ferromagnetism in of UH_3 and UD_3 more than 50 years ago encouraged/resulted the development of actinide research[2-6].

Although a great deal has been published on the properties of UH_3 and UD_3, little attempt has been made to describe these materials in terms of phonon spectra or density of states. Previous measurements include Surface Enhanced Raman Scattering (M. Piltch et al., *Philosophical Magazine*, Vol. 89, Nos. 22–24, 2009, 1947–1951) with limited and unresolved spectrum of UH3. Older neutron inelastic scattering experiments failed to observe transition lines and spectra are too weak to make a meaningful quantitative analysis[7-10]. Previous inelastic scattering by cold neutrons measurements by J. Rush et al. (J. Chemical Physics, vol. 45, 10, 3817, 1966) presents UH_3 and UD_3 spectra with barely resolved two or three peaks in the 600-1400 cm^{-1} range.

Uranium hydride (UH_3) and uranium deuteride (UD_3) synthesis involve direct reaction of depleted uranium metal with hydrogen or deuterium gas. All handling of the hydride powder is performed in a helium-atmosphere glovebox with water and oxygen contents less than 1 ppm and 5 ppm, respectively. The powder samples are loaded in annular aluminum sample holders (2 cm diam. X 10 cm height), and cooled down from room temperature to 10K in a top-loading, closed-cycle refrigerator before data collection. Vibrational spectra of the UH_3 and UD_3 were measured on the Filter Difference Spectrometer (FDS) at the Los Alamos Neutron Scattering Center (Los Alamos National Laboratory, USA). Due to the configuration of the instrument, an average over all the points in the Brillouin zone automatically takes place. For the neutron-nucleus scattering, there are no selection rules; all modes are observed and contribute to the phonon density of states. The experimental phonon spectra, measured in the 40-4000 cm^{-1} range, will be compared to the calculated spectra. The phonon spectra and density of states (DOS) will be obtained by means of first-principles calculations.

The mid-range neutron vibrational spectra of UH_3 and UD_3 is dominated by hydrogen dynamics. First and second harmonics are clearly visible in both spectra. These will allow determination of the potential energy surface of hydrogen in uranium hydride and evaluation of the anharmonicity of hydrogen dynamics. By applying a maximum Entropy reconstruction of the spectrum, the lower frequency band is resolved into a series of discrete modes, and higher frequency peaks are confirmed to be elemental. This is the first time that these modes have been observed (the J. Rush's 1996 neutron work article resolved only 2-3 peaks in the 600-1400 cm^{-1} band). Several extremely sharp phonons are present in the VDOS of UH_3 and UD_3, a proof of the existence of high amplitude of motion translational or librational modes. To the best of our knowledge, the experimental low frequency VDOS of uranium hydride has never been reported.

Vibrational modes above 500 cm^{-1} are due entirely to H motion (large mass of uranium compared to hydrogen). Below 500 cm^{-1}, few phonons involving translational motion of U and H show up strongly in the vibrational spectrum. The motion of H in UH_3 is harmonic, resulting in the overtones in the experimental spectrum.

ACKNOWLEDGMENT. This work has benefited from the use of the FDS beamline at the Lujan Center at Los Alamos Neutron Science Center, funded by the US DOE, Office of Basic Energy Sciences. Los Alamos National Laboratory is operated by Los Alamos National Security LLC under DOE contract No. DE-AC52-06NA25396.

References

[1] Rundle R.E., *J. Am. Chem. Soc*. **69**, 1719 (1947); 73, 4172 (1951)

[2] Trzebiatowski A. et al., *Chem*. **26** (1952) 110

[3] Gruen D. et al., *J. Chem. Phys*. **23**, 1708 (1955)

[4] Henry W. et al., *Phys. Rev*. **98**, 1200 (1955)

[5] Lin T. et al., *Phys. Rev*. **102**, 640 (1956)

[6] Henry W., *Phys. Rev*. **109**, 1976 (1958)

[7]. Karcevskii A. et al., *Teor. Fiz*. **36**, 636 (1959)

[8] Spedding H. et al., *Nucleonics* **4**, 4 (1949)

[9] Flotow H. E. et al., *Phys. Rev*. **164**, 755 (1957)

[10] B. C. Frazer et al., *Phys. Rev*.**140**, A1448 (1965).

1-63

X-ray photoelectron spectroscopy of 7-at.% gallium δ-stabilized plutonium

Thomas Venhaus

Los Alamos National Laboratory, Los Alamos, NM, USA

It has been shown [1] that the addition of gallium as a δ-phase stabilizer in plutonium has the effect of reducing the oxidation rate of the material. It is also known that the presence of oxygen in the gas phase dramatically reduces the rate of corrosion of plutonium in humid environments [2]. To study the behaviour of gallium at the near-surface region in controlled oxidation experiments, X-ray photoelectron spectroscopy (XPS) was performed on polycrystalline plutonium alloyed with 7 at.% gallium. The high Ga content used for this study allows clear identification of the photoelectron peaks and associated chemical shifts during reactions with 1-100 Langmuirs of oxygen. All experiments were performed with a Kratos Axis-Ultra XPS instrument fitted with a monochromatic Al K_a X-ray source (1486.7 eV). To account for any charge shifts, all XPS peak binding energies were calibrated by setting the Pu $4f_{7/2}$ trivalent peak (Pu_2O_3) binding energy to 424.4 eV [3]. The base pressure of the system is approximately 5×10^{-10} Torr. The sample was prepared by diamond saw cutting, followed by mechanical polishing down to a 600 grit silicon carbide paper. An acetone rinse was used to clean the sample prior to mounting and introduction into the XPS instrument. Prior to any oxygen gas exposure, a small area of the sample surface was sputter cleaned with 4 keV Ar^+ ions to remove the as-received oxide layer, which was comprised almost entirely of the Pu^{4+} state, and any contaminants left from the preparation steps. In addition to the sputtering cycles, the sample was heated in ultra-high vacuum for several hours at 423 K. The XPS analysis, with a spot size of approximately 300 × 700 microns, was performed within the sputter crater. Sputtering at room temperature produced a mixture of Pu^{3+} and metallic Pu photoelectron peaks, even at extended sputter times, and a small O 1s peak remained. Sputtering performed at low temperatures (180 K) was effective in producing a metallic Pu $4f_{7/2}$ photoelectron peak located at 422 eV, and a reduction of the O 1s photoelectron peak to below the detection limit. The sample temperature was maintained at 180 K for all oxygen gas exposures. The gallium $2p_{3/2}$ photoelectron peak was measured at a binding energy of 1116.5 eV on the sputter-cleaned surface. Low doses of oxygen (<1 Langmuir) resulted in a small shift of the gallium 2p photoelectron peaks to a higher oxidation state, followed by an elimination of the gallium photoelectron peaks at higher oxygen exposures. Sputter depth profiles revealed gallium had diffused to sub-surface layers following the oxidation of the plutonium surface, consistent with previous work at our laboratory on lower gallium content material. The gallium peak height suggests a concentration within this subsurface layer of nearly twice that found in the bulk. The gallium photoelectron peak locations were indicative of a non-oxidized state. The plutonium was observed to oxidize to Pu^{3+} at low doses, then to a mixture of Pu^{3+} and Pu^{4+} at higher doses.

References

[1] J. T. Waber, Plutonium Handbook, O.J. Wick, Editor (American Nuclear Society, La Grange Park, Illinois, 1980

[2] J. M. Haschke, T. H. Allen, L. A. Morales, Los Alamos Science, 26 (2000) 253

[3] H. G. Garcia Flores, P. Roussel, D. P. Moore, D. L. Pugmire, Surface Science 605 (2011) 314

1-64

Neutron Capture Cross Section on ^{236}U performed at the n_TOF facility at CERN

Mark James Vermeulen[1], Massimo Barbagallo[2], Carlos Guerrero[3], David Jenkins[1]

[1]University of York, York, UK, [2]Istituto Nazionale Fisica Nucleare, Bari, Italy, [3]European Organisation for Nuclear Research (CERN), Geneva, Switzerland

The accurate determination of the ^{236}U neutron capture cross section is of importance due to its relevance in nuclear systems. In the conventional U/Pu fuel cycle, the large abundance of ^{238}U provides a site for the build-up of transuranic elements. These minor actinides, such as neptunium, americium and curium, are a source of long lived radioactive waste. However, in the Th/U cycle, the site of the build-up of these waste products is on ^{236}U. Hence when data are to be used in reactor model codes to determine the proportions of nuclear waste after a reactor cycle, knowledge of the ^{236}U capture cross section is essential.

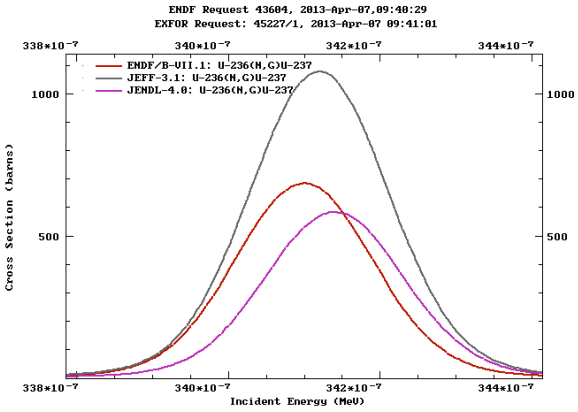

Figure 1 - Comparisons of the 3 main data libraries, (ENDF, JEFF and JENDL) showing discrepancies at the 34 eV resonance.

The current evaluations, such as ENDF, JEFF, JENDL, etc., are based on only a few measurements and cover an incomplete energy range. The different evaluations also show marked discrepancies. In the resolved resonance region, resonant cross sections can differ by up to 40% between evaluations, with resonances also not appearing at the same energies (see figure 3). Around the thermal region, there is only one set of data available, and in the unresolved resonance region, the evaluations also show marked differences.

For applications to the Th/U cycle, waste transmutation in ADS and Generation IV reactors, the accuracy on the ^{236}U capture cross section is simply unsatisfactory. The nuclear data community requests an accuracy of < 10% to be satisfactory for the design of these advanced nuclear systems.

Based on the need for new and accurate measurements, it was proposed to perform a measurement of the ^{236}U(n,γ) reaction at the neutron time of flight facility (n_TOF) at CERN. A world leading facility, n_TOF takes advantage of state of the art detection and acquisition systems. These, coupled with low background, a 185 m flight path and high instantaneous neutron flux, give rise to high resolution and statistics.

The experiment performed at n_TOF made use of the TAC (Total Absorption Calorimeter). This is a segmented array comprised of 40 BaF_2 crystals covering ≈95% of 4π, and is designed to absorb the complete γ-cascade from the de-excitation of the compound nucleus formed upon neutron capture. Indeed, it is this high segmentation along with the complete γ detection that enables the capture events to be discriminated against the various sources of background. The upper energy limit on the data the TAC can acquire is in the tens of keV range due to its high sensitivity to the so-called γ-flash (i.e. gamma-rays and relativistic charged particle emitted in the spallation process) .

The ^{236}U sample itself is of 99.85% enriched $^{236}U_3O_8$ in powdered form with a mass of 338 mg. It is contaminated by 0.1% ^{238}U and 0.05% ^{235}U. It is in the form of a powder compressed into a pellet 1 cm in diameter and 1 mm in thickness. This pressed pellet was then itself enclosed in an aluminium canning. Various experimental runs were performed during the ^{236}U TAC campaign. Alongside experimental runs with the ^{236}U in the canning, data were taken with an empty aluminium canning to determine the contribution from the aluminium.

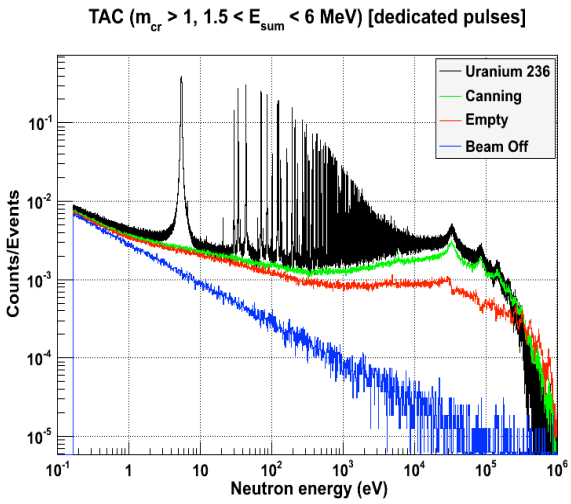

Figure 2 - Neutron energy spectra for uranium + canning, empty canning, beam off, and empty (beam on no target) experimental runs.

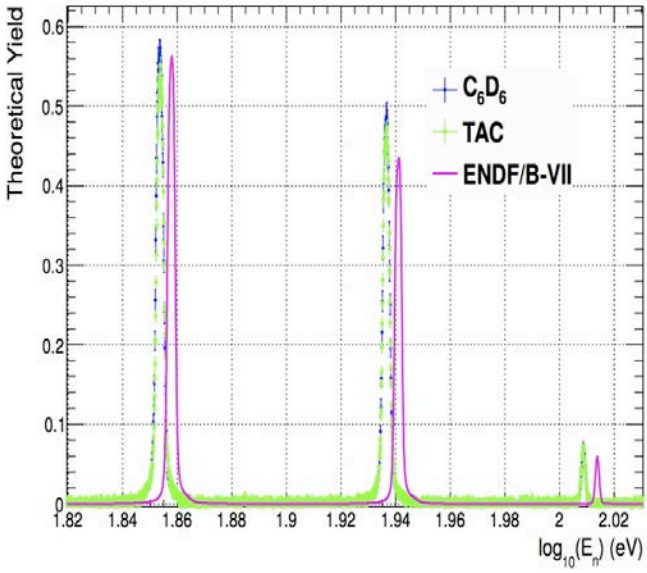

Figure 3 – Preliminary comparison of the experimental data from two experiments performed at n_TOF, alongside the ENDF/B-VII evaluation, in the resolved resonance region.

Runs were also done with a ^{197}Au sample for normalisation, a carbon sample for neutron sensitivity, beam off runs to determine environmental background and runs with the beam on but no target to see the contribution from structural materials. Figure 2 shows the neutron energy spectra obtained during these experimental runs. After background subtractions, a preliminary yield was been obtained. This has been compared with the ENDF/B-VII evaluations, as can be seen in figure 3. In the figure, it can be observed that there is a discrepancy between the data from the ENDF evaluation and with TAC data, both in terms of resonance energy and strength. The results are confirmed by the data collected at n_TOF with a pair of deuterated benzene (C_6D_6) scintillator detectors, analysed with a different technique – the pulse height weighting technique. Figure 3 shows that, for a subset of the total data, both sets of data from n_TOF agree well with each other and differ from the evaluation by a similar amount. This preliminary comparison could hint that the n_TOF results are indeed accurate, within a few percent, and that revisions to the evaluations may be needed, at least in the resolved resonance region.

In conclusion, accurate new data have been collected at n_TOF with two different detection systems, taking advantage of the convenient features of the facility, in particular the high instantaneous intensity and resolution of the neutron beam. Preliminary results indicate that the requested accuracy of less than 10% is within reach. Some differences relative to current evaluations are observed, which may call for a revision of the evaluated cross section libraries for this isotope, of relevance for the Th/U fuel cycle.

European Commission
EUR 26163 EN – Joint Research Centre – Institute for Transuranium Elements

9th International Conference on the Chemistry and Physics of the Actinide Elements (Actinides 2013)
21 - 26 July 2013, Karlsruhe, Germany
Abstract Booklet
Editor: Roberto Caciuffo

Publications Office of the European Union, Luxembourg

Catalogue Number LC-NA-26163-EN-N
EUR 26163 EN
ISBN 978-92-79-33192-3 (online)
doi:10.2789/16401

Abstract
The ACTINIDES 2013 conference was dedicated to providing a platform for discussion and information exchange for current research in the physics and chemistry of the actinide and the transactinide elements. Specific topics included fundamental materials science, chemistry, physics, environmental science, and application technologies. The conference consisted of presentations of new scientific results in plenary lectures, invited and contributed talks and presentations in poster formats. The ACTINIDES 2013 conference also offered an excellent opportunity to establish or renew contacts with colleagues during the scientific program, 2 poster sessions and the conference banquet program.

Online abstracts are available via direct link: http://actinides13.ine.kit.edu/28.php and
https://itu.conference-services.net/programme.asp?conferenceID=3032&language=en-uk
Navigate through the tabs "Programme", "Titles", "Presenters", and "Topics" to get an overview of the programme and the sessions times, a list of the contribution titles and of the presenting authors in alphabetic order, or sorted by topic. Clicking hyperlinks on any of these lists will bring you to individual session pages.

Abstracts are compiled in a booklet according to topics:
AT - Application Technologies, CH - Chemistry, ES - Environmental Science, MS - Materials Science, PH – Physics.
Search for Author name using Bookmarks toolbar in .pdf.

LC-NA-26163-EN-N

ISBN 978-92-79-33192-3

Publications Office